MEASUREMENT AND APPLICATION OF GEOMETRIC IMPERFECTIONS IN COLD-FORMED STEEL MEMBERS

by
Xi Zhao

A dissertation submitted to Johns Hopkins University in conformity with the requirements for the degree of Doctor of Philosophy

Baltimore, Maryland

August, 2016

Abstract

Cold-formed steel members provide a unique solution to framing walls and floors of buildings and are popular in low and mid-rise construction in North America. Members are formed from coils of thin sheet steel and cold bent into useful shapes. Advantages of cold-formed steel construction include ease of transportation and erection, thanks to its light-weight properties. This same light-weight property; however, creates a thin-walled member and such members are vulnerable to geometric imperfections. Strength and stiffness of thin-walled structural members can be impaired due to imperfections, which has inspired studies on imperfection sensitivity of cold-formed steel, including: measurement techniques, imperfection characterization, and numerical simulations.

In this study, an innovative imperfection measurement rig employing a laser triangulation technique is used to scan along targeted cold-formed steel members. The scan results in abundant measurement point clouds and these allow further exploration into the impact of geometric imperfections, especially for cross-section imperfections, which are constrained by conventional measurement techniques. In addition, the point clouds enable additional applications such as dimensional characterization and an ability to study the impact of different imperfection characterization approaches as compared to actual measured imperfections.

In this dissertation, a newly developed imperfection measurement rig is carefully detailed and the results illustrated with examples. Collected data from the laser-based imperfection measurement rig requires specific post-processing to achieve useful and reliable geometric information. The post-processing procedures generally comprise data trimming, surface registration, and feature recognition algorithms. Modifications to the surface registration algorithm, i.e. iterative closest point), are described along with development of the feature recognition algorithm. These

processing effects are demonstrated with three different section shapes of cold-formed steel members, i.e. C, Z, and Built-up C studs.

Dimensional variations, which are considered as primary geometric imperfections, are statistically summarized for future research studies. For the fist-time, correlation matrices for the dimensions are estimated from measured data. These correlation matrices can be used to improve simulations of realized member geometry that underpin reliability analysis of cold-formed steel members.

Based on measured point clouds, geometric imperfections are characterized into five classes when following conventional imperfection classification, i.e. bow (major axis bending), camber (minor axis bending), twist, flare/overbend, and crown. This method is carried out in this dissertation and compared with another characterization method known as modal imperfection characterization. Instead of using flare/overbend and crown as the cross-section imperfections, the cross-section buckling mode shapes in distortional and local buckling are utilized as the reference to the cross-section imperfections.

Imperfections based on MID measures exist along the longitudinal length of a specimen and can be interpreted as power spectrums in the frequency domain, which provide an insightful understanding on classified imperfections involved with multiple frequency (reciprocals of half-wave lengths) content. These results enable another imperfection modeling approach, the 1D spectral approach, and potentially improve prediction accuracy for member strength. Numerical modeling of imperfections comprising both traditional and 1D spectral approach has been carried out and is validated through material and geometric nonlinear shell finite element analysis on the true geometry. Taken together this thesis provides a new platform for measuring imperfections and dimensions of structural members, and demonstrates the use of this platform in enabling advanced

analysis methods on imperfect models of cold-formed steel members and improving the strength reliability predictions for cold-formed steel members.

Advisor: Professor Benjamin W. Schafer

Readers: Professor Lori Graham-Brady

Professor James K. Guest

Acknowledgement

I express my deep and sincere gratefulness to my advisor, Professor Benjamin Schafer, for his guidance, advice, and support in my research, my graduate program, and my life. He is very patient and friendly and always tries to understand my thoughts and ideas about research projects. He taught me how to conduct research and express my opinions properly. He taught me how to write a scientific article and make presentations at conferences. He saved me from the desperation and bouts of self-doubt, and he encouraged me to make accomplishments to regain my confidence. It is difficult for me to find a proper way to express my thankfulness to Professor Schafer, and I will use what he has taught me and the advice he has given me for the rest of my life. I also want to thank the members of my committee, Prof. Lori Graham-Brady, Prof. James Guest, and Prof. Mazdak Tootkaboni, for their willingness to serve on my thesis committee and help me with different aspects throughout my graduate study at Johns Hopkins University. I thank the National Science Foundation for the funding that was provided for this research work, I thank the members of the Department of Civil Engineering for providing a nice, supportive environment for study and research, and I thank the Creel Family Engineering Fellowship for the financial support that was provided.

I wish to express my appreciation to the staff members in the Department of Civil Engineering at Johns Hopkins, specifically Lisa Wetzelberger, Shamija Jackson, Deborah Lantry, and Vess Vassileva-Clarke, who are very helpful to me all of the time. I thank Nickolay Logvinovsky for his long-lasting technical support and training in conducting experiments in the Thin-Walled Structures Laboratory. He made my experience much better than it might have been. I also wish to acknowledge the help and encouragement provided the current and former students of this group, including Dr. Jiazhen Leng, Dave Fratamico, Dr. Shahab Torabian, Abdullah Mahmoud, Guanbo

Bian, Dr. Deniz Ayhan, Astrid Fischer, Dr. Vahid Zeinoddini, Dr. Yared Shifferaw, and Dr. Zhanjie Li, who shared many important thoughts and moments with me.

I am very happy to have such good friends who accompanied, helped, and supported me whenever I got stuck or felt trapped. I thank Yixin Gao, Lingling Tao, and Ting Su who grew with me and shared countless moments of happiness and sorrow together.

I thank my husband, Xuefeng Wang, for his unconditional support in both of my life and my research. Without his help and support, I would have had a much harder time completing my research and finishing my graduate study.

I thank my parents and grandparents who always trusted me and encouraged me to get over those challenging moments and to conquer various difficulties in every aspect of my life. I could never have gone so far without them at my side.

Xi Zhao

August, 2016

Preface

This dissertation is submitted to the Johns Hopkins University for the degree of Doctor of Philosophy. The work described in the dissertation was conducted by the author as a graduate student in the Department of Civil Engineering from September 2010 to August 2016 guided by Professor Benjamin Schafer.

The author claims that the work presented in the dissertation is original with proper references to acknowledge any information or ideas from other resources during the course of this research. Several supporting papers which are based on the work presented in the dissertation have been published together with Professor Benjamin Schafer and other co-authors as listed:

Journal:

X. Zhao, Tootkaboni, M., Schafer, B. W., "Development of a laser-based geometric imperfection measurement platform with application to cold-formed steel construction," *Experimental Mechanics*, 55: 1779-1790, 2015

X. Zhao, Schafer, B. W., "Laser-based cross section measurement of cold-formed steel members: model reconstruction and application. *Thin-Walled Structures* (Submitted), 2015

Conference:

Zhao, X., Schafer, B.W. "Non-contact Full-Field Measurement of Geometric Imperfections in Cold-formed Steel Member." *ASCE Engineering Mechanics Institute*. Northwestern University, Evanston, IL, 2013

L. E. McAnallen, D. A. Padilla-Llnao, X. Zhao, C. D. Moen, B. W. Schafer, and M. R. Eatherton, "Initial geometric imperfection measurement and characterization of cold-formed steel c-section

structural members with 3D non-contact measurement techniques," *AISC Annual Stability Conference,* Toronto, Canada, 2014.

Zhao, X., Schafer, B.W. "Laser scanning to develop three-dimensional fields for the precise geometry of cold-formed steel members," in *CCFSS*, St Louis, MO, 2014.

Zhao, X., Schafer, B.W., "Measurement geometry for Cee, Zee, and Built-up cold-formed steel members," in CCFSS, Baltimore, MD, 2016

Zhao,X., Tootaboni, M.P., Schafer, B.W., "High fidelity imperfection measurements and characterization for cold-formed steel members," in CIMS, Baltimore, MD, 2016

Table of Contents

List of Tables

List of Figures

Chapter 1 Introduction

1.1 History of cold-formed steel

The use of cold-formed steel, well-known for its light weight and easy erection, is increasing in today's structure market, especially in low- and mid-story buildings in America. There is a long history of the use of cold-formed steel in construction that was accompanied by advancements in the design specifications. Applications of cold-formed steel can be traced back to the 1850s in both the United States and Great Britain. However, the use of cold-formed steel members as structural members in buildings was documented several decades later after their first use. Built-up C sections of cold-formed steel were used as floor deck in Virginia Baptist Hospital in 1925 (Yu, 2000). There were two difficulties associated with the acceptance of cold-formed steel in the industry, i.e., the lack of a design methodology and the corresponding building codes at that time (SMDI, 2010). This dilemma was solved later by the Committee on Building Codes of the American Iron and Steel Institute (AISI) in 1938. Extensive research on structural members made of light-gage, cold-formed steel was conducted at Cornell University. Led by Professor George Winter, the research resulted in the development of an effective method for designing the appropriate width of structural members by incorporating geometric imperfections, residual stress, and different classes of buckling across various structural members and systems. The study resulted in the first Specification for the Design of Light Gage Steel Structural Members in 1946 and the first Design Manual for design engineers in 1949. The second edition of Specification (1956) was formally incorporated in the building codes, which provided the key to public acceptance of cold-formed steel products. AISI continually provides funding of research to broaden the design coverage and cultivate a cold-formed steel research and design community. Additional studies were conducted by Professor Pekoz at Cornell University as well as at other universities across the country, and the achievements of these researchers were published in conference proceedings and the journals of various engineering societies (Yu, 2000; SMDI, 2010).

There are several entities that promote the cold-formed steel industries' markets in the U.S. and worldwide. In the early 1990s, the expansion of residential construction and the increase in lumber prices created a potential market for cold-formed steel, especially considering its advantages, e.g., light weight, high strength, stiffness, fast and easy erection/installation, dimensional stability and durability, no formwork requirement, environmental friendliness, and energy efficiency (Yu, 2000; SMDI, 2010; SFIA 2016). In 1990, the North American Free Trade Agreement (NAFTA) was established, and the United States, Canada, and Mexico were bonded. The North American Specification for the Design of Cold-Formed Steel Structural Members was published in 2001; it was recognized by the American National Standards Institute in the U.S., the Canadian Standards Association in Canada, and Camara Nacional de la Industria del Hierro y del Aceroand in Mexico, and it was incorporated in the 2003 International Building Code. Publications and recognitions allow faster introduction of new technologies and more extensive markets worldwide. More countries started to draft and publish their own specifications on cold-formed steel after the North American Specification publications (SMDI, 2010). A significant amount of research related to cold-formed steel members has been conducted, and the Direct Strength Method (DSM), which includes mode interactions and Generalized Beam Theory (GBT) design methods, has been promoted extensively. The DSM, which is comprised of local, distortional, and global-mode design methods, was included in AISI S100-12 and was equivalent to an effective width method that was proposed decades ago. More research has been conducted in the cold-formed steel industry in the past five years than was conducted over the past several decades (Hancock, 2016)

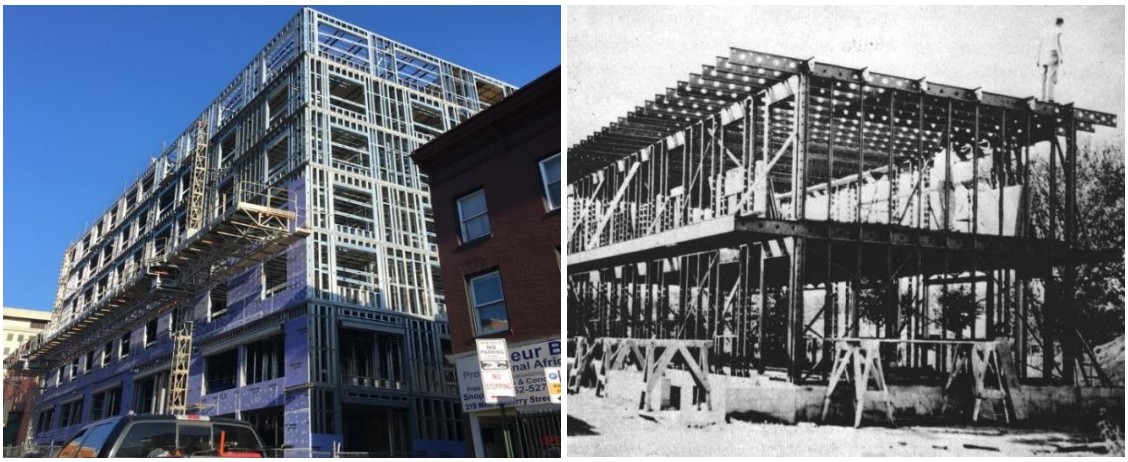

Figure 1. 1 Application of cold-formed steel members: (a) current cold-formed steel buildings; (b) first metal building with only cold-formed steel as major structural members (Yu, 2000)

1.2 Cold-formed steel members and applications

1.2.1 Manufacturing process

Three major manufacturing processes are used to produce cold-formed steel sections, i.e., cold-roll forming, press-brake operation, and bending-brake operation. Most structural members made of cold-formed steel, such as roofs, floors, and wall panels, are produced by the cold-roll forming process. The general procedures of cold-formed steel, cold-roll forming for example, consist of five steps:

- Raw steels are produced as the hot-rolled steel members.
- Molten steels are poured to slab and to form thinner strips.
- Zinc galvanization is applied on thinner strips to form a steel coil
- The large steel coil is slit into widths that match the desired dimensions.
- The required shapes of the cold-formed steel members are formed using various rollers at room temperature (Figure 1. 2).

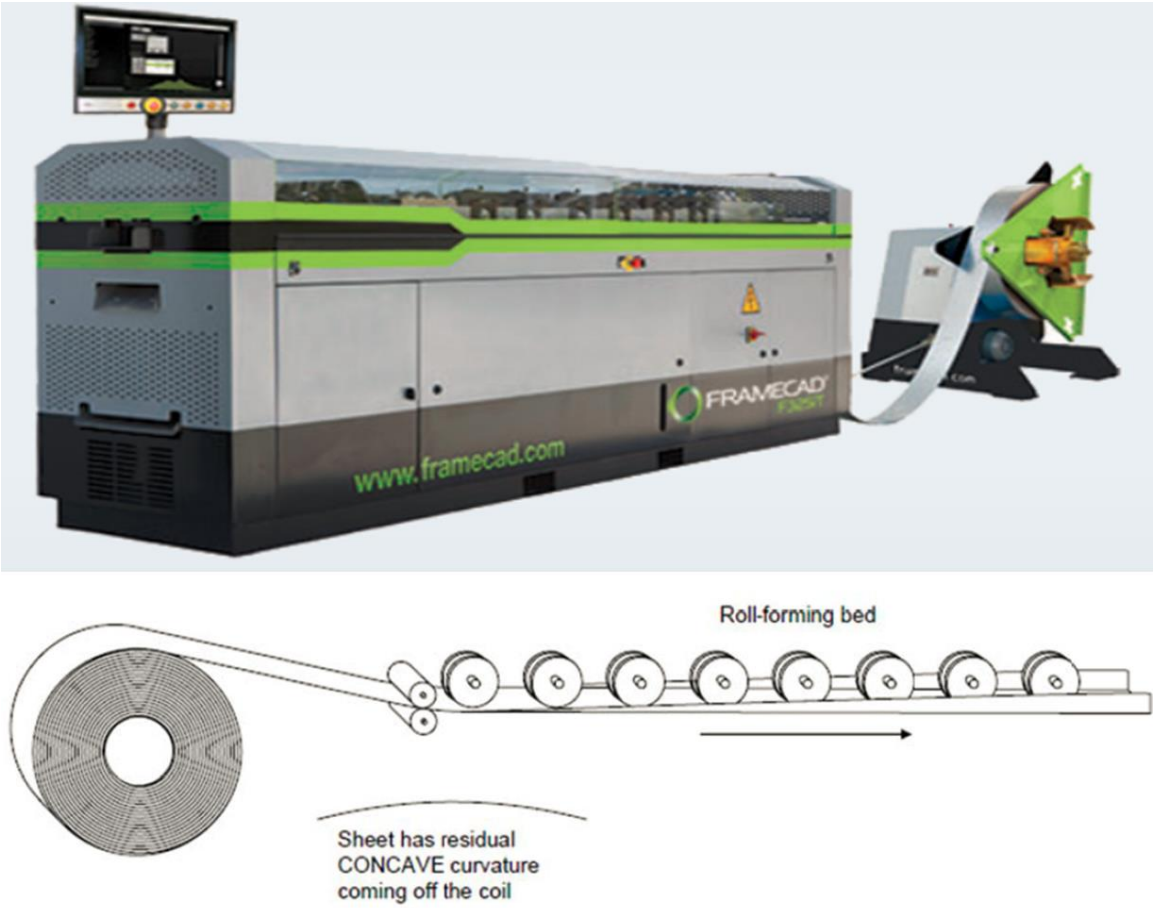

Figure 1. 2 Cold-roll forming process of cold-formed steel (FrameCad 2015, Zeinoddini 2011)

The manufacture process may lead to various primary imperfections (variations of dimensions along a specimen) and geometric and material imperfections for example residual stresses. A dimension standard has been used for quality control as shown in Figure 1. 3 & Table 1. 1.These standard is mainly for regular shape like Z and C members. It has strict restraint in deviations of dimensions in production. But it only includes global imperfections like camber. Other imperfections, such as local, distortional, twist and bow imperfections, are not included in the standard Metal Building Manufacturers Association (MBMA) 2012. These imperfections and residual stresses are generated in the production stage, i.e. coiling and cold-forming stages. Besides, additional imperfections can be produced in the transportation and constructions as well (Zeinoddini 2011).

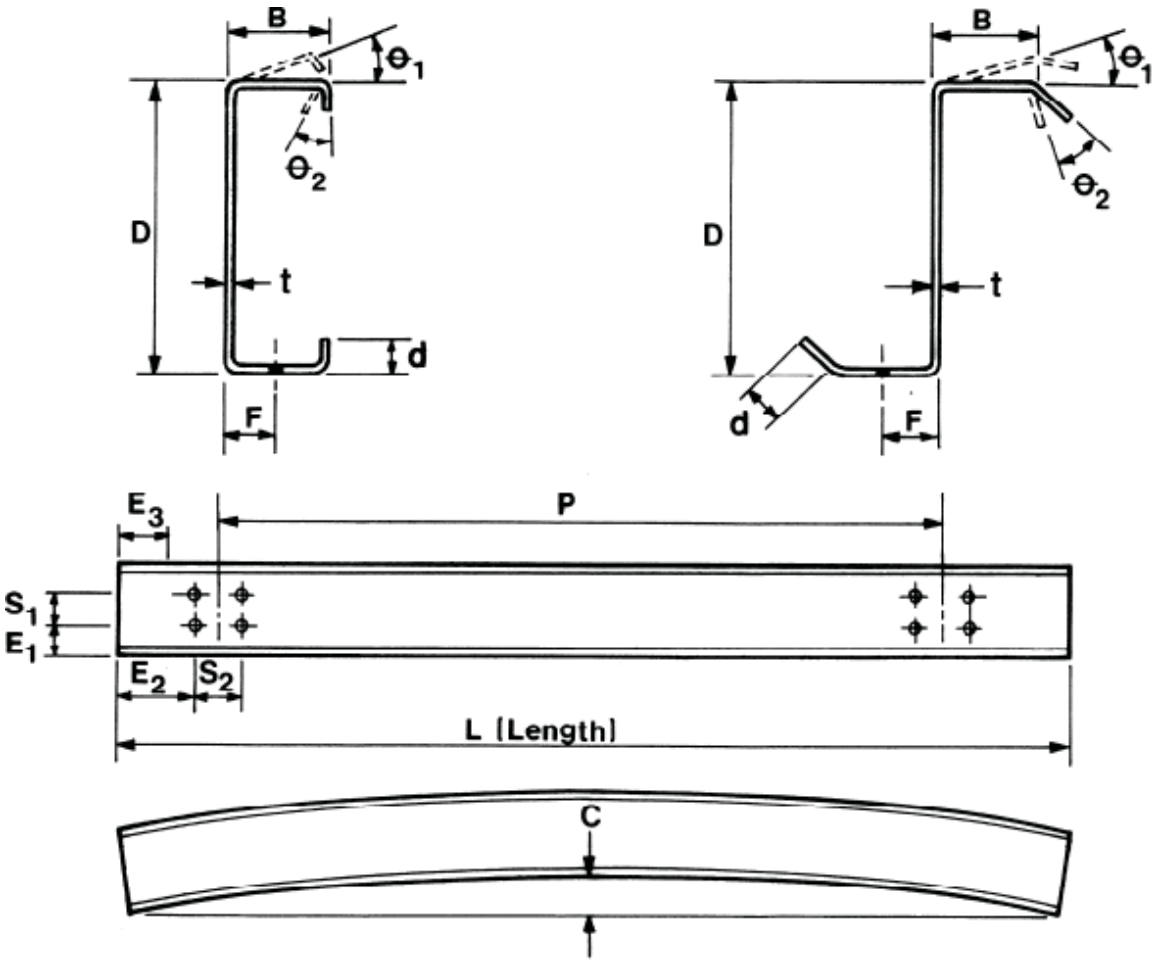

Figure 1. 3 Cold-formed structural members (MBMA 2012)

Table 1. 1 Tolerances of cold-formed structural members (MBMA 2012)

Formed Structural Members			
	Dimension	Tolerances	
		+	-
Geometry	D	3/16”	3/16”
	B	3/16”	3/16”
	D	3/8”	1/8”
	θ_1	3°	3°
	θ_2	5°	5°
Hole Location	E_1	1/8”	1/8”
	E_2	1/8”	1/8”
	E_3	1/8”	1/8”
	S_1	1/16”	1/16”
	S_2	1/16”	1/16”
	F	1/8”	1/8”
	P	1/8”	1/8”
Length (L)		1/8”	1/8”
Camber (C)		1/4” x L (ft)/10	
Minimum Thickness (t)		0.95 (Design t)	

1.2.2 Application of Cold-formed steel

Metal Buildings

Metal buildings generally are composed of steel products. Cold-formed steel makes up approximately 40-60% of the total steel in construction (SMDI 2010). Cold-formed steel members typically are used in the secondary systems of a building (Schafer 2011), as shown in Figure 1. 4, which support the roof and wall coverings and provide lateral stability to the primary rigid-frame members. However, in the last five decades, the situation has improved dramatically for cold-formed steel. More and more structural companies have begun to use cold-formed steel members to construct entire metal buildings. Companies provide entire building services in order to win the bid for building projects. Specific software and sample designs of buildings can be acquired from such companies. Tests of entire cold-formed steel buildings under seismic loads were conducted in the Thin-Walled Structures group at Johns Hopkins University, and the metal buildings performed well (Peterman 2014).

Figure 1. 4 Metal buildings comprised of hot-rolled steel and cold-formed steel members (SFIA 2015)

Wall Construction

Wall construction using cold-formed steel products usually relates to wall covering and wall framing. Panels of cold-formed steel with various shapes and textures are used extensively as coverings in metal buildings and office buildings. This type of cold-formed steel can satisfy both aesthetic and structural requirements. Wall framing has created a lot of research interests, where C-, Z, and Built-up sections can be used to bear loads (Liu et al. 2012, Fratamico et al. 2016). Cold-formed steel framing uses studs connected to the top and bottom tracks with either gypsum or wood boards for sheathe bracing or other channel bridging.

Figure 1. 5 Cold-formed steel framing (SFIA 2015)

Floor Construction

Floor constructions can be categorized as floor decks, steel joists (studs), and trusses with respect to floor covering, diaphragms, and floor framing. Floor decks using cold-formed steel have a great advantage as a working platform and a stay-in-place form that carries construction loads and the weights of other structural materials. Regarding floor framing, C sections can be used as load-bearing beams or tracks. The analysis of diaphragms was conducted intensively by Leng et al. (2012), where the high stiffness and strength of cold-formed steel framing were simulated and compared with observations during seismic testing in the CFS-NEES building.

Figure 1. 6 Floor deck of cold-formed steel (Metwood 2014)

Roof Construction

Roof panels of cold-formed steel can be used as a structural component of the roof to resist uplift wind and snow loads as well as transferring seismic loads to dissipate the energy of an earthquake. Cold-formed steel can be used for framing roofs as well, where Z and C members are used to support the roof panels. Roof framing of cold-formed steel members can effectively transfer lateral and vertical loads to the primary frames and brace the members of the primary frame. Trusses of cold-formed steel can be used in residential or light commercial buildings. They effectively provide load capacity to the roof structure with the desired design flexibility (SMDI 2010).

Figure 1. 7 Roof framing of cold-formed steel (SCI 2015)

1.3 Geometric imperfection sensitivity and tolerance in production

1.3.1 Geometric imperfection sensitivity study

Buckling analysis can be considered as a bifurcation problem in which a column can have two behavior pathways under compression. The column can be compressed until yielding failure in a perfect shape. However, in reality, the column may buckle under a smaller loading with a geometric disturbance, i.e., initial imperfections. This property of cold-formed steel has led to research interest specifically in buckling analysis and sensitivity to imperfections. An imperfection shape that resembles a buckling mode shape is considered to impair the load-bearing capacity of a cold-formed steel member (Figure 1.8). Imperfections can be categorized in three different classes i.e., local, distortional, and global imperfections. Global imperfections are divided into bow, camber, and twist imperfections. All of these imperfections correspond to specific critical buckling modes, i.e., local, distortional, and global buckling modes, respectively. Figure 1.8 shows that a perfect column can take twice as much load as those with different types of imperfections in collapse modeling of C studs. In the interest of getting better comparison, the modeling did not consider the material's nonlinearity.

There are arguments that structural studs can fail either in yielding or buckling. Short columns (small slenderness ratio) bear yield failure while long columns (large slenderness) undergo buckling failure. However, mid-length columns most likely are impaired by geometric imperfections. Figure 1.8c shows a typical strength vs. slenderness ratio curve. The figure indicates that the yield strength dominates before the slenderness ratio of λ1, while it is buckling weight after this slenderness ratio without imperfections. As imperfections are introduced, the decrease in material strength is apparent, and the biggest differences arise at the slenderness ratio of λ1. The structural member may fail earlier due to buckling instead of yielding at a smaller slenderness ratio compared to that of a perfect column.

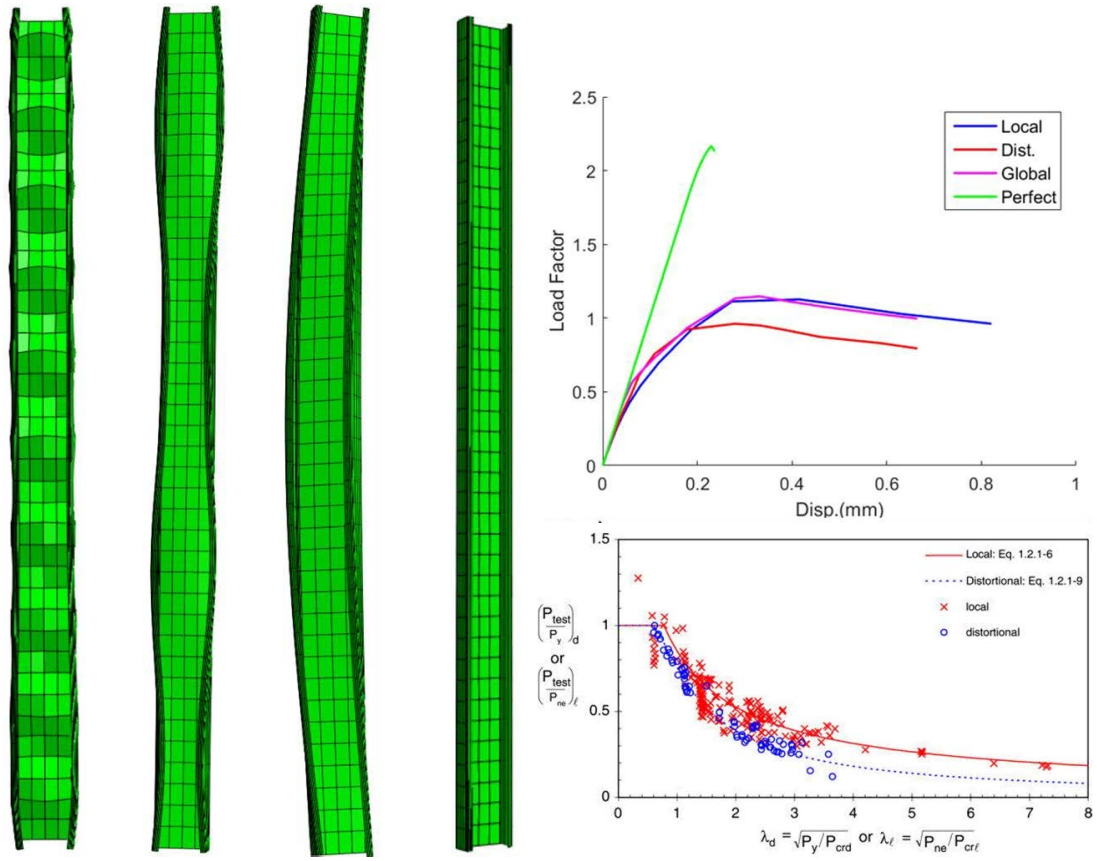

Figure 1. 8 Typical imperfections impact to cold-formed steel studs (a) imperfection types of cold-formed steel studs; (b) Impacts of imperfections;

1.3.2 Tolerance to imperfections for studs

ASTM (2015) introduces tolerances for steel studs, runners (tracks), and bracing for screw application of gypsum panel products and metal plaster bases. Imperfections of tolerance are not strictly connected to buckling modes. Global modes of imperfection can find their correspondence to bow, camber, and twist in the standard Figure 1. 9 and Table 1. 2. Local and distortional mode imperfections, however, may be re-categorized as flare/overbend and crown in cross-section imperfections. There are some overlapping tolerances between ASTM C955 and the fabrication tolerance of MBMA (2012), such as flange width, web width, and length. In fact, the general requirements are equivalent. This specification is designed mainly for C studs. Corresponding specification to other load-bearing members cannot be found, and, therefore, this specification is used as a reference for Z purlins and other built-up C sections in the following chapters.

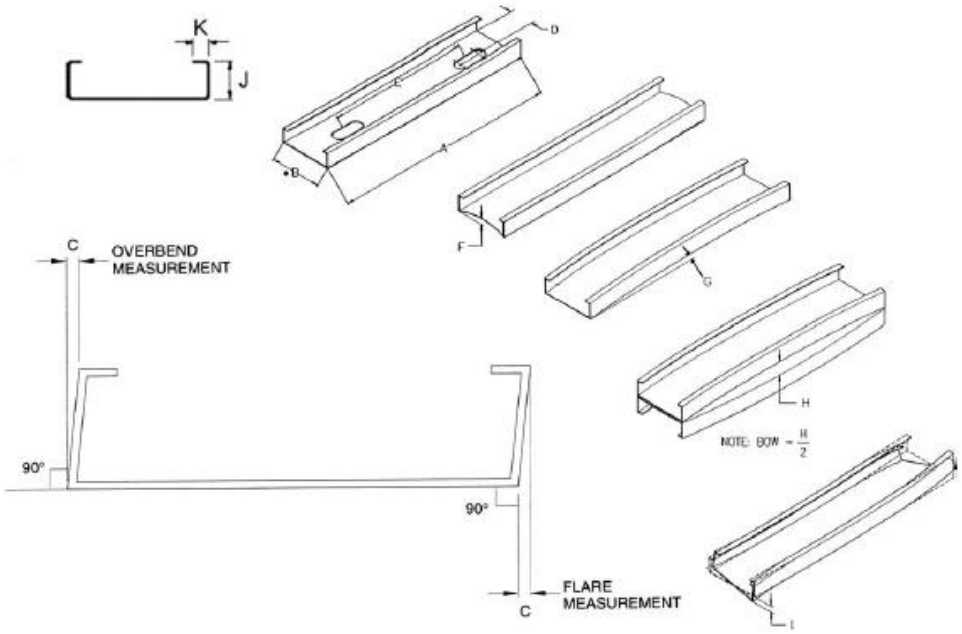

Figure 1. 9 Manufacturing tolerance of cold-formed steel members (ASTM 2015)

Table 1. 2 Manufacturing tolerance of cold-formed steel members (ASTM 2015)

Item	Studs, in, (mm)	Tracks, in. (mm)
Length	+3/32 (2.38)	+1/2 (12.7)
	-3/32 (2.38)	-1/4 (6.35)
Web Depth	+1/32 (0.79)	+1/32 (0.79)
	-1/32 (0.79)	+1/8 (4.18)
Flare	+1/16 (1.59)	+0 (0)
Overbend	-1/16 (1.59)	-3/32 (2.38)
Hole center Width	+1/16 (1.59)	NA
	-1/16 (1.59)	NA
Hole center Length	+1/4 (6.35)	NA
	-1/4 (6.35)	NA
Crown	+1/16 (1.59)	+1/16 (1.59)
	-1/16 (1.59)	-1/16 (1.59)
Camber	1/32 per ft (2.6 per m)	1/32 per ft (2.6 per m)
	1/2 max (12.7)	1/2 max (12.7)
Bow	1/32 per ft (2.6 per m)	1/32 per ft (2.6 per m)
	1/2 max (12.7)	1/2 max (12.7)
Twist	1/32 per ft (2.6 per m)	1/32 per ft (2.6 per m)
	½ max (12.7)	½ max (12.7)

1.4 Imperfection consideration in cold-formed steel design

Even though Karman et al. (1940) proposed an equation to predict structural members' behavior with geometric imperfection, the design method incorporate geometric imperfections after Winter's equation:

$$\rho = (1 - 0.22/\lambda)/\lambda \qquad \text{Eq 1.1}$$

where ρ is the effective portion of the cross-section, and $\lambda = \sqrt{(Fy/Fcr)}$ where Fy is the yield stress, and Fcr is the critical local buckling stress of the member.

The design curve of a cold-formed steel column was taken directly from the AISC column curve, so it has the same amount of imperfections as the hot-rolled steel columns. Some comparisons have

been conducted between the AISI column curve and curves with other magnitudes of imperfections (Zeinoddini 2011).

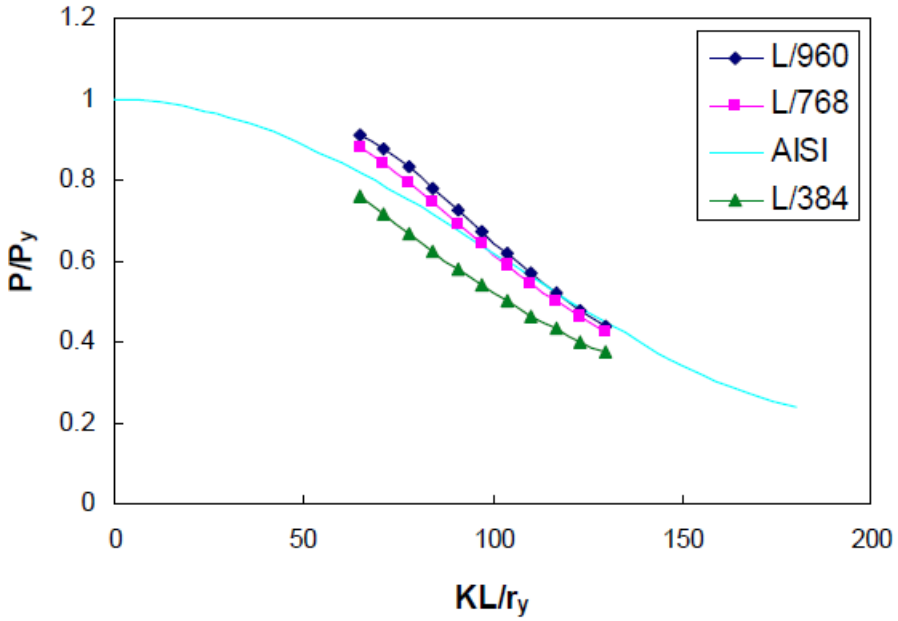

Figure 1. 10 Column curves for a typical C section stud (Zeinoddini 2011)

The Direct Strength Method (DSM) embeds geometric imperfections in AISI S100 (2012) in two ways. The first way is Direct Geometric Consideration of Initial Imperfections, in which initial imperfections are considered directly during the analysis for gravity-only load combinations. The second way is Consideration of Initial Imperfections through Application of Notional Loads in which notional loads are treated as lateral loads, are added to other lateral loads, and can be applied in all load combinations. The calculation of notional loads can be done with the equation below taken from AISI S100 (2012): $N_i = (1/240)\alpha\gamma_i$

where

α = 1.0 (LRFD or LSD)

= 1.6 (ASD)

N_i = Notional load applied at level i

γ_i = Gravity load applied at level i from LRFD, LSD, or ASD load combinations.

In this dissertation, the focus on geometric imperfections is not tightly connected to the design of cold-formed steel. More concern is directed toward imperfection measurements with advanced technologies and toward predictions of structural members' behaviors with certain amounts of imperfections. It would be interesting to thoroughly understand the imperfection sensitivity of cold-formed steel members with as-measured geometry.

Chapter 2 Review of imperfection measurement and application

In this chapter, thorough literature reviews are presented concerning the author's four major research stages, i.e., geometry measurement technologies, prior work in cold-formed steel imperfection measurement results, image processing for modern measurement methods, and application to finite element simulation. The literature review on geometry measurement technologies was focused on word done for cold-formed steel or thin-walled members. The literature review on cold-formed steel imperfection measurement identified imperfection characterization methods and a statistical summary based on specified imperfection patterns. The literature review on image processing was focused on reconstruction of 3D point clouds that are generated by the laser-measurement platform. The literature review of of applications to finite element simulation targeted imperfection sensitivity research that was related to the behavior of cold-formed steel members and imperfection modeling with the specified imperfection patterns.

2.1 Literature review on measurement technologies

Cold-formed steel members for civil building construction usually are understood as assemblages of plate structures, i.e., the shape is bent from a flat plate or coil, and the resulting geometry consists of nominally flat plates and sharp corners. This is in contrast to shell structures, which generally have at least one degree of curvature throughout. Plate and shell structures are known to have different levels of imperfection sensitivity (Calladine 1995); however, the large degree of elastic imperfection sensitivity for shells has resulted in much more extensive study of geometric imperfections and imperfection measurement for these structures; thus, background information on imperfection studies for both shell structures and cold-formed steel members is provided here.

In 1886, Ayrton and Perry (1886) published a seminal paper on the buckling of struts. In the paper, they indicated that the practical buckling load capacities of 'stocky' columns were much lower than

the theoretical ‘crush’ load. The ‘crush’ load generally was assumed to be larger than the buckling load based on Euler’s formula. The critical role that contributed to this result was revealed as an initial sinusoidal imperfection of the ‘stocky’ columns. The importance of geometric imperfections was brought into view from then on. Ayrton and Perry proposed a formula to describe the axial loading and initial imperfection based on the experiment that was used extensively in codes of practice for the design of structural steel work (Calladine, 1995). As techniques of aircraft engineering developed in the 1930s, greater interest developed in the buckling behavior of thin-shell metals. Karman et al. (1940) showed that the presence of a small initial imperfection can lead to a surprisingly large impact on the load-carrying capacity of thin-shell structures. This explained the discrepancy between the predictions of classical theory and the experimental observations on such structures. The study of sensitivity to imperfections produced breakthrough results when Koiter (1945) indicated that the observed degradation in shell strength, or the related “knock-down factor,” depends on the magnitudes and shapes of geometric imperfections. He showed that specific geometric imperfections reduced the load-carrying capacity of a thin-walled shell.

The direct connections between imperfections and the load-carrying capacity of thin-walled structures triggered many imperfection studies, and techniques for measuring initial imperfections underwent considerable development. A Caltech-centered group in the 1970s, e.g., Arbocz and Williams (1977) and a Delft, Netherlands-centered group in the 1980s e.g., Sebek (1981) conducted extensive and important imperfection surveys on large or full-scale cylindrical shells. These groups used Linear Variable Differential Transformer (LVDT) or displacement transducers as major measurement tools to detect the waviness of thin-shell cylinders in the radial direction. However, the longitudinal positions of the measurement tools were located by optical theodolite (Arbocz and Williams, 1977) or an electro-optical device that scanned a strip with equally-spaced cutouts (Sebek, 1981). As discussed in J. Singer et. al.’s book (Singer et al., 2002), contact-measurement tools were

not suitable for very thin structural members. Extra deflections might be produced when the LVDT probe or the displacement transducer's probe slid along the thin-walled surfaces. Berry et al. (1996) published their work in which they developed an imperfection measurement tool that used an automated scanning technique with a laser displacement meter. This setup avoided the disadvantages mentioned previously when they measured a thin-walled steel cylinder. The machine consisted of a laser displacement meter with an accuracy of 0.5 micrometer, a forming drum that held a cylinder internally, and a stepper motor. The stepper motor rotated the forming drum so that the thin-walled cylinder, which was welded to the forming drum, could rotate circumferentially. The laser displacement meter was mounted on a vertical, linear guiding system beside the forming drum. As the stepper motor rotated the forming drum, the laser meter scanned the cylinders circumferentially. When needed, the laser meter can move vertically to scan other cross sections of cylinders.

The applications of this measurement technique were not restricted to thin-walled cylindrical structures. As a matter of fact, contact and non-contact measurement techniques have been used for cold-formed steel members. Schafer & Pekoz (1998) prepared a setup to measure 11 lipped channel sections. A milling table was used to mount the targeted specimens, and a Direct Current Differential Transformer (DCDT) was used to take the measurements. A specimen on the milling table can move along its longitudinal direction driven by a servo motor, while the DCDT could slide across the cross section of a specimen at a constant speed. The setup enabled the DCDT to measure the waviness of a specimen across and along the specimen.

Conventional imperfection measurements utilizing LVDT-based, contact measurement cannot collect all of the required cross-section information. For example, the corners of the cross sections are difficult to assess with these types of methods. In addition, the time-consuming nature of current

methods has resulted in the database being relatively small. High-throughput methods also are needed to extend imperfection measurements out of the lab and into manufacturing facilities for quality control. All of these have led to an interest in full-field, non-contact measurements for thin-walled structural members.

McAnallen et al. (2014) and Zhao and Schafer (2014) displayed newly-developed, non-contact measurement methods, i.e., photogrammetry and laser triangulation techniques. Regarding photogrammetry, a lipped channel section was covered with unique and recognizable targets. Sets of photos were taken from multiple viewpoints around the specimen, and, then, they were processed using commercial software to identify all of the targets. These targets provided point clouds of measurement, allowing the construction of 3D models. Concerning laser triangulation, the laser is projected onto the section, and its reflection is detected. In this way, the relative distance between the head of the laser and the surface onto which it is projected can be estimated. The laser head can scan along the specimen, and full-field measurements can be obtained by rotating the specimen so that the surfaces of interest are scanned as they face then laser head. The author continues to develop laser measurement techniques, and details of this work are presented in Chapters 3 and 4.

2.2 Literature review on cold-formed steel imperfection characterization and modeling

2.2.1 Conventional imperfection characterization and traditional imperfection modeling

Constrained by the lack of appropriate techniques, researchers decades ago measured the global imperfections of cold-formed steel members irrespective of cross-section imperfections. Dat and Pekoz (1980) measured the ‘out-of-straightness’ of global members at the center of the web with reference to a straight line between the ends of their specimens for their column tests. Mulligan (1983) conducted similar imperfection measurements for his testing of short and long columns. Schafer and Pekoz (1998) measured 11 lipped channel sections via a DCDT and measured cross-

section imperfections. Young (2003) increased the fidelity of the measurements of imperfections significantly by using a single-point line laser to track longitudinal imperfections along five cross-section points, and, thus, he was able to assess both global deviations and cross-section imperfections in detail.

Conventional imperfections (a database that existed at that time) were compiled by Schafer and Pekoz (1998), and they categorized geometric imperfections into two groups, i.e., Type 1 (d1) and Type 2 (d2) with respect to the plate's 'out-of-flatness' and 'out-of-straightness.' This work was augmented by J.R. Vieira et al. (2011) who conducted measurements of both global and cross-section imperfections for a series of channel sections and used a position transducer on a manual linear stage to measure global imperfections for a large variety of channel sections. Zeinoddini and Schafer (2011) advanced the characterization of imperfections that were available at that time into global imperfections and cross-section imperfections (Figure 2. 1), where global imperfections include bow (G1), camber (G2), and twist (G3) imperfections, and cross-section imperfections consisted of Type 1 (d1) and Type 2 (d2) imperfections.

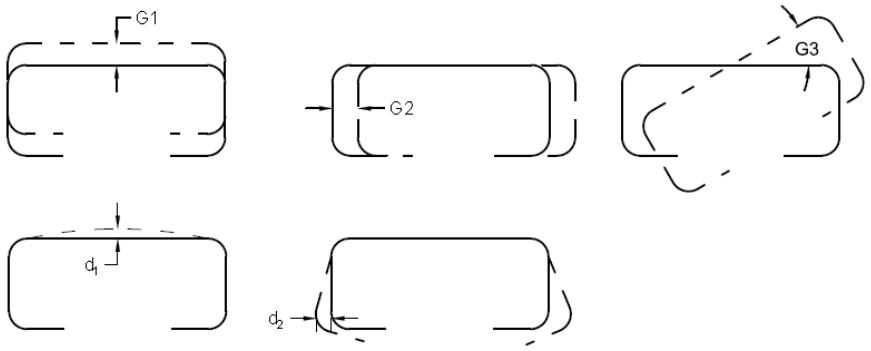

Figure 2. 1 Conventional characterization of imperfections.

These imperfections are statistically analyzed and simulated through Eq 2. 1, where α are taken from a provided statistical database, and mode shape φ from buckling analysis using the finite strip or finite element method. An easy way is to apply CUFSM and locate critical local and distortional

modes on analyzed signature curve. The x axis of the signature curve represents half-wave length and mode deformation shapes can be depicted after knowing the half-wave length (Figure 2. 2). Global mode imperfections are simply taking the entire length of a specimen as its half-wave length. The mode shapes on the other hand are simply translations along major and minor axis, and rotations about the longitudinal axis.

$$f(y) = \sum_{i=1}^{5} \alpha_i \phi_i(x, y, z) \qquad \text{Eq 2. 1}$$

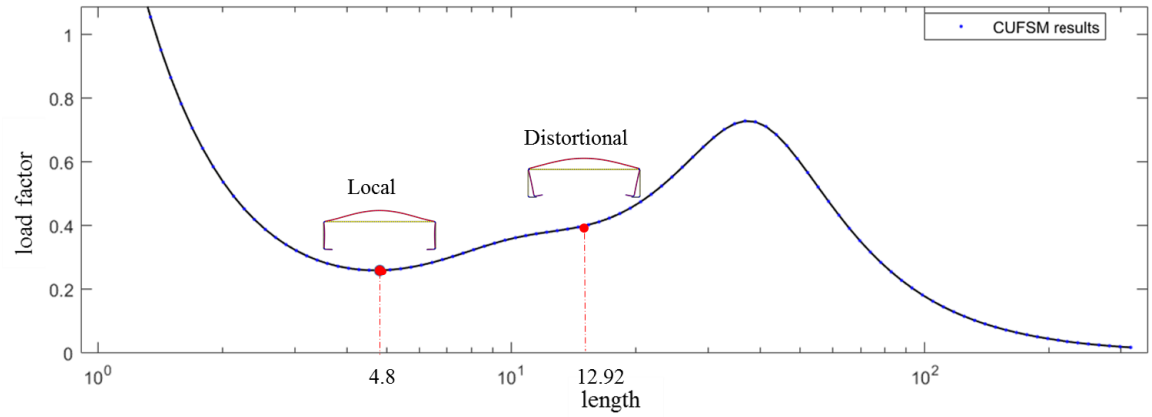

Figure 2. 2 Signature curve of a typical C section (half-wavelength in inches, load factor = P/P_y)

There are various ways to combine these imperfections while imperfection orientation is an important factor which may impact final strength prediction of simulated models. Another method which can be used is to combine two cross-section imperfections based on interaction between local and distortional modes (Dinis et al. 2007, Dinis and Camotim 2010). A coefficient C_i is used to scale its corresponding mode where C_i should satisfy the following equation:

$$\sqrt{C_L^{\,2} + C_D^{\,2}} = 1 \qquad \text{Eq 2. 2}$$

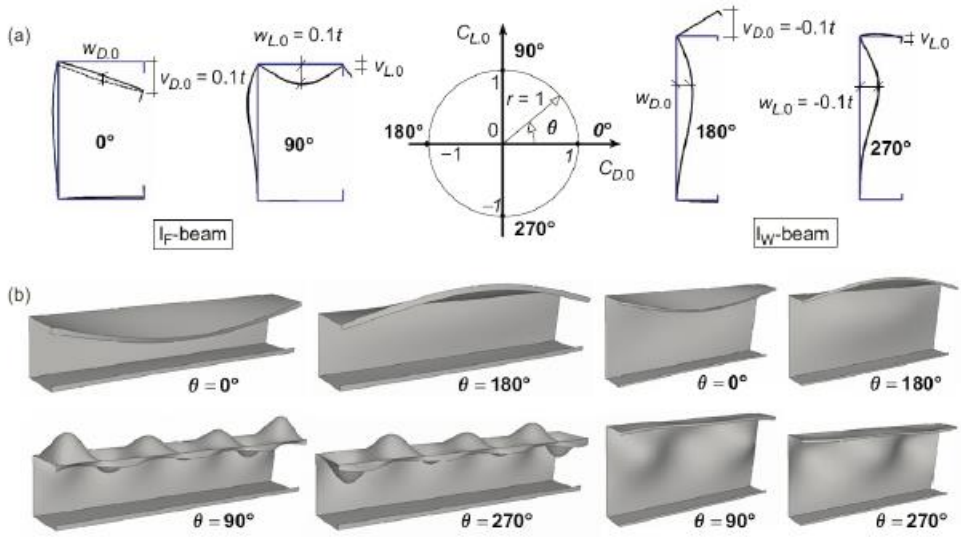

Figure 2. 3 (a) Initial imperfection representation in the C_D-C_L plane; (b) θ=0°, 90°, 180°, and 270° initial imperfection shapes (IF- and IW-beams) (Dinis and Camotim 2010)

The magnitudes of the imperfections can be determined from a statistical database or predefined magnitudes can be used, as shown in Figure 2. 3. Various combinations of local and distortional mode imperfections can be obtained simply by changing the angle θ of the CD-CL plane, which generates satisfactory coefficients to scale the predefined magnitudes of imperfections and sum these two simulated imperfections. This method can incorporate global mode imperfections since they have independent mode shapes. The advantages of these methods are that they consider interactions between the imperfections of two cross-section modes and they require no knowledge of half-wave lengths, which only can be obtained from finite-strip or finite-element methods.

2.2.2 Modal imperfection decomposition and 1D spectral simulation

The traditional modal approach is conservative for predicting strength in collapse modeling. An innovative simulation method, known as the 1D Modal Spectra approach, recently was proposed by Zeinoddini and Schafer (2012), and this approach provides a more formal decomposition of imperfections into buckling modes, and it includes a more accurate consideration of the longitudinal frequency in the measured imperfections.

The modal imperfection decomposition is based on the assumption that thin-walled, cold-formed steel-structural members can be impaired significantly by imperfection patterns to the critical buckling mode shapes, i.e., flexure of the minor axis, flexure of the major axis, torsion, and local, distortional buckling. Thereafter, five modes of imperfection were proposed, i.e., three global imperfections (G1, G2, and G3) and two cross-section imperfections (local and distortional), as shown in Figure 2. 4.

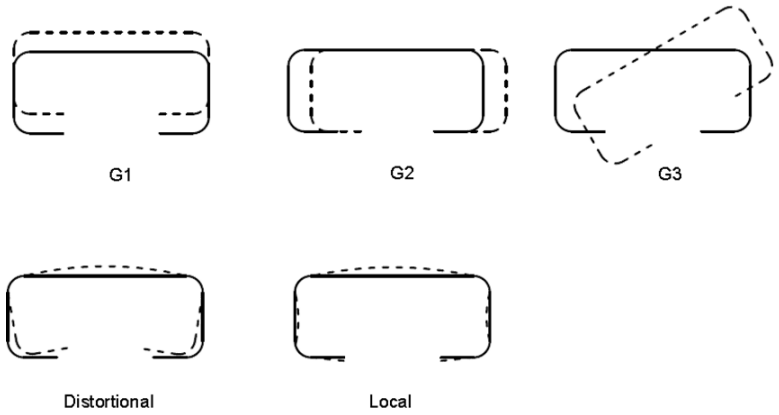

Figure 2. 4 Characterization of modal imperfection decomposition

$$f(y)=\sum_{i=1}^{5}\alpha_i(y)\phi_i(x,z) \qquad \text{Eq 2. 3}$$

where y represents the longitudinal position; α is the magnitude of the imperfection, which varies with y; φ_i is a cross-section deformation field with respect to the shapes of the mode; and f is the surface imperfection field of the measured cross section.

The advantage of this modal imperfection decomposition is that it directly uses information on the buckling modes when characterizing the imperfection. Its disadvantage is the shape of the buckling mode must be calculated in advance to perform the characterization, whereas traditional methods do not require such a calculation. The magnitudes of the imperfections (αi) along the model can be Fourier transformed into the frequency domain, where the reciprocal of the half-wave length (λ) of a buckling mode is the variant of magnitudes of imperfections that corresponds to a specific sinusoidal component.

Power spectra can be statistically summarized and a base power spectral density (PSD) can be formed by averaging power spectra from measurements. The base PSD can be used for high-accuracy imperfection modeling where mode shapes and magnitude α are given (Zeinoddini 2011).

$$\alpha_i(y) = \sqrt{2}\sum_{n=0}^{N-1}[A_n \cos(w_n y + \phi_n)] \quad \text{Eq 2. 4}$$

where

A_n is the magnitude at a specific frequency (w_n) from a statistical database

w_n is the corresponding frequency

y is the longitudinal position of a simulated member

ϕ_n is a random phase, which is uniformly distributed on an interval from 0 to 2π

The process is performed for each mode until five classified imperfections are generated and combined using Eq. 2.2. The 1D spectral approach has been reported to yield highly-accurate simulation of imperfections, and it will be examined carefully in Chapter 9.

2.3 Literature review related to image processing for modern measurement methods

Measurement techniques are categorized as contact and non-contact techniques. The contact measurement technique has been prevalent in structural engineering research over the past few decades. Researchers have used various devices to inspect the physical situations that exist in structural members or systems, and these devices include displacement sensors, rulers, calipers, and micrometers. Non-contact measurement techniques, such as photogrammetry, ultrasonic measurement and laser triangulation, have not been used extensively for various reasons. The development of techniques over the last two decades has resulted in more sophisticated non-contact measurement devices that are affordable for general use. Image processing using large measurement point clouds can be achieved with fast workstations and cloud computation. All of

these conditions allow the extensive application of non-contact measurement techniques, allowing them to compete with contact measurements in structural engineering.

Image-processing techniques are very highly-developed, especially in the computer vision, material inspection, and medical areas. They are still new and not fully developed in the structural engineering field. Image-processing techniques should be conducted in this discipline. One of the concerns is adapting existing image-processing algorithms so they can be used in structural studies, and another concern is the development of new image-processing algorithms for use in structural studies. Most objects in other fields have much smaller physical dimensions than structural members, which are quite large. Therefore, computation speed in image processing may be an issue, and proper algorithms must be selected or developed. The valuable findings of multi-disciplinary researchers should be carefully identified, studied, and evaluated to determine their potential use in structural engineering. With proper treatment, large point clouds from laser measurement may provide in-depth understanding of the behaviors of structural members and more reliable and accurate predictions.

When laser triangulation techniques are used to measure geometric imperfections in cold-formed steel members, two major processing stages, i.e., surface registration and feature recognition, are used so that there is better access to measurement data. The goal of surface registration is to reconstruct 3D models of target specimens using scanned measurement data from different directions. Even though a reconstructed model contains all of the required geometric information, easy access to each measurement of cross-section geometric information still requires further processing, which highlights the need for feature recognition. The major goal is to automatically identify the different geometric features of a reconstructed model, including the true dimensions of a cross section that can be measured accurately. Only topics of image processing related to surface

registration and feature recognition are reviewed partially in this study of cold-formed steel. The lists of research papers and algorithms are so extensive that all of them cannot be fully explored. In addition, some of the latest developments may not be included due to time constraints.

2.3.1 Surface registration

Early surface registration may require two kinds of data, i.e., 3D data in a sensor coordinate system and 3D data in a model coordinate system. The 3D data in a sensor coordinate system, which describes a *data shape*, may correspond to some part of the *model shape* depicted by the 3D data in a model coordinate system. The key concern is how to optimize rotation and translation in order to align, or register, the shape of the *model* and the shape of the *data* to minimize the distance between the two shapes.

Besl and Mckay (1991), and Chen and Medioni (1991) proposed an algorithm that can effectively register different 3D data into a full model. The name of this method is Iterative Closest Point or Iterative Correspondent Points (ICP) algorithm. The basic concept is to compare roughly aligned *sensor data*, *S*, to *model data, M*, and estimate the distance metric, *d*, between an individual sensor's data, say [redacted], and *model data M*. The mathematical expression is denoted as:

[redacted] Eq 2. 5

[redacted] Eq 2. 6

where [redacted] is the closest point in *M* that yields the minimum distance;

$$R = C(S, M)$$ Eq 2. 7

R is the resulting set of closest points, and *C* is the closest point operator.

The least squares registration is computed as:

[redacted] Eq 2. 8

$S = \vec{q}(S)$ Eq 2. 9

where $\vec{q}$ is the optimized transformation values that correspond to the minimum distances for the given closest point pairs and data shape data. The optimized transformation obtained in each iteration is applied to *S* for registration.

The overall procedures are following:

1. Initial alignment to guarantee sensor data are well-aligned with model data.
2. Compute the closest points using Eq 2. 1 and Eq 2. 10.
3. Compute the registration using use Eq 2. 4.
4. Apply the registration using Eq 2. 5.
5. Terminate the iteration when the change in the mean-square error falls below a preset threshold $\tau > 0$ specifying the desired precision of the registration.

The algorithm shows a good convergence and can determine a local minimum with respect to the mean-square distance objective function all the time. Also, this algorithm works irrespective of whether there is a rigid-form surface or a free-form surface. It can be used for any representations of geometric data, such as point sets, line segment sets, and implicit curves. (Besl and McKay, 1991). However, the original ICP algorithm has limitations as well. The proposed algorithm is sensitive to outliers. Highly uncertain measurements are assumed to be rejected in advance. The boundary points may be influential to the algorithm, which requires that the range of the sensor data should always stay inside the model's data.

If there are multiple local minima, the iteration may be terminated and algorithm may converge into local minima, and optimization goal eventually may fail. The initial alignment should be good enough to reject other potential minima from the beginning.

The potential of ICP has attracted multi-disciplinary researchers to use it and develop it further. Rusinkiewicz and Levoy (2001) categorized six different variants that can affect the performance of the ICP algorithm, i.e. :

1. Points selection or resampling
2. Points match
3. Weighting penalization
4. False match rejection
5. Error metric assignment
6. Error metric minimization

As mentioned in Pulli (1999), general combination variants (1) use random sampling of points on both sensor data and model data; (2) match each selected point from one dataset to another with searching radii within a 45° range from normal from the reference surface; (3) uniformly weight point pairs; (4) reject pairs that contain edge vertices and a percentage of the pairs with the largest point-to-point distances; (5) form a point-to-point metric; and (6) apply the 'select-match-minimize' iteration for the alignment and transform.

Many researchers have developed some variants in order to achieve their image processing goal. The most influential developments focused on the selection of points and matching points, which was carefully reviewed by the author. The former affects accuracy, especially for noisy and/or incised planes (Figure 2. 5a). However, the latter affects both accuracy and convergence rate (Figure 2. 5b). Selection of points is necessary considering a dense point cloud taken from a laser. If all available data are used (Besl and McKay, 1991), the computation becomes incredibly large, while uniform subsampling (Turk and Levoy, 1994) may lead to aliasing geometric information. For example, a curve may require much denser sampling than a plane, and a complex geometry

generally contains both features. Regarding this situation, some researchers, for example, Johnson and Herbert (1997), proposed sampling data based on their geometric features, and this approach was used in the author's research. Rusinkiewicz and Levoy (2001) suggested normal-space sampling, in which selected points should have as large a distribution of normals as possible. This method can sample data effectively without reducing robustness or adversely impacting the computational cost (Figure 2. 6), so it will be implemented in future research. In Trimmed ICP proposed by Chetverikov et al. (2002), a pre-defined number of estimated matching pairs is used to expedite computation and improve accuracy. Additional features, such as curvature and moment invariants, are used to improve the correspondence search (Bendels et al., 2004).

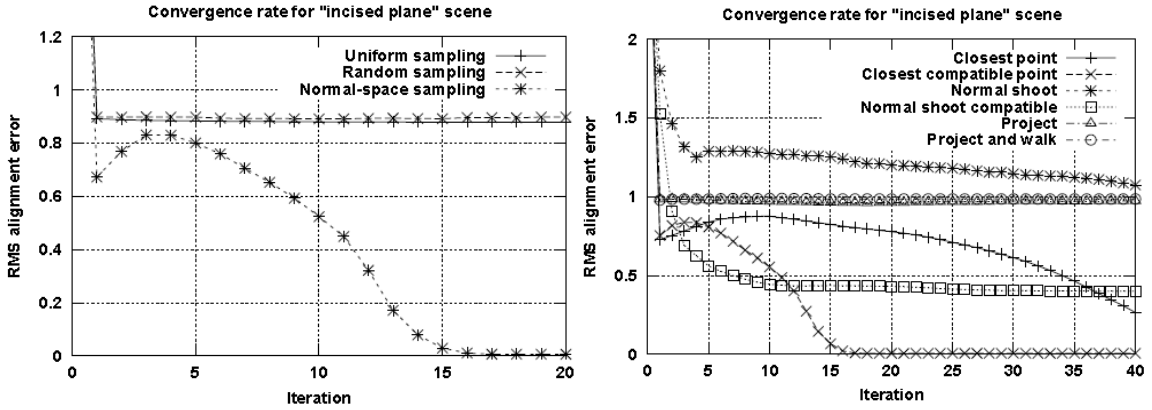

Figure 2. 5 Comparison of convergence rate and RMS alignment error: (a) Points Selection; (b) Points Match (Rusinkiewicz and Levoy, 2001)

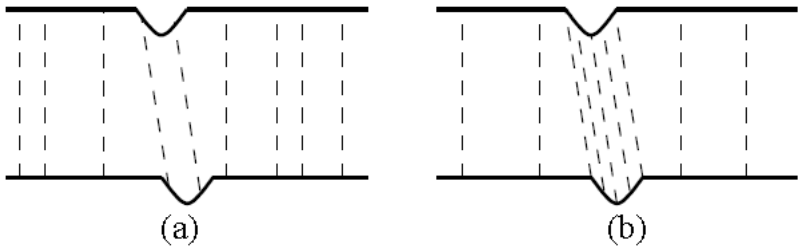

Figure 2. 6 Comparison between sampling methods: (a) random sampling; (b) normal-space sampling (Rusinkiewicz and Levoy, 2001)

Point match is the most important variant that determines the performance of the ICP registration algorithm. There are various point-match methods. The basic method is to find the closest point through point-to-point search, i.e., comparing all of the points in both the model and sensor data selected from the last step (Besl and McKay, 1991). This computation can be accelerated through a k-d tree and/or close-point caching (Simon, 1996). Chen and Medioni (1991) proposed 'normal shooting,' which uses the intersections between the source point's normals and the destination surface, i.e., point-to-plane. Other than these two fundamental methods, various advanced matching methods have been developed, such as 'projection' and 'projection and walk' (Rusinkiewicz and Levoy, 2001). The projection is carried out by projecting the sensor points onto the model data from the perspective of the destination mesh's range camera. 'Projection and walk' got its name from a search that is conducted in the model range data. The results of the comparison of all of these searching algorithms are shown in Figure 2. 7.

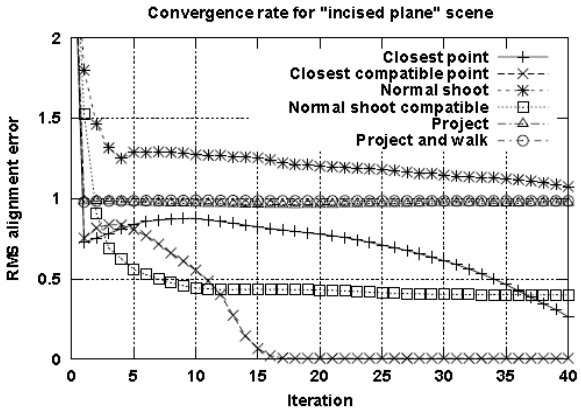

Figure 2. 7 Comparison of several matching algorithms (Rusinkiewicz and Levoy 2001).

Almhdie et al. (2007) proposed an algorithm called the 'Comprehensive Iterative Closest Point' (CICP) algorithm, which sorts the distance metrics in ascending order within the entire matrix. During the matching procedure, previously assigned points from the sensor data are removed from the comparison list so that the list can be narrowed down gradually. This method can effectively lower the cost of computation while maintaining the accuracy of the computation.

As mentioned before, there has been a lot of research related to surface registration. It is worth exploring this research to determine the best way to apply these results to structural engineering areas.

2.3.2 Feature recognition

There are many terminologies relative to feature recognition, such as feature/corner/edge detection, feature extraction, and even curve segmentation. There are various goals of feature recognition. It may be used for the reconstruction of 3D models, the extraction of specific features, or the validation of signatures when image point clouds are taken by cameras or range lasers. These techniques have been explored extensively and developed in computer vision, robotic controls, and medical imaging. Some of these techniques are discussed briefly in this section, and they inspired the development of feature recognition.

Harris detector

The Harris detector is used extensively and has been thoroughly developed in feature extractions/detections, especially in images taken by cameras. This method was proposed by Harris and Stephens (1988) to extract specific features from an image. This purpose triggers an automatic recognition algorithm that a computer vision system can use to identify corners, edges, and flat regions.

The procedures start by defining a window function with certain dimension (unit width in general) as shown in Figure 2. 8. The window function moves around the target on x-y plane and 2nd gradients of four corners of the window function can be estimated. A second moment matrix therefore can be formed:

$$M(p,r)=\sum_{r} w(r)\begin{bmatrix} I_x^{\,2}(p,r) & I_xI_y(p,r) \\ I_yI_x(p,r) & I_y^{\,2}(p,r) \end{bmatrix} \quad \text{Eq 2. 10}$$

where p is a point inside the window function, r is the shift of the target, and w(r) is the weighting function, which can be a uniform function or a Gaussian function.

As shown in Figure 2. 8, if the window function is on edge, there is no change along the edge direction; if the window function moves on 'flat' region, there are no changes in all directions; if the window function is on corner, significant change can occur in all directions. These changes also present in the second moment matrix with small transformation Eq 2.8.

$$M = R^{-1}\begin{bmatrix} \lambda_1 & 0 \\ 0 & \lambda_2 \end{bmatrix} R \quad \text{Eq 2. 11}$$

where Determine(M) = $\lambda_1+\lambda_2$

Trace(M) = $\lambda_1\ \lambda_2$

R = Determine (M)-kTrace(M)

If R is positive, the window function is located in the corner regions; if R is positive (both λ1 and λ2 are large); if R is negative in the edge regions (λ1 >> λ2 , λ2 << λ1) and in the flat regions if R is very small (both λ1 and λ2 are small). Harris detectors are more specific to corners when precise localization is required.

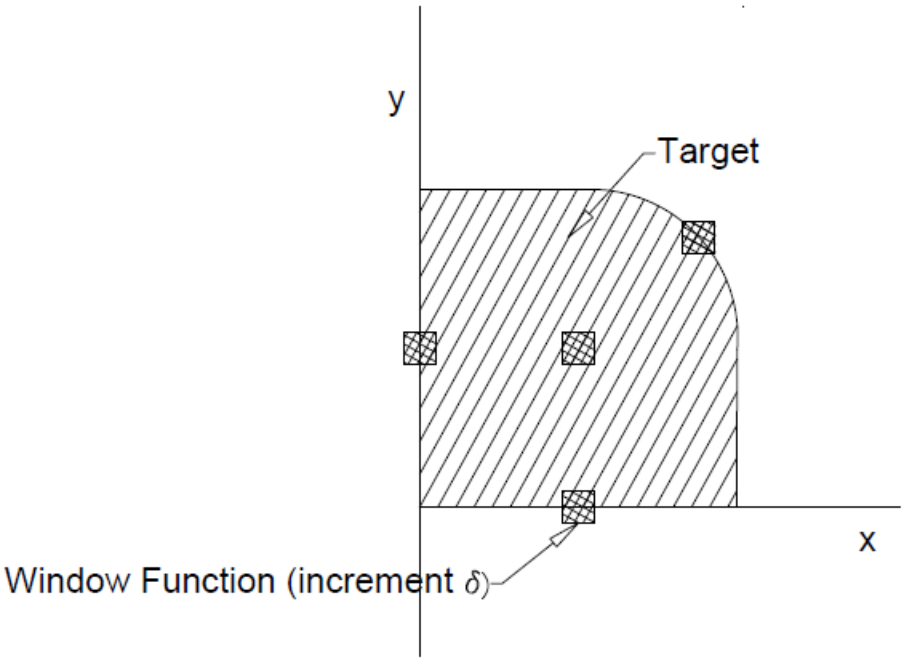

Figure 2. 8 Example of a Harris Detector

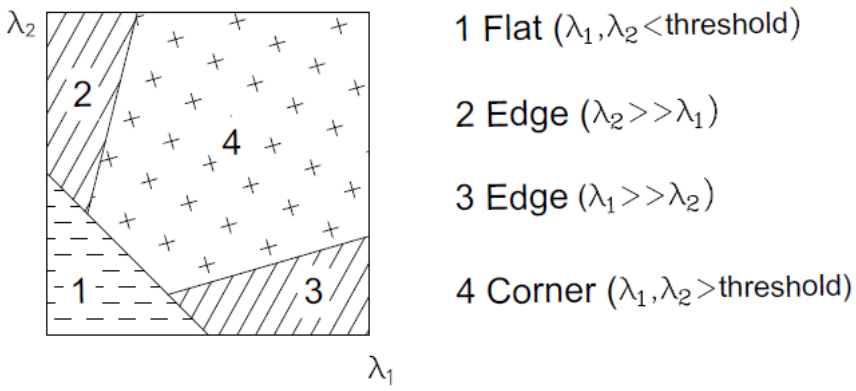

Figure 2. 9 Auto-correlation principal curvature space

Normal-aligned radial feature (NARF)

Steder et al. (2011) proposed a method, which they called the 'normal-aligned radial feature (NARF) algorithm, to extract the desired features from random 3D point clouds generated by laser scanners. This method is implemented in three steps, i.e., border extraction, interest point extraction, and NARF descriptor.

Border extraction mainly relies on the variation in the tracking distance between neighboring points. A heuristic is utilized to determine the typical 3D distance to adjacent points, which stay within boundaries. A score is estimated from the 3D distance of inspected points and the typical distance. The larger the score, the greater the possibility of a border becomes. As the border point is categorized, a non-maximum suppression is used to obtain the exact position of the border.

As the second step, the extraction of interest points aims at extracting points with significant changes on the surface measured from different perspectives. This step is a key to the successful extraction of features at a fast computational speed. A score is evaluated to the surface changes at extracting points' positions as well as a dominant direction for the change incorporating border information from previous step. Variations in the directions are calculated, and potential interest points can be determined by setting a threshold. A non-maximum suppression is applied, similar to border extraction, to finalize the extraction of the points of interest.

The third step is to define a feature descriptor so that a desired geometry with a unique local coordinate frame at the point can be extracted from point clouds. A normal-aligned range value patch is calculated at the interest point. A star pattern is overlaid onto the patch, and each ray of the pattern indicates a value in the NARF descriptor.

This method can be used to determine different images, and the interest point extraction inspired the author to develop a specific feature-recognition algorithm.

Chapter 3 Development of Imperfection Measurement Rig[1]

Motivated by full-field measurement of a cold-formed steel member, a 3D laser imperfection measurement rig is designed and built at the Thin-Walled Structures Laboratory in Johns Hopkins University. The newly developed measurement rig is intended to collect an entire geometry (external surface) of any targeted specimen. It is expected that measured point clouds have high resolution across and along the sections, so that any desired imperfections can be identified. This chapter details concepts and consideration, mechanic design and control, machine calibration, and accuracy verification through analysis of variance (ANOVA). Design drawings for major components of imperfection measurement rig are attached in the appendix (Ap. 1).

3.1 Design of test set-up and its considerations

Cold-formed steel members are the targeted specimen in this research where geometries and imperfections are required for study. Conventional stylus-type measurement rig is constrained to provide satisfactory cross-section configuration. Local and distortional type imperfections, which may have an impact on short- or medium-length cold-formed steel members, such as C, Z, and BUC members, cannot be accurately depicted. In turn, structural behaviors, such as strength, deformation, etc., cannot be precisely predicted from simulated models. Motivated from precise prediction to structural members' behaviors, a full-field geometric imperfection measurement platform is conceived. This platform is required to capture all characteristic geometries of targets: for example, corners, web, flanges, etc. Second, the measurement path is repeatable because there

1. This chapter published on Experimental Mechanics in 2015 (Zhao al. etc. 2015)

is no direct contact between the measurement machine and targeted specimens. Most importantly, the measurement accuracy should be less than 0.13 mm (0.005 in.) so as to catch small waviness and to defeat contact measurement sensors.

These three considerations inspired the author to design and build up an imperfection measurement rig, as below (Figure 3. 1).

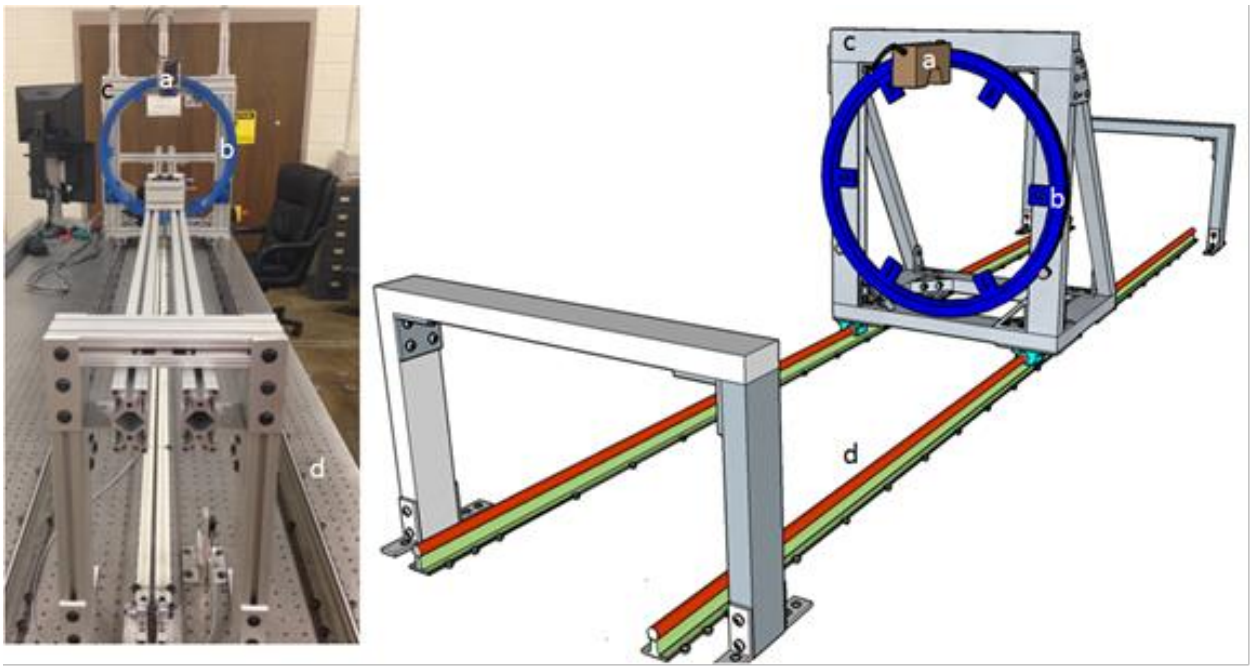

Figure 3. 1 Noncontact geometric imperfection measurement rig for cold-formed steel members picture and rendering, including the following details: (a) laser scanner; (b) large dimension rotary stage; (c) linear stage and support frame; (d) precision rails for linear stage and linear motion system

The rig includes a laser scanner, a rotary stage, a linear stage, and a triangular support frame. The laser scanner is a 2D line laser that generates 800 points per reading, covering widths up to 240 mm. The laser is positioned on the 635 mm diameter rotary stage. This allows the laser to scan different segments of a target specimen, e.g., corner radius in a cold-formed steel member. The support frame where the rotary stage is attached is heavy and wide enough to carry the rotary ring

without tipping and provide only minor forces on the linear guides. Specimens are placed on a support beam to minimize gravity deflections. The linear motion system drives the support frame and positions the laser along the length. Full-field geometric information of a target specimen can be achieved by scanning the specimen at multiple circumferential directions and by registering various individual scans from local coordinate systems into a global coordinate system.

This imperfection measurement rig is satisfactory but with two limitations: 1. The imperfection rig can measure any specimen of at most 250 mm in width or depth and 3 m long; 2. The scanning process must be carried out in a dark environment because the laser scanner is sensitive to ambient light where stray reflection may occur.

3.1.1 Linear motion

The linear stage system consists of a motion system (Figure 3. 2) and a linear guide system (Figure 3. 3) where more details of design can be found in the appendix (Ap. 1). The linear motion system, as shown in the Figure 3. 2, has a structure comprising two encoders at the two ends and the drive chain and sprocket stay in between. Encoder 2 is embedded inside the motor (GM9236S019) system. Two shaft couplers are used to connect the motor, the drive chain, and sprocket and Encoder 1 (ENS1J-B28). The signal of Encoder 1 is used as the motion control feedback to control the motor, while the signal of Encoder 2 (HEDS-91X0) is used as the laser position feedback to trigger the laser scanner. The linear guide system is designed to provide smooth motion with double rails and

four ball bearing supports. Supporting rails belong to aluminum support rail assembly, the part number of which is SRA12 CTL from Thomson. Shaft diameter is 19.05 mm (3/4 in.) with total length 3048 mm (120 in.). The support rails have a roundness of 0.00203 mm (0.00008 in.) and straightness of 0.0254 mm (0.001 in.). While the four ball bearing supports, from Thomson with part number TWN12OPN, can self-adjust deviation of motion when the heavy infrastructure moves along the rails. The triangular support frame (Figure 3. 3) sits on the four ball bearing supports, materials of which are aluminum from 80/20 Inc. The mechanical control is discussed in Section 3.2.1, including control consideration and connection diagram.

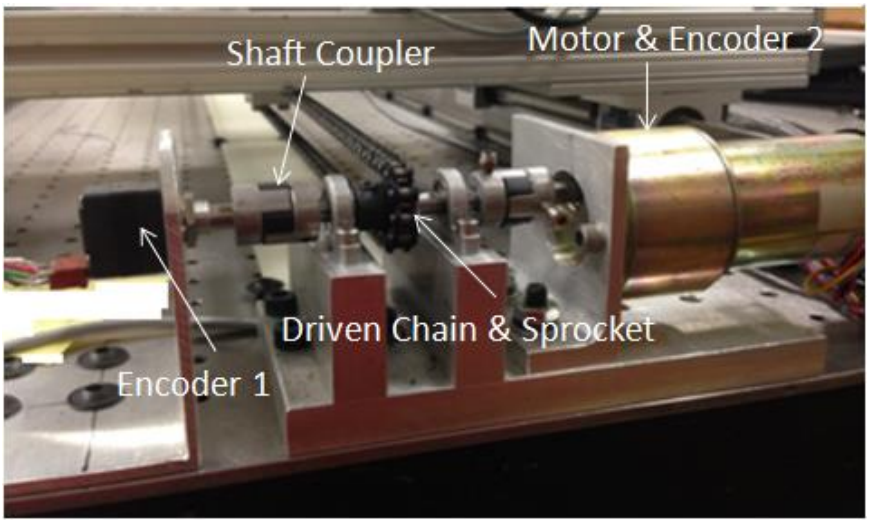

Figure 3. 2 Linear motion system

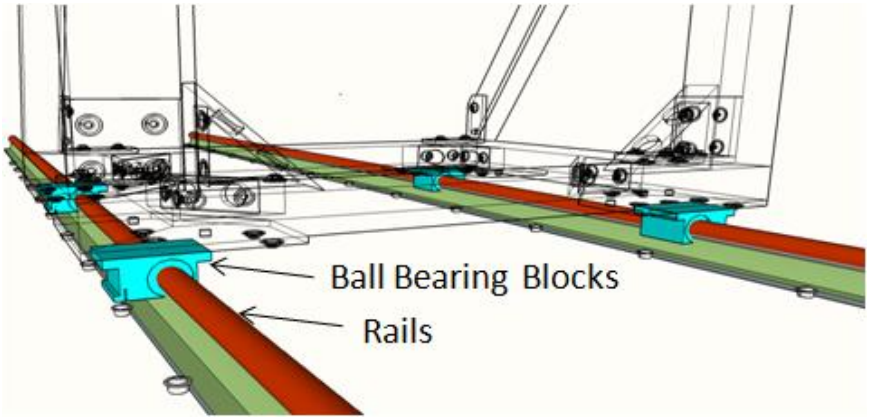

Figure 3. 3 Linear guide system

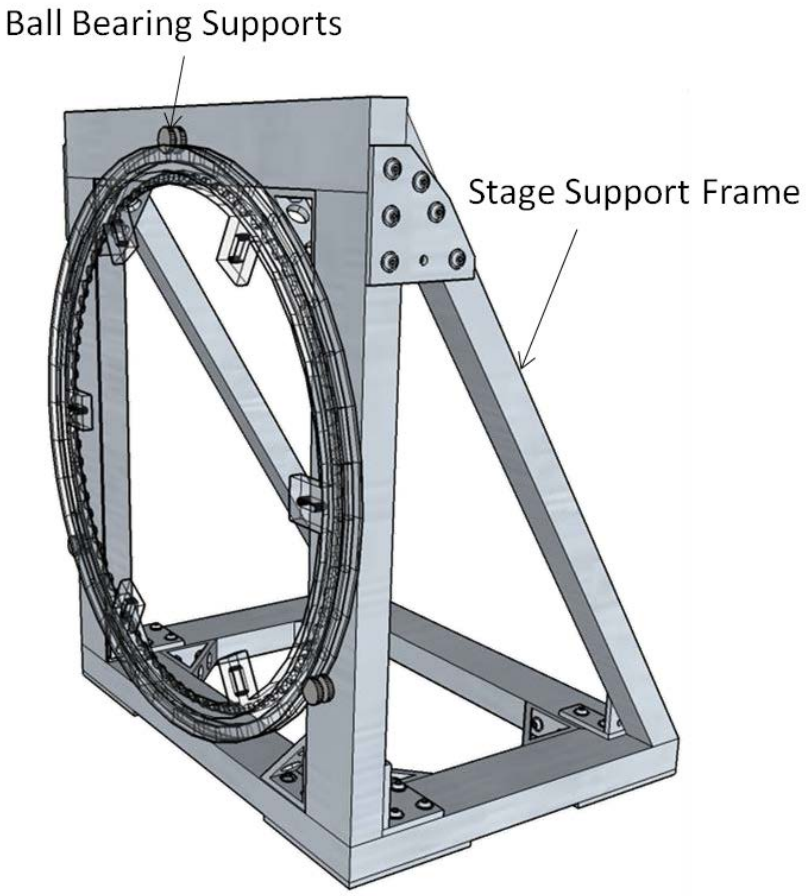

Figure 3. 4 Stage support frame

3.1.2 Rotary motion

The rotary stage system, as shown in Figure 3. 5, is intended to rotate the laser head to any desired angle. The rotary stage system consists of a large diameter rotary ring, a timing belt affixed to the rotary ring, and a stepper motor (Long Motor 23HS9430). The rotary ring, as shown in 4a, has a diameter of 635 mm (25 in.) where the timing belt is affixed. The timing belt is in 32 pitches with 800 teeth in total. The face width is 4.76 mm (3/16 in.) and overall height is 4.76 mm (3/16 in.). It is made of nylon, which is flexible and capable to be glued on the steel rotary ring. This rack is replaceable and can be easily mounted on the steel ring with glue. If the rack is worn and replaced, calibration for the machine will be required. Calibration details are included in Section 3.3.1. A spur gear, with 17.48 mm (0.688 in.) pitch diameter, is mounted on the shaft of the stepper motor and grips the timing belt. A rotary ring with double rails (Figure 3. 5) is selected for the rotary system. The V-shaped rails better grip the roller bearings that hold the rotary ring and transmit the heavy loads to the support frame. The double rails can effectively prevent out-of-plane vibration when the rotary ring is driven. The rotary ring is made of cast iron, which is heavy due to its dimension and density. It is stable and still when moving along linear guide rails. This minimizes potential dynamic noise of scanning in motion and guarantee measurement precision as required. The rotary ring is connected with the triangle support frame through three alloy steel shoulder screws forming an equilateral triangle. This alloy steel shoulder screw has 9.525 mm (3/8 in.) in shoulder diameter, 44.45 mm (1-3/4 in.) in shoulder length, and 21.17 mm (5/6” -18) in thread size,

part number of which is 91259A630 from McMaster-Carr. Detailed sizing drawings can be found in the appendix (Ap.1).

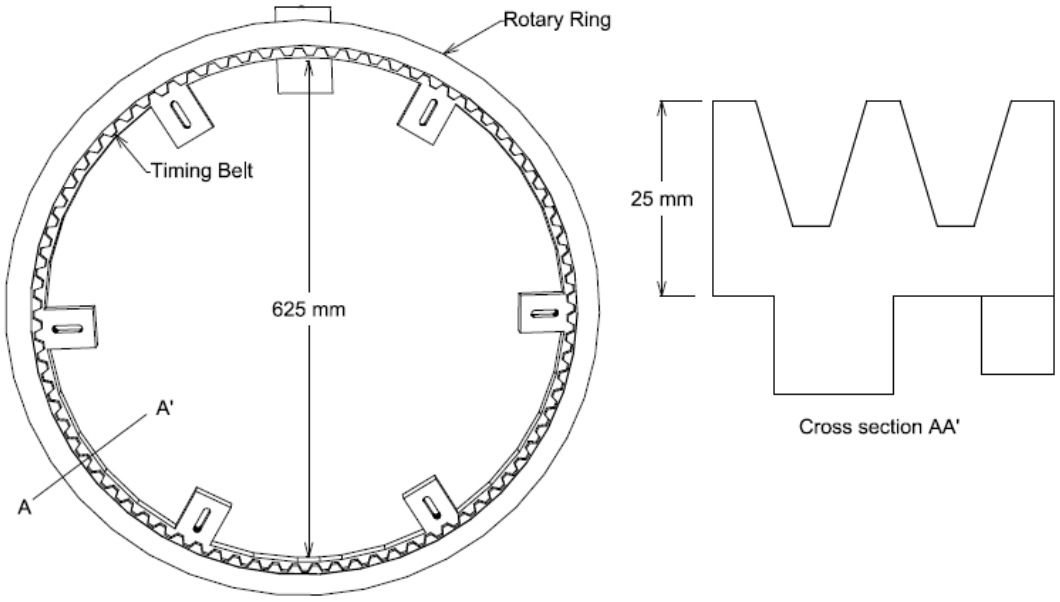

Figure 3. 5 Detail of steel ring employed for rotary laser stage

3.1.3 Laser

Laser scanning employs triangulation technique, where a source and a detector compose the scanner, to accomplish displacement measurement. A commercial laser scanner (Keyence LJ-V7300), which consists of a blue semiconductor laser source and a CMOS detector (Figure 3. 6), is utilized in this work. The detected signal is compared with a reference to determine the relative distance to the target. The laser scanner's working range is between 155 mm (6 in.) and 445 mm (17.5 in.) away from laser head. This Keyence line laser can obtain the detected signal over its scanned cross section at once, with a resolution over its cross section of 0.3 mm (0.008 in.). The double-polar

function embedded in the laser scanner can effectively remove stray reflections during scanning on a shiny surface: for example, zinc-galvanized cold-formed steel. The line laser's scanning width depends on the depth of scan from the head to the specimen and varies from 110 mm (4.33 in.) to 240 mm (10 in.), as shown in Figure 3. 6; there are 800 points at the largest width.

The accuracy of the laser depends on the distance to the target both vertically and horizontally, as shown in Figure 3. 6. Highest accuracy, 0.1 mm (0.005 in.), is achieved when the target is 155mm (6 in.) to 300 mm (11.8 in.) away from the laser head. The laser head is able to profile the target at high frequencies (up to 16 kHz), which allows it to continuously scan in the longitudinal direction, as discussed in Section 3.2.

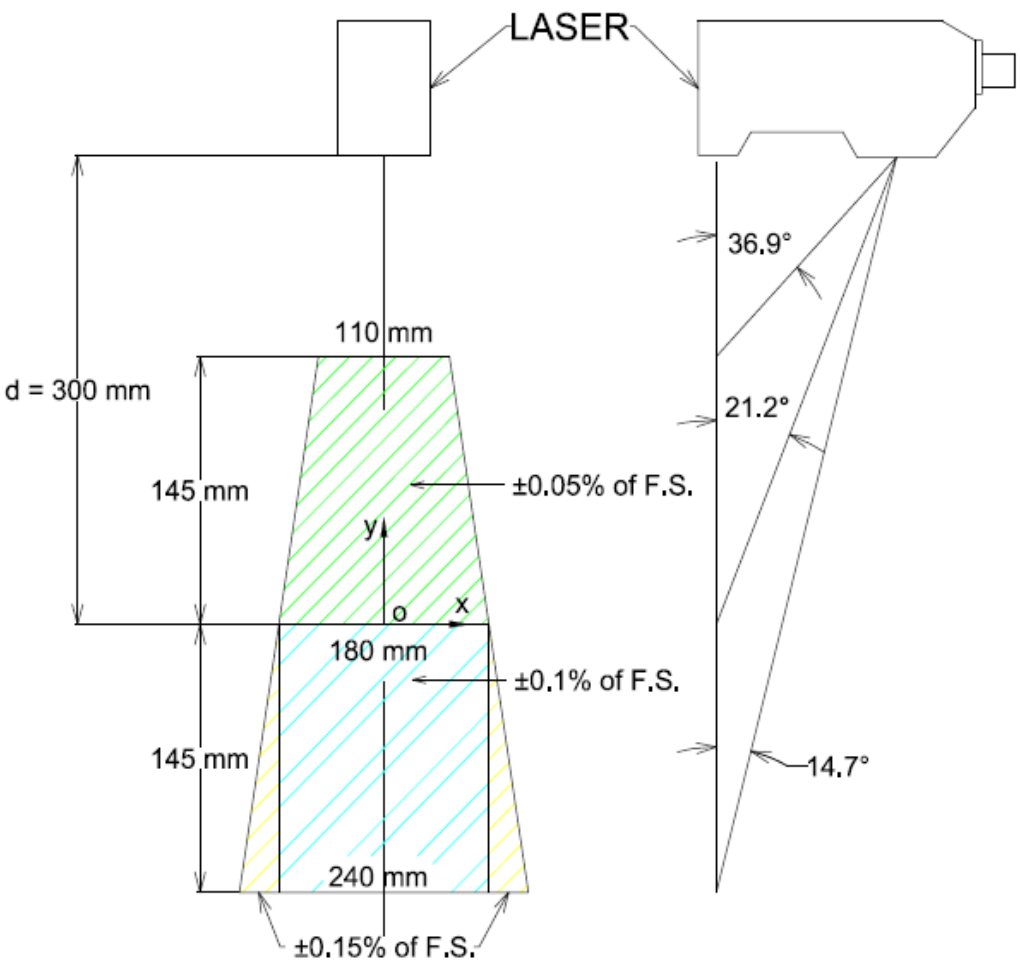

Figure 3. 6 Measurement accuracy and scan range for Keyence LJ-V7300, adapted from (KEYENCE) (note F.S. indicates full scale accuracy which is 0.09 mm at d=300 mm)

3.2 Motion control of test set-up

The automation of the geometric measurement platform is realized by a LabVIEW program through the control system depicted in Figure 3. 7. A data acquisition (DAQ) system (NI 6343) connecting to a PC is the center of the control system. The DAQ board connects to a stepper motor driver (M542) and a DC motor driver (MODEL 4212), which sends a pulse signal and an analog control signal, respectively. The stepper motor controller converts the pulse signal to a stepper motor control signal, to power the stepper motor, which rotates the rotary ring to a desired position. The

DC motor driver converts the analog control signal to a large power signal to drive the DC motor; the speed of the DC motor is changed with the signal. The rotation angle of the DC motor, which indicates the longitudinal position of the laser scanner, is fed back to the DAQ board and the laser scanner controller through Encoder 2 and Encoder 1 (Figure 3. 2), respectively. The signal from Encoder 1 is used for linear motion real-time control, and that from Encoder 2 is used for controlling laser measurements. Pulses from Encoder 2 can switch the laser on and off. When the rising edge of a pulse is detected, the laser is triggered, and a laser line is projected on a scanned surface. Measurements of a cross section where a laser line is projected and reflected to the detector of the laser head are collected by the laser controller and sent to the computer. With the calibration of the encoder-triggered laser scanning, the distance between adjacent profiles of measurement from the laser is known, so the longitudinal position of the target specimen can be calculated. Details are provided in Section 3.3.

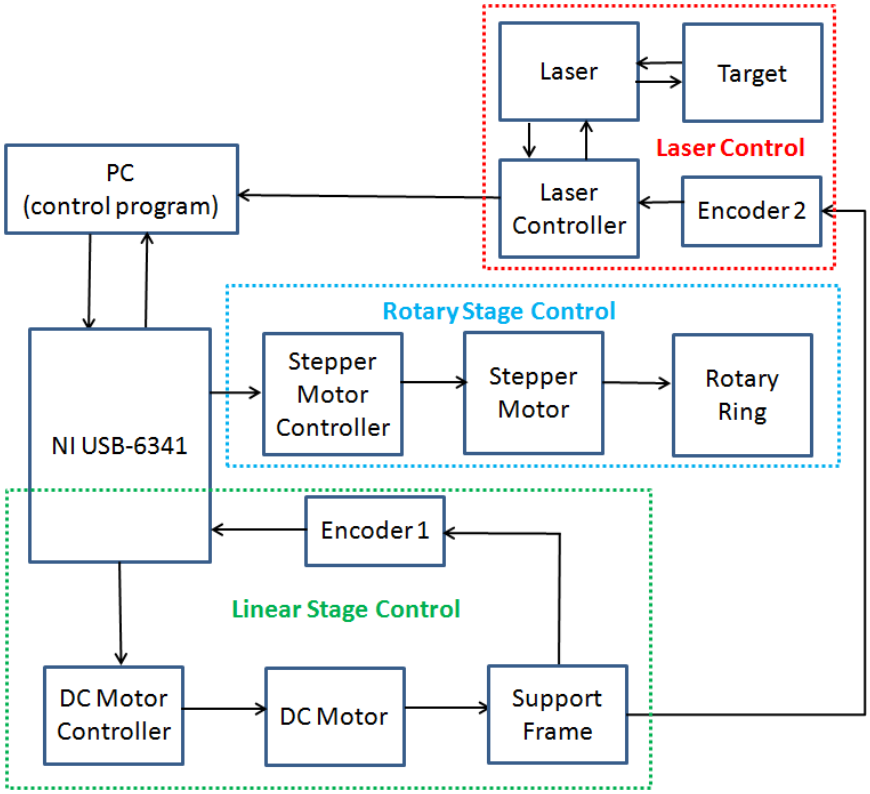

Figure 3. 7 Overall block diagram of imperfection measurement rig

3.2.1 Linear motion

The linear motion control aims for precise fixed position control (Figure 3. 8). The target position is input from the control program in the PC. The DAQ board receives the command from the PC, and converts the command to the analog signal for the DC motor driver. The DC motor driver then controls motion of the DC motor. The motion from the DC motor is fed back to the control program through Encoder 1 and the DAQ board. Because the feedback signal from the encoder is in a square-wave format, which is counted by the counter terminal on the DAQ board, a factor is applied to the feedback signal to convert counts to the longitudinal position of the laser scanner. Therefore, the difference Δd between the target position and the feedback position can be calculated. A function

of Δd is used as the command to control the DC motor. The difference Δd is first converted to error e by a constant empirical parameter K_1 ($K_1 = 9.73$) and then converted to the control signal d_v by the function $K_2(e)$. Because there is strong nonlinearity of the dynamics of the DC motor, a linear function for $K_2(e)$ is not enough to control the system. A sliding mode control therefore is used. The function $K_2(e)$ is a piecewise function of e (Figure 3. 9). Error for this final system is addressed in Section 3.3.

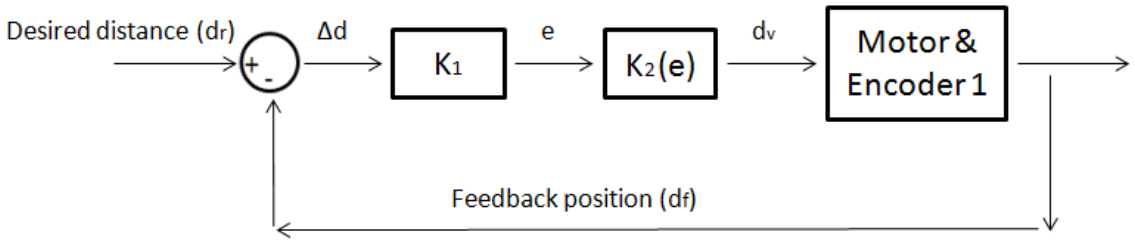

Figure 3. 8 Simplified block diagram of linear motion controller

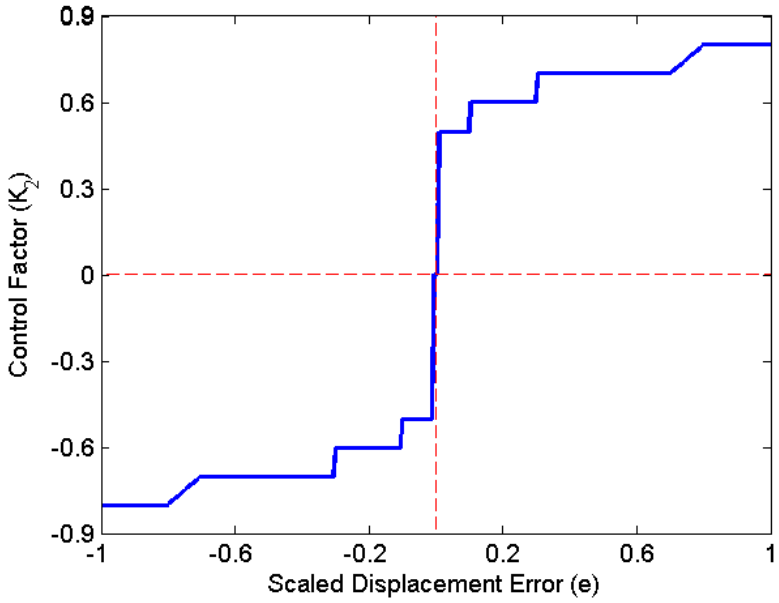

Figure 3. 9 Controlling linear position error, sliding mode of K_2

3.2.2 Rotary motion

Similar to the linear motion control, the rotary stage control is a precise fixed position; however, the control law for the rotary stage is relatively simpler. The target angle is assigned from the control program in the PC and sent to the stepper motor driver. The driver sends the corresponding control signal to the stepper motor. This enables the stepper motor to go until reaching a certain position. Calibration is carried out such that the parameter to convert the number of steps to the angular position of the laser scanner mounted on the rotary ring is found.

3.3 Calibration and accuracy verification

3.3.1 Calibration

Linear stage calibration

Linear position of the laser system is determined through two encoders attached to the drive shaft of the liner motion system, as shown in Figure 3. 2. As depicted in structure of Figure 3. 2, Encoder 1 provides the primary feedback to the linear motion system and Encoder 2 provides triggering for the laser. The linear motion calibration is aided by two measurement standards: a caliper with a range up to 635 mm (25 in.) and an accuracy of 0.127 mm (0.005 in.), and a digital dial gauge with a range up to 25 mm (1 in.) and an accuracy of 0.0127 mm (0.0005 in.). The standards are installed along the linear rails, as shown in Figure 3. 10, and allow for precise measurement of the triangular support frame over two distinct distance ranges.

(a) digital caliper for >10 mm movement (b) dial gauge for <10 mm

Figure 3. 10 Calibration of linear motion system

Encoder 1 Calibration

Encoder 1 provides the primary longitudinal measurement for the linear motion system. Rotation count on the encoder is converted to displacement along the linear rails through calibration with the caliper and dial gauge measurement standard (Figure 3. 10a&b) and the results are provided in Figure 3. 11a. Repeated several times, the response is linear and the linear calibration coefficient is subsequently used for the measurement platform.

Encoder 2 Calibration

Encoder 2 is used to trigger the laser so that measurements occur at discrete intervals along the length even if the velocity/time of scanning has some variation. In addition, Encoder 2 also provides, through calibration, a measurement of longitudinal laser location. Rotation count on the encoder is converted to displacement along the linear rails through calibration with the caliper measurement standard (Figure 3. 10a), and the results are provided in Figure 3. 11b. Similar to Encoder 1, the movements are repeated several times, the response is linear, and the linear calibration coefficient is subsequently used for the measurement platform.

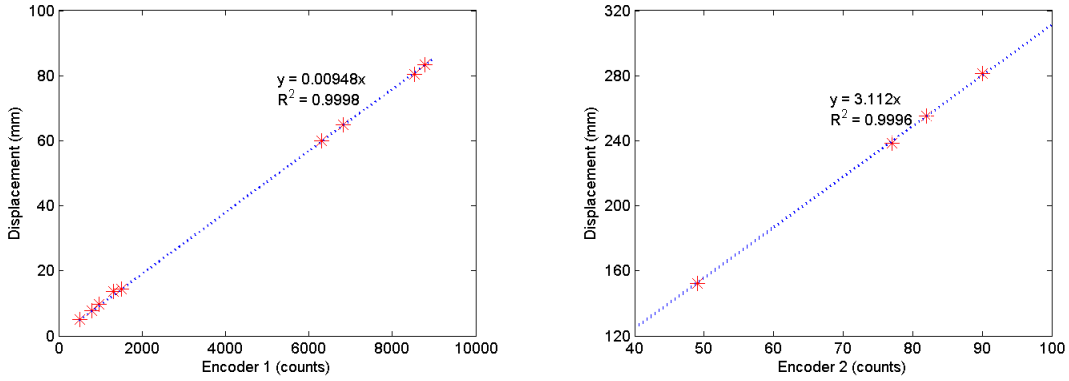

(a) Encoder 1 scale factor and fit (b) Encoder 2 scale factor and fit

Figure 3. 11 Linear calibration factors and results for encoders

Rotary Stage Calibration

Calibration of the stepper motor, which provides rotation of the rotary ring, is completed using a simple inclinometer clamped directly to the laser head mount, as shown in Figure 3. 12. The inclinometer has an accuracy of 0.01°. A series of rotation trials are conducted and the counts from the stepper motor are plotted against the rotation angle in Figure 3. 13a. A linear calibration coefficient is established by regression and subsequently employed for control of the rotary ring.

Figure 3. 12 Calibration setup (with clamped digital angle) for rotary motion system

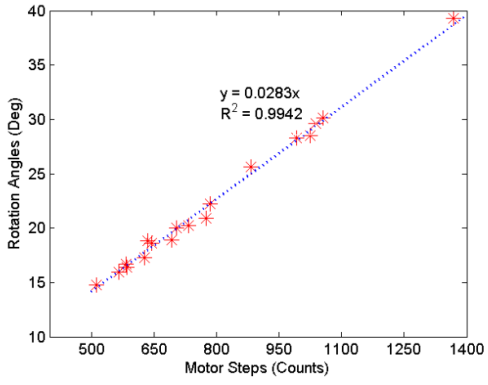

(a) scale factor and fit in terms of motor steps

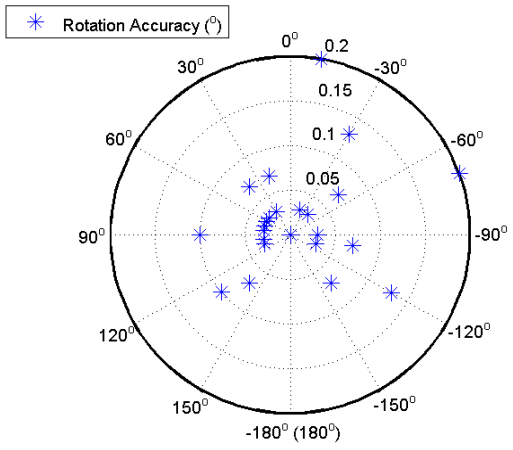

(b) rotary stage accuracy in °

Figure 3. 13 Rotary stage calibration results

Motion of the rotary stage system is imperfect. The rotary ring is heavy; the timing belt, as mentioned in Section 3.1.2, is made of nylon; and there is some friction in the lateral guides. This leads to some concern regarding repeatability and hysteresis in the rotary system. Therefore, accuracy between command and actual rotation of the rotary stage is studied beyond the initial calibration. Starting always from 0° (vertical), angles between -140° and 140° are studied at 10° increments, and the difference between desired and actual rotation recorded and provided in Figure 3. 13b. The maximum observed error is 0.2° and the mean error from all rotations is 0.04°.

3D registration framework

Even though there are tons of methods to register two overlapped surface from laser scanning, there is always a prior requirement, that is, these two surfaces have to be aligned as closely as possible. Mentioned in the beginning of this chapter, common cold-formed steel members require several entries of scanning at different directions, the line laser of which provides 800 readings in a local coordinate system located a distance d (d = 300 mm) from the laser head. This local reading must be converted into global coordinates so that multiple readings may be combined to provide the complete scan. Ignoring initially the longitudinal location (Y) and dealing with a specific cross section (X–Z plane), Figure 3. 14 provides the coordinate systems and notation used to make this basic transformation from local to global coordinates for the laser measurement.

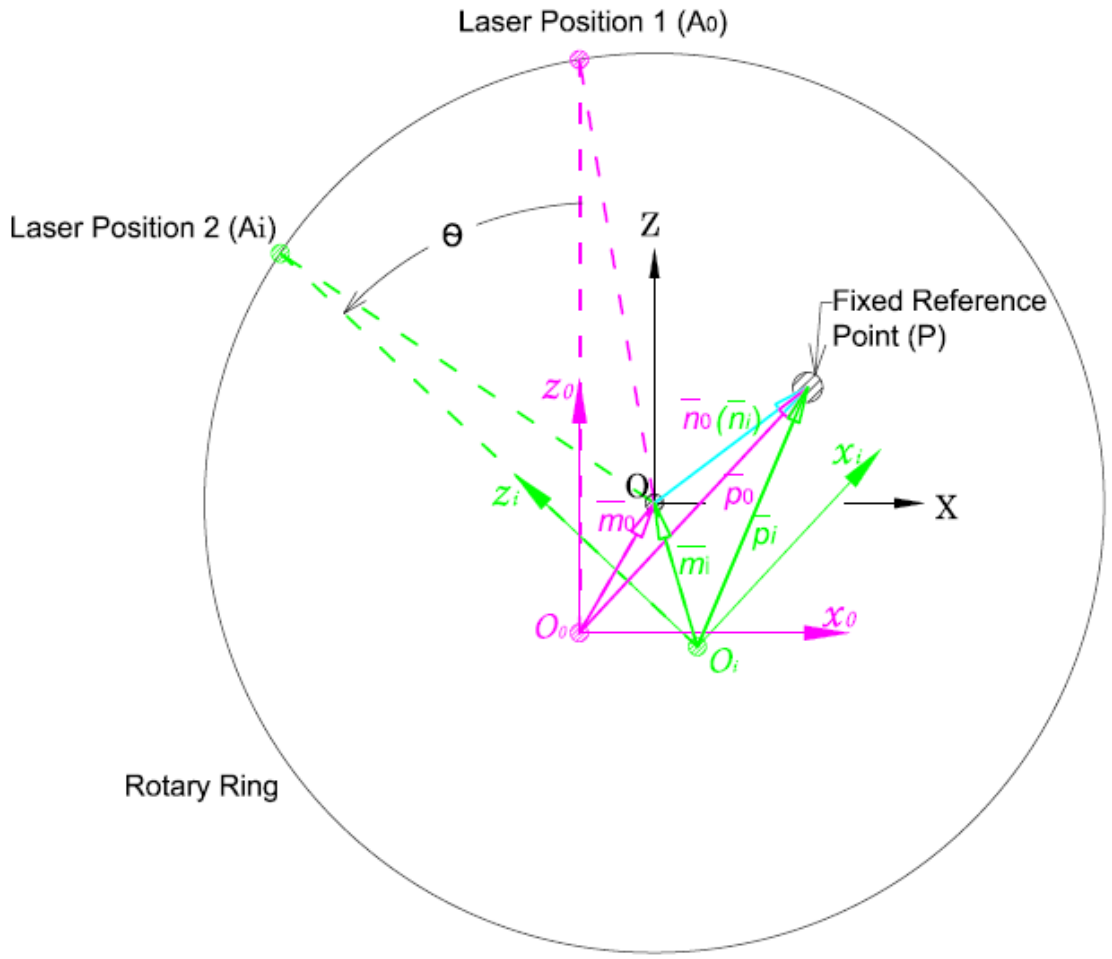

Figure 3. 14 Global coordinates (X,Z) and laser local coordinates (x,z) for different measurements (note, only single point laser at center of line laser illustrated for clarity)

The initial local coordinates: x_0,z_0 are defined by the origin of the laser readings at an angle of 0°. The z_0 axis of the local coordinate system is vertical and perpendicular to horizontal ground. The global coordinates X,Z are translated from the initial local coordinates following a vector $\bar{m}_0$ so that the origin of the global coordinates, O, is located at the center of the rotary ring. Note the line O_0A_0 (d = 300 mm) that passes through the origin of the local measurement coordinates does not coincide with the radius OA_0 (R = 281.2 mm) at the center of the rotary ring; thus there is a constant

distance OO_0 (r = 18.2 mm) between the origin of the laser local coordinates and the center of the rotary ring.

As the laser rotates to any angle θ, the center line of the laser O_iA_i also rotates θ along the circumferential axis of the rotary ring. This results in radius OA_i and a distance OO_i between the origin of the new i^{th} laser local coordinates and the center of the rotary ring. The angle between OA_i and O_iA_i is the same as that between OA_0 and O_0A_0. The radius of the rotary is constant so that OA_0 equals OA_i. The distance (OO_i) and the angle between the origin of laser local coordinates and the center of rotary ring in position 2 equals the distance (OO_0) and angle in position 1. To register all local measurements into global coordinates, a fixed reference point P is established. In the initial coordinates x_0, z_0 the fixed reference point P is measured, and the position vector $\bar{p}_0$ is established. The distance between local coordinates origin to the rotary center is $\bar{m}_0$, which is unknown. The free vector $\bar{n}_0$ from O to P must follow:

$$\bar{m}_0 + \bar{n}_0 = \bar{p}_0 \qquad \text{Eq 3. 1}$$

For the laser at any non-zero angle θ_i, the fixed reference point P is measured in the new local coordinates: x_i,z_i and a new position vector $\bar{p}_i$ is obtained. The position vector $\bar{m}_i$ for the rotary center O should have the same vector expression as $\bar{m}_0$ since the two vectors both deviate an angle α from the z_0 axis and z_i axis and are both equal to the distance r. Thus:

$$\bar{m}_0 = \bar{m}_i = \bar{m} \qquad \text{Eq 3. 2}$$

Further, similar to Eq. 1:

$$\bar{m}_i + \bar{n}_i = \bar{p}_i \qquad \text{Eq 3. 3}$$

Noting, by simple rotation:

$$\bar{n}_i = T_i \bar{n}_0 \qquad \text{Eq 3. 4}$$

where $T_i = \begin{bmatrix} \cos\theta_i & \sin\theta_i \\ -\sin\theta_i & \cos\theta_i \end{bmatrix}$

Substituting Eq. 4 into Eq. 3 and recognizing the equality of Eq. 2:

$$\bar{m} + T_i \bar{n}_0 = \bar{p}_i \ , \ i = 0,1,2, \ldots \qquad \text{Eq 3. 5}$$

Considering the measurement noise in an actual experiment, we may define the error between the independently determined p_i and that determined through the transformation as:

$$e_i = \bar{p}_i - \bar{m} - T_i \bar{n}_0 \qquad \text{Eq 3. 6}$$

$$E = \sum e_i^T e_i \qquad \text{Eq 3. 7}$$

By minimizing Eq. 7, $\bar{m}$ may be found such that the relationship between O_0 and O is identified.

With $\bar{m}$ known, a laser reading (Figure 3. 15) in local coordinates ($\bar{l}_i$) (i.e. $x_i, z_i,$) may be translated to the rotary center by adding $\bar{m}$ and then rotated to the final global coordinate system with T_i, i.e. a laser reading in the global coordinate system, L_i (i.e. X_i, Z_i), is as follows:

$$\bar{L}_i = T_i(\bar{l}_i - \bar{m}) \qquad \text{Eq 3. 8}$$

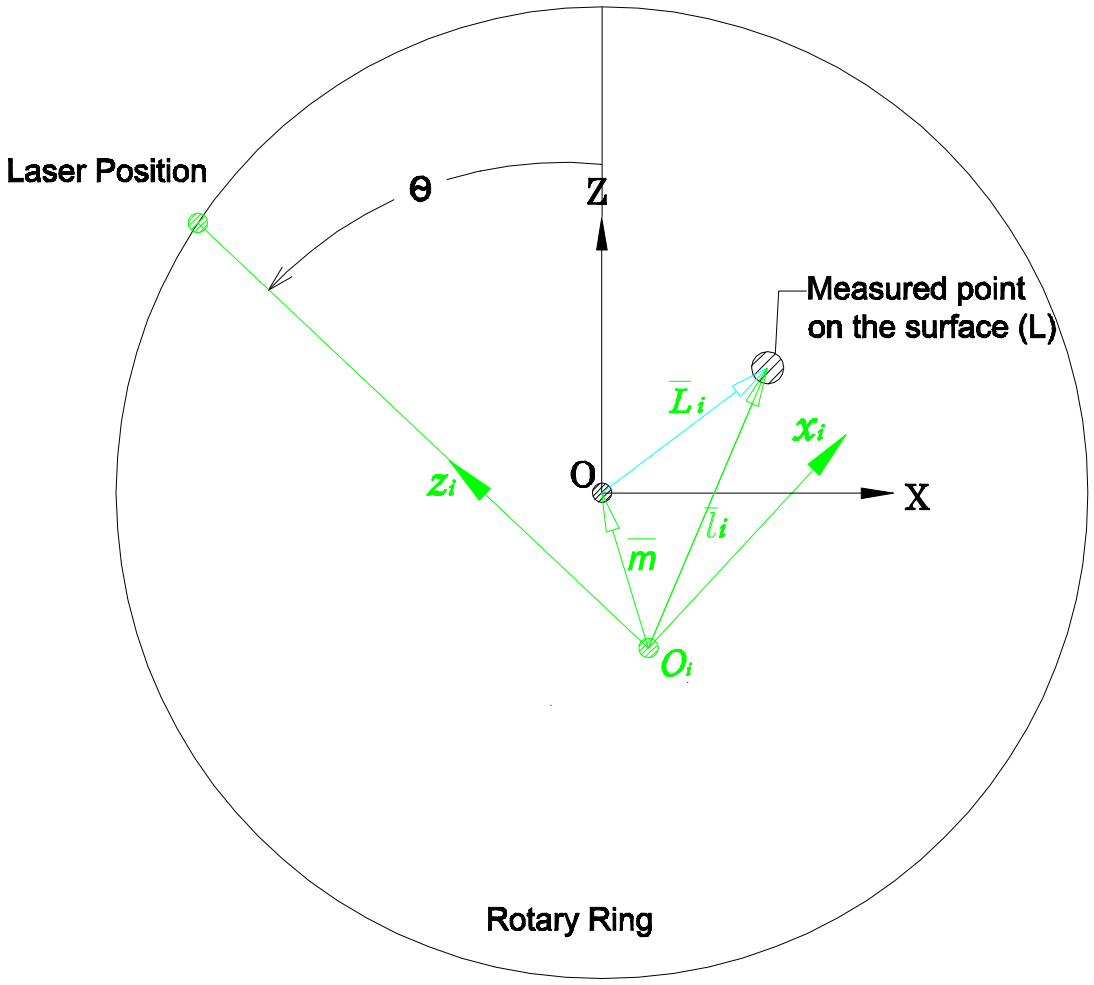

Figure 3. 15 Global coordinates $\bar{\boldsymbol{L}}_{\boldsymbol{i}}(\boldsymbol{X}_{\boldsymbol{i}},\boldsymbol{Z}_{\boldsymbol{i}})$ and laser local coordinates $\boldsymbol{l}_{\boldsymbol{i}}(\boldsymbol{x}_{\boldsymbol{i}},\boldsymbol{z}_{\boldsymbol{i}})$ for different measurements

3D registration calibration

A calibration setup is designed to experimentally find $\bar{m}$ per the procedure of the previous section. As shown in Figure 3. 16, a 0.0625 mm (1/16 in.) thin string is tied to two clamps that grip to a support beam to establish the reference point. The reference point is scanned at 25 angles (0°) to ±120° with an increment of ±10° and at eight locations along the length. From this data and employing Eqs. (5)–(7) the position vector $\bar{m}$ is estimated to be $\bar{m} = (6.368\ \text{mm}, 17.016\ \text{mm})^T$. With $\bar{m}$ established the local to global transformation is provided

through Eq. 8. The measurements at any corresponding angle θ can be transformed and translated; following the registration matrix, to the global coordinates so that different measurement surfaces can be registered in the global coordinates.

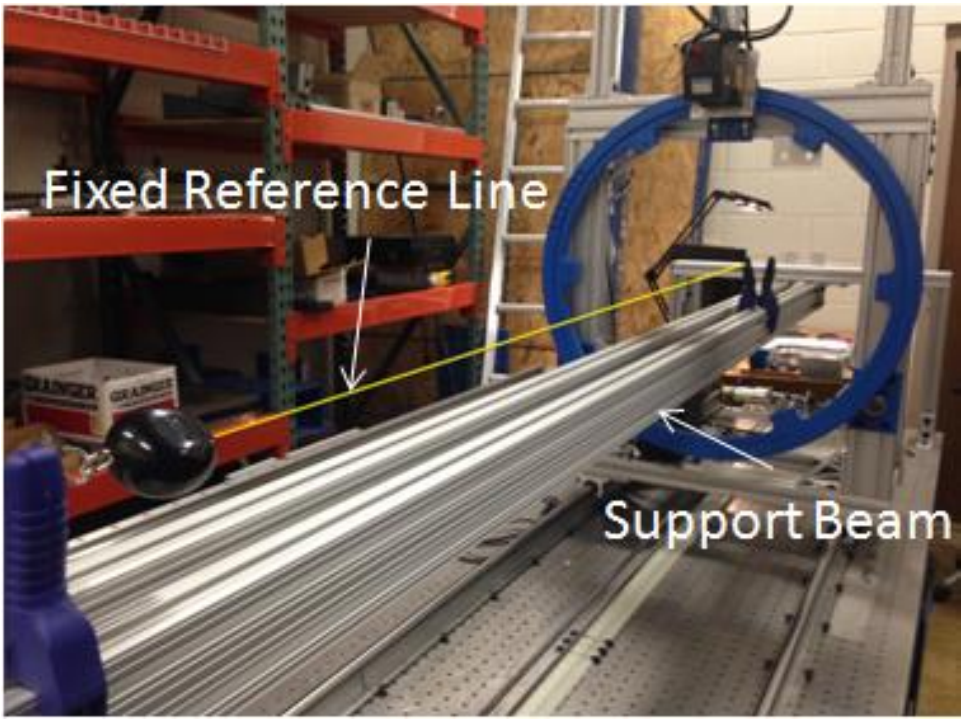

Figure 3. 16 Calibration setup for 3D registration study

3.3.2 Accuracy Verification

The global registration leading to Table 3. 1 assumes the relative position vector $\bar{m}$ between origins of the laser local coordinates and the center of the rotary ring is constant. The validity of this assumption is tested by a statistical hypothesis test using analysis of variance (ANOVA).

Table 3. 1 Registration Table

Angle (°)	x (mm)	z (mm)	Angle (°)	x (mm)	z (mm)
0	-6.368	-17.016	-10	-3.317	-17.863
10	-9.226	-15.652	-20	-0.164	-18.168
20	-11.804	-13.812	-30	2.993	-17.92
30	-14.023	-11.552	-40	6.059	-17.128
40	-15.816	-8.942	-50	8.942	-15.816
50	-17.128	-6.059	-60	11.552	-14.023
60	-17.92	-2.993	-70	13.812	-11.804
70	-18.168	0.164	-80	15.652	-9.226
80	-17.863	3.317	-90	17.016	-6.368
90	-17.016	6.368	-100	17.863	-3.317
100	-15.652	9.226	-110	18.163	-0.164
110	-13.812	11.804	-120	17.92	2.993
120	-11.552	14.023			

Validation of Calibration Model

Specifically, 25 different θ angles are used to estimate $\bar{m}$ (i.e. $\hat{m}_j$) at a given location. This estimation is performed for 7 different independent locations of the reference point, *p*. Thus we postulate that the null hypothesis, H_0: $m_j = \bar{m}$ for all j = 1,2,…,7. The F-statistic (Figure 3. 17) can be formed by taking F(6,168). At a 95% confidence level if the calculated F values are smaller than 2.15, then H_o is true. Since $\bar{m} = (\bar{x}, \bar{z})^T$ is a vector, two F values, calculated from Table 3. 2, are 0.428 and 1.006 corresponding to $\bar{x}$ and $\bar{z}$ respectively. Both values are smaller than the critical F value, thus the null hypothesis is accepted and a constant $\bar{m}$ is justified by the observations.

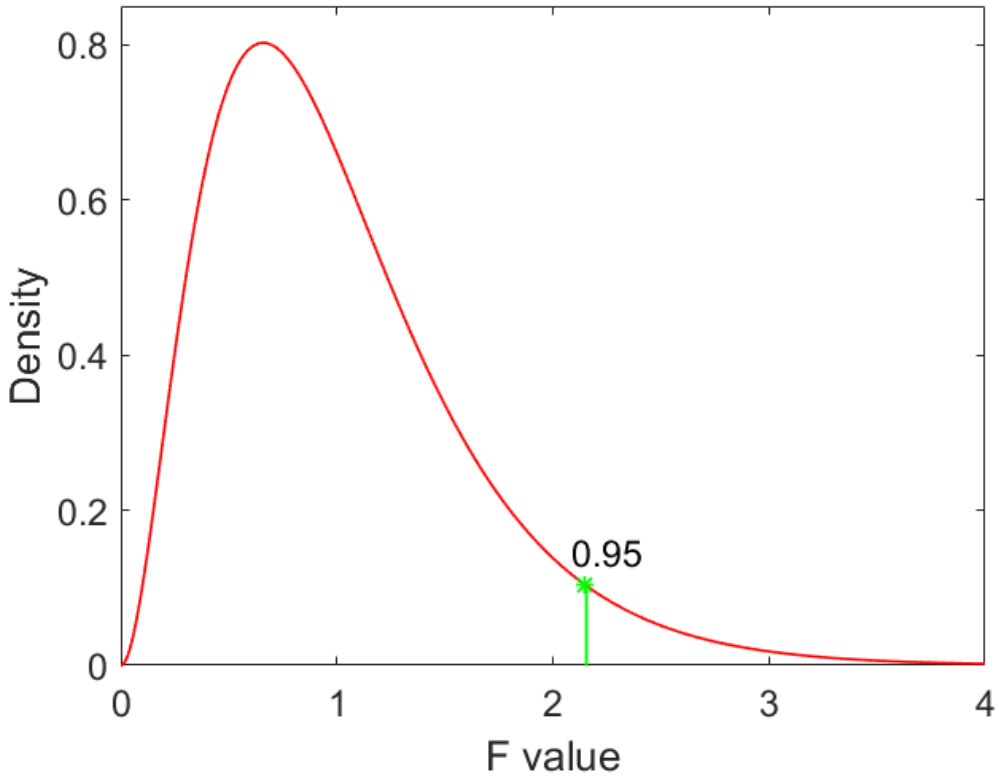

Figure 3. 17 Density plot for $F(6,168)$

Table 3. 2 ANOVA Table for fixed model, single factor, fully randomized experiment

Source of Variation	Sum of Squares (SS)	Degree of Freedom (DF)	Mean Square (MS)	F
Between samples	$SS_B = \sum_j^k n_j(\hat{m}_j - \bar{m})^2$	$DF_B = k - 1$	$MS_B = \frac{SS_B}{DF_B}$	$\frac{MS_B}{MS_w}$
Within samples	$SS_w = \sum_j^k \sum_i^{n_j}(m_{ji} - \hat{m}_j)^2$	$DF_w = (n_j \times k) - k$	$MS_w = \frac{SS_w}{DF_w}$	
Total	$SS_T = \sum_j^k \sum_i^{n_j}(m_{ji} - \bar{m})^2$	$DF_T = (n_j \times k) - 1$		

Evaluation of registration estimation

The total variance in $\bar{m}$ can be estimated as follows:

$$var(m_{ji}) = \frac{SS_T}{DF_T} = \left(\sigma_{Xji}{}^2, \sigma_{Zji}{}^2\right)^T = (0.2022, 0.0819)^T \quad \text{Eq 3. 9}$$

where $\sigma_{Xji} = 0.45$ mm and $\sigma_{Zji} = 0.29\ mm$. The accuracy of reconstruction model is:

$$e = \sqrt{\sigma_{Xji}{}^2 + \sigma_{Zji}{}^2} = 0.533\ mm\ . \quad \text{Eq 3. 10}$$

Considering the radius (R = 281.2 mm) of the rotary ring, this small deviation of the rotary center estimation is small. The estimation therefore is satisfactory and good for initial surface registration.

3.4 Manual to Imperfection Measurement Rig

Laser scanning generally requires a lot of patience and carefulness. When a researcher starts to scan a specimen, for example, a *z*-shaped section, s/he should always keep in mind that scanning results directly determine efficiency of post-image processing and accuracy of desired geometric information. Poor scanning may result in noisy or even misleading physical configuration of a reconstructed model. A responsible researcher should always take care of laser scanning as taking care of a new-born baby.

Regarding the scanning environment, as previously mentioned, the scanning process should be carried out in a dark environment without disturbance of ambient light. A single room is assigned to the imperfection measurement platform in the Thin-Walled Structures Laboratory. It is

guaranteed that no disturbance exists from other ongoing structural experiments. Even though the platform sits on an optical table, which can maximally eliminate potential noise transmitted through the ground, the researcher should keep in mind that a heavy working hydraulic actuator or an oil pump in the neighbor room may potentially contaminate measurement data in the longitudinal and cross-section directions. In conclusion, geometry measurement on the imperfection measurement rig should be carried out in a dark and quiet environment.

Laser-safety glasses should be worn all the time, even if the scanning laser in this platform is remarked as Class II whose blink reflex will limit the exposure to no more than 0.25 s and is safe for general use. Researchers who conduct the measurement are not allowed to stare at laser beam directly any time.

Laser and motion stages (rotary and linear stages) must warm up for at least 15 min by turn on two switches, as shown in Figure 3. 18.

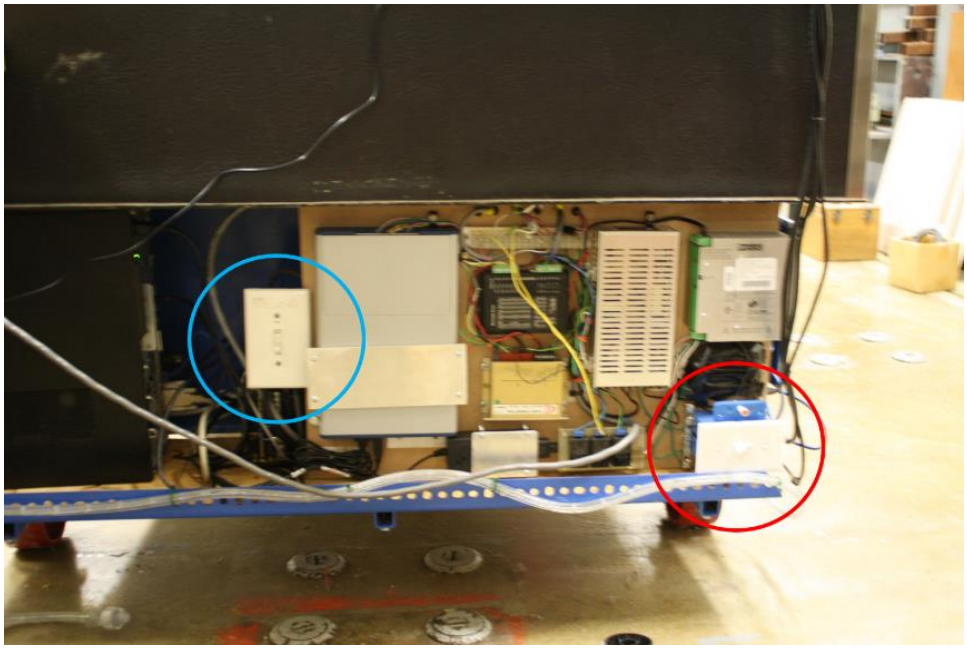

Figure 3. 18 Switches to laser and motion control

Two software should be launched, i.e., LJ-Navigator 2 for laser control, and LabVIEW for motion control. Front panel for motion control is easy to understand. There is one input for the laser rotated to a desired angle (degree) and an input for the target longitudinal travel distance (inch). Ranges of rotation angles are -140° to 140°. However, it is recommended that scan angles should be controlled within 120° to keep acceptable circumferential motion inaccuracy from accumulated command errors. Range of travel distance is up to 7-1/2 feet. It is recommended that the length of specimen should be controlled within 7 feet. A quick start-up procedure of using both software is introduced briefly. It is highly recommended that researchers should always look up to the LJ-V7300 user manual in order to accommodate the LJ-Navigator 2 and laser for the best scanning effect of target specimens.

1. Open LabVIEW and LJ-Navigator

2. Click white arrow at top of screen in LabVIEW

3. Enter a random displacement to start movement and get initial sensor readings prepared for scanning. The collected data is able to tell if the specimen is parallel to the longitudinal direction as well as target scan cross-section region is achieved from current specimen's placement. Besides, the end of specimen should be against the little metal bolt, as shown in Figure 3. 19.

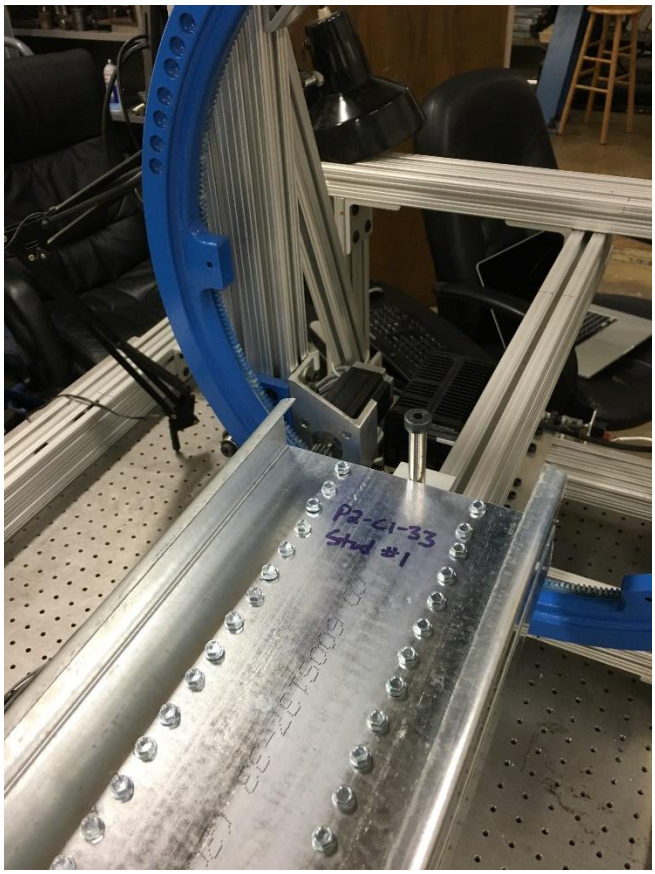

Figure 3. 19 Placement of specimen on imperfection measurement rig

4. Bring rig back to zero position. Click *Batch Stop*, *Clear Memory*, and *Batch Start* in that order at the bottom of the LJ_Navigator3 screen.

5. Click **Direct Setting** on *LJ-Navigator 3* to open options interface
6. **Trigger mode** determines whether it scan only in motion or continuously even in static conditions.
7. Start at **continuous mode** for preparation in scanning as in step 2 at the beginning of a scan entry for a specific type of specimen. It is noted that in the **Direct Setting** window, there are various programming for specific scan directions to a nominally-identical cold-formed steel member; user must select (big button top-left of the window) the mask for the appropriate scan angle before scanning.
8. Change image-mask boundaries of scan in **Imaging Setting → Image Mask → Head A tab**
9. Switch to **Encoder Mode**
10. Move scanner back to zero and potential manual operation may be required.

Figure 3. 20 Starting point of imperfection rig

11. Click **Clear Memory**

12. Click **Batch Start**

13. Enter a new displacement and/or angle

14. Click **Batch Stop**

15. Click **Motor Stop**

16. Click rightmost button in lower bottom window pointed by green arrow as shown in Figure 3.

    21 (Save Profile Data With CSV Format)

17. If desired, check the 3D image by clicking the button near to the CSV format button as shown in Figure 3. 21 pointed by a red arrow.

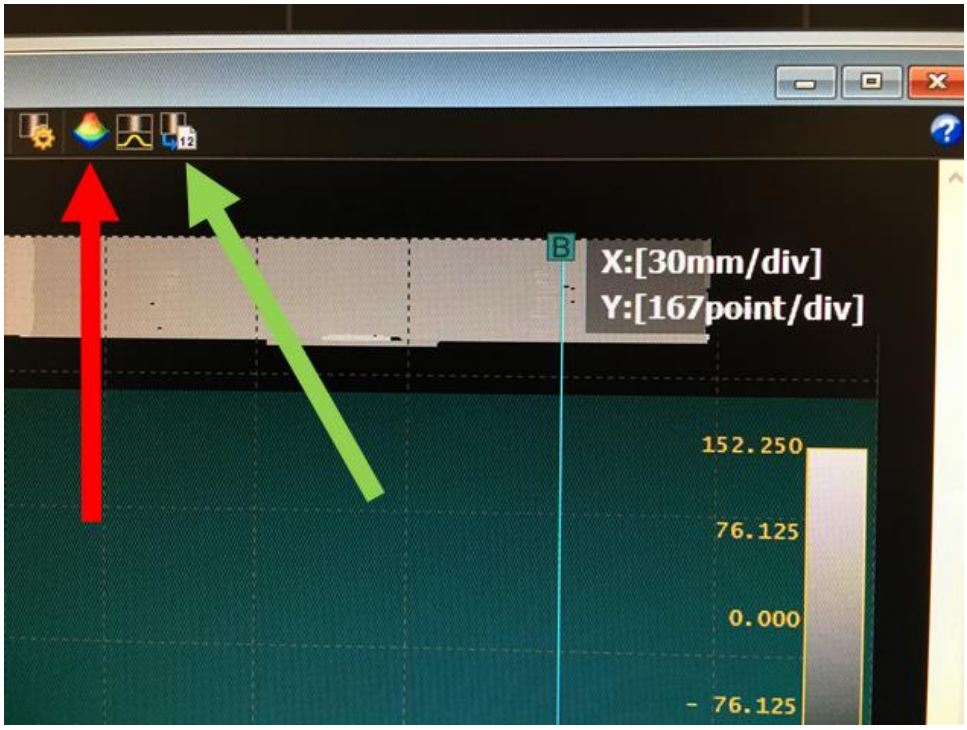

Figure 3. 21 Visualization and storage of measurement data

18. Name Format: angledegree_scandate_specimenname (must have >= 2 digits in angle)
19. Example Name: angle00_070515_600S137
20. Clicking Motor Stop zeroes the displacement
21. Must change program to a new angle if not using zero
22. Click Clear Memory and Batch Stop before each new test.

A preliminary scan should be executed before formal scan of target specimen. There are many nominally identical structural members required to be tested. It is worth spending half or one hour to find appropriate scan views in order for the full-field catch of geometry. For example, a 600 series z-shaped stud may require five directions of scan entries, as in the Figure 3. 22, so as to obtain scan pieces (Figure 3. 23), which cover needed physical information of an interested specimen.

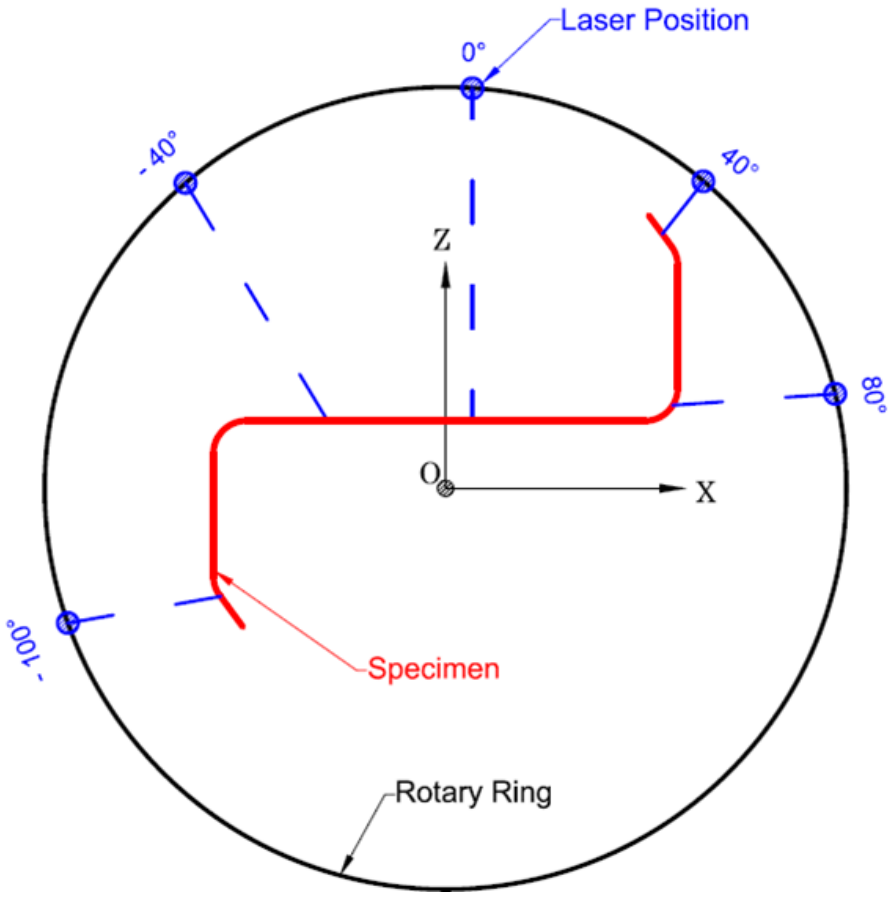

Figure 3. 22 Measurement angles of view in a scan

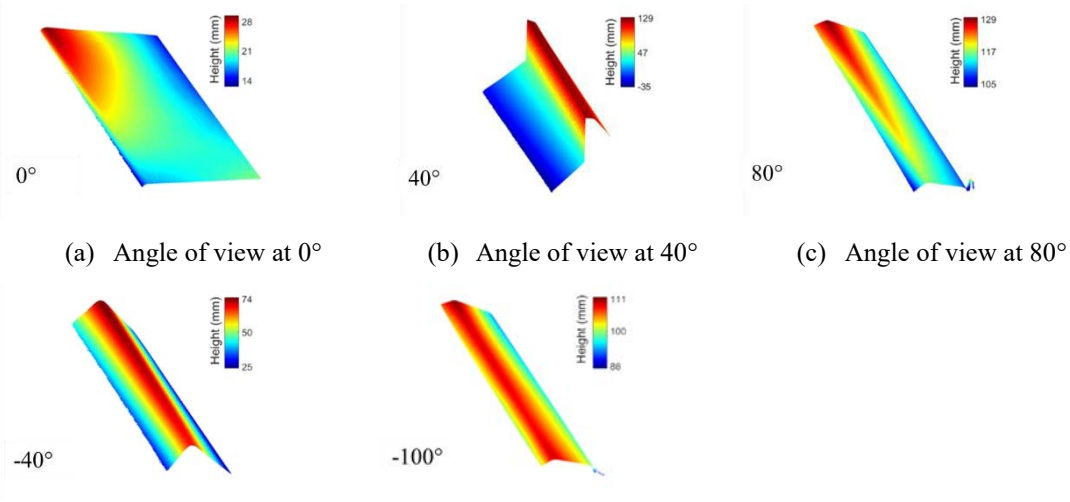

(a) Angle of view at 0° (b) Angle of view at 40° (c) Angle of view at 80°

(d) Angle of view at -40° (e) Angle of view at -80°

Figure 3. 23 Raw data from laser measurement

There is a key requirement to pick up proper scanning angles, that is, a scanned surface must share overlap regions with its adjacent surface. For example, as shown in Figure 3. 23, a surface at 0° angle of view should overlap with surfaces at 40° and -40°. While the surface at angle 40° is required to share a common area with the surface at -100°, it is same for surfaces at -40° and -100°. On the other hand, improper scan directions can lead to poor measurements where obvious abrupt points or bubbles show up in the measurement surface.

3.5 Conclusions

This chapter details the design of a measurement platform for scanning the imperfect geometry of relatively large parts with high precision using a line laser mounted on translational and rotary stages. The intended application is the geometric measurement of cold-formed steel members as used in the construction of buildings. The mechanical realization of the platform is demonstrated

in the paper by detailing its three major components: laser scanner, linear motion system, and rotary stage system. Control and calibration for each component is provided. The platform can accurately scan a part up to 3 m in length and 250 mm in diameter as configured. Multiple scans are required to build-up the geometry - data of surfaces measured from different angles of view are transformed from local coordinates associated with the laser scanner to global coordinates, a process requiring calibration as detailed herein. A multi-pass scan of a z-shaped cold-formed steel member is provided as an example to demonstrate the efficacy of the measurement platform. The point cloud of the part provides data for performing additional analysis on dimensions, plate imperfections, etc., and can form the geometric basis for direct finite element simulations.

Chapter 4 Model Reconstruction and Feature Recognition

This chapter intends to explain image-processing concepts and procedures for data collected from the laser measurement rig. Collected measurement data requires pre-processing before formal image processing, such as data format conversion, invalid data removal, etc. All of these pre-processing steps are discussed in Section 4.1. The next step is rigid surface registration where measurement segments are realigned and transformed to a defined coordinate system. Section 4.2 details the optimization algorithm called the iterative closest point (ICP) application to specific measurement point clouds. Limitations of the algorithm and corresponding solutions are discussed as well. Moreover, the manual of self-programmed GUI is included for future learning purposes. A novel feature recognition method, similar in sprint of gradients that drive the Harris detector, is implemented. Further development of this feature recognition method is stated with noise elimination and outliers' removal in Section 4.3. Example studies for three shapes of structural members are demonstrated in Section 4.4, where each member experiences the entire image-processing steps.

4.1 Pre-processing step

4.1.1 Data Conversion

The data collected from the laser scanner are in a *comma separated values* format (.csv). Image-processing environment is carried out in MATLAB, which requires imported data in *Excel Worksheet* format (.xlsx)[1]. Thus all saved files have to be converted into the *Excel Worksheet* format. A function called *CSV2Excel.m* is applied with its script posted in the appendix (Ap. 2). A graphic user interface (GUI) is created to perform conversions, as shown in Figure 4. 1. This GUI can select multiple *CSV* files when the "Select" button is clicked. The click of the conversion button can convert all selected files into the *Excel Worksheet* format.

1. Following image processing programs can only read .xlsx file so that all .csv files are converted.

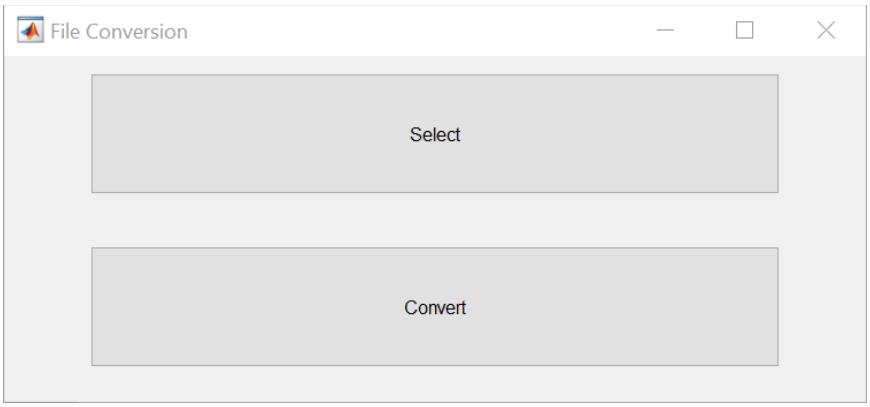

Figure 4. 1 Conversion GUI

4.1.2 Data Trimmer

This step is an important pre-processing step, which is targeted at removal of most invalid data from measurements. Invalid data can be generated during scanning. The line laser projects 800 points per cross section with scan widths up to 10 inches (240 mm). Objects at different scan directions may not occupy all these laser points. Instead, laser points may be projected on other articles in the environment or beyond effective scan range. The former therefore results in an outlier, and the latter produces invalid data *-999.99* (Figure 4. 2).

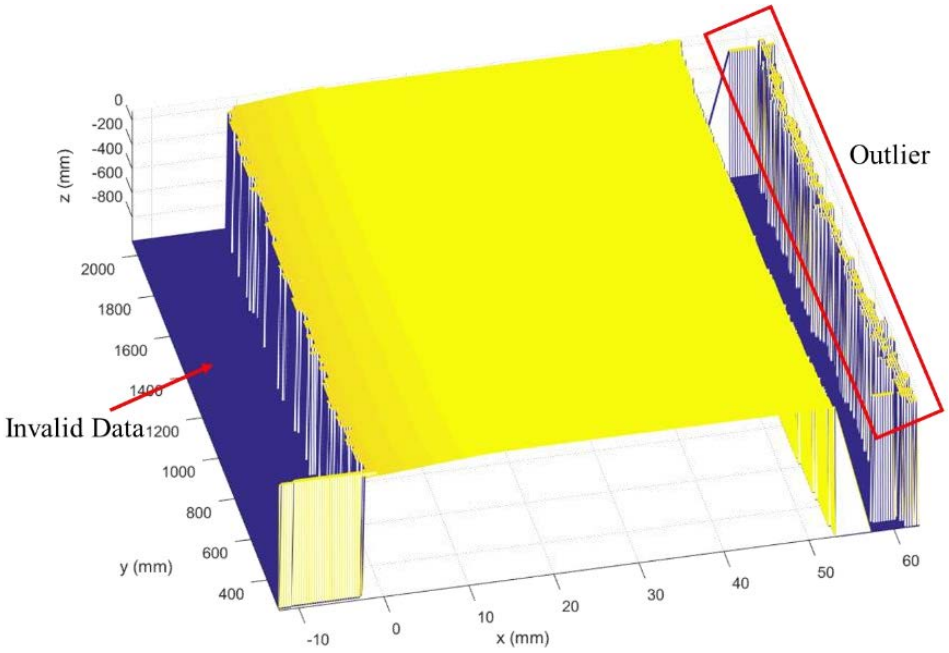

Figure 4. 2 Raw measurement with outlier and invalid data shown

A data trimmer process can be executed by design lower and upper boundaries of x, y, z coordinates respectively. A GUI system (Figure 4. 3) created by the main function, *impost1.m* (script is attached in appendix Ap.2), can be competent for the goal of invalid data removal. As shown in Figure 4. 3, Inputting proper boundary limits can delete most of the unwanted data, i.e., outlier and invalid data. This step does not provide a noise-filtering process.

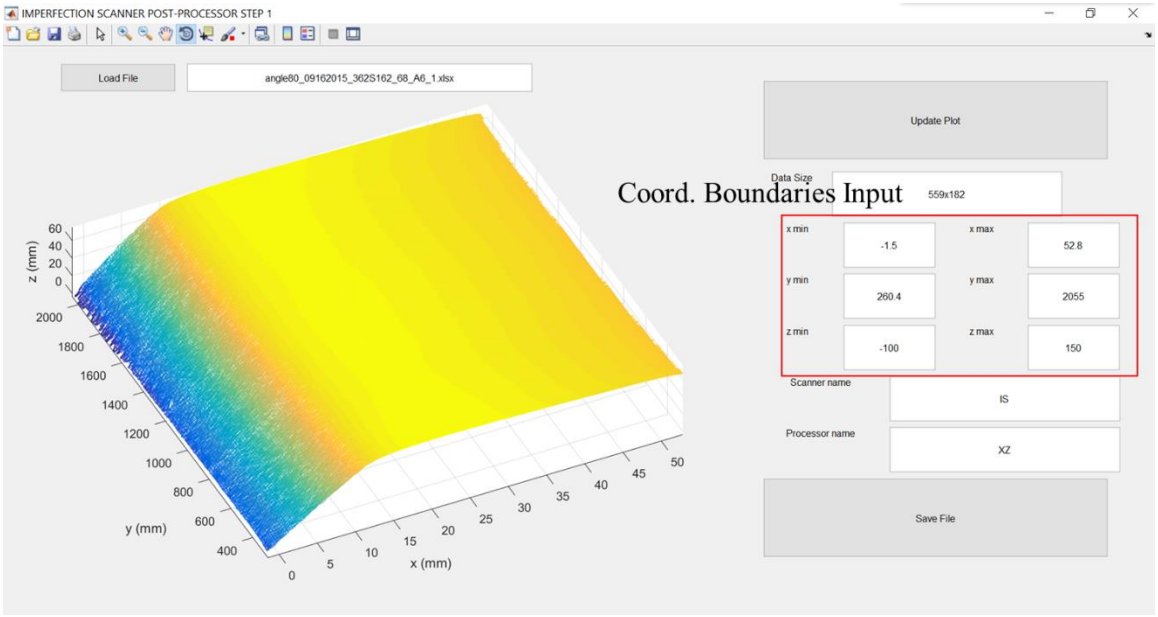

Figure 4. 3 Data trimmer GUI and result demonstration

If data files are properly named in the format, as discussed at the beginning of Chapter 3, renaming the data file is not required. Otherwise, data must be renamed following the format: angle*XX*_MMDDYY_*specimen name*. Users can click "Save File" and trimmed data together with other information are saved as cell arrays with a unified name *datafile*. The first cell of the data file is about general information, including specimen name, corresponding scanning angle, scanning data, name of scanner and processor. While the second and fourth cell arrays correspond to measurement points coordinates z, x, and y, respectively.

4.2 Surface Registration

As depicted in the Chapter 3, the 3D laser imperfection measurement rig in the Thin-Walled Structures Laboratory is composed of a rotating 2D laser range scanner, which typically scans an object from one direction at a time (Figure 4. 4a & b). Complex geometry requires more than one scan entry in order to collect entire sections' information. Entry numbers toward a specific object depend upon the complexity of its geometry. A lipped C stud only requires five angles (Figure 4. 6), i.e., 0°, 40°, -40°, 120°, -120°, while a back-to-back lipped C demands nine angles (Figure 4. 7). Scanned directions do not require strict symmetry as a Z purlin, measurement directions of which are 0°, 40°, -40°, 80°, -100°, as shown in Figure 4. 5.

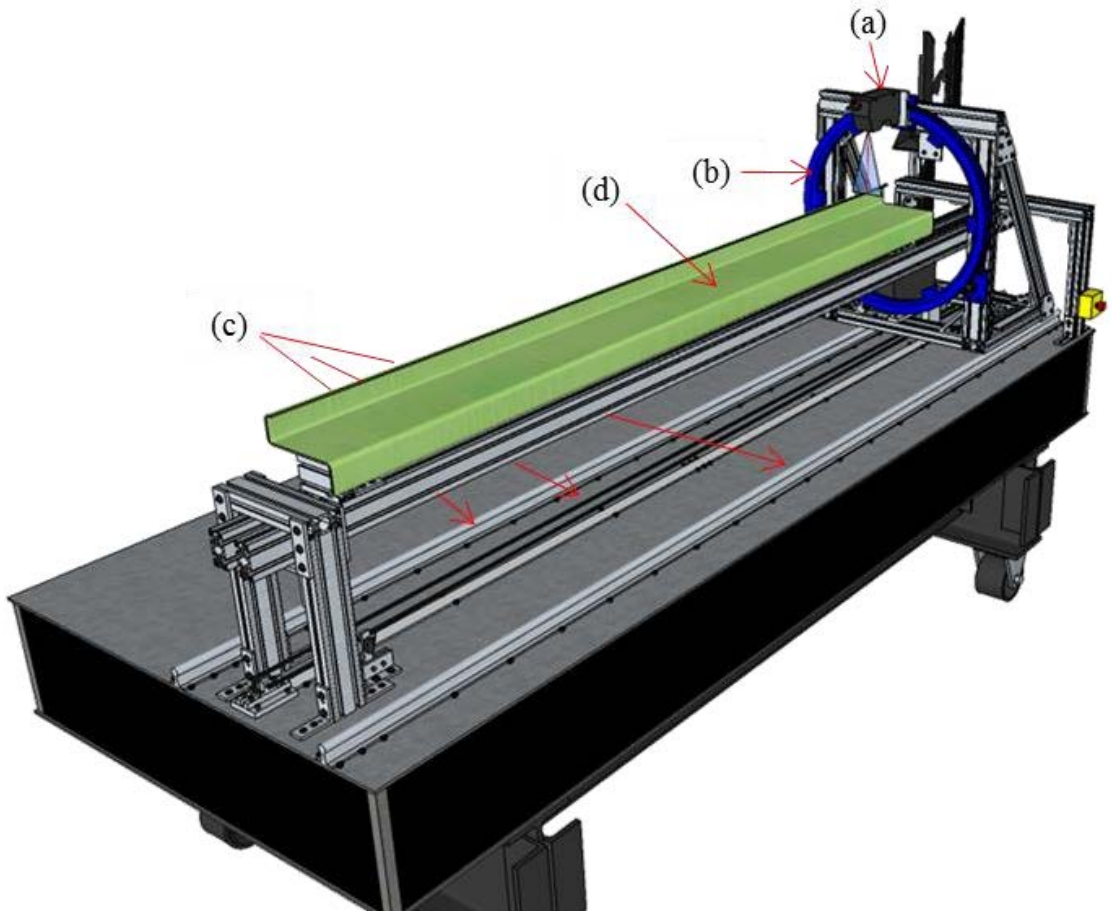

Figure 4. 4 Laser-Based Imperfection Measurement Platform: (a) laser scanner; (b) large rotary stage; (c) linear motion system; (d) Z-shape specimen

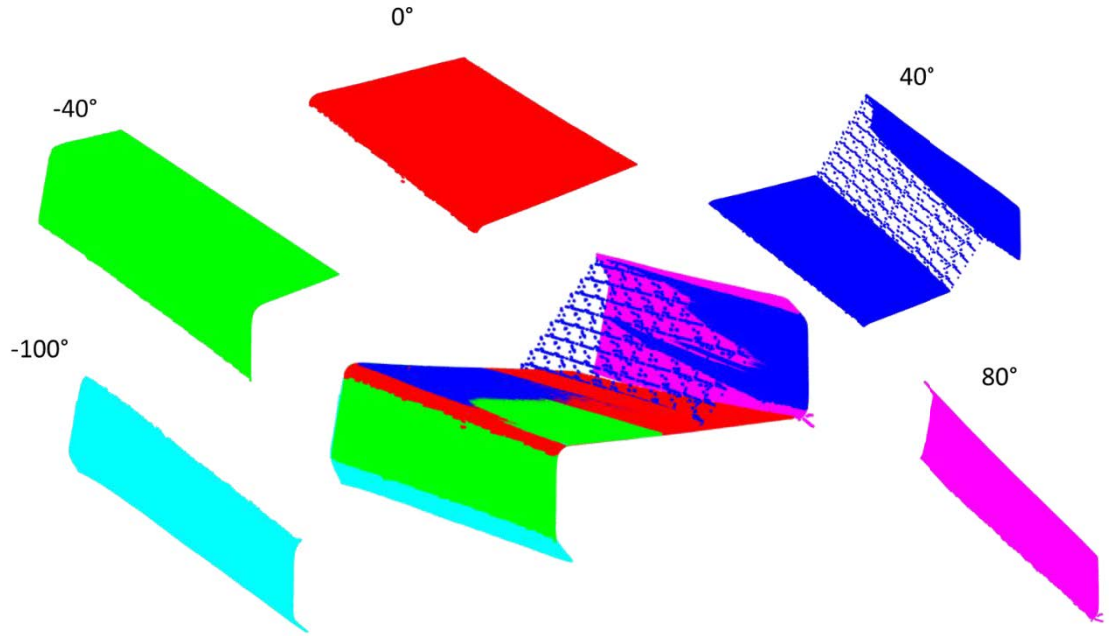

Figure 4. 5 Five different scans used to develop Z sections

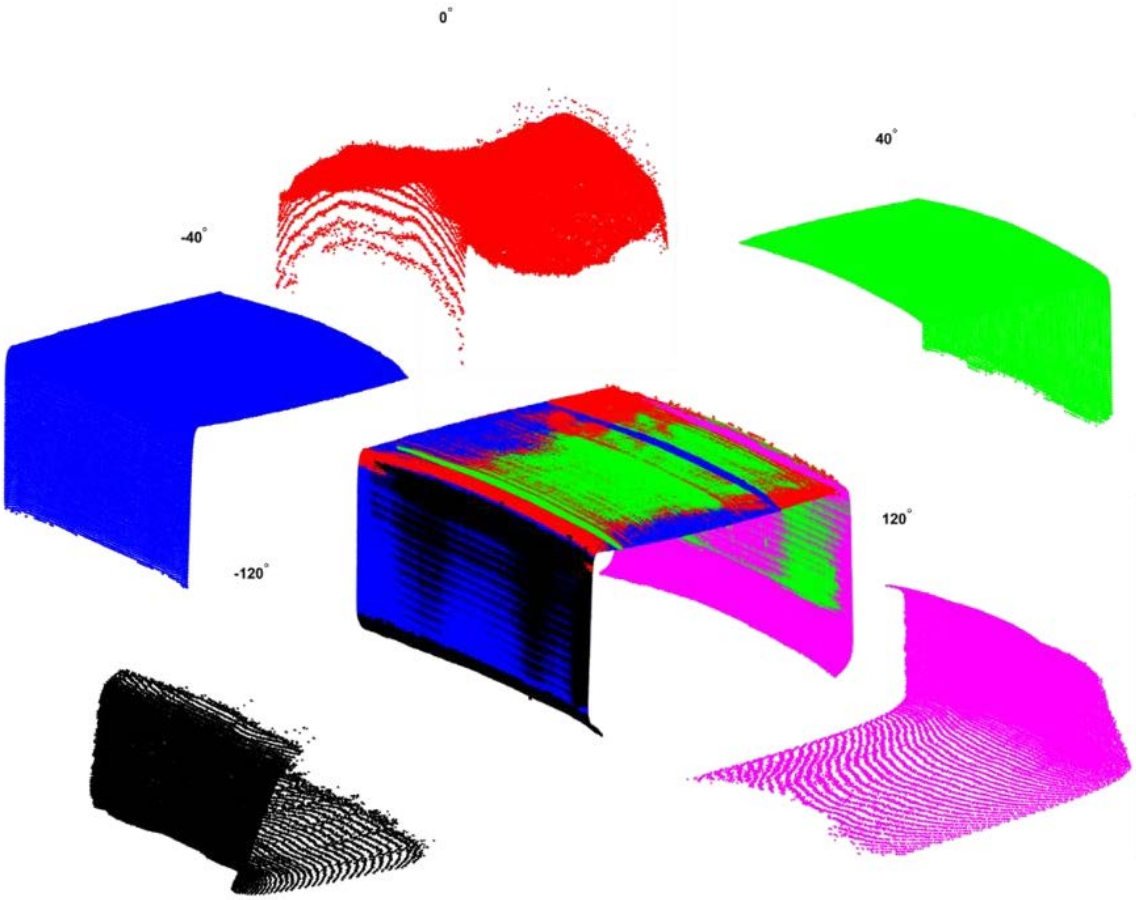

Figure 4. 6 Five different scans used to develop C sections

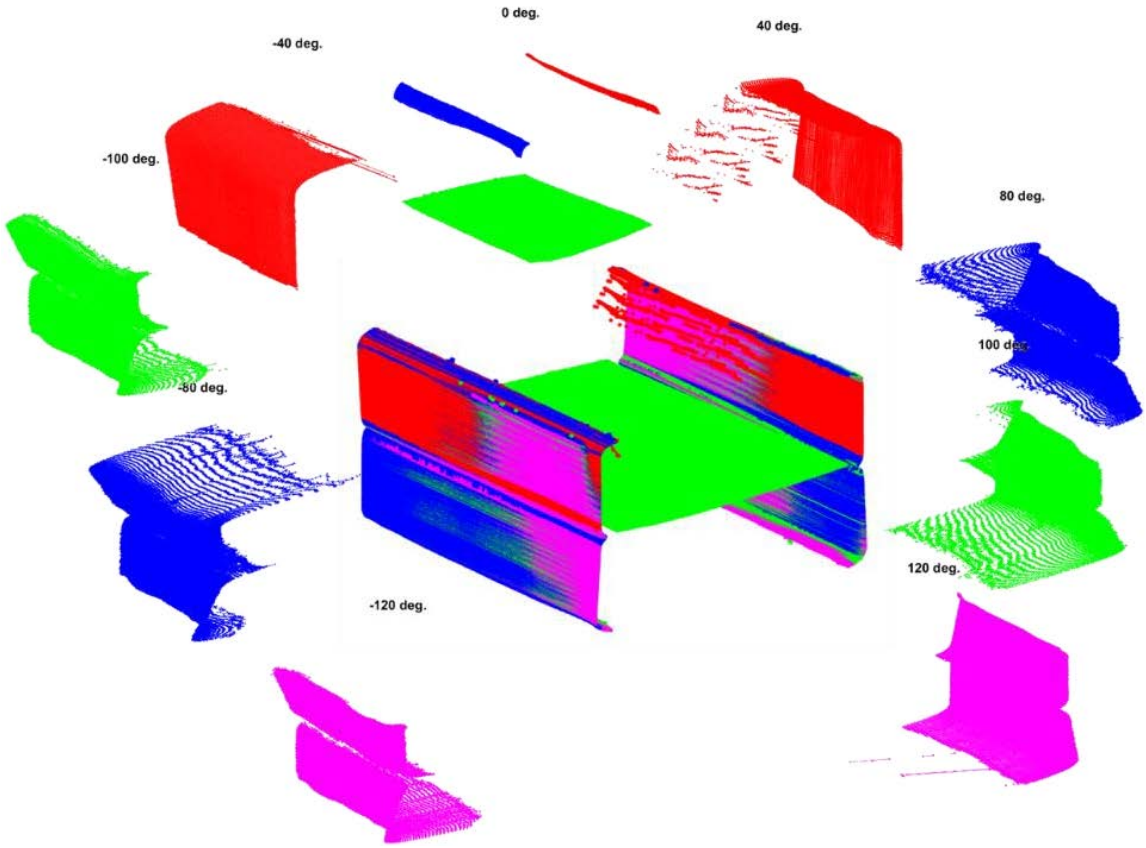

Figure 4. 7 Nine different scans used to develop BUC

Scanned pieces are located in local sensor coordinates systems and have to be realigned or transformed into a self-defined global coordinate system. The realignment or transformation of surface is called “surface registration.” Translations and transformations of specific measurement segments can be estimated from various methods such as geometric features, gradients and normal variations of surface, colors, heat map, etc. Regarding the characteristics of laser measurement point clouds, only geometric information is required so that geometric features are utilized for transformation values’ optimization.

4.2.1 Surface registration with modified ICP

To start with surface registration, an initial guess should be utilized. Because the platform comprises a position encoder installed on linear stage (Figure 4. 4c), longitudinal positions of scanned surfaces can be accurately recorded toward measurement data. The sensor coordinates system of a measured surface 0° is taken as a global coordinate system. Six degrees of freedom (three rotations and three translations) can be minimized to 3 degrees of freedom [one rotation along longitudinal direction (y); two translations on cross-section plane (x, z)]. Thus only three quantities of initial guess are needed for the laser measurement platform. These quantities are obtained from the calibration mentioned in Chapter 3. They can assure target measurement planes are close enough to the reference planes for utilizing the iterative closest point (ICP) algorithm. Fundamental concepts and general procedures of ICP are discussed in Chapter 2. This section details modified ICP on 3D data taken from the laser measurement platform.

A reference plane is selected at the beginning, which shares obvious geometric features with the target plane in general. Overlapping areas with obvious features are extracted from both reference and target planes with a user-defined window function (Figure 4. 8). The reference surface is considered to be "correct" and is used to compare distance of cropped areas with target surface. The goal is to minimize distance, known as "error," between the reference and the target.

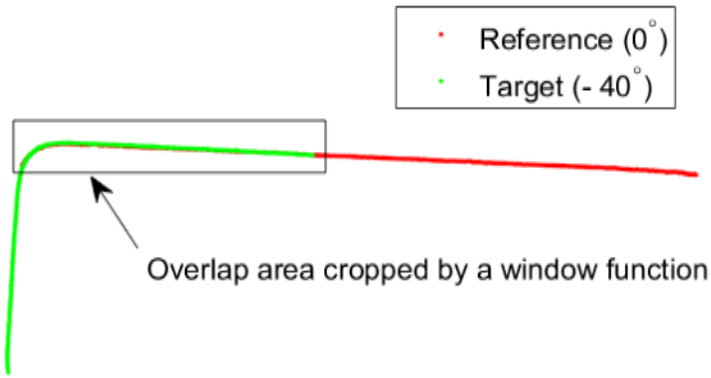

Figure 4. 8 Feature extraction for ICP

Regarding the 2D cross section, the cropped set of reference data is designated as the "Model" ***M***, and the cropped target data as ***D*** (Besl and Mckay 1991). The user-defined window function cropping data should guarantee that points range of ***D*** should be a subset to that of ***M***. The objective of ICP is to minimize the distance between ***D*** and ***M***, i.e.:

$$e = \left\| \overline{D} - \overline{M} \right\| \qquad \text{Eq 4. 1}$$

where $\overline{D}$ is an updated $n\times 2$ array transformed from ***D*** through 76;

$$\overline{D}^T = \begin{bmatrix} \cos\theta_y & \sin\theta_y \\ -\sin\theta_y & \cos\theta_y \end{bmatrix} D^T + \begin{bmatrix} x_t \\ z_t \end{bmatrix} \qquad \text{Eq 4. 2}$$

where θ_y is a rotation angle and x_t and z_t are translation values along the x and z axes;

$\overline{M}$ is an updated $m\times 2$ array screened from ***M*** such that points in $\overline{M}$ correspond to points in $\overline{D}$ in terms of closest distance. A special search algorithm is coded for finding the closest point pair between $\overline{M}$ and $\overline{D}$ in each iteration for the purpose of computation rate acceleration (Figure 4. 9). All points in ***M*** are utilized to find distance from $\overline{D}$ so that correspondence $\overline{M}$ is created in the first iteration. Starting from second iteration, every point in $\overline{M}$ is searched in proximity of the closest point in the previous iteration once $\overline{D}$ is updated. Weighting values of the estimated correspondence pairs are unified to all pairs. However, in the future updated algorithm, boundary effects will be minimized and specific penalization weighting factors will be carefully selected.

Because the rotation angle is one of the factors in error function minimization, a trust region reflective nonlinear least-squares algorithm [Eq. (2)] is utilized in registration. Iteration of ICP is terminated when error variation $\Delta\|e\| < 10^{-6}$. The result of the minimization is similar to that

depicted in Figure 4. 9b. Total iteration time for the minimization is less than 0.1s on a desktop computer, and the algorithm is found to be suitable for model optimization with the larger point cloud sets developed experimentally. There is a drawback that local minima may contribute to termination of algorithm. Future algorithms may adopt perturbations in the initial conditions and then select the best result (Simon 1996).

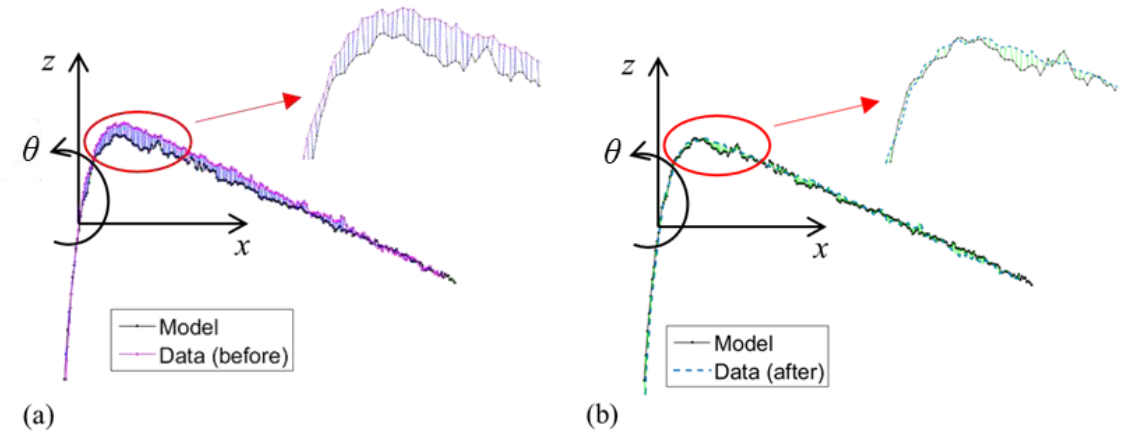

Figure 4. 9 Illustration of ICP algorithm: (a) before applying ICP (b) after applying ICP.

Similar to a 2D cross section, a 3D surface is registered with six variables: three rotations and three translations. As previously mentioned, the registration can be reduced to three variables: two translations along x and z axes (cross section plane) and a rotation along the y axis (longitudinal direction). Unlike Figure 4. 9, for a three-dimensional object such as surface Ω_t compared with reference surface Ω_r in Figure 4. 10, the translations and rotation are not independent at each cross-section. A single set of error minimized values for the entire surface are required.

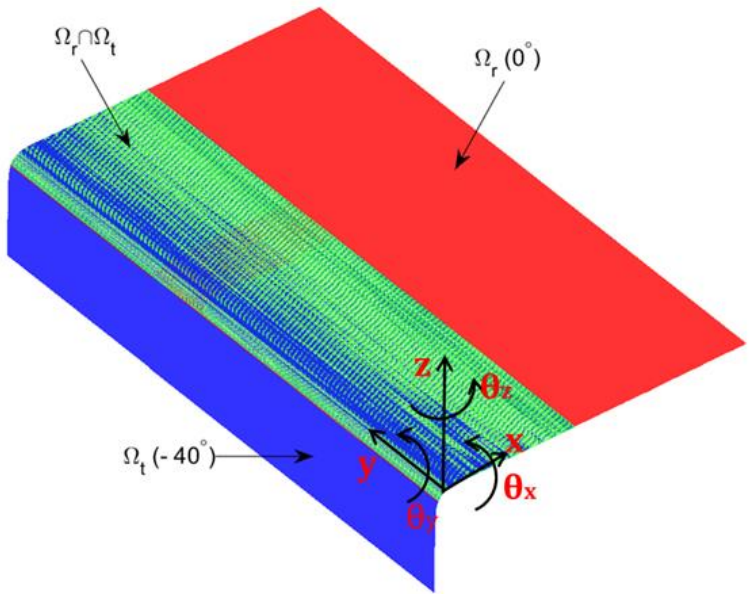

Figure 4. 10 3D Surface Registration: Ω_r is the reference surface, and Ω_t is the target surface. They overlap at $\Omega_o = \Omega_r \cap$ [redacted]

A pre-defined window (Figure 4. 11a) extract shared area between the reference surface, Ω_r, and the target surface, Ω_t. It is assumed that the 3D "Data" is a rigid body in which all cross sections in "Data" are taken into consideration during registration. Similar error function, as shown in Eq. (3), is employed where all points in the window are summed up. Iterations of error minimization are executed until optimized transformation values θ_y, x_t, z_t are found. Surface registration results have been shown in (Figure 4. 11b).

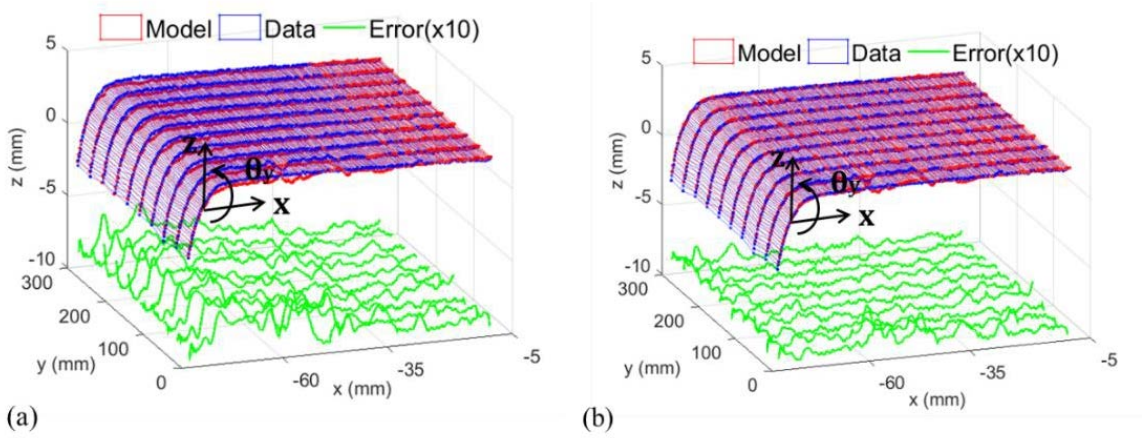

Figure 4. 11 A 3D example with ICP optimization where green curves display errors between 'Model' and 'Data' a) before ICP optimization; b) after ICP optimization

4.2.2 Manual to Implemented GUI system

A GUI system is implemented for easy access to surface registration, as illustrated in Figure 4. 12, where the MATLAB script is attached in the appendix (Ap. 2). There is a waiting list called *All Files* showing all data segments to be processed. The *Plotted Files* show the processed segments with corresponding image realizations shown on left side of the GUI. ICP optimization in addition to surface registration is placed on the right side of the GUI. There are reference lists and target lists located on the top of right side GUI. The reference list provides well-registered segments; the target surface (sensor surface) bar lists measured segments that wait for registration. The window function, as mentioned in Section 4.2.1, extracts overlapped regions from the reference surface and target surface via definition of upper and lower limits of x and z coordinates. These two surfaces are roughly aligned from translations and rotation, the values of which are calibrated in advance. As the user selects the reference and target surface and inputs the x/z limits, ICP optimization can start by clicking *Optimize!* The estimated transformation values are given, which can be inputted in the lower part of right-side GUI for registration. One can choose to save multiple segments or a single segment by checking the optional box. The saved file containing cell array is similar to the file saved from *Data Trimmer*. If *Single* is checked, the first cell stores general information of

processed data; the second stores x coordinates of a registered segment; the third stores y coordinates (longitudinal direction); and the fourth stores z coordinates.

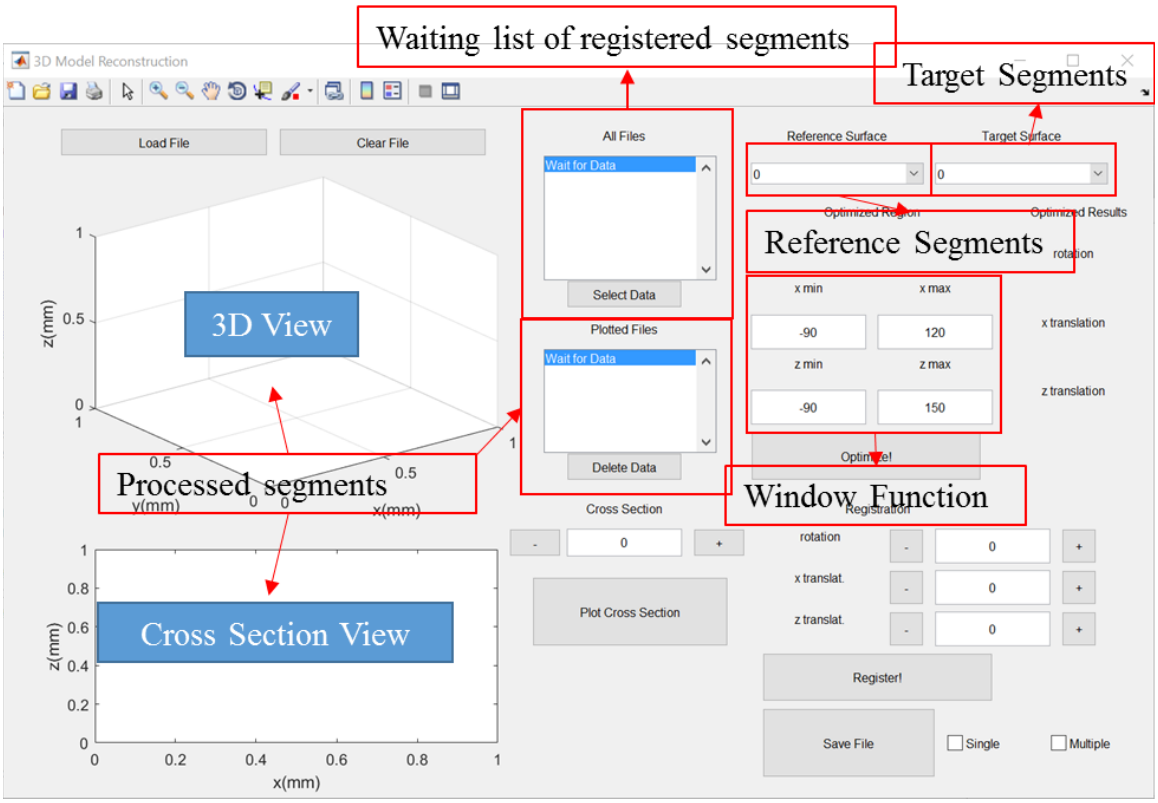

Figure 4. 12 Interface of surface registration using ICP optimization

4.3 Feature Recognition

Feature recognition is targeted at identifying geometric features with certain geometric characteristics. In the research of imperfection measurement of cold-formed steel members, the major geometric features are flat elements and curved elements (Figure 4. 13a). With the feature recognition, one can easily find important dimension information for high-fidelity modeling, quality inspections, primary geometric imperfections, etc. (Figure 4. 13b).

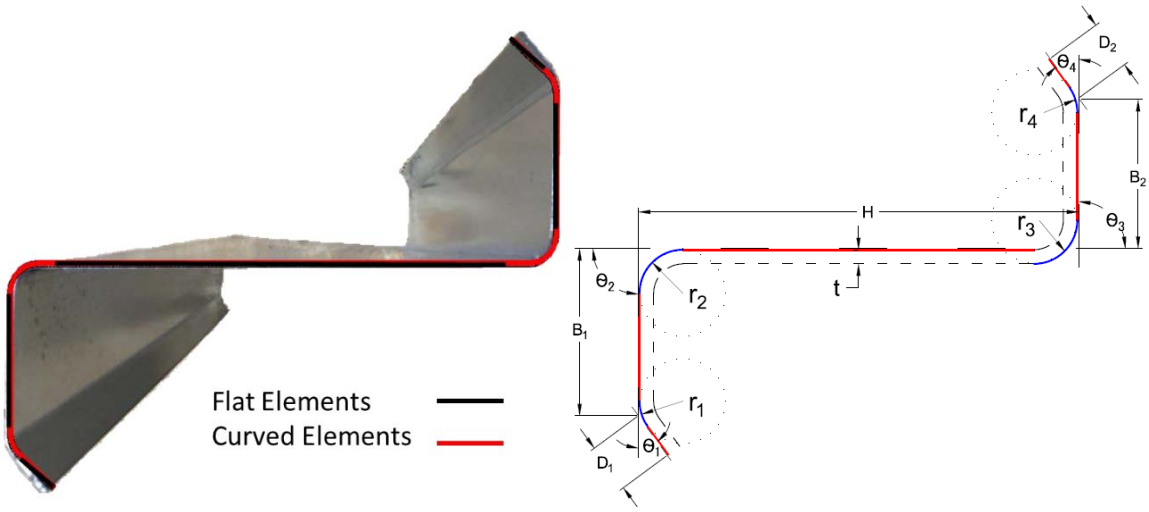

Figure 4. 13 Typical structural members with corners and flat elements (a) goal of feature recognition; (b) dimension findings from feature recognition.

There are two versions of feature recognitions with knowledge advancement of the author. The original version is presented in Zhao et al. (2016) and is briefly described in Section 4.3.1. The current version is carefully discussed in Section 4.3.2.

4.3.1 Original Version of Feature Recognition

Each cross section of a 3D cold-formed steel model has been sorted and recorded after surface registration. Feature recognition therefore can be performed with a 3D point cloud model in the unit of cross section. The procedures comprise three steps: removal of outliers, detection of corner points, and determination of corner regions. Figures in this section are taken from Zhao et al. (2016).

Removal of Outliers

Optical measurements are sensitive to their surrounding environments, such as ambient light, scanned surface, test setup, etc., results of which sometimes contain various outliers. A simple threshold cannot remove all outliers. Manual removal, on the other hand, is tedious considering outliers vary along cross sections. Smoothing and filtering functions can compromise accuracy. An automatic outlier removal algorithm is proposed with two tests. Each registered cross section (at a

fixed *y* value) is tested with the algorithm, proceeding point-to-point from one end of cross section (Figure 4. 14a). The first test (T1) can identify outliers that are outside of a specified angular region (2α) from the current point; the following test (T2) again recognizes outliers that are outside a specified threshold radial distance, as shown in Figure 4. 14b. For a valid present point (p_o in Figure 4. 14b), the next closest point is evaluated; if it is outside of the 2α angle or outside of the *a* radius, it is treated as an outlier, and a linearly interpolated point will replace it when the next valid point that satisfies the T1 and T2 tests is discovered. The angular region and threshold radius vary with shape of scanned specimens, measurement environment, and scanned surfaces. For the example of Figure 4. 14, α=75.5°, *r*=2.95 mm was selected. The process is repeated for all cross sections along *y*.

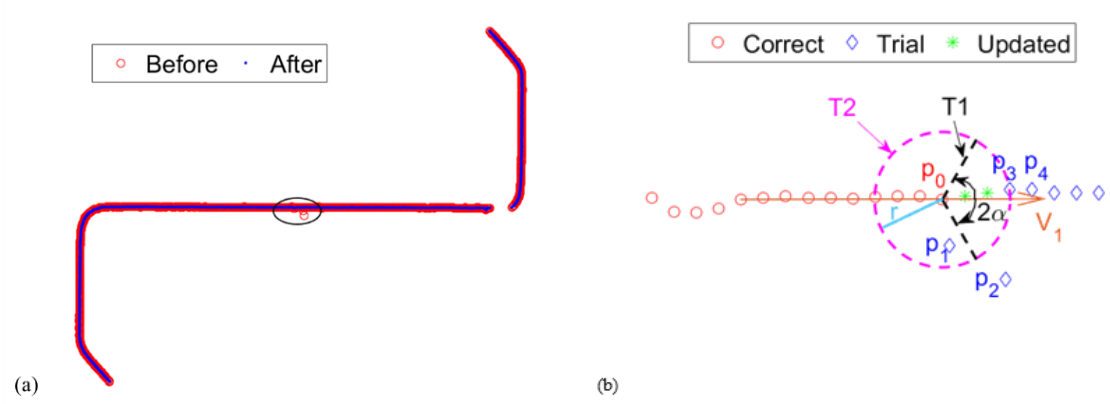

Figure 4. 14 A method to remove outliers of a cross section (a) a cross section before and after removal of outliers; (b) procedures of outliers' removal. A small break between the web and the right flange since the scanner can only take external side measurements is present. This break does not affect further applications.

Corner point detection from variation of direction vectors

As each cross section is evaluated from end to end, a present direction vector, q_i, built up from the points over length scale, *h*, may be ascertained. Variation in this direction vector along the cross section gives a way to estimate the presence of curves in the section as illustrated in Figure 4. 15. Particularly the change in angle β may be calculated from:

$$\sin\beta_i = \frac{q_i \times q_{i-1}}{\|q_i \times q_{i-1}\|}$$ Eq 4. 3

In the interest sections a length scale for the vector q equal to $2t$, or 10 points along the section, is used.

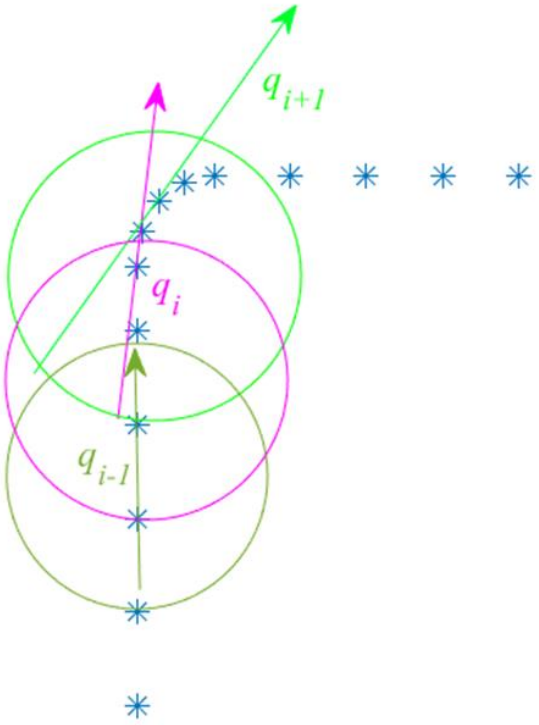

Figure 4. 15 Variations of direction vectors: q_{i-1}, q_i, q_{i+1}

A typical realization of sin(β) for a cross-section of the example cross section, Z, is illustrated in Figure 4. 16b. The four corners are identified as deviations from 0 in the example section. A small break shows up in the data near the right flange/web junction as only the external side of the specimen is exposed to the sensor. This contributes to additional noise in the sin(β) realization near this location.

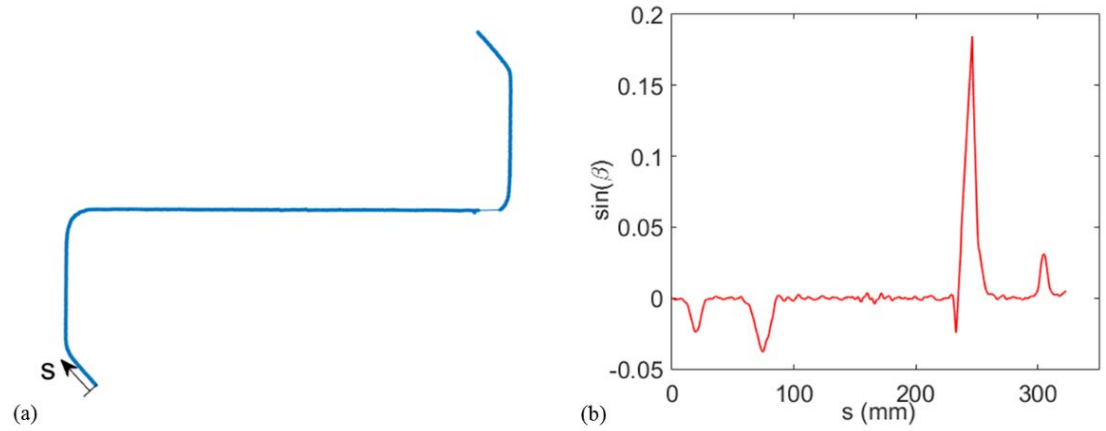

Figure 4. 16 Finding variations of a typical cross section of a structural member: (a) definition of a natural coordinate system; (b) variations sin β along natural coordinate s.

Determination of corner regions

A threshold of 0.006 radian for |sin(β)| (Figure 4. 17a) is chosen to determine the corner regions (Figure 4. 17b). The largest four areas above the threshold are identified as the corner regions, knowing that this section has only four corner regions. This neglects the spurious region such as the one near the small break in the data. Therefore, all other points different from corners can be sorted as the flats of the section.

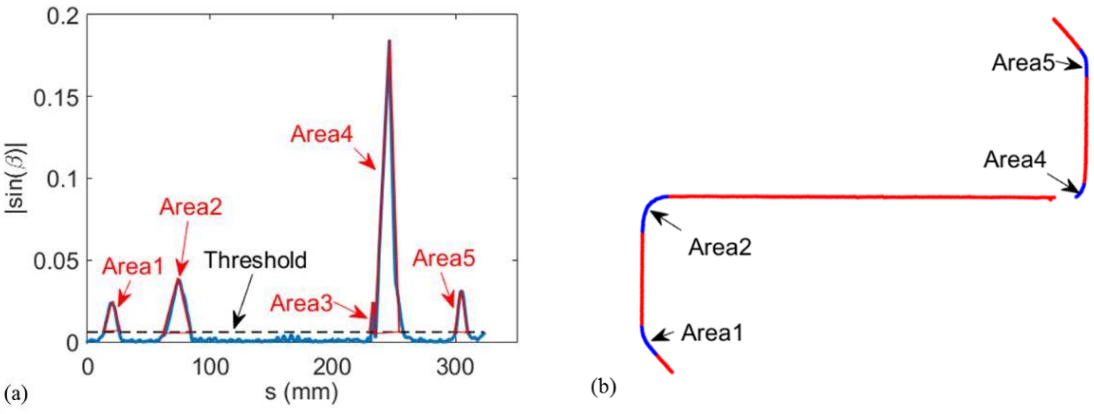

Figure 4. 17 Determination of corner regions: (a) potential corner regions from a threshold; (b) determination four corner regions by areas' comparison.

This feature recognition algorithm prevails towards a registered 3D point-cloud model. Cross sections of the 3D model is processed one by one and $|\sin(\beta)|$ is computed and evaluated to find corner regions leading to feature recognition for the entire model depicted in Figure 4. 18.

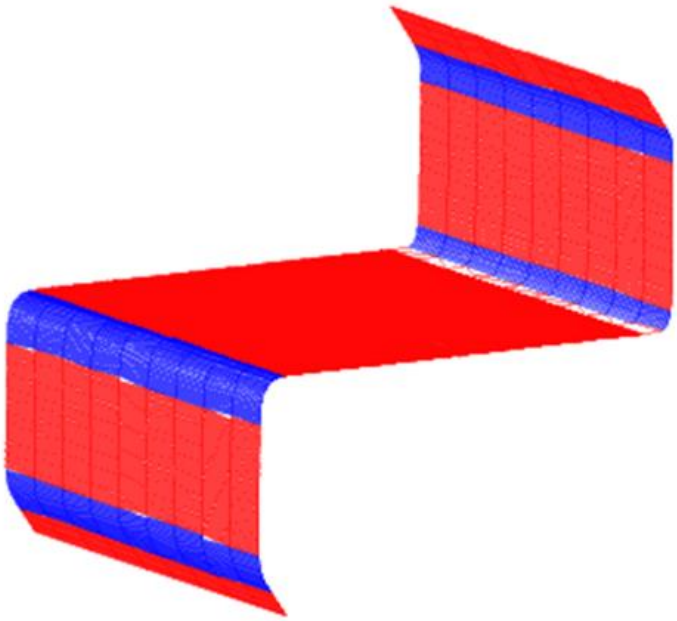

Figure 4. 18 Result of a 3D model under feature recognition. (corner regions in blue, flat regions in red)

There are two drawbacks of the original version of feature recognition. The first drawback is that it is not flexible in recognizing corners. The algorithm is restrained to four corners recognition. If more or less corners are recognized, parametric study of the corner threshold has to be intensively carried out, which is typically time consuming. The second drawback is the instability of potential corner points' search in the algorithm. The search angles and radius have to be carefully set, and input data should be well cleaned in advance. Otherwise, a death loop of search can occur, and time may be wasted.

4.3.2 Current Version of Feature Recognition

As the author obtains more experience and knowledge toward feature recognition, a new algorithm (the script is shown in the appendix (Ap.2) is proposed, which is more adaptive and robust. The

method requires four steps to process geometric features: (1) specific features should be categorized at the beginning, i.e., knowledge of numbers of corners and flats; (2) manual selection of data at a sensor view correspond to specific geometric features with best resolution; (3) outliers and noise removal are specially designed, methods of which are similar with the old version but more efficient and effective; (4) multiple feature-identifications tests are conceived and executed to guarantee features selection. The following contexts explain all these procedures in a careful manner using complicated geometry, back-to-back lipped c channels (BUC), for illustration.

Feature Categorization

This is step is relatively simple but important. It is necessary to recognize numbers and positions of geometric features in a cross section. In the example of Figure 4. 19, the BUC has eight corners (Figure 4. 19b), which separate lips, flanges, and a web (available data contains raw data where surfaces are exposed to the sensor). Each feature, knowing their relative locations and characteristics, is denoted and saved for the second step.

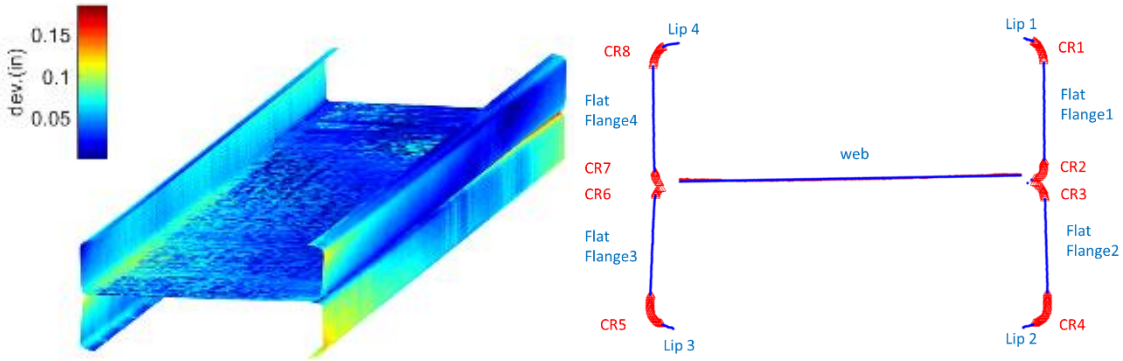

Figure 4. 19 Example of feature categorization: (a) typical BUC registered model; (b) geometric features in a cross-section view.

Manual selection of measurement segments

Considering restrained measurement directions, selections of measurement data from various directions are executed manually. As illustrated in Figure 4. 7, there are many measurement segments taken from different directions, nine segments for BUC, for example. The measurement scheme is carefully selected to ensure there are enough points to cover all geometric information, with scan resolution in consideration as well. The goal of manual selection therefore is to pick up the best-resolution data corresponding to specific features from a series of measurements. Take BUC as an example, corner regions may employ right out of nine measurements (Figure 4. 19b): *CR1* from 40°, *CR2* from 100°, *CR3* from 80°, *CR4* from 120°, *CR5* from -120°, *CR6* from -80°, *CR7* from -100°, *CR8* from -40°. While flat regions may employ seven out of nine measurements: *Lip1* from 0°, *Lip2* from 120°, *Lip3* from -120°, *Lip4* from 0°, *FF1* (flat flange 1) from 100°, *FF2* from 80°, *FF3* from -80°, *FF4* from -100°.

This step is important because it can easily have an impact on noise filtering/removal together with feature recognition effects. Pre-processing sometimes may be required. Again take BUC as an example. Measurements from angles 80, 100, -80, and -100 generally contain too much geometric information to reduce computation efficiency and hinder feature identification in the fourth step. Therefore, proper pieces are extracted from a measurement segments, as illustrated in Figure 4. 20, a surface taken from an 80° angle. All these extractions are carried out in the unit of a cross section. However, these preprocesses vary relying on shapes of specimens. The advantage of preprocess results is closely connected to the following processing convenience; thus the preprocess is worth much attention.

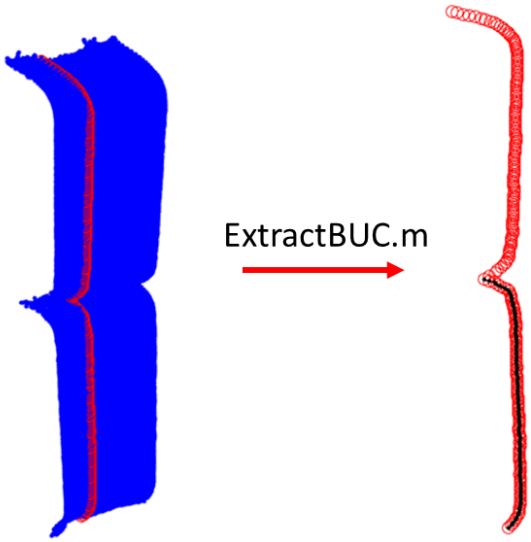

Figure 4. 20 Preprocess of BUC for selection

Outliers and Noise Removal

Outliers and noise removal are the keys to feature recognition. Three different methods may be applied to measurement pieces to effectively remove noise or outliers. The easiest way is to set a threshold and directly cut data boundaries to eventually obtain clean data. This removal method can be utilized only when features are not sensitive to boundary conditions. As is shown in Figure 4. 21, these two segments (angles 40° and -40°) have good resolution in corner regions, while boundaries are not in the interest. Thus this straightforward method is applied. It should be noted that data from 40° and -40° directions may not go through the pre-processing.

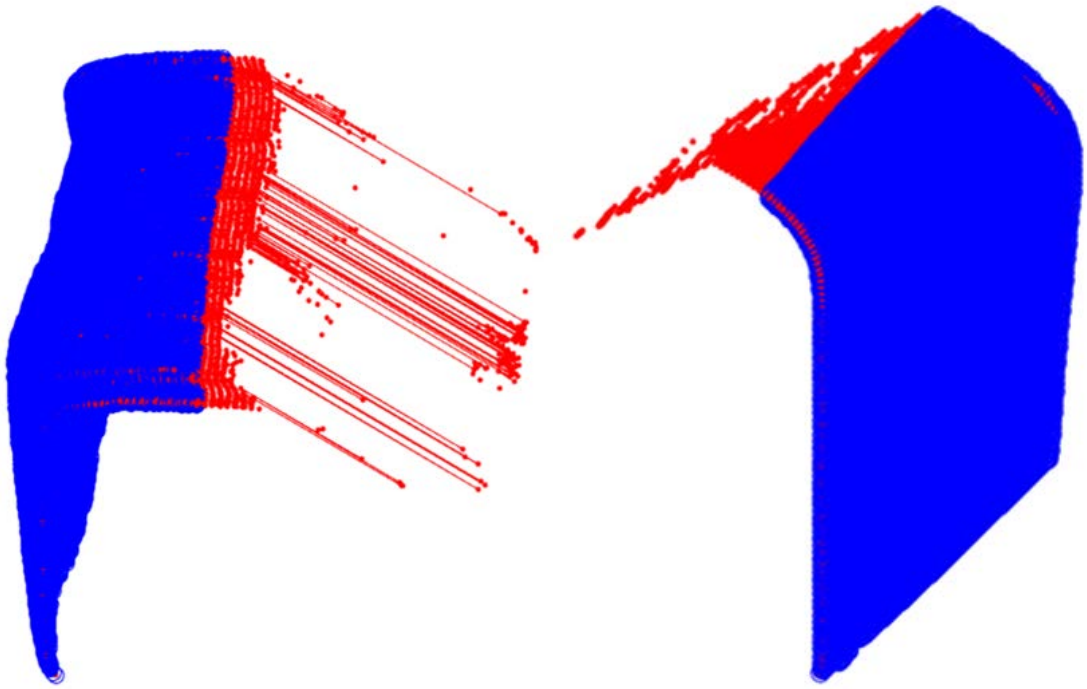

Figure 4. 21 Outliers removal by setting threshold (segments taken from 40° and -40°)

The second outliers' removal algorithm is slightly complicated in which four sub-steps proceed. The first sub-step is to smooth data along the specimen. Missing data in the boundary is detected and complemented meanwhile. The second sub-step is to extract data in the purpose of fast noise removal. The third sub-step is cross-sectional smoothing. This step is similar to the method used in the original version of feature recognition (Figure 4. 14b) where data along cross sections, point-to-point, are removed and resorted. The final step is to remove noise on the boundary. Outliers on the boundary have relatively large gradients. A threshold can be set to gradients from the extracted data and points with larger gradients are dismissed as noise. This algorithm is mainly designed for measurements at angle 120° and -120° (lip regions). The example (BUC sections) displayed in the Figure 4. 22 are preprocessed and upper flanges of sections are excluded.

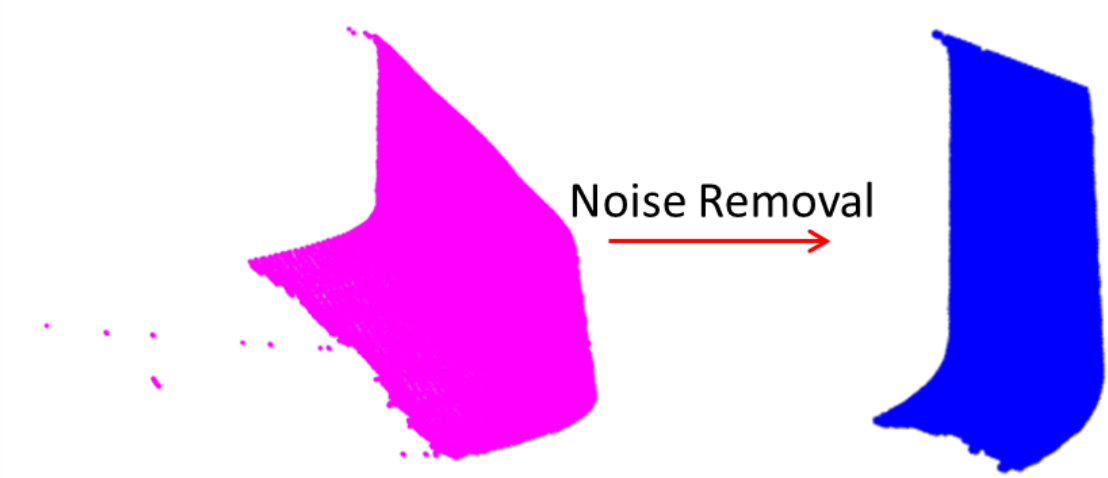

Figure 4. 22 Results of outliers and noise removal using method 2

The third method is embedded in the main feature recognition algorithm to all measurements before processing. In this step, both outlier removal and points resorting (the same as the old version presorting algorithm Figure 4. 14b) are applied. The target of the third noise filter method is to not only remove the outlier for the example in Figure 4. 23 but also smooth/resort the obvious error points. Considering that the presorting algorithm is sensitive to the outlier, removals of outliers are executed in advance to avoid misleading information in presorting algorithm.

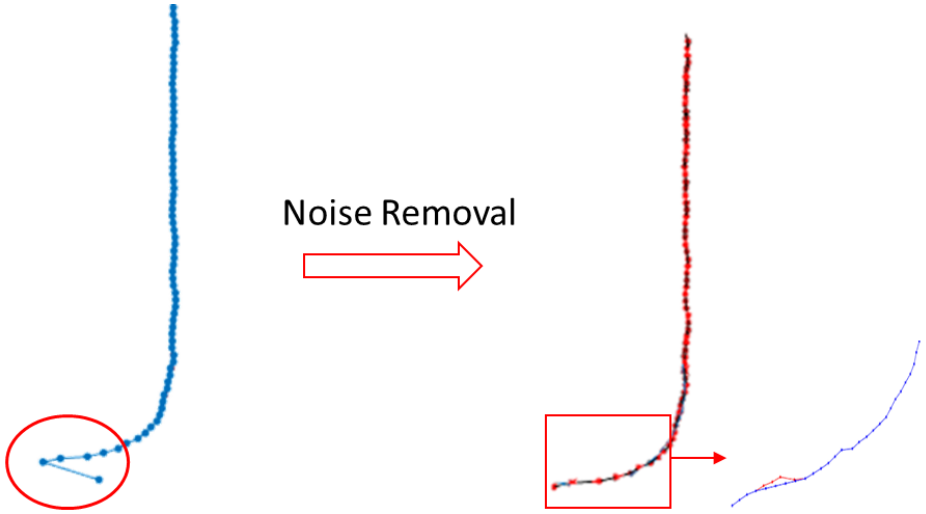

Figure 4. 23 Noise removal using the third method of filtering (cross section from 3D example shown in Figure 4.22)

The procedure of outliers' removal is as follows:

(1) A point i in a cross section can be denoted as (x_i, z_i), its previous point i-1 is denoted as (x_{i-1}, z_{i-1}), and the next point i+1 is denoted as (x_{i+1}, z_{i+1}). Point i+1 is denoted as potential outlier if the following relationship is reached (Eq 4. 4 or Eq 4. 5):

$$x_{i-1} - x_i > \frac{(x_i - x_{i+1})}{4} \quad \text{Eq 4. 4}$$

if the trend of x_i is decreasing from mid part to the end of cross section.

$$x_{i-1} - x_i < \frac{(x_i - x_{i+1})}{4} \quad \text{Eq 4. 5}$$

if the trend of x_i is increasing from mid part to the end of cross section.

It is important to note that the test should start from the mid-part of the cross section approaching the end. If not, errors show up in the processing results.

(2) An acceptance to potential improper point i+1 is executed to stop function if point i satisfy the following equation (Eq 4. 6 or Eq 4. 7):

$$x_i < \min_{x \in X}(x) + \frac{(\max_{x \in X}(x) - \min_{x \in X}(x))}{2} \quad \text{Eq 4. 6}$$

if the trend of x_i is decreasing from mid part to the end of cross section.

$$x_i > \min_{x \in X}(x) + \frac{(\max_{x \in X}(x) - \min_{x \in X}(x))}{2} \quad \text{Eq 4. 7}$$

if the trend of x_i is increasing from mid part to the end of cross section.

(3) If the point i is qualified from either Eq 4. 6 or Eq 4. 7, the points after current correct point i are fed into the following test algorithms. A search radius is defined in which r points forward are used to fit a circle and fit a linear line. Fitted errors are found as e_1 and e_2 with respect to

the fitted curve and fitter line. Standard deviations of errors are also estimated and denoted as s_1 and s_2. If either of tests below is satisfied, the point *i* forward (not include point i) are considered as outliers thereafter.

$$s_1 < s_2 \quad \text{Eq 4. 8a}$$

$$e_1 < s_1 \times f_1 \quad \text{Eq 4. 9b}$$

$$s_1 > s_2 \quad \text{Eq 4. 10a}$$

$$e_2 < s_2 \times f_2 \quad \text{Eq 4. 11b}$$

Regarding to Eq. 4.8a, the forwarding points show more linear property from its errors in comparison. However, if Eq. 4.8b cannot be satisfied, it indicates potential outliers may be just noisy points. Otherwise, the potential outliers are accepted. Similar to Eq. 4.9, where forward points starting from point i+1, if both equations (Eq. 4.9a and Eq. 4.9b) are fulfilled, the forwarding points are considered as outliers and removed.

After outliers are removed from cross sections, it is time to filter noise using presorting algorithm mentioned in old version. Procedures are similar and applied to 3D models in the unit of cross section, results of a cross section is shown in Figure 4.23.

Feature Identification

This step is the final step of feature recognition. A dual identifications algorithm is designed to guarantee correct recognized curve points. This algorithm executes recognition from one cross section to another. The main identification (Figure 4. 24) starts from selection of a length scale of points (similar to the original version). It is always assumed that end points are nicely smoothed and false points are rejected. Starting from the end-point segments, a series of circles are fitted along the segments. The curvature obtained from a segment is denoted as the curvature of the end

point of that segment. The fitting errors together with fitting curvatures are compared to a pre-defined threshold, i.e., threshold 1 and threshold 2, respectively. Threshold 1 uses fitting errors for initial screening; threshold 2 uses curvatures for corner points' selection. If fitting errors of segments are larger than in threshold 1, these segments are rejected from a potential corner, and all of their curvatures are set to zero. Following comparisons, dismiss points from corner points whose curvatures are below threshold 2. Thus points above threshold 2 are considered as temporary corner points. In general, because curvature value is allocated to the end point, it requires indices of corners moving backward about $n/2$ (total number of points in that segment is n).

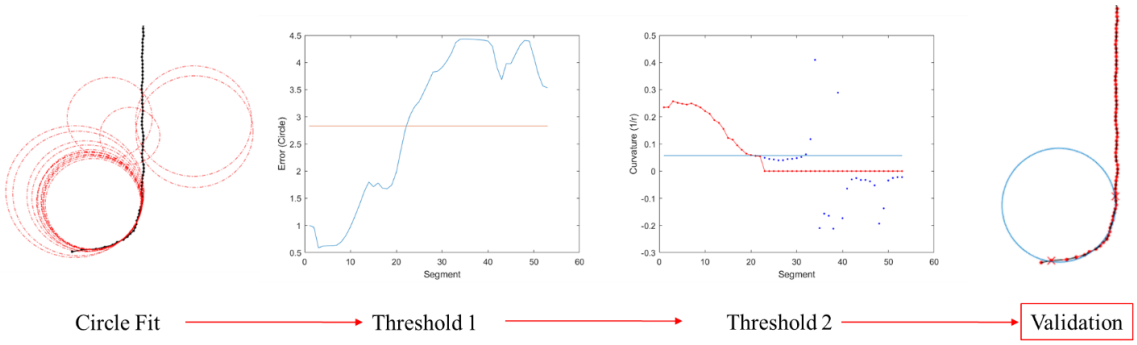

Figure 4. 24 Procedures of feature identifications

The temporary corner points need to be validated through two tests before entitlement. The first validation (Figure 4. 25) is to examine coordinates of temporary corner boundaries along the cross sections. A sliding threshold (green dash) is determined from smoothing coordinates by subtracting or adding standard deviations of coordinates (x or z) corresponding to end or beginning boundaries. If the coordinates locate outside the threshold, the corner points of that cross section have to be evaluated together with the other information from the second validation. The second validation (Figure 4. 26) is to compare radii along cross sections with a sliding threshold. The threshold calculation is similar to that of the first validation. Again, if radii stay beyond or below the threshold, the validation fails and the corner of that cross section has to be re-evaluated in the second feature identification algorithm.

In the second feature identification, the order index of the re-evaluated cross section is found so as to find its nearest two cross sections whose corner points pass two validations. The beginning and end point coordinates are obtained from the two correct corners and are used to find corresponding points with closest coordinates on the fake corner. A circle is fitted to the corner region with new boundaries, and the radius of the cross section is updated together with new boundary indices thereafter. A remedy is to update the corner region from its neighbors if the second feature identification cannot achieve the goal (this remedy is rarely used).

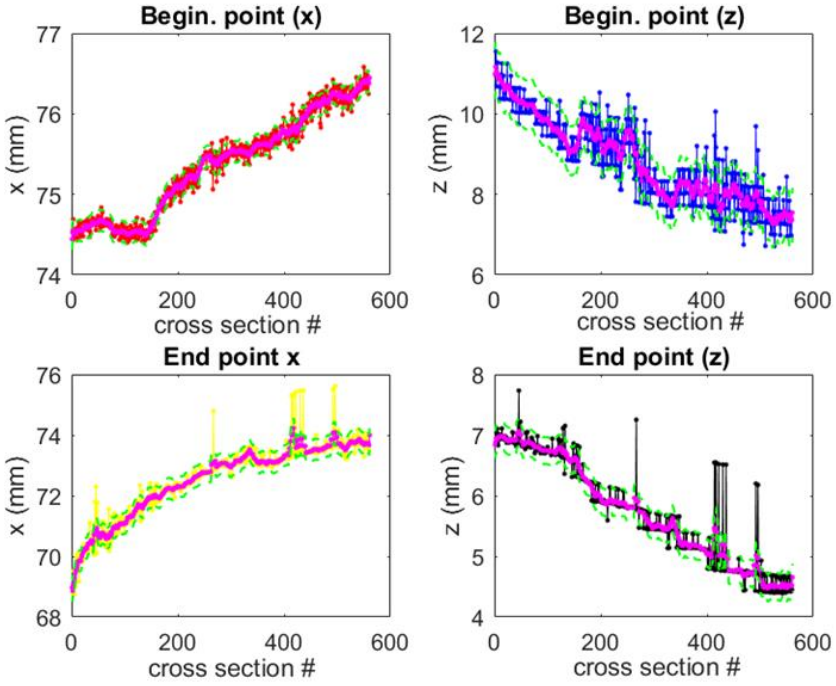

Figure 4. 25 First validation for potential second feature identification

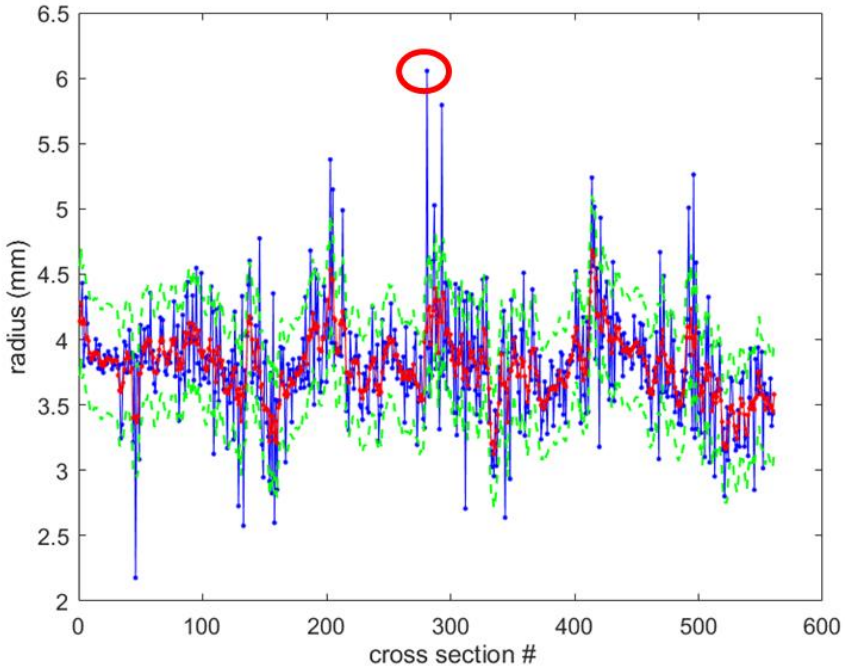

Figure 4. 26 Second validation for potential feature identification

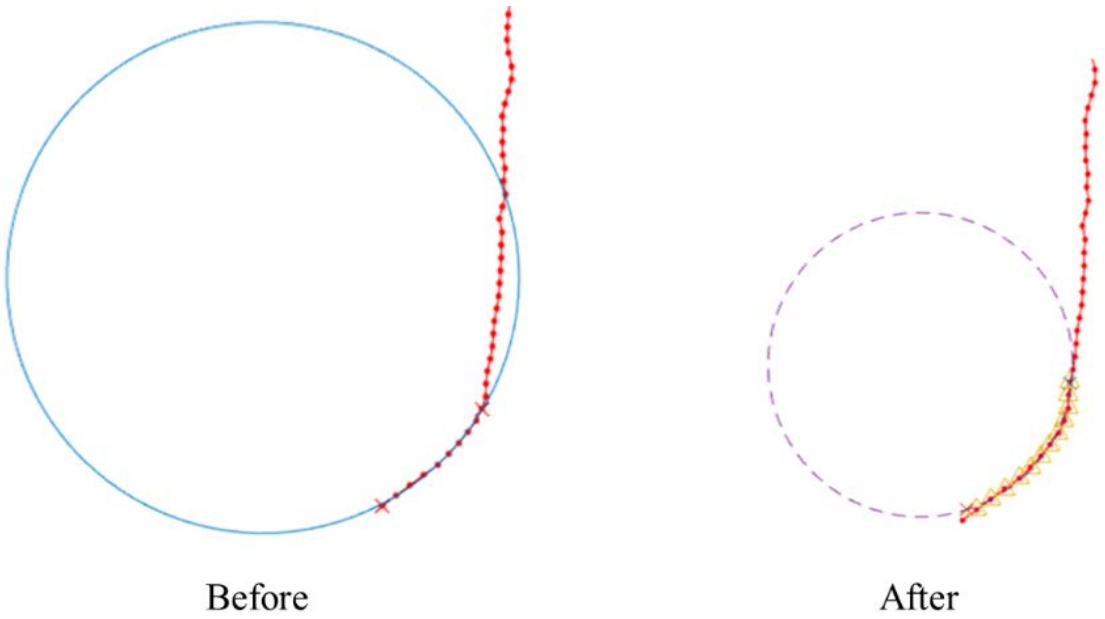

Figure 4. 27 Result of second feature identification

After the second feature identification algorithm, correct corners can be found, as shown in Figure 4.27. Achievement from the feature recognition can be applied to dimension analysis, as discussed in Chapter 6.

4.4 Example Study

The example study goes through three different shapes of cold-formed steel members, i.e., Z, C, and built-up channel section (BUC). Measurement direction schemes are different among Z, C, and BUC sections. The first two pre-process steps, i.e., data conversion and data trimmer, are left out because the procedures are simple and repetitive, as described in Section 4.1. More explanations are given in surface registration and feature recognition for three members, respectively. Besides, the original version algorithm of feature recognition utilizes Z members, while the current version algorithm is applied to C and BUC.

4.4.1 Z

Z purlins generally require scans from five directions in order to attain full geometric information of the specimen (Figure 4. 5), i.e. 0°, -40°, 40°, 80°, -100°. The five measurement segments are first registered through a surface registration GUI with ICP algorithm embedded (Section 4.2.2). The reference and target point pairs are processed in sequence: 0° and 40°, 40° and 120°, 0° and -40°, -40° and -120°. A segment at the 0° direction is set as a reference by nature. Other segments considered as targets are utilized as references after proper surface registration.

Feature recognition is explained in Section 4.3.1. The only two factors are the threshold to presort and filter noises from presorting algorithm, i.e., α=75.5°, r=2.95. The categorized results are shown in Figure 4. 18.

4.4.2 C

Surface registration to C sections is similar to that of Z sections. Global coordinates are taken from sensor coordinates at 0°. The registration process is started with 0° and its adjacent segments -40° or 40° (Figure 4. 6). After all data loaded from *All Files* (Figure 4. 12), data at 0° is selected as a reference, and then measurements at 40° are chosen as targets. As a window function is defined by users, optimization can start and registrations can be done. The procedures are repeated to a next pair of references and targets, say 40° and 120°, 0° and -40°, -40° and -120°, until the entire target data can be properly registered into the global coordinates.

Regarding to feature recognition, C members do not require the specific data extraction algorithm as BUC. Measurements from 40° and -40° only require a threshold removal method (method 1 in *Noise and Outlier Removal* in Section 4. 3. 2). The result is shown in Figure 4. 28.

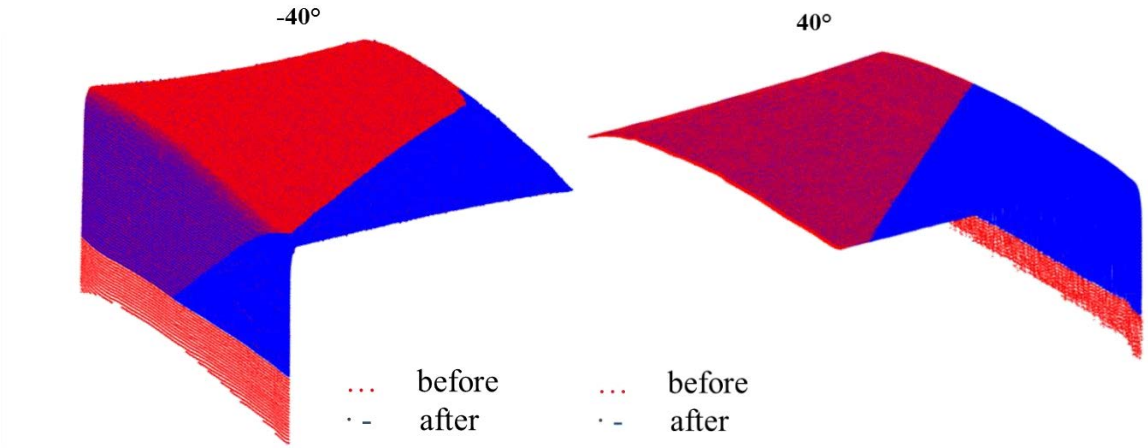

Figure 4. 28 Processed results of measurements at angle 40° and -40° using method 1 in *Noise and Outlier Removal* in section 4.3.2

On the other hand, segments from directions of 120° or -120° require additional care along the edge. Method 2 in *Noise and Outlier Removal* in Section 4.3.2 is applied so that only outliers are

eliminated at boundaries. The processed results from measurements are demonstrated in Figure 4. 29.

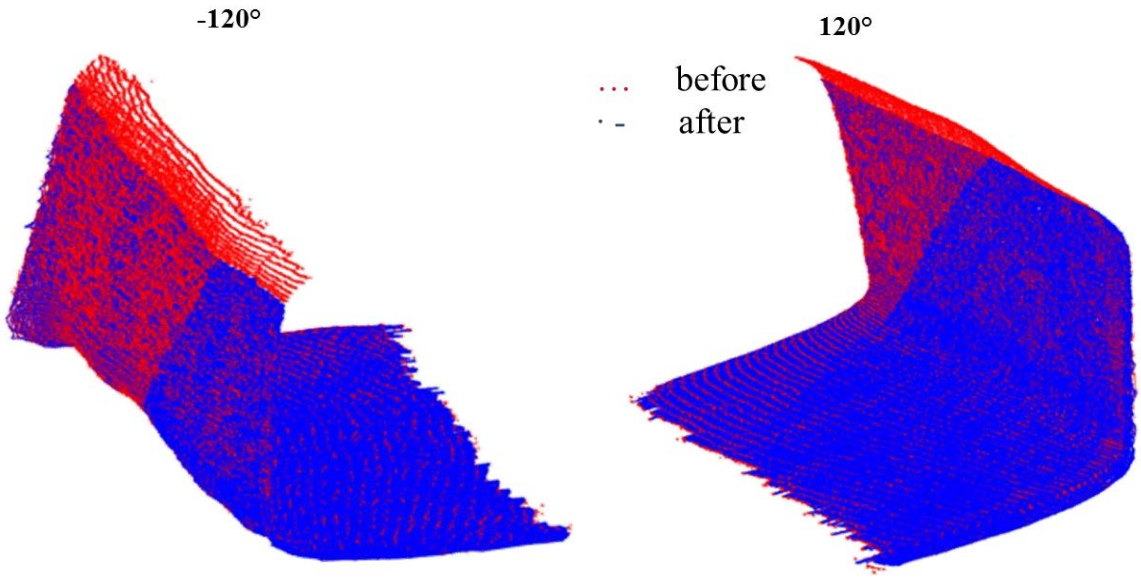

Figure 4. 29 Processed results of measurements at angle 120° and -120° using method 2 in *Noise and Outlier Removal* in section 4.3.2

The "clean" measured segments then are recognized using feature identification. Post-progress is required when all segments have been processed; a corner is identified and validated per segment. As previously mentioned, each segment may have advantageous parts of measurements; for example, measurements at 40° or -40° have better resolution in corners near a web, while measurements at 120° and -120° have better resolutions in corners close to the lips, and measurements from the 0° direction provide the best resolution in web information. Thus a reconstructed plan has formed: a 3D model can take a web from 0°, corners near a web from 40° and -40°; flanges comprising both ±40° and ±120°, or simply between ±40° and ±120°, corners near lips from ±120°. A reconstructed model is achieved (Figure 4. 30).

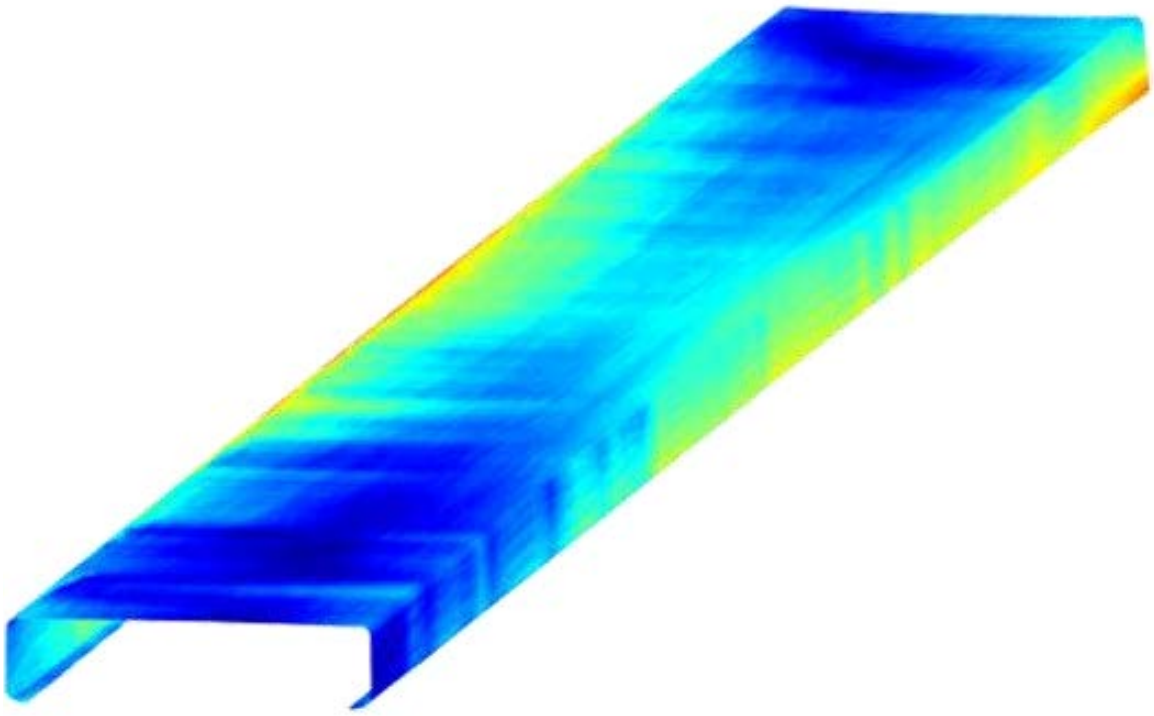

Figure 4. 30 Reconstructed C stud after surface registration and feature recognition

4.4.3 BUC

Similarly, but more complicated, BUC requires nine-direction measurements. Again, global coordinates are taken from sensor coordinates at 0°. The registration starts from 0° and its adjacent segments from -40° or 40° (Figure 4. 6). Data at 0° are selected as a reference, and the measurement at 40° is chosen as a target. With proper window function defined, optimization starts and registration can be done. Registration procedures are repeated for pairs of references and targets, say 40° and 100°, 100° and 80°, 80° and 120°, 0° and -40°, -40° and -100°, -100° and -80°, -80° and -120°, until all nine measurement segments are processed and the registration job is done.

BUC sections compared to C sections are much more complicated with total nine measured segments processed. The upper C has outside lips and an inside web exposed to the sensor; the lips and a web must be separated from the segment taken at 0° direction and in-between noises have to

be automatically removed (Figure 4. 31). Regarding segments at 40° or -40° direction, similar to C, only a threshold is set up to remove problematic points (Figure 4. 32). Data measured at 120° or -120° can be processed with method 2 as C's procedures (Figure 4. 33). It can be observed that some data is missing from -120° due to scan environment. This absent part can be interpolated later in the feature recognition whose radius is generally larger than other cross sections.

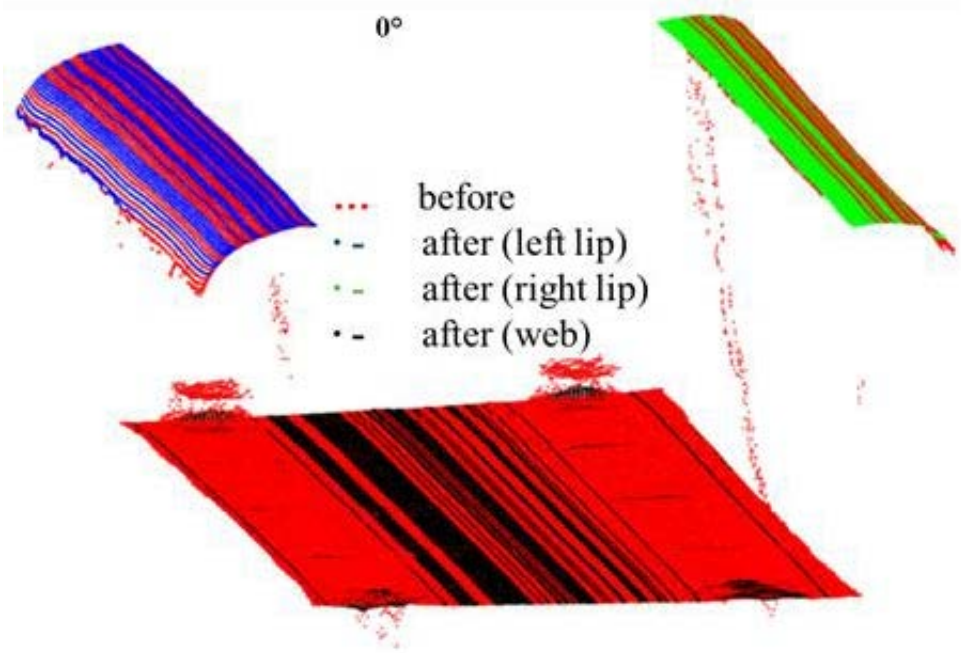

Figure 4. 31 Processed results of measurements at angle 0° where lips and a web are separated.

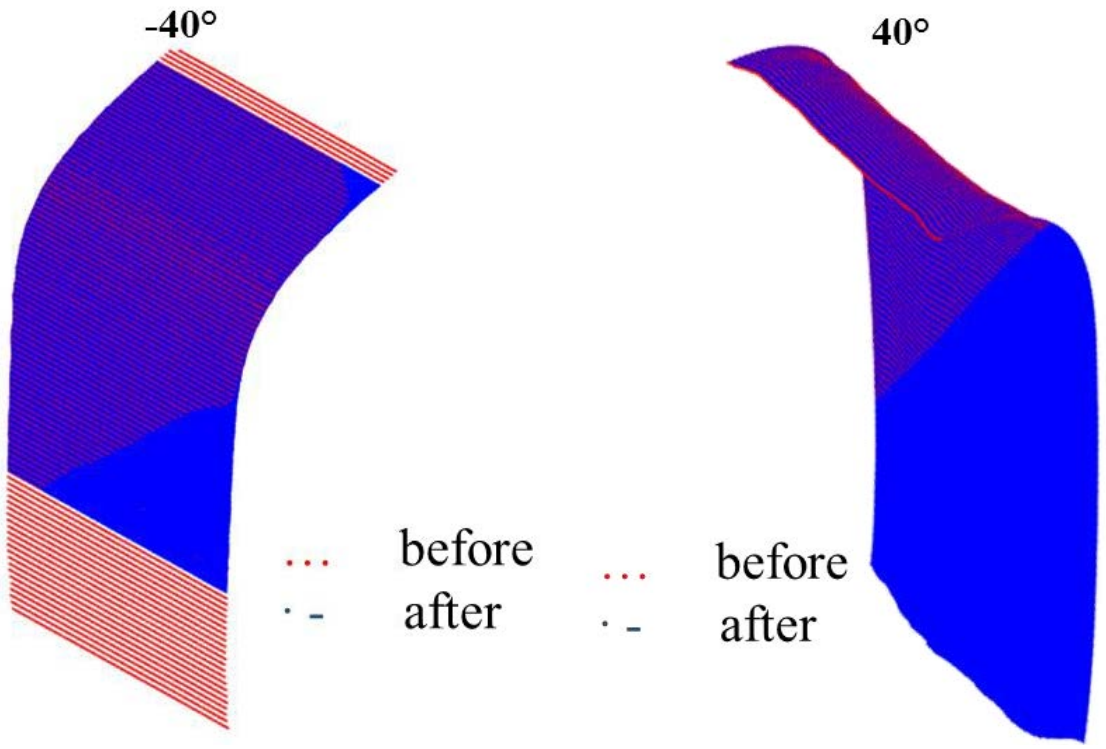

Figure 4. 32 Processed results of measurements at angle 40° and -40° using method 1 in *Noise and Outlier Removal* in section 4.3.2

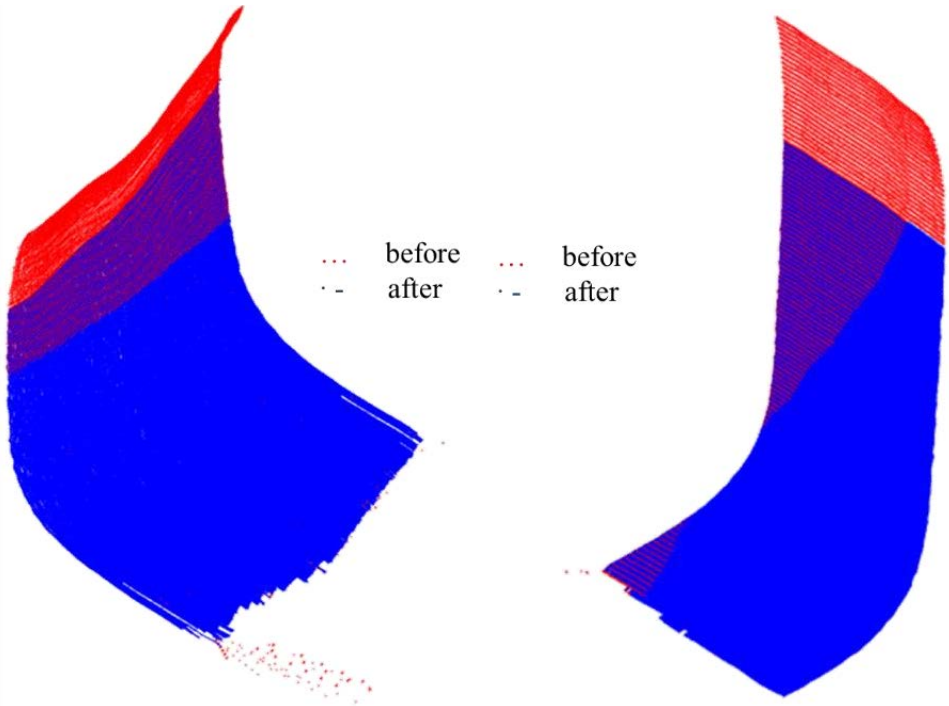

Figure 4. 33 Preprocessed results of measurements at angle 120° and -120° using method 2 in *Noise and Outlier Removal* in section 4.3.2

Measurements at 80° or -80°, and 100° or -100° require an additional data extraction process before removing noises. The extraction results are displayed in Figure 4. 34 and Figure 4. 35. These segments are intended to be processed in method 3 in *Noise and Outliers Removal* in Section 4.3.2.

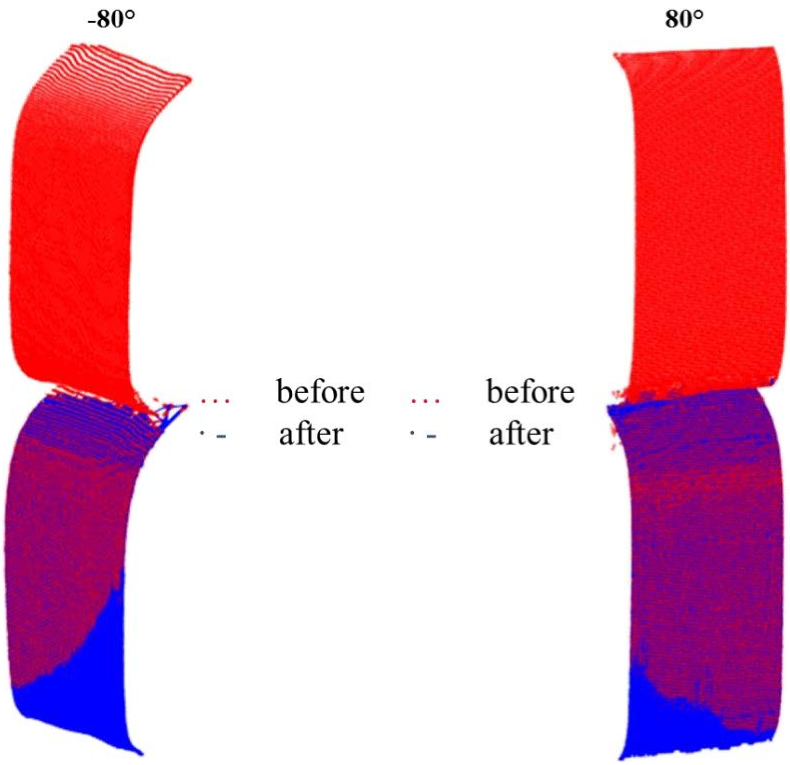

Figure 4. 34 Processed results of measurements at angle 80° and -80° after data extraction

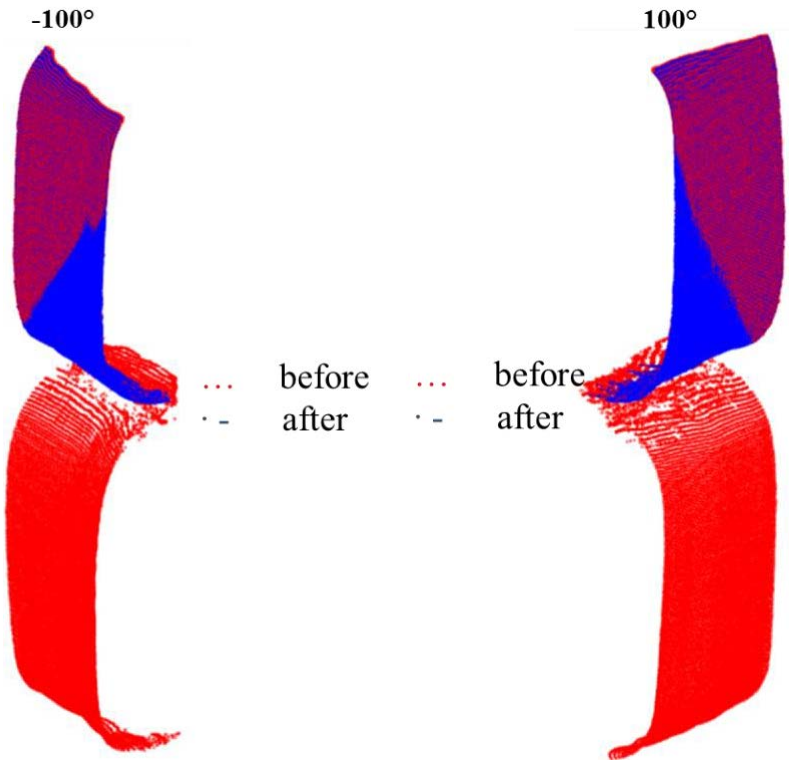

Figure 4. 35 Processed results of measurements at angle 100° and -100° after data extraction

The feature identification process of BUC is exactly the same compared with that of C but more tedious. Feature recognition can be applied to one segment with only one corner region each time. There are only four corners in C; thus, feature recognition is processed four times, while eight corners of BUC thus require eight times' process. The post-progress is more complicated as well. The BUC model can be divided into five regions: webs, top right-side region (include upper right lip, upper flange, and two corners), top left-side region, bottom right side region, and bottom left side region. Webs and upper lips' information are taken from the measurement at direction 0°. Upper flanges can be taken from segments at ±100° directions since they have better resolution in general and bottom flanges utilize segments from ±80° angles of view. Bottom lips can be taken from measurements at ±120° directions. As for the corners, top corners near lips are contributed by measurements at ±40° directions; top corners near the upper web are data at ±100° angles of view; bottom corners near lips are contributed by measurements at ±120° directions; and bottom corners

near the web are from measurements at ±80° directions. In combination of these geometric information, a 3D model can be reconstructed for BUC sections (Figure 4. 36).

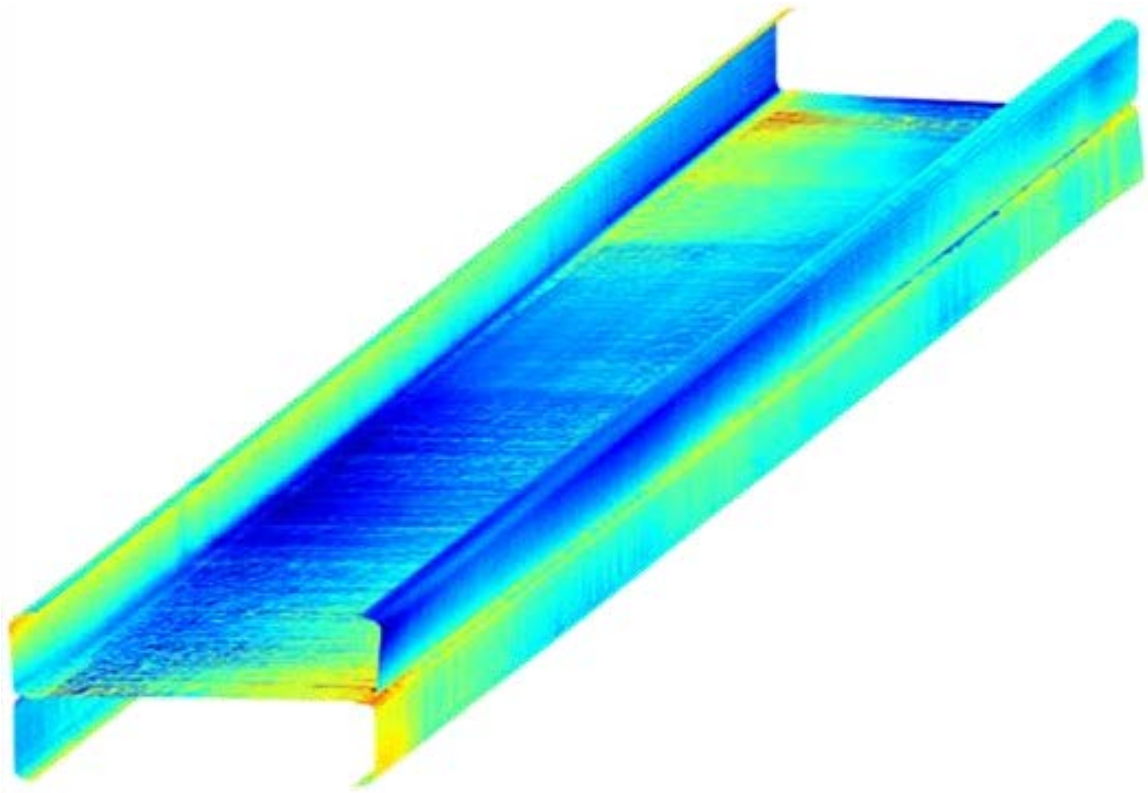

Figure 4. 36 Reconstructed BUC stud after surface registration and feature recognition

4.5 Conclusions

Modern laser-based measurements may be used to create accurate three-dimensional point clouds of cold-formed steel parts. If care is taken in the post-processing, it is possible to create highly accurate representations and even identify key features of the cross-section automatically. A straightforward implementation of an iterative closest point algorithm, coupled with additional methods to filter noise, are successfully employed to stitch multiple point clouds together with minimal error into a point cloud of a complete cold-formed steel part. A scanned cold-formed steel zee purlin is provided as an example. An automated procedure is also developed for identifying features (corners and flats) in the point cloud. The fully registered point cloud enables a variety of

potential automated applications, three of which are demonstrated: calculation of dimensions, calculation of imperfections, and development of shell finite element models with as-measured imperfections as the model's initial state. Automated calculation of dimensions has excellent potential for quality assurance and quality control methods in manufacturing, and in the provided example gives novel insights on corner radius and lip length dimensions of the example zee shapes. Imperfections are unavoidable and the registered point cloud provides an efficient means to quantify simple or complex imperfection patterns. In the studied examples, the initial twist in the specimens is noted as particularly large. Using the point cloud to drive a shell finite element model is a powerful means to align modeling with reality, and a method is developed to perform the necessary transformations.

Chapter 5 Introduction to studied sections

This chapter provides manufactured geometric information, material properties, and test set-up instrumentation of cold-formed steel members that were scanned by the laser imperfection measurement platform. Three types of structural members are introduced in this chapter, i.e., Z, C, and built-up channel (BUC) sections. The geometric information focuses on cross-section shape and manufacturing dimensions which will be compared with laser measurements in a later chapter. Regarding material properties and the configuration of the test setup, they will be used with reference to finite element analysis.

5.1 Z

Z sections are commonly used in metal buildings, where they serve as purlins and girts (Figure 5. 1). Torabian et al. (2016) conducted a thorough study of the behaviors of beam-column Z sections, where 700Z225-48 specimens were carefully measured and tested. The researcher conducted the measurement part of 700Z225-48, where 19 specimens that were 48 in long were placed on the imperfection measurement rig and scanned by the laser. The measurement results were summarized statistically and provided for numerical simulations, which were compared with the test results. Thus, the research in this dissertation includes Z sections as one of example studies.

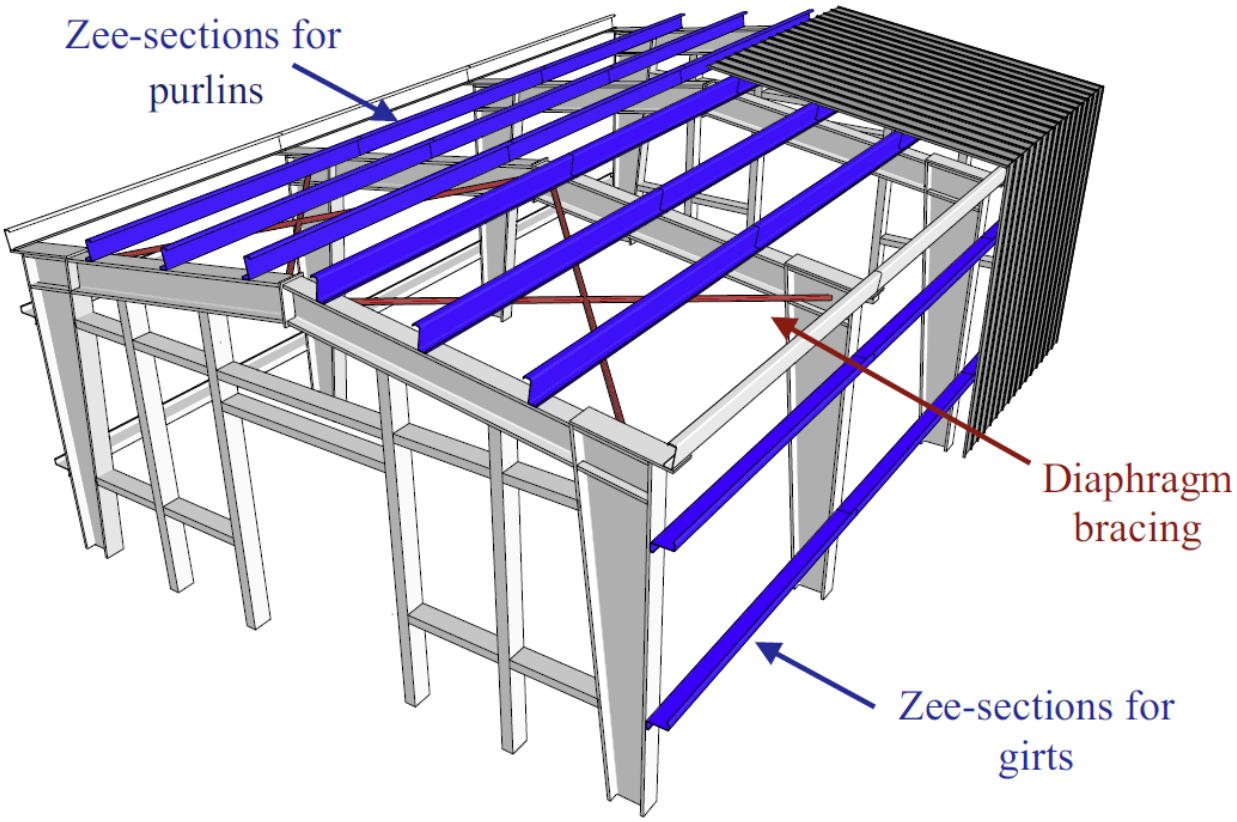

Figure 5. 1 Application of Z-sections in steel frame buildings (Torabian et al. 2016)

5.1.1 Geometric Information

Cold-formed structural members contain a web, two flanges, two lips, and four corners, as shown in Figure 5. 2. The Z section is a point-symmetric geometry with its centroid in the center of its web. Specific ZZ sections are scanned in cooperation with beam-column testing in the Thin-Walled Structures Laboratory (Torabian et al. 2016).

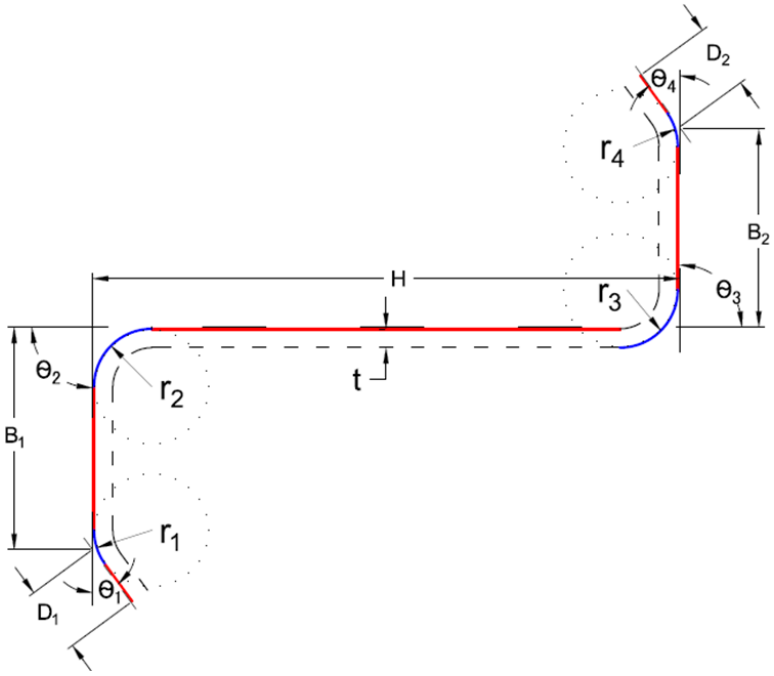

Figure 5. 2 Definition of the dimensions of a Z section

The dimensions of the scanned ZZ sections are listed in Table 5. 1. There were 19 Z sections that were 48 in (1219.2 mm) long that were studied in this research. In general, the web height of the true dimension was well-controlled, approaching the manufactured dimensions. However, the angles and radii of corners and the lip lengths may differ greatly compared to its nominal shape.

Table 5. 1 Nominal dimensions of the Z-sections that were studied

Out-to-Out Dimensions of Z (700Z225-60)					
H (inch)	7	**r_1 (inch)**	0.3725	**θ_1 (°)**	48
B_1 (inch)	2.25	**r_2 (inch)**	0.3725	**θ_2 (°)**	90
B_2 (inch)	2.25	**r_3 (inch)**	0.3725	**θ_3 (°)**	90
D_1 (inch)	0.766	**r_4 (inch)**	0.3725	**θ_4 (°)**	48
D_2 (inch)	0.766	**t (inch)**	0.06		

5.1.2 Material Properties

Modeling of structural behaviors, e.g., collapse modeling, generally requires inputs about the properties of the materials, such as Young's modulus, yield stress, Poison ratios, and ultimate stress. In order to obtain these properties, coupon testing is required for specific types of structural members (Torabian et al. 2016). Coupons to be tested (Figure 5. 3) are taken from flanges and a web of the same series of Z sections, i.e., 700Z225-60. Uniaxial tension testing is conducted in which 12 coupons are tested using an MTS machine in the Thin-Walled Structures Laboratory (Torabian et al. 2015). The properties of materials are determined using the coupon tests and stress-strain curves, such as those shown in Figure 5. 4. The yield stress, F_y = 79.85 ksi, is estimated using the 0.2% offset approach. The ultimate stress, F_u = 84.89 ksi, is obtained from the maximum value of the stress-strain curve. Poisson's ratio is assumed to be 0.3 and Young's modulus is rounded up to 29,500 ksi.

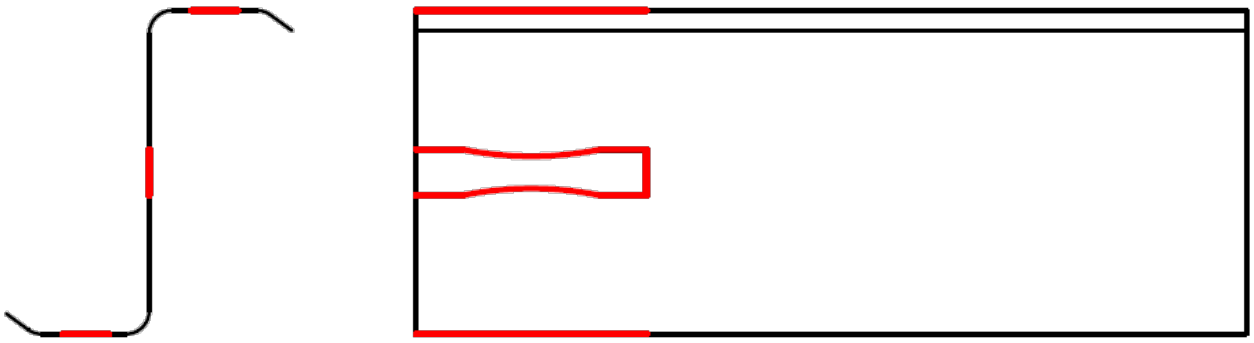

Figure 5. 3 Coupon test samples of Z sections

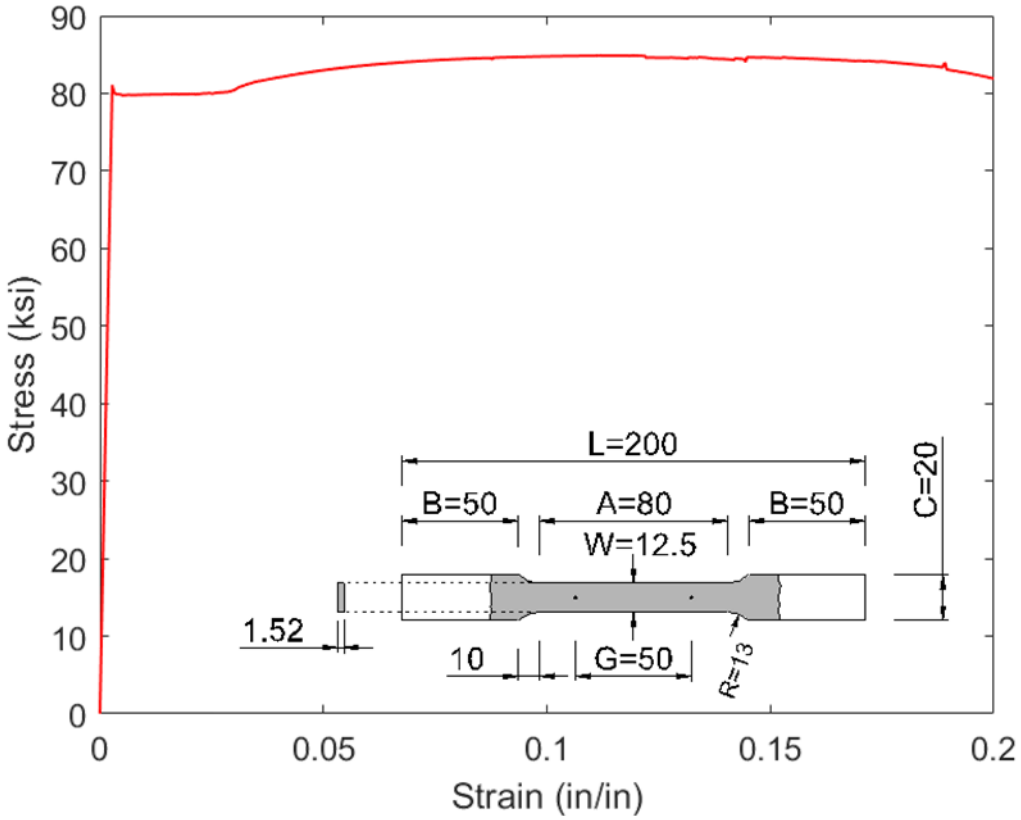

Figure 5. 4 Stress-strain curve of Z (Torabian et al. 2016)

5.1.3 Post-measurement testing for modeling

The goal of Z-section testing is to precisely predict the strength of cold-formed steel beam-columns. Motivated by this goal, a test setup was designed and built in Thin-Wall Structures Laboratory (Figure 5. 6). This test setup used MTS standard swivel joints to provide controlled, eccentric, compressive loading to the Z sections. The special designs of the clamps and loading plates can accommodate eccentricity in both axes. Figure 5. 5 shows the directions and magnitudes of eccentricity in the tests. The link that connects the loading plates and the tested members allows both rotation and longitudinal translation. Thus, the boundary condition can be considered as pin-pin end restraints. The distance between loading and the boundaries of the actual compressed members is 6.25 inches, which is used in numerical modeling in which the boundary condition of the MPC-Beam constraint is used in the finite element analysis using ABAQUS.

Deformations until failure occurs during testing are tracked by displacement sensors that are set up around the members being tested. Loads can be measured through load cells and recorded through National Instrument DAQ systems. The data that are collected are compared to the results of numerical simulations in order to validate the simulation results.

No.	Loading condition: θ_{MM} Target angle (deg.)		Test specimen Z700-12-	ϕ_{PM} Target angles (deg.)	θ_{MM-m} Measured angles (deg.)	ϕ_{PM-m} Measured angles (deg.)	P_u Peak load kN
1			1	25.0	277.1	24.0	109.8
2			2	50.0	277.3	49.3	92.8
3			3	81.0	277.0	81.3	37
4			22	81.0	277.0	81.0	32.3
5	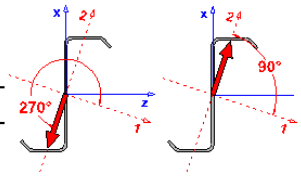	Axial load and Minor axis bending	21[a]	83	89.9	83.0	31.5
6			4[a]	60	81.9	61.8	79.7
7			5[a]	77	80.9	77.5	49.7
8			6[a]	85	81.4	85.8	21.3
9	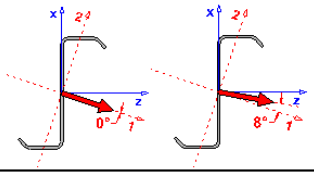	Axial load and Major axis/ Geometric Major axis bending	7	30.0	352.2	30.2	93.1
10			8	55.0	1.3	55.1	68.2
11			9	75.0	0.8	75.0	34.7
12			19[b]	55.0	5.1	54.7	72.1
13			20[b]	75.0	9.7	75.1	39.4
14	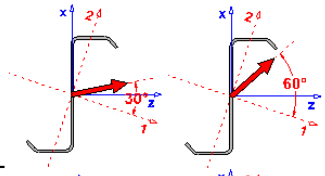	Axial load and Bi-axial bending	10	40.0	25.4	38.0	93.8
15			11	75.0	30.9	75.1	42.8
16			12	40.0	60.1	39.0	109.8
17			13	75.0	59.8	74.9	55.0
18	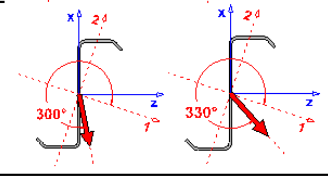		14	40.0	301.7	39.0	88.8
19			15	75.0	300.5	74.7	43.1
20			16	40.0	327.0	41.0	83.9
21			17	75.0	330.4	75.0	34.3
22		Column	18	0.0	77.8	3.4	131.8

Figure 5. 5 Test configuration matrix of Z sections (Torabian et al. 2016)

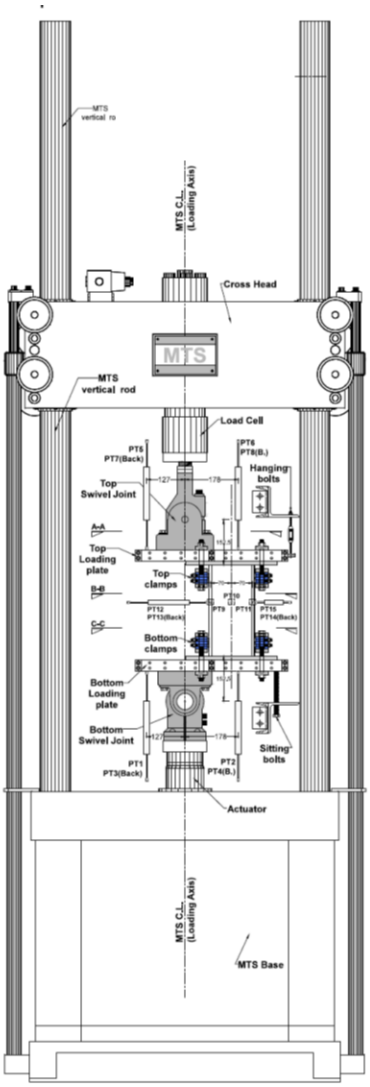

Figure 5. 6 Configuration of the instrumentation used in the test setup for the Z section (Torabian et al. 2016)

The test results under different boundary conditions are provided, as shown in the load vs. displacement curves in Figure 5. 7. Figure 5. 7 a, b, and c correspond to axial load and minor axis bending; axial load, major axis bending, and axial load only; and axial load and bi-axial bending, respectively. Various test observations were made, and common deformations began with lip deformations, and the Z sections failed in flexural, distortional buckling. More conclusions are available in Torabian et al. (2016).

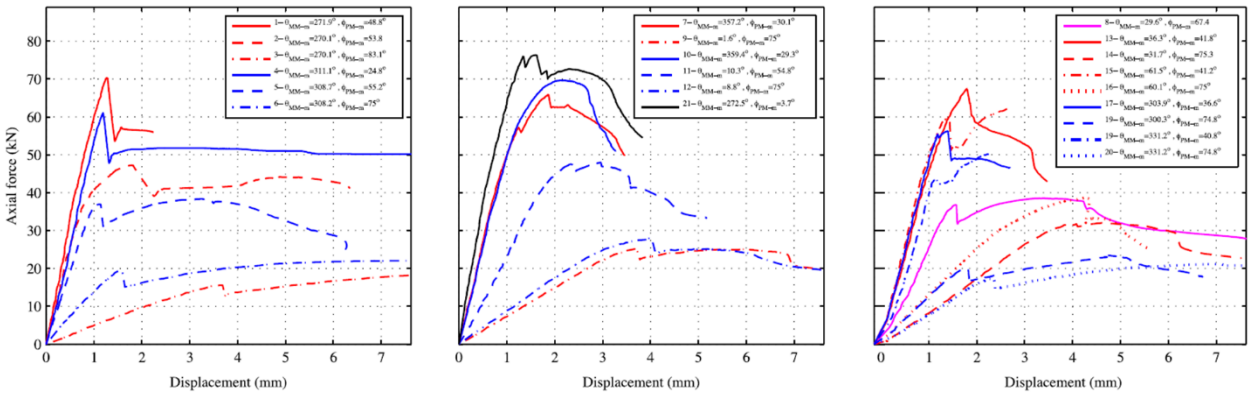

Figure 5. 7 Test results of load vs. displacement of 700Z225-48: (a) axial load and minor axis bending; (b) axial load, major axis bending, and axial load only; (c) axial load and bi-axial bending (Torabian et al. 2016)

5.2 C

C sections are used extensively in different low- and mid-level buildings. They can be used in both first- and second-order structural systems. In this dissertation, two categories of C sections were studied and reported for geometric measurements, i.e., 362S162-68 and 600S137-54. Fourteen specimens of 362S162-68 and 14 specimens of 600S137-54 were scanned carefully and reconstructed. All of the dimension information and the geometric imperfections were processed thoroughly. This information served as a reference of built-up sections and allowed comparisons with the results of earlier studies of the imperfections of C sections. Then, these two sections were attached together with a fastener and constructed as built-up sections, which are discussed in section 5.3.

5.2.1 Geometric Information

Similar to Z sections, C sections consist of a web, two flanges, two lips, and four corners, as shown in Figure 5. 8. The C section is singly-symmetric geometry, so its centroid does not coincide with the shear center. No specific testing was conducted for the C sections. Nevertheless, these sections constitute built-up channel (BUC) sections for the loading tests. Therefore, the dimensions and the properties of the material, as determined by coupon testing, still are required for numerical

modeling. The test setup is explained in Section 5.3, while all of the other fundamental information is presented in this section.

Figure 5.6 shows the definition of the out-to-out dimensions of C sections. The manufacture dimension table (Table 5. 2) compares the measurements with those resulting from the statistical analysis in chapter 6

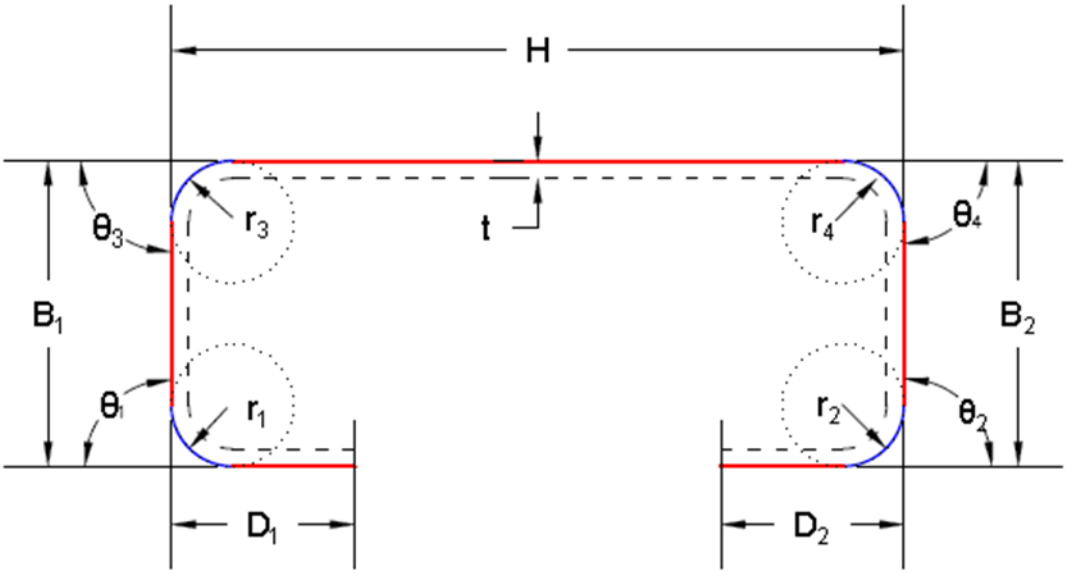

Figure 5. 8 Dimension definition of C

Table 5. 2 Nominal dimensions of C sections

Out-to-Out Dimensions of C (362S162-68)					
H (inch)	3.625	**r_1 (inch)**	0.1783	**θ_1 (°)**	90
B_1 (inch)	1.625	**r_2 (inch)**	0.1783	**θ_2 (°)**	90
B_2 (inch)	1.625	**r_3 (inch)**	0.1783	**θ_3 (°)**	90
D_1 (inch)	0.5	**r_4 (inch)**	0.1783	**θ_4 (°)**	90
D_2 (inch)	0.5	**t (inch)**	0.0713		
Out-to-Out Dimensions of C (600S137-54)					
H (inch)	6	**r_1 (inch)**	0.1415	**θ_1 (°)**	90
B_1 (inch)	1.375	**r_2 (inch)**	0.1415	**θ_2 (°)**	90
B_2 (inch)	1.375	**r_3 (inch)**	0.1415	**θ_3 (°)**	90
D_1 (inch)	0.375	**r_4 (inch)**	0.1415	**θ_4 (°)**	90
D_2 (inch)	0.375	**t (inch)**	0.0566		

5.2.2 Material Properties

Similar to Z sections, the coupons that were tested (Figure 5. 9) were taken from flanges and a web of the same series of C sections, i.e., 362S162-68 and 600S137-54. Uniaxial tension testing was conducted on 12 twelve coupons using the MTS machine in Thin-Walled Structures Laboratory (Fratamico et al. 2016). The properties of the materials were determined through the coupon tests and the stress-strain curves that are shown in Figure 5. 10. The yield stresses, i.e., F_{y1} = 60.85 ksi and F_{y2} = 57.31 ksi, were estimated using the 0.2% offset approach with respect to 362S162-68 and 600S137-54. The ultimate stresses, F_{u1} = 78.81 ksi and F_{u2} = 69.91 ksi, were obtained from the maximum value of stress-strain curve with respect to 362S162-68 and 600S137-54. Poisson's ratio is assumed to be 0.3, and Young's modulus was rounded up to 29,500 ksi.

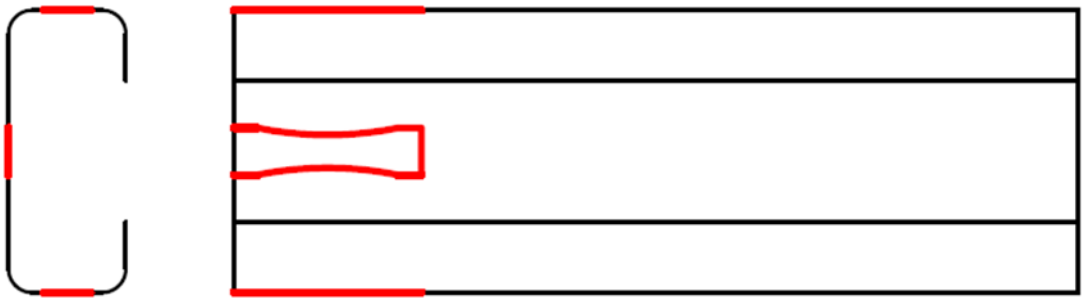

Figure 5. 9 Coupon tests of C sections (Fratamico 2017)

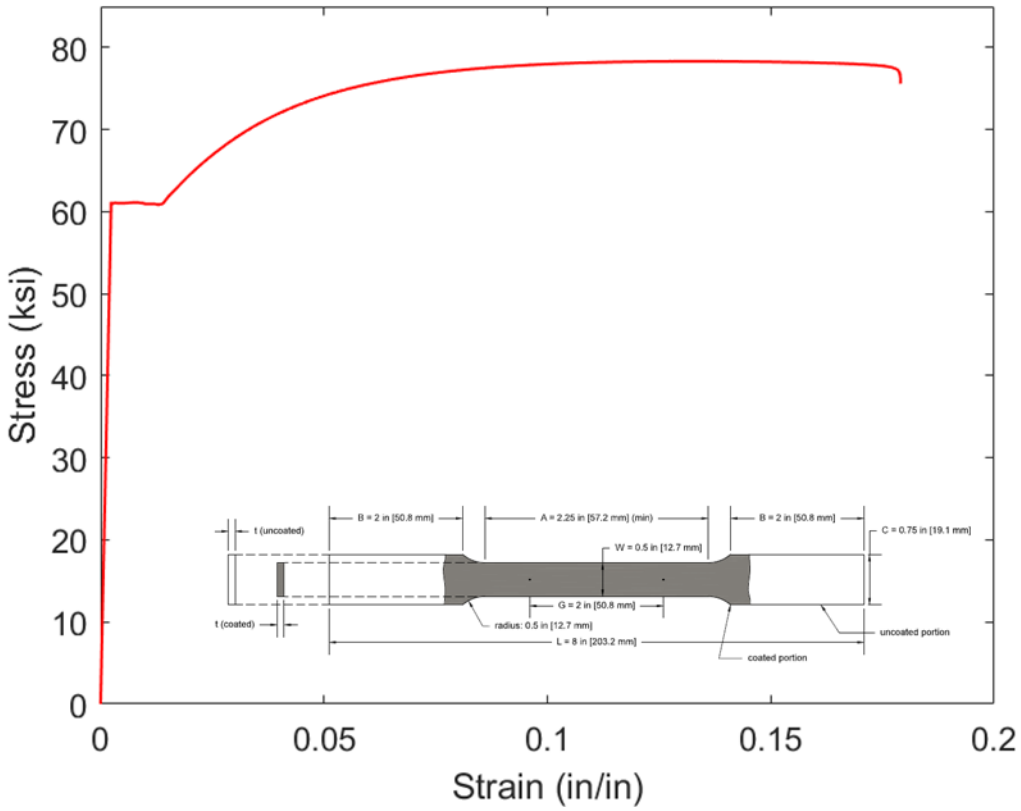

Figure 5. 10 Stress-strain curve of C sections (Fratamico et al. 2016)

5.3 BUC

BUCs' members are composed of two back-to-back lipped channels connected with fasteners. These types of sections are used extensively in cold-formed steel framing, such as roof, floor, and

wall framing. Interesting research proposed by Fratamico et al. (2016) was conducted in the Thin-Walled Structures Laboratory at Johns Hopkins University. BUCs with different fastener spacing and layouts, i.e., sheathed/unsheathed plans, were tested under axial loading. Similar to Z sections, the test results of BUCs were compared with the results of numerical simulations. In order to make this comparison, thorough 3D geometric measurements were required so that the true dimensions and imperfections could be utilized. The manufacturing dimensions can be taken directly from the corresponding C sections. The laser measurement platform can be used to obtain direct scans of the BUC's members, and their dimensions can be determined from reconstructed models.

5.3.1 Geometric Information

It has been observed that BUCs can be treated simply as two, back-to-back C sections, but with more dimension quantities. Ideally, the external surfaces of the webs should be in close contact with each other. The BUC should contain a top section and a bottom section and be divided into five regions (Figure 5. 12), i.e., RR1, RR2, RR3, RR4, and RR5. This division is to facilitate feature recognition and determining the dimensions when processing the huge amount of laser measurements from 50 specimens.

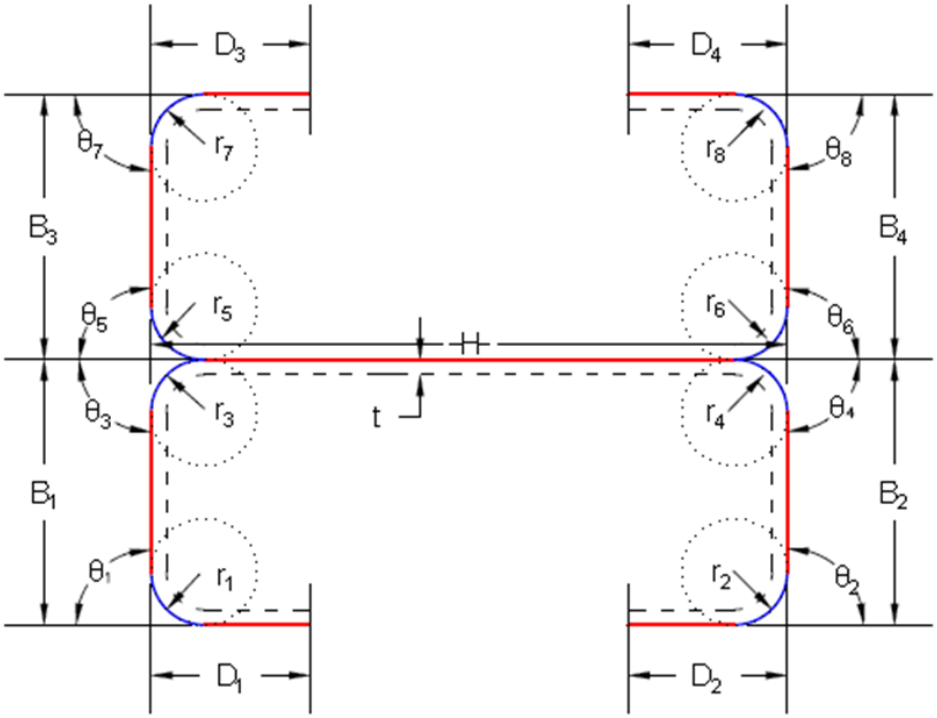

Figure 5. 11 Definition of the Dimensions of BUC

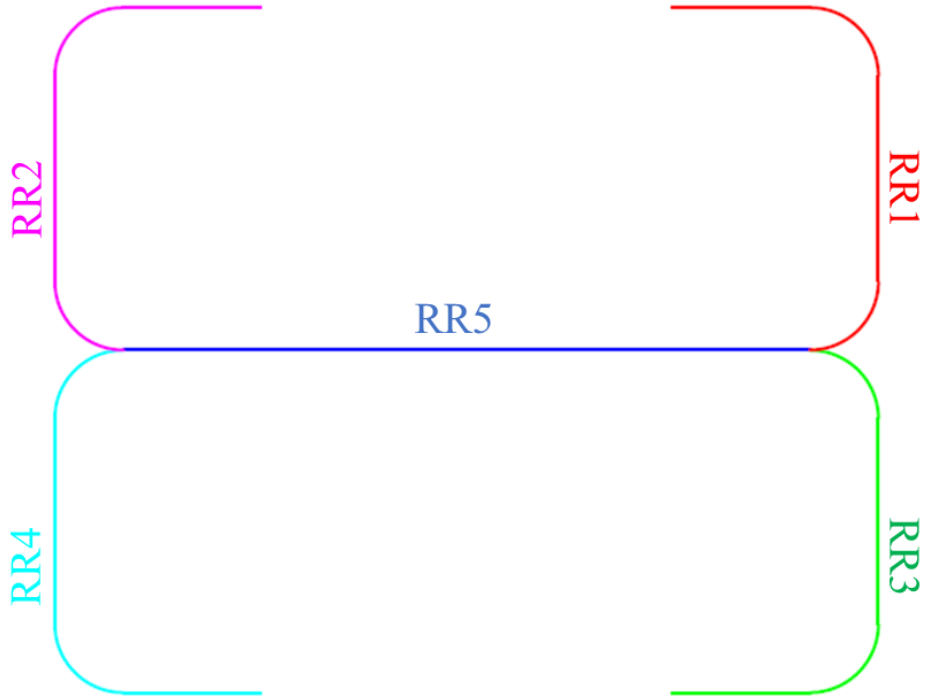

Figure 5. 12 Scanned processing regions of BUC

5.3.2 Post-measurement Test Setup

Similar to the Z-section test setup, the tests of a BUC column loading it onto an MTS machine with the two ends connected to a single track (Fratamico et al. 2016). The purpose of this test is to determine the effects of the fasteners on the built-up sections. Therefore, concentric loading is applied with different fastener plans and different sheathing board attachment. The MTS machine (Figure 5. 13) can take up to 6-ft columns, so all of the members that were tested were trimmed from 8 to 6 ft. The fastener plan and sheathed/unsheathed test plan are shown in Figure 5. 14 in which cases 1 to 4 are unsheathed, and cases 5 to 8 are sheathed. Figure 5. 15 shows the test setup for the sheathed and unsheathed BUCs. The boundary conditions of the test were wrapping-fixed and local-pin fixed. The numerical simulation of BUC is similar to that of the boundary conditions of the Z tests, i.e., an MPC-Beam with two reference point on the centroids of both end cross sections. Regarding fastener modeling, springs are assumed in finite element modeling via ABAQUS. More modeling details are presented in Chapter 9. Due to the restraints of time, dimensions, imperfections, and true-geometry, the modeling of unsheathed BUC members was studied in this research. Numerical modeling was validated through true-geometry modeling and compared with the experimental results (Fratamico et al. 2016).

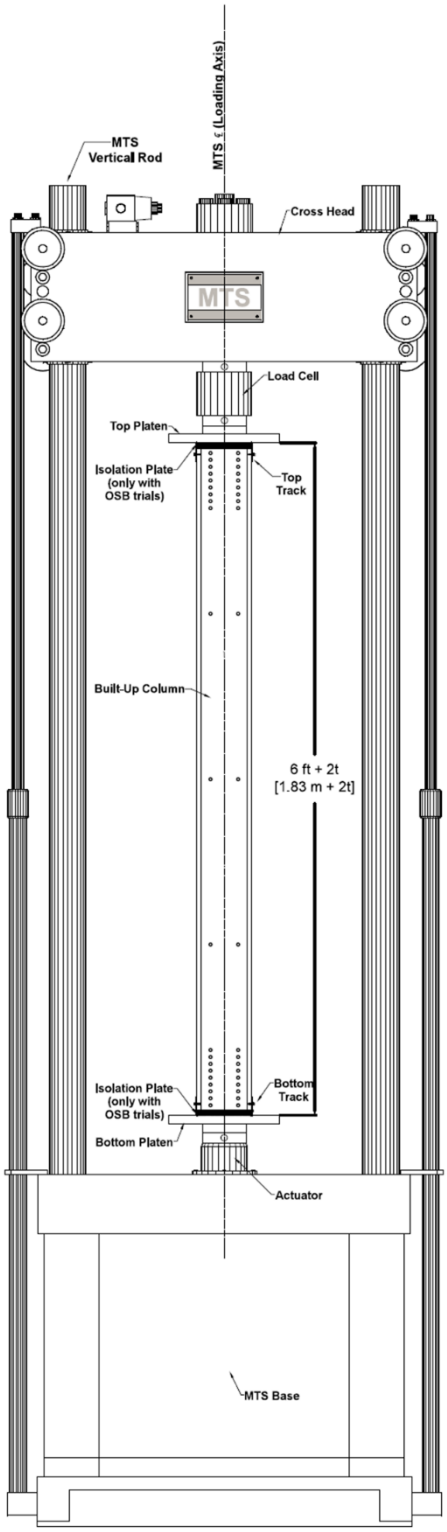

Figure 5. 13 Configuration of the instrumentation for the test setup (Fratamico et al. 2016)

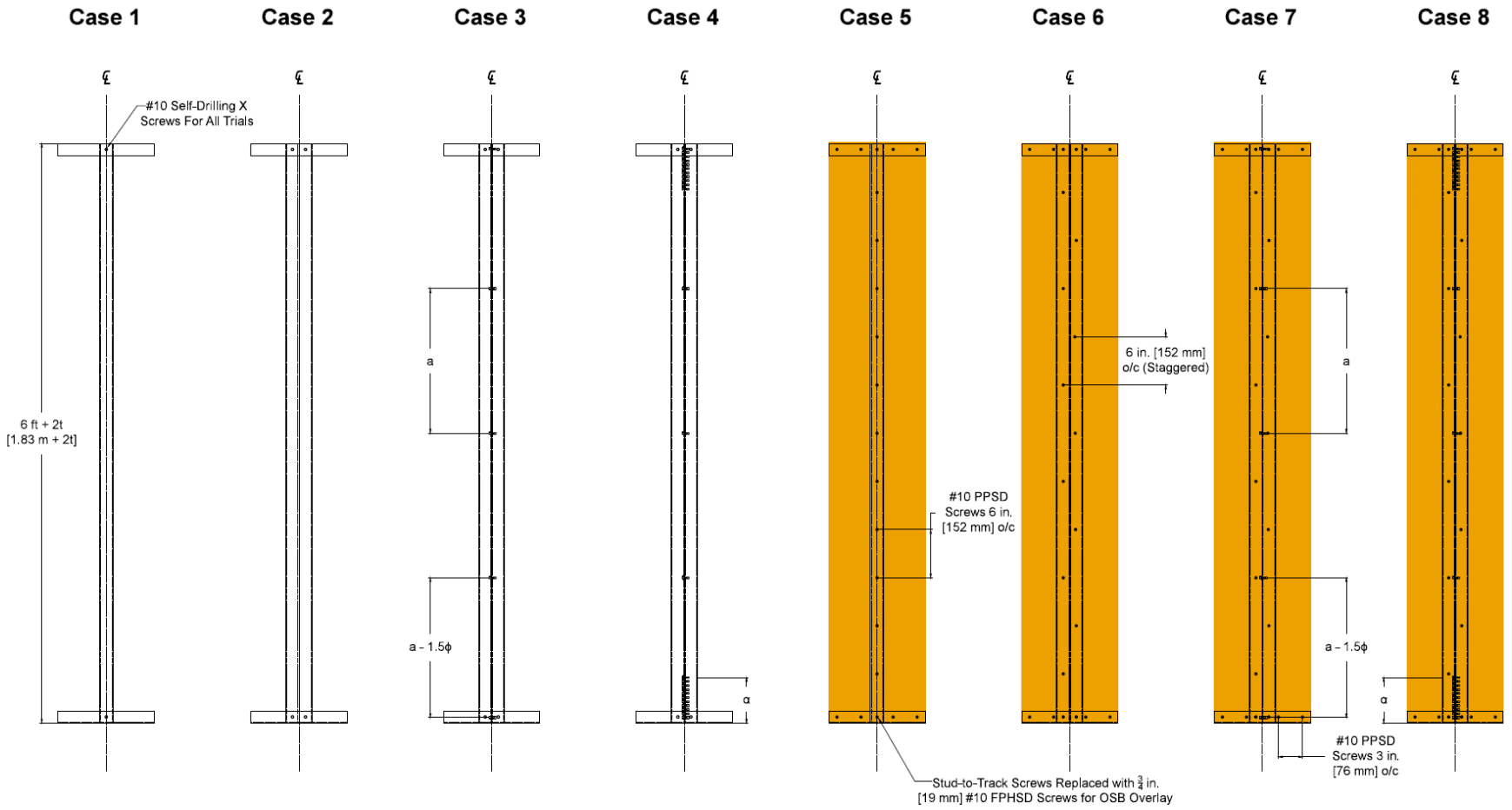

Figure 5. 14 Information from the test specimens for use in finite element modeling (Fratamico et al. 2016)

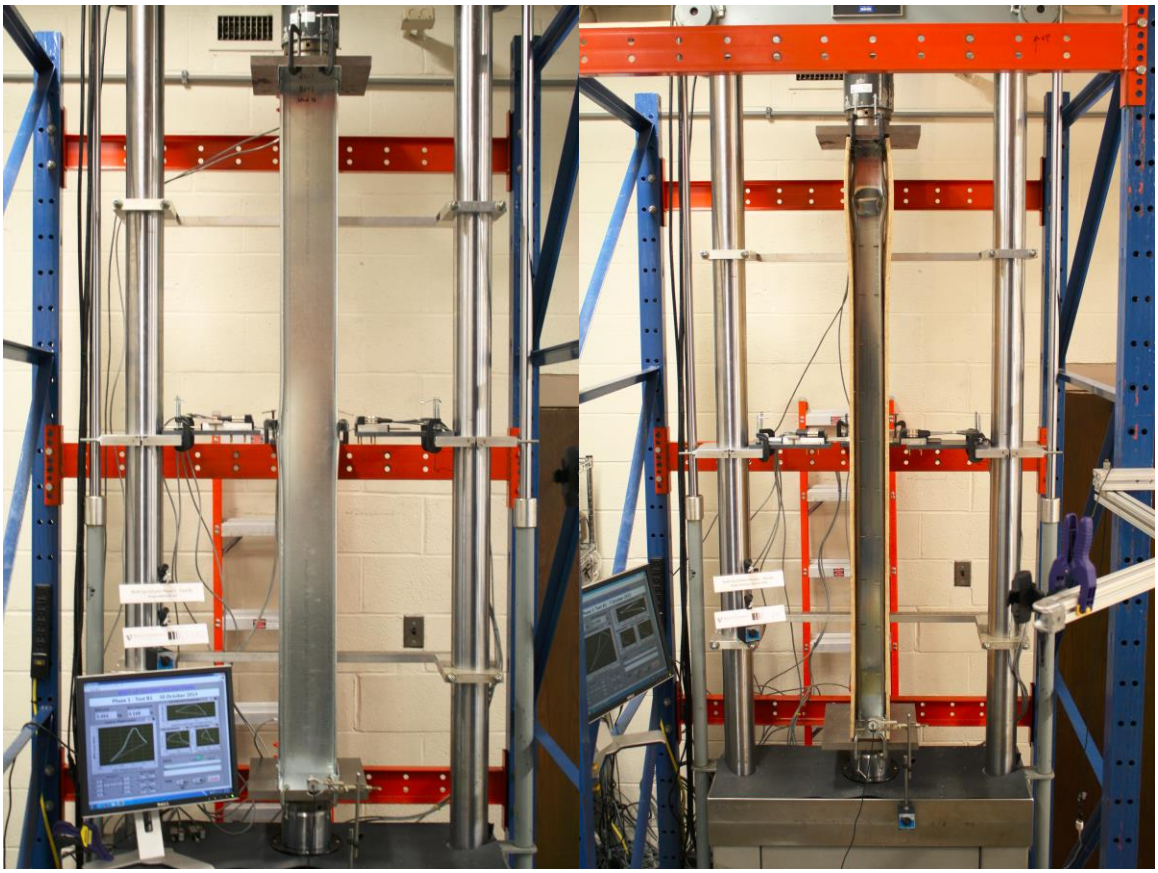

Figure 5. 15 Tests of unsheathed and sheathed built-up sections (Fratamico et al. 2016)

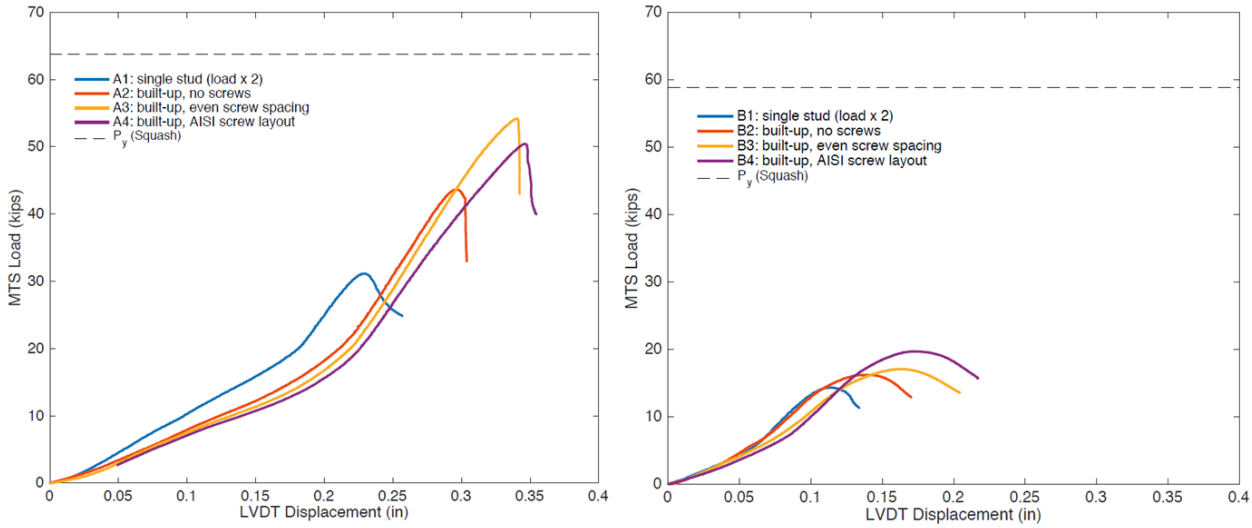

Figure 5. 16 Load vs. displacement for unsheathed columns: (a) 362S162-68; (b) 600S137-54 (Fratamico et al. 2016)

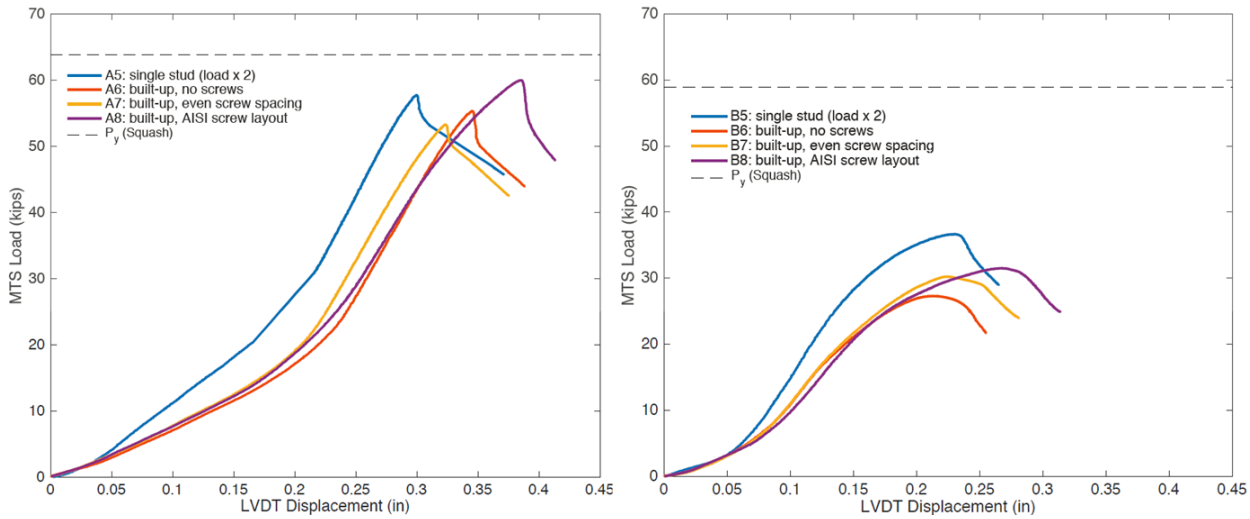

Figure 5. 17 . Load vs. displacement for sheathed columns: (a) 362S162-68; (b) 600S137-54 (Fratamico et al. 2016)

Figure 5. 16Various shapes of failure modes can be observed, such as local buckling and flexural buckling of then web. Similar to Z sections, deformation generally starts from the lip of the BUCs, and 362S162-68 was able to bear much larger loads in both the sheathed and unsheathed conditions. The sheathed plan had a higher load capacity in the AISI screw layout, but the unsheathed plan had better load capacity in even screw spacing. However, all of these sections failed before the yield point. More information is available in Fratamico et al. (2016).

5.4 Conclusions

This chapter displays several cold-formed steel members which were scanned, processed, and simulated in this research. Three shapes and five types of steel members are introduced, that is, Z, C (362S162-68), C (600S137-54), BUC (362S162-69), and BUC (600S137-54). Geometric information, manufacturing dimensions for example, is provided together with material properties. Coupon testing of both C sections and Z sections were conducted in the Thin-Walled Structures Laboratory at Johns Hopkins University, which discovered material properties, such as stiffness, yielding, and stress-strain relationships of studied cold-formed steel members. C sections are used

to form BUC sections. As a result, BUC sections have same material properties as C sections. Post-measurement testing is discussed in this chapter for Z sections and BUC sections. Z sections were tested for beam-column study where different levels of eccentricities were assigned to nominally identical Z members. BUC sections were tested under concentric compression where different fastener plans and sheathing plans were assigned to those members. C sections were not tested experimentally.

Chapter 6 Measurement of Dimensions

As mentioned in Chapter 5, measuring the dimensions of cold-formed steel members is very important since variations in the dimensions can have adverse effects on structural performance, such as strength and stiffness, by changing the geometric properties, such as area and moment of inertia. Conventional measurements may only survey three to five cross sections along the specimens due to technology constraints. Thus, many uncertainties exist in conventional measurements, such as biased samples, reading errors, and system errors. However, models reconstructed from laser measurements can deal with most of these limitations due to the large point clouds of 3D models. In this chapter, the strength of laser measurement toward true geometry is demonstrated by discussing three types of geometries, i.e., Z, C, and BUC.

6.1 Z

6.1.1 Dimension Estimation and constraints

For the zee section studied here, there are 13 quantities that can be calculated from a given cross section, as shown in Figure 6. 1. Radii r_1, r_2, r_3, and r_4 are estimated from corners that are found from the feature-recognition algorithm, as described in Chapter 4. Best-fit linear segments are fit to other regions, such as lips, flanges, and web, the intersections of which are used for estimating out-to-out dimensions. A constraint of laser measurement is that only a surface exposed to the laser scanner can be surveyed. Thus, only the external side of the zee section was measured, as shown by the solid line in the figure. The internal surface (dashed line in the figure) was generated from the offset of the external surface by a defined thickness. Another constraint was noted in that the laser measurement rig was unable to handle the thickness measurement, and the nominal thickness had to be assumed when estimating dimensions and conducting finite element modeling in a later chapter.

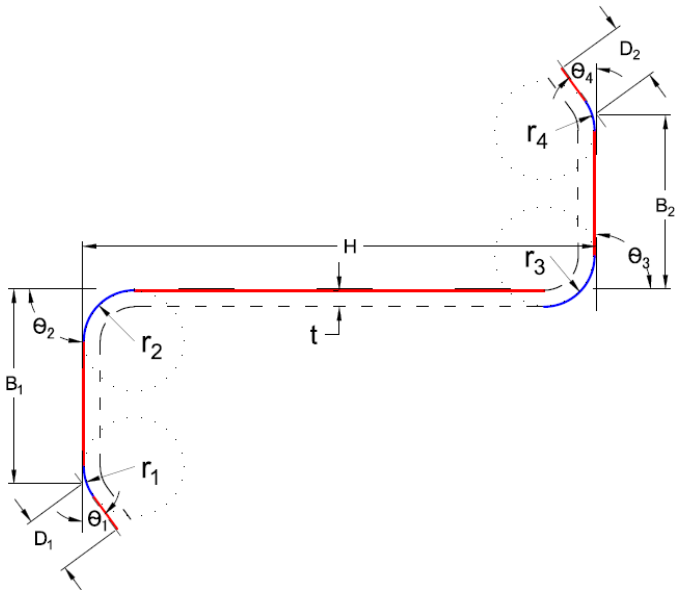

Figure 6. 1 Definition of the dimensions of Z shape purlin section

6.1.2 Dimension Results

Nineteen specimens of Z sections (700Z225-60) were studied, and the results are reported in this section. The sample specimen had a nominal length of 4 ft (48 in), a depth of 7 in, a flange width of 2.25 in, and a thickness of 0.060 in. Typical dimensions along the length are demonstrated in Figure 6. 2 a and b. It can be observed that the Z specimens manufactured from one steel sheet generally contained similar dimensions. For example, θ_1 in specimen 1 was wavy and ranged from 40° to 45°, whereas the number of waves in specimen 2 resembled that of specimen 1 and ranged from 39° to 45° (slightly different). This situation occurred in all Z sections. In addition, from both radii and angles, interesting phenomena can be observed in that corners near the web could be much better controlled than those next to the lips. Better quality control is presented from both magnitude deviations and noise level. Both θ_1 and θ_4 had poor-quality manufacturing since they were much smaller than the nominal angle of 48°. Also, r_1 and r_4 were much noisier than r2 and r3. This might suggest that different levels of variations in dimension simulation should be considered in modeling and that quality control should be considered in manufacturing.

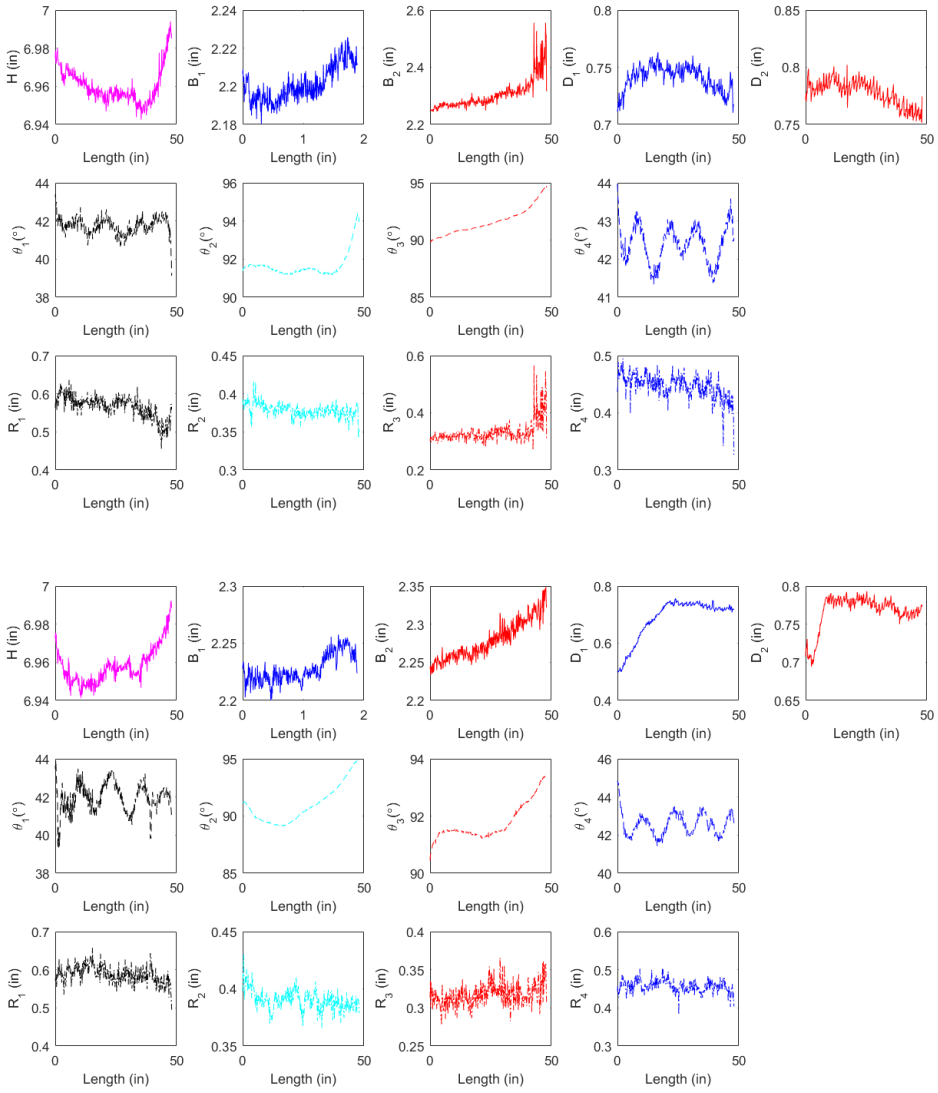

Figure 6. 2 Typical variations of dimensions along the length of Z sections: (a) Specimen 1; (b) Specimen 2.

6.1.3 Statistical study of dimensions

Table 6.1 provides the statistical summary of the dimensions that were measured, including 19 nominally-identical Z sections with densities of 356 cross sections along the 48-in length. Histograms and cumulative distribution functions (CDF) for different dimensions, i.e. web (H), left flanges (B_1), right flanges (B_2), left lip (D_1), right lip (D_2), radii (R_1, R_2, R_3, R_4), and corner angles (θ_1, θ_2, θ_3, θ_4). Dimensions from laser and manual measurements were summarized statistically and

compared with the nominal dimensions. It was observed that the mean values of web height from the laser were much closer to the nominal value than the manual measurements. There were large differences between the laser and the manual measurements of radii, especially for corners near the lips. Manual measurements, using a radius gage, were not as accurate as the laser measurement. Measured angles of corners near lips had huge deviations from the nominal dimensions as well, which explained the large differences between the true and nominal radii.

Table 6. 1 Statistical dimension summary from laser measurements of Z purlins

Dimension		H (in)	B_1 (in)	B_2 (in)	D_1 (in)	D_2 (in)	R_1 (in)	R_2 (in)	R_3 (in)	R_4 (in)	θ_1 (°)	θ_2 (°)	θ_3 (°)	θ_4 (°)
Laser[a]	5%	6.95	2.20	2.25	0.64	0.76	0.53	0.37	0.30	0.42	40.7	89.5	90.2	41.7
	10%	6.95	2.21	2.25	0.68	0.76	0.55	0.38	0.30	0.43	41.0	89.8	90.6	41.8
	50%	6.96	2.23	2.28	0.73	0.78	0.58	0.40	0.32	0.45	41.8	90.9	91.4	42.4
	75%	6.96	2.24	2.31	0.74	0.78	0.59	0.40	0.33	0.46	42.2	91.6	91.9	42.8
	90%	6.97	2.25	2.34	0.75	0.79	0.61	0.41	0.36	0.48	42.7	92.9	92.9	43.1
	Mean	6.96	2.23	2.29	0.72	0.78	0.58	0.40	0.33	0.45	41.8	91.1	91.5	42.4
	Std	0.01	0.02	0.04	0.04	0.02	0.03	0.01	0.04	0.02	0.8	1.3	1.3	1.0
Manual[b]	5%	6.89	2.11	2.11	0.69	0.73	0.39	0.34	0.28	0.31	40.6	86.6	86.9	40.5
	10%	6.90	2.19	2.17	0.70	0.74	0.39	0.34	0.28	0.31	40.9	87.0	87.1	41.0
	50%	6.91	2.25	2.27	0.73	0.76	0.39	0.34	0.28	0.31	42.1	88.6	88.2	42.1
	75%	6.92	2.27	2.29	0.74	0.78	0.39	0.34	0.28	0.31	42.5	89.2	88.8	42.6
	90%	6.93	2.29	2.31	0.77	0.81	0.39	0.34	0.28	0.31	43.1	89.9	89.7	43.2
	Mean	6.91	2.25	2.27	0.74	0.77	0.39	0.34	0.28	0.31	42.1	88.7	88.7	42.2
	Std	0.01	0.05	0.06	0.03	0.02	0.00	0.00	0.00	0.00	0.74	1.06	1.05	0.82
Nominal		7.00	2.25	2.25	0.77	0.77	0.37	0.37	0.37	0.37	48	90	90	48
L. vs. M.[d](%)		0.7	-0.9	0.9	-2.7	1.3	**48.7**	**17.6**	**17.9**	**45.2**	-0.7	2.7	3.2	0.5
L. vs. N.[e] (%)		-0.6	-1.1	1.9	-6	0.7	**56.1**	**6.8**	**-11**	**22.3**	**-12**	-1.3	-1.7	**-11**
M. vs. N.[f] (%)		-1.3	0.0	0.9	-3.9	0.0	**5.4**	**-8.1**	**-24.3**	**-16.2**	**-12.3**	-1.4	-1.4	**-12.1**

Note:

a. Laser measurements from 356 cross sections x 19 specimens;

b. Manual measurements from 5 cross sections x 19 specimens;

c. Thickness t was 0.06 in.

d. % Difference was estimated as |[mean(laser)-mean(manual)]/[mean(manual)]x100%|

e. % Difference was estimated as |[mean(laser)-nominal]/[nominal]x100%|

f. % Difference was estimated as |[mean(manual)-nominal]/[nominal]x100%|

g. The bold font indicate % difference larger than 5%

The distributions, particularly of the lip, were non-Gaussian. The length of the lip was the dimension that was the most difficult to control when roll-forming, but it has an important impact on the stability of the cross-section. Knowledge of the expected dimensional distributions could be used to examine the reliability of these sections to actual fabrication in a manner that, to date, has been impossible.

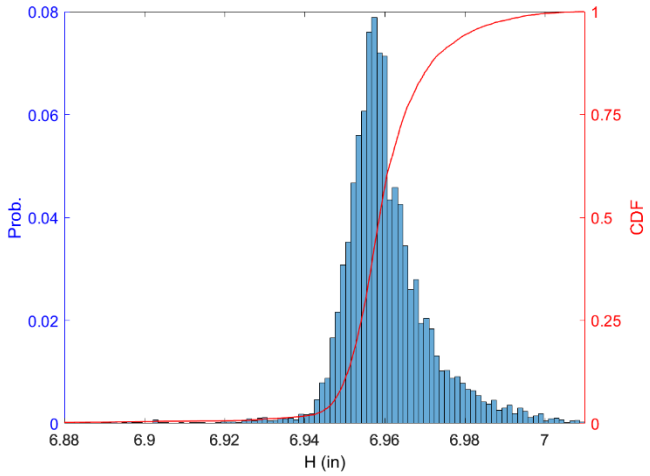

Figure 6. 3 Statistical summary of web height (H) [700Z225-60]

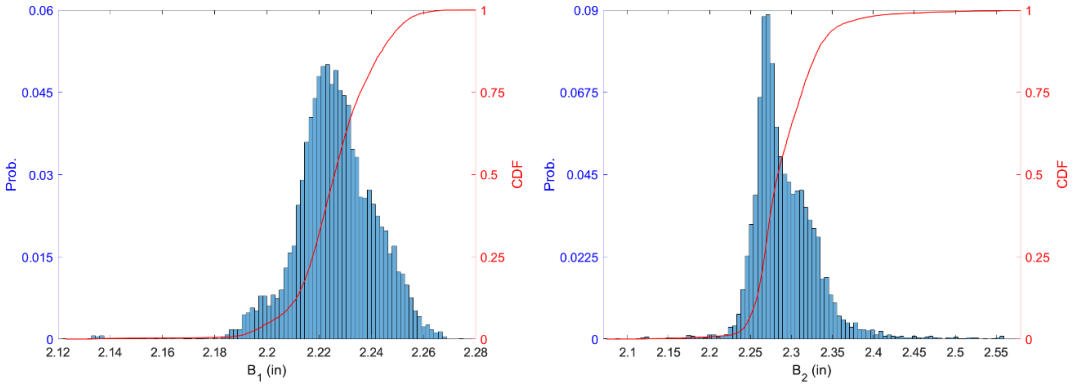

Figure 6. 4 Statistical summary of flanges (B_1 & B_2) [700Z225-60]

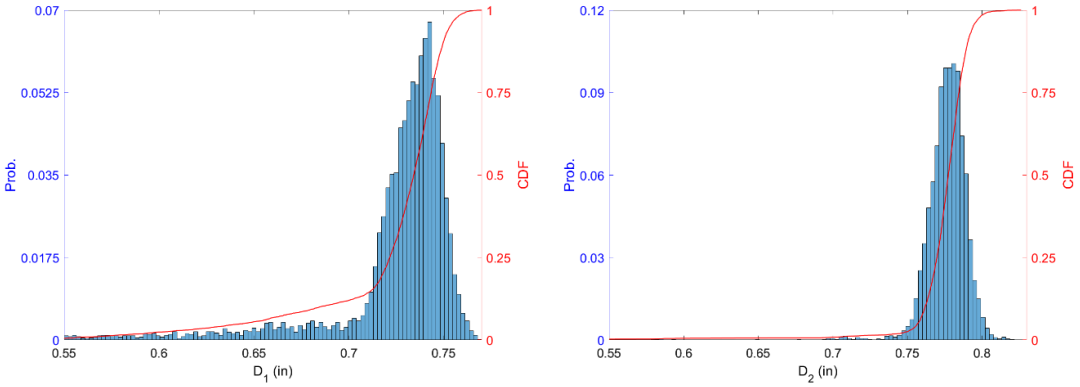

Figure 6. 5 Statistical summary of lips (D_1 & D_2) [700Z225-60]

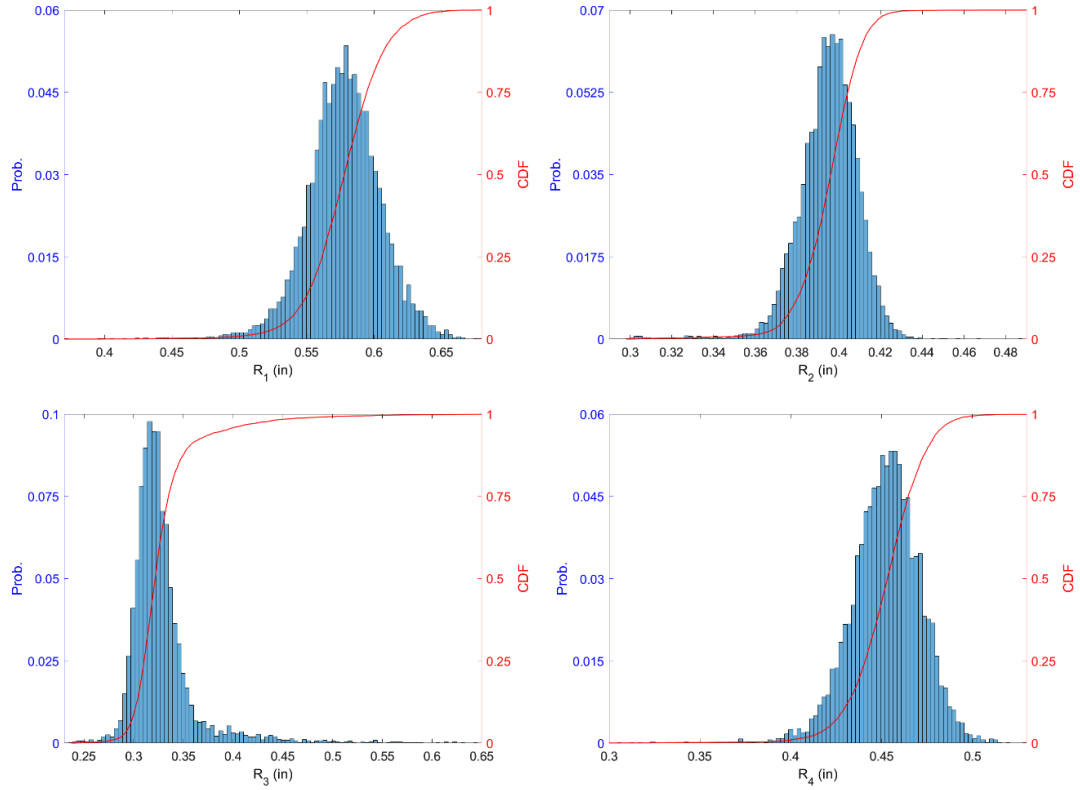

Figure 6. 6 Statistical summary of outside radii (R_1, R_2, R_3, R_4) [700Z225-60]

Traditional manual measurements are very difficult for estimating the radius of the corner and the length of the lip. Short lips with some inclination always require additional aids, such as a plate, and measuring a large radius with a radius gage requires a lot of manual judgment and guessing. Manual judgments may vary even if the measurements are done by the same person. Laser

measurements, however, have the advantage of large point clouds. There is no need to worry about the various dimensional definitions and uncertainties when estimating dimensions from laser measurements because they are produced from a specific algorithm with constant criteria. Moreover, laser measurements can have more data for further study, e.g., correlation analyses, than manual measurements.

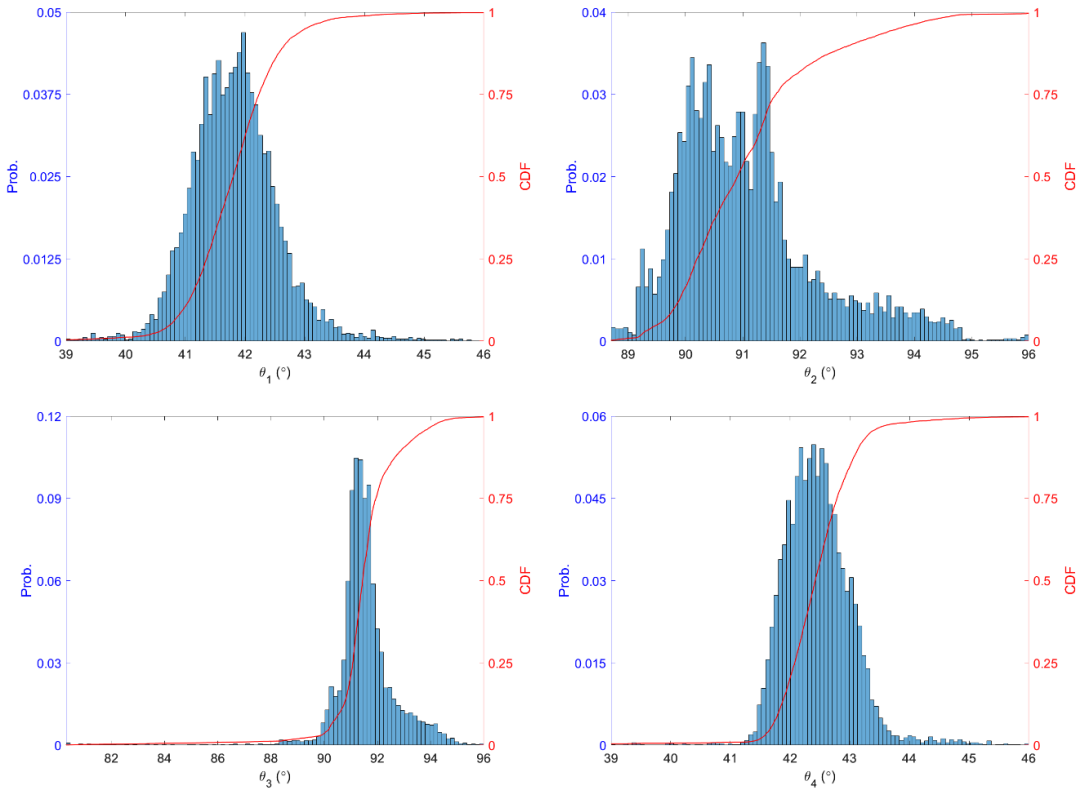

Figure 6. 7 Statistical summary of outside angles (θ_1, θ_2, θ_3, θ_4) [700Z225-60]

6.1.4 Correlation Study and Significance

Correlations among different dimensions deserve some attention since they can be used as the foundation of dimension-simulation studies. Fisher (2016) used an assumed correlation matrix from variations of dimensions from the design values to generate large amounts of simulated dimensions, and the results were used to determine the impacts of strength and stiffness. Inspired by this idea, a correlation matrix with significance estimation (p-value) was produced from a Pearson linear

correlation among variations of dimensions' quantities with respect to Z, C, and BUC. Variations are from differences between measured dimensions and the mean of measured dimensions. A comparison of the correlation matrix between true geometry and the scenario assumed by Fisher (2016) was conducted for C studs, and the results are reported in Section 6.2.4. This section is focused on the correlation of the dimensions of Z sections. Each dimension quantity of Z sections contains over 6,000 samples from 19 specimens and 365 cross sections. The results are demonstrated in Tables 6.2 and 6.3. An obvious correlation (> 0.4 or < -0.4) was observed among several pairs. The largest correlations were from θ_2 - H, θ_3-B_2. The correlation was significant in most cases (< 5%); the exceptions were B_2-D_2, D_2-H, R_2-H, D- θ_2, and θ_2-R_3.

Table 6. 2 Correlation Matrix of Z purlins

ρ	D_1	D_2	B_1	B_2	H	R_1	R_2	R_3	R_4	θ_1	θ_2	θ_3	θ_4
D_1	1.0	0.2	0.0	0.2	-0.1	-0.2	0.0	0.1	-0.2	-0.2	0.0	0.1	-0.1
D_2	0.2	1.0	-0.1	0.0	0.0	0.1	0.1	-0.1	-0.1	0.1	-0.2	0.3	0.6
B_1	0.0	-0.1	1.0	0.4	0.2	-0.2	0.3	0.1	0.0	0.0	0.4	0.4	0.1
B_2	0.2	0.0	0.4	1.0	**0.5**	**-0.6**	-0.3	**0.7**	**-0.6**	-0.1	0.6	0.8	0.2
H	-0.1	0.0	0.2	0.5	1.0	-0.4	0.0	0.2	-0.2	-0.1	0.7	0.6	0.2
R_1	-0.2	0.1	-0.2	-0.6	-0.4	1.0	0.4	-0.3	**0.7**	-0.1	**-0.5**	**-0.5**	-0.1
R_2	0.0	0.1	0.3	-0.3	0.0	0.4	1.0	-0.2	0.4	0.1	-0.3	-0.2	0.0
R_3	0.1	-0.1	0.1	0.7	0.2	-0.3	-0.2	1.0	-0.3	0.0	0.2	0.2	0.0
R_4	-0.2	-0.1	0.0	-0.6	-0.2	0.7	0.4	-0.3	1.0	0.1	-0.3	**-0.5**	-0.3
θ_1	-0.2	0.1	0.0	-0.1	-0.1	-0.1	0.1	0.0	0.1	1.0	-0.2	-0.2	0.2
θ_2	0.0	-0.2	0.4	0.6	0.7	-0.5	-0.3	0.2	-0.3	-0.2	1.0	**0.6**	0.1
θ_3	0.1	0.3	0.4	0.8	0.6	-0.5	-0.2	0.2	-0.5	-0.2	0.6	1.0	**0.4**
θ_4	-0.1	0.6	0.1	0.2	0.2	-0.1	0.0	0.0	-0.3	0.2	0.1	0.4	1.0

Table 6. 3 P-value for correlation study of Z purlins

p-val	D_1	D_2	B_1	B_2	H	R_1	R_2	R_3	R_4	θ_1	θ_2	θ_3	θ_4
D_1	1.00	0.00	0.01	0.00	0.00	0.00	0.01	0.00	0.00	0.00	0.38	0.00	0.00
D_2	0.00	1.00	0.00	0.14	0.07	0.00	0.00	0.00	0.00	0.00	0.00	0.00	0.00
B_1	0.01	0.00	1.00	0.00	0.00	0.00	0.00	0.00	0.05	0.02	0.00	0.00	0.00
B_2	0.00	0.14	0.00	1.00	0.00	0.00	0.00	0.00	0.00	0.00	0.00	0.00	0.00
H	0.00	0.07	0.00	0.00	1.00	0.00	0.33	0.00	0.00	0.00	0.00	0.00	0.00
R_1	0.00	0.00	0.00	0.00	0.00	1.00	0.00	0.00	0.00	0.00	0.00	0.00	0.00
R_2	0.01	0.00	0.00	0.00	0.33	0.00	1.00	0.00	0.00	0.00	0.00	0.00	0.00
R_3	0.00	0.00	0.00	0.00	0.00	0.00	0.00	1.00	0.00	0.66	0.00	0.00	0.00
R_4	0.00	0.00	0.05	0.00	0.00	0.00	0.00	0.00	1.00	0.00	0.00	0.00	0.00
θ_1	0.00	0.00	0.02	0.00	0.00	0.00	0.00	0.66	0.00	1.00	0.00	0.00	0.00
θ_2	0.38	0.00	0.00	0.00	0.00	0.00	0.00	0.00	0.00	0.00	1.00	0.00	0.00
θ_3	0.00	0.00	0.00	0.00	0.00	0.00	0.00	0.00	0.00	0.00	0.00	1.00	0.00
θ_4	0.00	0.00	0.00	0.00	0.00	0.00	0.00	0.00	0.00	0.00	0.00	0.00	1.00

6.2 C

6.2.1 Dimension Estimation Procedures

Similar to the Z section, 13 quantities of dimensions were calculated from a given cross section, as shown in Figure 6. 8. Compared to the Z section, the C section can obtain a continuous geometry with the entire external surface being accessible by the scanner. Thus, the measurement error can be controlled better. As corners with radii are identified from feature recognition algorithm and a 3D model is reconstructed, a linear curve is fitted to each flat region, i.e., flat web, flat flanges, and flat lips. Coordinates (x and z) of intersections among adjacent fitted curves are used to find relative distances, which are taken as corresponding to the out-to-out dimensions. The scans of the C section have the same restraints as those of Z sections, i.e., information about the internal surfaces is missing, and the thickness measurements must be made manually.

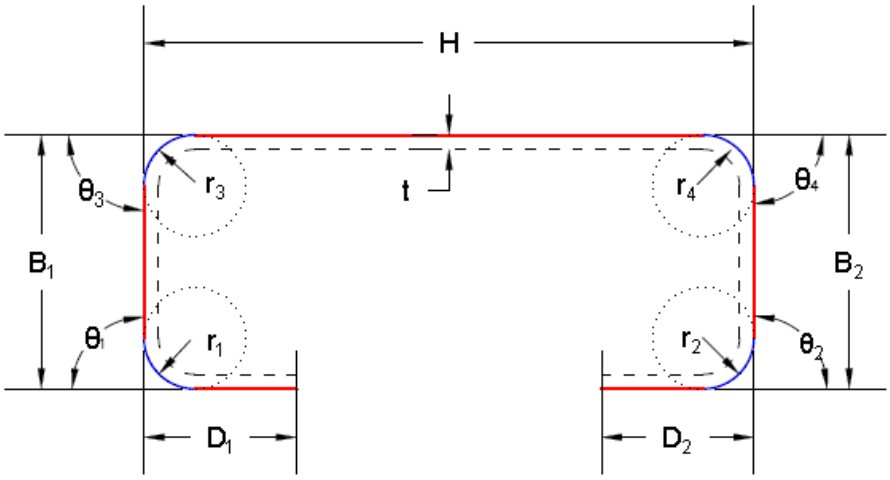

Figure 6. 8 Definition of the dimensions of C sections

6.2.2 Dimension Results

Two types of C sections were evaluated in the dimension studies, and the lengths of both were 6 ft (72 in). Their nominal dimensions were different, i.e., 362S162-68 had web depth, flange width, lip width, and thickness of 3.625, 1.625, 0.5, and 0.0713 in, respectively, whereas 600S137-54 had web depth, flange width, lip width, and thickness of 6, 1.375, 0.375, and 0.0566 in, respectively. Figure 6. 9 a and b show typical variations of the dimensions along the lengths of two 362S162-68 specimens; Figure 6. 10 shows the typical variations for 600S137-54 specimens. Two phenomena can be observed by comparing the two types of specimens, i.e., 1) in general, lip lengths are much noisier than web heights and flange width and 2) radii close to the web contain less disturbance. The 600S137-54 C sections had less 'noise,' especially in angles next to the webs. It may be worthwhile to study the noise distribution of dimensions in additional samples.

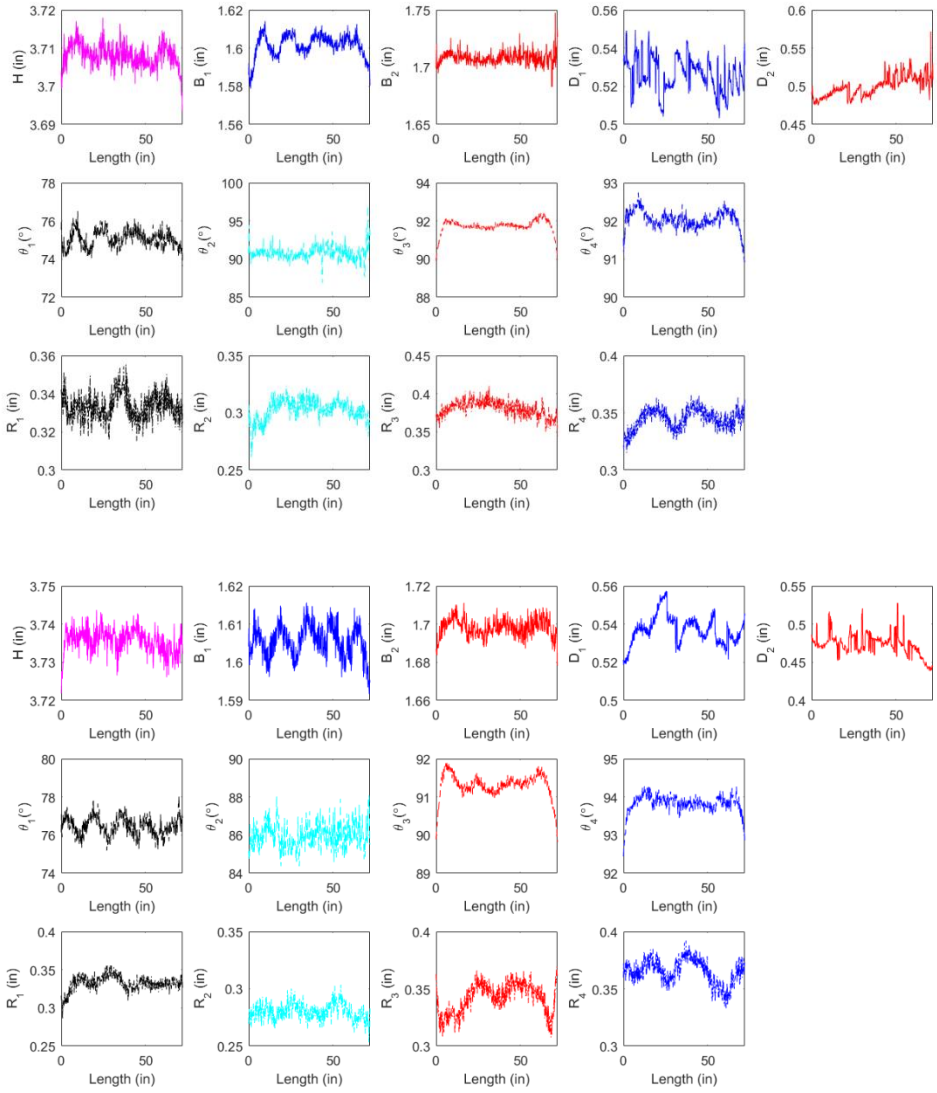

Figure 6. 9 Typical variations of dimensions along the length of C sections [362S162-68]: (a) Specimen 1; (b) Specimen 2

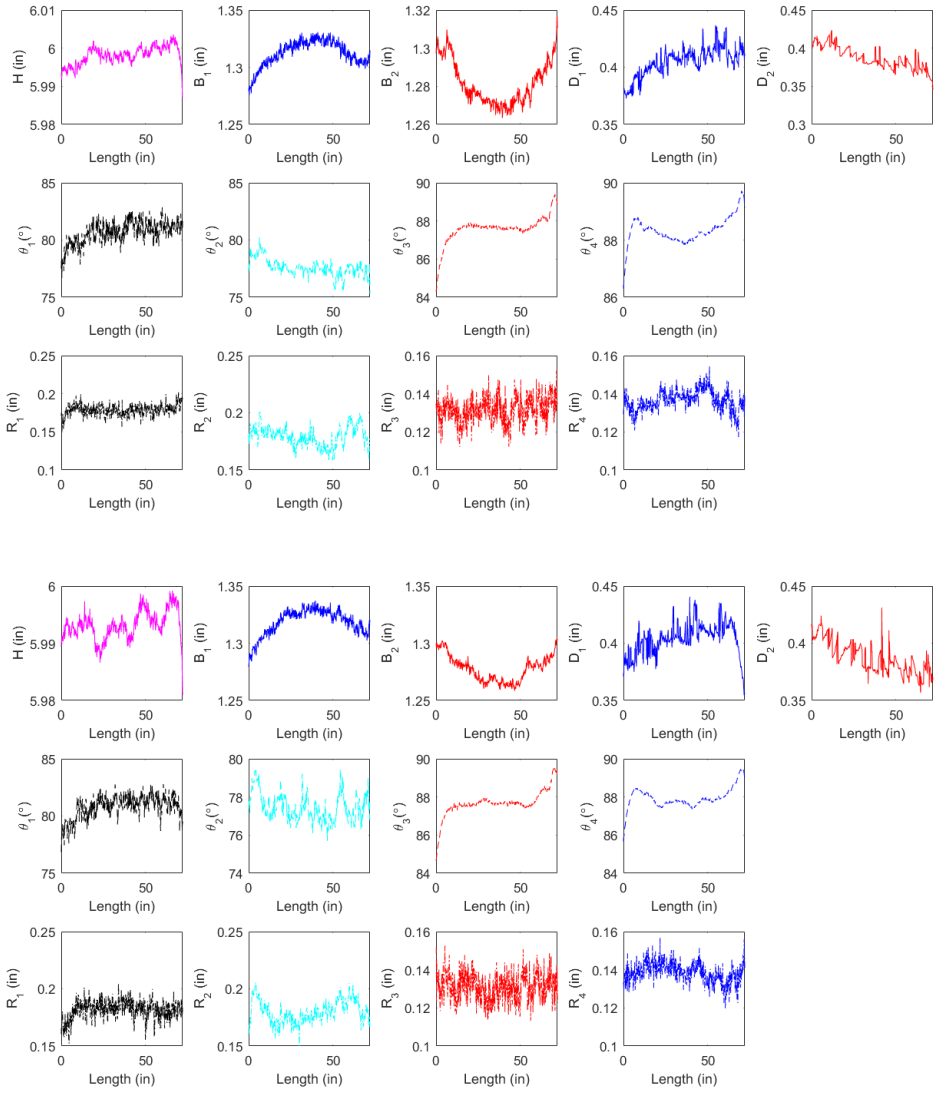

Figure 6. 10 Typical variations of dimensions along the length of C sections [600S137-54]; (a) Specimen 1; (b) Specimen 2

6.2.3 Statistical study of dimensions

Reading from Table 2a and b, it seems that 600S137-54 had better control in web height and radii R1, R2, R3, and R4, reporting only 0.1, 28.4, 29.1, -2.4, and -1% vs. 2.6, 79.2, 52.5, 94.6, and 86%, respectively. Corners adjacent to the web are in a strict quality control and approach to manufacturing dimensions (angles and radii). However, it may be concluded that poorer control exists in small dimensions than with the two types of studs' flange widths and web heights. Larger

web depths contribute to smaller deviations of the radii. However, angles, especially those next to lips, may have worse deviations, which can be generated easily during manufacturing and transportation.

Table 6. 4a Summary of the statistical dimensions of the C-shape section [Stud: 362S162-68]

Dimension		H (in)	B_1 (in)	B_2 (in)	D_1 (in)	D_2 (in)	R_1 (in)	R_2 (in)	R_3 (in)	R_4 (in)	θ_1 (°)	θ_2 (°)	θ_3 (°)	θ_4 (°)
Laser[a]	5%	3.71	1.58	1.68	0.52	0.45	0.30	0.26	0.32	0.29	74.4	85.5	90.9	91.9
	10%	3.71	1.59	1.69	0.52	0.46	0.31	0.26	0.33	0.30	74.7	85.8	91.1	92.2
	50%	3.72	1.60	1.70	0.54	0.48	0.32	0.27	0.35	0.34	75.6	87.2	91.6	93.0
	75%	3.73	1.61	1.70	0.54	0.49	0.33	0.28	0.36	0.35	76.0	87.9	91.8	93.5
	90%	3.74	1.61	1.71	0.55	0.50	0.34	0.29	0.38	0.37	76.4	88.9	92.1	94.0
	Mean	3.72	1.60	1.70	0.53	0.48	0.32	0.27	0.35	0.33	75.6	87.3	91.6	93.1
	Std	0.01	0.01	0.01	0.01	0.02	0.01	0.01	0.02	0.03	0.7	1.4	0.4	0.7
Nominal		3.63	1.63	1.63	0.50	0.50	0.18	0.18	0.18	0.18	90	90	90	90
L. vs. N. (%)[c]		2.6	-1.6	2.6	**6.9**	-3.6	**79.2**	**52.5**	**94.6**	**86**	**-16**	-3	1.7	3.4

Note:

a. Laser measurements from 548 cross sections x 14 specimens

b. Thickness, t, is 0.0588 in

c. % Difference is estimated as |[mean(laser)-nominal]/[nominal]x100%|

d. Bold font indicates % difference values larger than 5%

Table 6. 5b Statistical dimension summary of C shape section [Stud: 600S137-54]

Dimension		H (in)	B_1 (in)	B_2 (in)	D_1 (in)	D_2 (in)	R_1 (in)	R_2 (in)	R_3 (in)	R_4 (in)	θ_1 (°)	θ_2 (°)	θ_3 (°)	θ_4 (°)
Laser[a]	5%	5.99	1.29	1.26	0.37	0.37	0.17	0.17	0.12	0.13	77.6	76.4	86.3	87.5
	10%	6.00	1.30	1.27	0.38	0.37	0.17	0.17	0.12	0.13	78.4	76.7	87.1	87.7
	50%	6.01	1.32	1.28	0.40	0.39	0.18	0.18	0.13	0.14	80.4	77.7	87.7	88.1
	75%	6.01	1.33	1.29	0.41	0.40	0.18	0.19	0.14	0.14	81.0	78.3	87.9	88.4
	90%	6.02	1.33	1.30	0.42	0.41	0.19	0.19	0.14	0.14	81.5	79.2	88.3	88.8
	Mean	6.01	1.32	1.28	0.40	0.39	0.18	0.18	0.13	0.14	80.2	77.8	87.6	88.2
	Std	0.01	0.01	0.01	0.01	0.01	0.01	0.01	0.01	0.01	1.23	1.07	0.71	0.6
Nominal		6.00	1.38	1.38	0.38	0.38	0.14	0.14	0.14	0.14	90	90	90	90
L. vs. N. (%)[c]		0.1	-4.3	**-7.2**	**5.3**	2.6	**28.5**	**28.5**	-0.0	-0.0	**-11**	**-13**	-2.6	-2

Note:

a. Laser measurements from 548 cross sections x 14 specimens

b. Thickness, t, is 0.0588 in

c. % Difference is estimated as |[mean(laser)-nominal]/[nominal]x100%|

d. Bold font indicates % difference values larger than 5%

Histograms as well can provide another view of the variations of dimensions. Most dimensions, especially those in the 600S137-54 studs, were non-Gaussian with distinct distribution curves. These particular distributions may be either from measurement errors, scans of some studs in opposite directions, or from true deviations of dimensions. Considering each type of C studs, about 7,672 cross sections (14 studs/per type x 548 cross sections/per stud) are involved. Histograms of web heights in 362S162-68 had more than one peak. It is difficult to explain the situation directly from the one histogram of web height in Figure 6.11 unless histograms of two radii (R3 and R4) in Figure 6.14 are taken into consideration. The R3 histogram shows a second peak between the [0.38, 0.4] interval in the x direction (in); the R4 histogram has a second peak between [0.36, 0.38]. The two peaks have distances from the first peaks of 0.03 and 0.04 in with respect to R3 and R4. They have a 0.01 in difference, and this characteristic can be observed in the web height histogram in Figure 6.11 as well. It shows that the web heights are affected from the variations of R3 and R4 and thus has three peaks in the web height's histogram.

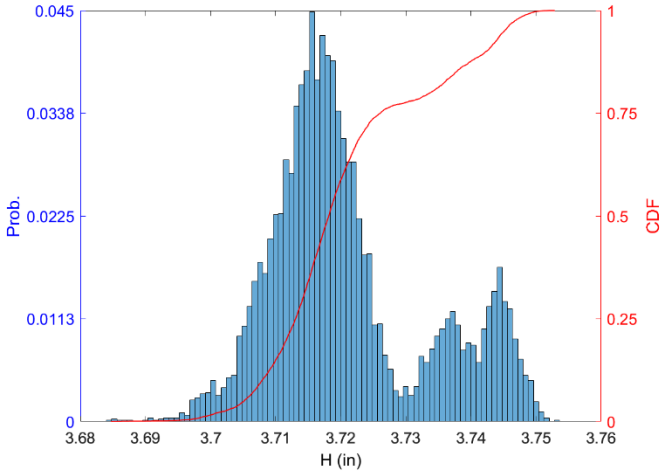

Figure 6. 11 Statistical summary of web height (H) [362S162-68]

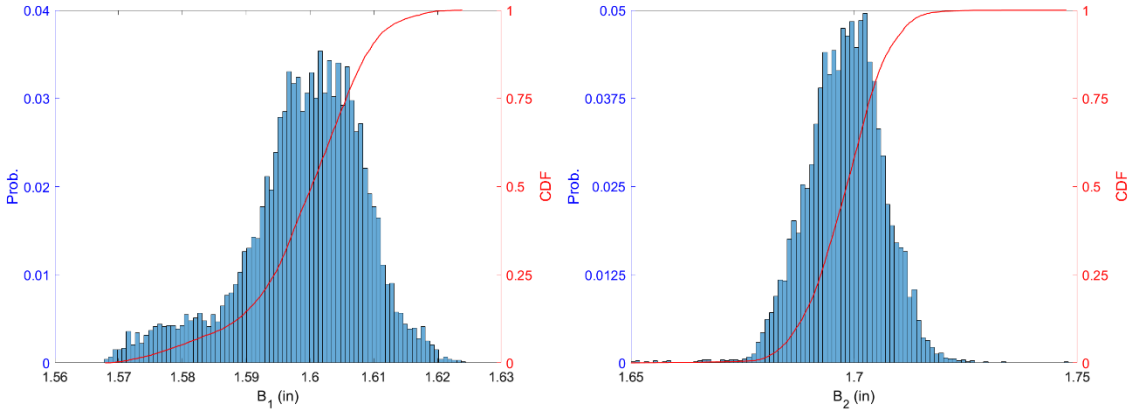

Figure 6. 12 Statistical summary of flange width (B_1 & B_2) [362S162-68]

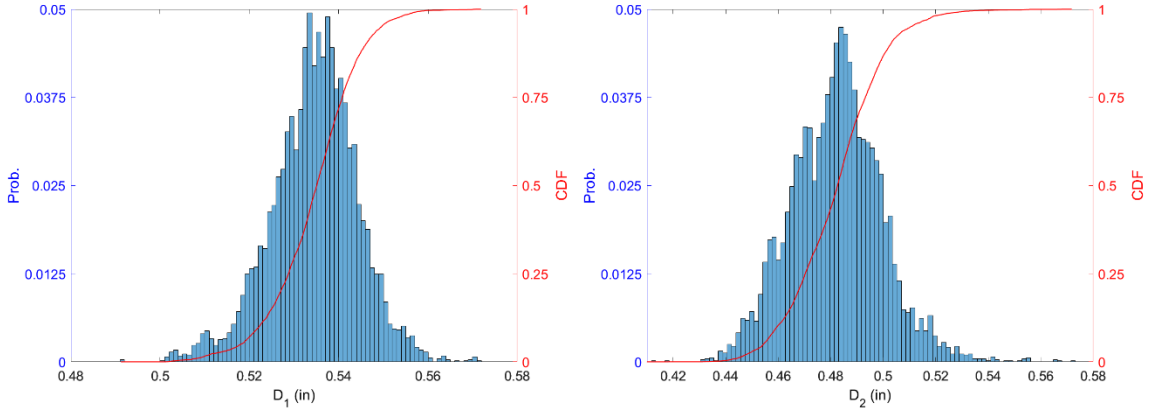

Figure 6. 13 Statistical summary of lip lengths (D_1 & D_2) [362S162-68]

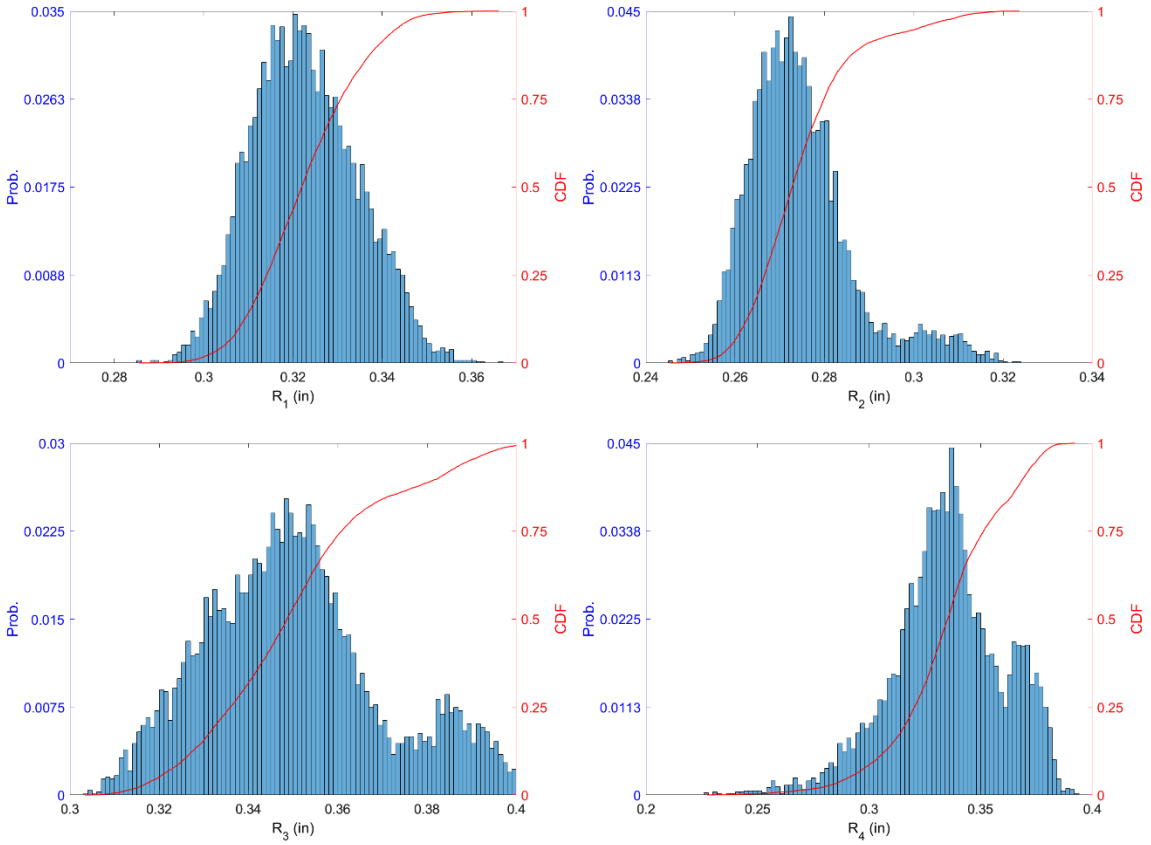

Figure 6. 14 Statistical summary of radii (R_1, R_2, R_3, R_4) [362S162-68]

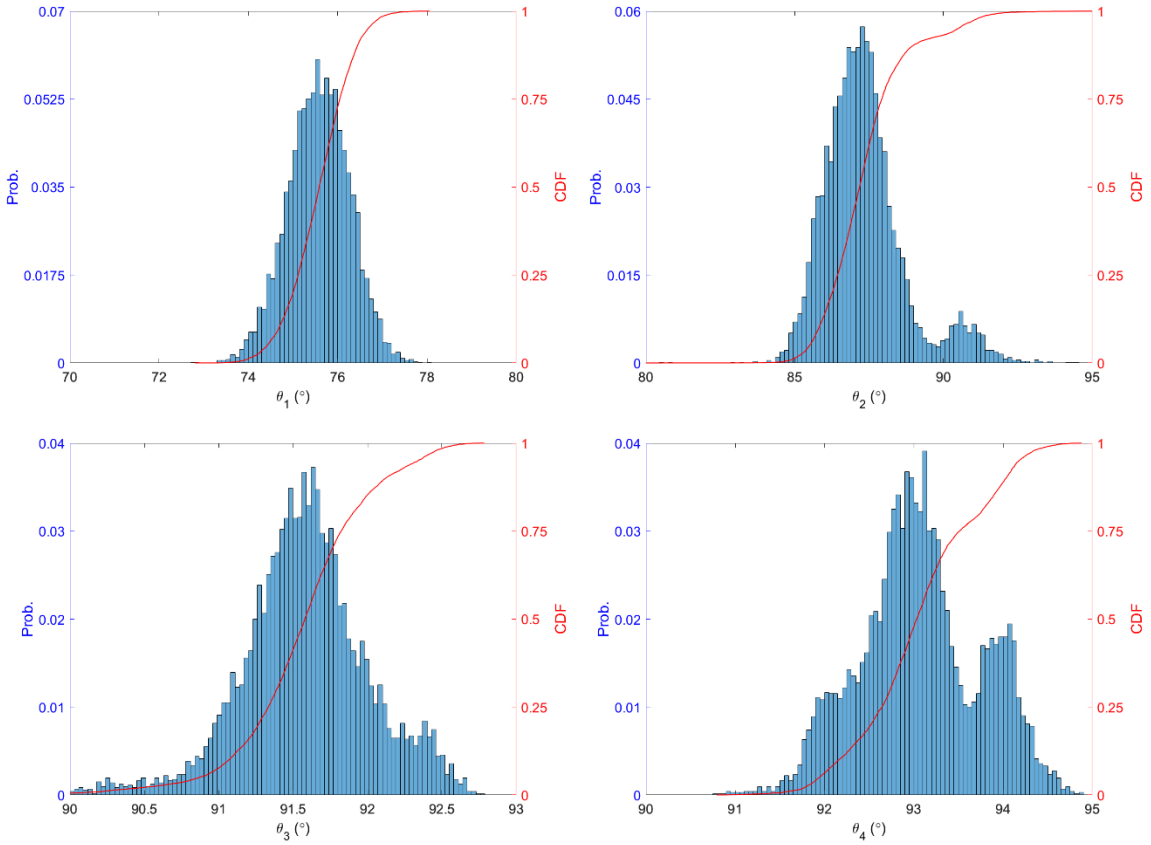

Figure 6. 15 Statistical summary of angles (θ_1, θ_2, θ_3, θ_4) [362S162-68]

Regarding 600S137-54, the web height has two peaks on its histogram, which can be attributed to two groups of 600S137-54. The actual deviation between the two groups was around 0.01 in, which may be contributed by two different batches. Flanges and lips, however, display interesting phenomena. Histogram distributions between right-side dimensions and left-side dimensions are offset. For example, the histogram of the left-side flange (B_1) has a peak at 1.33 in, and it has a left tail; the histogram of the right-side flange (B_2) has a peak at 1.28 in, and it has a right tail. Distributions of radii of 600S137-54 seem more Gaussian than any of the other histograms. Histograms of angles near the web, i.e., θ_1 and θ_2, have their peaks in the interval [87°, 89°], indicating better control than the angles near the lips, i.e., θ_3 and θ_4. The histogram of θ_1 has a long left tail at least to 75°; the histogram of θ_2 has a long right tail up to 82°.

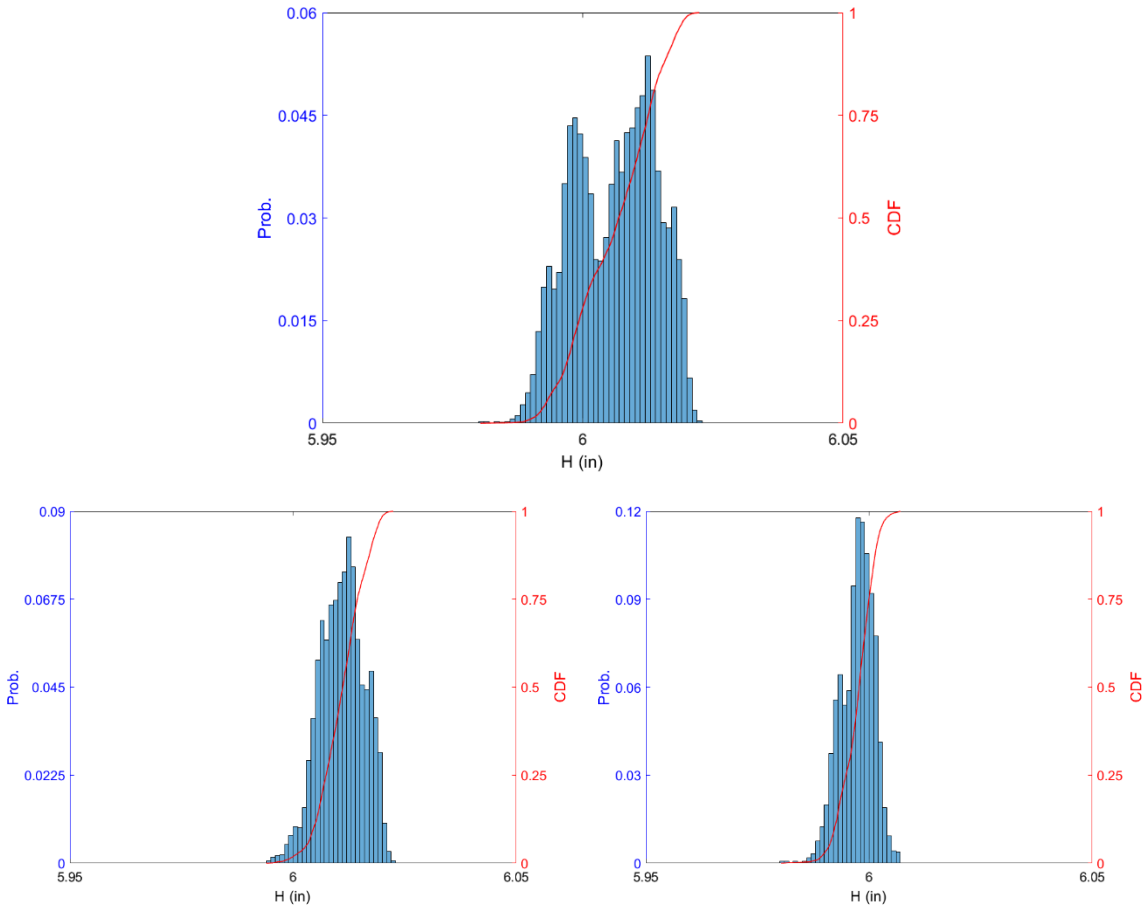

Figure 6. 16 Statistical summary of web height (H) [600S137-54]; (a) specimens 1- 14; (b) specimens 1-4; (c) specimens 5-14

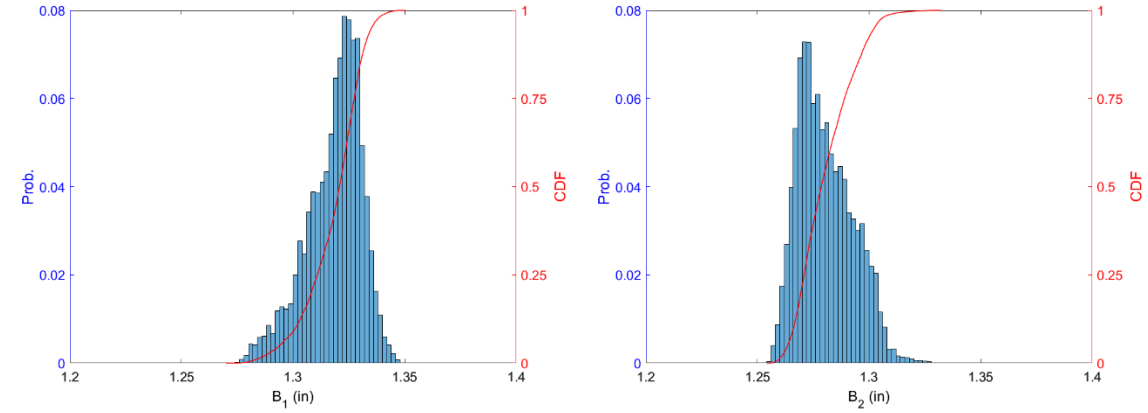

Figure 6. 17 Statistical summary of flanges (B_1 and B_2) [600S137-54]

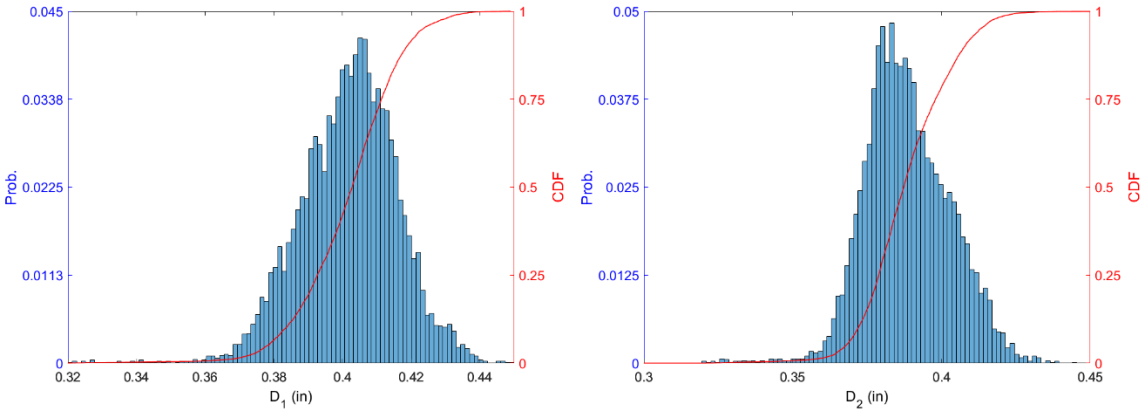

Figure 6. 18 Statistical summary of lip lengths (D_1 and D_2) [600S137-54]

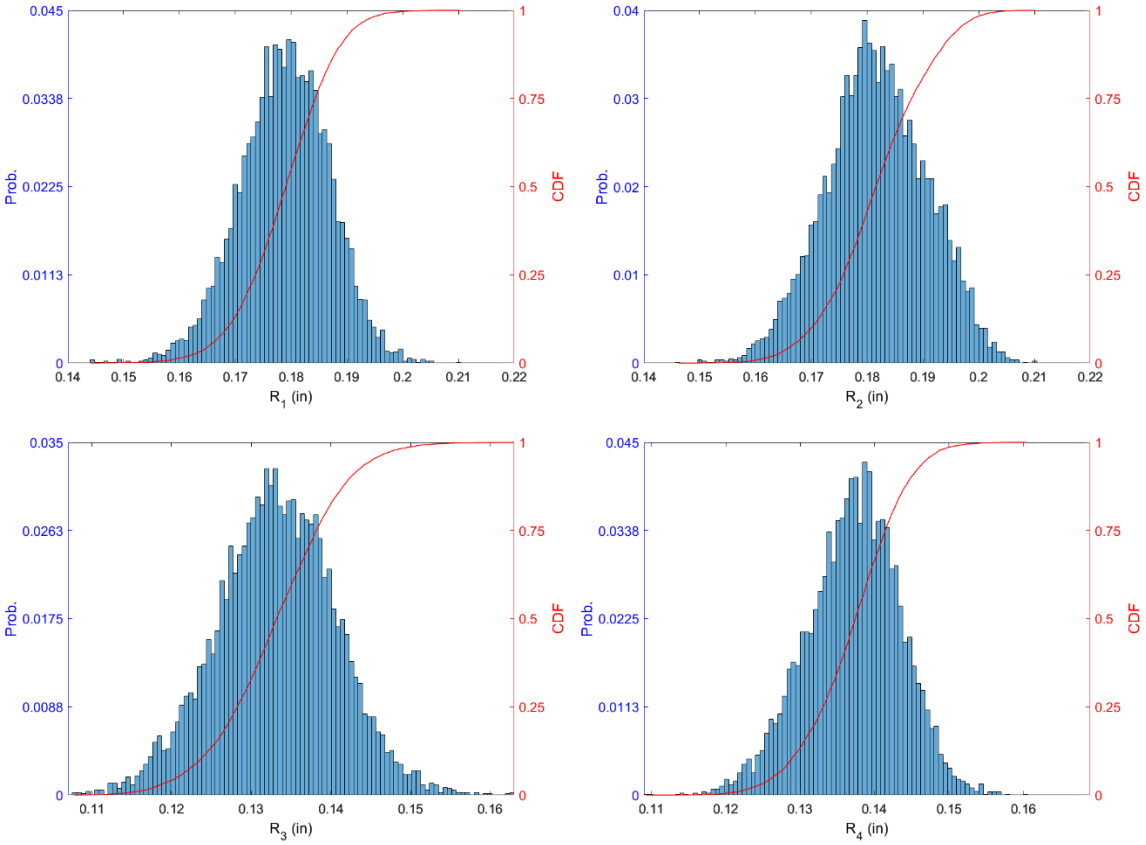

Figure 6. 19 Statistical summary of outside radii (R_1, R_2, R_3, R_4) [600S137-54]

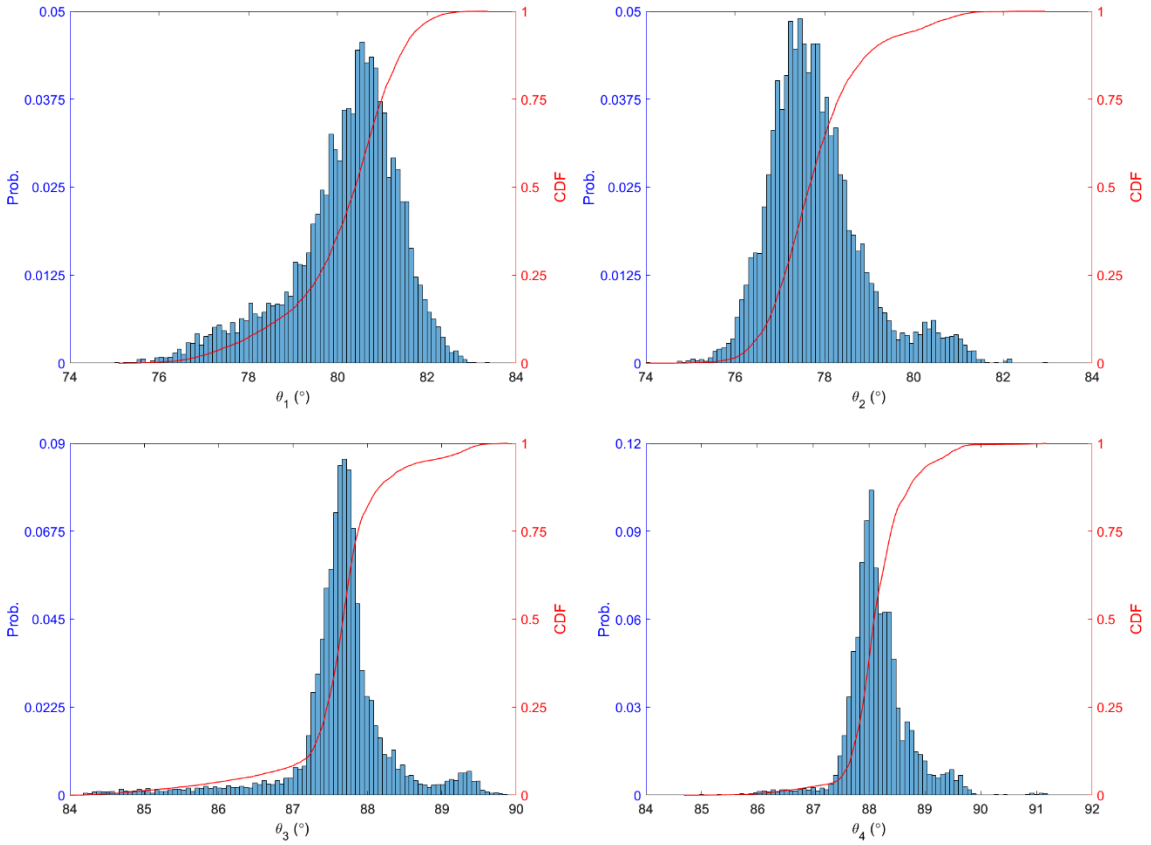

Figure 6. 20 Statistical summary of outside angles (θ_1, θ_2, θ_3, θ_4) [600S137-54]

6.2.4 Correlation Study and Significance

Similar to Z sections, correlation studies have been done for C sections as well. By combining the dimensional variations of both types of specimens, convincing correlation results can be obtained that follow traditional Pearson linear correlation theory, in which a correlation matrix can be formed for all 13 quantities. The matrix is symmetric, and data from the upper right triangle of the matrix is enough for analysis. Values in the green grids are positive correlation factors, and values in the blue grids are negative correlation factors. Values in bold font are larger than 0.4 or smaller than -0.4. The threshold of the p-value was set as 0.5%, where a reliable correlation factor should have a smaller p-value than the criterion. Compared to Z purlins, C sections contribute to more stable results and provide a firm relationship among dimensions.

B_1 is highly negative-correlated with B_2, and D_1 is highly negative-correlated with D_2. The findings from the correlation matrix verify the observations from the histograms of two types of C studs. In addition, B_1 shares a strong negative correlation with B_2, where the correlation factor is -0.65.

An interesting comparison was conducted between the correlation matrix from measurement (Table 6.6) and that from the assumption made by Fischer (2016). Fischer assumeed correlations among dimensions as follows: (1) two lips are negative correlated with the correlation factor -1, (2) the same-side flanges and lips are negative correlated, and (3) lips are negative correlated with the web height and correlation factors are -0.5

The true geometry validates Fischer's first assumption, but it disagrees with the other two assumptions. Same-side flanges and lips are not strongly correlated, but they do have a positive correlation factor. This may be contributed by the strong negative correlation between two flanges due to misalignment of the steel sheet during manufacturing. Web height is not strongly correlated with lip lengths. An interesting phenomenon can be observed that web height is positively-correlated with the left-side lip and negatively-correlated with the right-side lip. This further supports the assumption of misalignment of the steel sheet.

Table 6. 6 Correlation Matrix of C studs [362S162-68 & 600S137-54]

ρ	D_1	D_2	B_1	B_2	H	R_1	R_2	R_3	R_4	θ_1	θ_2	θ_3	θ_4
D_1	1.0	**-0.5**	0.3	**-0.4**	0.2	0.1	-0.1	0.0	0.1	0.3	-0.3	0.3	0.2
D_2	-0.5	1.0	-0.2	0.2	-0.4	-0.1	0.2	-0.1	-0.3	-0.2	**0.4**	-0.4	-0.5
B_1	0.3	-0.2	1.0	**-0.7**	0.2	0.0	0.0	0.1	0.1	**0.5**	-0.2	**0.5**	0.0
B_2	-0.4	0.2	-0.7	1.0	0.0	0.0	0.3	0.1	0.2	-0.3	0.3	-0.1	0.3
H	0.2	-0.4	0.2	0.0	1.0	0.0	-0.1	0.1	**0.6**	0.1	-0.3	0.3	**0.6**
R_1	0.1	-0.1	0.0	0.0	0.0	1.0	0.2	0.1	0.3	0.1	0.1	0.1	0.1
R_2	-0.1	0.2	0.0	0.3	-0.1	0.2	1.0	0.4	0.2	-0.1	**0.4**	0.1	-0.1
R_3	0.0	-0.1	0.1	0.1	0.1	0.1	0.4	1.0	0.2	-0.2	0.2	0.1	-0.1
R_4	0.1	-0.3	0.1	0.2	0.6	0.3	0.2	0.2	1.0	0.2	-0.2	0.1	0.5
θ_1	0.3	-0.2	0.5	-0.3	0.1	0.1	-0.1	-0.2	0.2	1.0	**-0.5**	0.2	0.2
θ_2	-0.3	0.4	-0.2	0.3	-0.3	0.1	0.4	0.2	-0.2	-0.5	1.0	-0.1	-0.4
θ_3	0.3	-0.4	0.5	-0.1	0.3	0.1	0.1	0.1	0.1	0.2	-0.1	1.0	**0.5**
θ_4	0.2	-0.5	0.0	0.3	0.6	0.1	-0.1	-0.1	0.5	0.2	-0.4	0.5	1.0

Table 6. 7 P-value for correlation study of C studs

p-val	D_1	D_2	B_1	B_2	H	R_1	R_2	R_3	R_4	θ_1	θ_2	θ_3	θ_4
D_1	1.00	0.00	0.00	0.00	0.00	0.00	0.00	0.51	0.00	0.00	0.00	0.00	0.00
D_2	0.00	1.00	0.00	0.00	0.00	0.00	0.00	0.00	0.00	0.00	0.00	0.00	0.00
B_1	0.00	0.00	1.00	0.00	0.00	0.00	0.21	0.00	0.00	0.00	0.00	0.00	0.01
B_2	0.00	0.00	0.00	1.00	0.00	0.00	0.00	0.00	0.00	0.00	0.00	0.00	0.00
H	0.00	0.00	0.00	0.00	1.00	0.93	0.00	0.00	0.00	0.00	0.00	0.00	0.00
R_1	0.00	0.00	0.00	0.00	0.93	1.00	0.00	0.00	0.00	0.00	0.00	0.00	0.00
R_2	0.00	0.00	0.21	0.00	0.00	0.00	1.00	0.00	0.00	0.00	0.00	0.00	0.00
R_3	0.51	0.00	0.00	0.00	0.00	0.00	0.00	1.00	0.00	0.00	0.00	0.00	0.00
R_4	0.00	0.00	0.00	0.00	0.00	0.00	0.00	0.00	1.00	0.00	0.00	0.00	0.00
θ_1	0.00	0.00	0.00	0.00	0.00	0.00	0.00	0.00	0.00	1.00	0.00	0.00	0.00
θ_2	0.00	0.00	0.00	0.00	0.00	0.00	0.00	0.00	0.00	0.00	1.00	0.00	0.00
θ_3	0.00	0.00	0.00	0.00	0.00	0.00	0.00	0.00	0.00	0.00	0.00	1.00	0.00
θ_4	0.00	0.00	0.01	0.00	0.00	0.00	0.00	0.00	0.00	0.00	0.00	0.00	1.00

Table 6. 8 Simulation of correlation matrix (Fischer, 2016)

ρ	D_1	D_2	B_1	B_2	H
D_1	1.00	-1.00	-1.00	0.00	-0.50
D_2	-1.00	1.00	0.00	-1.00	-0.50
B_1	-1.00	0.00	1.00	0.00	0.00
B_2	0.00	-1.00	0.00	1.00	0.00
H	-0.50	-0.50	0.00	0.00	1.00

6.3 BUC

6.3.1 Dimension Estimation Procedures

Calculations of dimension procedures resemble those of C calculations, i.e., radii estimation is completed in the feature recognition where corners' features are configured. Flat regions are fitted by linear lines, and intersection coordinates are obtained. Adjacent intersections are used to estimate out-to-out dimensions, such as webs, flanges, and lips. Variations of adjacent directions of linear curves (assuming fitting lines following cross sections) are tracked to find angles of recognized corners. These procedures are conducted in the lower sections as a whole followed by the upper sections.

Different from pure C sections, external webs cannot be scanned since they are attached by fasteners. Small parts near the corners of the upper internal web are missing, since the sight of the scanner was blocked by the upper lips. Information of the lower webs cannot be collected since they are not exposed to the scanner. Therefore, it is always assumed that upper and lower C sections are well attached and that they have identical web shapes.

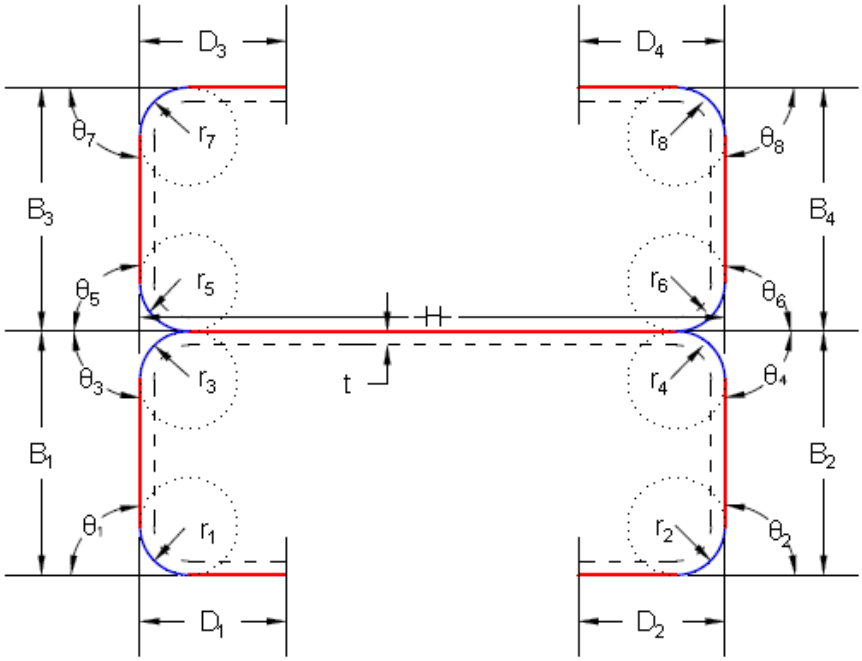

Figure 6. 21 Definition of the dimensions of BUC

6.3.2 Dimension Results

Dimensions along length of BUCs are very similar to those of C sections, except that lips on the upper sections always contain less noise in 362S162-68 and more noise in 600S137-54. However, theoretically, the upper and lower sections should have the same levels of noises. This may be an interesting issue that requires future scanning studies. Other conclusions can be made similar to those of C sections. Corners near webs were cleaner than those farther away from webs. Large dimensions generally have better control than small dimension quantities.

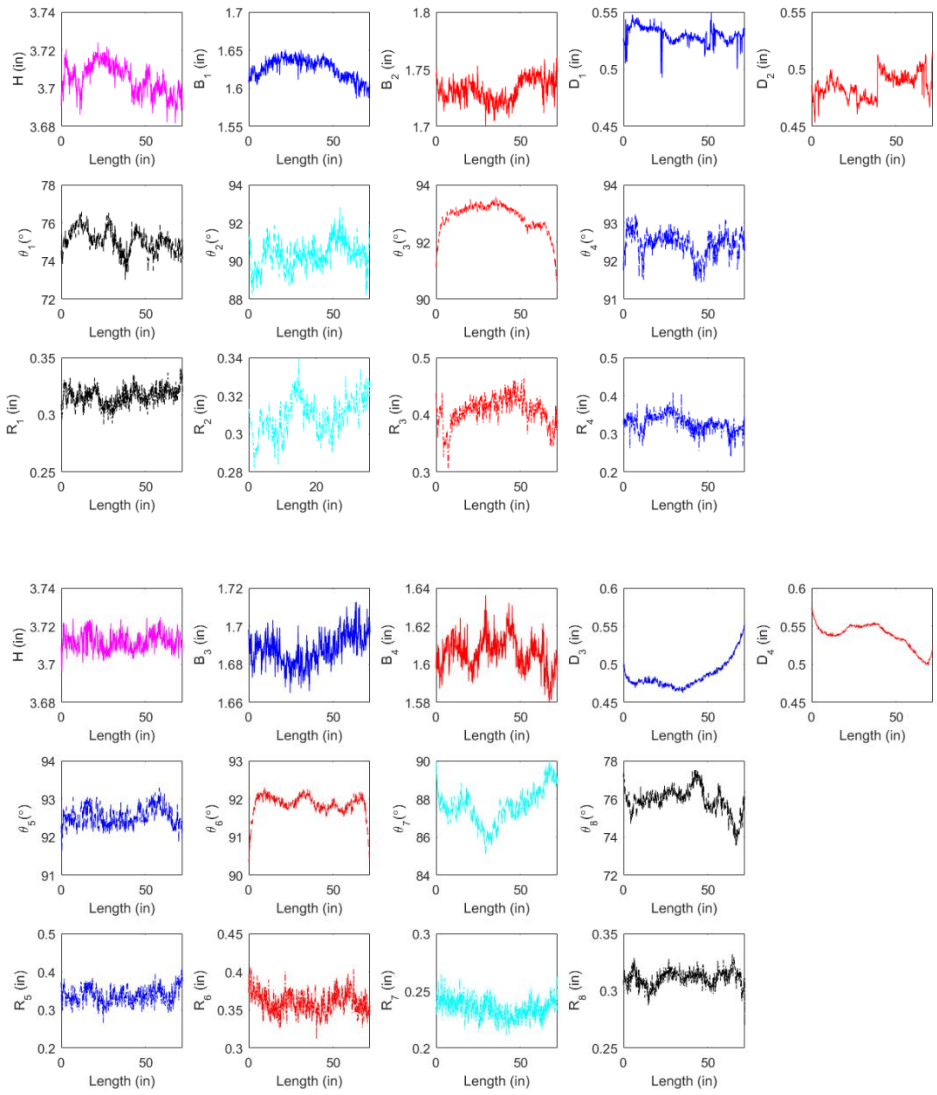

Figure 6. 22 Typical dimension variations along the length of BUC sections [362S162-68]

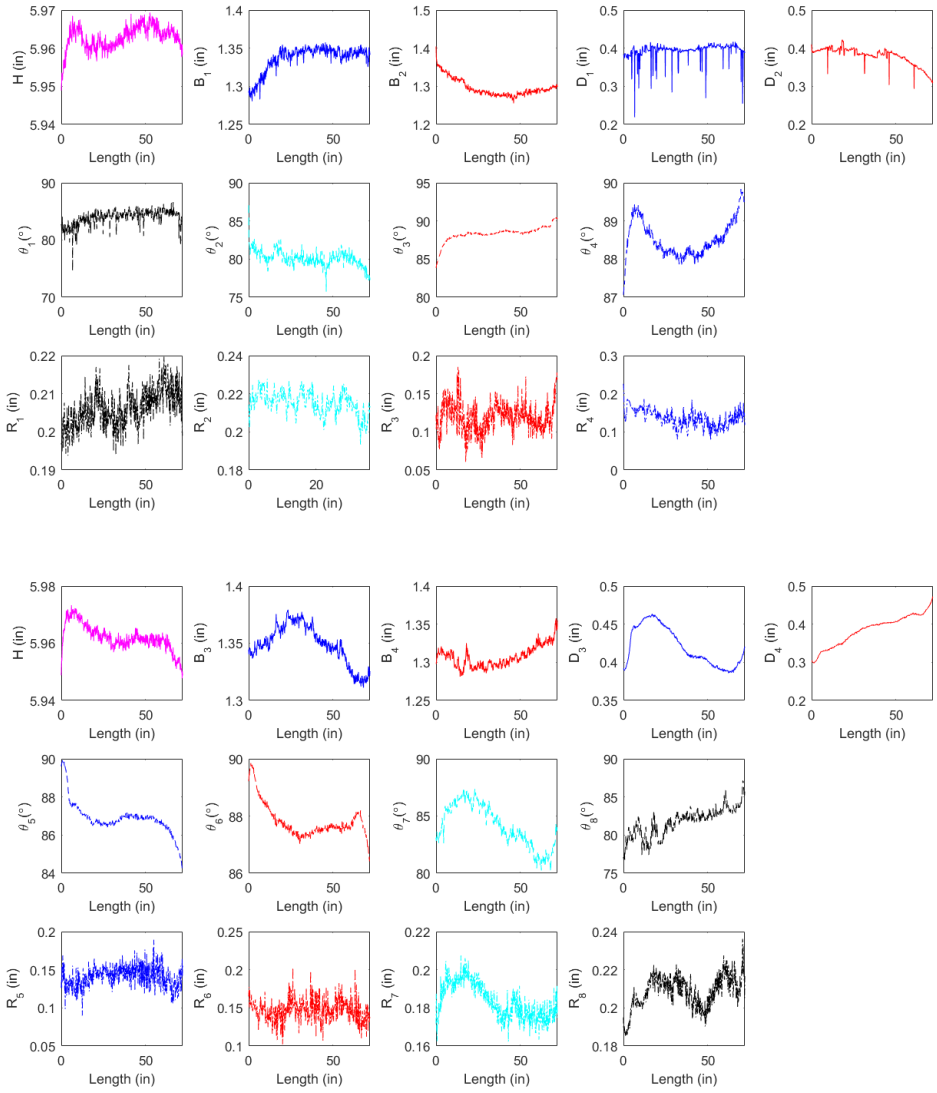

Figure 6. 23 Typical dimension variations along the length of BUC sections [600S137-54]

6.3.3 Statistical study of dimensions

he statistical summary table seems very similar to those of C sections. There are four 362S16-68 and four 600S137-54 BUC sections that are put on the plates. Each BUC member is six feet in length and is comprised of lower and upper sections. Single sections contain exactly the same nominal dimension as those of the C sections studied earlier. Therefore, some of the conclusions are similar to those for C sections. The differences in the corners were very similar to C sections.

Inside corners are in better shape than corners near the lips. However, the radii in 362S162-68 indicated poor quality control, and they generally were much larger than the nominal dimensions.

Table 6. 9a Summary of the statistical dimensions of BUC sectionS [Stud: 362S162-68]

Dimension (Lower)		H (in)	B_1 (in)	B_2 (in)	D_1 (in)	D_2 (in)	R_1 (in)	R_2 (in)	R_3 (in)	R_4 (in)	θ_1 (°)	θ_2 (°)	θ_3 (°)	θ_4 (°)
Laser[a]	5%	3.70	1.59	1.67	0.47	0.46	0.30	0.23	0.33	0.31	74.4	83.5	90.8	92.1
	10%	3.70	1.60	1.69	0.49	0.47	0.31	0.23	0.33	0.32	74.7	83.8	90.9	92.3
	50%	3.71	1.63	1.72	0.53	0.48	0.32	0.27	0.36	0.34	76.1	88.3	92.4	92.9
	75%	3.72	1.64	1.73	0.54	0.49	0.33	0.29	0.39	0.36	77.1	90.2	93.1	93.5
	90%	3.72	1.65	1.74	0.54	0.51	0.34	0.32	0.41	0.37	78.2	91.1	93.3	93.9
	Mean	3.71	1.62	1.71	0.52	0.49	0.32	0.27	0.37	0.34	76.3	87.9	92.3	93.0
	Std	0.01	0.02	0.02	0.02	0.03	0.01	0.03	0.03	0.02	1.29	2.76	0.85	0.59
Nominal		3.63	1.63	1.63	0.50	0.50	0.18	0.18	0.18	0.18	90	90	90	90
L. vs. N. (%)		2.4	0.0	**5.5**	**4.2**	-2.6	**79.2**	**50.9**	**105**	**91**	**-15**	-2.3	2.5	3.3
Dimension (Upper)		H (in)	B_3 (in)	B_4 (in)	D_3 (in)	D_4 (in)	R_5 (in)	R_6 (in)	R_7 (in)	R_8 (in)	θ_5 (°)	θ_6 (°)	θ_7 (°)	θ_8 (°)
Laser[a]	5%	3.69	1.66	1.59	0.47	0.51	0.28	0.33	0.22	0.29	91.2	90.7	86.3	73.7
	10%	3.69	1.67	1.59	0.47	0.51	0.30	0.33	0.23	0.29	91.5	91.0	86.6	74.0
	50%	3.71	1.69	1.61	0.49	0.53	0.33	0.36	0.25	0.31	92.4	91.7	87.9	75.6
	75%	3.72	1.70	1.61	0.50	0.54	0.34	0.38	0.27	0.31	92.8	92.0	88.6	76.3
	90%	3.72	1.70	1.62	0.52	0.55	0.36	0.39	0.27	0.32	93.2	92.2	89.4	77.0
	Mean	3.71	1.69	1.61	0.49	0.53	0.33	0.36	0.25	0.31	92.3	91.6	87.9	75.6
	Std	0.01	0.01	0.01	0.02	0.02	0.03	0.02	0.02	0.01	0.67	0.53	1.10	1.18
Nominal		3.63	1.63	1.63	0.50	0.50	0.18	0.18	0.18	0.18	90	90	90	90
L. vs. N. (%)[b]		2.3	3.8	-1.1	-1.3	**6.5**	**82**	**101**	**69.8**	**55.6**	2.6	1.8	-2.3	-16

Note:

a. Laser measurements from 548 cross sections x 4 specimens

b. Thickness, t, is 0.0712 in

c. % difference is estimated as |[mean(laser)-nominal]/[nominal]x100%|

d. Bold font indicates % difference larger than 5%

Table 6.8b Summary of the statistical dimensions of BUC sections [Stud: 600S137-54]

Dimension (Lower)		H (in)	B_1 (in)	B_2 (in)	D_1 (in)	D_2 (in)	R_1 (in)	R_2 (in)	R_3 (in)	R_4 (in)	θ_1 (°)	θ_2 (°)	θ_3 (°)	θ_4 (°)
Laser[a]	5%	5.96	1.30	1.27	0.36	0.34	0.19	0.20	0.10	0.10	81.2	78.5	87.3	88.0
	10%	5.96	1.32	1.28	0.38	0.36	0.20	0.20	0.10	0.11	81.9	79.0	88.0	88.1
	50%	5.96	1.34	1.30	0.40	0.38	0.20	0.21	0.13	0.14	84.1	80.2	88.5	88.6
	75%	5.97	1.35	1.31	0.40	0.39	0.21	0.22	0.15	0.15	84.8	80.9	88.7	89.0
	90%	5.97	1.36	1.33	0.41	0.40	0.21	0.22	0.17	0.16	85.3	81.9	89.3	89.4
	Mean	5.96	1.34	1.30	0.39	0.38	0.20	0.21	0.14	0.14	83.9	80.3	88.5	88.7
	Std	0.00	0.02	0.02	0.02	0.02	0.01	0.01	0.02	0.02	1.33	1.27	0.92	0.61
Nominal		6.00	1.38	1.38	0.38	0.38	0.14	0.14	0.14	0.14	90	90	90	90
L. vs. N. (%)		-0.6	-2.5	**-5.4**	3.6	0.2	**45.7**	**52**	-1.6	0.9	**-6.8**	**-10**	-1.4	-1.4
Dimension (Upper)		H (in)	B_3 (in)	B_4 (in)	D_3 (in)	D_4 (in)	R_5 (in)	R_6 (in)	R_7 (in)	R_8 (in)	θ_5 (°)	θ_6 (°)	θ_7 (°)	θ_8 (°)
Laser[a]	5%	5.95	1.30	1.28	0.37	0.28	0.12	0.12	0.15	0.19	77.5	87.2	79.4	77.3
	10%	5.96	1.32	1.29	0.38	0.30	0.12	0.13	0.16	0.19	78.5	87.4	79.8	78.3
	50%	5.96	1.35	1.30	0.41	0.38	0.14	0.15	0.18	0.20	85.2	87.7	83.2	81.2
	75%	5.97	1.35	1.31	0.45	0.40	0.15	0.16	0.19	0.21	86.8	88.0	84.6	82.6
	90%	5.97	1.37	1.32	0.46	0.42	0.16	0.16	0.19	0.22	87.1	88.7	86.1	83.7
	Mean	5.96	1.34	1.30	0.42	0.37	0.14	0.15	0.18	0.20	83.6	87.9	83.0	81.0
	Std	0.00	0.02	0.01	0.03	0.05	0.01	0.01	0.01	0.01	3.82	0.57	2.21	2.39
Nominal		6.00	1.38	1.38	0.38	0.38	0.14	0.14	0.14	0.14	90	90	90	90
L. vs. N. (%)[c]		-0.6	-2.4	**-5.2**	**10.1**	-3.1	1.3	3.8	**28.6**	**47.5**	**-7.1**	-2.4	**-7.8**	-10

Note:

a. Laser measurements from 548 cross sections x 4 specimens;

b. Thickness t is 0.0588 in.

c. % Difference is estimated as |[mean(laser)-nominal]/[nominal]x100%|

d. Bold font indicate % difference larger than 5%

Histograms provide a very interesting point in that some of them consist of similar distribution as the C sections while others do not, especially the upper sections. Histograms of flanges or lips of one side are offset from those of the other side, as seen in C, i.e., B_1 is offset from B_2, B_3 is offset from B_4, D_1 is offset from D_2, and D_3 is offset from D_4. Unusual observations have been made to histograms of radii, where the highly non-Gaussian distribution maintains two or three peaks in the histograms (R_2, R_6, and R_7). Since criteria are constant during feature recognition and the dimensional definitions are unchanged in the estimation, the potential reasons are small sample size

and existing noises. More study in future research is required to determine the explanations for these unexpected results.

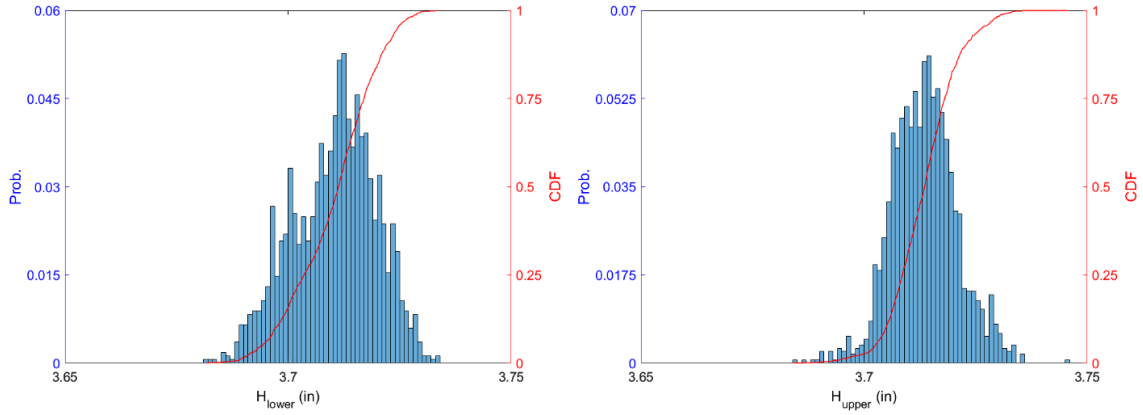

Figure 6. 24 Statistical summary of web height (H) [362S162-68]

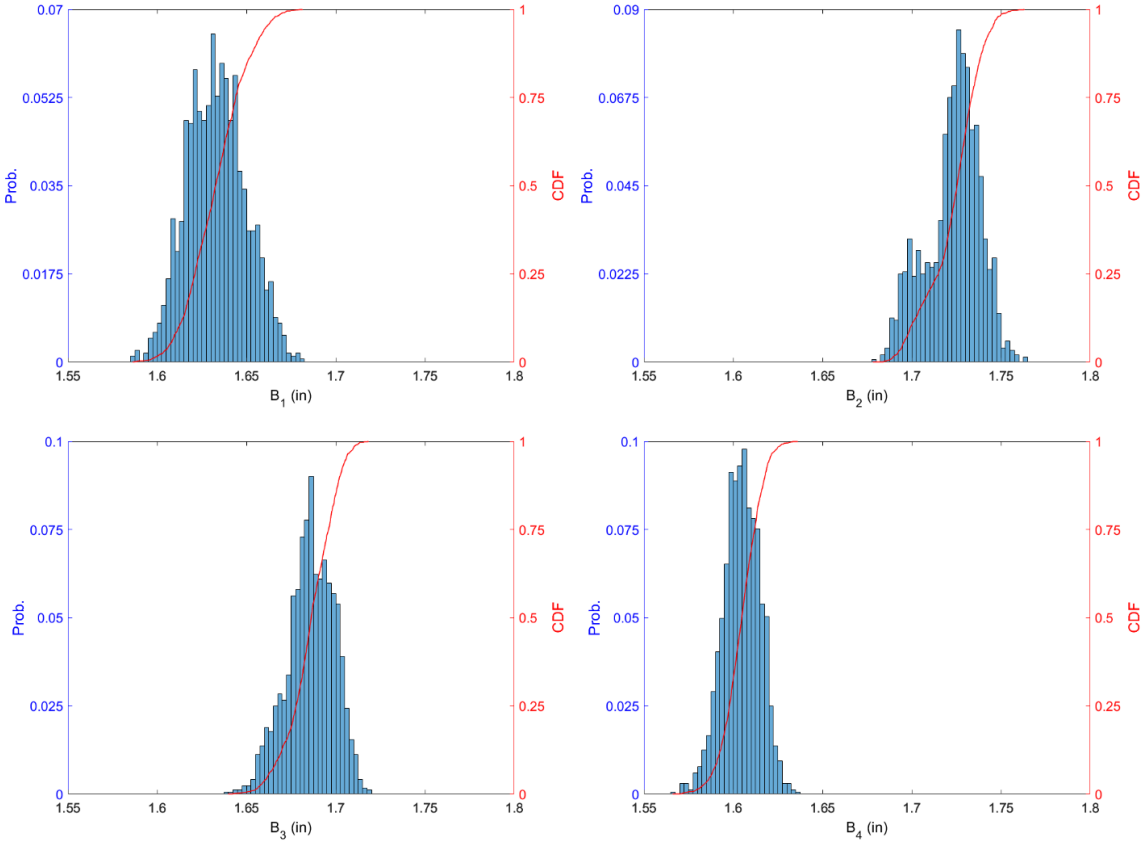

Figure 6. 25 Statistical summary of flange width (B_1, B_2, B_3, B_4) [362S162-68]

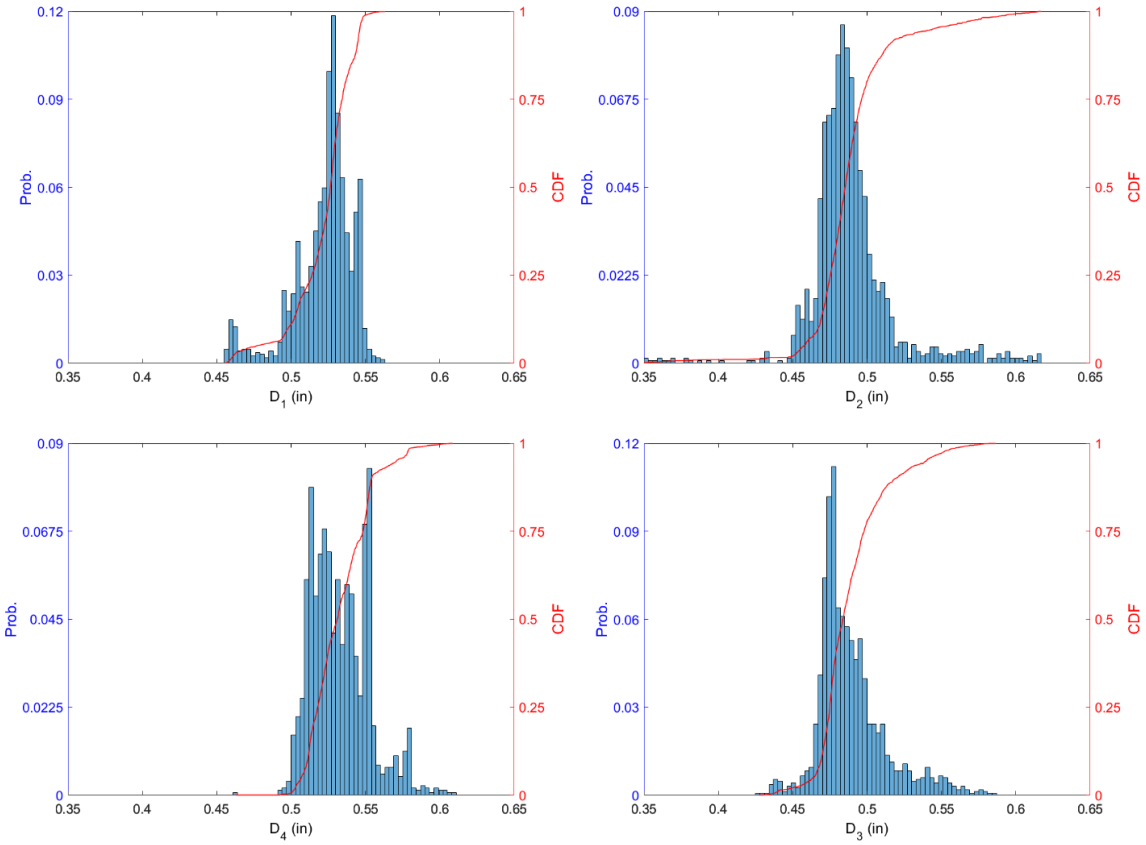

Figure 6. 26 Statistical summary of lip lengths (D_1, D_2, D_3, D_4) [362S162-68]

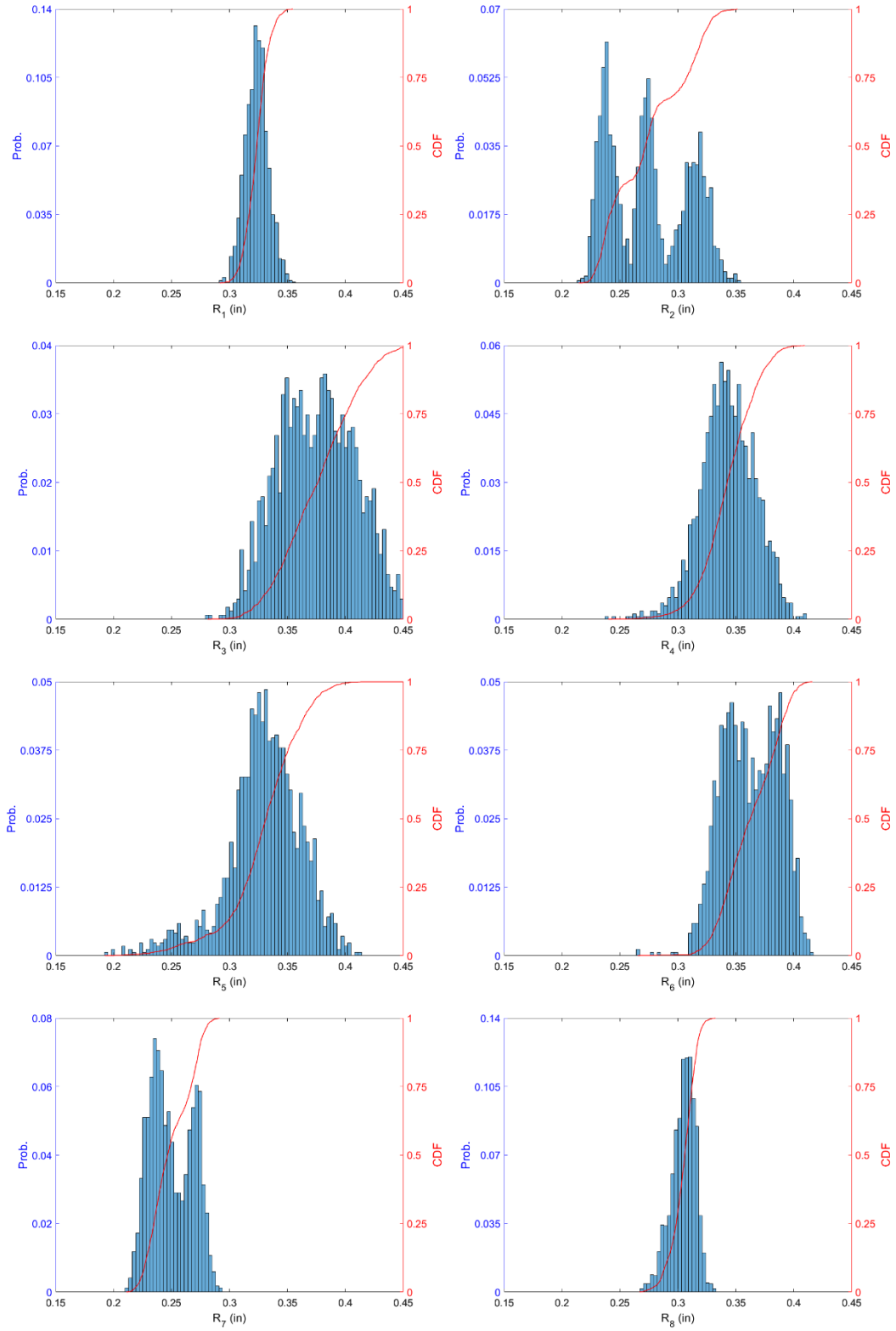

Figure 6. 27 Statistical summary of radii (R_1, R_2, R_3, R_4, R_5, R_6, R_7, R_8) [362S162-68]

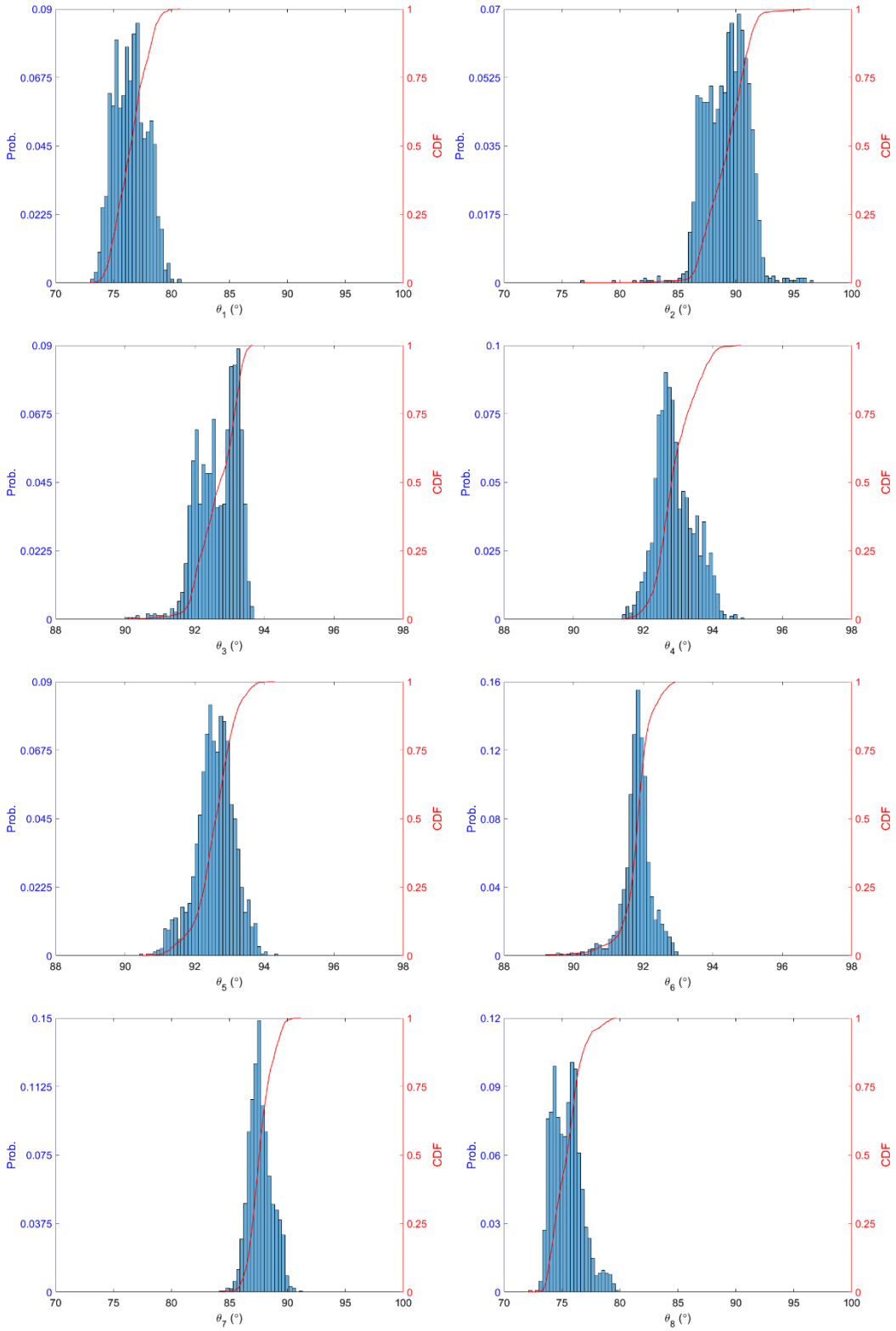

Figure 6. 28 Statistical summary of angles (θ_1, θ_2, θ_3, θ_4, θ_5, θ_6, θ_7, θ_8) [362S162-68]

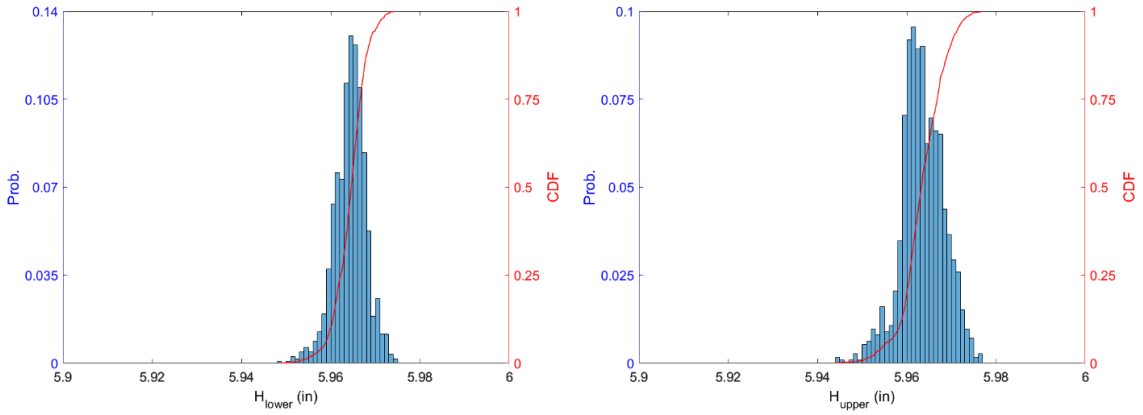

Figure 6. 29 Statistical summary of web height (H) [600S137-54]

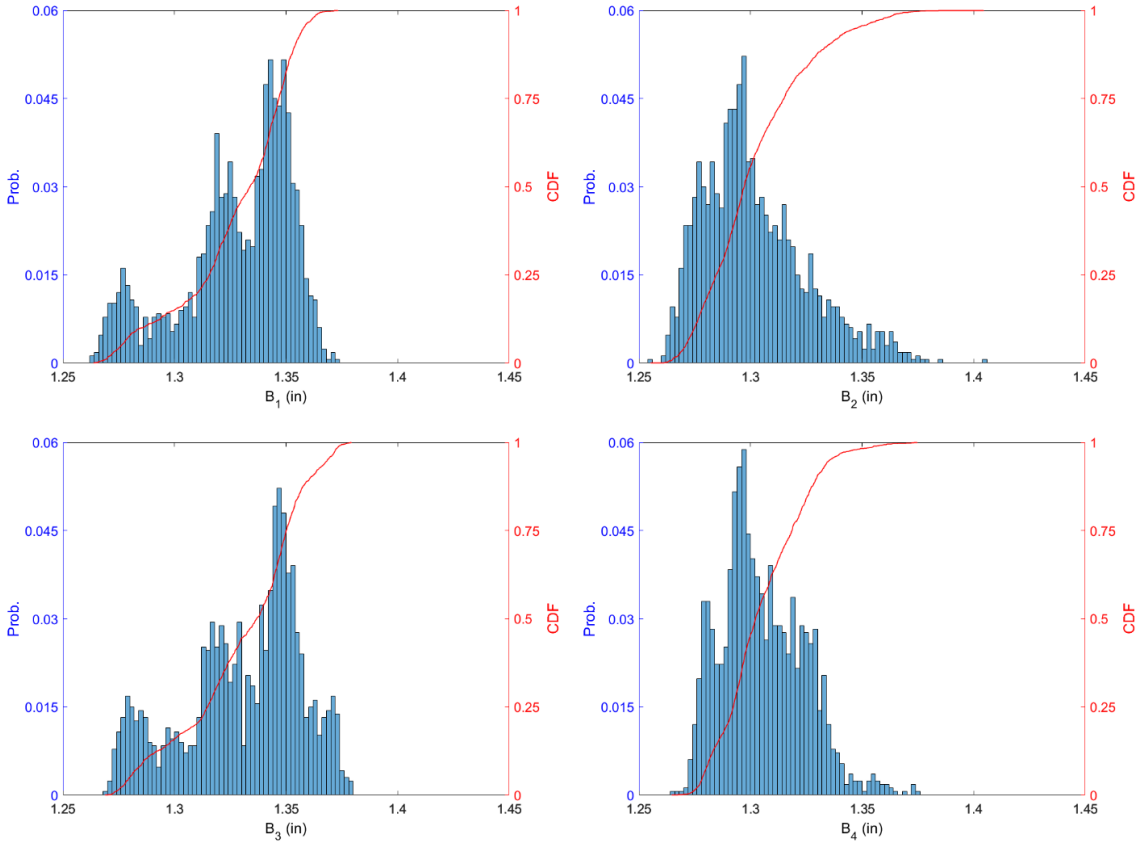

Figure 6. 30 Statistical summary of flanges (B_1, B_2, B_3, B_4) [600S137-54]

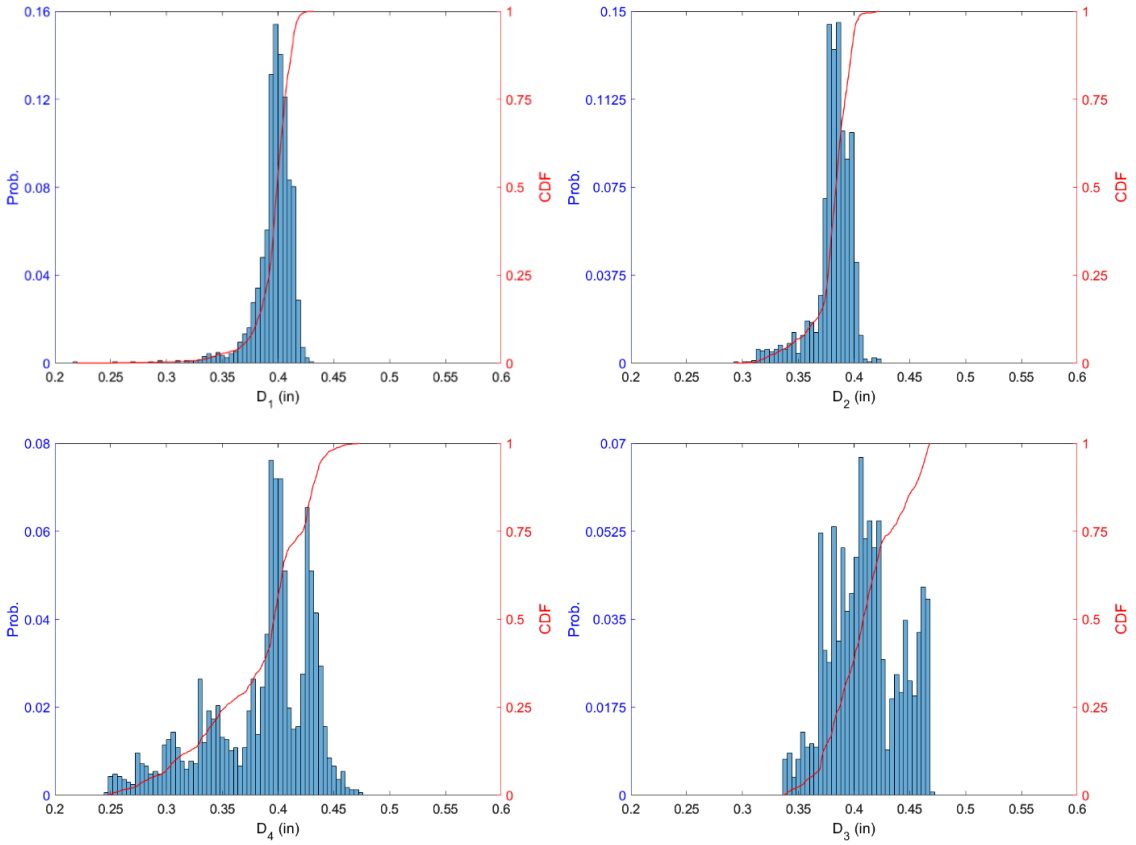

Figure 6. 31 Statistical summary of lip lengths (D_1, D_2, D_3, D_4) [600S137-54]

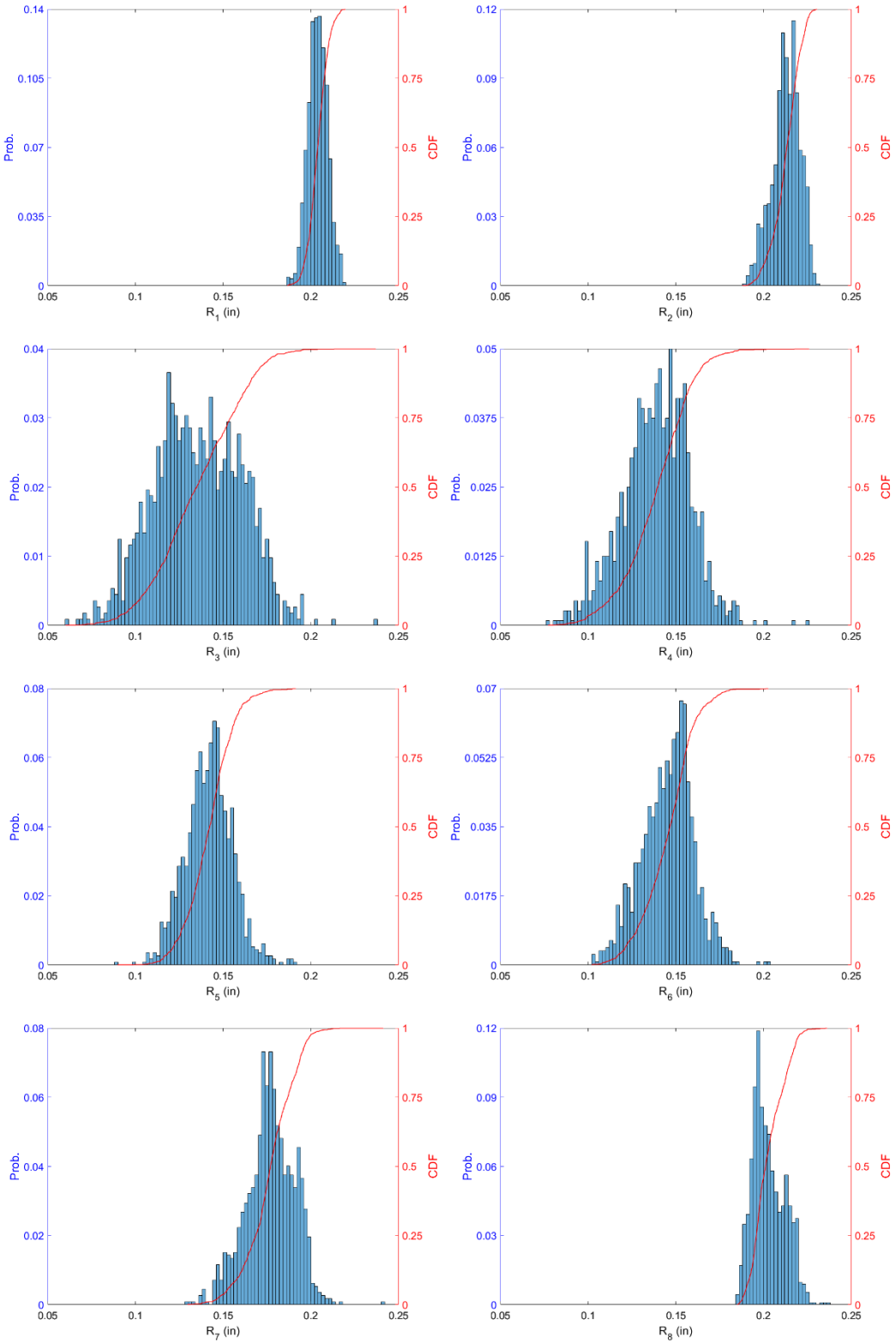

Figure 6. 32 Statistical summary of radii (R_1, R_2, R_3, R_4, R_5, R_6, R_7, R_8) [600S137-54]

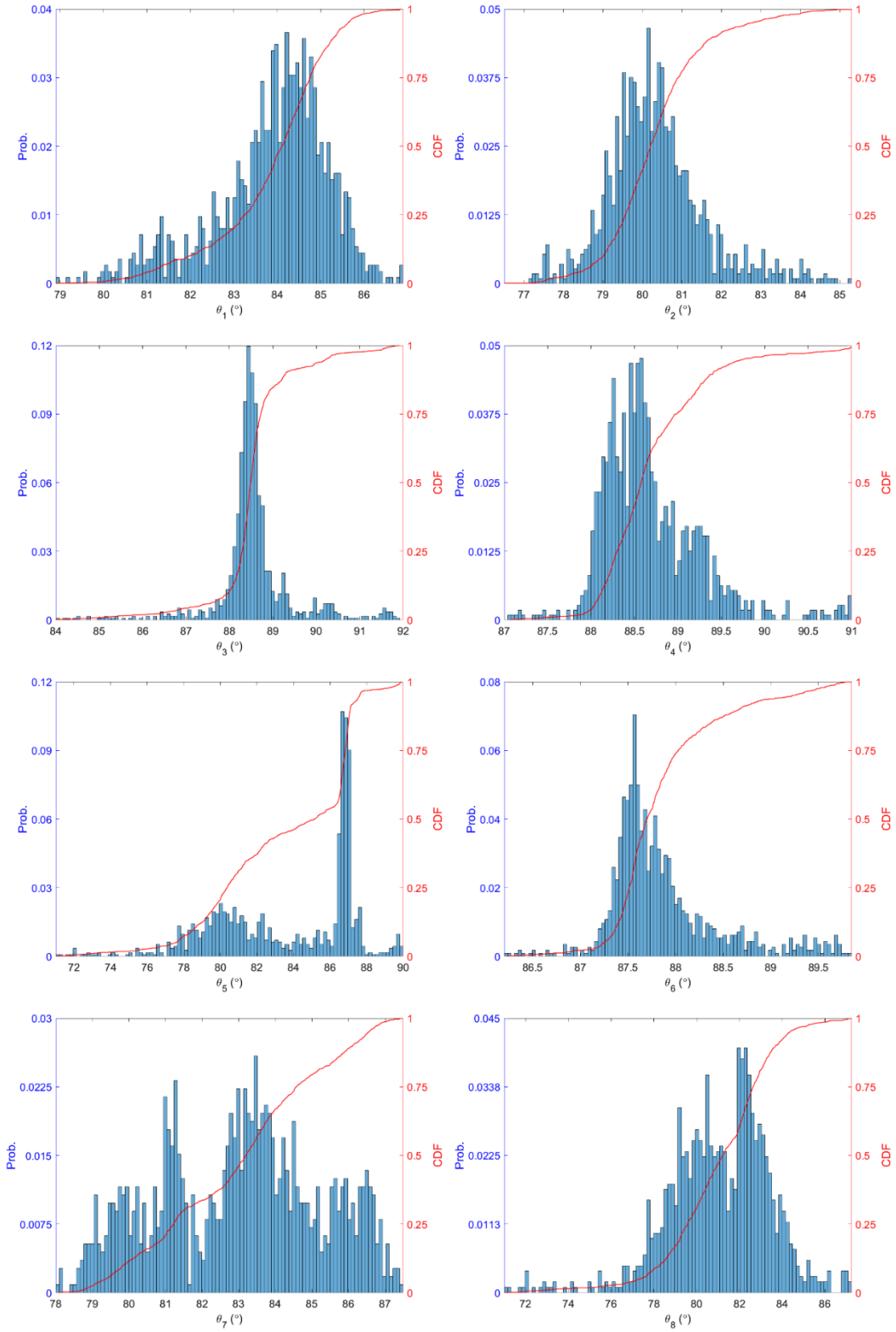

Figure 6. 33 Statistical summary of angles (θ_1, θ_2, θ_3, θ_4, θ_5, θ_6, θ_7, θ_8) [600S137-54]

The histograms of 600S137-54 are highly non-Gaussian, especially the corner angles. Control of corner angles seems to be a challenge, since deformations can occur during manufacturing and transportation. Measurement noises, especially in the lower sections, must be studied carefully due to the existence of outliers. Noise removal functions must be developed further so that the impacts of noises or outliers can be minimized.

6.3.4 Correlation Study and Significance

A correlation study was conducted, and findings similar to those from C sections were obtained. Correlation factors (Table 6. 10) between lips were -0.43 (lower section) and -0.50 (upper section), whereas they were -0.49 in C sections. Different from C sections, BUC sections seem to have strong correlations between radii/angles and flanges, webs, and lips. For example, a strong positive correlation was observed between same-side corner angles and lips in both the lower and upper sections, i.e., 0.5 and 0.7, 0.8 and 0.5, respectively.

Poor significances (Table 6. 11) were found between B_2 and D_1, H and D_1, and θ_1 and H in the lower section. Poor significances also were found between B_3 and D_3, R_6 and D_4, R_8 and D_4, R_7 and R_6, R_8 and D_4, θ_6 and R_7, θ_8 and R_8, and θ_8 and θ_7 in the upper section of BUC. These p-values in Table 6. 11 correspond to the correlation factors (see Table 6. 10) of dimensions are all in weak correlation. Thus, it is difficult to conclude that these pairs had weak correlations. Certainly, more samples are required for the correlation study of BUCs. However, the correlation results from BUCs are supposed to be similar to those of C sections, even though small changes may occur when the BUC sections are being built.

Table 6. 10 Correlation Matrix of BUC studs [362S162-68 & 600S137-54]

ρ	D_1	D_2	B_1	B_2	H	R_1	R_2	R_3	R_4	θ_1	θ_2	θ_3	θ_4
D_1	1.0	**-0.4**	0.2	0.0	0.0	0.2	-0.1	-0.3	0.2	0.2	-0.2	0.2	-0.1
D_2	-0.4	1.0	0.1	0.1	0.1	0.2	-0.4	-0.1	-0.2	0.2	-0.2	-0.1	**0.5**
B_1	0.2	0.1	1.0	0.2	0.2	0.4	-0.1	0.1	-0.2	0.9	-0.4	**0.6**	**0.6**
B_2	0.0	0.1	0.2	1.0	**-0.5**	0.3	0.1	-0.1	**0.5**	0.4	-0.1	-0.2	**0.7**
H	0.0	0.1	0.2	-0.5	1.0	-0.2	0.3	-0.2	**-0.7**	0.0	0.4	0.4	**-0.4**
R_1	0.2	0.2	0.4	0.3	-0.2	1.0	**-0.6**	-0.4	**0.5**	**0.6**	**-0.8**	-0.3	**0.6**
R_2	-0.1	-0.4	-0.1	0.1	0.3	-0.6	1.0	0.1	-0.2	-0.3	**0.7**	0.3	-0.4
R_3	-0.3	-0.1	0.1	-0.1	-0.2	-0.4	0.1	1.0	-0.3	-0.1	0.1	0.3	-0.1
R_4	0.2	-0.3	-0.2	0.5	-0.7	0.5	-0.2	-0.3	1.0	0.1	-0.4	**-0.7**	0.3
θ_1	0.2	0.2	0.9	0.4	0.0	0.6	-0.3	-0.1	0.1	1.0	**-0.5**	0.3	**0.8**
θ_2	-0.2	-0.2	-0.4	-0.1	0.4	-0.8	0.7	0.1	-0.4	-0.5	1.0	0.2	**-0.6**
θ_3	0.2	-0.1	0.6	-0.2	0.4	-0.3	0.3	0.3	-0.7	0.3	0.2	1.0	-0.1
θ_4	-0.1	0.5	0.6	0.7	-0.4	0.6	-0.4	-0.1	0.3	0.8	-0.6	-0.1	1.0
	D_3	D_4	B_3	B_4	H	R_5	R_6	R_7	R_8	θ_5	θ_6	θ_7	θ_8
D_3	1.0	**-0.5**	0.0	**-0.4**	0.1	0.3	-0.3	0.3	-0.4	-0.1	0.0	**0.8**	-0.3
D_4	-0.5	1.0	-0.1	0.3	-0.3	0.3	0.0	0.1	0.0	-0.4	**-0.4**	-0.2	**0.8**
B_3	0.0	-0.1	1.0	-0.2	**-0.5**	-0.3	0.0	-0.2	0.2	0.2	**-0.5**	0.1	-0.1
B_4	-0.4	0.3	-0.2	1.0	-0.1	0.2	**0.4**	0.3	-0.1	-0.4	0.3	-0.2	**0.5**
H	0.1	-0.3	-0.5	-0.1	1.0	0.2	0.3	-0.2	-0.4	**0.6**	**0.8**	-0.2	-0.4
R_5	0.3	0.3	-0.3	0.2	0.2	1.0	-0.2	**0.5**	**-0.5**	-0.3	0.2	**0.5**	0.3
R_6	-0.3	0.0	0.0	0.4	0.3	-0.2	1.0	0.0	-0.2	0.2	**0.4**	-0.4	0.1
R_7	0.3	0.1	-0.2	0.3	-0.2	0.5	0.0	1.0	**-0.6**	-0.4	0.0	**0.5**	0.2
R_8	-0.4	0.0	0.2	-0.1	-0.4	-0.5	-0.2	-0.6	1.0	-0.1	-0.3	**-0.5**	0.0
θ_5	-0.1	-0.4	0.2	-0.4	0.6	-0.3	0.2	-0.4	-0.1	1.0	**0.4**	**-0.4**	**-0.5**
θ_6	0.0	-0.4	-0.5	0.3	0.8	0.2	0.4	0.0	-0.3	0.4	1.0	-0.2	**-0.4**
θ_7	0.8	-0.2	0.1	-0.2	-0.2	0.5	-0.4	0.5	-0.5	-0.4	-0.2	1.0	0.0
θ_8	-0.3	0.8	-0.1	0.5	-0.4	0.3	0.1	0.2	0.0	-0.5	-0.4	0.0	1.0

Table 6. 11 P-value for correlation study of BUC studs [362S162-68 & 600S137-54]

p-val	D_1	D_2	B_1	B_2	H	R_1	R_2	R_3	R_4	θ_1	θ_2	θ_3	θ_4
D_1	1.00	0.00	0.00	0.97	0.45	0.00	0.00	0.00	0.00	0.00	0.00	0.00	0.00
D_2	0.00	1.00	0.00	0.00	0.00	0.00	0.00	0.00	0.00	0.00	0.00	0.00	0.00
B_1	0.00	0.00	1.00	0.00	0.00	0.00	0.00	0.01	0.00	0.00	0.00	0.00	0.00
B_2	0.97	0.00	0.00	1.00	0.00	0.00	0.00	0.01	0.00	0.00	0.02	0.00	0.00
H	0.45	0.00	0.00	0.00	1.00	0.00	0.00	0.00	0.00	0.05	0.00	0.00	0.00
R_1	0.00	0.00	0.00	0.00	0.00	1.00	0.00	0.00	0.00	0.00	0.00	0.00	0.00
R_2	0.00	0.00	0.00	0.00	0.00	0.00	1.00	0.00	0.00	0.00	0.00	0.00	0.00
R_3	0.00	0.00	0.01	0.01	0.00	0.00	0.00	1.00	0.00	0.00	0.00	0.00	0.01
R_4	0.00	0.00	0.00	0.00	0.00	0.00	0.00	0.00	1.00	0.00	0.00	0.00	0.00
θ_1	0.00	0.00	0.00	0.00	0.05	0.00	0.00	0.00	0.00	1.00	0.00	0.00	0.00
θ_2	0.00	0.00	0.00	0.02	0.00	0.00	0.00	0.00	0.00	0.00	1.00	0.00	0.00
θ_3	0.00	0.00	0.00	0.00	0.00	0.00	0.00	0.00	0.00	0.00	0.00	1.00	0.00
θ_4	0.00	0.00	0.00	0.00	0.00	0.00	0.00	0.01	0.00	0.00	0.00	0.00	1.00
	D_3	D_4	B_3	B_4	H	R_5	R_6	R_7	R_8	θ_5	θ_6	θ_7	θ_8
D_3	1.00	0.00	0.94	0.00	0.00	0.00	0.00	0.00	0.00	0.00	0.30	0.00	0.00
D_4	0.00	1.00	0.00	0.00	0.00	0.00	0.21	0.00	0.52	0.00	0.00	0.00	0.00
B_3	0.94	0.00	1.00	0.00	0.00	0.00	0.10	0.00	0.00	0.00	0.00	0.00	0.01
B_4	0.00	0.00	0.00	1.00	0.00	0.00	0.00	0.00	0.00	0.00	0.00	0.00	0.00
H	0.00	0.00	0.00	0.00	1.00	0.00	0.00	0.00	0.00	0.00	0.00	0.00	0.00
R_5	0.00	0.00	0.00	0.00	0.00	1.00	0.00	0.00	0.00	0.00	0.00	0.00	0.00
R_6	0.00	0.21	0.10	0.00	0.00	0.00	1.00	0.21	0.00	0.00	0.00	0.00	0.00
R_7	0.00	0.00	0.00	0.00	0.00	0.00	0.21	1.00	0.00	0.00	0.07	0.00	0.00
R_8	0.00	0.52	0.00	0.00	0.00	0.00	0.00	0.00	1.00	0.00	0.00	0.00	0.19
θ_5	0.00	0.00	0.00	0.00	0.00	0.00	0.00	0.00	0.00	1.00	0.00	0.00	0.00
θ_6	0.30	0.00	0.00	0.00	0.00	0.00	0.00	0.07	0.00	0.00	1.00	0.00	0.00
θ_7	0.00	0.00	0.00	0.00	0.00	0.00	0.00	0.00	0.00	0.00	0.00	1.00	0.31
θ_8	0.00	0.00	0.01	0.00	0.00	0.00	0.00	0.00	0.19	0.00	0.00	0.31	1.00

6.4 Conclusions

In this chapter, results have been presented from the study of the dimensions of cold-formed steel members from laser measurements, including Z, C, and BUC sections. Z sections had both laser and manual measurements. It was observed that the laser measurements were more reliable, produced more data, and provided constant estimates of the dimensions. Correlation matrixes were formed among dimensional quantities, and they identified the true relationships among all dimensional quantities. The correlation matrix of C sections was compared with the general

assumptions of dimensional correlations. Disagreements existed with most assumptions with the exception of *two lips being negatively correlated*. More research is needed on BUC sections with better noise control and a larger study group. The current findings can effectively aid the dimensional study of cold-formed steel sections and can be used to evaluate fabrication factors in current designs in which Monte Carlo simulations of dimensions can be conducted with a more reliable database and true correlations.

Chapter 7 Imperfection fields: traditional representation

The traditional imperfection approach claims that structural behaviors of cold-formed steel members are only sensitive to imperfection corresponding to the shape of first buckling-mode classes, i.e., local, distortional, bow, camber, twist. Various imperfections are surveyed along a specimen in a corresponding buckling mode, the maxima of which are taken as magnitudes of the classified imperfection modes and used in modeling with specified half-wave lengths, while all other imperfection findings are dismissed, and the modeling method only offers conservative simulation results. It is the foundation of the 1D spectral method (Chapter 8) and contains two characterization methods. More literature reviews of the traditional imperfection approach are found in Chapter 2.

7.1 Conventional imperfection characterizations

7.1.1 Conventional imperfection definition

Geometric imperfection characterization plays an important role in advanced cold-formed steel modeling using shell finite elements. Conventional imperfection characterizations categorize imperfections, as shown in Figure 7. 1, Figure 7. 2, and Figure 7. 3 with respect to Z, C, and BUC: Type 1 (d_1), Type 2 (d_2), and member bow (G1), camber (G2), and twist (G3) (Schafer and Pekoz,1998; Zeinoddini and Schafer, 2011). BUC compared with Z and C members are relatviely complicated, considering it contains upper and lower sections, while the calculation procedures are similar except for the double computations in C and Z. Imperfection simulations of cold-formed steel members can be correlated to failure mode shape for study of imperfection sensitivity. Cross-section imperfection in the simulation adopts a corresponding failure mode shape, as shown in Figure 7. 1, Figure 7. 2, and Figure 7. 3. Longitudinal imperfection, on the other hand, adopts corresponding sinusoical components of failure modes whose amplitude is scaled to the desired imperfection magnitude. Maximum magnitudes of imperfections are taken from measurements per

cold-formed steel member and are statistically summarized for such traditional modal imperfection simulations (Zeinoddini and Schafer, 2012). The simulated imperfection described above can be obtained through Eq. 1, where maganitude α is taken from a database, and mode shape φ is taken from the failure mode shape in buckling analysis using the finite strip or finite element method. The constraint of the traditional modal approach is over-conservative in predicting the strength in the collapse modeling.

$$f(y)=\sum_{i=1}^{5}\alpha_i\phi_i(x,y,z) \qquad \text{Eq 7. 1}$$

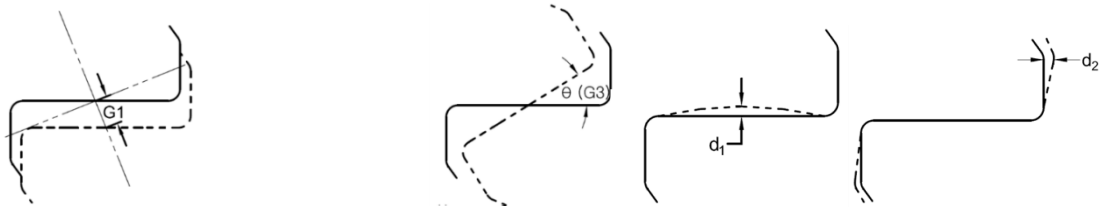

Figure 7. 1 Imperfection definition of Z sections; (a) Bow Imperfection - G1; (b) Camber Imperfection - G2; (c) Twist Imperfection - G3; (d) Type 1 Imperfection - d_1; (e) Type 2 Imperfection - d_2

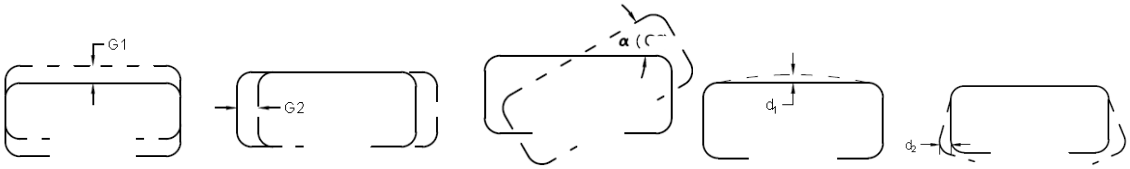

Figure 7. 2 Imperfection definition of C sections; (a) Bow Imperfection - G1; (b) Camber Imperfection - G2; (c) Twist Imperfection - G3; (d) Type 1 Imperfection - d_1; (e) Type 2 Imperfection - d_2

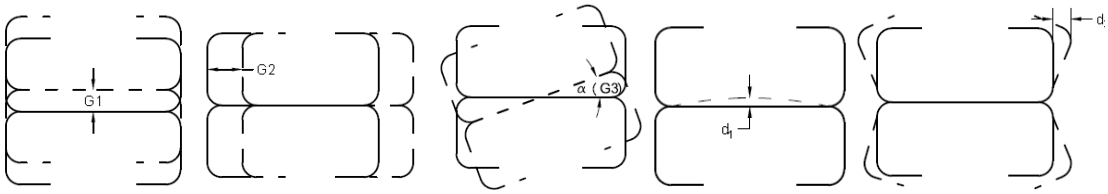

Figure 7. 3 Imperfection definition of BUC sections; (a) Bow Imperfection - G1; (b) Camber Imperfection - G2; (c) Twist Imperfection - G3; (d) Type 1 Imperfection - d_1; (e) Type 2 Imperfection - d_2

7.1.2 Conventional imperfection results

Z

A total of 19 *Z* sections (700Z225-60) were processed and reported in this part. Findings from conventional imperfection characterizations are intended for use in modeling, the results of which are compared with those from the other method, called the *modal imperfection decomposition approach* (MID). *Z* purlins, 700Z225-60, have a nominal length of 4 feet (1219 mm), depth of 7.00 in. (177.8 mm), flange width of 2.25 in. (57 mm), and thickness of 0.060 in. (1.52 mm). Figure 7. 4 shows that cross-sectional imperfections along the length are relatively noisier than global imperfections along lengths. Some pointed protuberances prevail in the Type 1 imperfections to all scanned specimens. These noises are eliminated for final statistical summary. Type 2 imperfections have c compared with Type 1. Precision of Type 1 (out-of-flatness) imperfection estimation seems to have stricter requirements on accurate measurement than that of Type 2. It is understandable because Type 1 imperfections are estimated from the raw measurement; Type 2 imperfections, on the other hand, are calculated from the distance between the end of the fitted linear line for the flat flange and the end of a perfect flat flange. With the linear regression fitting process, most of noise on flange can be eliminated. Thus Type 2 seems to have fewer imperfections than Type 1. It is always set at the ends of the bow (G1) and camber (G2) into zero because they are simply translations of centroids along the length of specimens. Besides, these two imperfections are generally fitted with a half-sine wave where structural members are the most imperfection-sensitive. Twist (G3), unfortunately, demonstrates a different shape compared with traditional assumptions. It is always monotonically increasing or decreasing along the length. A half cosine wave may better describe the twist. Maxima of these imperfections are selected for statistical summary in Section 7.1.3.

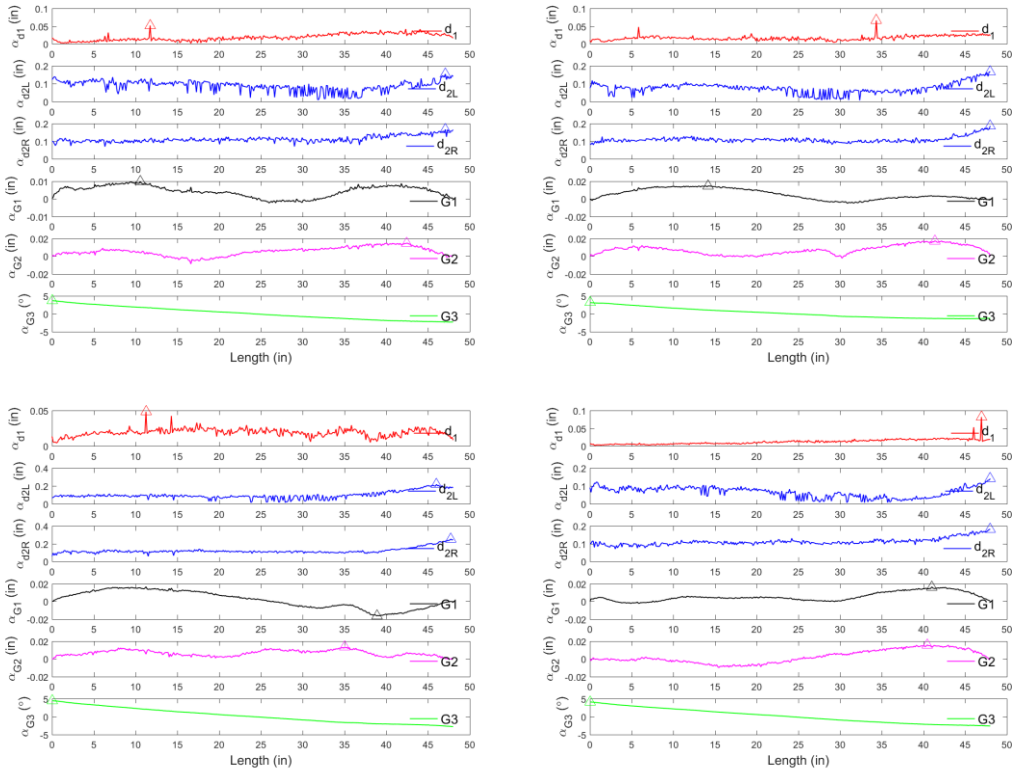

Figure 7. 4 Typical conventional imperfections along length of Z sections

C

The following procedures are described in the previous section. In two sections, the first, 362S162-68, has a nominal length of 6 ft, depth of 3.62 in., flange width of 1.62 in., and thickness of 0.0713 in.; and the second, 600S137- 54, has a nominal length of 6 ft, 6 in. of web depth, 1.375 in. of flange width, and a thickness of 0.0566 in. Conventional imperfection definitions (G1, G2, G3, d_1, and d_2) are identified along the studs, as shown in Figure 7. 5 and Figure 7. 6). Maximum values are taken into account for the statistical summary tables in Section 7.1.3. Compared with Z purlins, Type 1 and Type 2 have less noises in the C studs. Besides, the maxima of the cross-section imperfections approach two ends per section. An interesting phenomena arises when comparisons are made between the two types of C studs. Type 1 imperfections of 362S162-68 appear smoother compared with those of 600S137-54. This proves that Type 1 imperfections are sensitive to noise of measurements. 600S137-54 has a longer depth contributing to more points on the web, which

increase probability of measurement noises. The maxima of G1 in 600S137-54 are shown in the mid-span per section. This may show better half-sine wave fitting.

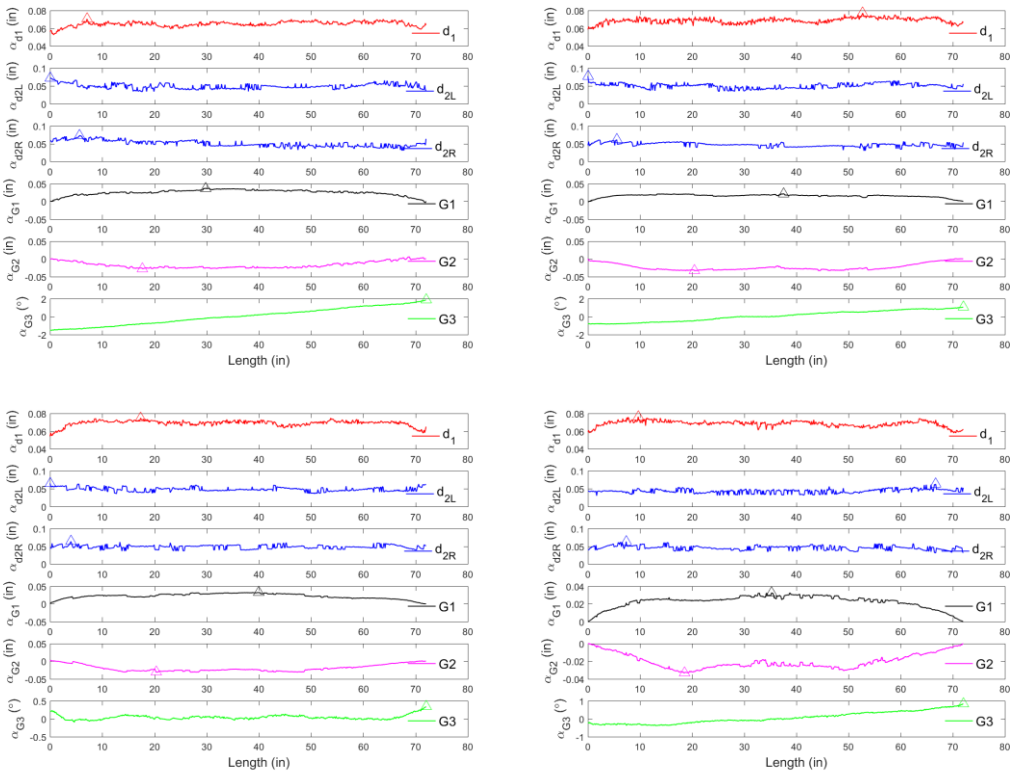

Figure 7. 5 Typical conventional imperfections along length of 362S162-68 of C sections.

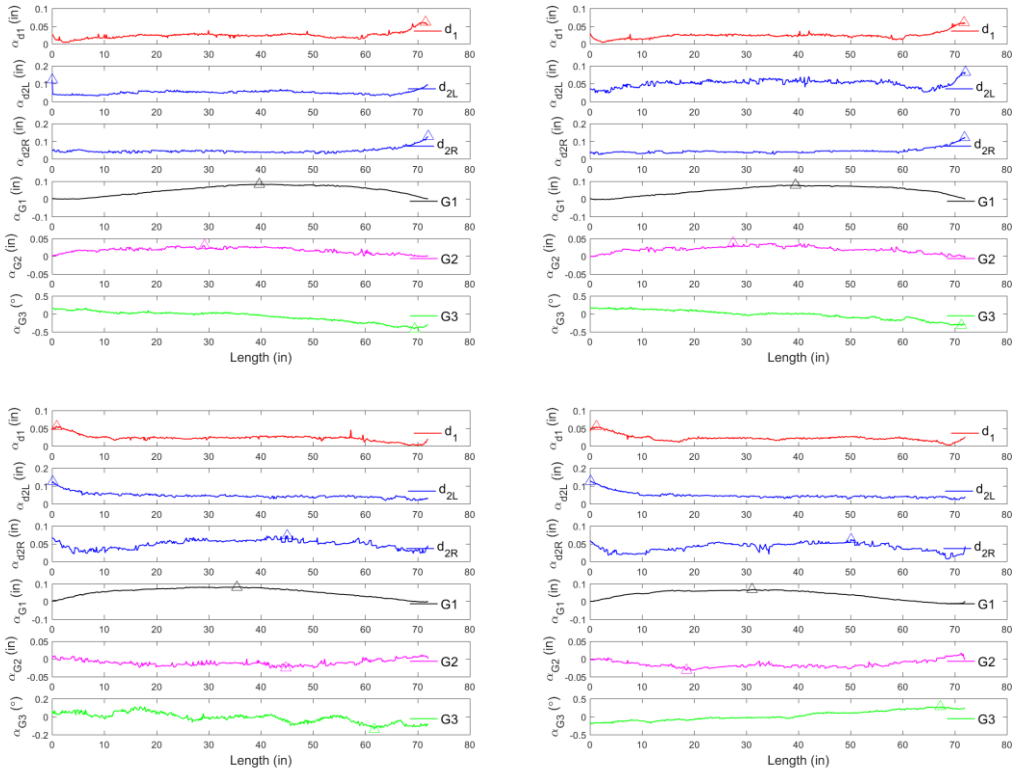

Figure 7. 6 Typical conventional imperfections along length of 600S137-54 of C sections

BUC

Similar to C sections, BUC comprises 362S162-68 and 600S137-54 C studs. The trend of curves is similar to C studs. However, G1 and G2 shows more noise compared with C studs, which can be attributed to the construction process. Lower-section cross-section imperfections are heavier polluted compared with those of the upper cross sections. There are several possibilities, such as measurement techniques, reflections, or scanning outliers from the supporting frames (targets are lying down on the supported beams).

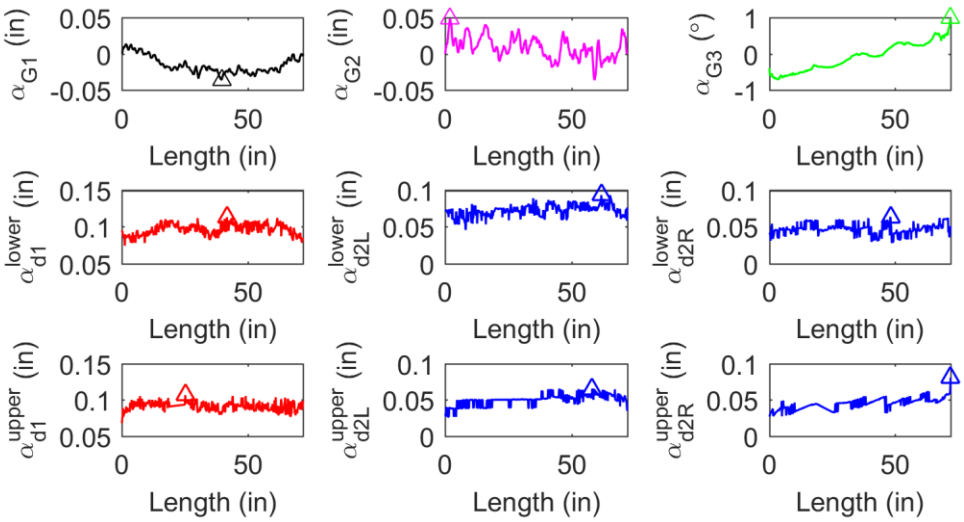

Figure 7. 7 Typical conventional imperfections along length of 362S162-68 of BUC

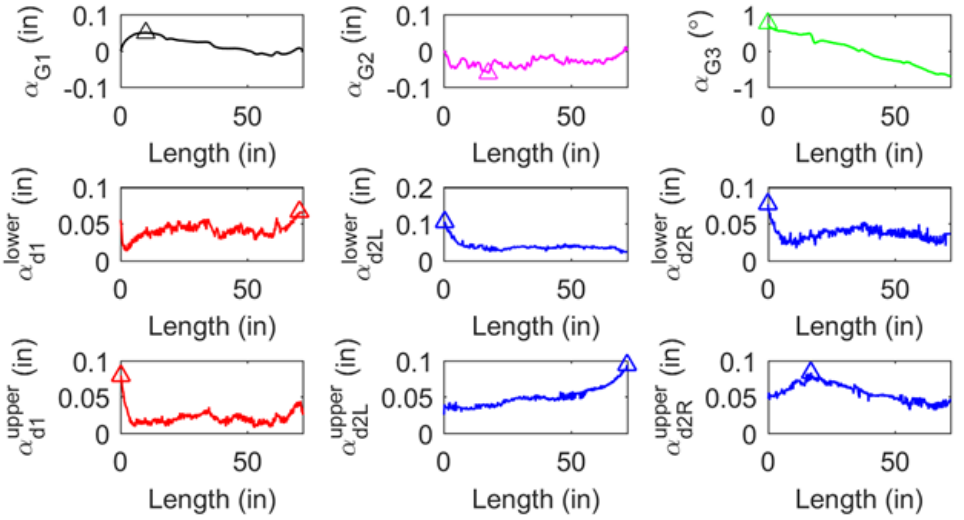

Figure 7. 8 Conventional imperfections along length of 600S137-54 of BUC

7.1.3 Statistical summary

Z

Repeating the imperfection characterization procedures to Z purlins, there are more than 7000 cross sections' Repeating the imperfection characterization procedures to *Z* purlins, there are more than 7000 cross-section imperfections obtained. These findings are then summarized into histograms with CDF in Table 7. 1. From Figure 7. 9 to Figure 7. 14, there are two subgraphs in each figure: one (named as general imperfections) is summarized from imperfections over all cross sections (G1 and G2 exclude imperfections smaller than one tenth of maxima per specimen); the other is generated from maximum values of specimens, i.e., 19 specimens for Z purlins. General imperfections are designed only for statistical purpose but do not contribute to the statistical summary table. Distribution of general imperfections are highly non-Gaussian. From the perspective of the researcher, a statistical summary of general imperfections of Type 1 and Type 2 can be effectively useful because these types of imperfections are more localized and cannot be normalized along length. Regarding the summary table (Table 7.1), it can be observed that 50% cross-section imperfections are much larger when compared with Zeinoddini's 50% and even tolerance. Potential sources to differences in measurement specimens are in a Z shape instead of C shape, high density of measurements per cross section, and measurement noise. There are global imperfections, as G1 and G2 are all smaller than the request tolerances. However, 50% of G2 imperfections are two times more than in Zeinoddini's conclusion. Again, Z sections are much easier to be distorted in transportation and installment, and its twist magnitudes can be surprisingly large relative to C sections.

Table 7. 1 Statistic summary of geometric imperfections of Z sections

Z	Type 1[a]	Type 2[b]		G1	G2	G3
700S48	d_1/t	d_{2L}/t	d_{2r}/t	L/δ	L/δ	°/ft
25%	1.10	2.24	2.58	3901	3585	1.83
50%	1.26	2.38	2.81	3557	2815	2.07
75%	1.49	2.47	3.04	2755	2606	2.25
95%	1.81	2.83	4.20	1245	961	2.45
99%	1.97	3.63	6.11	1245	961	2.71
mean	1.30	2.42	3.02	3465	3087	2.06
Std. Dev.	0.34	0.41	0.86	1183	1170	0.33
Zeinoddini 50%[c]	0.31	0.75	0.75	2909	4010	0.09
c955[d]	1.04	1.04	1.04	960	960	0.51

Note:

a. Type 1 for conventional imperfections indicates crown imperfections.

b. Type 2 for conventional imperfections indicates over-bend or flare imperfections.

c. Measured values can be referred to in Zeinoddini (2011).

d. Reference tolerances from ASTM (2015) for C sections: G1 (bow) and G2 (camber) are L/960; G3 is 1/32 in./ft of a specimen, in addition for d1 (crown) = 1/16 in., and d2 (flare) = 1/16 in., C tolerances are reported here as similar tolerances for Z do not exist.

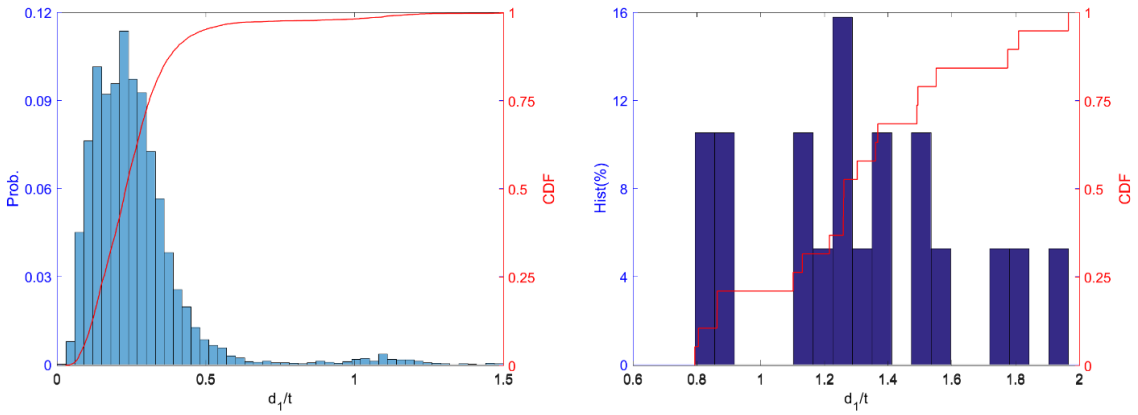

Figure 7. 9 Typical statistical summary of Type 1 of Z sections (700Z225-48): (a) imperfections along length; (b) maximum imperfection per section

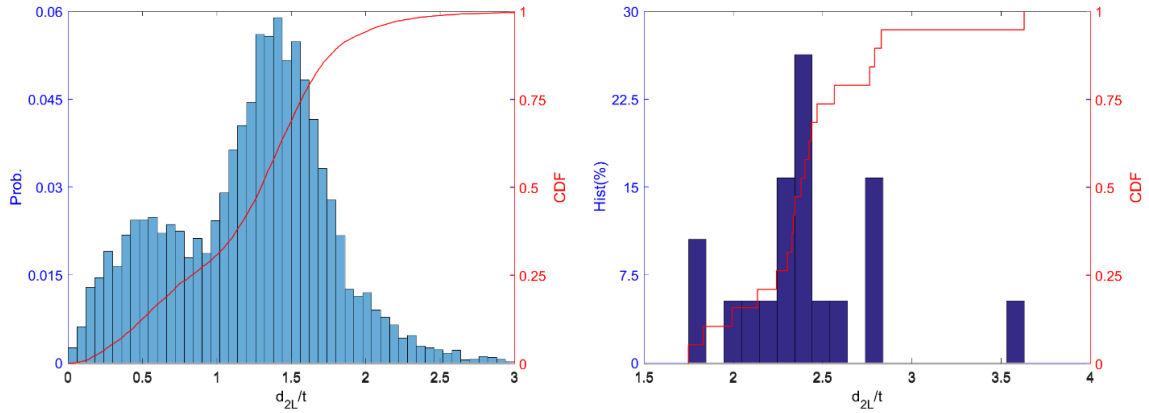

Figure 7. 10 Typical statistical summary of Type 2 (left flange) of Z sections (700Z225-48): (a) imperfections along length; (b) maximum imperfection per section

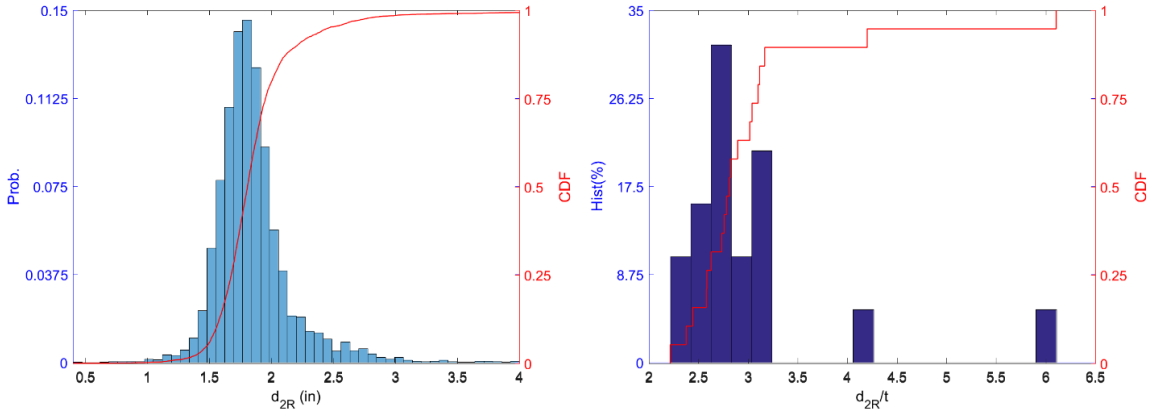

Figure 7. 11 Typical statistical summary of Type 2 (right flange) of Z sections (700Z225-48): (a) imperfections along length; (b) maximum imperfection per section

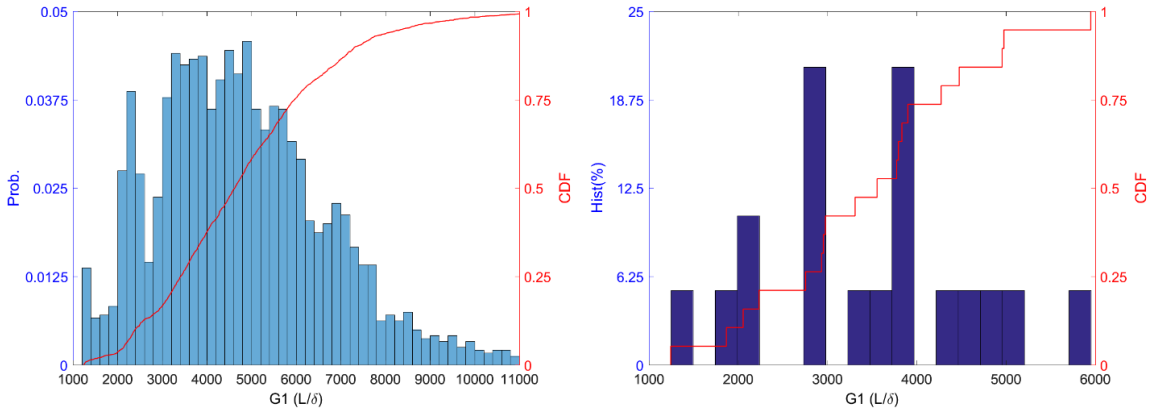

Figure 7. 12 Typical statistical summary of bow (G1) of Z sections (700Z225-48): (a) imperfections along length; (b) maximum imperfection per section

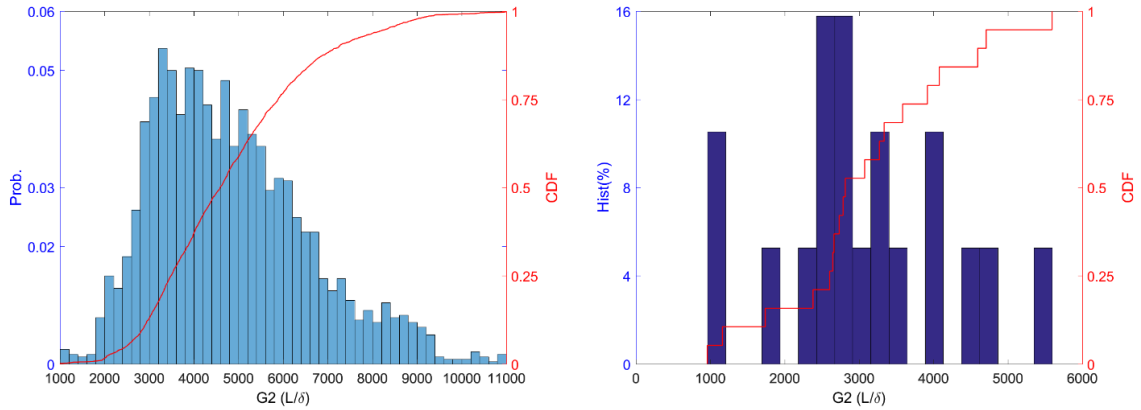

Figure 7. 13 Typical statistical summary of camber (G2) of Z sections (700Z225-48): (a) imperfections along length; (b) maximum imperfection per section

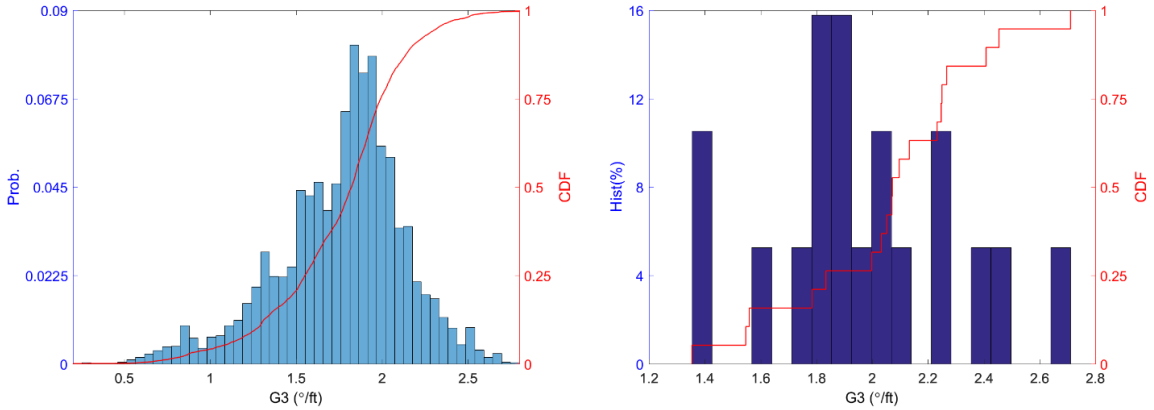

Figure 7. 14 Typical statistical summary of twist (G3) of Z sections (700Z225-48): (a) imperfections along length; (b) maximum imperfection per section

C

As previously mentioned, there are two types of C sections: 362S162-68 and 600S137-54 are both scanned and processed and each comprises 14 specimens in the group. Each specimen contains around 550 cross sections; the total number of cross sections used for the general imperfection statistical summary is around 7700. Following the conventional imperfection characterization, abundant histograms can be obtained for 362S162-68 (Figure 7. 15 to Figure 7. 20) and for 600S137-54 (Figure 7. 21 to Figure 7. 26). Maximum values per imperfections are statistically analyzed in Table 7. 2 (362S162-68) and Table 7. 3 (600S137-54).

Recalled from the Z statistical summary, twist imperfections of 362S162-68 and 600S137-54 are much smaller and generally stay within tolerance. However, they are still larger than in Zeinoddini's results. Type 1 of 362S162-68 contains a larger value when a 50% imperfection is compared with the tolerance and Zeinoddini's 50% results. Type 2 imperfections, however, approach to tolerance in c955 when a 50% imperfection is used. Moreover, global imperfection G2 from the summary is much larger than in Zeinoddini's conclusion. However, both G1 and G2 are smaller than tolerance.

Regarding the distribution of general imperfections, Type 2 imperfections from left flanges and right flanges have a similar distribution shape as well as magnitude. Type 1 shows a better Gaussian distribution while G1, G2, and G3 are still non-Gaussian with long tails on the right side.

Table 7. 2 Statistical summary of geometric imperfections of C sections (362S162-68)

C	Type 1[a]	Type 2[b]		G1	G2	G3
362S162-68	d_1/t	d_{2l}/t	d_{2r}/t	L/δ	L/δ	°/ft
25%	1.04	0.89	0.89	2988	2687	0.23
50%	1.06	0.92	0.93	2271	2497	0.31
75%	1.08	1.05	1.02	2162	2160	0.44
95%	1.10	1.09	1.04	1969	1169	0.57
99%	1.11	1.11	1.21	1969	1169	0.61
mean	1.06	0.98	0.97	2547	2482	0.36
Std. Dev.	0.03	0.09	0.10	458	646	0.15
Zeinoddini 50%[c]	0.31	0.75	0.75	2909	4010	0.09
c955[d]	0.92	0.92	0.92	960	960	0.99

Note:

a. Type 1 for conventional imperfections indicates crown imperfections.

b. Type 2 for conventional imperfections indicates over-bend or flare imperfections.

c. Measured values can be referred to in Zeinoddini (2011).

d. Reference tolerances from ASTM (2015) for C sections: G1 (bow) and G2 (camber) are L/960; G3 is 1/32 in./ft of a specimen, in addition for d1 (crown) = 1/16 in., and d2 (flare) = 1/16 in.

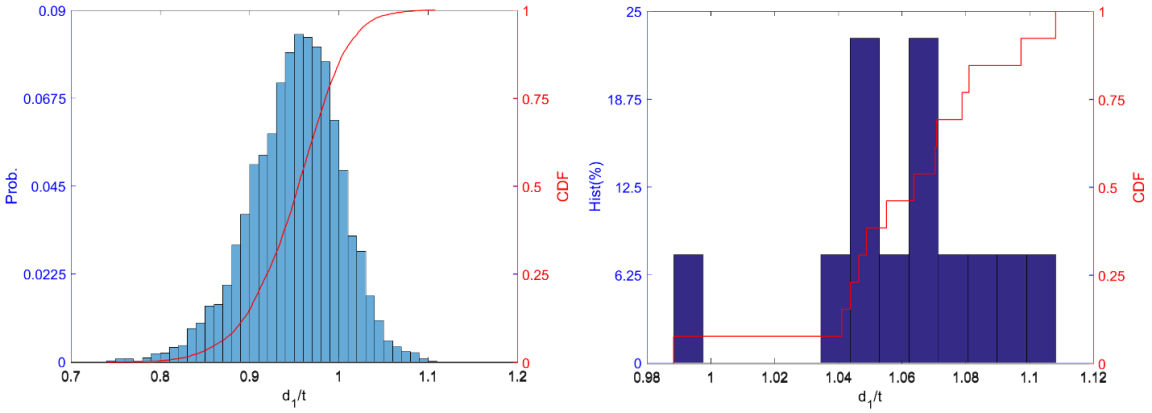

Figure 7. 15 Typical statistical summary of Type 1 of C sections (362S162-68): (a) imperfections along length; (b) maximum imperfection per section

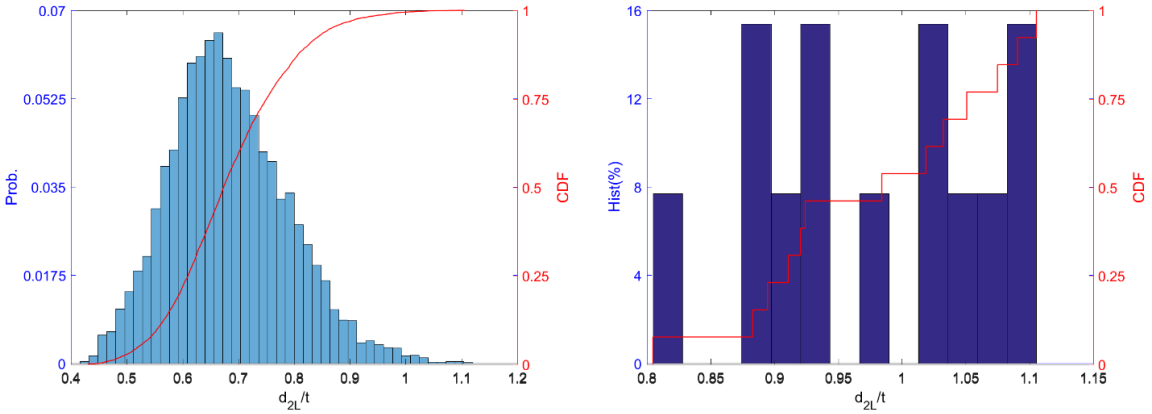

Figure 7. 16 Typical statistical summary of Type 2 (left flange) of C sections (362S162-68): (a) imperfections along length; (b) maximum imperfection per section

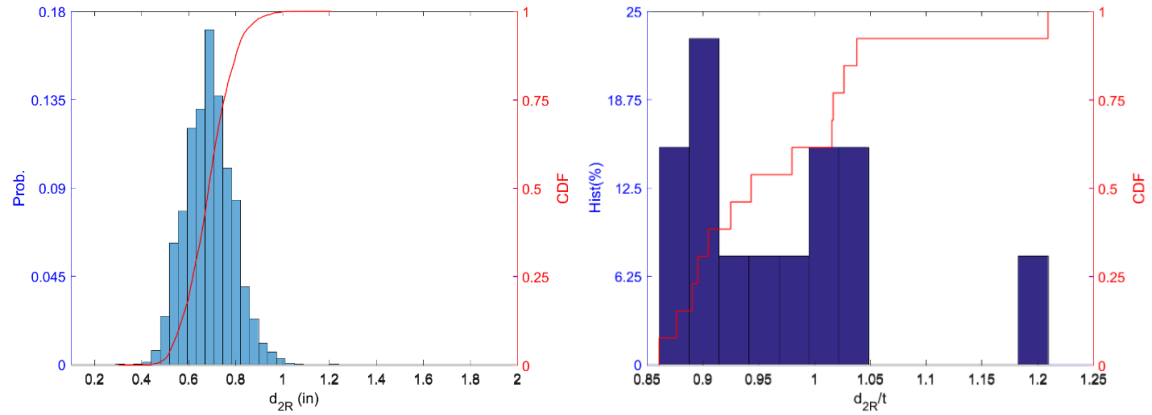

Figure 7. 17 Typical statistical summary of Type 2 (right flange) of C sections (362S162-68): (a) imperfections along length; (b) maximum imperfection per section

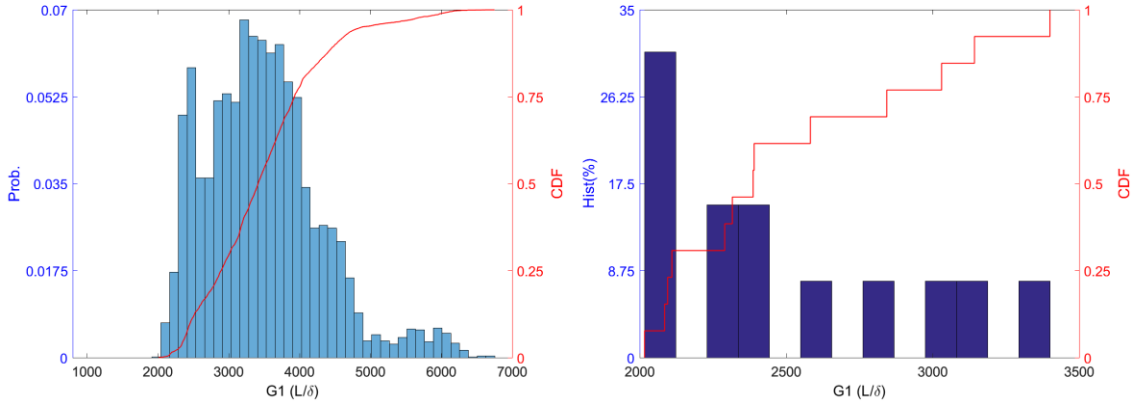

Figure 7. 18 Typical statistical summary of bow (G1) of C sections (362S162-68): (a) imperfections along length; (b) maximum imperfection per section

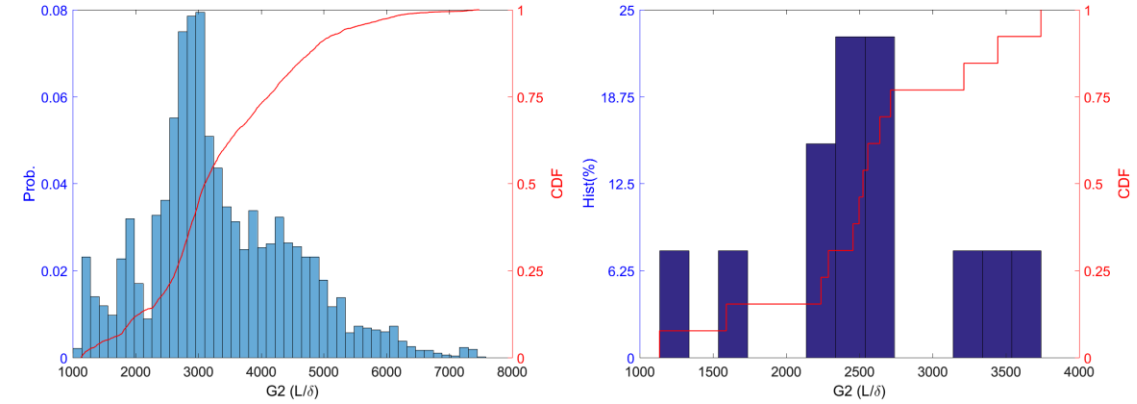

Figure 7. 19 Typical statistical summary of camber (G2) of C sections (362S162-68): (a) imperfections along length; (b) maximum imperfection per section

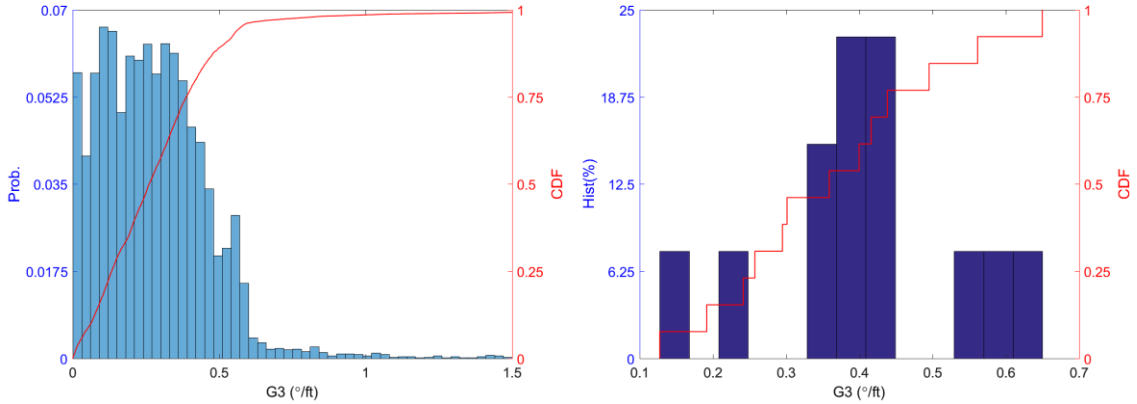

Figure 7. 20 Typical statistical summary of twist (G3) of C sections (362S162-68): (a) imperfections along length; (b) maximum imperfection per section

Compared with 362S162-68, 600S137-54 has larger Type 2 imperfections, and both Type 2 imperfections are out of tolerance. Besides, bow (G1) imperfections are much larger with respect to 362S162-68, Zeinoddini's results, and standard tolerance. On the other hand, twist (G3) imperfections are much smaller than 362S162-68 and 700Z225-60. It may be concluded that single-symmetric geometry is stiffer in torsion than double-symmetric geometry, and torsion resistance of 600S137-54 is higher than that of 362S162-68, while shorter flanges of 600S137-54 impair bending resistance and corner stiffness with respect to bow (G1) and out-of-straightness (Type 2). distributions of general imperfections of 600S137-54 resemble those of 362S162-68 except Type 1 has long tail on right side.

Table 7. 3 Statistical summary of geometric imperfections of 600S137-54 (C)

C	Type 1[a]	Type 2[b]		G1	G2	G3
600S137-54	d_1/t	d_{2L}/t	d_{2r}/t	L/δ	L/δ	°/ft
25%	0.95	1.46	1.38	882	2422	0.07
50%	0.97	2.09	1.66	863	2239	0.09
75%	1.07	2.17	2.11	835	2024	0.11
95%	1.10	2.20	2.26	817	1543	0.14
99%	1.11	2.25	2.29	817	1543	0.15
mean	1.00	1.88	1.76	879	2394	0.09
Std. Dev.	0.08	0.39	0.42	70	577	0.03
Zeinoddini 50%[c]	0.31	0.75	0.75	2909	4010	0.09
c955[d]	1.15	1.15	1.15	960	960	0.60

Note:

a. Type 1 for conventional imperfections indicates crown imperfections.

b. Type 2 for conventional imperfections indicates over-bend or flare imperfections.

c. Measured values can be referred to in Zeinoddini (2011).

d. Reference tolerances from ASTM (2015) for C sections: G1 (bow) and G2 (camber) are L/960; G3 is 1/32 in./ft of a specimen, in addition for d1 (crown) = 1/16 in., and d2 (flare) = 1/16 in.

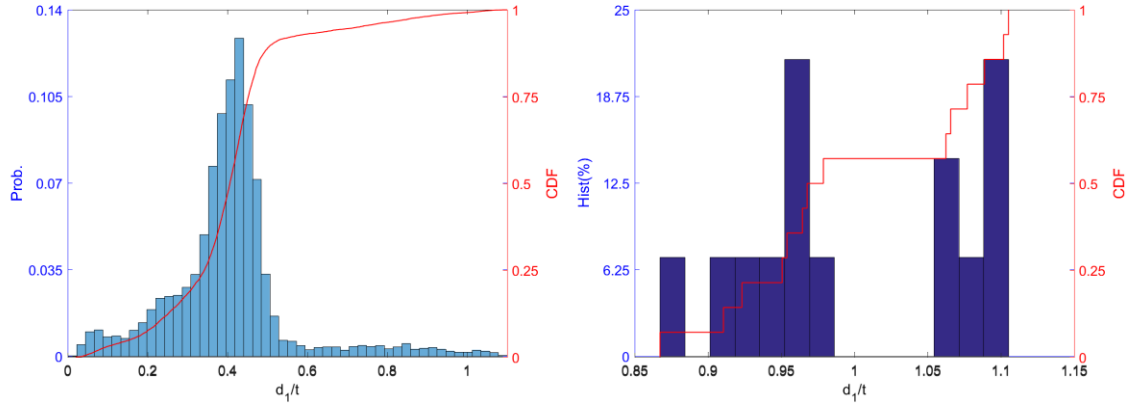

Figure 7. 21 Typical statistical summary of Type 1 of C sections (600S137-54): (a) imperfections along length; (b) maximum imperfection per section

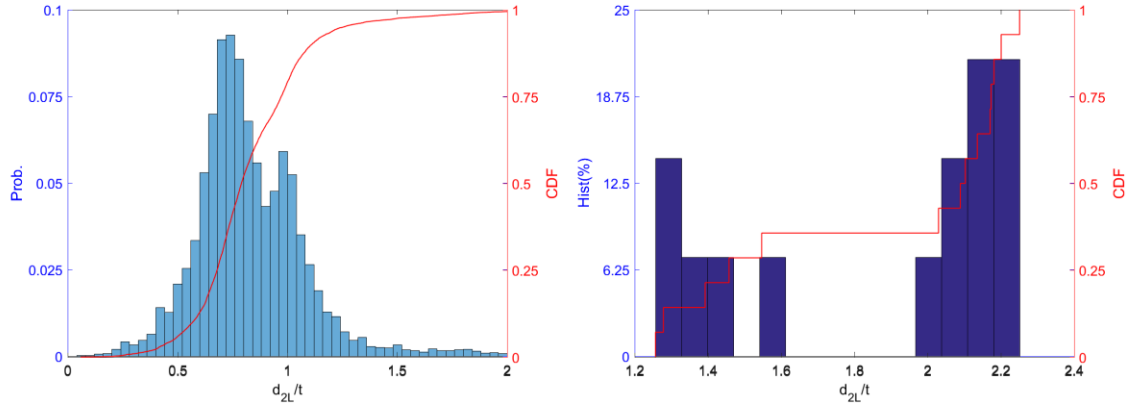

Figure 7. 22 Typical statistical summary of Type 2 (left flange) of C sections (600S137-54): (a) imperfections along length; (b) maximum imperfection per section

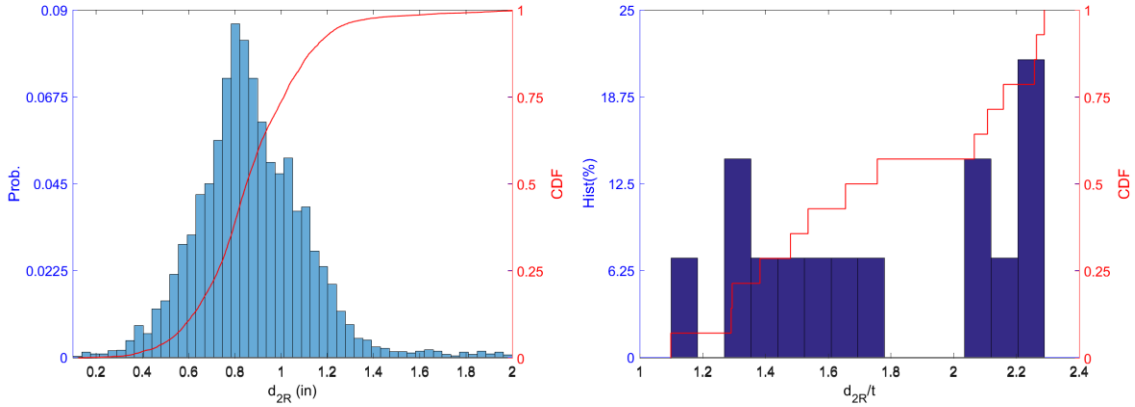

Figure 7. 23 Typical statistical summary of Type 2 (right flange) of C sections (600S137-54): (a) imperfections along length; (b) maximum imperfection per section

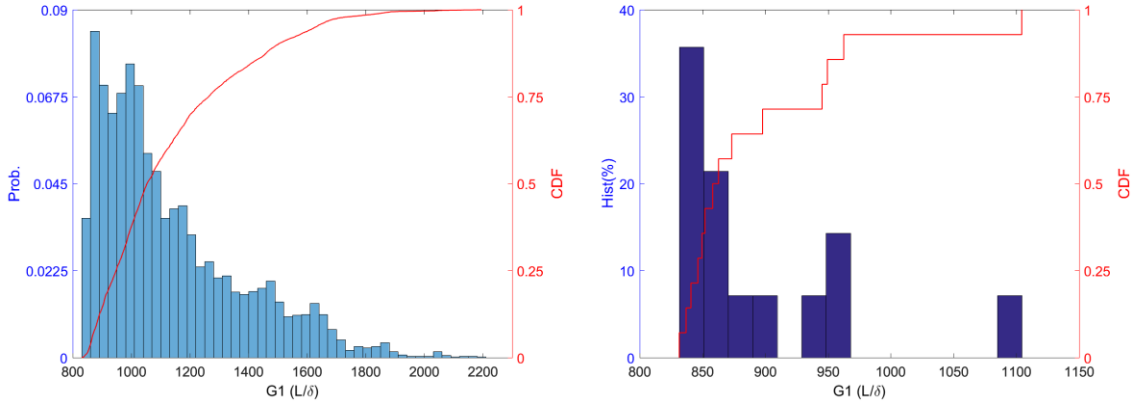

Figure 7. 24 Typical statistical summary of bow (G1) of C sections (600S137-54): (a) imperfections along length; (b) maximum imperfection per section

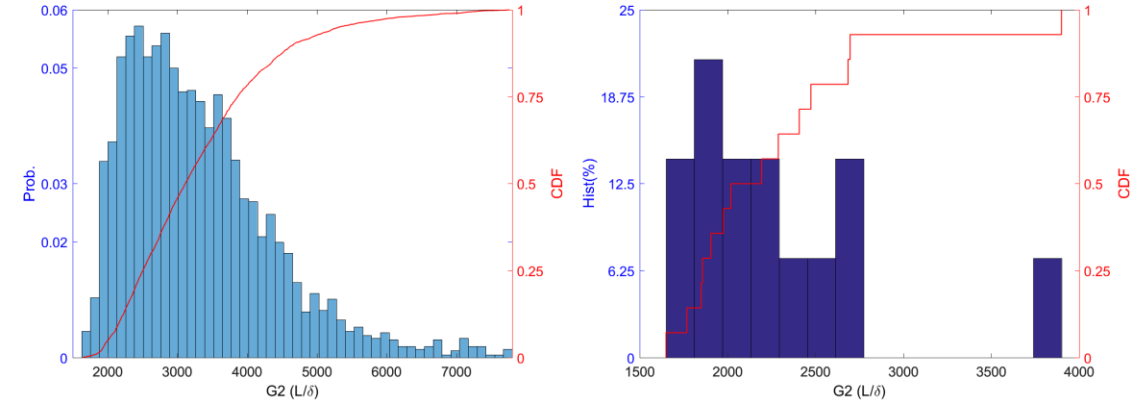

Figure 7. 25 Typical statistical summary of camber (G2) of C sections (600S137-54): (a) imperfections along length; (b) maximum imperfection per section

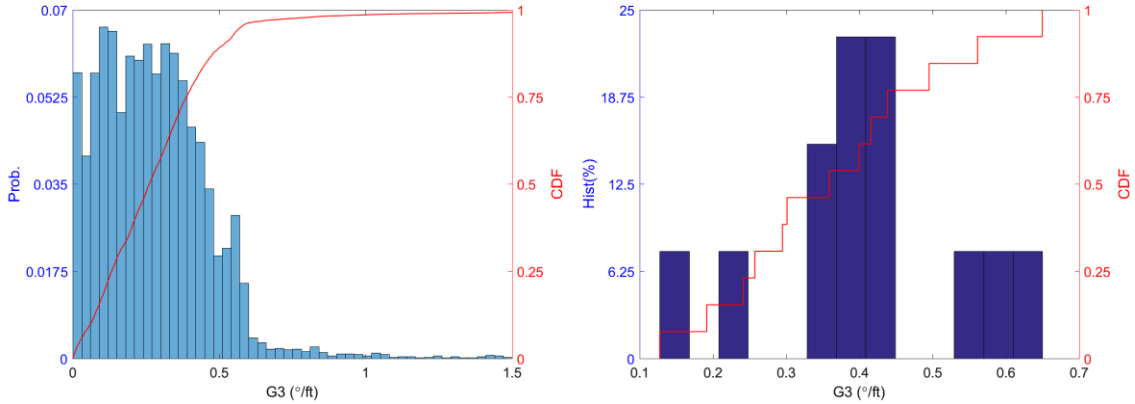

Figure 7. 26 Typical statistical summary of twist (G3) of C sections (600S137-54): (a) imperfections along length; (b) maximum imperfection per section

BUC

Compared with Z purlins and C studs, the sample size of BUC members is limited to four in 362S162-68 and 600S137-54 groups, respectively. Restrained by the measurement techniques, Type 1 imperfections of lower sections may not reflect its true situation. As shown in Table 7. 4, Type 1 imperfections (50% level) of 362S162-68 are much larger than in Zeinoddini's 50% results and tolerances. This may be contributed by the post-manufacturing when two C sections are tied together with screws and nuts. Again, Zeinoddini's data and the tolerance are used for reference only because they are not designed for built-up C members. Type 2 imperfections are generally small, except for the left flange of lower sections. The interesting thing is that global imperfections such as bow (G1) are small, while (G2) is much larger when they are compared with Zeinoddini's findings and the tolerance of c955. Twist (G3) is smaller than the tolerance but much larger than in Zeinoddini's report.

Table 7. 4 Statistical summary of geometric imperfections of BUC (362S162-68)

BUC	Type 1[a]			Type 2[b]			G1	G2	G3
362S162-68	d_1^{upper}/t	d_1^{lower}/t	d_{2L}^{upper}/t	d_{2r}^{upper}/t	d_{2L}^{lower}/t	d_{2r}^{lower}/t	L/δ	L/δ	°/ft
25%	1.13	1.49	0.49	0.51	1.21	0.39	6448	2032	0.33
50%	1.33	1.59	0.67	0.68	1.29	0.50	4847	1609	0.44
75%	1.49	1.77	0.79	0.76	1.31	0.71	2007	1476	0.48
95%	1.57	1.94	0.82	0.80	1.56	0.72	2007	1476	0.66
99%	1.57	1.94	0.82	0.80	1.56	0.72	2007	1476	0.66
mean	1.38	1.70	0.69	0.69	1.34	0.58	4990	1805	0.48
Std. Dev.	0.19	0.20	0.15	0.13	0.15	0.16	2147	309	0.14
Zeinoddini 50%[c]	0.31	0.31	0.75	0.75	0.75	0.75	2909	4010	0.09
c955[d]	0.92	0.92	0.92	0.92	0.92	0.92	960	960	0.99

Note:

a. Type 1 for conventional imperfections indicates crown imperfections.

b. Type 2 for conventional imperfections indicates over-bend or flare imperfections.

c. Measured values can be referred to in Zeinoddini (2011).

d. Reference tolerances from ASTM (2015) for C sections: G1 (bow) and G2 (camber) are L/960; G3 is 1/32 in./ft of a specimen, in addition for d1 (crown) = 1/16 in., and d2 (flare) = 1/16 in., C tolerances are reported here as similar tolerances for BUC do not exist.

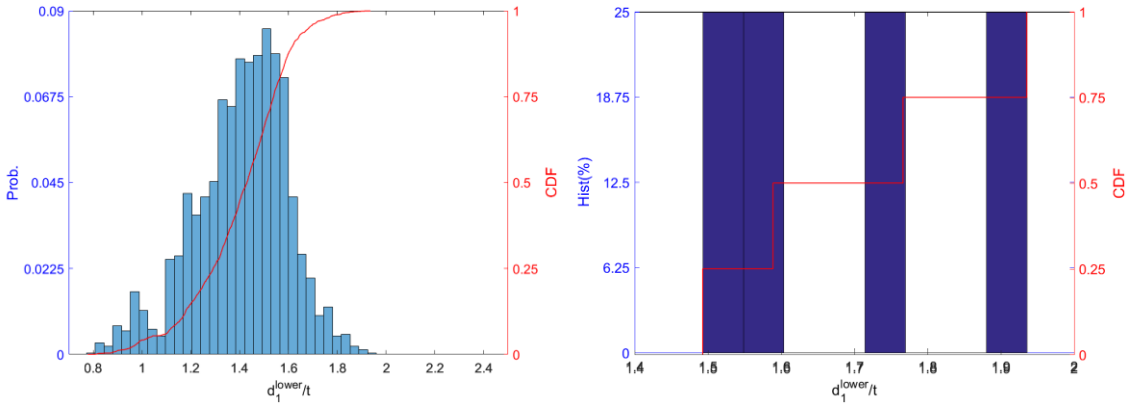

Figure 7. 27 Typical statistical summary of Type 1 (lower section) of BUC sections (362S162-68): (a) imperfections along length; (b) maximum imperfection per section

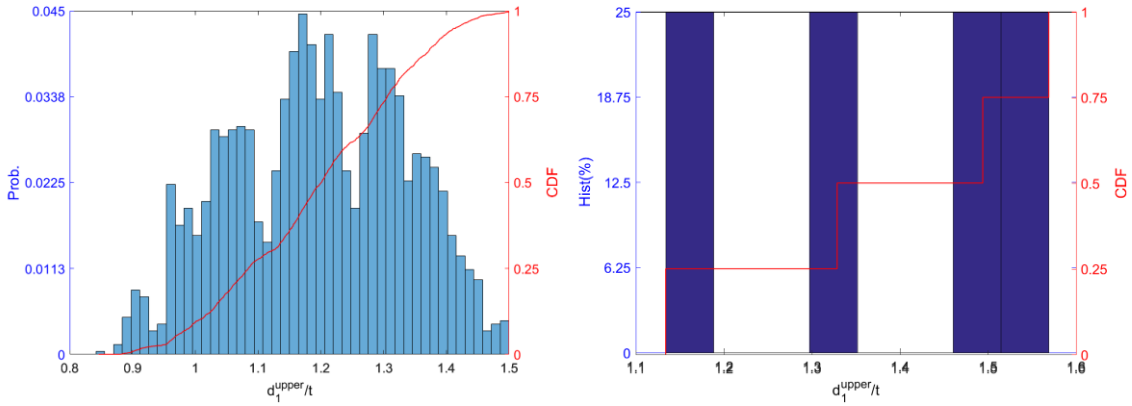

Figure 7. 28 Typical statistical summary of Type 1 (upper section) of BUC sections (362S162-68): (a) imperfections along length; (b) maximum imperfection per section

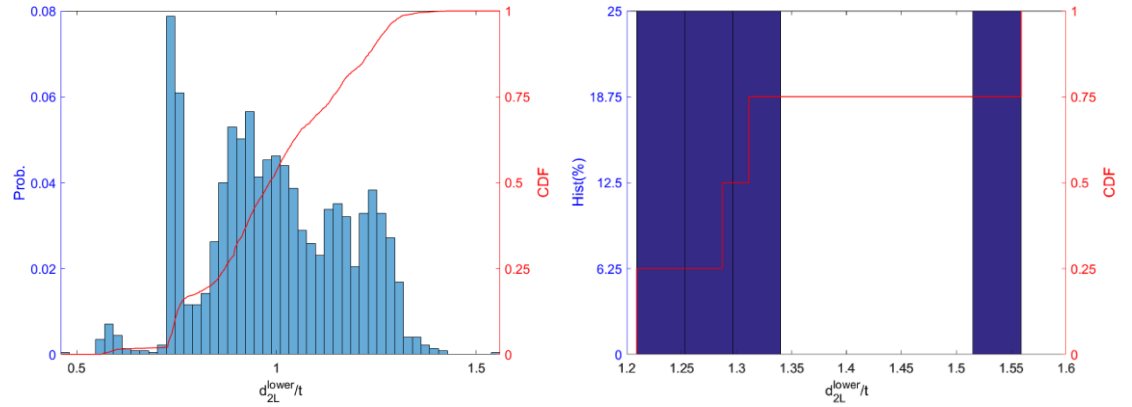

Figure 7. 29 Typical statistical summary of Type 2 (lower section, left flange) of BUC sections (362S162-68): (a) imperfections along length; (b) maximum imperfection per section

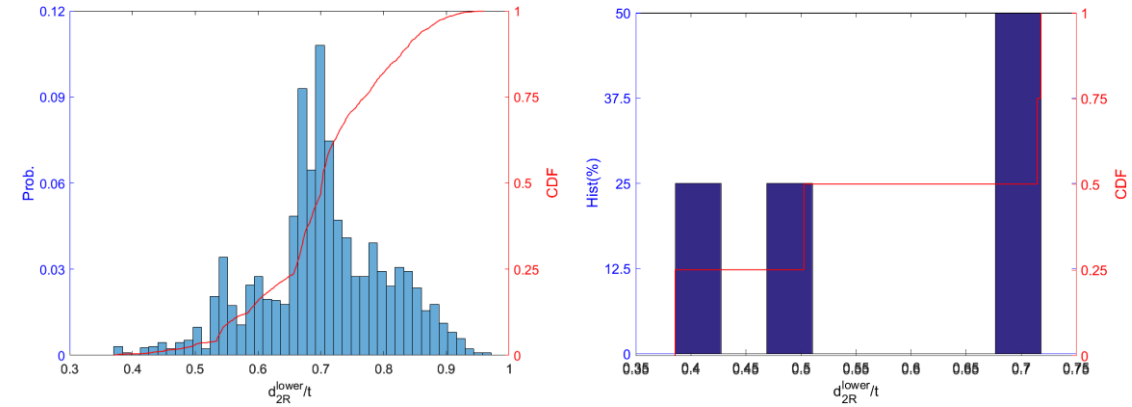

Figure 7. 30 Typical statistical summary of Type 2 (lower section, right flange) of BUC sections (362S162-68): (a) imperfections along length; (b) maximum imperfection per section

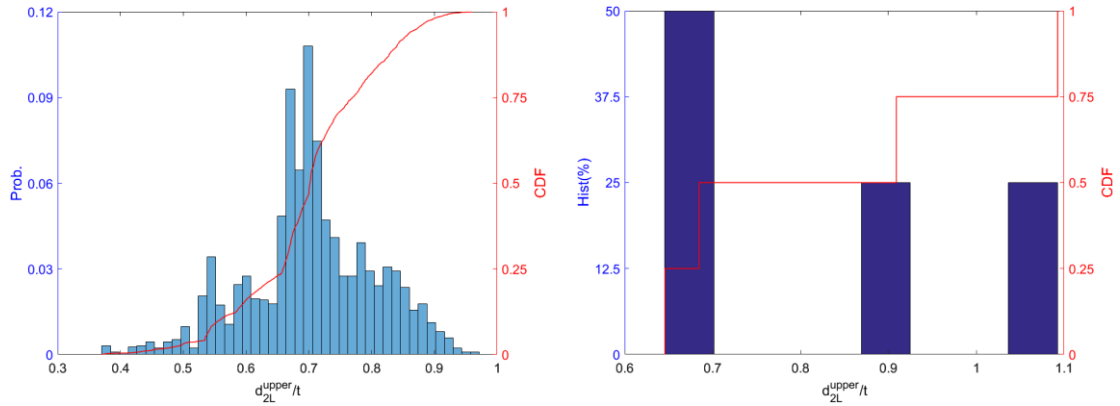

Figure 7. 31 Typical statistical summary of Type 2 (upper section, left flange) of BUC sections (362S162-68): (a) imperfections along length; (b) maximum imperfection per section

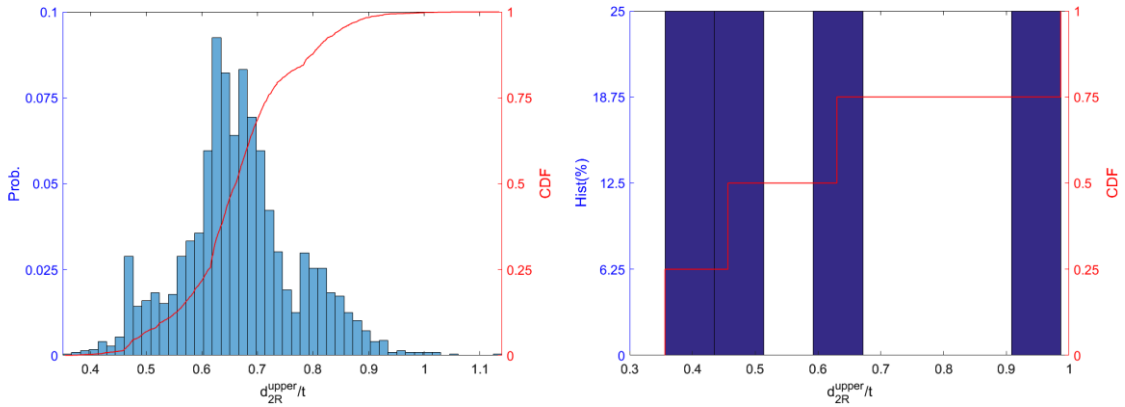

Figure 7. 32 Typical statistical summary of Type 2 (upper section, right flange) of BUC sections (362S162-68): (a) imperfections along length; (b) maximum imperfection per section

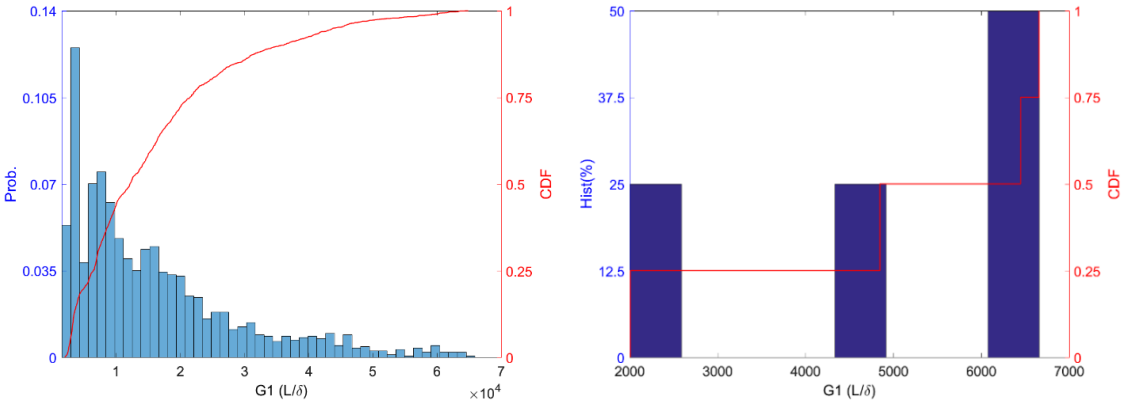

Figure 7. 33 Typical statistical summary of bow (G1) of BUC sections (362S162-68): (a) imperfections along length; (b) maximum imperfection per section

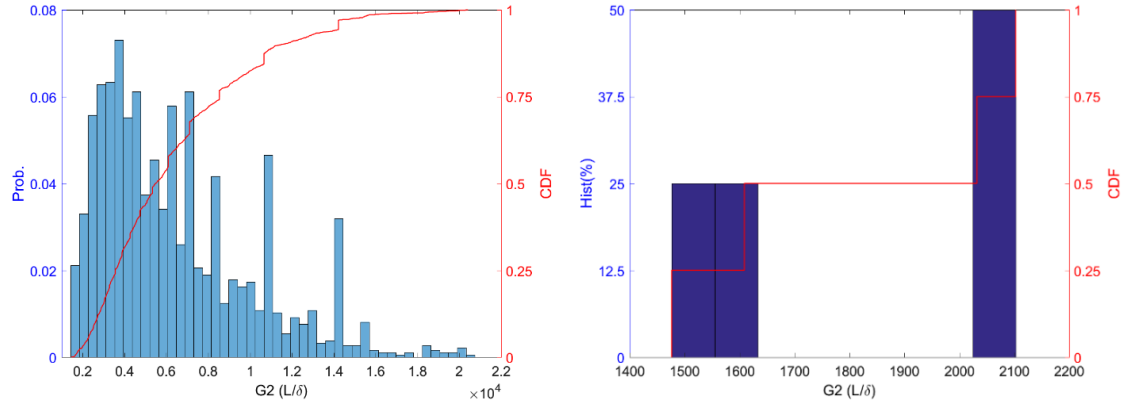

Figure 7. 34 Typical statistical summary of camber (G2) of BUC sections (362S162-68): (a) imperfections along length; (b) maximum imperfection per section

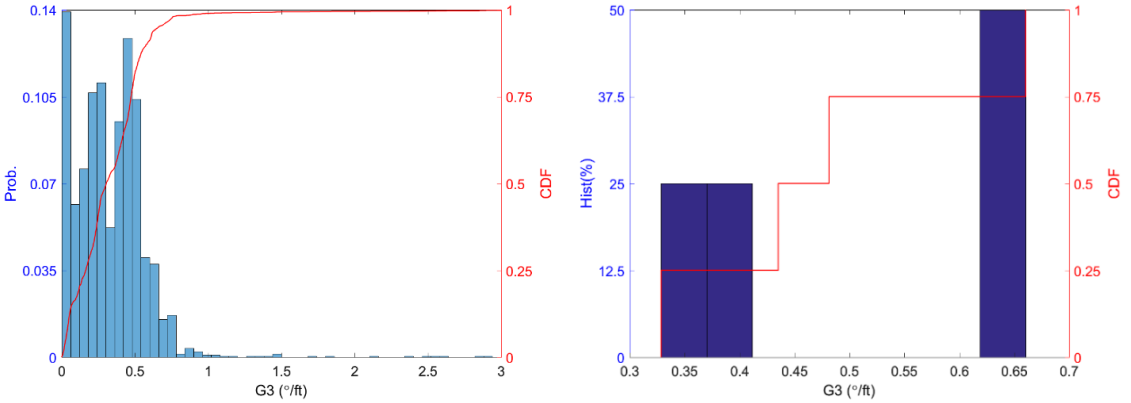

Figure 7. 35 Typical statistical summary of twist (G3) of BUC sections (362S162-68): (a) imperfections along length; (b) maximum imperfection per section

Compared with 362S162-68, 600S137-54 of BUC shares similar comparison results as those of C sections. However, imperfections of G1 improves, but G2 imperfections become worse. The 50% cross-section imperfections (Type 1 and 2) are all within the tolerance. A potential difference may be attributed to the post-manufacturing process. Distributions of imperfections in Figure 7. 36 to Figure 7. 44 are not very typical. Sample sizes of scanned BUC should increase, and more studies should be carried out here.

Table 7. 5 Statistical summary of geometric imperfections of BUC (600S137-54)

BUC	Type 1[a]		Type 2[b]				G1	G2	G3
600S137-54	d_1^{upper}/t	d_1^{lower}/t	d_{2L}^{upper}/t	d_{2r}^{upper}/t	d_{2L}^{lower}/t	d_{2r}^{lower}/t	L/δ	L/δ	°/ft
25%	0.39	0.71	0.65	0.36	0.79	0.61	2646	1181	0.17
50%	0.49	0.78	0.68	0.46	1.30	1.05	1438	922	0.19
75%	1.20	1.04	0.91	0.63	1.82	1.18	1322	803	0.25
95%	1.39	1.17	1.09	0.99	1.87	1.33	1322	803	0.34
99%	1.39	1.17	1.09	0.99	1.87	1.33	1322	803	0.34
mean	0.87	0.93	0.83	0.61	1.45	1.04	2172	1079	0.24
Std. Dev.	0.50	0.21	0.21	0.28	0.51	0.31	952	272	0.08
Zeinoddini 50%[c]	0.31	0.31	0.75	0.75	0.75	0.75	2909	4010	0.09
c955[d]	1.15	1.15	1.15	1.15	1.15	1.15	960	960	0.60

Note:

a. Type 1 for conventional imperfections indicates crown imperfections.

b. Type 2 for conventional imperfections indicates over-bend or flare imperfections.

c. Measured values can be referred to in Zeinoddini (2011).

d. Reference tolerances from ASTM (2015) for C sections: G1 (bow) and G2 (camber) are L/960; G3 is 1/32 in./ft of a specimen, in addition for d1 (crown) = 1/16 in., and d2 (flare) = 1/16 in., C tolerances are reported here as similar tolerances for BUC do not exist.

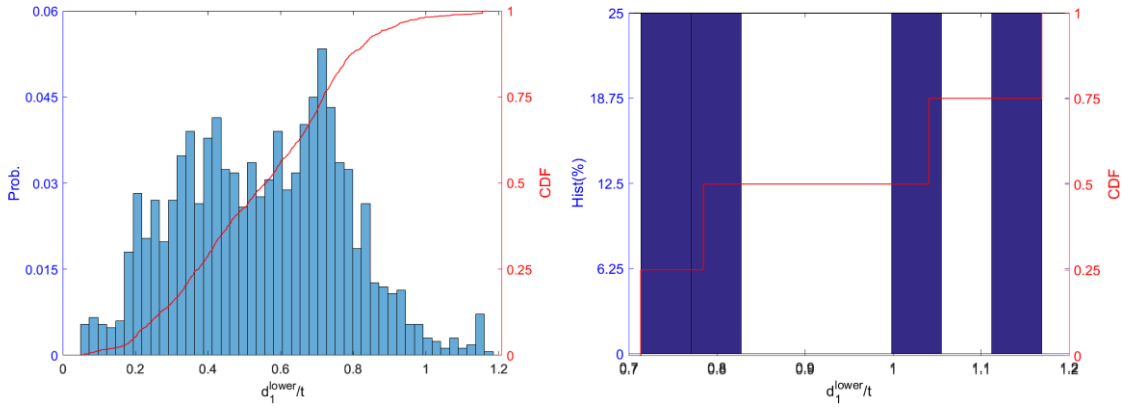

Figure 7. 36 Typical statistical summary of Type 1 (lower section) of BUC sections (600S137-54): (a) imperfections along length; (b) maximum imperfection per section

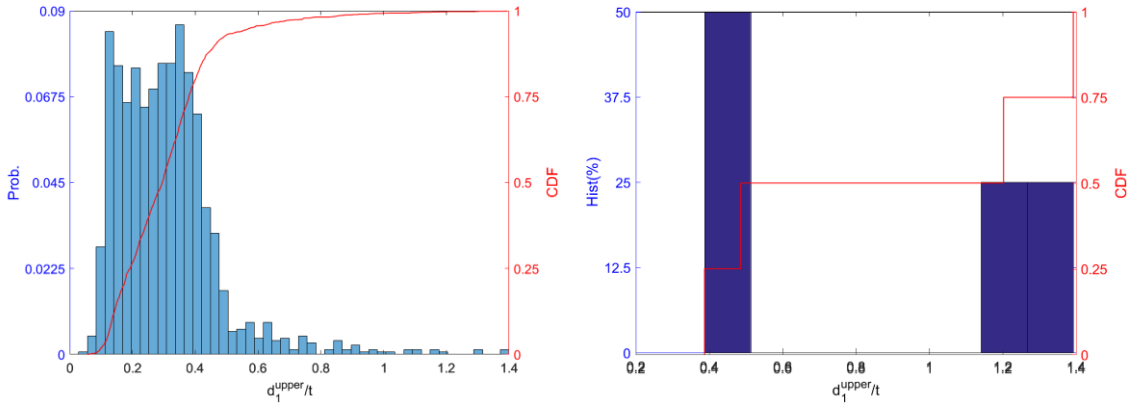

Figure 7. 37 Typical statistical summary of Type 1 (upper section) of BUC sections (600S137-54): (a) imperfections along length; (b) maximum imperfection per section

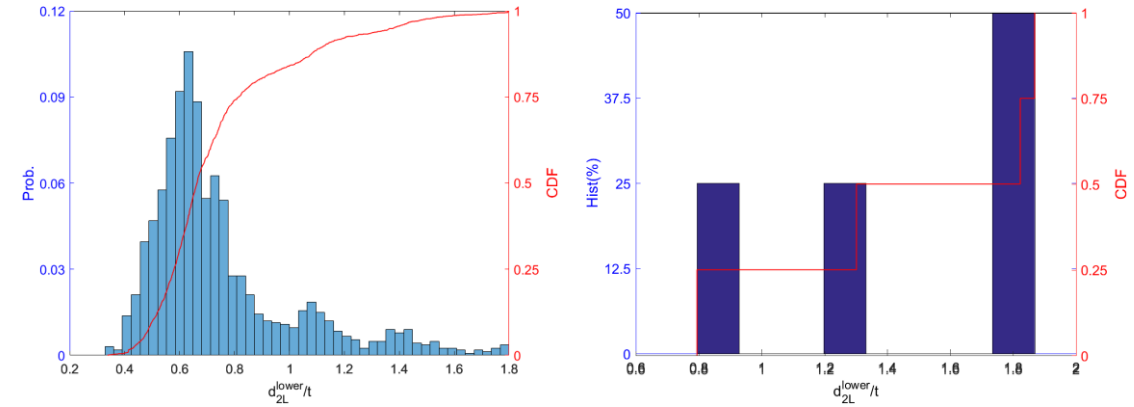

Figure 7. 38 Typical statistical summary of Type 2 (lower section, left flange) of BUC sections (600S137-54): (a) imperfections along length; (b) maximum imperfection per section

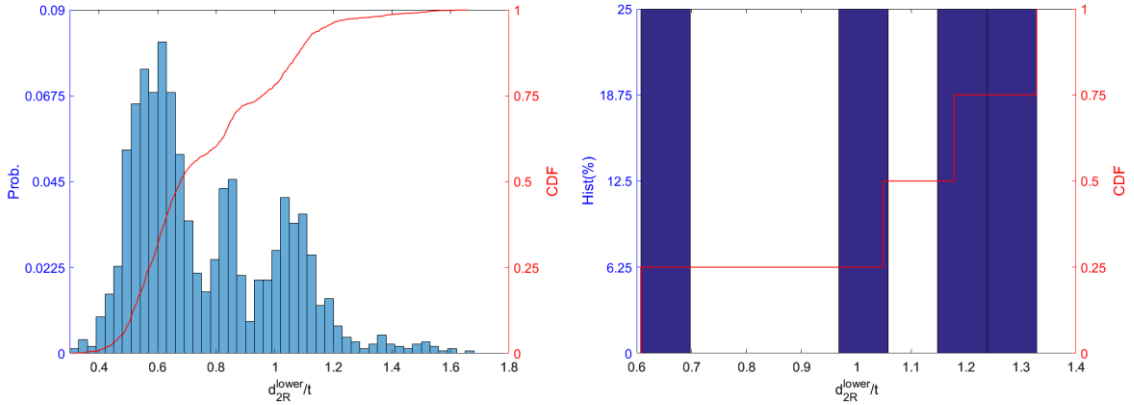

Figure 7. 39 Typical statistical summary of Type 2 (lower section, right flange) of BUC sections (600S137-54): (a) imperfections along length; (b) maximum imperfection per section

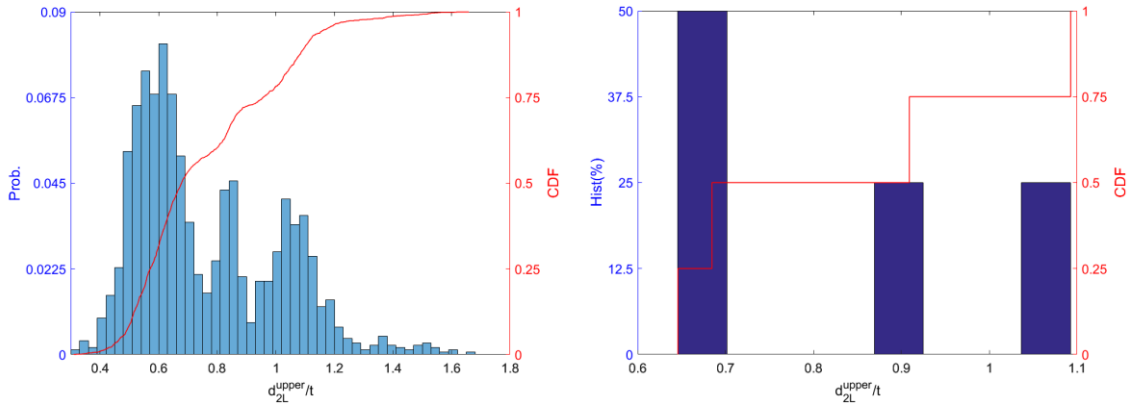

Figure 7. 40 Typical statistical summary of Type 2 (upper section, left flange) of BUC sections (600S137-54): (a) imperfections along length; (b) maximum imperfection per section

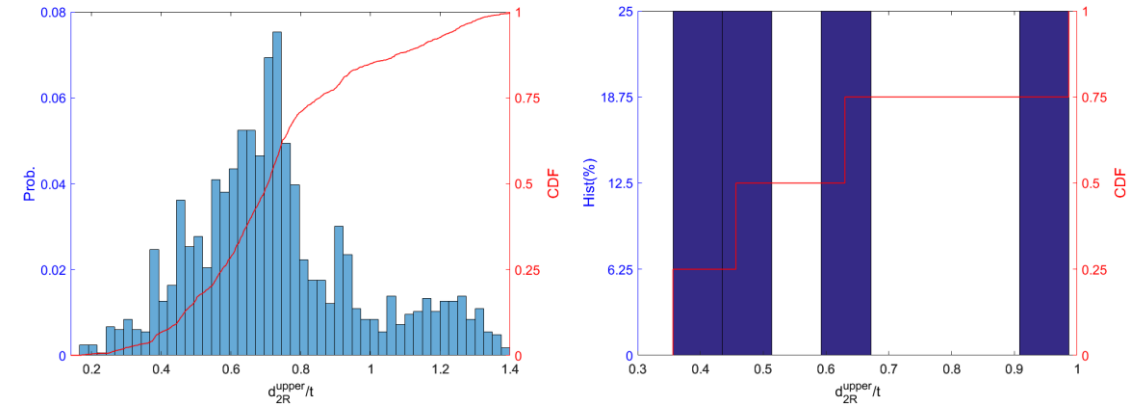

Figure 7. 41 Typical statistical summary of Type 2 (upper section, right flange) of BUC sections (600S137-54): (a) imperfections along length; (b) maximum imperfection per section

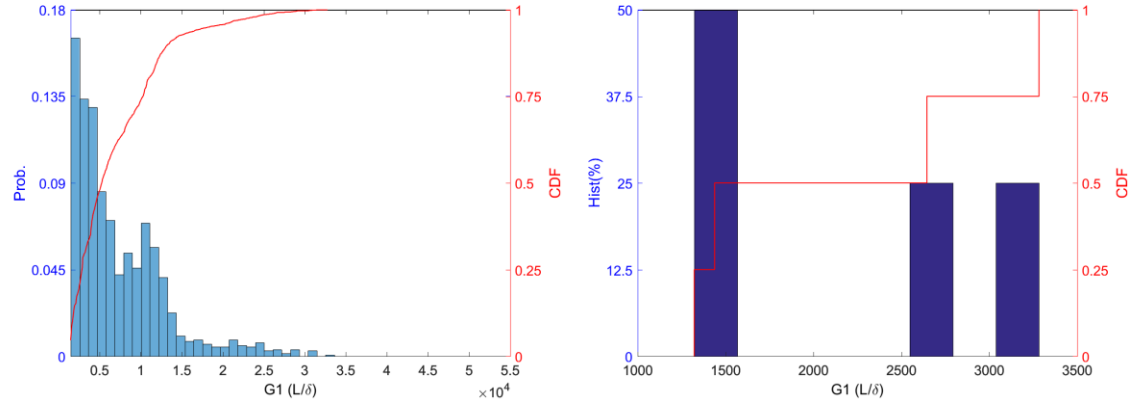

Figure 7. 42 Typical statistical summary of bow (G1) of BUC sections (600S137-54): (a) imperfections along length; (b) maximum imperfection per section

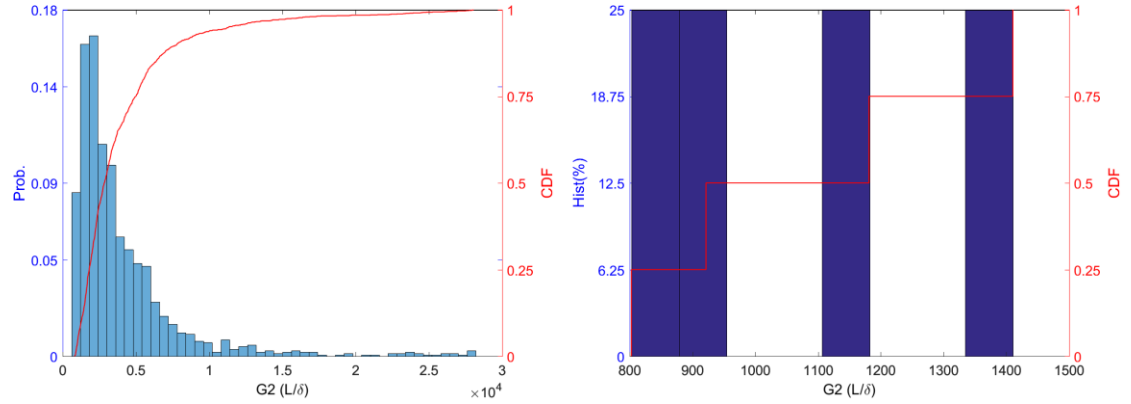

Figure 7. 43 Typical statistical summary of camber (G2) of BUC sections (600S137-54): (a) imperfections along length; (b) maximum imperfection per section

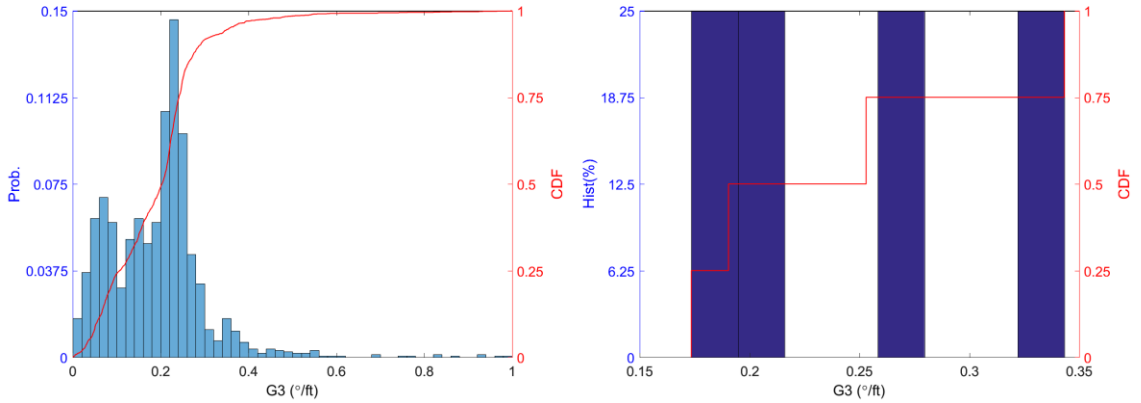

Figure 7. 44 Typical statistical summary of twist (G3) of BUC sections (600S137-54): (a) imperfections along length; (b) maximum imperfection per section

7.2 Model imperfection characterization

Buckling of cold-formed steel members generally may be characterized as occurring across three classes: global, distortional, or local. Global deformations can be categorized as major-axis bending, minor-axis bending, and torsion. Local and distortional deformations both include cross-section deformations with local buckling strongly associated with bending of the local plates and distortional buckling a combination of bending and membrane deformations in the plates (Schafer 2002).

Thin-walled cold-formed steel structural members are sensitive to imperfections, especially when the imperfection patterns are reasonably affine to the aforementioned buckling mode shapes (Zeinoddini and Schafer 2012). This motivated a new method to formally characterize imperfections based on 1st mode buckling shapes across the buckling classes. Surface imperfections in a cross section are formally decoupled into 5 different modes, i.e. G1, G2, G3, distortional, and local with the cross-section shape determined based on the maximum cross-section deformation of the 1st buckling mode in each class (Figure 7. 47, Figure 7. 50, Figure 7. 53). The resulting imperfection may be expressed as follows:

$$f(y) = \sum_{i=1}^{5} \alpha_i(y)\phi_i(x,z) \qquad \text{Eq 7. 2}$$

where y represents longitudinal position, α is the imperfection magnitude, which varies with y, φ_i is a cross-section deformation field with respect to the mode shapes, and f is the surface imperfection field of the measured cross section.

The advantage of this modal imperfection decomposition is that it directly utilizes information on the buckling modes when characterizing the imperfection. The disadvantage is that the buckling mode shape must be calculated in advance to perform the characterization—traditional methods do not require such a calculation. The obtained imperfection magnitudes (αi) along the 3D model can be Fourier transformed into the frequency domain, as shown in Figure 7. 45, where the x axis represents the reciprocal of the half-wave length (λ) of a buckling mode and the y axis represents magnitudes of imperfections (amplitude) corresponding to a specific half-wave length. Power spectra can be statistically summarized, and a base power spectral density (PSD) from that may be used for high-accuracy imperfection simulations (Zeinoddin, 2011).

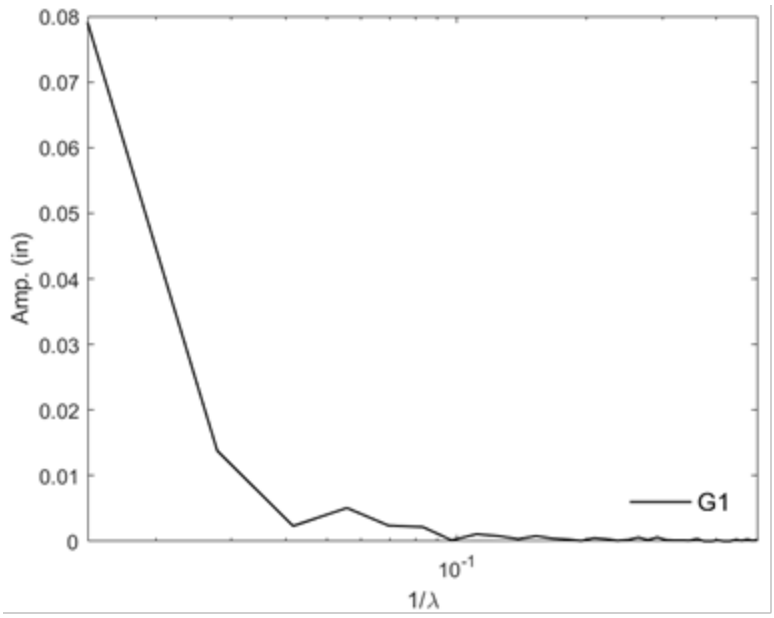

Figure 7. 45 Example mode imperfection in frequency domain (λ in in.)

7.2.1 Modal imperfection definition

The first step in the decomposition is formation of the cross-section shapes, i.e., ϕ_i, for G1, G2, G3. This step is done manually because the shapes are simply rigid body movements of the section. For local and distortional, a surrogate finite strip model is used in CUFSM. Specifically, the method of Li et al. (2011) is employed: a straight-corner model is used with the constrained finite strip method to find the critical local or distortional buckling half wavelength. This is followed by a proper round-corner model on the idealized geometry at the mesh density desired and at the critical half-wavelength determined in the constrained finite strip model. Results are then taken directly from the analysis, which are conceptually illustrated in Figure 7. 46, Figure 7. 49, and Figure 7. 52, corresponding to Z, C, and BUC, respectively.

Regarding the Z sections, major and minor axes of bending should be identified at first. Variations of centroids are tracked and then decomposed along major and minor axes. The first buckling mode shapes with respect to five classes are demonstrated in Figure 7. 47. These buckling mode shapes

are identified through CUFSM, as described in the procedures above, half-wave lengths of which will be used in Chapter 8.

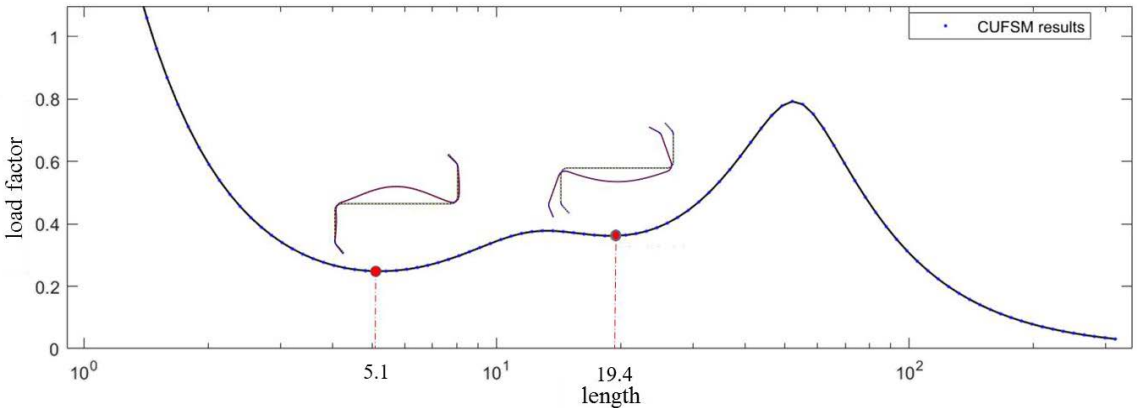

Figure 7. 46 Signature curve of Z section (half-wavelength in in., load factor P/P_y)

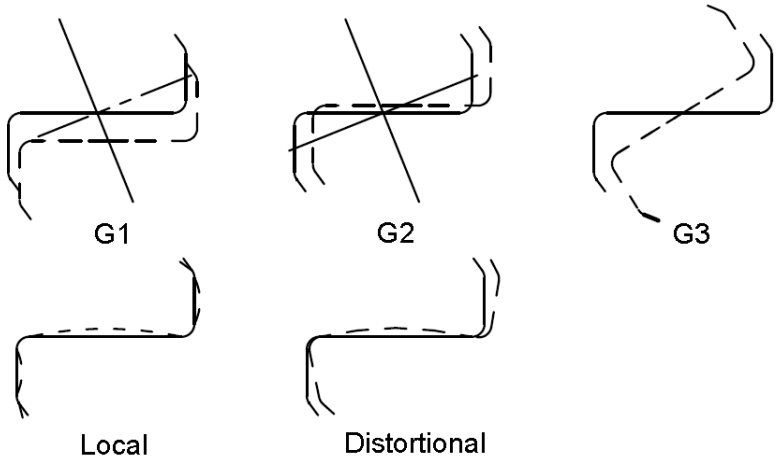

Figure 7. 47 Imperfection characterization of Z sections by MID

With the cross-section ϕ_i with maximum deformation normalized as 1, magnitudes (α_i) can be found for each mode of imperfections from linear regression against the imperfect 3D point cloud. A typical result is depicted for a given cross-section in Figure 7. 48. The procedure is repeated across all cross sections, providing the magnitude as a function of length, $\alpha_i(y)$, results of which will be shown in the next section..

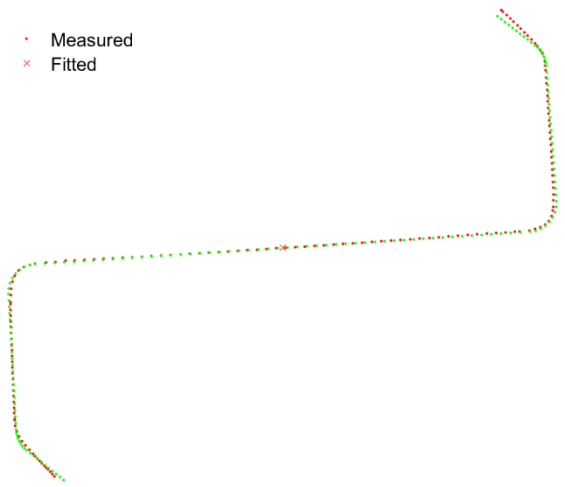

Figure 7. 48 A typical fitting cross section of Z section from MID

C sections and BUC sections have similar procedures as Z sections. Lowest points of load factor along a signature point are located, and mode shapes thus can be found from CUFSM analysis (Figure 7. 49 and Figure 7. 52). The first buckling mode shapes (local and distortional modes) thus can be identified. G1 and G2 are relatively easier to find for C and BUC because they can be simply decomposed along vertical (z) and horizontal (c) directions. Findings of imperfection magnitudes are estimated from normalized mode shapes. Combinations of five modes to a specific cross sections can be close to the true geometric cross sections (Figure 7. 51 and Figure 7. 54).

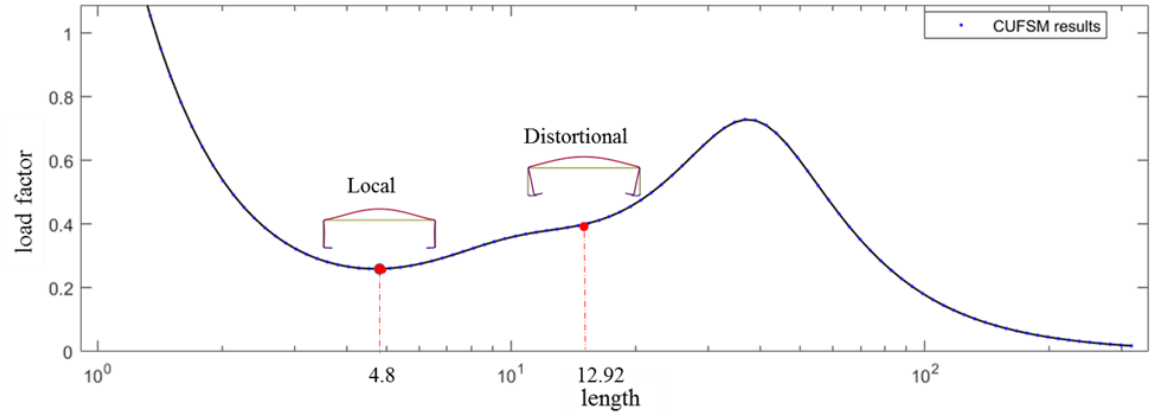

Figure 7. 49 Signature curve of C section (half-wavelength in in., load factor P/P_y)

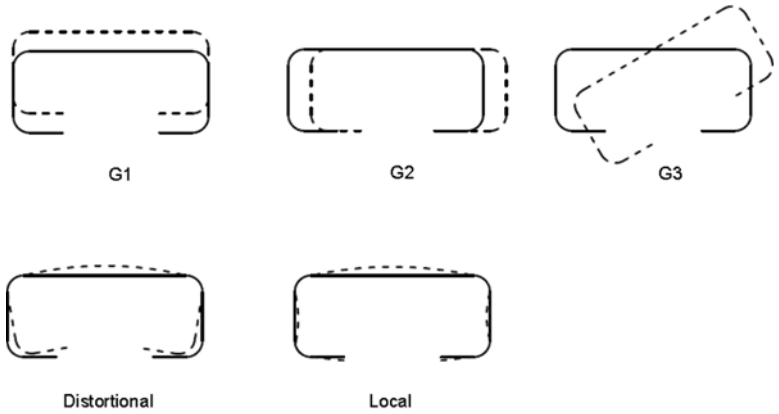

Figure 7. 50 Imperfection characterization for C by MID

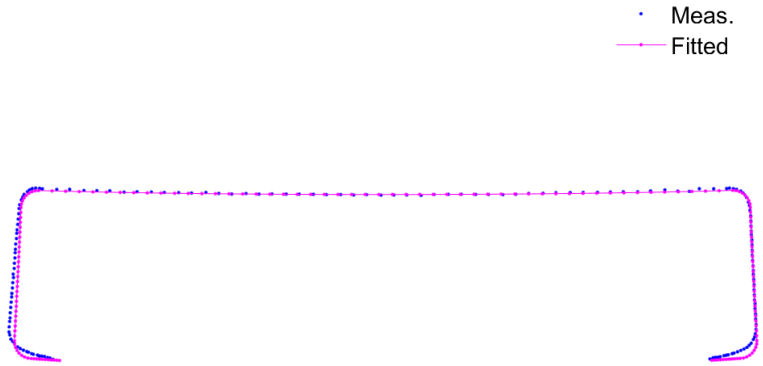

Figure 7. 51 typical fitting cross section of C section from MID

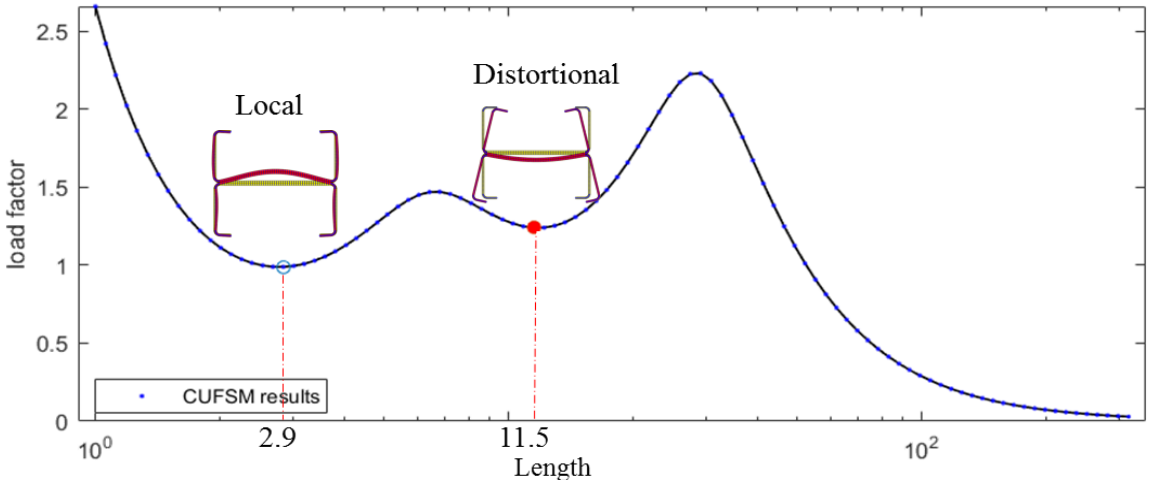

Figure 7. 52 Signature curve of BUC section (half-wavelength in in., load factor P/P_y)

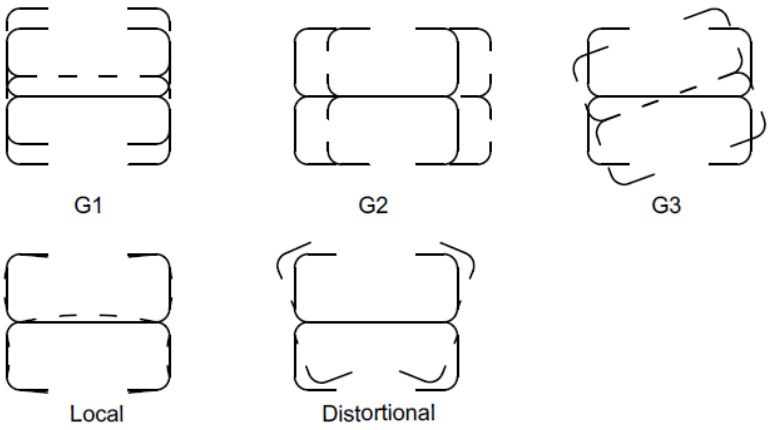

Figure 7. 53 Imperfection characterization for BUC by MID

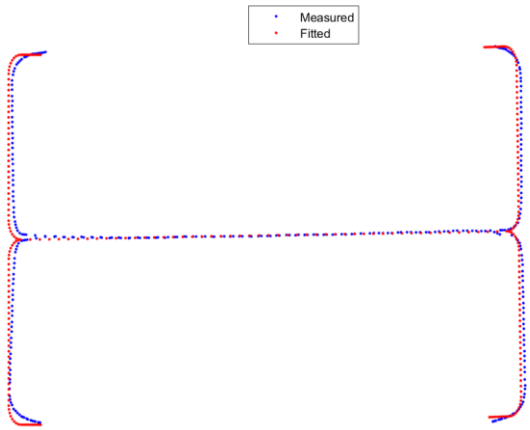

Figure 7. 54 A typical fitting cross section of BUC section from MID

7.2.2 Modal imperfection results

Z

Based on CUFSM analysis, a distinct critical sine half-wavelength for local buckling is 5.1 in. and distortional buckling is 19.4 in. Identified cross-section mode shapes incorporating global imperfections, five mode imperfections of 19 specimens of 700Z225-60 are realized and posted in Figure 7. 55. Cross-sectional imperfections of MID are much smoother and less noisy in comparison with Type 1 and 2 in conventional imperfection characterization. Curves of local and distortional imperfections generally have three half-waves along specimens. Besides, imperfections at both ends fluctuate more strongly as compared with the mid-span. Recalling conventional imperfection results, it is obvious that cross-section imperfections through MID are much smoother and smaller. Regarding the global mode imperfections, even though there are some minor difference due to rounding error or noise (<1%), the magnitudes obtained from both methods are supposed to be identical due to the orthogonal property of global modes imperfections. Therefore, global imperfection results (G1, G2, G3) of MID share same quantities of conventional imperfections.

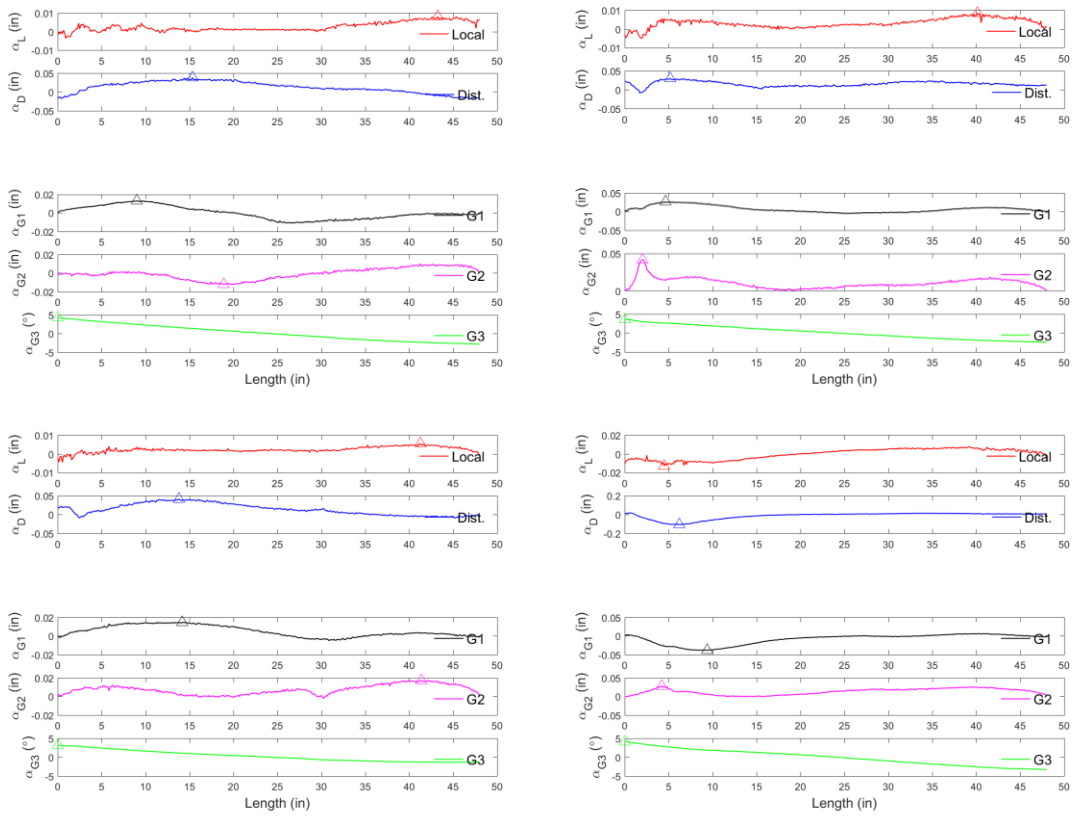

Figure 7. 55 Typical modal imperfections along length of Z sections

C

Five modes of C sections as Z sections are identified per specimen. The following procedures are described in the previous section: two sections, 362S162-68 and 600S137-54, have been modeled in CUFSM. Based on the signature curves from the CUFSM analysis, distinct critical sine half-wavelengths of local buckling are 2.8 in. and 4.8 in., respectively, for the 362S162-68 and 600S137-54; and those for distortional buckling are 12.9 in. and 12.9 in., respectively.

There are 14 specimens of 362S162-54 participating in the modal imperfection decomposition. Compared with the Z sections' results, a half-wave shape shows up in local and distortional imperfections, and imperfections along the length are smoother and smaller, relatively. Bow (G1) and camber (G2) imperfections seem to keep a half sine wave shape over length. In comparison

with the results of conventional imperfection characterization, cross-section imperfections are much smoother, especially for Type 1 distortional imperfections comparisons.

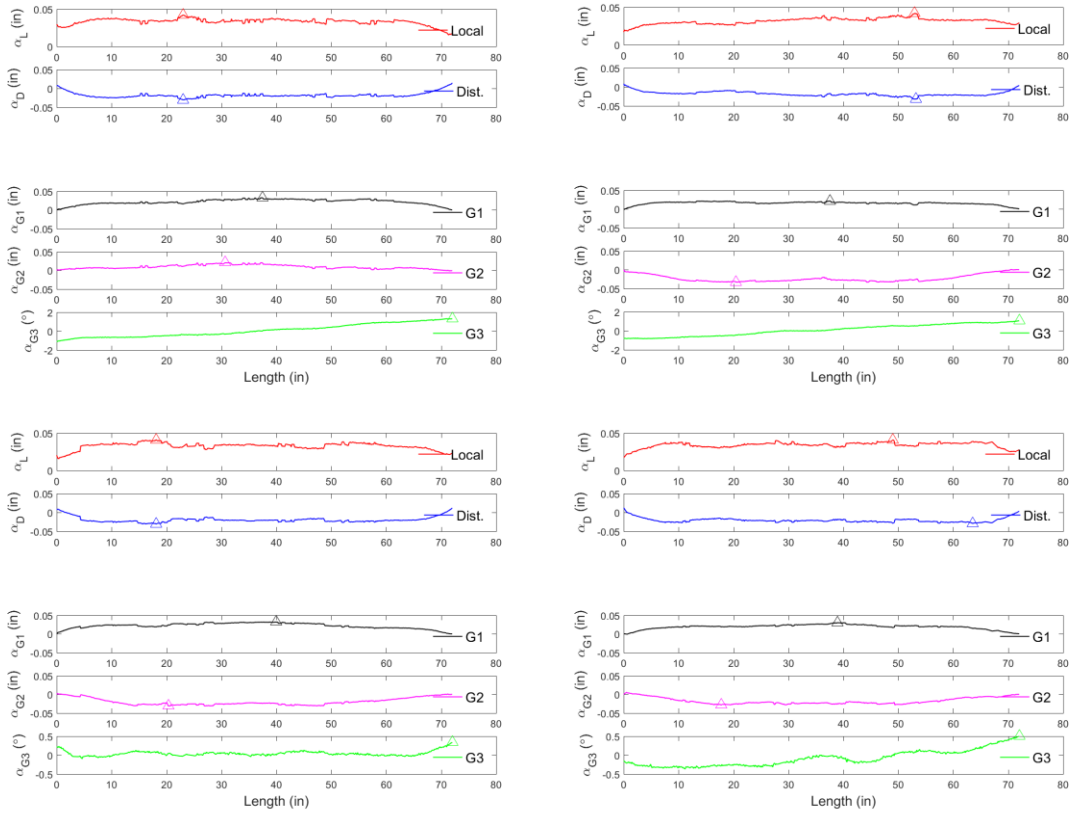

Figure 7. 56 Typical modal imperfections along length of C sections (362S162-68)

On the other hand, 600S137-54 displays different waves in cross-section imperfections. A full sine wave appears along the length. The magnitudes of imperfections are mostly larger than that of 362S162-68 except twist. Besides, camber (G2) imperfections seem a bit noisier compared with 362S162-68 but still much better than results from a conventional imperfections approach.

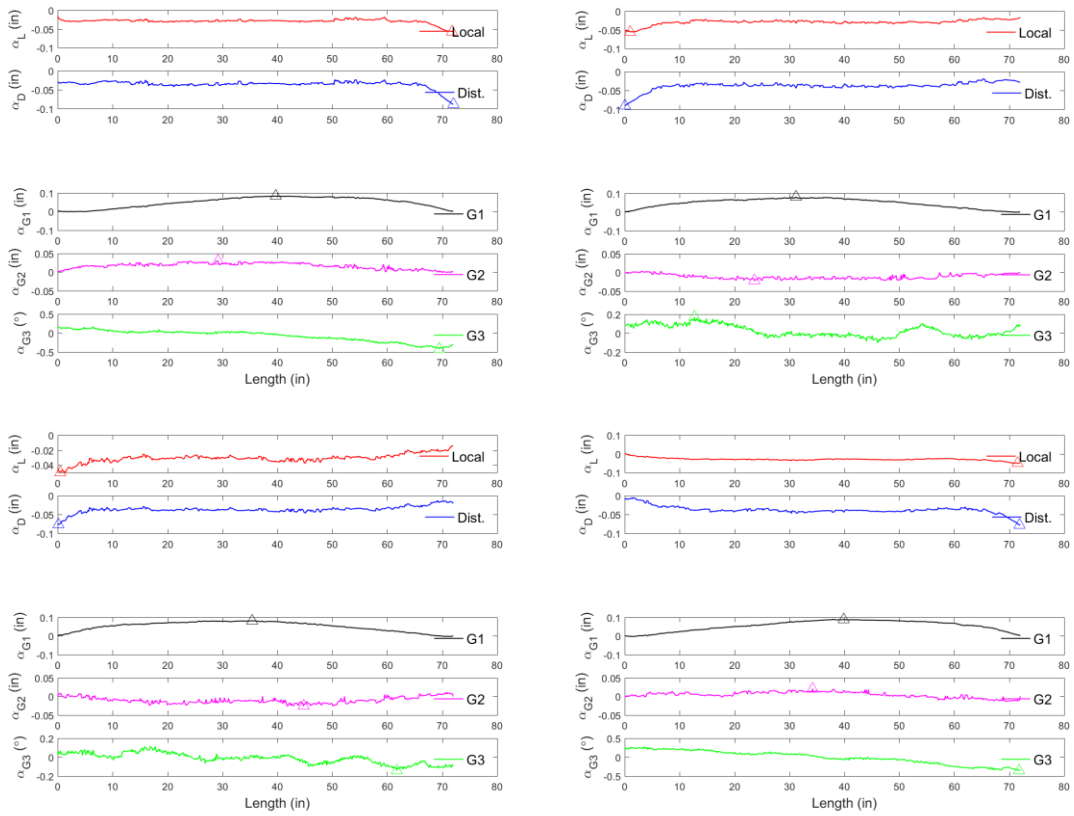

Figure 7. 57 Typical modal imperfections along length of C sections (600S137-54)

BUC

There are restrained specimens of BUC studied in this part, i.e., four 362S162-68 and 600S137-54. Generally speaking, imperfection curves of classified modes are similar to those of C sections. In comparison with results of a conventional imperfection method, fewer quantities are required to identify. There are nine quantities to be surveyed because there are upper and lower sections of BUC members. The results from conventional imperfection methods are polluted and have a lot of noises along the length. While it turns out that imperfections from MID are cleaner with better realization of imperfections along length. It also saves a lot of computation time because it only requires five modes identified.

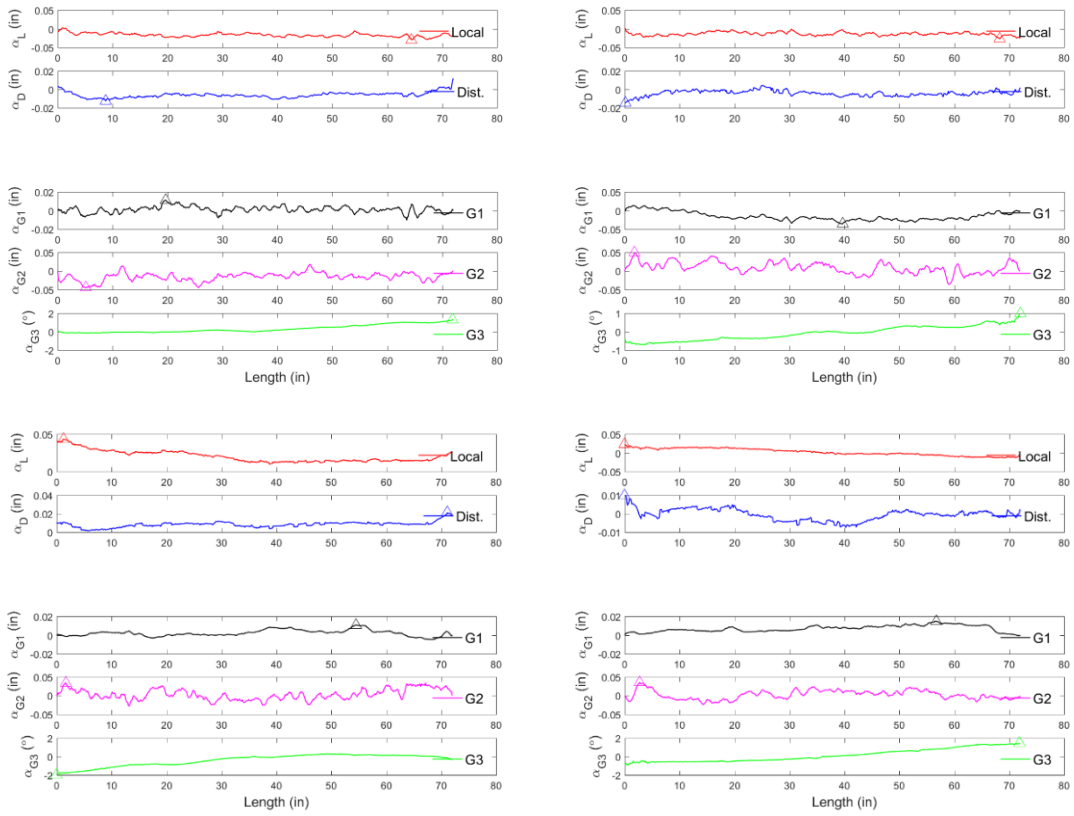

Figure 7. 58 Modal imperfections along length of BUC sections (362S162-68)

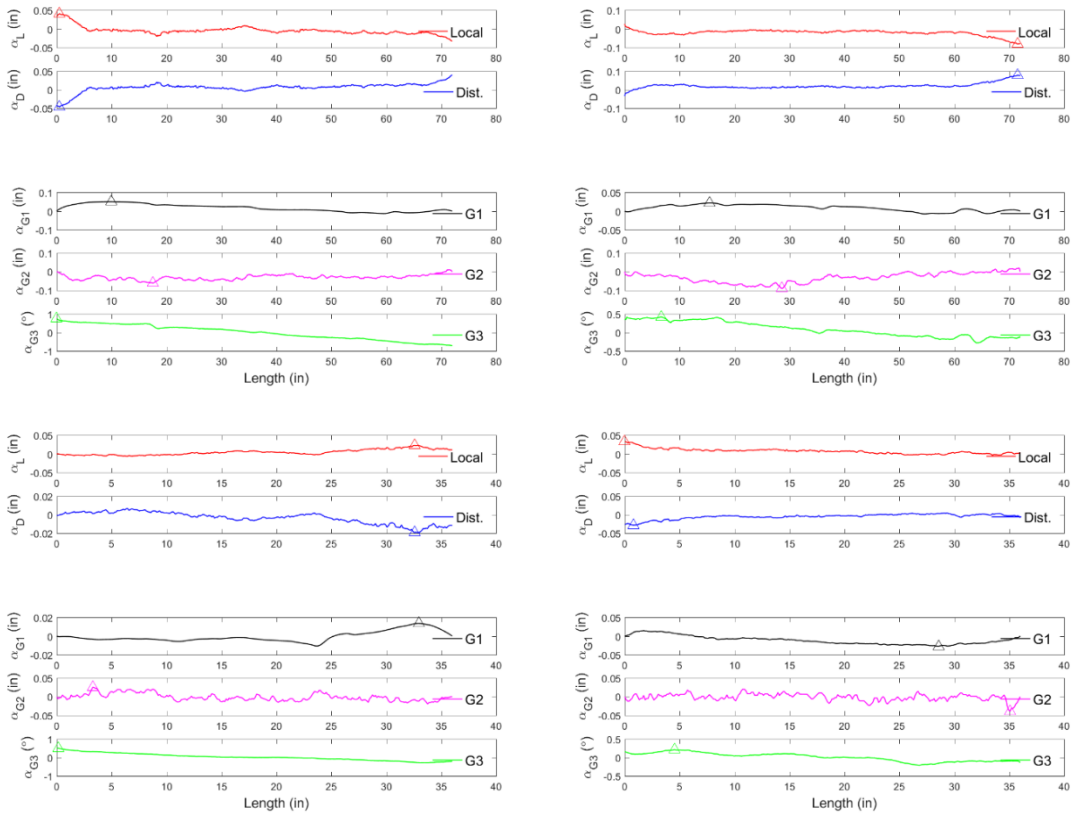

Figure 7. 59 Modal imperfections along length of BUC sections (600S126-54)

7.2.3 Statistical Summary

Z

There are 19 nominally identical 4-feet-long (1219 mm) 700Z225-60 members, which were measured with 373 cross sections per member. A statistical examination of the 7087 α_i magnitudes is provided for this nominally identical case. Histograms of local mode magnitude α_L are provided in Figure 7. 60. The local imperfection magnitude α_L is smaller than the out-of-flatness magnitude (d_1) and presents a less Gaussian-shaped distribution trend. Extrema for the modal imperfection decomposition method provide a fine histogram and approximated CDF.

The ASTM C955 tolerances are for C sections but used here for Z sections as a reference. As noted before, for extreme values in a specimen, the conventional imperfections are an upper bound on

the MID magnitudes for local and distortional and are essentially identical for global G1, G2, and G3.

Table 7. 6 Statistical summary of modal imperfections of Z sections (700Z225-60)

Z	Local[a]	Distortional[b]		G1	G2	G3
700S225-48	d_{local}/t	$d_{dist.}/t$		L/δ	L/δ	°/ft
25%	0.14	0.39		3901	3585	1.83
50%	0.17	0.50		3557	2815	2.07
75%	0.23	0.57		2755	2606	2.25
95%	0.34	0.68		1245	961	2.45
99%	0.34	1.77		1245	961	2.71
mean	0.19	0.55		3465	3087	2.06
Std. Dev.	0.07	0.32		1183	1170	0.33
Zeinoddini 50%[c]	0.31	0.75	0.75	2909	4010	0.09
c955[d]	1.04	1.04	1.04	960	960	0.51

Note:

a. Local imperfections for modal imperfections correlate to Type 1/crown imperfections.

b. Distortional imperfections for modal imperfections correlate to Type 2/ over-bend or flare imperfections.

c. Measured values can be referred to in Zeinoddini (2011).

d. Reference tolerances from ASTM (2015) for C sections: G1 (bow) and G2 (camber) are L/960; G3 is 1/32 in./ft of a specimen, in addition for d_1 (crown) = 1/16 in., and d_2 (flare) = 1/16 in., conventional C tolerances are reported here as similar tolerances for Z as well as modal imperfections do not exist.

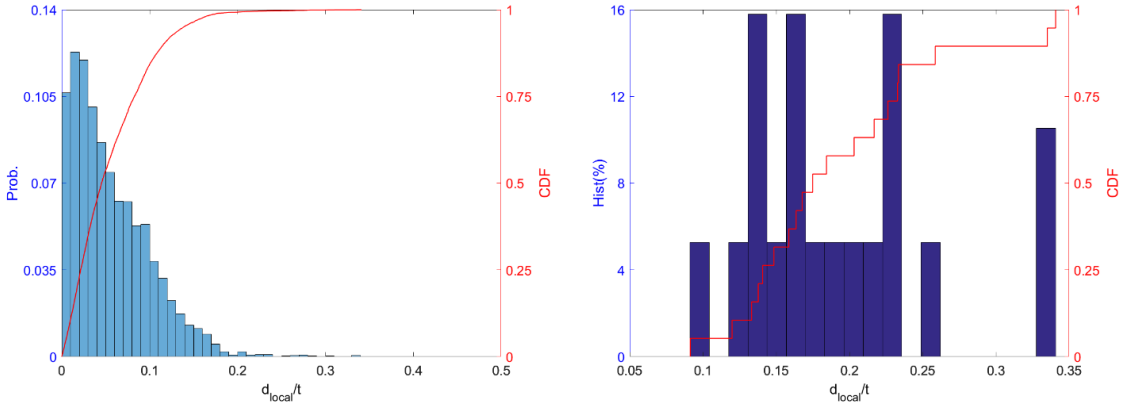

Figure 7. 60 Typical statistical summary of local imperfection of Z sections (700Z225-48): (a) imperfections along length; (b) maximum imperfection per section

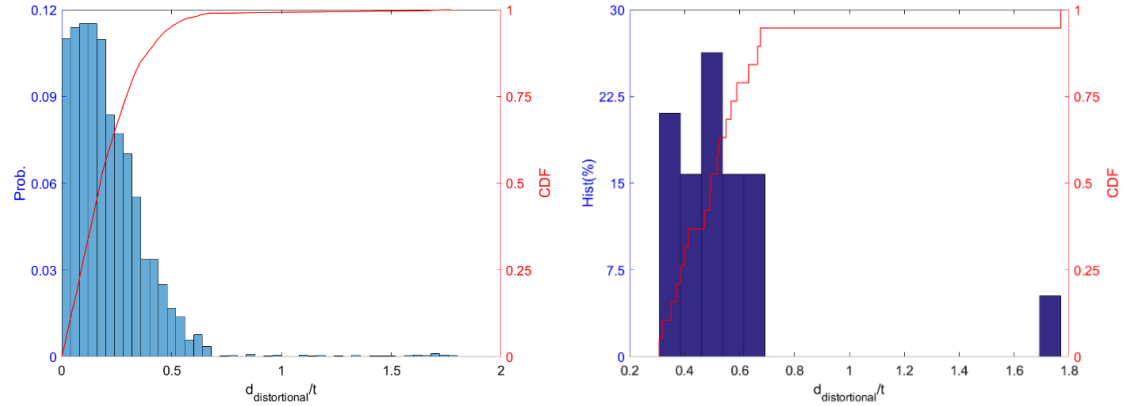

Figure 7. 61 Typical statistical summary of distortional imperfection of Z sections (700Z225-48): (a) imperfections along length; (b) maximum imperfection per section

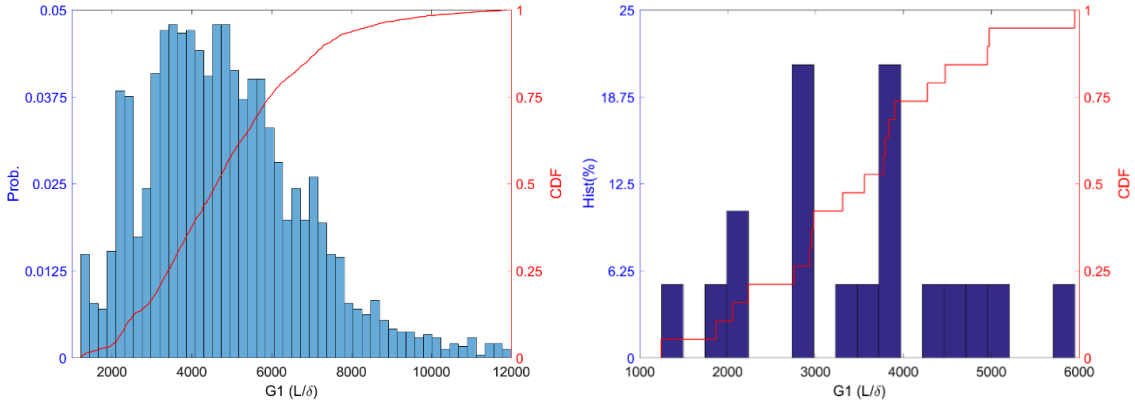

Figure 7. 62 Typical statistical summary of bow (G1) of Z sections (700Z225-48): (a) imperfections along length; (b) maximum imperfection per section

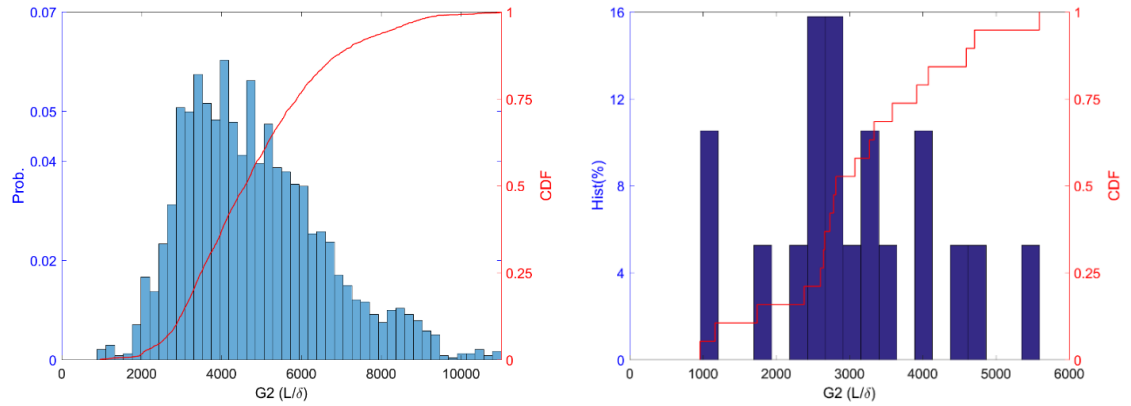

Figure 7. 63 Typical statistical summary of camber (G2) of Z sections (700Z225-48): (a) imperfections along length; (b) maximum imperfection per section

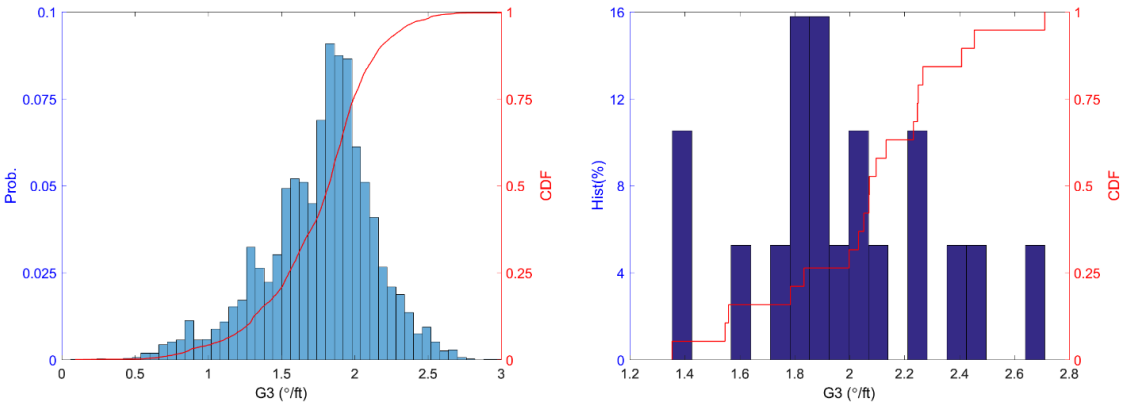

Figure 7. 64 Typical statistical summary of twist (G3) of Z sections (700Z225-48): (a) imperfections along length; (b) maximum imperfection per section

C

As previously mentioned, cross-section imperfections from MID are generally smaller than the conventional imperfection method. The local imperfection of 362S162-68 shows better Gaussian-shape distribution compared with conventional imperfection method. It has a longer tail on the left side of distribution. The median of 362S162-68, as shown in Table 7. 7, is larger than Zeinoddini's median value. However, both local and distortional imperfections stay within ASTM c955 tolerance.

Table 7. 7 Statistical summary of modal imperfections of C sections (362S162-68)

C	Local[a]	Distortional[b]		G1	G2	G3
362S162-68	d_{local}/t	$d_{dist.}/t$		L/δ	L/δ	°/ft
25%	0.56	0.40		2988	2687	0.23
50%	0.58	0.43		2271	2497	0.31
75%	0.59	0.43		2162	2160	0.44
95%	0.61	0.45		1969	1169	0.57
99%	0.63	0.61		1969	1169	0.61
mean	0.58	0.43		2547	2482	0.36
Std. Dev.	0.03	0.06		458	646	0.15
Zeinoddini 50%[c]	0.31	0.75	0.75	2909	4010	0.09
c955[d]	0.92	0.92	0.92	960	960	0.99

Notes:

a. Local imperfections for modal imperfections correlate to Type 1/crown imperfections.

b. Distortional imperfections for modal imperfections correlate to Type 2/ over-bend or flare imperfections.

c. Measured values can be referred to in Zeinoddini (2011).

d. Reference tolerances from ASTM (2015) for C sections: G1 (bow) and G2 (camber) are L/960; G3 is 1/32 in./ft of a specimen, in addition for d_1 (crown) = 1/16 in., and d_2 (flare) = 1/16 in., conventional C tolerances are reported here as similar tolerances for modal imperfections do not exist.

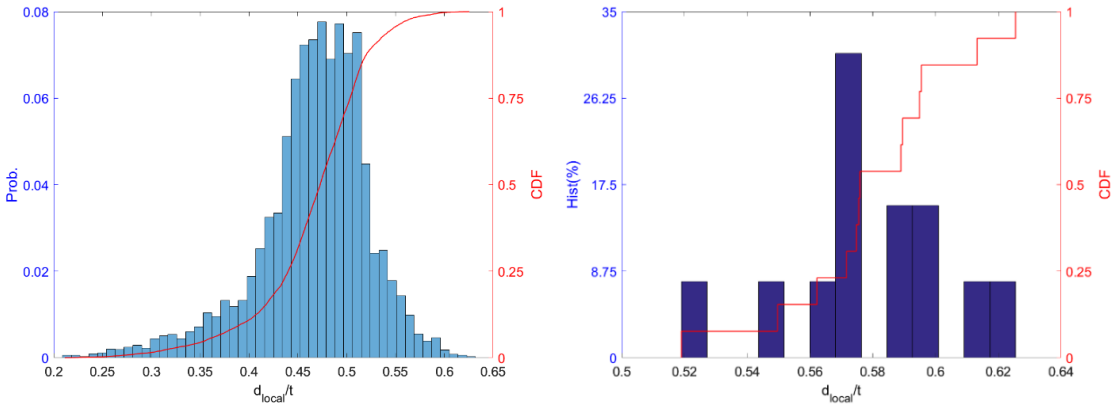

Figure 7. 65 Typical statistical summary of local imperfection of C sections (362S162-68): (a) imperfections along length; (b) maximum imperfection per section

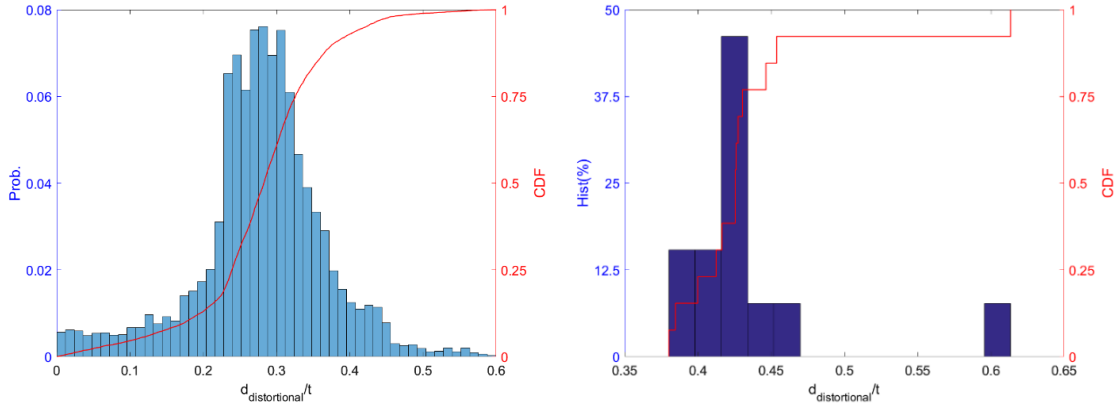

Figure 7. 66 Typical statistical summary of distortional imperfection of C sections (362S162-68): (a) imperfections along length; (b) maximum imperfection per section

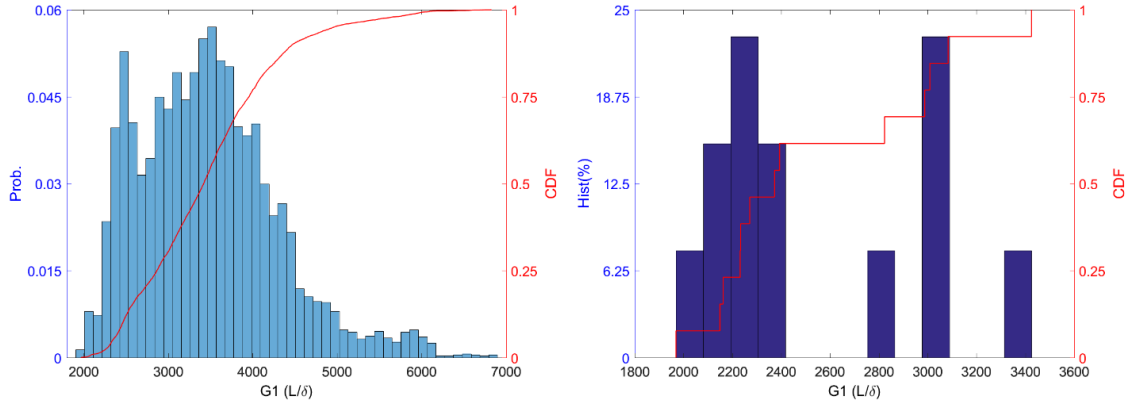

Figure 7. 67 Typical statistical summary of bow (G1) of C sections (362S162-68): (a) imperfections along length; (b) maximum imperfection per section

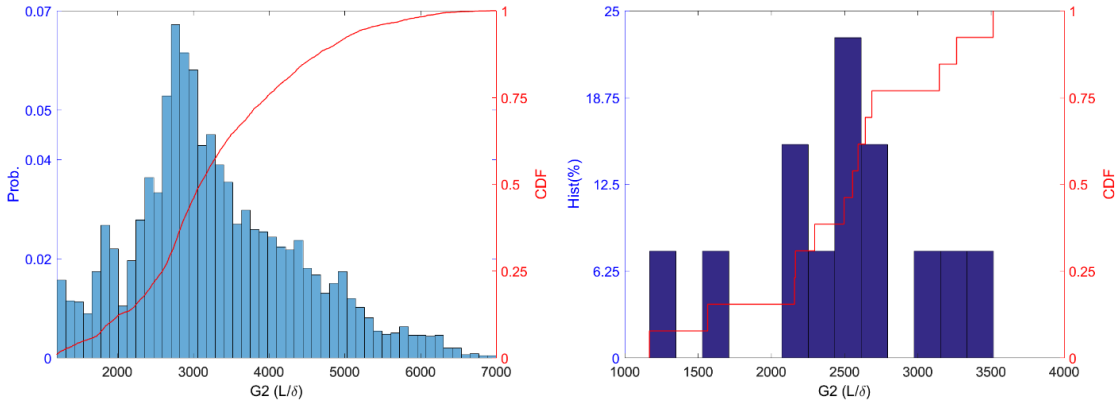

Figure 7. 68 Typical statistical summary of camber (G2) of C sections (362S162-68): (a) imperfections along length; (b) maximum imperfection per section

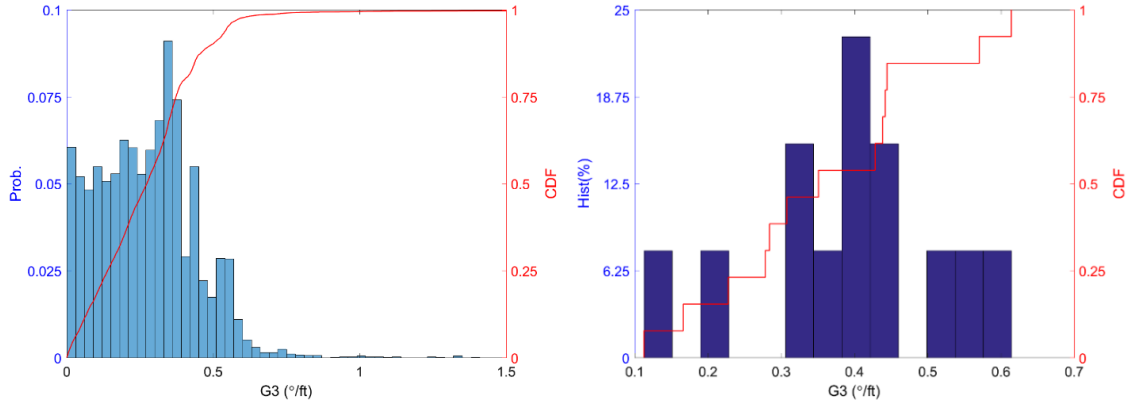

Figure 7. 69 Typical statistical summary of twist (G3) of C sections (362S162-68): (a) imperfections along length; (b) maximum imperfection per section

A similar conclusion can be compared with the results of the modal imperfection method in comparison with the conventional imperfection method. 600S137-54 has much larger median values in cross-section imperfection, especially in distortional imperfection compared with 362S162-68. However, in comparison with the conventional imperfection method, magnitudes of local and distortional imperfection are much smaller, even though distortional imperfections are still larger than ASTM c955 tolerance.

Table 7. 8 Statistical summary of modal imperfections of 600S137-54

C	Local[a]	Distortional[b]		G1	G2	G3
600S137-54	d_{local}/t	$d_{dist.}/t$		L/δ	L/δ	°/ft
25%	0.90	1.37		882	2422	0.07
50%	0.95	1.45		863	2239	0.09
75%	0.98	1.54		835	2024	0.11
95%	1.02	1.60		817	1543	0.14
99%	1.04	1.73		817	1543	0.15
mean	0.95	1.47		879	2394	0.09
Std. Dev.	0.05	0.12		70	577	0.03
Zeinoddini 50%[c]	0.31	0.75	0.75	2909	4010	0.09
c955[d]	1.15	1.15	1.15	960	960	0.60

Notes:

a. Local imperfections for modal imperfections correlate to Type 1/crown imperfections.

b. Distortional imperfections for modal imperfections correlate to Type 2/ over-bend or flare imperfections.

c. Measured values can be referred to in Zeinoddini (2011).

d. Reference tolerances from ASTM (2015) for C sections: G1 (bow) and G2 (camber) are L/960; G3 is 1/32 in./ft of a specimen, in addition for d_1 (crown) = 1/16 in., and d_2 (flare) = 1/16 in., conventional C tolerances are reported here as similar tolerances for modal imperfections do not exist.

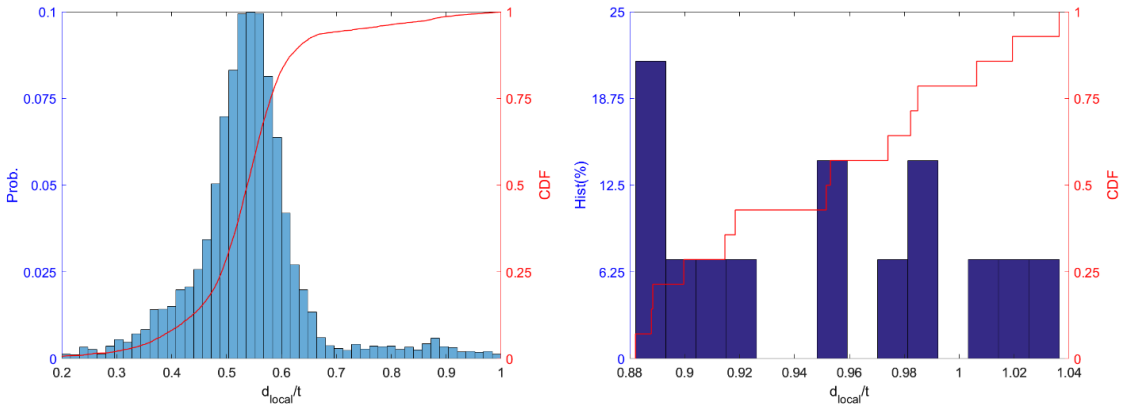

Figure 7. 70 Typical statistical summary of local imperfection of C sections (600S137-54): (a) imperfections along length; (b) maximum imperfection per section

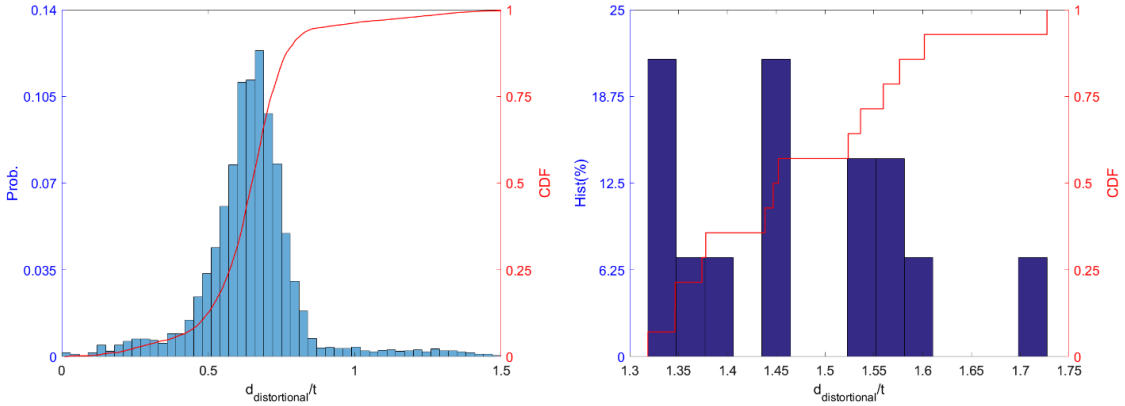

Figure 7. 71 Typical statistical summary of distortional imperfection of C sections (600S137-54): (a) imperfections along length; (b) maximum imperfection per section

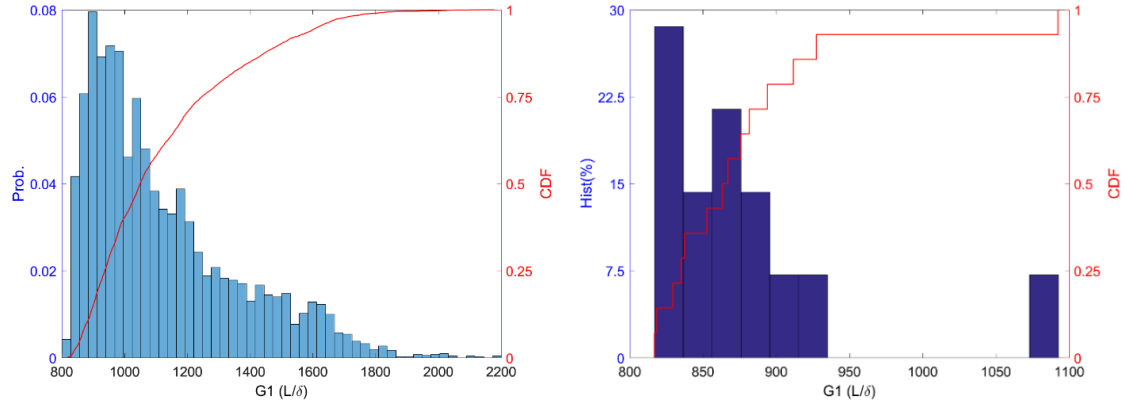

Figure 7. 72 Typical statistical summary of bow (G1) of C sections (600S137-54): (a) imperfections along length; (b) maximum imperfection per section

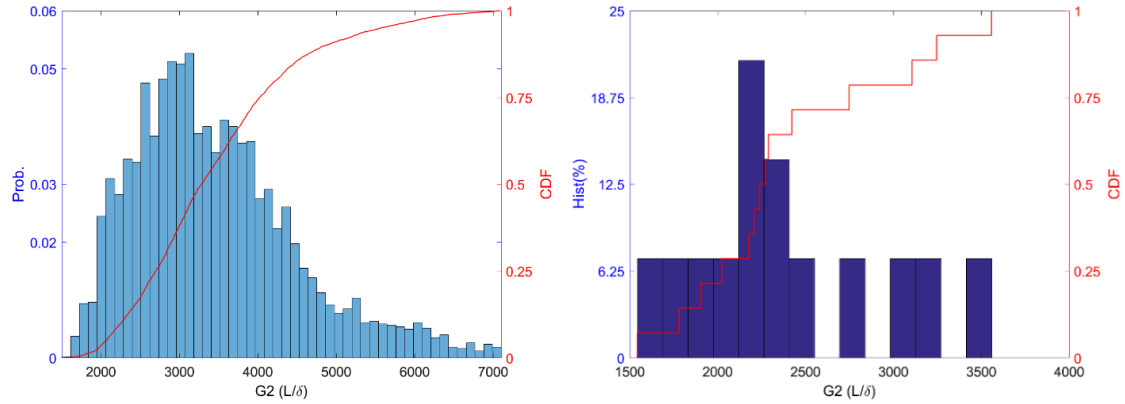

Figure 7. 73 Typical statistical summary of camber (G2) of C sections (600S137-54): (a) imperfections along length; (b) maximum imperfection per section

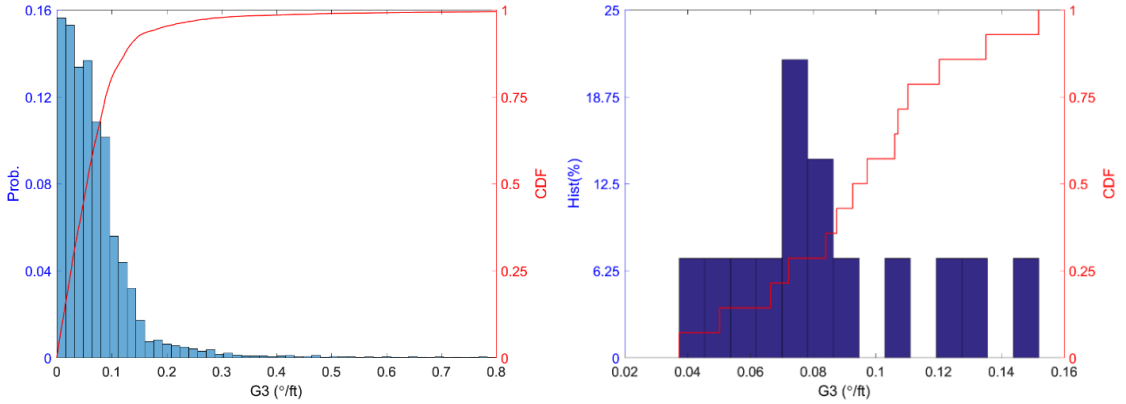

Figure 7. 74 Typical statistical summary of twist (G3) of C sections (600S137-54): (a) imperfections along length; (b) maximum imperfection per section

BUC

Compared with C sections, BUC sections have much smaller local imperfections. The median value of local imperfections is similar to Zeinoddini's result, and it is one-fourth of the conventional imperfection method. Distortional imperfections of 362S162-68, on the other hand, are one-third of the C sections and one-fifth of conventional imperfection method.

Table 7. 9 Statistical summary of modal imperfections of BUC sections (362S162-68)

BUC	Local[a]	Distortional[b]		G1	G2	G3
362S162-68	d_{local}/t	$d_{dist.}/t$		L/δ	L/δ	°/ft
25%	0.32	0.14		6448	2032	0.33
50%	0.34	0.16		4847	1609	0.44
75%	0.34	0.18		2007	1476	0.48
95%	0.66	0.20		2007	1476	0.66
99%	0.66	0.20		2007	1476	0.66
mean	0.32	0.14		4990	1805	0.48
Std. Dev.	0.34	0.16		2147	309	0.14
Zeinoddini 50%[c]	0.31	0.75	0.75	2909	4010	0.09
c955[d]	0.92	0.92	0.92	960	960	0.99

Note:

a. Local imperfections for modal imperfections correlate to Type 1/crown imperfections.

b. Distortional imperfections for modal imperfections correlate to Type 2/ over-bend or flare imperfections.

c. Measured values can be referred to in Zeinoddini (2011).

d. Reference tolerances from ASTM (2015) for C sections: G1 (bow) and G2 (camber) are L/960; G3 is 1/32 in./ft of a specimen, in addition for d_1 (crown) = 1/16 in., and d_2 (flare) = 1/16 in., conventional C tolerances are reported here as similar tolerances for BUC as well as modal imperfections do not exist.

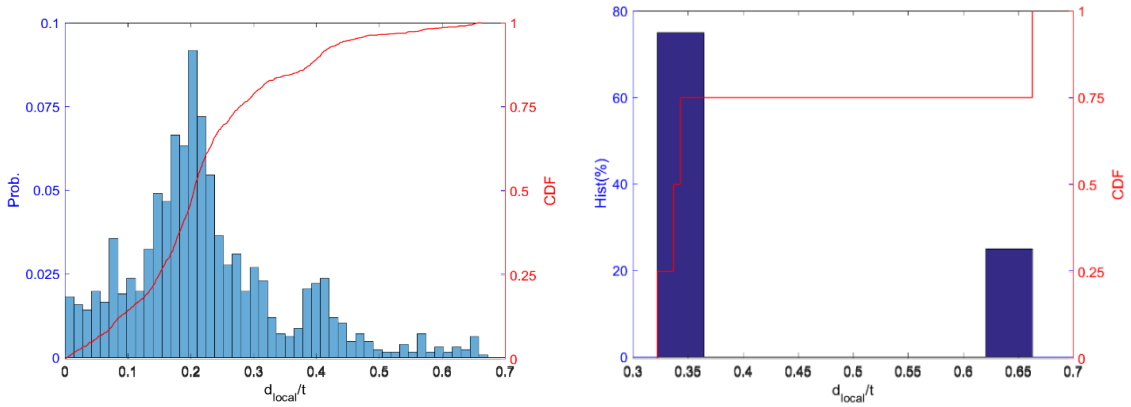

Figure 7. 75 Typical statistical summary of local imperfection of BUC sections (362S162-68): (a) imperfections along length; (b) maximum imperfection per section

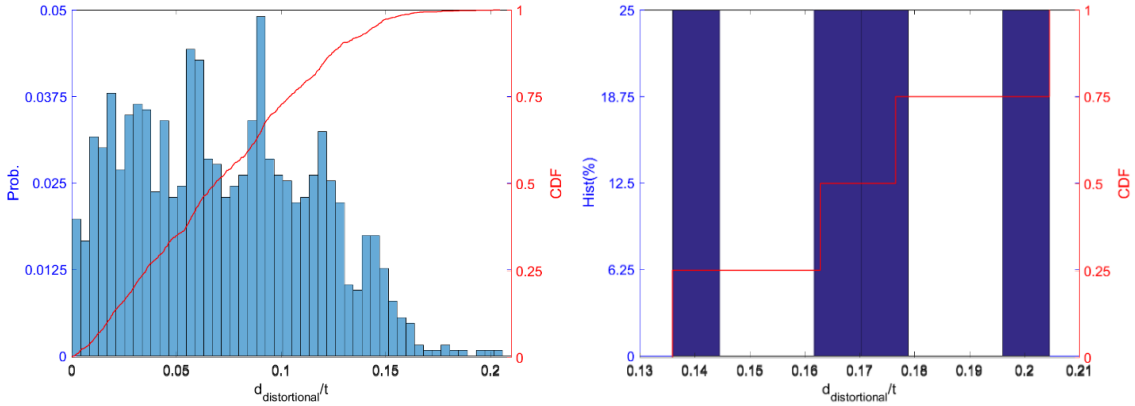

Figure 7. 76 Typical statistical summary of distortional imperfection of BUC sections (362S162-68): (a) imperfections along length; (b) maximum imperfection per section

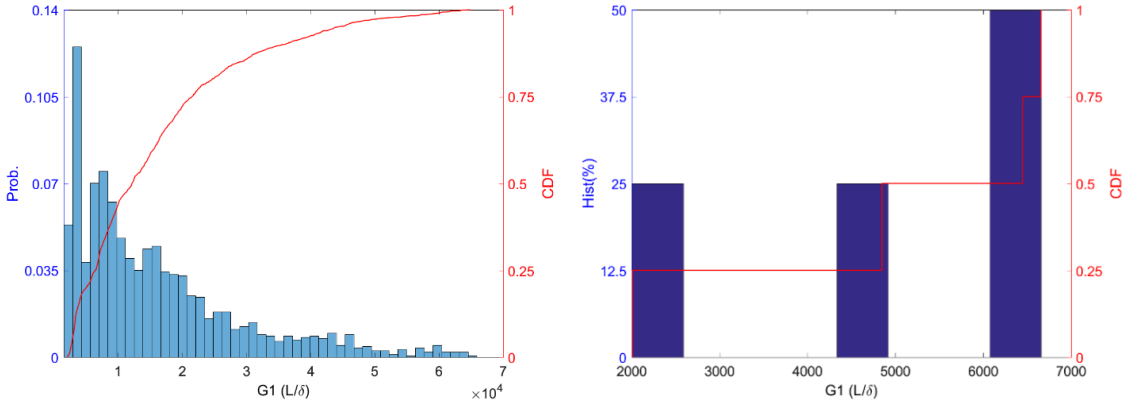

Figure 7. 77 Typical statistical summary of bow (G1) imperfection of BUC sections (362S162-68): (a) imperfections along length; (b) maximum imperfection per section

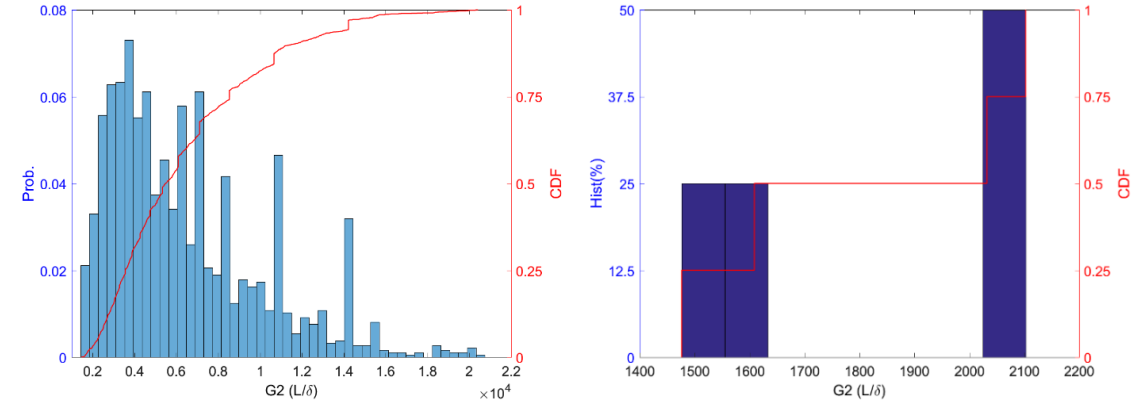

Figure 7. 78 Typical statistical summary of camber (G2) imperfection of BUC sections (362S162-68): (a) imperfections along length; (b) maximum imperfection per section

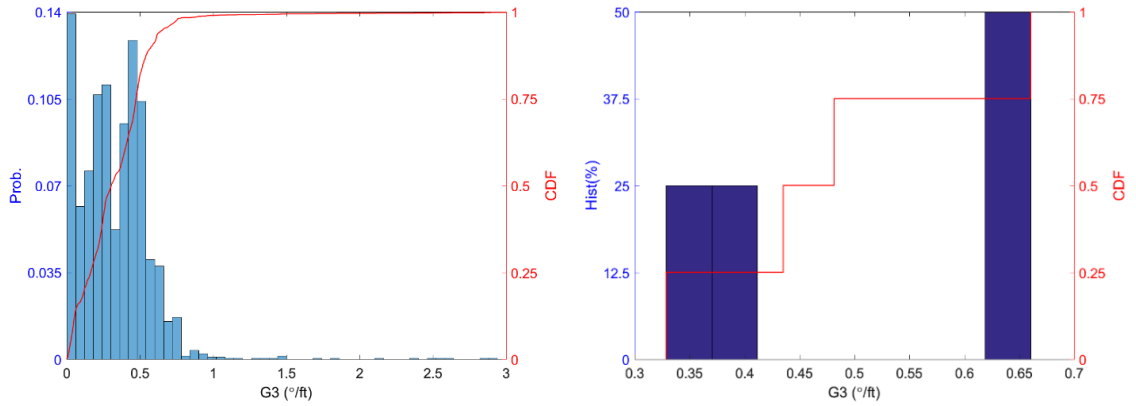

Figure 7. 79 Typical statistical summary of twist (G3) imperfection of BUC sections (362S162-68): (a) imperfections along length; (b) maximum imperfection per section

It is surprising that the median value of modal imperfections of 600S137-54 is larger than one Type 1 imperfection via conventional method. Potential reasons attribute to sample size and large cross-section shapes. BUC members generally contain upper and lower cross sections. Local imperfection realization therefore may not be accurately estimated in comparison with Z and C sections. Besides, distortional imperfections do not differ too much from those of conventional imperfections compared with situations in the Z and C sections. General imperfections of both 600S137-54 and 362S162-68 for all five identified modes have long tails on the right side of the distributions, which have very different statistical performance in comparison with other two type of sections. More samples should be included in BUC members for better statistical analysis in future.

Table 7. 10 Statistical summary of modal imperfections of BUC sections (600S137-54)

BUC	Local	Distortional		G1	G2	G3
600S137-54	d_{local}/t	$d_{dist.}/t$		L/δ	L/δ	°/ft
25%	0.40	0.34		2646	1181	0.17
50%	0.58	0.50		1438	922	0.19
75%	0.72	0.82		1322	803	0.25
95%	1.43	1.39		1322	803	0.34
99%	1.43	1.39		1322	803	0.34
mean	0.78	0.76		2172	1079	0.24
Std. Dev.	0.45	0.46		952	272	0.08
Zeinoddini 50%	0.31	0.75	0.75	2909	4010	0.09
c955	1.15	1.15	1.15	960	960	0.60

Note:

a. Local imperfections for modal imperfections correlate to Type 1/crown imperfections.

b. Distortional imperfections for modal imperfections correlate to Type 2/ over-bend or flare imperfections.

c. Measured values can be referred to in Zeinoddini (2011).

d. Reference tolerances from ASTM (2015) for C sections: G1 (bow) and G2 (camber) are L/960; G3 is 1/32 in./ft of a specimen, in addition for d_1 (crown) = 1/16 in., and d_2 (flare) = 1/16 in., conventional C tolerances are reported here as similar tolerances for BUC as well as modal imperfections do not exist.

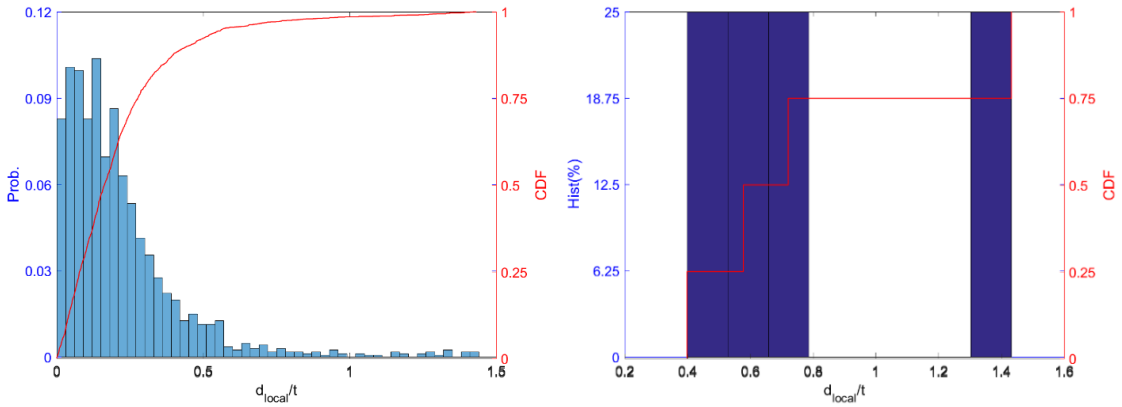

Figure 7. 80 Typical statistical summary of local imperfection of BUC sections (600S137-54): (a) imperfections along length; (b) maximum imperfection per section

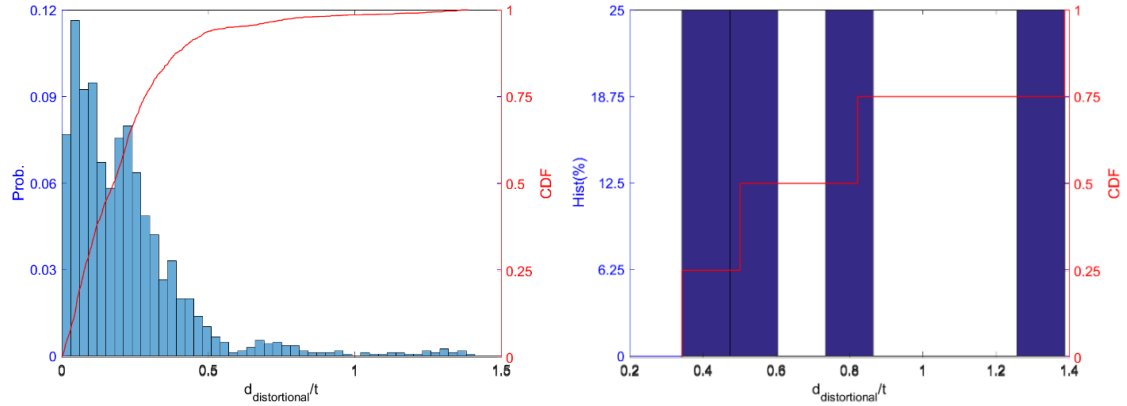

Figure 7. 81 Typical statistical summary of distortional imperfection of BUC sections (600S137-54): (a) imperfections along length; (b) maximum imperfection per section

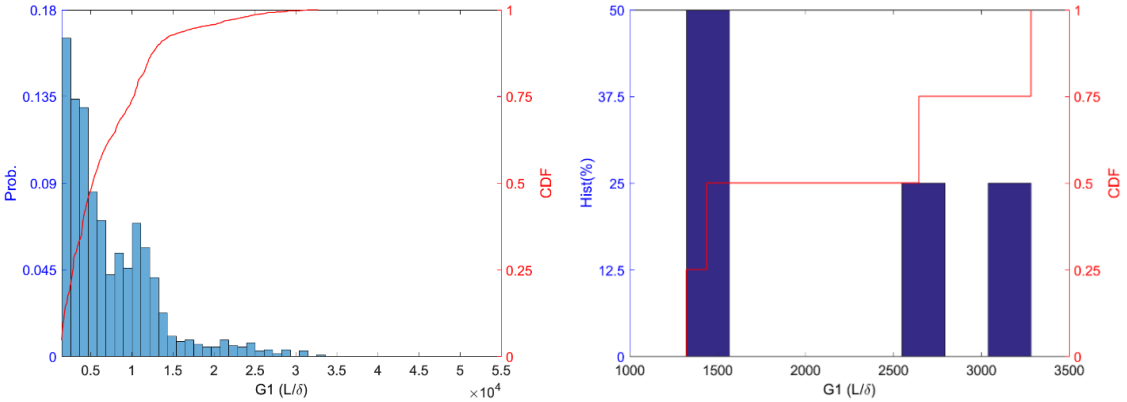

Figure 7. 82 Typical statistical summary of bow (G1) imperfection of BUC sections (600S137-54): (a) imperfections along length; (b) maximum imperfection per section

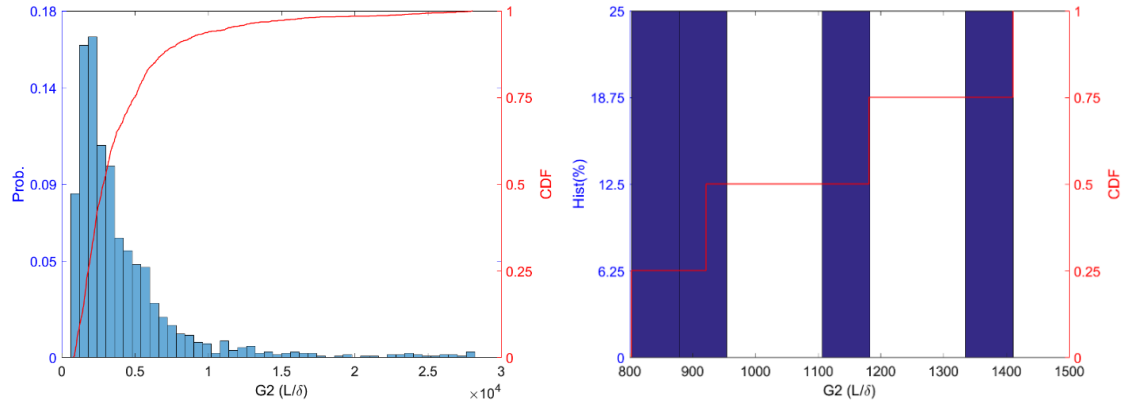

Figure 7. 83 Typical statistical summary of camber (G2) imperfection of BUC sections (600S137-54): (a) imperfections along length; (b) maximum imperfection per section

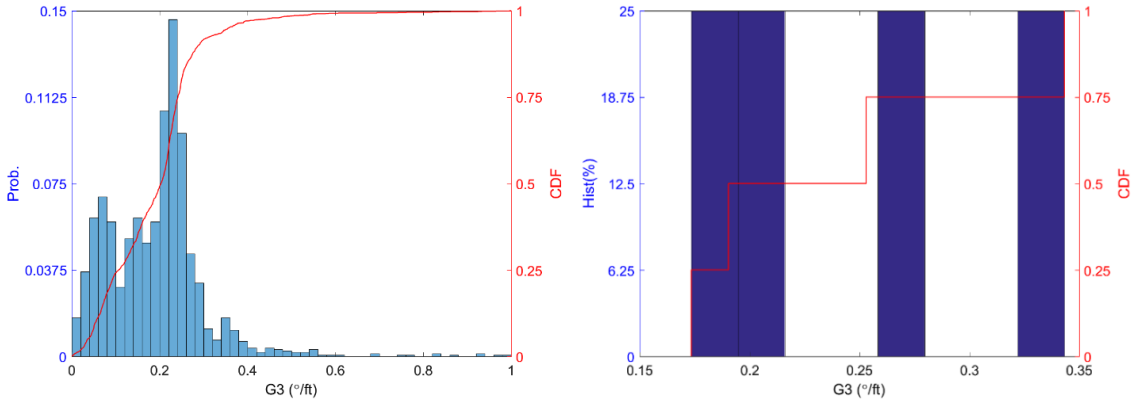

Figure 7. 84 Typical statistical summary of twist (G3) imperfection of BUC sections (600S137-54): (a) imperfections along length; (b) maximum imperfection per section

7.3 Discussions

Note that fitting shapes from a five-mode combination cannot perfectly match the measured cross section. True geometry contains more sinusoidal components of imperfections other than the five corresponding sinusoids of failure modes. Small deviations, such as lip imperfections, may not be comprised in these five mode shapes. These deviations eventually generate errors in the cross-section fitting. While the fitting errors should not affect imperfection sensitivity of the simulation because those five modes are most critical. Five modes of imperfections correlate to the five first-mode buckling shapes, which bear the lowest buckling loads in comparison with higher-mode buckling.

Besides, imperfections estimated from MID are much smaller than those from conventional imperfection characterizations. Two attributes may lead to this situation: (1) conventional imperfection characterizations may include imperfections other than corresponding five modal imperfections; (2) MID imperfections can dismiss noises from measurements especially to cross-sectional imperfections.

Imperfections from both MID and conventional method disagree with Zeinoddini's data (Zeinoddini 2011). This may come from large quantities of measured specimens but sparse data per section from manual measurements.

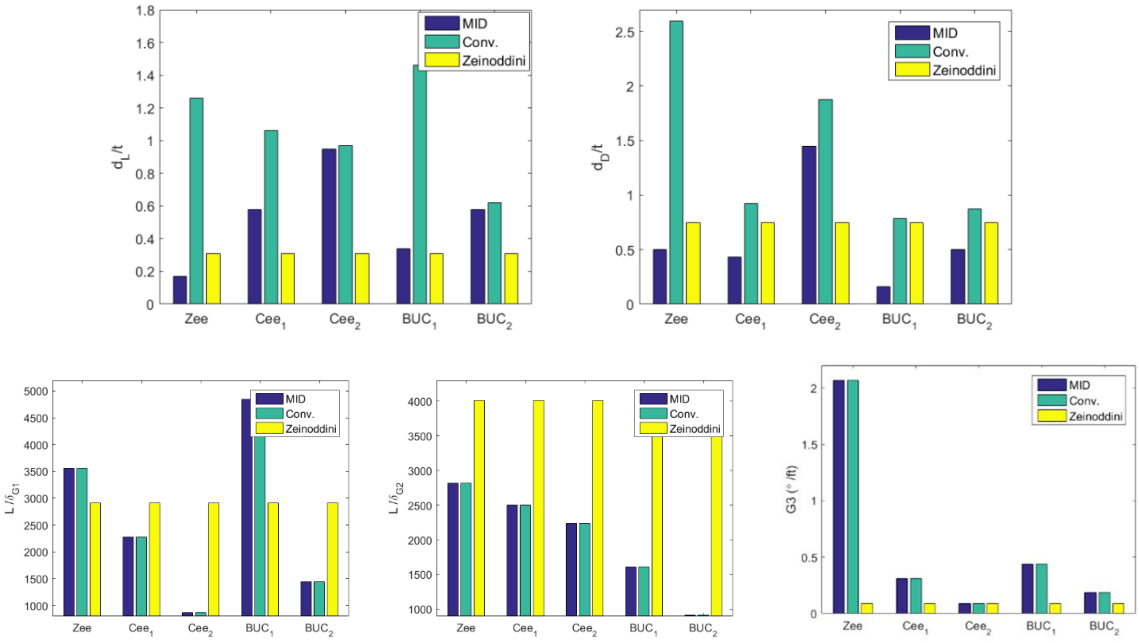

Figure 7. 85 Comparisons between conventional imperfection characteristics and MID

7.4 Conclusions

The strength and response of cold-formed steel members is sensitive to geometric imperfections. A new laser scanner-based imperfection measurement rig created by the authors allows for reasonably high-throughput and high-accuracy 3D point clouds of member geometry. With some care take in post-processing this data may be converted to operational 3D models and the imperfections characterized. Twenty-eight C sections consisting of two nominal geometries and nineteen Z sections consisting of a single nominal geometry were processed to examine their imperfection content. Two processing methods were employed: conventional and modal imperfection decomposition (MID). The conventional method uses plate out-of-flatness (d_1), plate out-of-straightness (d_2), and member bow, camber, and twist while the MID method uses local and distortional modes, as well as global modes of minor-axis flexure, major-axis flexure, and torsion.

Given the fidelity of the measurements the imperfections are examined along the member length as well as for extrema (largest magnitude in a given specimen). Considering extrema, the conventional method is shown to provide an upper bound imperfection approximation compared with MID. Besides, imperfections from MID are reused to fit the true-geometry cross sections. Obvious errors can be observed on lip deviations since characterized imperfections do not contain lip deviations' information. Future work should pay attention on lip deviations where many failures of experimented members start. Results from MID imperfections are further explored in the Chapter 8 where Fourier transformation is applied to imperfections from MID. It provides another perspective to geometric imperfections of cold-formed steel members as well as simulations.

Chapter 8 Imperfection fields: 1D Spectral Representation

8.1 Concept of 1D spectral representation

As discussed in chapter 7, traditional imperfection representation assumes that a corresponding class of imperfections can relate to only one sinusoidal component longitudinally. For example, a global imperfection, bow (G1), may be represented by a half sinusoidal wave, the length and magnitudes of which are its overall length of the specimen and the statistical values of the maxima of the classified imperfections per specimen. This representation of imperfections may not be adequate for cross-section deviations and other global imperfections, such as camber and twist (Zeinoddin, 2011). In chapter 7, it was observed that classified imperfections may contain waves of different frequencies along its length, Z sections for example. There should be a way that can correlate imperfections with multiple sinusoidal components along the length.

Inspired from this idea, 1D spectral representation of imperfection are introduced by Zeinoddini and Schafer (2012), method of which successfully have multiple sinusoidal components representing classified imperfections. Fourier transformation is employed to a specimen's imperfections characterized by modal imperfection decomposition (MID).

$$\alpha_i(y) \overset{FFT}{\leftrightarrow} \chi(f) \qquad \text{Eq 8. 1}$$

Instead of using regular frequency, the frequency axis (x axis) adopt reciprocals of half-wave lengths as its representation as shown in Figure 8. 1. The frequencies can be calculated as following where n is the corresponding number order of transformed point, and L is the overall length of specimen.

$$f = \frac{n}{L} \qquad \text{Eq 8. 2}$$

The magnitudes of Fourier-transformed imperfections are taken from their absolute values, while phase contents are not considered in this chapter. One pre-step is required before Fourier transformation is conducted, i.e., imperfections from measurements must be complemented with their asymmetry by considering that longitudinal imperfections use half sine-wave as their unit. Thus, the magnitudes of the Fourier transformations can be calculated as follows:

$$Mag(f) = \frac{|\chi(f)|}{N} \qquad \text{Eq 8. 3}$$

where N is the total number of points in the complete data from above step.

In this work, a simple assumption was made that is different from previous research, i.e., the twist (G3) of a specimen should be represented by a cosine wave instead of a sine wave. This assumption is generated from the observations in Chapter 7 for both the decomposition of modal imperfections and the conventional approaches for characterizing imperfections, which, in turn, mirror symmetrical twist imperfections along a specimen, as shown in Figure 8. 2. The imperfections at mid-span length always offset to zero, and, thus, a cosine wave fits the twist for a full-length Fourier-transformation wave quite well. The Fourier-transformation procedure of twist is exactly the same as other classified imperfections (Eq 8. 2 and Eq 8. 3).

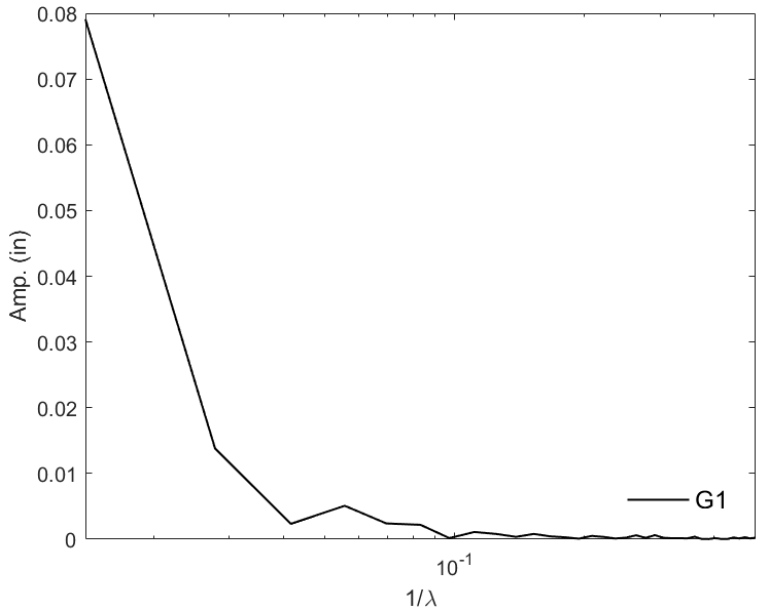

Figure 8. 1 Example mode imperfection in frequency domain (λ in in.)

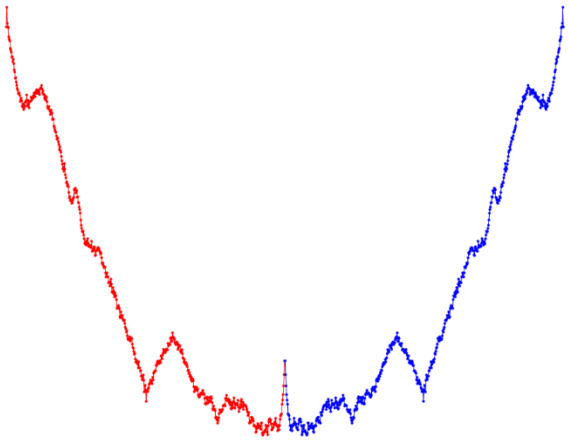

Figure 8. 2 Complement of imperfections for Fourier Transformations

8.2 Results of 1D spectral representation

As in chapter 7, Three different shapes of specimens are studied in this chapter, i.e., Z, C, and BUC sections. In this chapter, 19 700Z225-60 of Z, 14 362S162-68 and 14 600S137-54 of C, and 4 362S162-68 and 4 600S137-54 of BUC sections are studied and the corresponding manufactured

and measured dimensions are shown in chapters 5 and 6. A single member's Fourier transformation, i.e., 1D spectral realization, is presented for better understanding of the energy distributions of imperfections in the frequency domain. First, Z sections are presented, and that is followed by C sections and BUC members.

8.2.1 1D spectral representation of a single specimen

By following the procedures described in Section 8.1, 1D spectral characterizations that correspond to five modes of imperfections can be achieved. As described before, it is always assumed that the specific mode may comprise only one half-wavelength. The frequency of the class of imperfections can be calculated by taking the reciprocal of the corresponding half-wavelength, i.e., 1/L for global imperfections bow (G1), camber (G2), and twist (G3), $1/\lambda_L$ for local imperfections, and $1/\lambda_D$. Employing the 1D spectral approach, the previous assumption seems to be inaccurate, especially for cross-section imperfections, i.e., local and distortional imperfections.

Z

Z sections are described in this section, and the results of 19 specimens are presented in Figure 8. 3. Global imperfections seem to be comprised of one, two, and sometimes three major frequency contents. The frequencies' maximum magnitudes may not always be located in 1/L, but they are always near 1/L. This differs from the one half-wavelength assumption. However, cross-section imperfections turn out to be very different from what might be expected. If there is only one major half-sine wave in a local imperfection, the peak energy should occur at the corresponding reciprocal frequency of the corresponding half-wavelength, λL. But the 1D spectral curves prove that higher-energy (magnitudes) imperfections assemble in the first two or three frequencies. And imperfections are much smaller in the corresponding frequencies of the local and distortional imperfections.

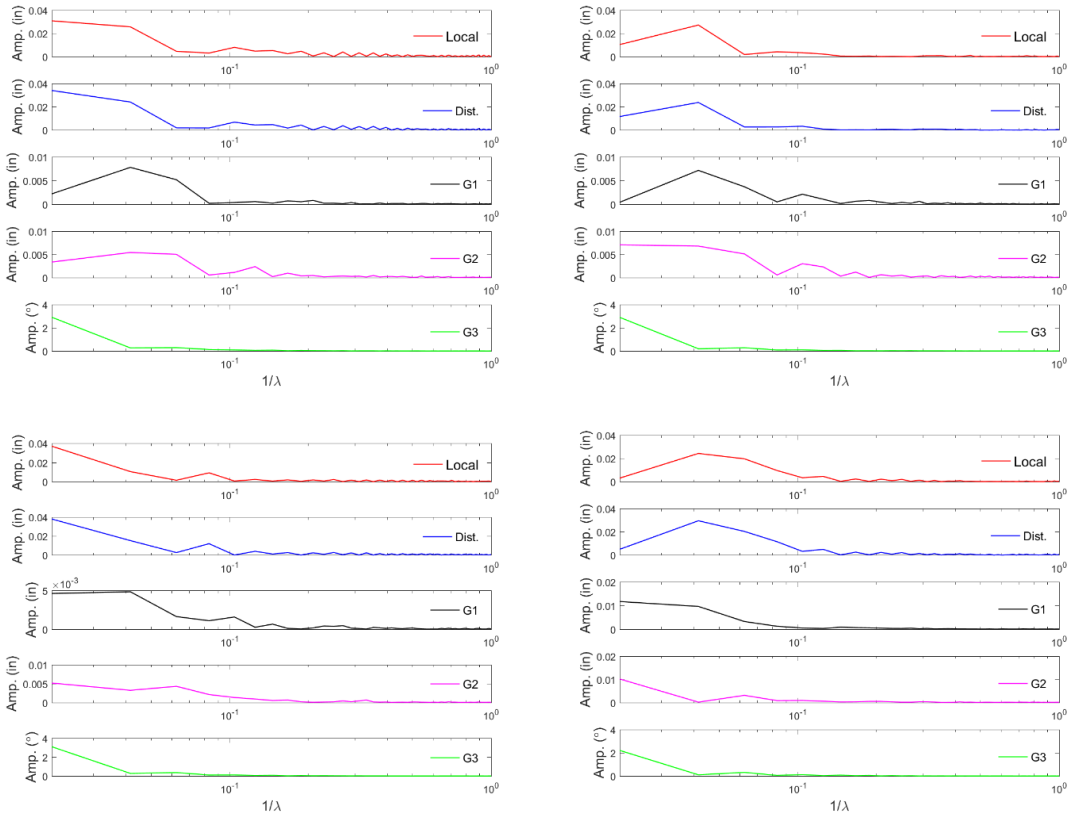

Figure 8. 3 Typical 1D spectral realization of Z sections (700Z225-60)

C

C sections are described in this section, and they are comprised of two groups of specimens, as shown in Figure 8. 4 and Figure 8. 5 for 362S162-68 and 600S137-54, respectively. Different from Z sections, C sections share a similar phenomenon in that their maximum magnitudes occur at the 1/L frequency. However, imperfections also exist at other frequencies, and they cannot be dismissed, especially the cross-section imperfections. Compared to 362S162-68, the power spectral densities of the local imperfections of 600S137-54 fluctuate noticeably near the corresponding local half-wavelength, λ_L.

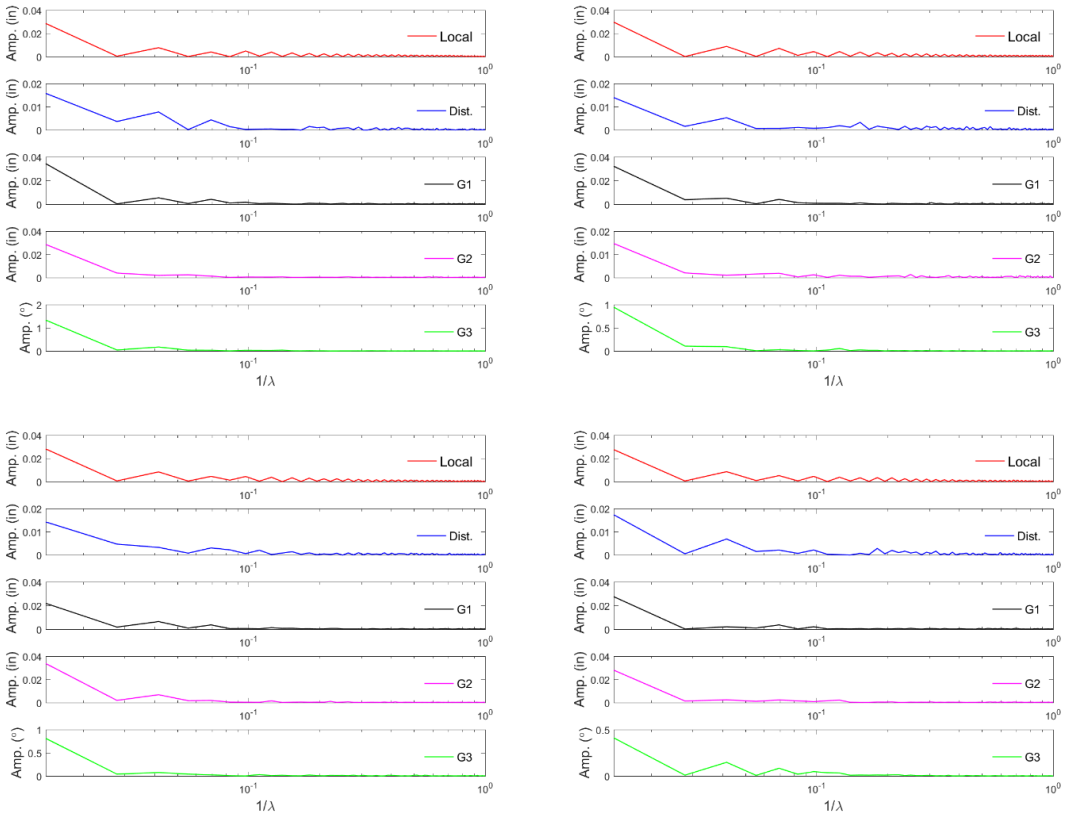

Figure 8. 4 1D spectral realization of C sections (362S162-68)

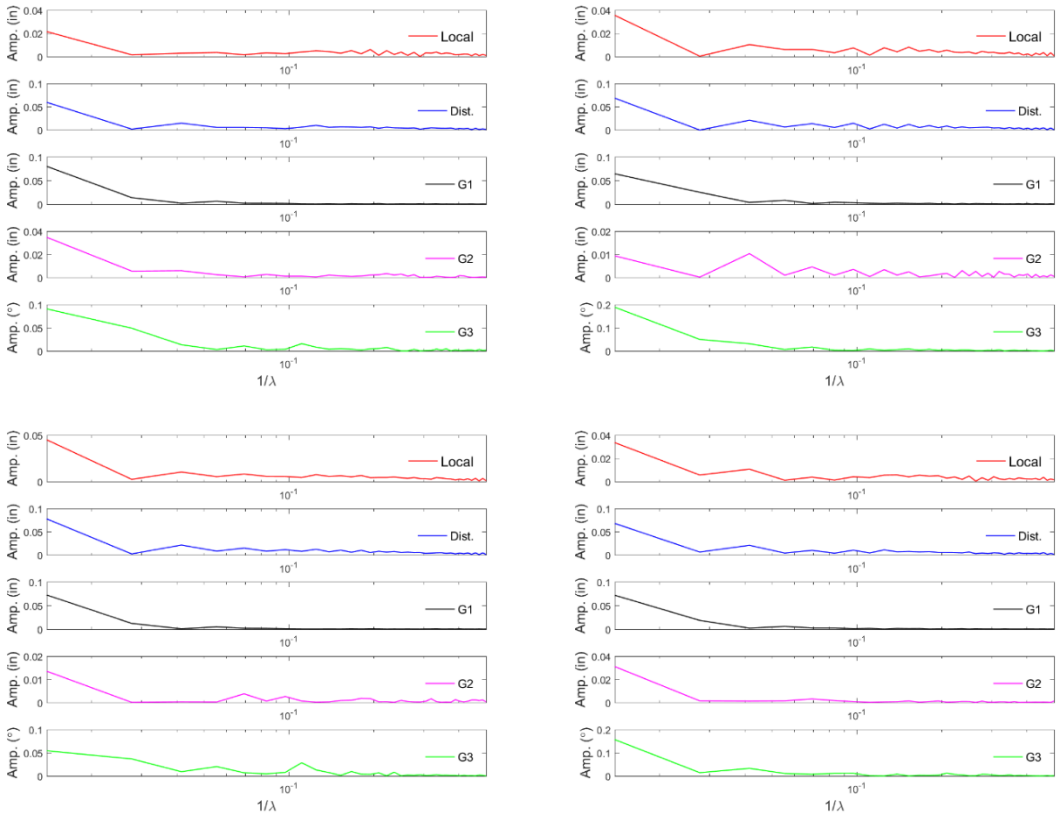

Figure 8. 5 1D spectral realization of C sections (600S137-54)

BUC

BUC sections are individually different in the 1D spectral approach. It may be difficult to reach a precise conclusion concerning current findings. Regarding the local imperfections of 362S162-68, three PSD curves had maximum values in 1/L, but the fourth curve showed its peak at the second frequency. Concerning distortional imperfections, the fourth curve again was distinctly different, with its maximum values occurring at the third frequency. The global imperfections' camber (G2) of 362S162-68 contained four different situations. The first curve was similar to the previous C sections; the second curve had a flat platform across three frequencies; the third curve reached its peak at the fourth frequency; and the fourth curve resembled the second curve, but it fluctuated much more at the higher frequencies.

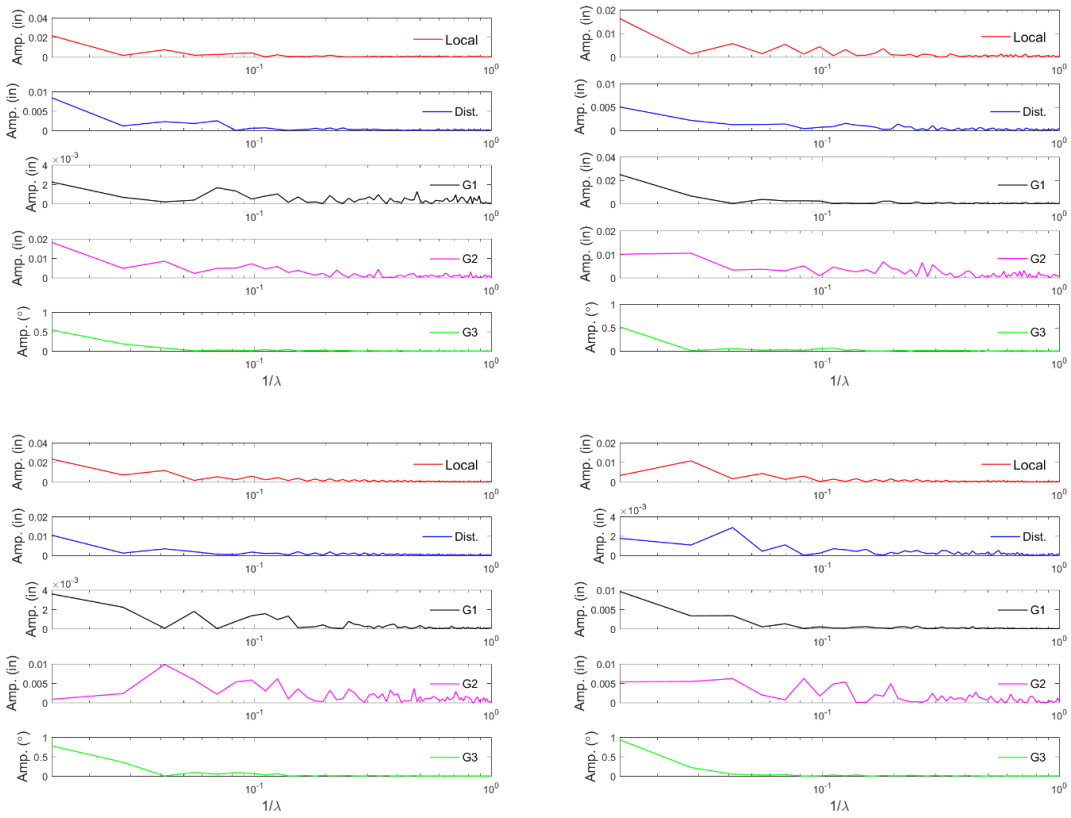

Figure 8. 6 1D spectral realization of BUC sections (362S162-68)

Similar to 362S162-68, 600S137-54 had non-uniform PSD curves across all four specimens. It is difficult to draw any conclusions based on the current sample sizes. It may worthwhile to increase the BUC sample size so that precise conclusions can be obtained to guide future numerical imperfection simulation in modeling.

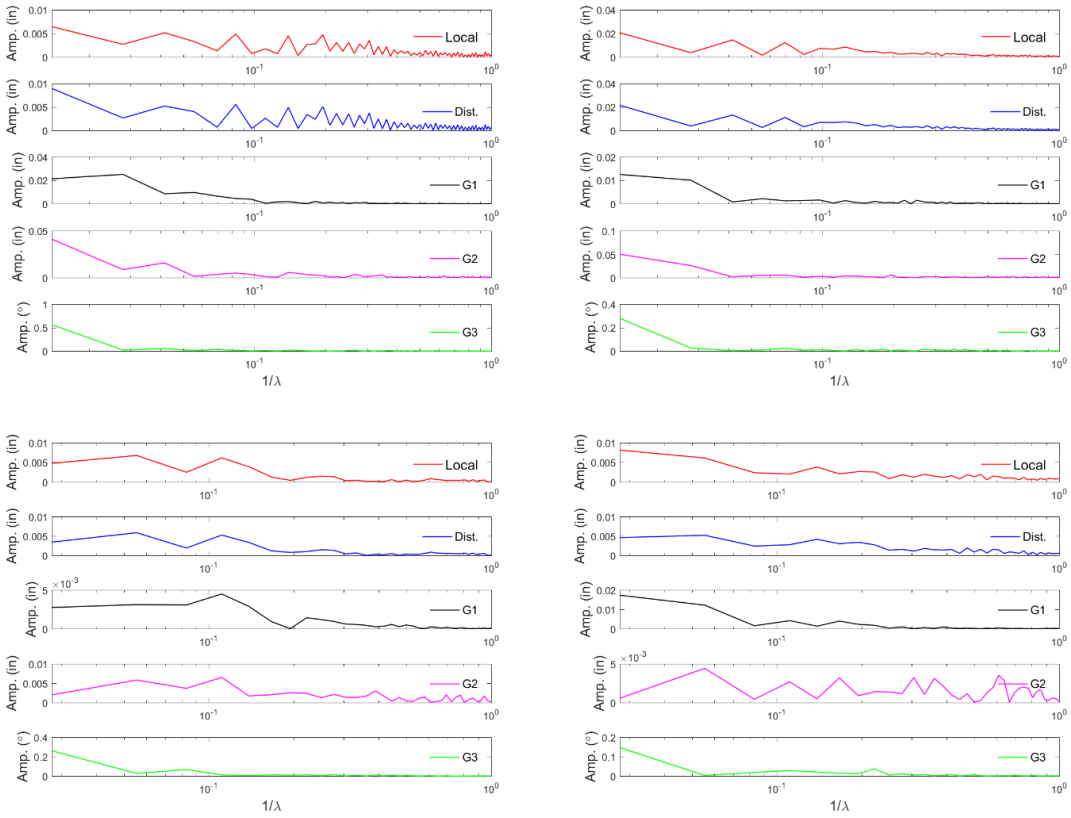

Figure 8. 7 1D spectral realization of BUC sections (600S137-54)

8.2.2 Comparisons with traditional imperfection representation

Zeinoddin (2011) proposed five equations to represent the power spectrum of local, distortional, bow, camber, and twist through the 1D spectral approach. The base spectra were estimated from over 100 C sections with various dimensions. These equations are called Design PSD, and they are plotted in Figure 8. 8 through Figure 8. 12. In order to understand the two methods of representing imperfections, detailed comparisons are depicted in Figure 8. 8 - Figure 8. 12 with respect to 700Z225-60, 362S162-68 (C), 600S137-54 (C), 362S162-68 (BUC), and 600S137-54 (BUC), respectively.

Z

When 1/λ is larger than 0.1 in., Design PSD resembles the spectral curves of local imperfections, but the maximum magnitudes of Design PSD are twice as large as the local imperfection curves. However, at the frequency that corresponds to local imperfections, both the magnitude from the characterization of conventional imperfections and the magnitude obtained with modal imperfection decomposition approaches are larger than the magnitudes of the spectra. Regarding distortional imperfections, it seems that the traditional approach in the related frequency coincides with the maximum magnitudes of the spectra of the 19 specimens. 50% The MID value of 50% was close to the peaks of the spectra. Discrepancies in the spectra of global imperfections G1 and G2 made comparisons difficult. Design PSD seems too large in its depiction of G1, but it predicted the magnitudes of the G2 spectra quite well. Concerning G3, Design PSD has a very small magnitude when compared with the spectra of 700Z225-60, but its frequency coincided with the results of the traditional approach and with 700Z225-60.

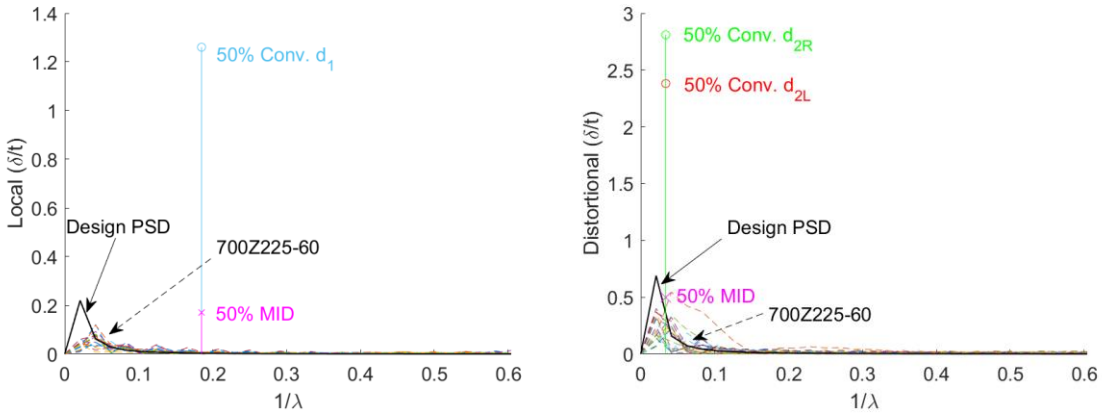

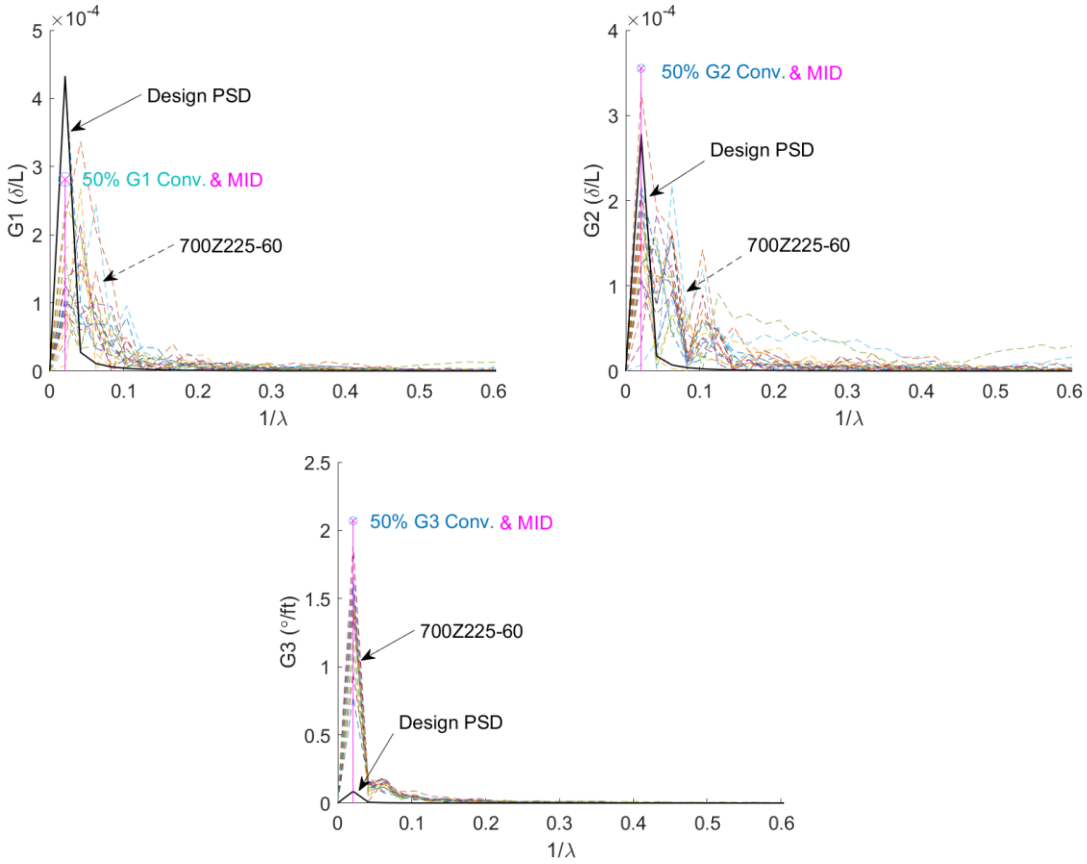

Figure 8. 8 Comparisons among 1D spectral, design PSD, and traditional representation of Z sections (700Z225-60)

C

Similar to Z sections, 362S162-68 (C) had extremely small magnitudes in corresponding frequency in local imperfections (Figure 8. 9). Fifty percent of the imperfections from MID obtained magnitudes that were similar to those of 362S162-68 irrespective of frequency. However, Design PSD provided values that were about one-third of those of 362S162-68. Focusing on distortional spectrum plots, 50% MID again resembled the median of 365S162-68 (14 specimens) in magnitude. However, Design PSD produced values that were larger than 365S162-68. Design PSD's values coincided with the medians of both the magnitudes and frequencies of the G1 and G2 imperfection spectra. But it was much smaller than the results of the traditional approaches as well as the actual 365S162-68 spectra.

Different situations occurred with 600S137-54 (C). The spectra of both local and distortional imperfections shared their energy along multiple frequencies. Therefore, in general, the 50% MID values were larger than the maxima of the spectra. However, the magnitudes at the corresponding traditional frequencies of local and distortional imperfections were much more obvious than the spectra. Design PSD successfully predicted the spectra of distortional G2 and G3 imperfections, but it had smaller values in local and G1 imperfections.

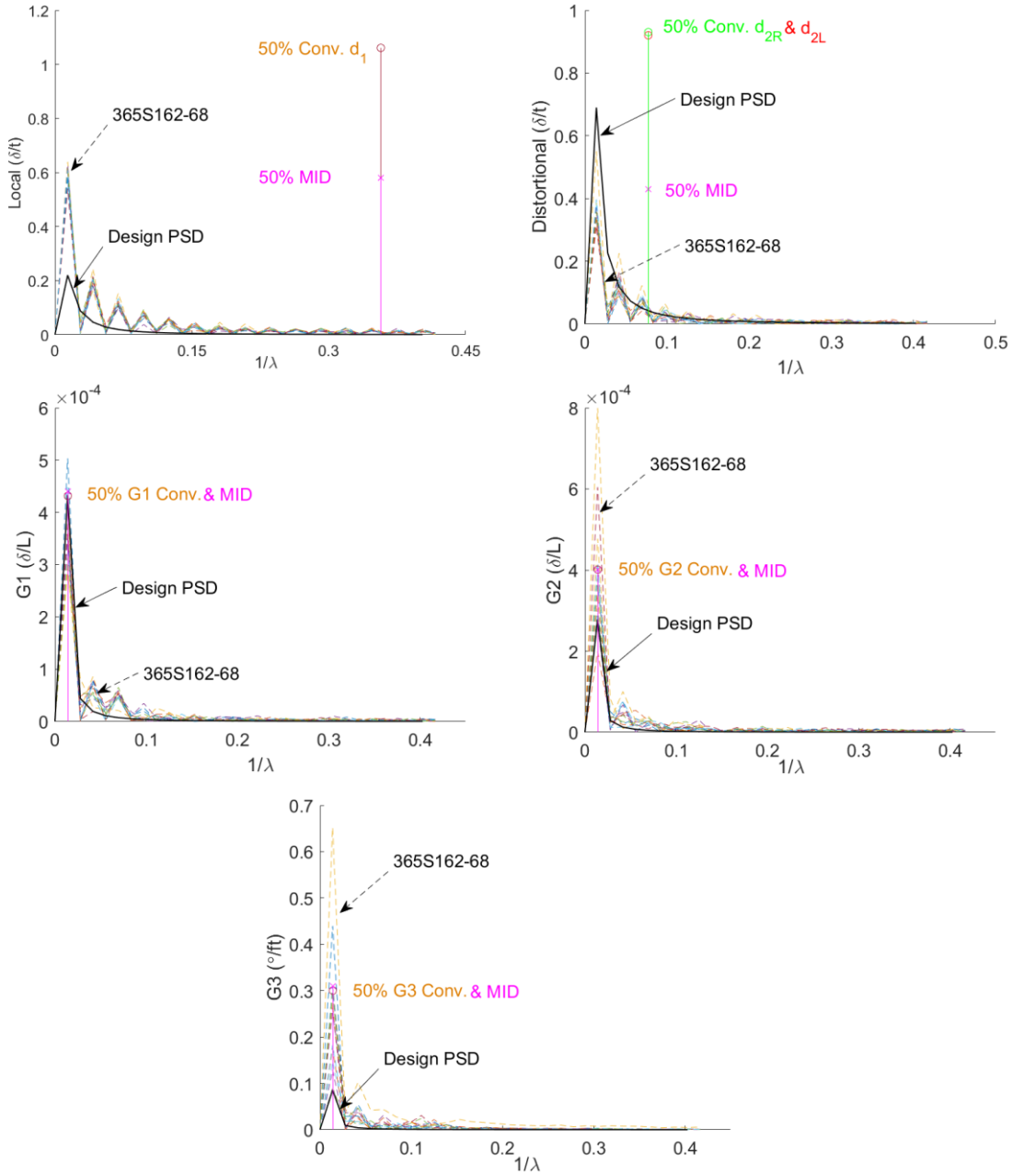

Figure 8. 9 Comparisons of 1D spectral, Design PSD, and traditional representation of C sections (362S162-68)

Local imperfections of 600S137-54 behaved similarly to 362S162-68, i.e., the maxima of the spectra were similar and larger than Design PSD (Figure 8. 10). However, the magnitudes at the corresponding traditional imperfection frequency were larger than those of 362S162-54. Distortional imperfections, unlike 362S162-68, coincided with Design PSD; however, the median values from both traditional representations were much larger than the both the maximum spectra for 600S137-54 and the value at the corresponding traditional frequency ($1/\lambda_D$). Design PSD provided values for the global imperfections of G1 and G2 that were 50% of the median values of 600S137-54 and both traditional methods. However, twist (G3) of Design PSD coincided with the maximum values of the measurements except that there were other frequencies in 600S137-54.

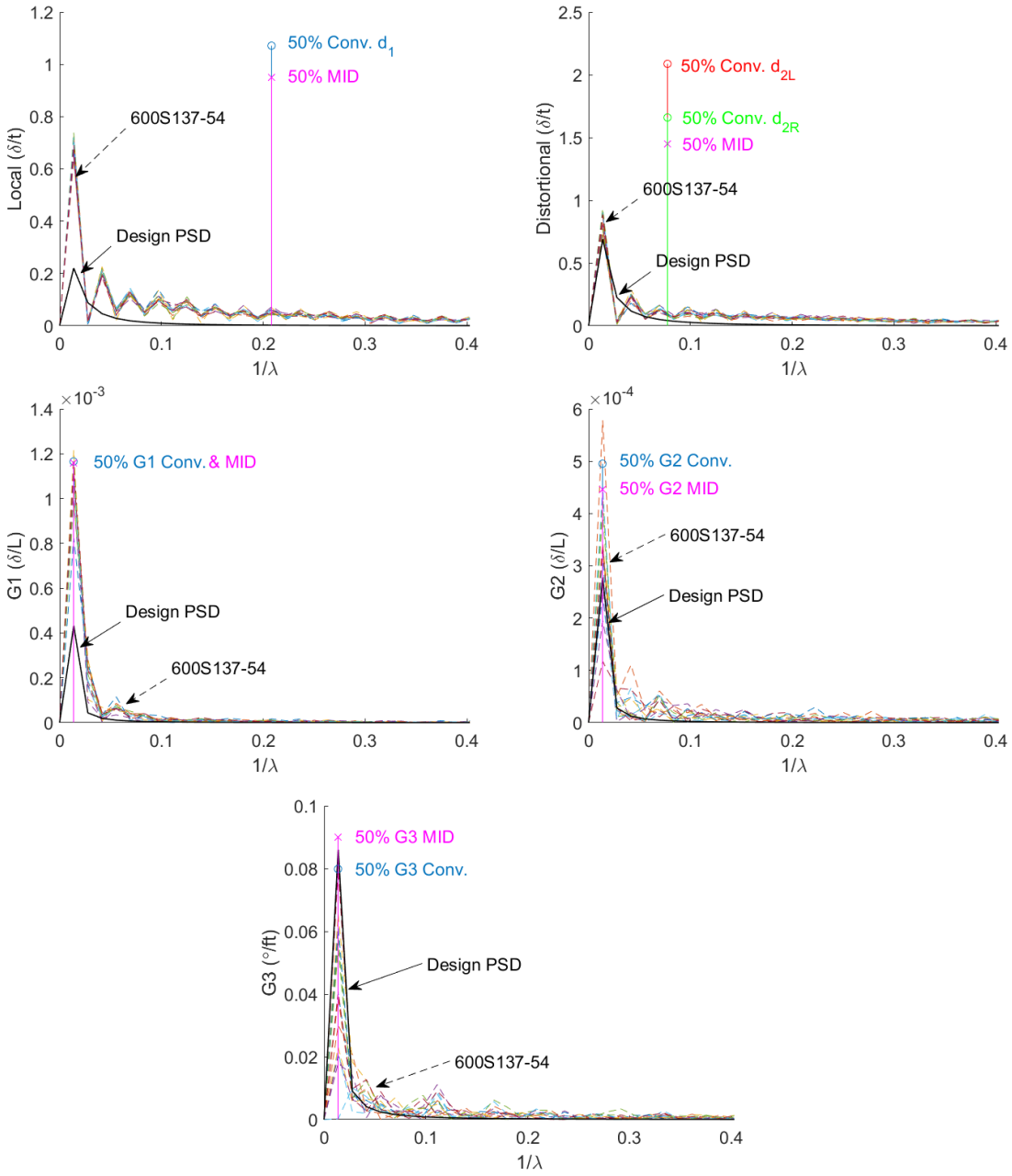

Figure 8. 10 Comparisons among 1D spectral, design PSD, and traditional representation of C sections (600S137-54)

BUC

Built-up C sections performed differently from the other two sections, i.e., Z and C sections. An obvious difference between the Design PSD and measurements (362S162-68 and 600S137-54) was the disagreement about the maxima's frequencies. The 362S162-68 specimens had similar magnitudes as Design PSD for local, G1, and G2. However, the distortional imperfections of 362S162-68 and 600S137-54 were much closer to 50% MID, but their corresponding frequencies of the maxima were different. The size of the samples was an issue, and some trends occurred that cannot be conclusively confirmed in the current study. Unfortunately, this may impair the mathematical presentation of the spectra in the following sections.

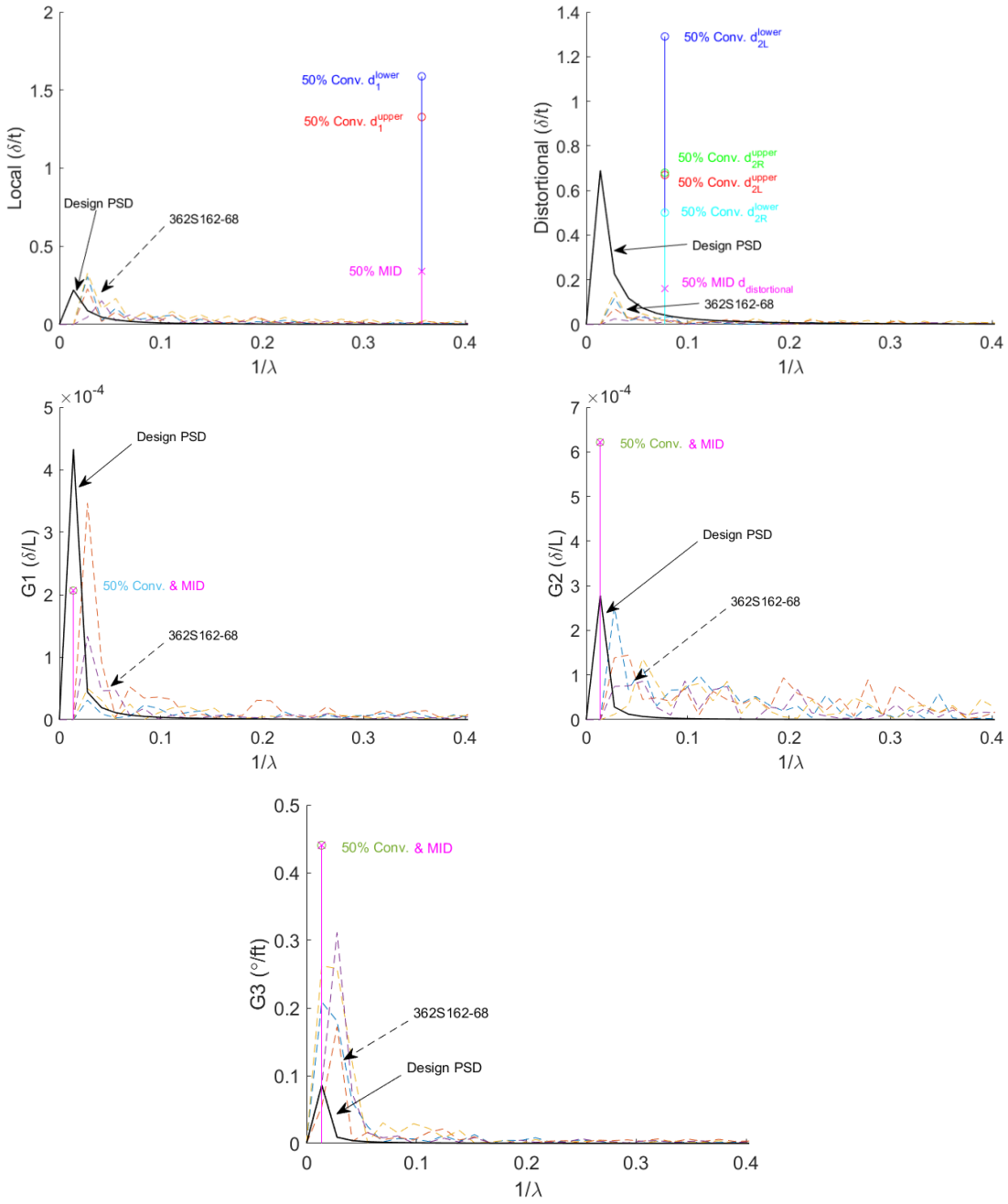

Figure 8. 11 Comparisons among 1D spectral, design PSD, and traditional representation of BUC sections (362S162-68)

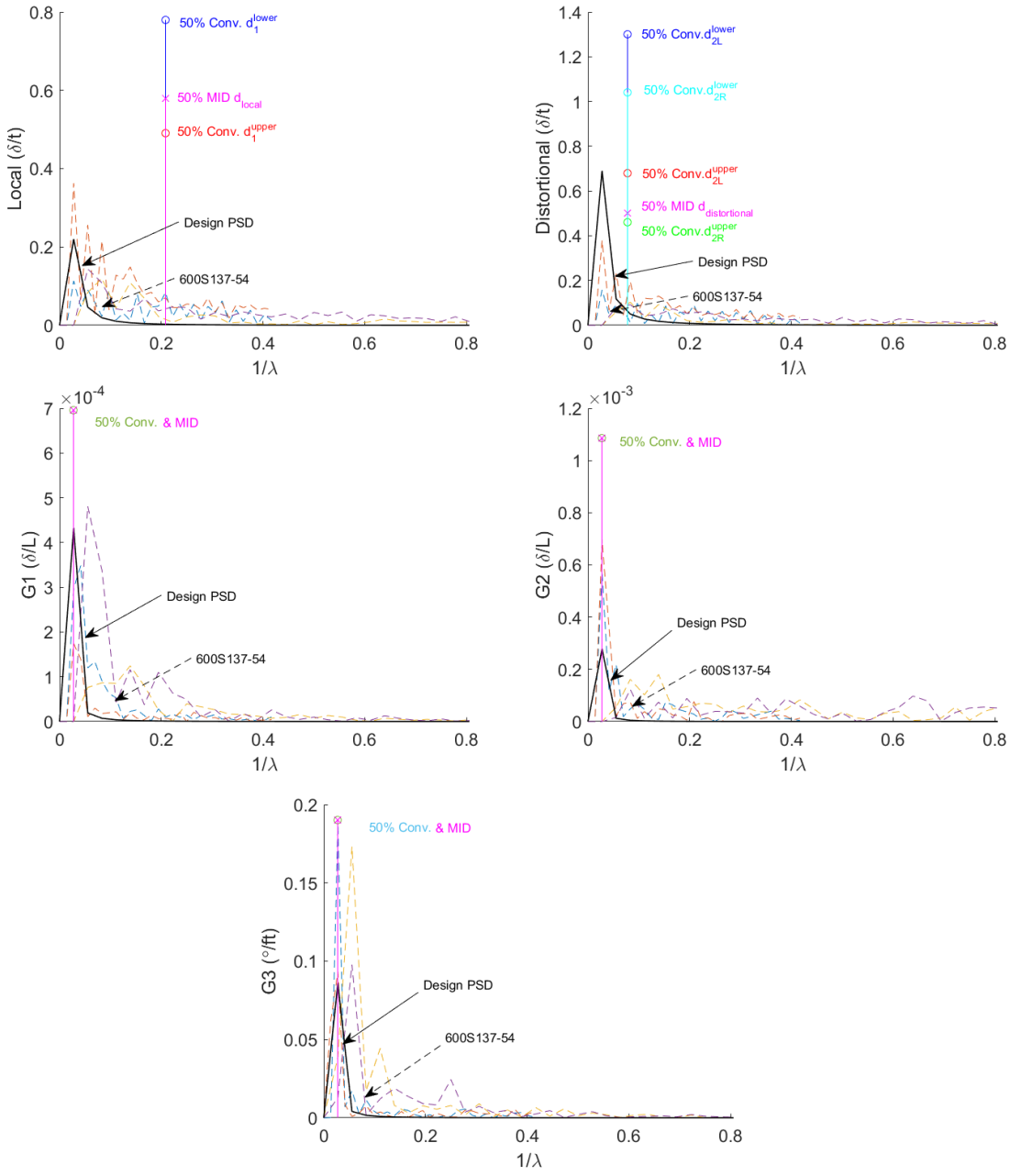

Figure 8. 12 Comparisons among 1D spectral, design PSD, and traditional representation of BUC sections (600S137-54)

8.3 Mathematical expression

The comparison plots presented above demonstrate that sections with nominally-identical dimensions have similar magnitudes and frequencies. It is desirable to find a mathematical expression for each type of section that may be considered for use in future simulations of imperfections in structural modeling. The mathematical equations are intended to provide the magnitudes at the required range of frequencies, and the phases were assigned for the combination of the modes.

Z

The average of five modes of imperfections of Z sections was taken from 19 specimens. The mean spectra, i.e., the base power spectra, were fitted with the reciprocals of polynomials with normalized maximum values of numerators. Therefore, the corresponding mathematical expressions for Z sections could be determined, as shown in Eq 8. 4 – Eq 8. 8. The simulated curves were compared with Design PSD, and the observations showed that Design PSD provided the upper bounds of the magnitudes within 0.05 (1/λ) frequency of 700Z225-60, with the exception of twist (G3).

$$PSD_{local} = \frac{0.06}{-32x^2 + 90.5x - 0.9} \quad \text{Eq 8. 4}$$

$$PSD_{Dist} = \frac{0.23}{-25.1x^2 + 89.9x - 0.9} \quad \text{Eq 8. 5}$$

$$PSD_{G1} = \frac{1/7653}{381.1x^2 + 32.6x + 0.2} \quad \text{Eq 8. 6}$$

$$PSD_{G2} = \frac{1/6580}{118x^2 + 38.5x + 0.1} \quad \text{Eq 8. 7}$$

$$PSD_{G3} = \frac{1.41}{1663x^2 + 150.3x - 2.9} \quad \text{Eq 8. 8}$$

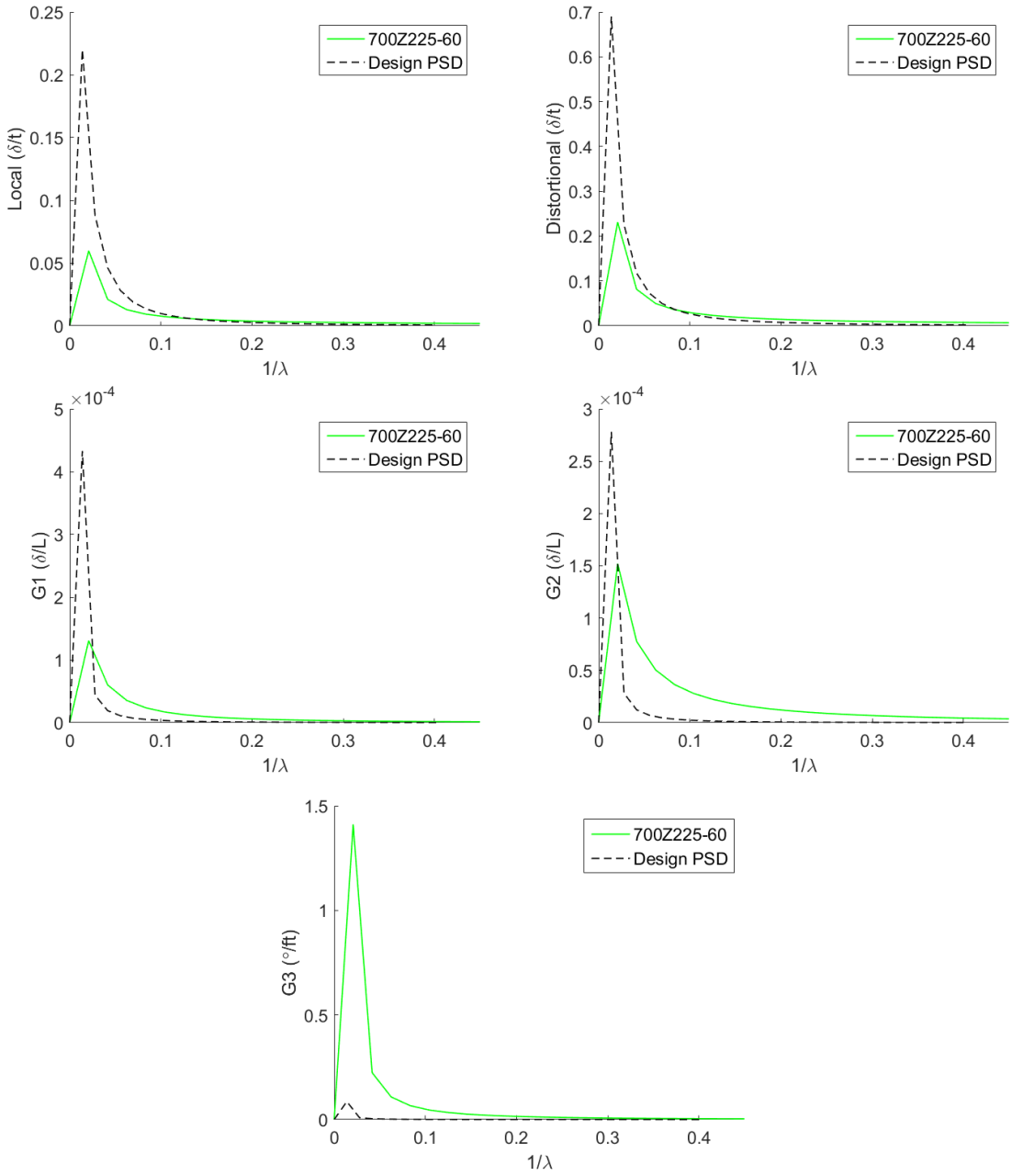

Figure 8. 13 Comparisons of mathematical realizations between Z sections and design PSD

C

Originally, it was planned to develop an equation for the specific mode imperfections for both sections. However, the results presented above show that different dimensions could produce totally opposite conclusions from the mathematical presentations. Thus, two groups of equations were derived based on the base spectra of 365S162-68 and 600S137-54, respectively. The equations were compared with Design PSD obtained from Zeinoddin (2011). Design PSD had the smallest magnitudes of local imperfections and camber (G2) imperfections. Regarding global imperfections, the three spectra seemed similar, with reciprocals larger than 0.1.

365S162-68

$$PSD_{local} = \frac{0.61}{120.8x^2 + 100.7x - 0.4} \quad \text{Eq 8. 9}$$

$$PSD_{Dist} = \frac{0.37}{598.5x^2 + 79.2x - 0.2} \quad \text{Eq 8. 10}$$

$$PSD_{G1} = \frac{1/2586}{1017.9x^2 + 174.1x - 1.6} \quad \text{Eq 8. 11}$$

$$PSD_{G2} = \frac{1/2524}{-93x^2 + 406.9x - 4.6} \quad \text{Eq 8. 12}$$

$$PSD_{G3} = \frac{0.27}{984.2x^2 + 223.7x - 2.3} \quad \text{Eq 8. 13}$$

600S137-54

$$PSD_{local} = \frac{0.69}{-35.2x^2 + 79.3x - 0.1} \quad \text{Eq 8. 14}$$

$$PSD_{Dist} = \frac{0.83}{-73.9x^2 + 81.8x - 0.1} \quad \text{Eq 8. 15}$$

$$PSD_{G1} = \frac{1/920}{2412.3x^2 + 361.7x - 4.5} \quad \text{Eq 8. 16}$$

$$PSD_{G2} = \frac{1/2999}{-122.3x^2 + 244.1x - 2.4} \quad \text{Eq 8. 17}$$

$$PSD_{G3} = \frac{0.039}{79.9x^2 + 114.4x - 0.6} \quad \text{Eq 8. 18}$$

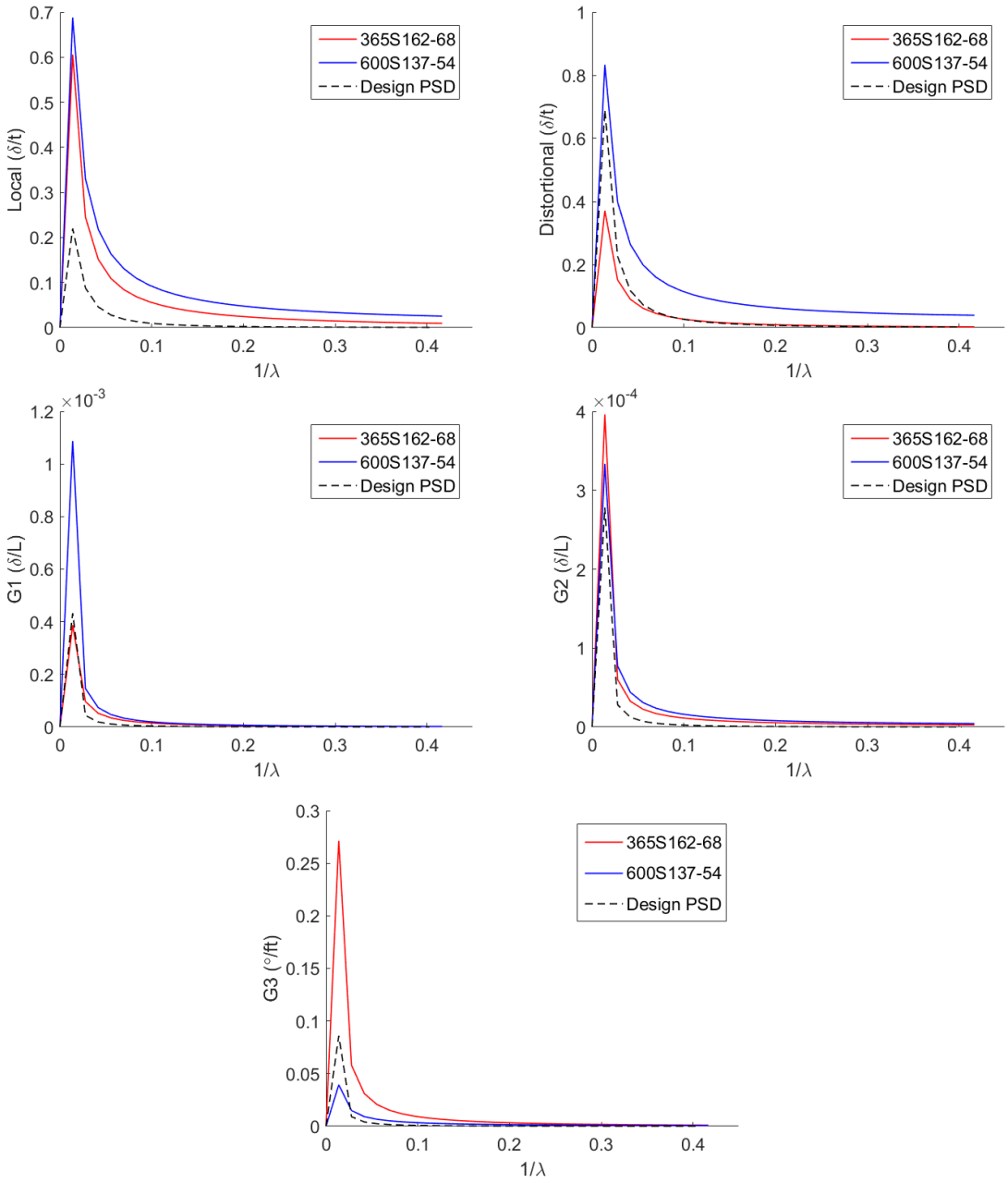

Figure 8. 14 Comparisons of mathematical expressions between C sections and design PSD

BUC

Compared to the C and Z sections, built-up members have much more energy at frequencies other than the peak frequcncy; the spectra of 600S137-54, 365S162-68, and 600S137-54 coincided as 1/λ larger than 0.2 for bow imperfections (G1) and larger than 0.1 for camber imperfections (G2). Regarding twist imperfections (G3), Design PSD was only 10% of the maximum values of 600S137-54 and 365S162-68.

365S162-68

$$PSD_{local} = \frac{0.23}{38.8x^2 + 46.5x - 0.3} \quad \text{Eq 8. 19}$$

$$PSD_{Dist} = \frac{0.09}{-61.7x^2 + 57.8x - 0.6} \quad \text{Eq 8. 20}$$

$$PSD_{G1} = \frac{1/7126}{-152x^2 + 121.8x - 2.26} \quad \text{Eq 8. 21}$$

$$PSD_{G2} = \frac{1/8385}{4.7x^2 + 10.8x - 0.7} \quad \text{Eq 8. 22}$$

$$PSD_{G3} = \frac{0.23}{348.8x^2 + 50.2x - 0.7} \quad \text{Eq 8. 23}$$

600S137-54

$$PSD_{local} = \frac{0.24}{-9.2x^2 + 16.6x + 0.5} \quad \text{Eq 8. 24}$$

$$PSD_{Dist} = \frac{0.27}{-12.2x^2 + 17.4x + 0.5} \quad \text{Eq 8. 25}$$

$$PSD_{G1} = \frac{1/4095}{238x^2 + 84.7x - 1.5} \quad \text{Eq 8. 26}$$

$$PSD_{G2} = \frac{1/1581}{-132x^2 + 130.3x - 2.5} \quad \text{Eq 8. 27}$$

$$PSD_{G3} = \frac{0.14}{-272.1x^2 + 212.7x - 4.6} \quad \text{Eq 8. 28}$$

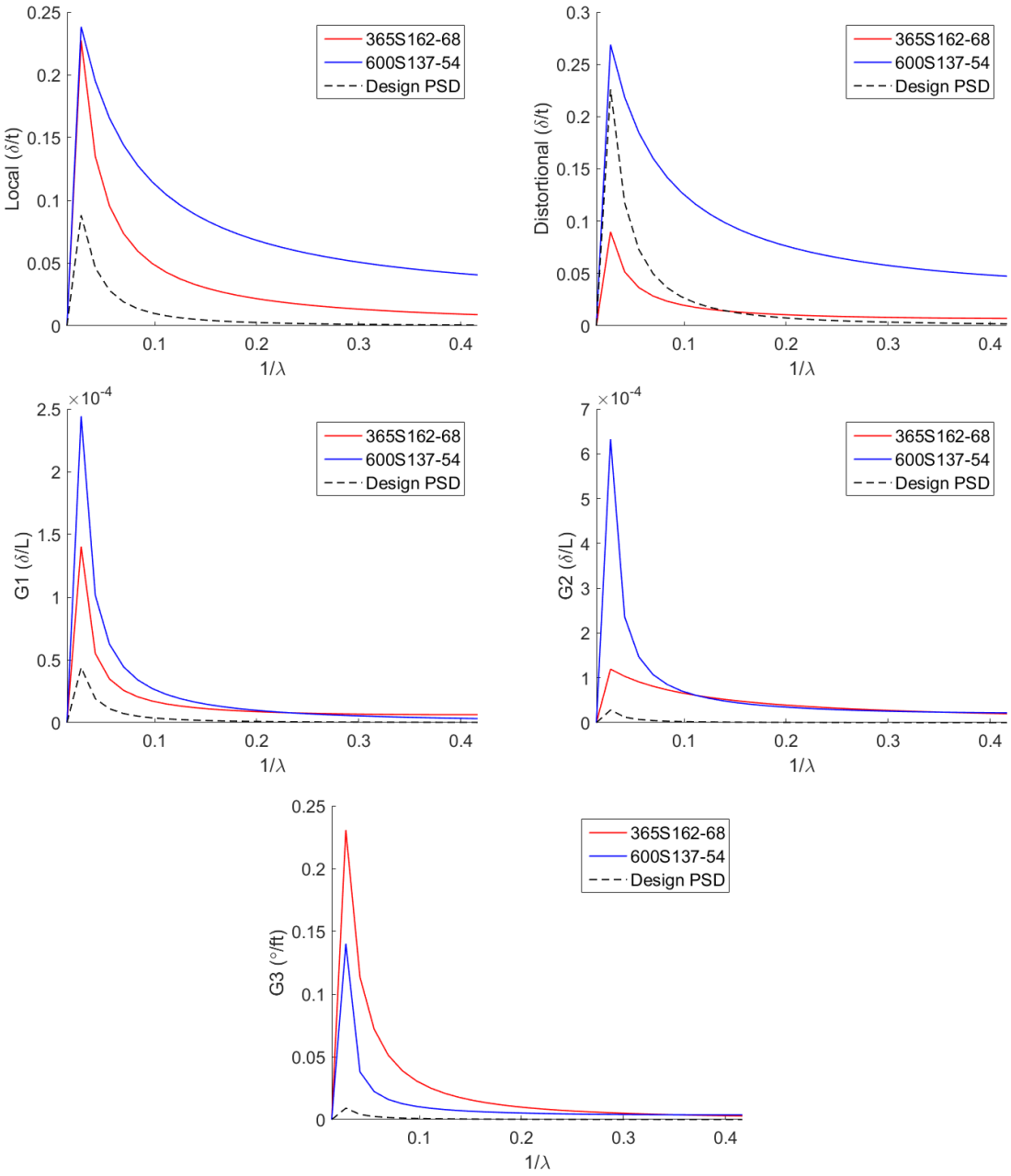

Figure 8. 15 Comparisons of mathematic realizations between BUC sections and design PSD

8.4 Conclusions

This chapter provides an insightful analysis of the characterized imperfections in the frequency domain, where lower frequencies, i.e., frequencies lower than the frequency of local buckling, were of greater interest. The use of extrema for defining imperfection magnitudes in shell finite element simulations seeded with buckling mode imperfections often ignores frequency content of real imperfections. Following from previous work (Zeinoddini, 2011) the use of simplified functions for defining imperfection power spectral density (PSD) across the buckling modes is explored as a means to maintain frequency content in addition to cross-section buckling mode shapes. Resolution of the data in the frequency axis can be as small as the reciprocal of the member's full length. For example, if the length of a C section is 72 in., the resolution is 0.0139. The 1D spectral representation disagreed with the traditional representation, especially in cross-section imperfections, i.e., local and distortional imperfections. Cross-section imperfections should be reviewed carefully, and simulations using from two representations are compared in Chapter 9. It was concluded that different PSD equations must be proposed for different types and shapes of cold-formed steel members.

Further work is needed to compare simulated imperfections across shell finite element models and tests and additional imperfection measurements are needed to expand the statistical foundation for the use of the PSD approach in MID-based imperfection modeling.

Chapter 9 Collapse simulation of cold-formed steel members

The aim of this chapter is to bridge the actual measured geometry, characterize imperfections from the traditional and 1D spectral approaches, and collapse modeling in finite element analysis. A preliminary study of collapse simulation by three types of models is presented in this chapter, i.e., true geometry, imperfection simulation using the traditional approach, and imperfection simulation using the 1D spectral approach. The procedures in using measured data and characterized imperfections are discussed in section 9.1. The results of the preliminary study are presented in section 9.2, and the traditional and 1D spectral approaches are compared.

9.1 Procedures of collapse simulation

9.1.1 Collapse modeling of members with true geometry

There are six steps to convert an actual geometry from laser measurement to a finite element model. The first step is to determine the centerline of each cross section in a measurement Z section and develop a centerline model (Figure 9. 1). Taking a typical Z section with a thickness of 0.06 in as an example, the points measured by the laser scanner provide information about the entire outer face of the Z section. The finite element analysis requires a centerline model so that the outer-face point clouds must be translated through its face normal by half of the thickness, i.e., 0.03 in. Since it is assumed that the measurements of longitudinal position are accurate, the normal vectors for translations can be estimated in the 2D sense, i.e., in the cross section plane. Normal vectors to flat regions can be calculated directly from the orthogonal directions to the linear curves; While a corner should be fitted with an arch so that normal vectors can be equivalent to the directions of the radii (from arch to the center).

When the centerline model has been established, resampling of points, also called 'node formation,' is started from both the cross-section plane and the longitudinal direction (Figure 9. 2). A pre-

defined list of element numbers for each geometric feature is provided before node formation. As illustrated in the Figure 9. 2, the cross section obtains an element list in which a lip should comprise two elements, a corner has two elements, a flange has four elements, and a web has nine elements; the longitudinal direction receives an element list that a 3D model has nine rows of elements. The resampling should always start with an interpolation along its mesh direction. When the dimensions of each of the geometric features are known, the positions of the nodes can be calculated. Then, interpolated points that are close to those calculated positions are selected as nodes of the finite-element models. The node formation procedures are terminated when the mesh of both the cross-sectional and longitudinal directions is finished.

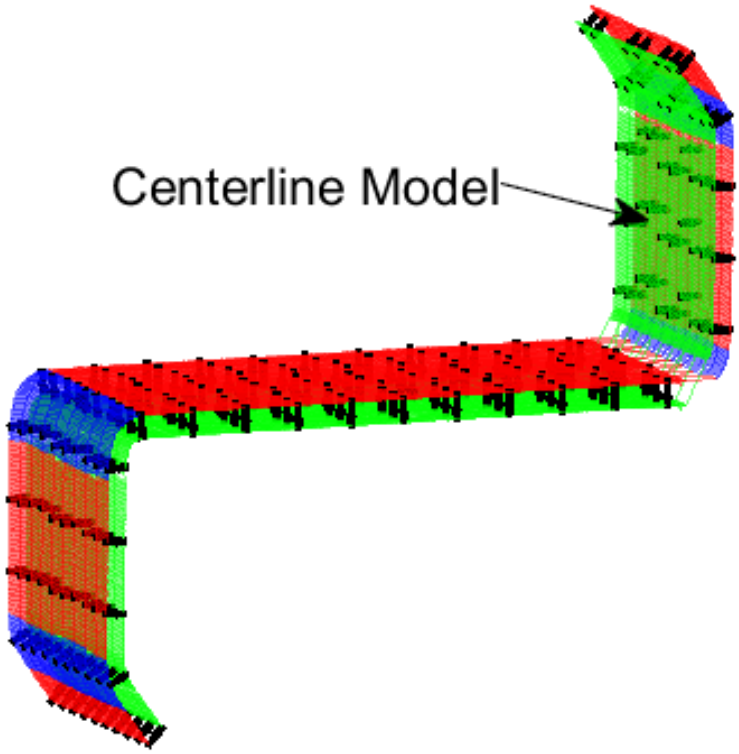

Figure 9. 1 Formation of a centerline model

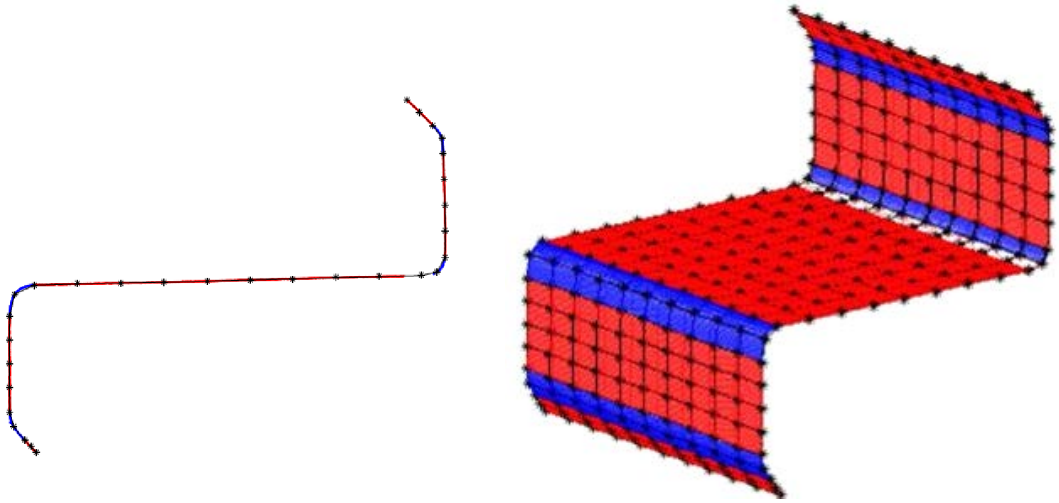

Figure 9. 2 Nodal formation of a finite element model

The third step is to define the elements of the finite element models. This requires assignment of the types of elements. Typical elements for cold-formed steel members are S4, S4R, and S9R5, which comprise 4, 4, and 9 nodes in an element unit.

Material properties, known as plastic matrix, Young's matrix, and Poisson ratios, are critical for analysis. Coupon testing was conducted to identify all of these quantities. There were two shapes and three types of cold-formed steel members, i.e., Z (700Z225-60), C (362S162-68), and C (600S137-54); the quantities of materials are listed in Table 9. 1:

Table 9. 1 Properties of materials in the preliminary study

700Z225-60		362S162-68		600S137-54	
E (ksi)	**υ**	**E (ksi)**	**υ**	**E (ksi)**	**υ**
29580	0.3	29500	0.3	29500	0.3
Plastic Matrix					
σ (ksi)	**ε**	**σ (ksi)**	**ε**	**σ (ksi)**	**ε**
81.27406	0	55.9209	0	44.9234	0
80.77135	0.008939	61.0789	0.0007	52.764	0.0005
81.57181	0.017878	61.249	0.0012	56.1954	0.0012
82.80677	0.026818	61.6086	0.0107	58.1038	0.003
85.17766	0.035757	63.3866	0.0141	57.8625	0.004
86.87825	0.044696	65.0141	0.0166	57.9291	0.0083
88.35571	0.053635	66.952	0.0199	58.0733	0.0098
89.64809	0.062574	69.1773	0.024	58.7859	0.0131
90.8162	0.071514	71.923	0.0298	61.646	0.0217
91.86298	0.080453	74.5595	0.0365	65.3653	0.035
92.88578	0.089392	77.2445	0.0448	68.3958	0.0488
93.82312	0.098331	79.0406	0.0517	70.8007	0.062
94.70614	0.10727	81.2389	0.0621	73.0097	0.0763
95.25566	0.11621	83.5452	0.0761	74.6479	0.0883
96.05889	0.125149	85.7756	0.0934	75.3695	0.0939
97.01143	0.134088	87.4163	0.1087	77.0412	0.1084
97.75368	0.143027	88.9035	0.1247	80.1462	0.1392
98.30948	0.151966	91.0582	0.1525	82.3186	0.1641
98.86071	0.160906	91.3122	0.1568	84.2328	0.1884

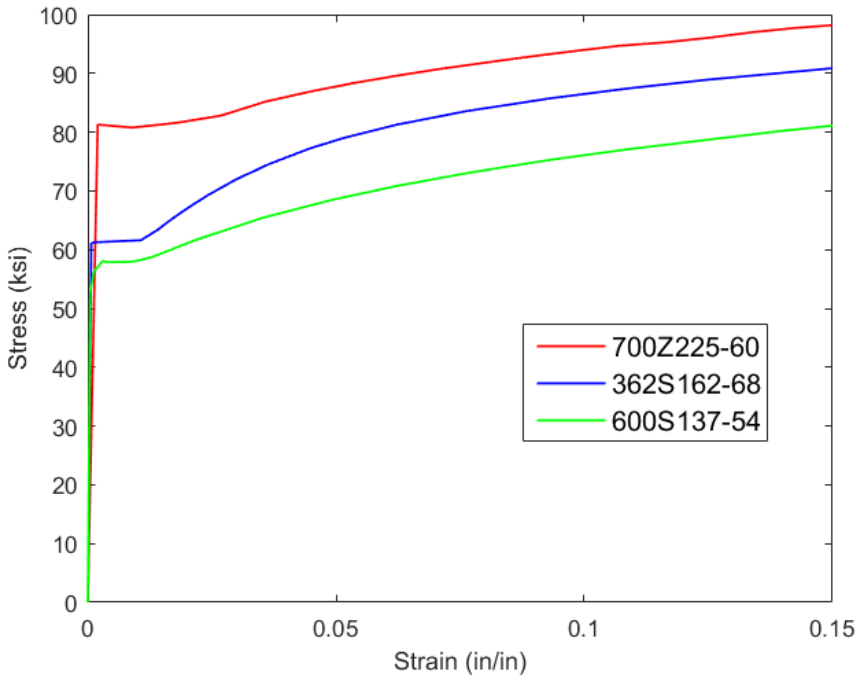

Figure 9. 3 Stress-strain curves of modeling from coupon testing

The fifth step is to define the steps in the analysis. Since post-buckling analysis is required for cold-formed steel members, geometric non-linearity and the material's non-linearity must be considered. Three different methods can be used, i.e., the modified Riks method, the stabilize method, and the quasi-static method. The stabilize method is a little bit tricky, since an artificial damping coefficient is required that generally must be estimated by trial and error. The quasi-static method treats collapse modeling in a slow, dynamic environment where cold-formed steel analysis is rarely used, and abrupt changes occur in some models. Thus, the modified Riks method was chosen for use. For the purpose of comparison, arc-length definitions were fixed for a specific type of model (Table 9. 2).

Table 9. 2 Arc-length definitions using the modified Riks method

	Initial	Total	Minimum	Maximum
700Z225-60	0.0001	1	1e-12	0.001
362S162-68	0.0001	1	1e-8	0.01
600s137-54	0.0001	1	1e-8	0.01

The final step is to determine the boundary conditions. Again, all models were assumed to be simply supported and warping fixed, where two reference nodes at both ends are defined to control end-plate nodes. One reference point was fixed in all three translation degrees of freedom. The other reference point was a defined displacement that the model should reach eventually.

All of the above information was integrated and used as input to the ABAQUS software, and a true geometry model was established, as shown in Figure 9. 4. The, the six steps in the procedure described above were allowed to use point clouds of measured geometry to be analyzed in finite element approaches through the ABAQUS software.

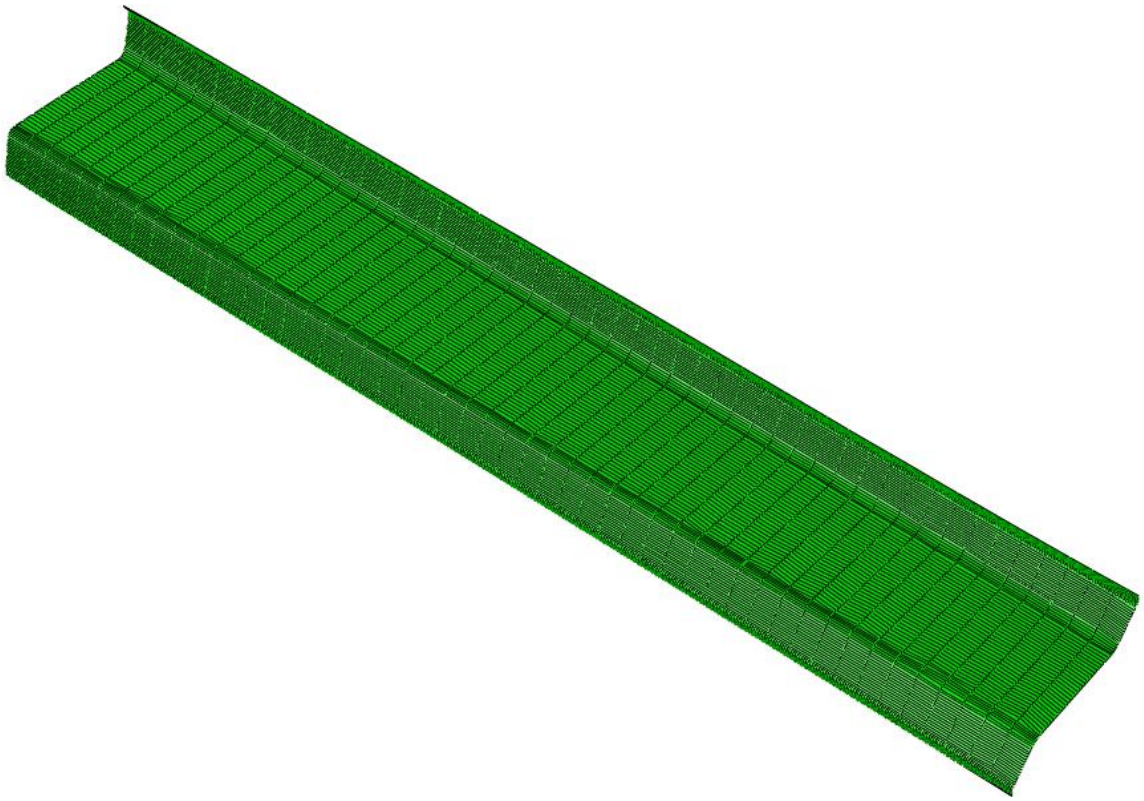

Figure 9. 4 A finite element model of a true geometry in ABAQUS

9.1.2 Collapse modeling of members with imperfection simulation (traditional representation)

Chapter 7 provided statistical summaries of imperfections from traditional representation, i.e., fixed magnitudes in corresponding modes and varied with determined shapes in a specific frequency half-wavelength. To start the imperfection simulation, a model with nominal dimensions was established with nodes and elements ready. The imperfections were considered to add corresponding nodes to distort the model. Five modes of imperfections, i.e., local, distortional, bow, camber, and twists, were simulated, and cross-section deformation shapes were obtained from the corresponding buckling mode shape (Figure 9. 5). The deformation of a mode shape is normalized as a unit and then multiplied by the magnitudes of the imperfections from a statistical summary table. The results from these operations were added to the nodes of the model, thereby achieving the simulation of imperfection.

Regarding the preliminary study, the boundary conditions, arch length definitions, and material properties remain the same as those described in Section 9.1.1.

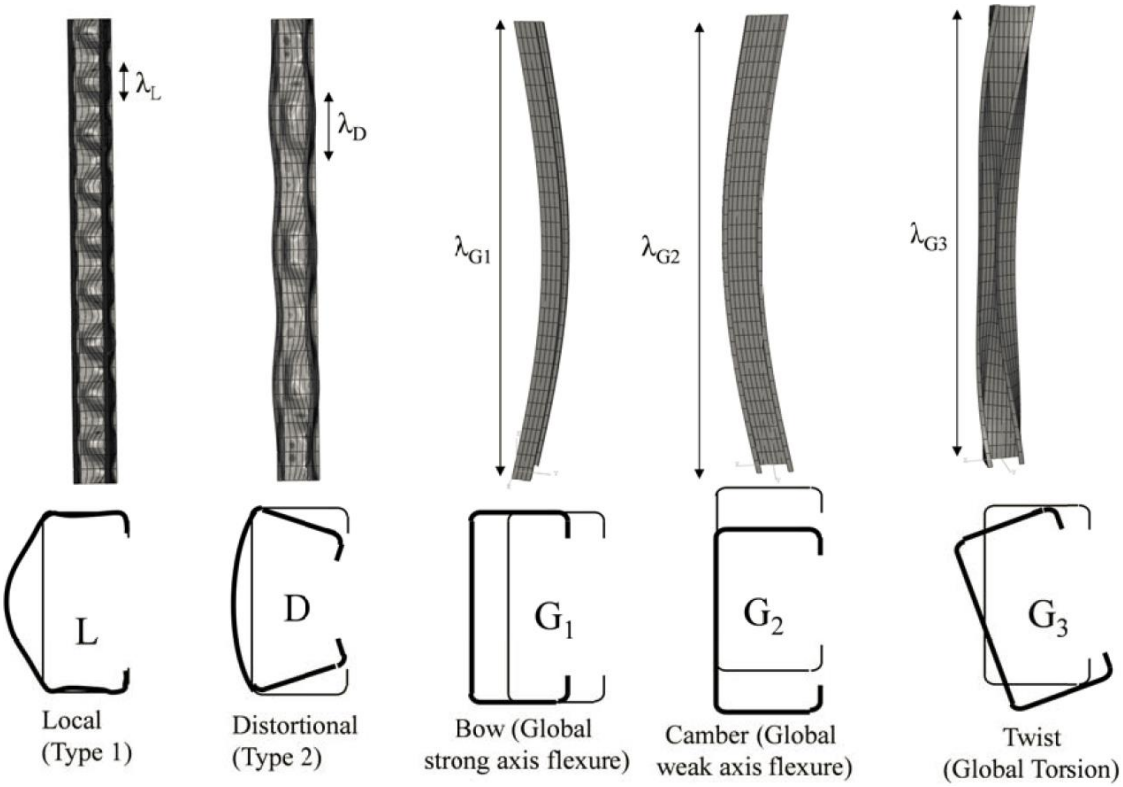

Figure 9. 5 Imperfection simulations using traditional approach (Zeinoddini 2011)

9.1.3 Collapse modeling of members with imperfection simulation (1D spectral representation)

Collapse modeling using the 1D spectral approach is different from the traditional approach. Instead of assuming only one frequency for the corresponding imperfection mode, the classified mode imperfection in the 1D spectral approach is assumed to contain multiple frequencies. More details are provided in Chapter 2, where there is a thorough literature review, and in Chapter 8, where the concepts and calculation procedures are presented. To begin the imperfection simulation, a series of base power spectra, with respect to local, distortional G1, G2, and G3, is obtained by estimating the medians of the power spectra from classified, measured imperfections (Figure 9. 6). The magnitudes of the first 10 frequencies are maintained for further analysis, the energy of which cannot be ignored because it occupies more than 95% of the classified imperfections.

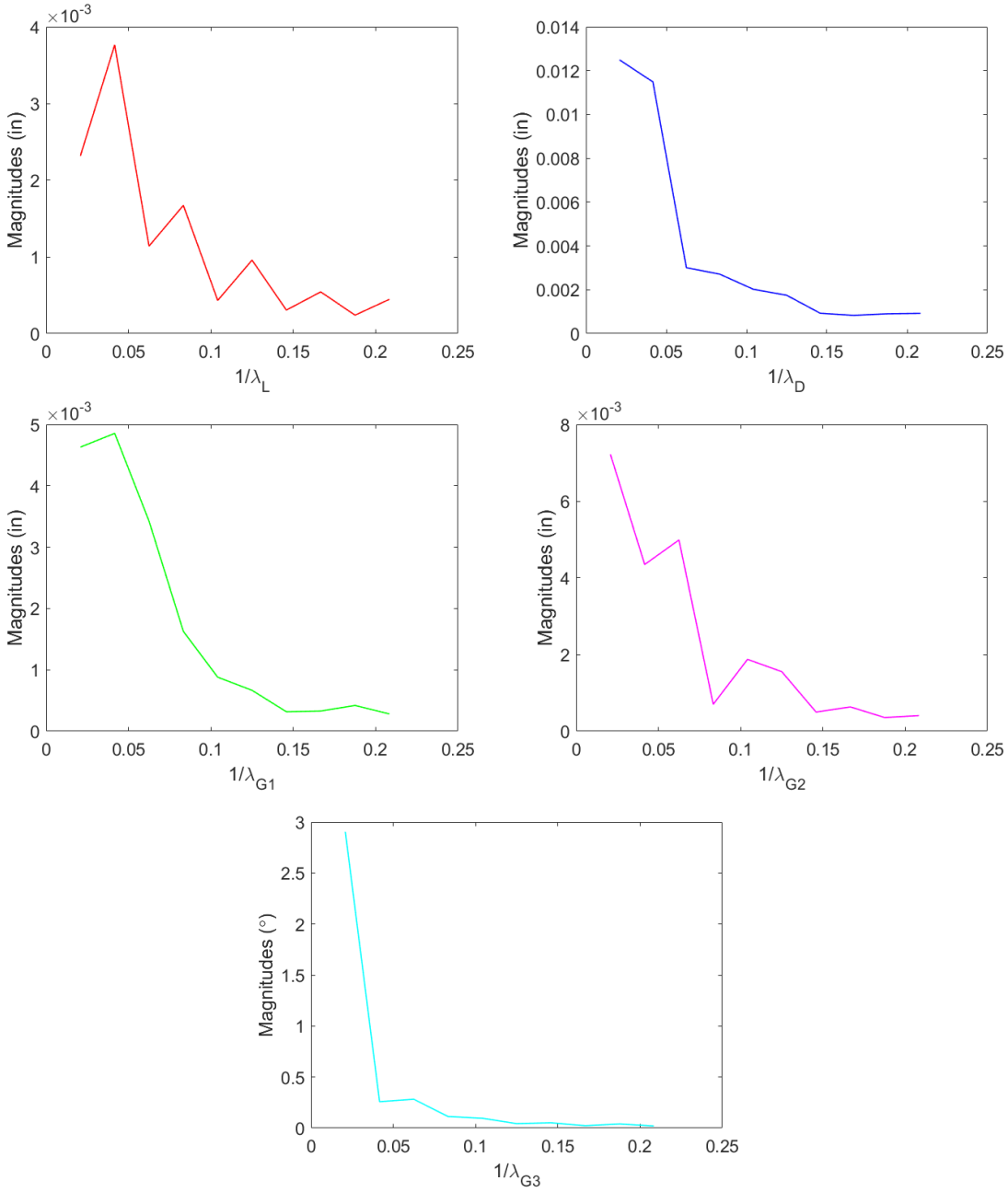

Figure 9. 6 Typical base power spectra of five modal imperfections

Magnitudes from the above base power spectrum are expressed as A_n in Eqs. 9. 2-9. 3. In the preliminary study, phases for combinations in a mode imperfection were simplified as zero. Mode 1 to mode 4, i.e., local, distortional, G1, and G2, respectively, use Eq. 9. 2 to combine the modes. Mode 5, as concluded from the last chapter, should be simulated with a cosine wave and Eq. 9. 3 is

used thereafter. The value of α can be determined simply by summing the multiple waves, as shown in Figure 9. 7. Simulated imperfections of all of the specimens can be achieved from Eq. 1, where the cross-section deformation mode shapes, ϕ, are known in advance. The imperfections that are obtained are added directly onto the corresponding nodes of the simulated finite-element models.

$$f(y)=\sum_{i=1}^{5}\alpha_i(y)\phi_i(x,z) \quad \text{Eq 9. 1}$$

$$\alpha_i(y)=\sum_{n=0}^{N-1}[A_n \sin(w_n y+\varphi_n)] \quad \text{Eq 9. 2}$$

$$\alpha_i(y)=\sum_{n=0}^{N-1}[A_n \cos(w_n y+\varphi_n)] \quad \text{Eq 9. 3}$$

where

A_n is the magnitude at specific frequency (w_n) from a statistical database;

w_n is the corresponding frequency;

y is the longitudinal position of a simulated member; and

φ_n is a random phase that is distributed uniformly over an interval [0 2π]

It should be noted that all of the spectra here are the absolute values from the Fourier transformation, and more details are available in Chapter 8.

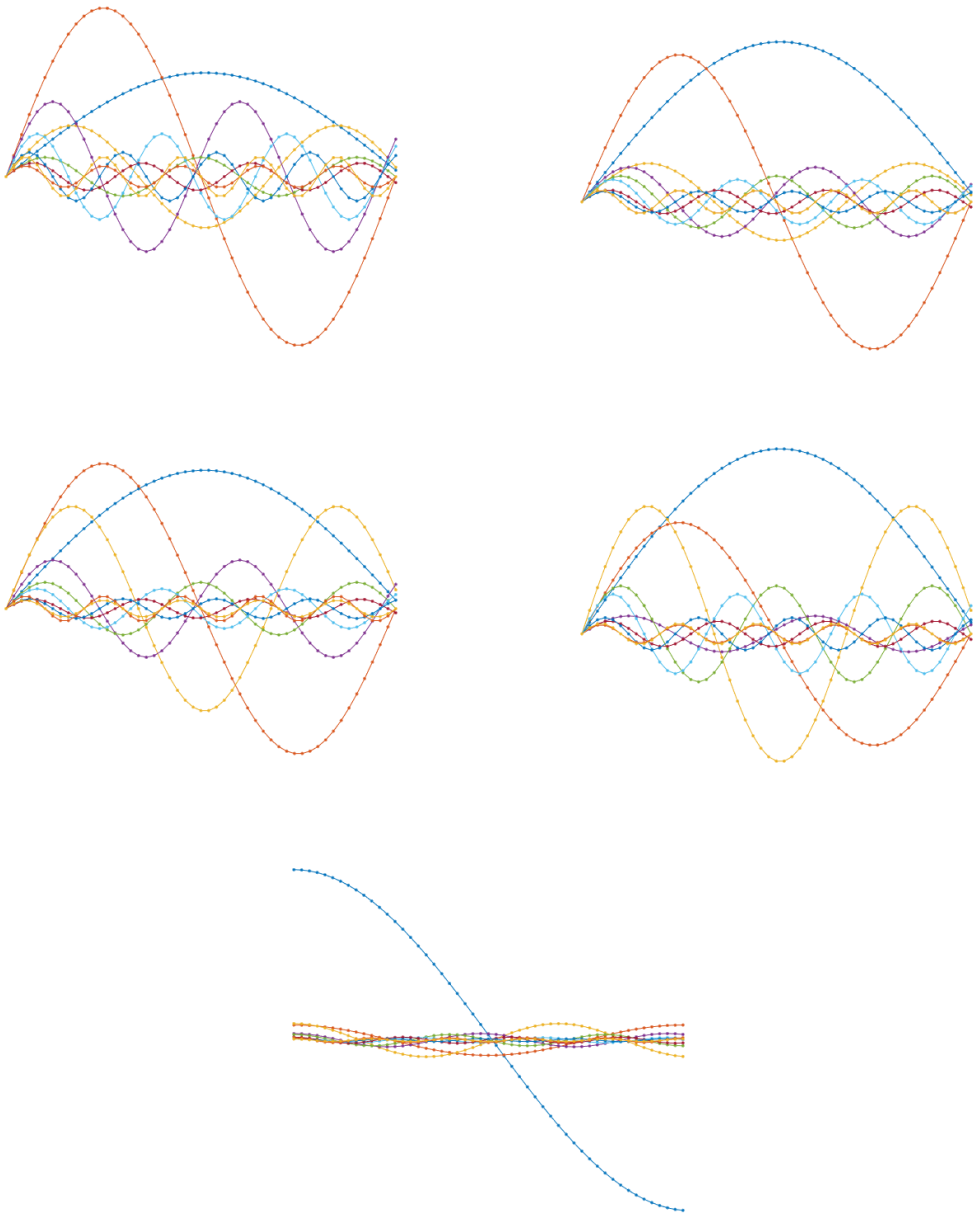

Figure 9. 7 Magnitudes combinations correspond to local, distortional, G1, G2, and G3 imperfections

As nodes with imperfections are obtained, all other procedures to establish a finite element model are similar to the procedures in the previous two sections, such as element definition, material properties, boundary conditions, and analysis method for defining the length of a specific arch.

9.2 Results and discussions

The three modeling methods described above were used for both the Z and C sections. The built-up sections were not included in this modeling due to the limited number of samples. The results of true geometry are presented in section 9.2.1, the traditional imperfection simulation is in section 9.2.2, and the 1D spectral imperfection simulation is in section 9.2.3. The discussion of each follows the presentations of the results.

9.2.1 Results of true-geometry models

Z

Ten Z sections were scanned and used for the true-geometry, finite-element modeling. Figures 9.7 - 9.10 show the typical models, where deformations are scaled automatically. Failures of Z sections typically started from the lip and the end with large distortion of the flange. Imperfect true geometry may contribute to the differences in the local deformations; the large, local imperfections shown in Figure 9.10 can lead to a distinct failure mode beyond expectation. Deformation modes of the models were taken from the step at 0.09 in of end displacement. Figure 9.11 shows that the corresponding load-displacement curve was unique when compared to the other three curves provided by models 1-3. Unlike the distortional failure mode, model 4 failed much earlier due to a small dent around the end of the specimen.

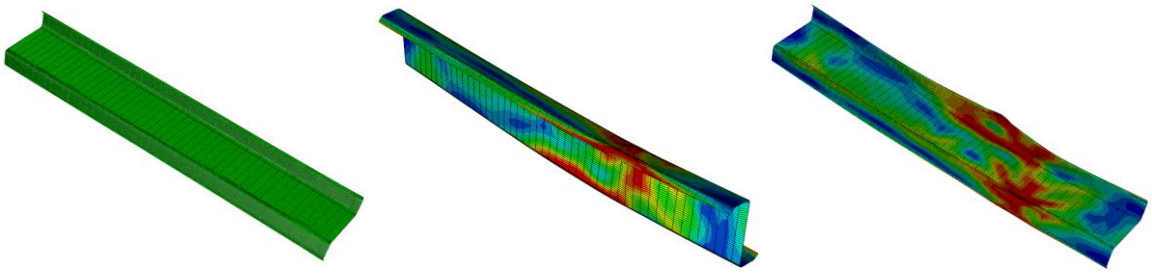

Figure 9. 8 Collapse modeling of model 1 at displacements 0.09 in. of a Z section: (a) pre-test model; (b) after-test model in view 1; (c) after-test model in view 2 (von-Mises stress).

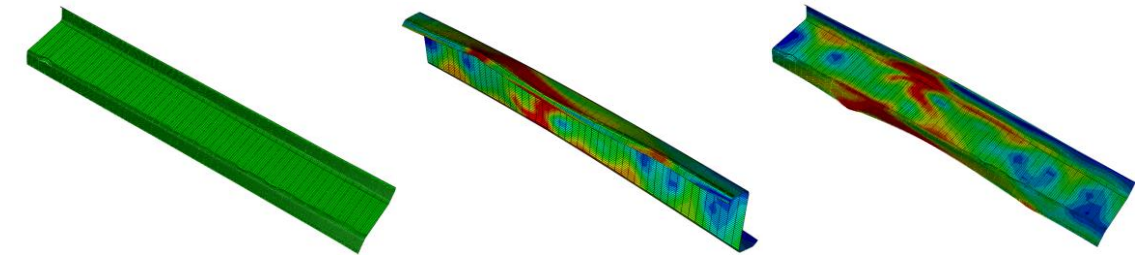

Figure 9. 9 Collapse modeling of model 2 at displacements 0.09 in. of a Z section: (a) pre-test model; (b) after-test model in view 1; (c) after-test model in view 2 (von-Mises stress).

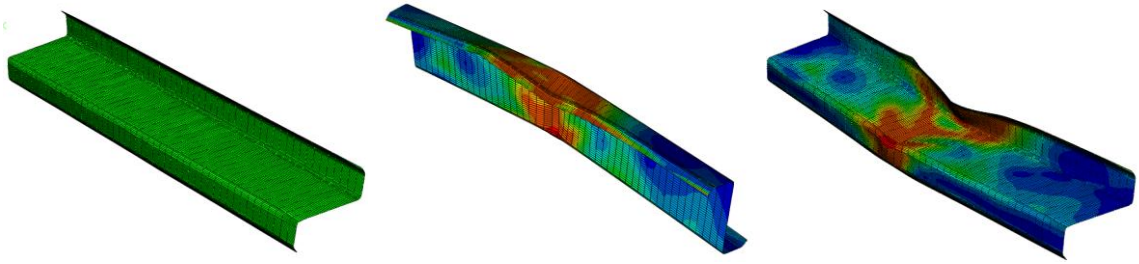

Figure 9. 10 Collapse modeling of model 3 at displacements 0.09 in. of a Z section: (a) pre-test model; (b) after-test model in view 1; (c) after-test model in view 2 (von-Mises stress).

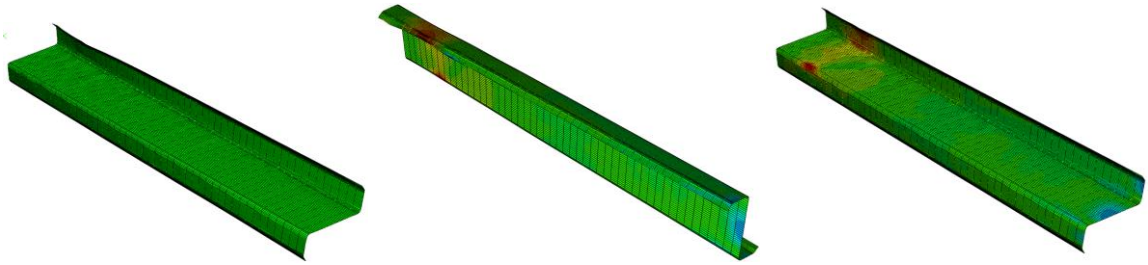

Figure 9. 11 Collapse modeling of model 1 at displacements 0.09 in. of a Z section: (a) pre-test model; (b) after-test model in view 1; (c) after-test model in view 2 (von-Mises stress).

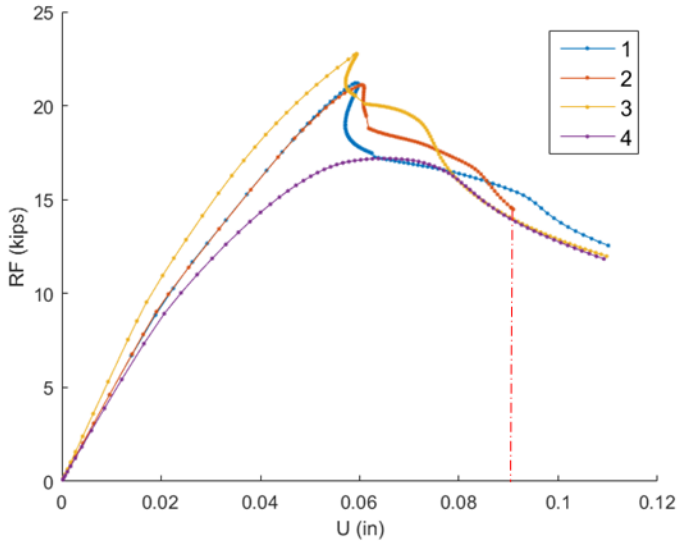

Figure 9. 12 Load-displacement curves correspond to collapse models 1-4 of Z sections

Curve 1, 2, 3, and 4 in the Figure 9. 12 correspond to model 1, 2, 3 and 4 of true geometries of Z sections as shown in Figure 9. 8 to Figure 9. 11. These curves show us that stiffness of models are varied, same to the peak loads.

C (362S162-60)

Even though the failure shapes were slightly different, all four of the models shown in Figures 9.13 - 9.16 failed in lip buckling, which eventually resulted in collapse. The shapes of the deformations were extracted from the step at 0.3 in of end displacement. The load-displacement curves shown in Figure 9.17 are similar to those for Z. The curves of all four models were similar, but minor differences were apparent in the shapes of the deformations in the post-buckling stage. Directions and positions of deformation along the specimens varied among the specimens.

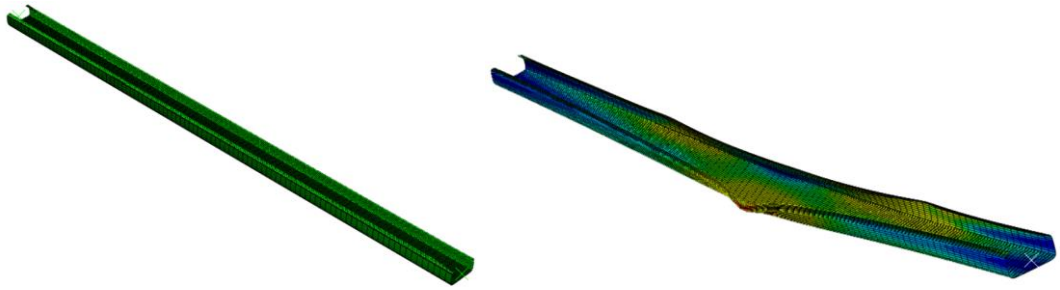

Figure 9. 13 Collapse modeling of model 1 at displacement 0.3 in of a C section (362S162-68): (a) pre-test model; (b) after-test model (von-Mises stress).

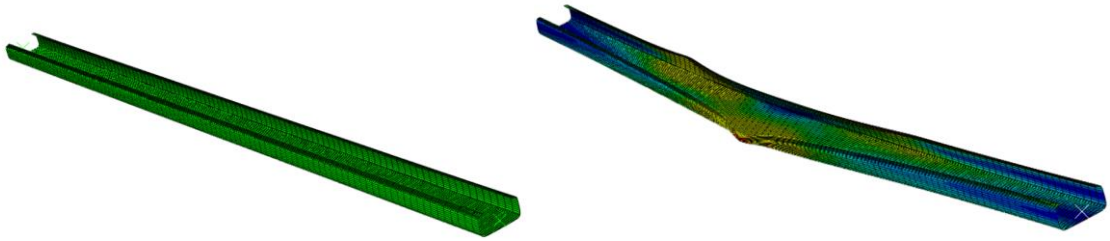

Figure 9. 14 Collapse modeling of model 2 at displacement 0.3 in of a C section (362S162-68)): (a) pre-test model; (b) after-test model (von-Mises stress).

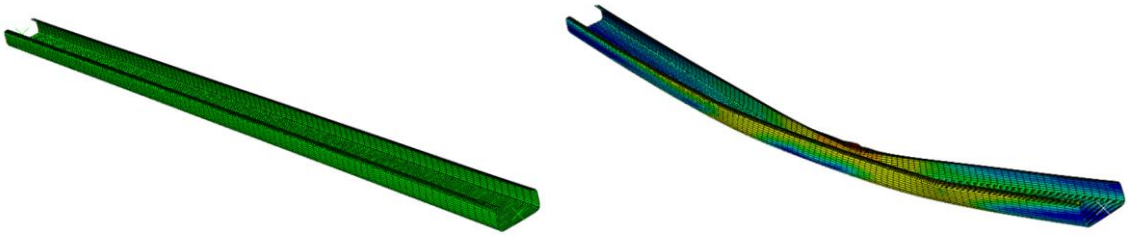

Figure 9. 15 Collapse modeling of model 3 at displacement 0.3 in of a C section (362S162-68)): (a) pre-test model; (b) after-test model (von-Mises stress).

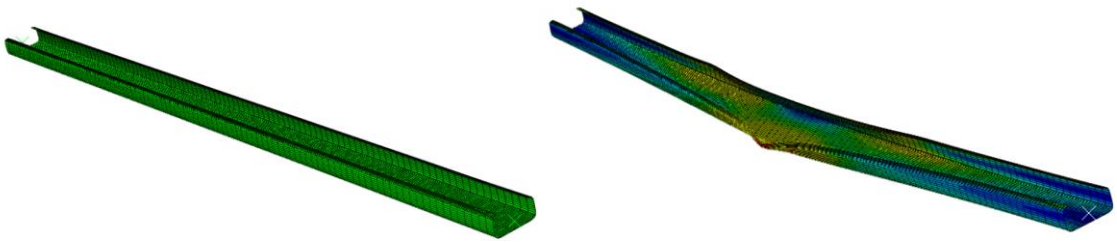

Figure 9. 16 Collapse modeling of model 4 at displacement 0.3 in. of a C section (362S162-68)): (a) pre-test model; (b) after-test model (von-Mises stress).

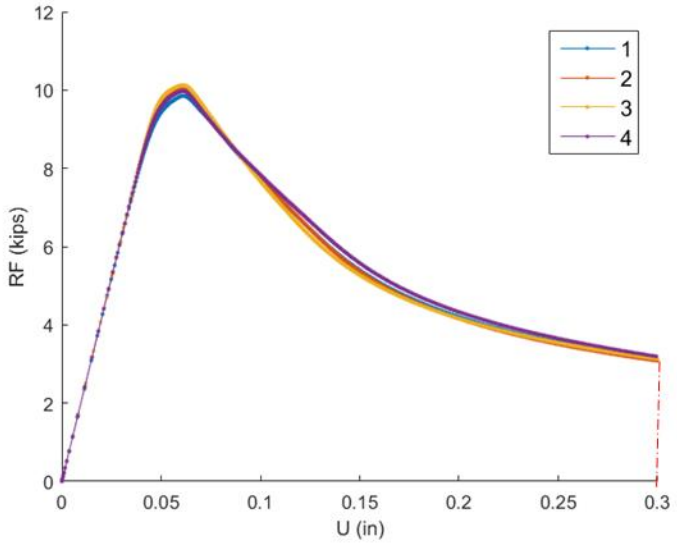

Figure 9. 17 Load-displacement curves correspond to collapse models 1-4. of a C section (362S162-68)

C (600S137-54)

Type 600S137-54 specimens had similar shaped failure modes as 362S162-68, with lip buckling at the beginning. As shown in Figure 9. 18 - 9.21, its catastrophic deformation resulted from global buckling along its major axis, where deformation shapes were extracted from the step at 0.35 in of end displacements. Figure 9. 22 shows that the failure curves have obvious differences in the peak stage and the post-buckling stage.

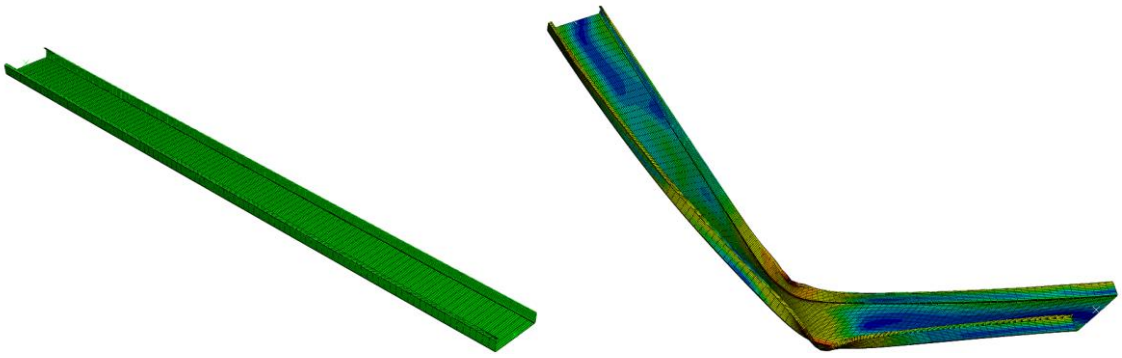
Figure 9. 18 Collapse modeling of model 1 at displacement 0.35 in. of a C section (600S137-54)): (a) pre-test model; (b) after-test model (von-Mises stress).

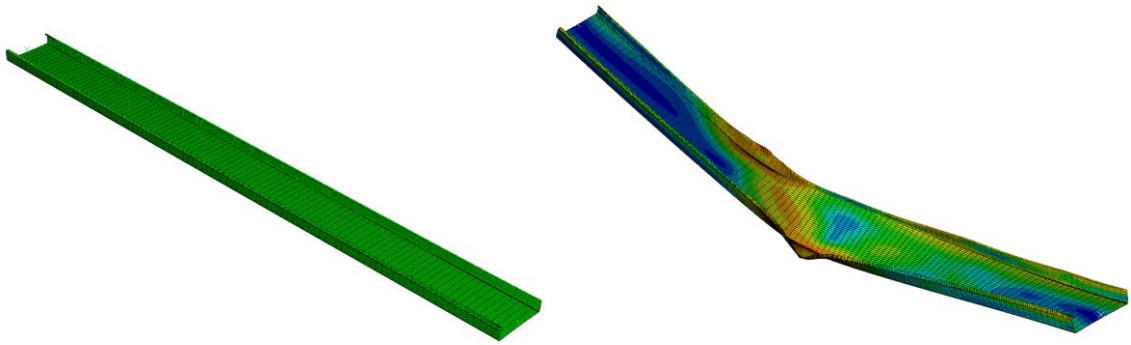

Figure 9. 19 Collapse modeling of model 2 at displacement 0.35 in. of a C section (600S137-54)): (a) pre-test model; (b) after-test model (von-Mises stress).

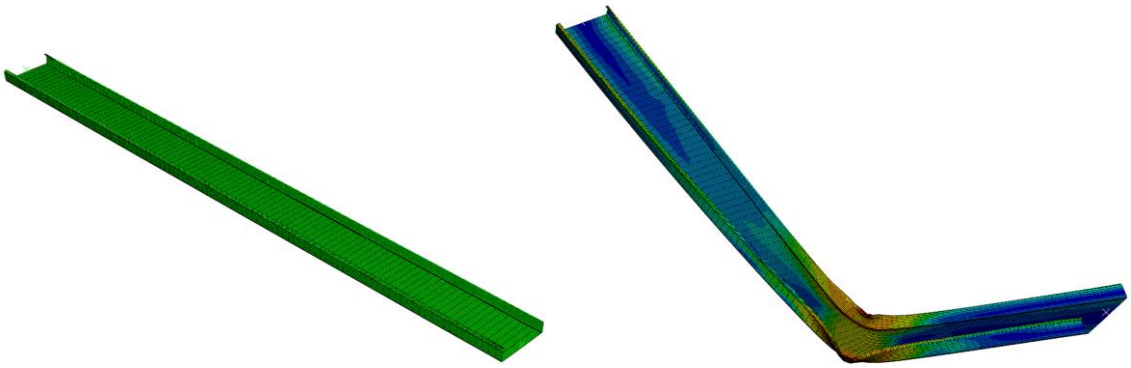

Figure 9. 20 Collapse modeling of model 3 at displacement 0.35 in. of a C section (600S137-54) (a) pre-test model; (b) after-test model (von-Mises stress).

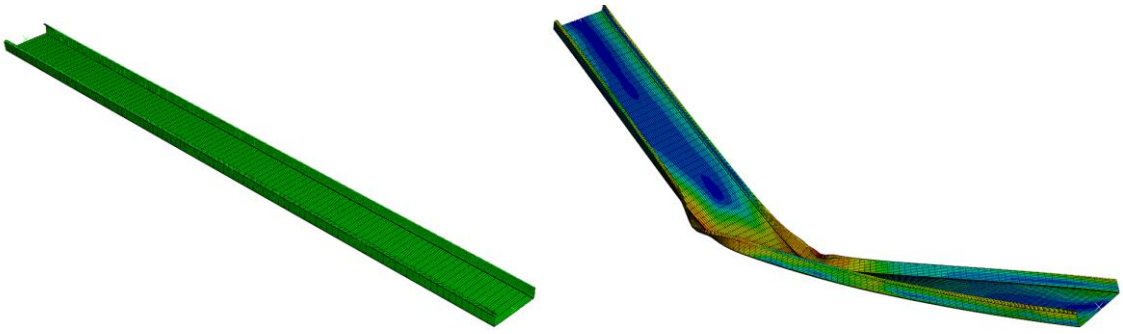

Figure 9. 21 Collapse modeling of model 4 at displacement 0.35 in. of a C section (600S137-54) (a) pre-test model; (b) after-test model(von-Mises stress).

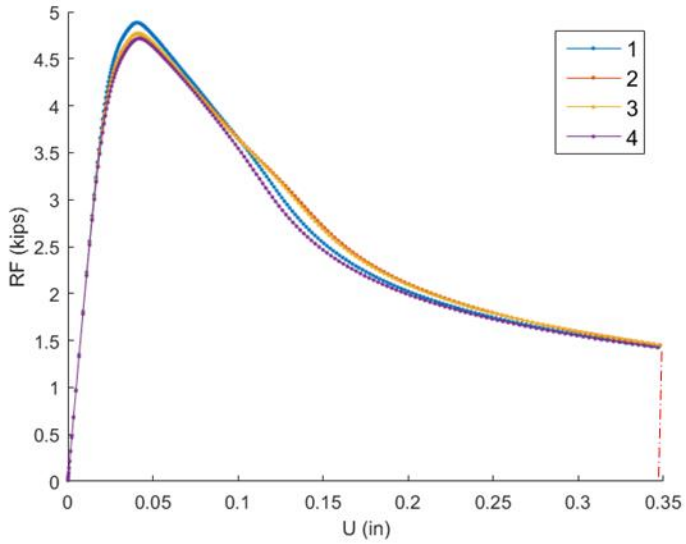

Figure 9. 22 Load-displacement curves correspond to collapse models 1-4 of a C section (600S137-54)

9.2.2 Results of simulated models using traditional representation

Single mode imperfections are simulated one by one. It is interesting to find dominant imperfection modes when compared to the true geometry results. Combinations of imperfection modes are not included in this dissertation, but will be part of future work.

Z

Five characteristic imperfection modes were simulated in traditional representation, i.e., single sinusoidal components were assigned to corresponding imperfection modes. The magnitudes of the imperfections were taken from the statistical summaries of conventional imperfections. Figure 9. 23 - 9.27 show the results. Failures occurred from five different modes, but the main causes of failure were lip buckling and distortional buckling. However, the deformation shapes for the two main causes were very different. Failure Mode 1, known as local buckling, occurs in lip buckling, and the shape of the failure indicates both lip buckling and local buckling. Failure Mode 2, known as distortional buckling, occurs in distortional buckling, and the shape approaches the shape of distortional buckling. The two ends of the mode 2 model are critical, and they are marked in red

colors. Imperfections of mode 3 and mode 4 have similar failures, but the shapes are different. Even though the imperfection in mode 5 was large, the model still failed in a lip deformation that was accompanied by distortional buckling.

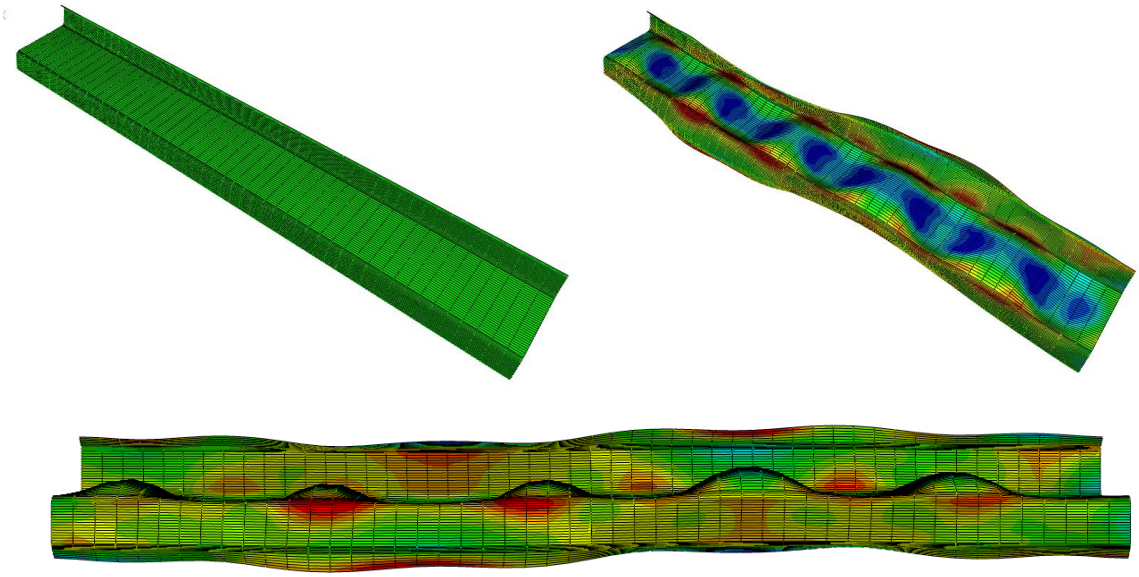

Figure 9. 23 Collapse modeling of mode 1 of Z in traditional representation

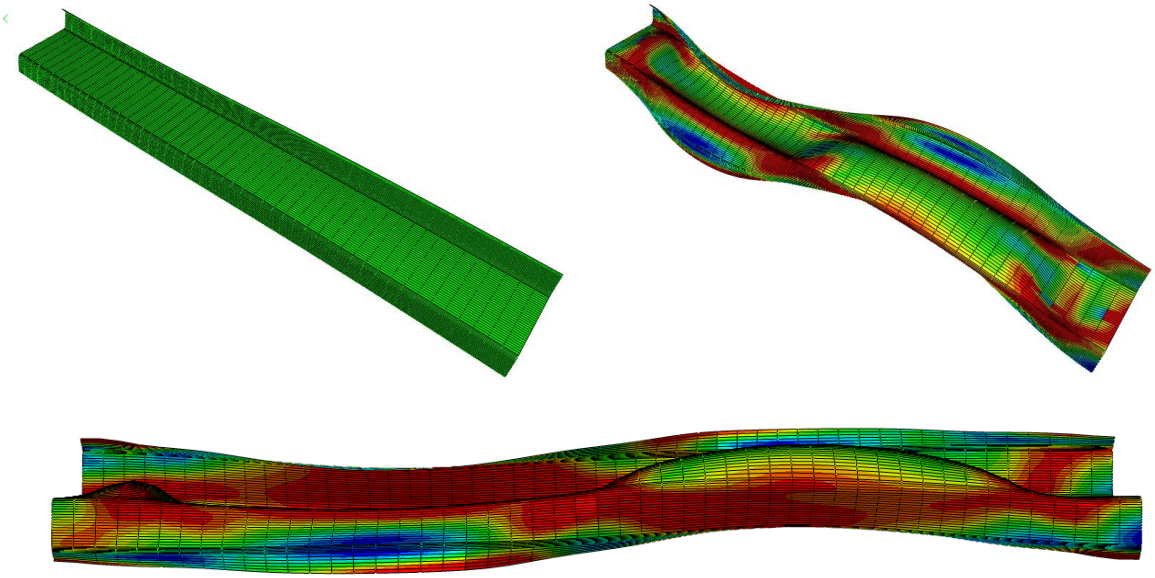

Figure 9. 24 Collapse modeling of mode 2 of Z in traditional representation

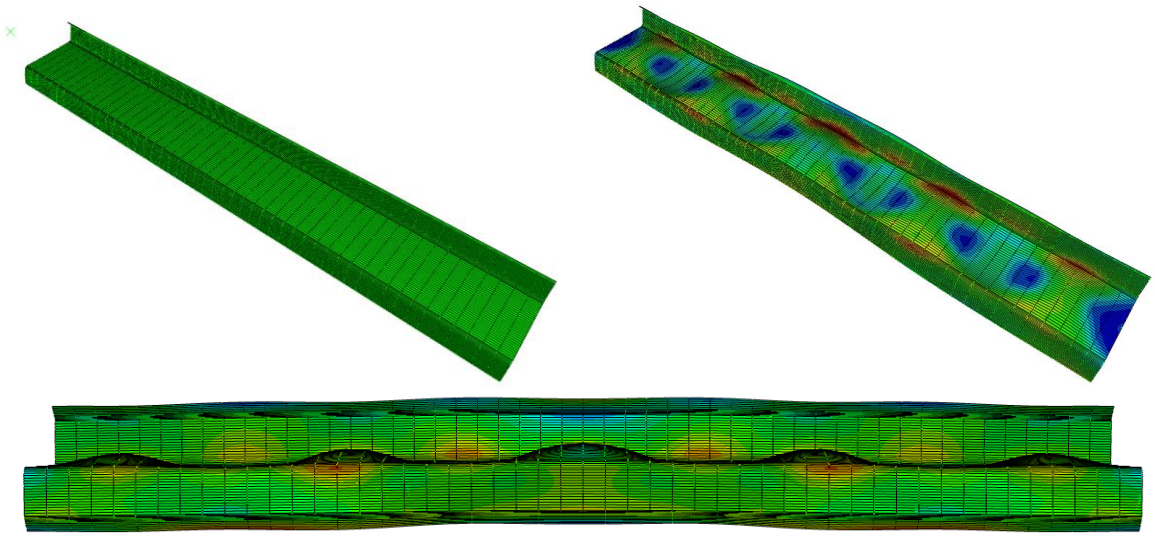

Figure 9. 25 Collapse modeling of mode 3 of Z in traditional representation

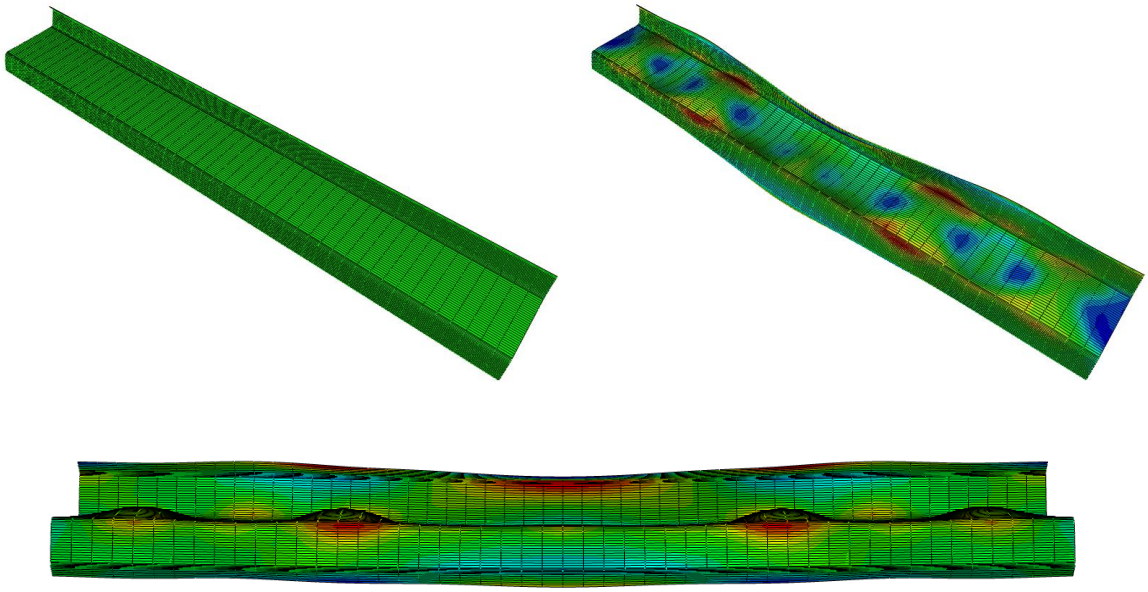

Figure 9. 26 Collapse modeling of mode 4 of Z in traditional representation

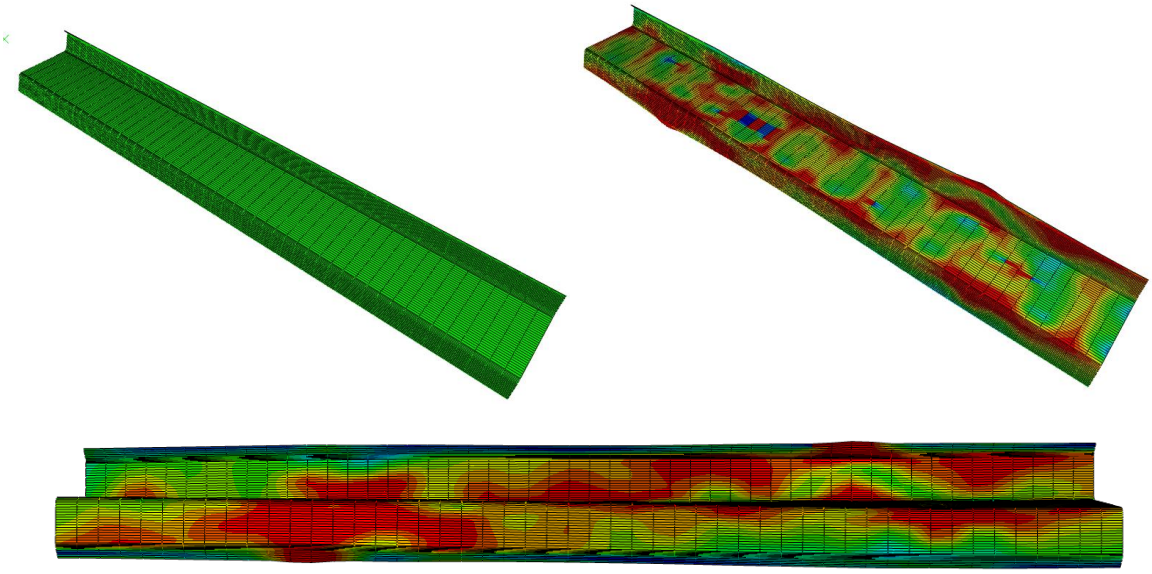

Figure 9. 27 Collapse modeling of mode 5 of Z in traditional representation

C (362S162-68)

Conventional imperfections seem to make no contribution to the failures of C sections (362S162-68), but they did affect the shapes of the failures. Models with mode imperfections fail in flexure buckling along their minor axis, with the exception of mode 5. Figure 9. 28 shows that the deformation contains local buckling along the specimen, and it also can be observed from the web's waviness. Figure 9. 29 shows that the failure of the model started with distortion of the lips, but failure eventually occurred in global buckling. The modeling of imperfections with mode 5 was impressive. A torsion failure occurred in this model.

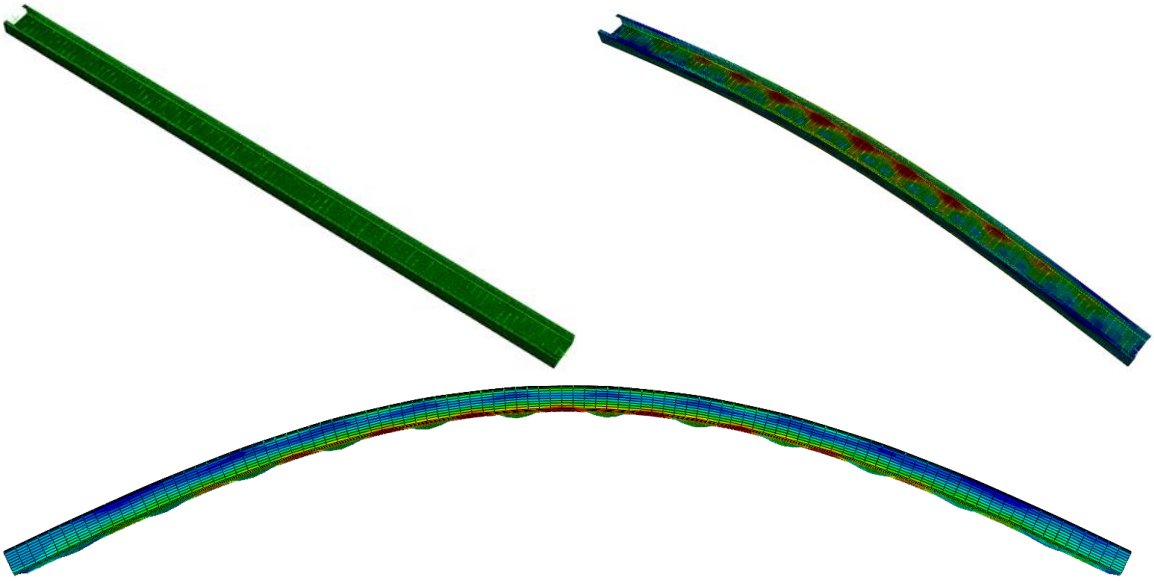

Figure 9. 28 Collapse modeling of mode 1 of C (362S162-69) in traditional representation

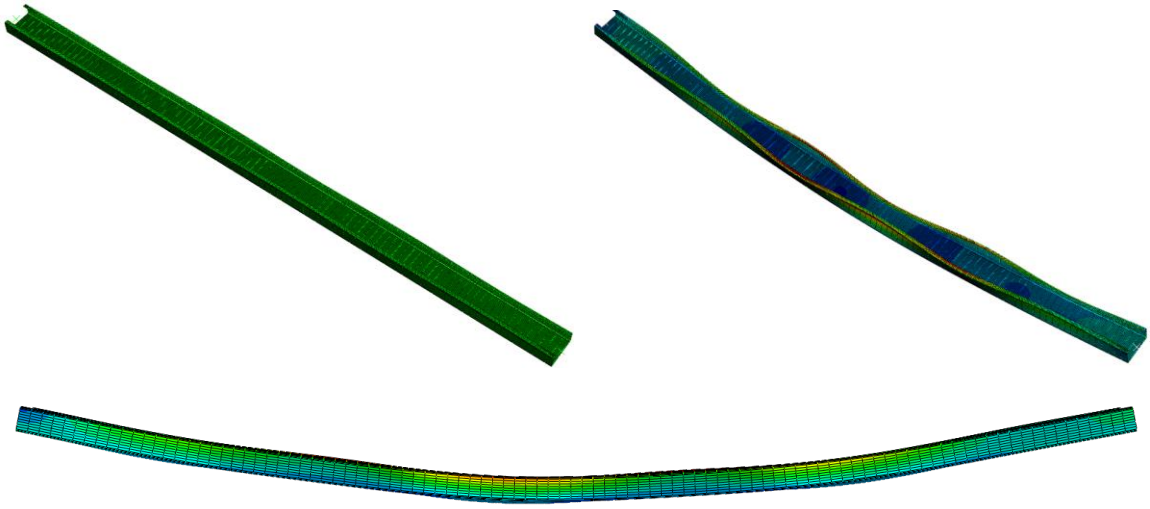

Figure 9. 29 Collapse modeling of mode 2 of C (362S162-69) in traditional representation

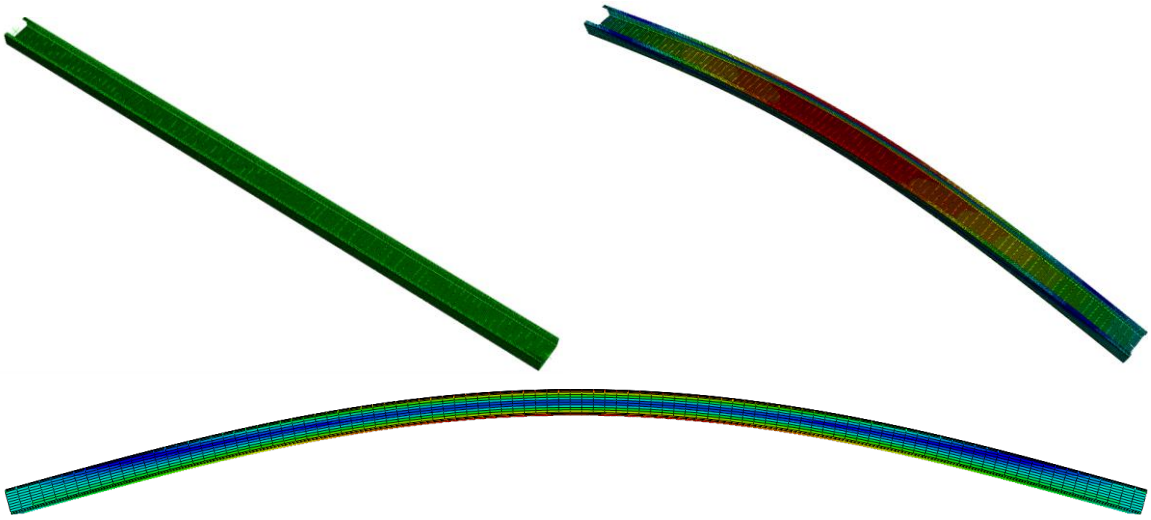

Figure 9. 30 Collapse modeling of mode 3 of C (362S162-69) in traditional representation

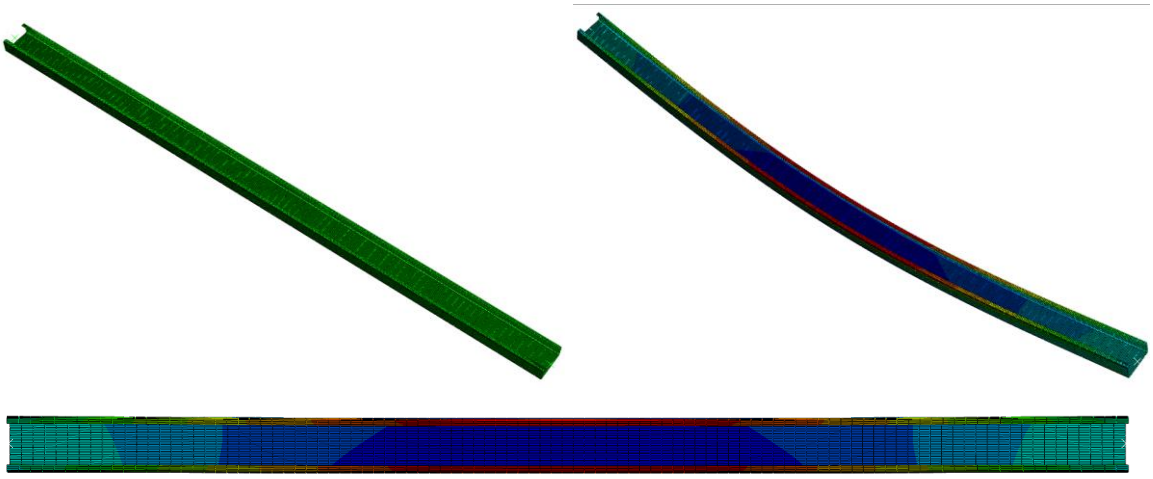

Figure 9. 31 Collapse modeling of mode 4 of C (362S162-69) in traditional representation

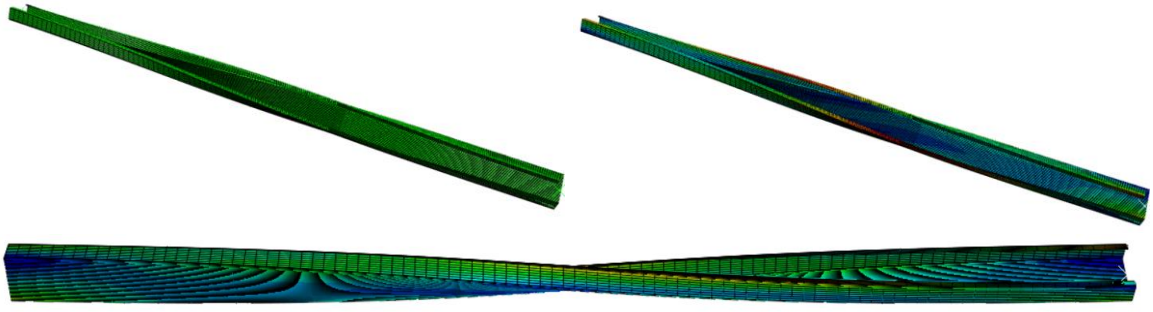

Figure 9. 32 Collapse modeling of mode 5 of C (362S162-69) in traditional representation

C (600S137-54)

Similar to 362S162-68, conventional imperfections did not contribute to the determination of modeling failures of specimens; rather they affected the shapes of the failures. The models with imperfections failed in global buckling along the minor axis except for mode 5. Figure 9. 33 shows that the deformation contained local buckling along the specimen, which also can be observed from the web's waviness. Mode 5 of imperfection of 600S137-54 had a result that was similar to that of 362S162-68, in which torsion failure was dominant.

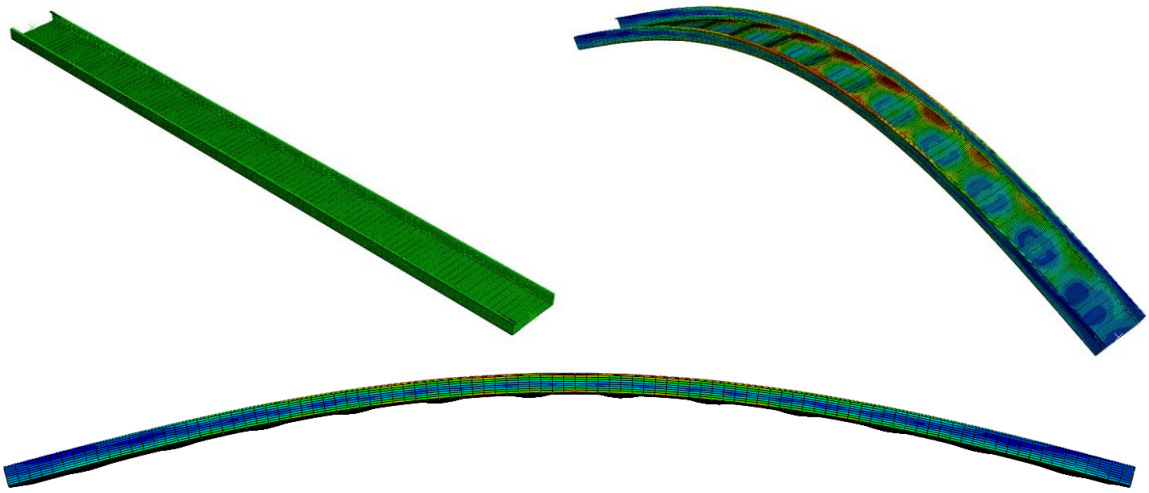

Figure 9. 33 Collapse modeling of mode 1 of C (600S137-54) in traditional representation

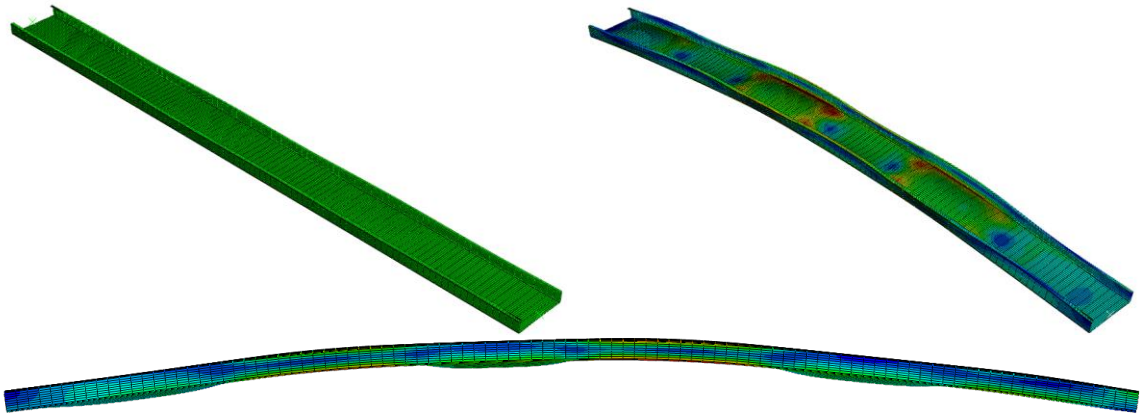

Figure 9. 34 Collapse modeling of mode 2 of C (600S137-54) in traditional representation

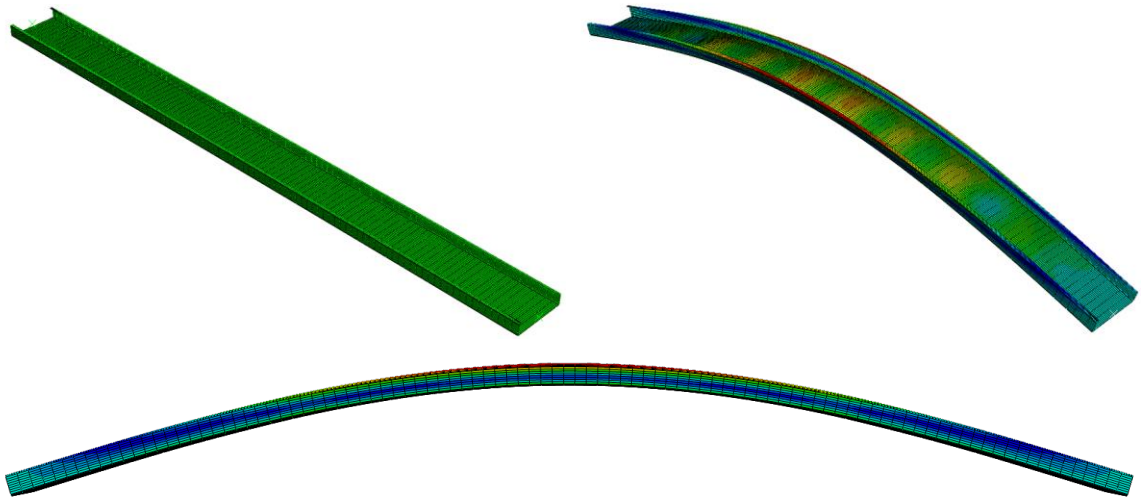

Figure 9. 35 Collapse modeling of mode 3 of C (600S137-54) in traditional representation

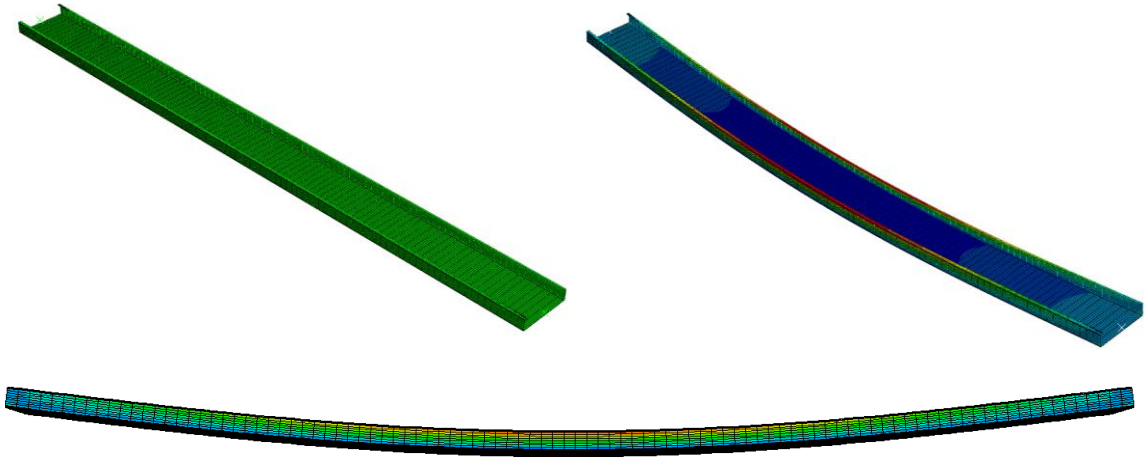

Figure 9. 36 Collapse modeling of mode 4 of C (600S137-54) in traditional representation

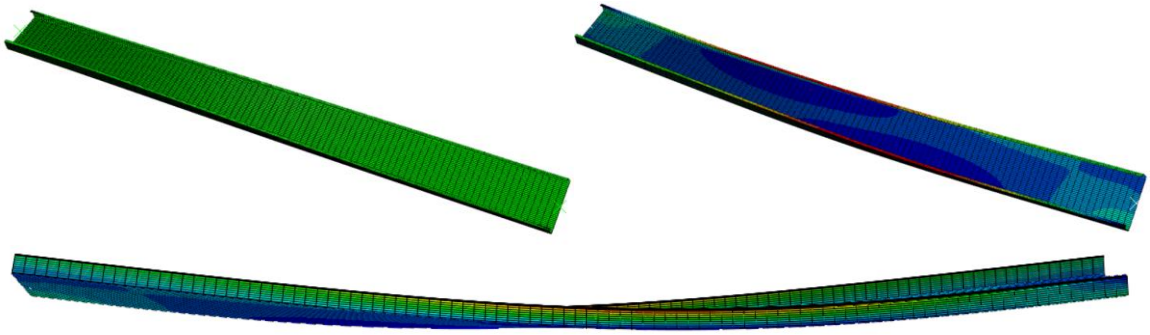

Figure 9. 37 Collapse modeling of mode 5 of C (600S137-54) in traditional representation

9.2.3 Results of simulated models using 1D spectral representation

Z

Compared to the traditional representation, the 1D spectral representation provides different results, especially with respect to the shapes of the modes. The most differences occurred in modes 3 and 4, where large deformations of the lips contribute to the ultimate failure of the model.

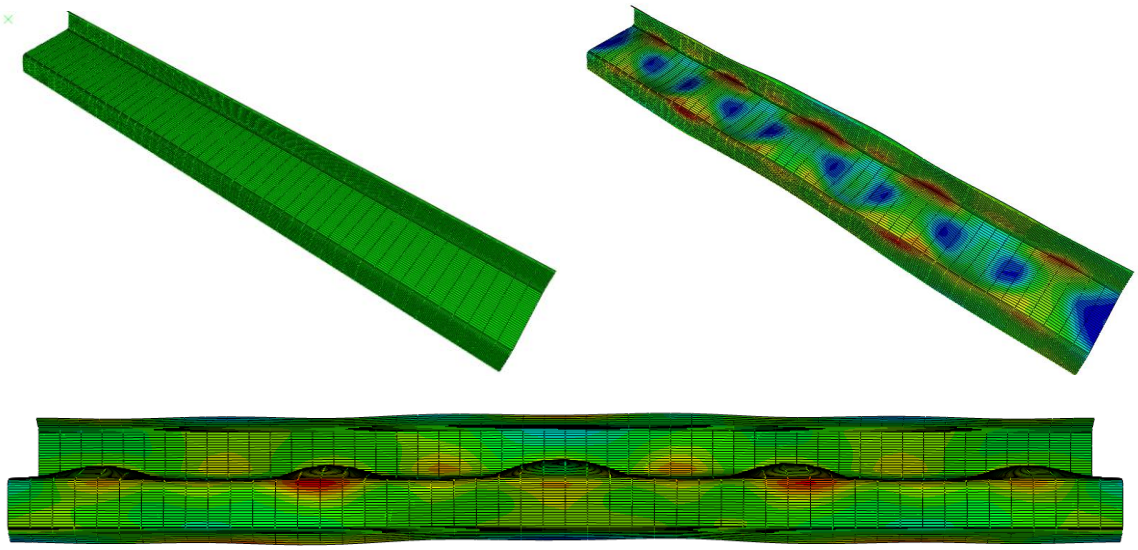

Figure 9. 38 Collapse modeling of mode 1 of Z in 1D spectral representation

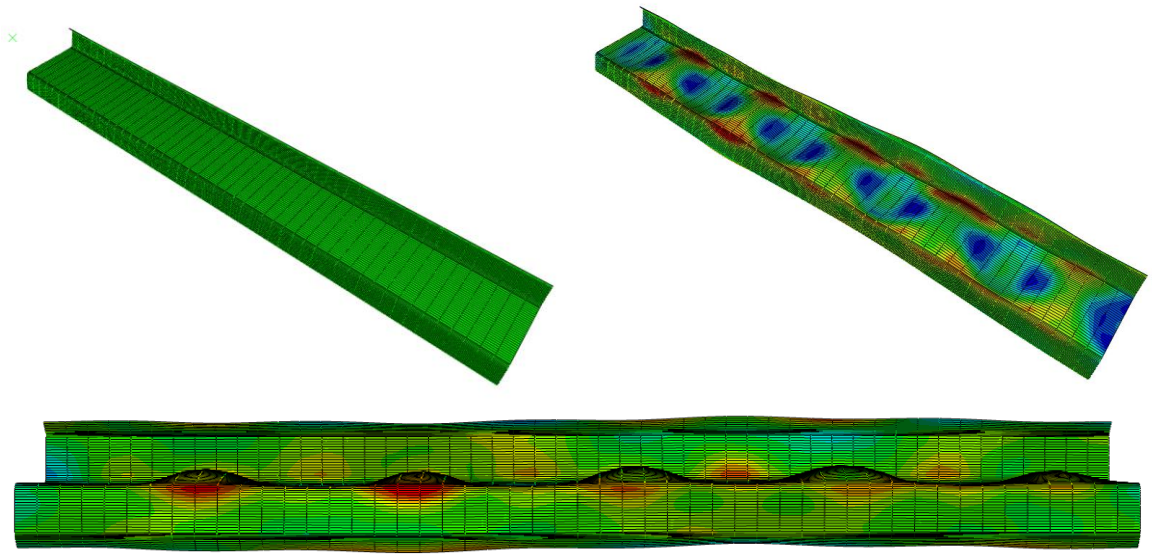

Figure 9. 39 Collapse modeling of mode 2 of Z in 1D spectral representation

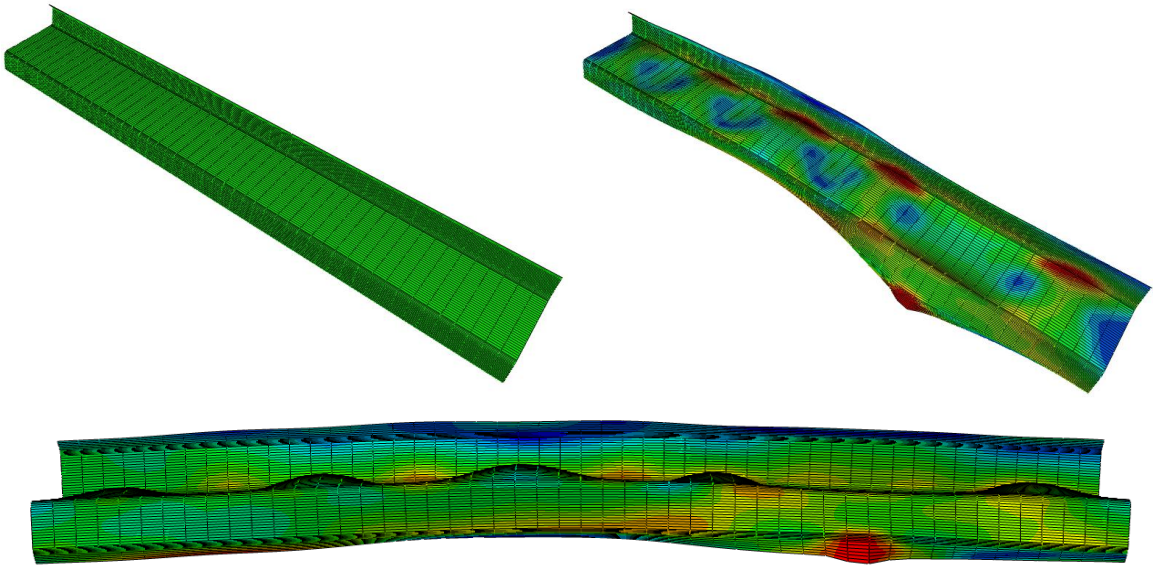

Figure 9. 40 Collapse modeling of mode 3 of Z in 1D spectral representation

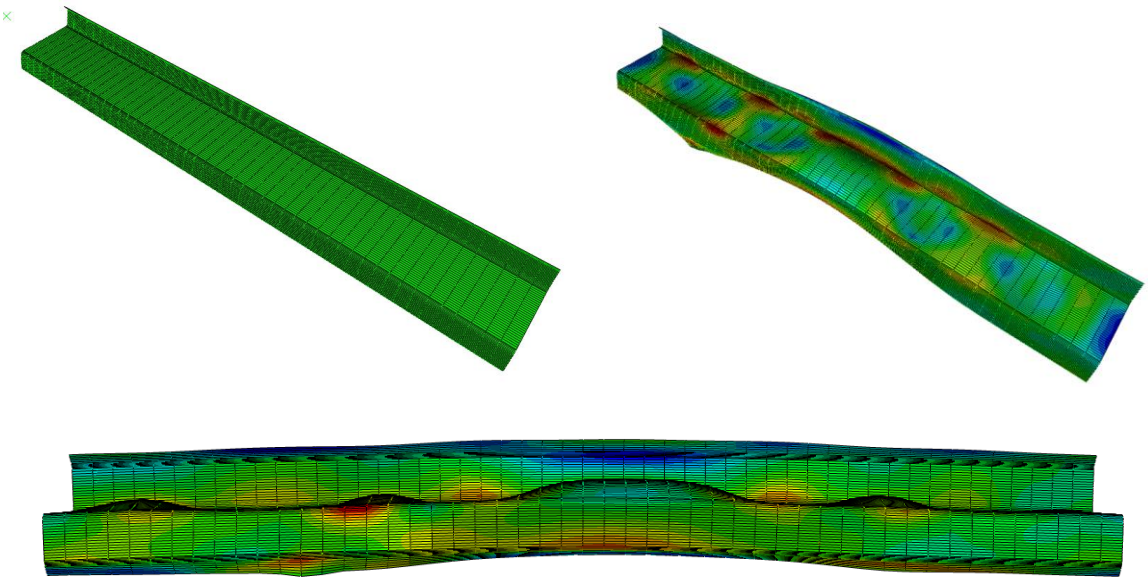

Figure 9. 41 Collapse modeling of mode 4 of Z in 1D spectral representation

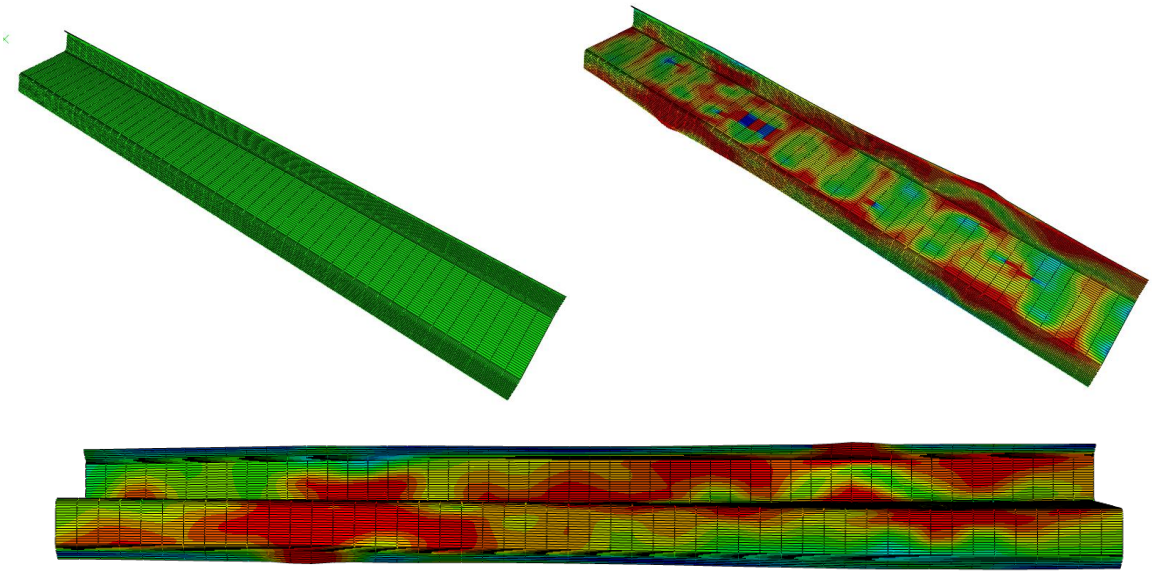

Figure 9. 42 Collapse modeling of mode 5 of Z in 1D spectral representation

C (362S162-68)

For 362S162-68, the 1D spectral approach was used to simulate its imperfections for collapse modeling. However, the imperfections of 362S162-68 did not contribute to the failure shapes or the

failure modes. All models with mode 1-5 imperfections finally failed in flexure buckling along their minor axes.

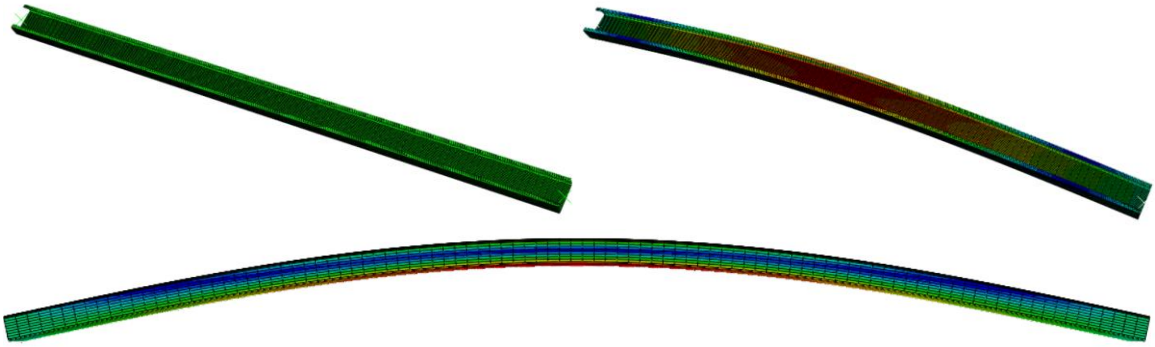

Figure 9. 43 Collapse modeling of mode 1 of C (362S162-68) in 1D spectral representation

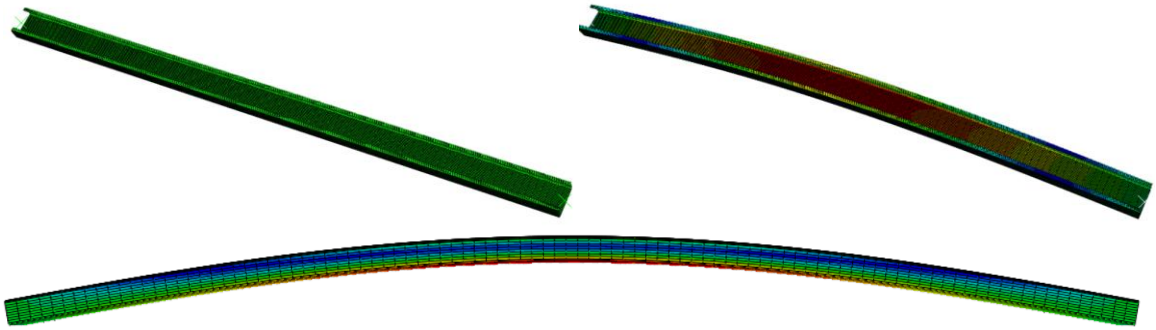

Figure 9. 44 Collapse modeling of mode 2 of C (362S162-68) in 1D spectral representation

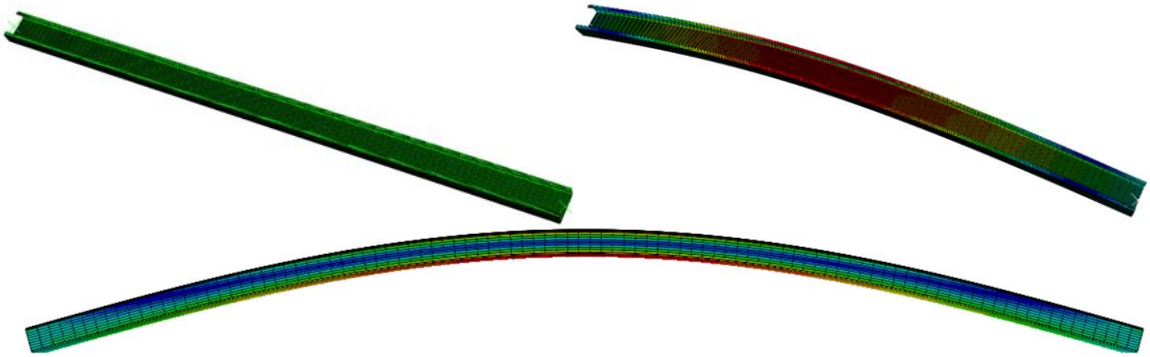

Figure 9. 45 Collapse modeling of mode 3 of C (362S162-68) in 1D spectral representation

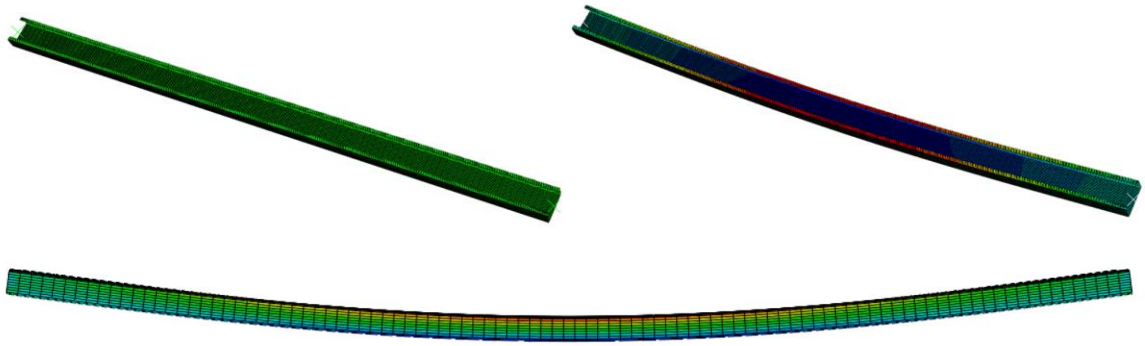

Figure 9. 46 Collapse modeling of mode 4 of C (362S162-68) in 1D spectral representation

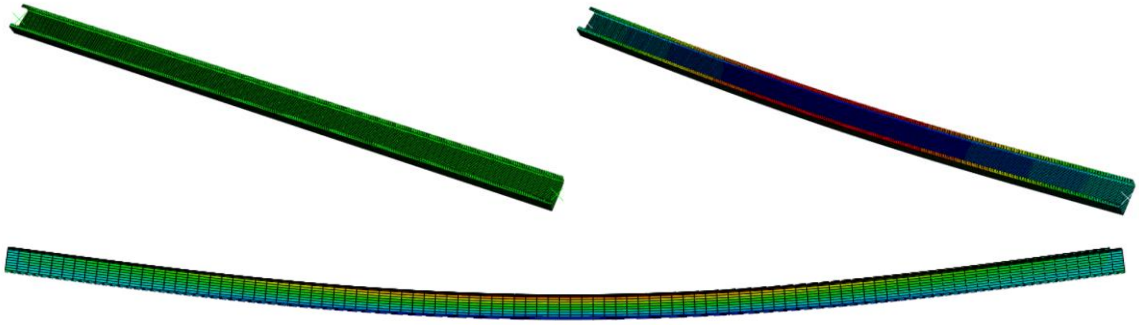

Figure 9. 47 Collapse modeling of mode 5 of C (362S162-68) in 1D spectral representation

C (600S137-54)

Both the failure modes and shapes of 600S137-54 were very similar to those of 362S162-68. The only differences were observed for the web deformation. These models still fail in global buckling, while imperfections may contribute to some local deformations, as shown in Figure 9. 48 - 9.52. An interesting finding was the shapes of modes 4 and 5 in the collapse model; they were very similar even though the types of imperfection were different.

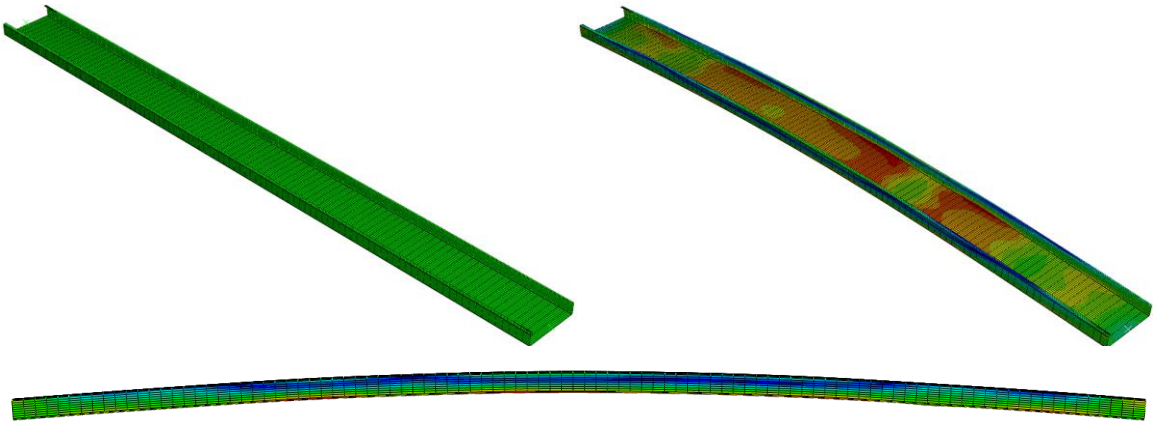

Figure 9. 48 Collapse modeling of mode 1 of C (600S137-54) in 1D spectral representation

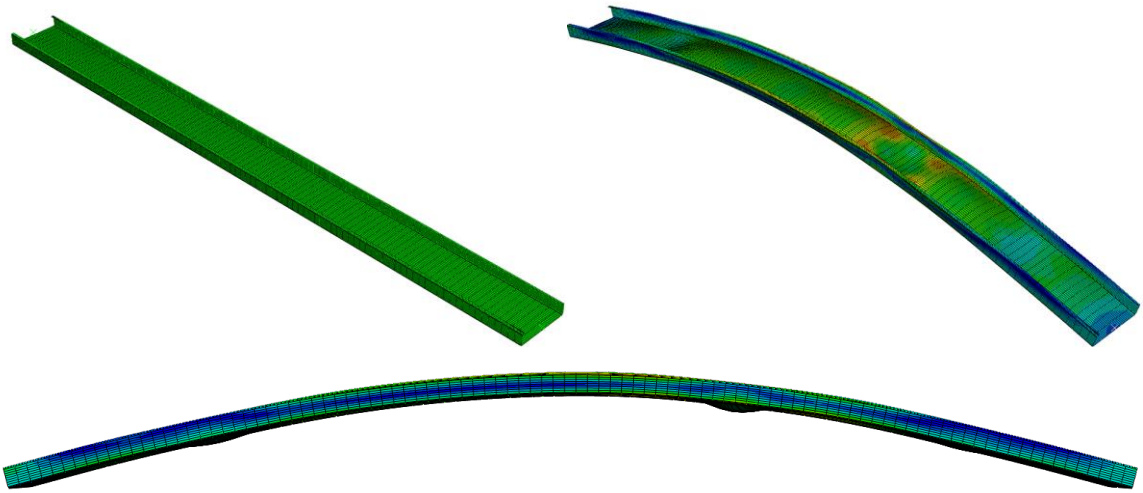

Figure 9. 49 Collapse modeling of mode 2 of C (600S137-54) in 1D spectral representation

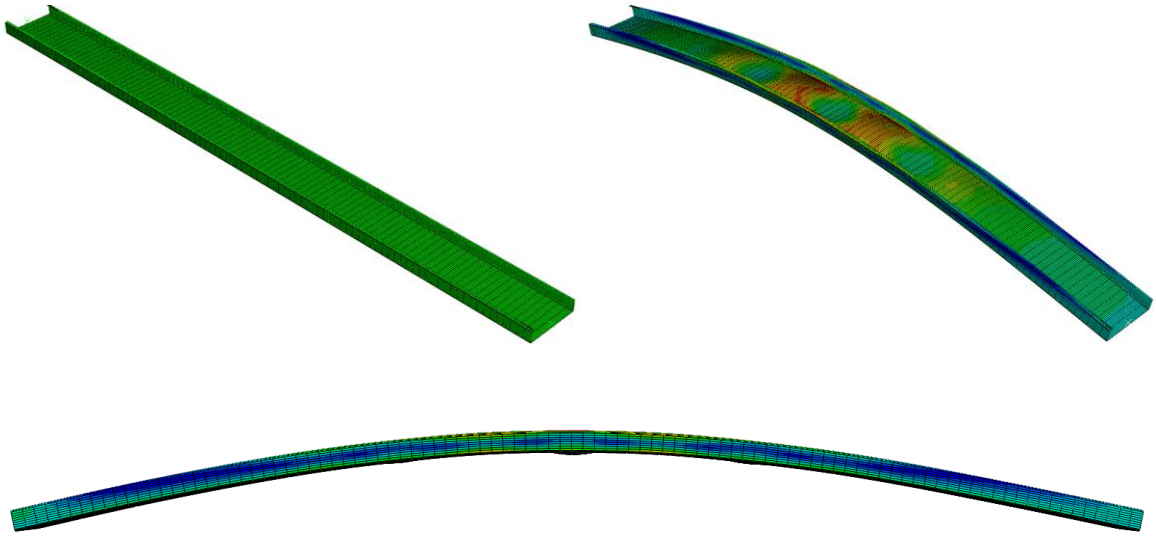

Figure 9. 50 Collapse modeling of mode 3 of C (600S137-54) in 1D spectral representation

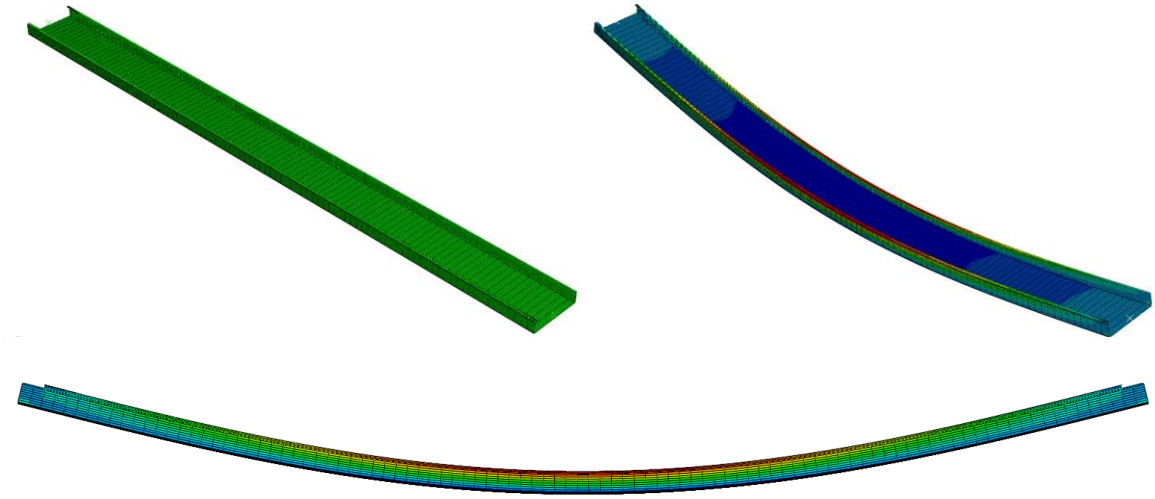

Figure 9. 51 Collapse modeling of mode 4 of C (600S137-54) in 1D spectral representation

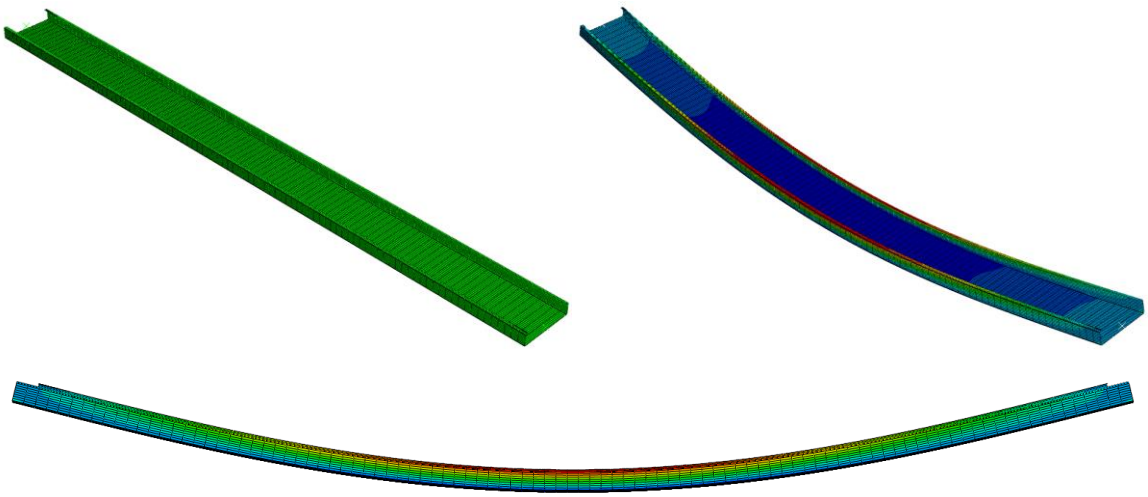

Figure 9. 52 Collapse modeling of mode 5 of C (600S137-54) in 1D spectral representation

9.2.4 Discussion

Peak load from two representations are compared regarding to three types of section, i.e. 700Z225-60, 362S162-68, and 600S137-54. The failure mode shapes from two methods are very different. However, when compared to its peak load, there aren't much difference. Local imperfections have difference between traditional and 1D spectral approach are 6%, 28.1%, and 27% with respect to 700Z225-60, 362S162-68, and 600S137-54; distortional imperfections are 7.6%, 6.3%, and 3.8%, G1 are 3.2%, 3%, and 3.12%; G2 are 4.03,0.1%, and 0.0%; and G3 are 0.01%, 20.49%, and 1.25%.

In comparing the differences, the Z section, which was 4 ft long, seemed to be more sensitive to local and distortional imperfections, while the C section (362S162-68) was more sensitive to local and twist imperfections, and the C section (600S137-54) was more sensitive to local imperfections. Overall, the simulated model with the 1D spectral approach had a higher load capacity. The traditional approach may have been too conservative. These conclusions may change with changes in the the length of specimens, magnitudes of imperfections, and loading conditions. Additional studies should be conducted to compare the traditional approach and the 1D spectral approach with different combinations of imperfection modes and additional types of specimens.

Table 9. 3 Load capacity from collapse modeling simulated with median imperfections from two methods

Ultimate load (kips)	Traditional Approach			1D Spectral Approach		
Single-mode imperf.	700Z225-60	362S162-68	600S137-54	700Z225-60	362S162-68	600S137-54
Local	27.60	7.67	4.06	25.85	9.83	5.16
Dist.	25.37	9.49	4.86	27.30	10.08	5.05
G1	24.62	9.69	4.81	25.41	9.98	4.66
G2	23.98	10.38	5.88	24.94	10.39	5.88
G3	21.14	8.62	5.80	21.14	10.39	5.88

Comparisons were made for the true geometry and single mode simulation via the 1D spectral approach, where the dominant mode of imperfections was determined by comparing the ultimate loads from the models. Figure 9. 53 and 9.54 show the comparisons of the results of the Z sections. Mode 5 imperfections, i.e., twist (G3), were dominant among all of the imperfection modes in the Z sections. However, Figure 9.54 shows that the displacement-load curves are different. The initial stiffness between the two curves differed slightly, considering that the lack of other mode imperfections may affect a member's stiffness.

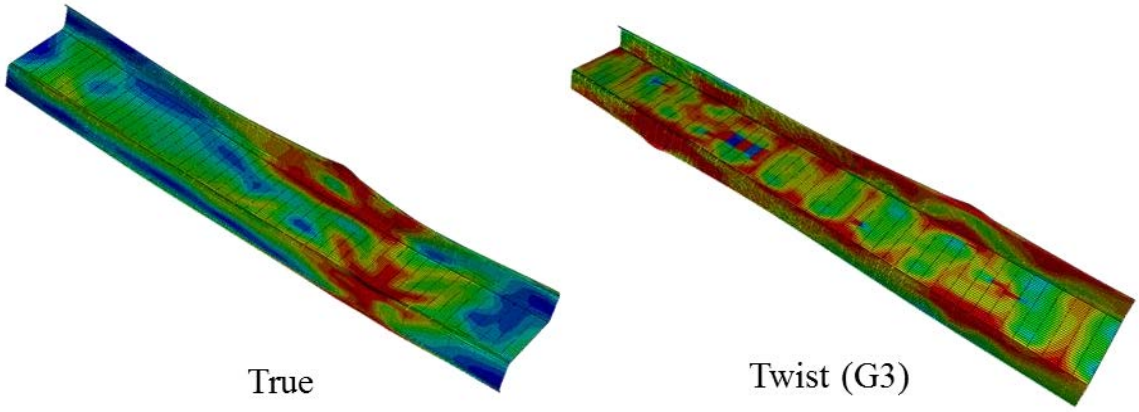

Figure 9. 53 Comparisons between true geometry and model in 1D spectral representation of Z sections at the peak load

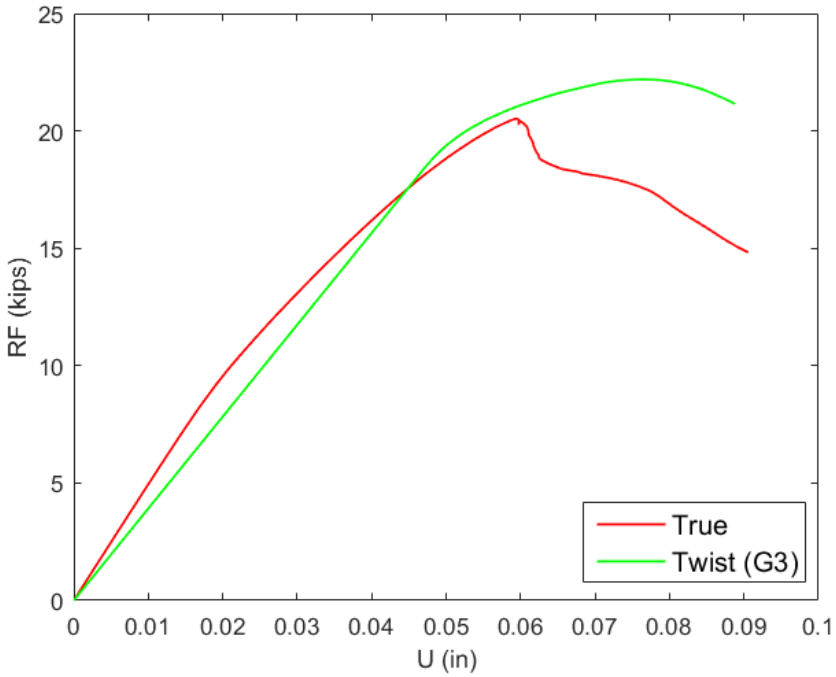

Figure 9. 54 Load-displacement curves of true geometry and model in 1D spectral representation of Z sections

Similarly, two C sections, 362S162-68 and 600S137-54, were compared. Figure 9. 55 and Figure 9. 57 show that the distortional mode imperfection and the bow imperfection were dominant in the simulated model of 362S162-68 and of 600S13-54, respectively. Load-displacement curves of 362S162-68 showed that the initial stiffness of the two curves had a smaller difference than those of the Z sections. However, the model with distortional-mode imperfections showed an unusual phenomenon in the post-buckling stage, i.e., the curve stayed almost horizontal in a long displacement, as shown in Figure 9. 56. Load-displacement curves of 600S137-54 in Figure 9. 58 show that there was a huge difference between the two models in the post-buckling stage.

All of these comparisons show that load capacity may be determined by a single, dominant mode. However, deformation shapes and post-buckling behaviors may require combinations of mode imperfections so that predictions can be made accurately.

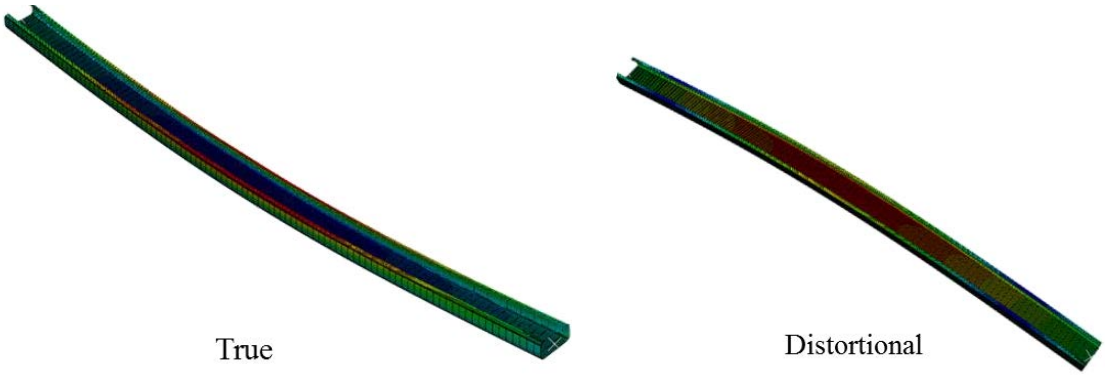

Figure 9. 55 Comparisons between true geometry and model in 1D spectral representation of C sections (362S162-68) at the peak load

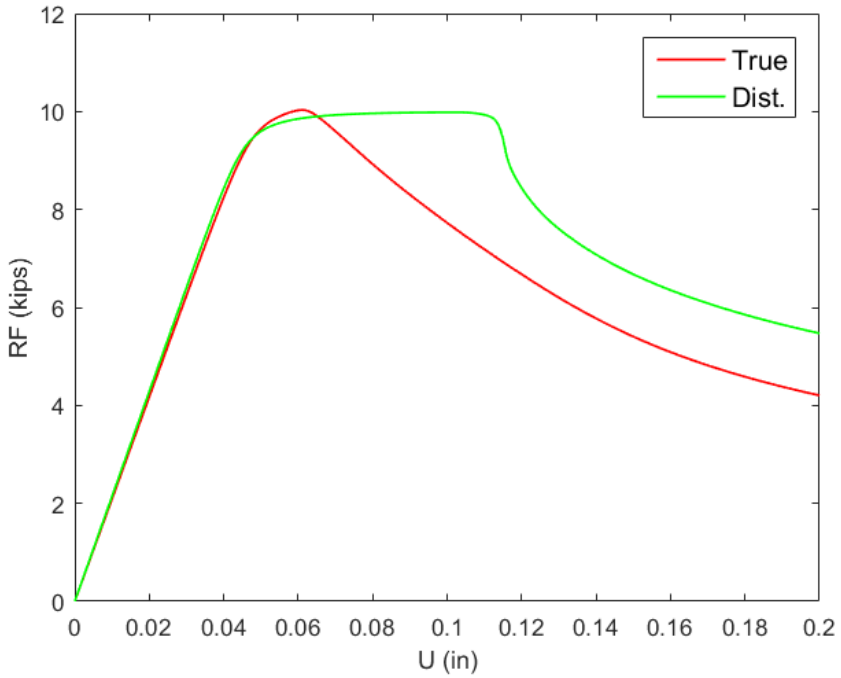

Figure 9. 56 Load-displacement curves of true geometry and model in 1D spectral representation of C sections (362S162-68)

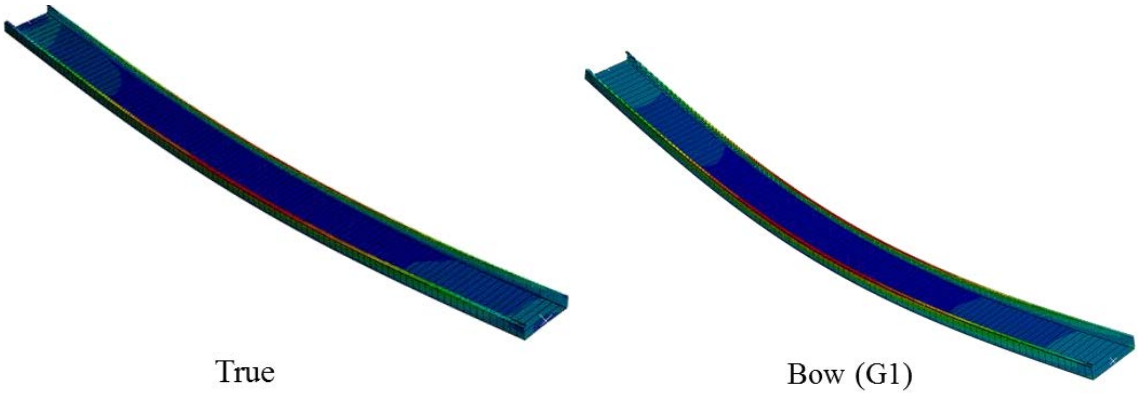

Figure 9. 57 Comparisons between true geometry and model in 1D spectral representation of C sections (600S137-54) at the peak load

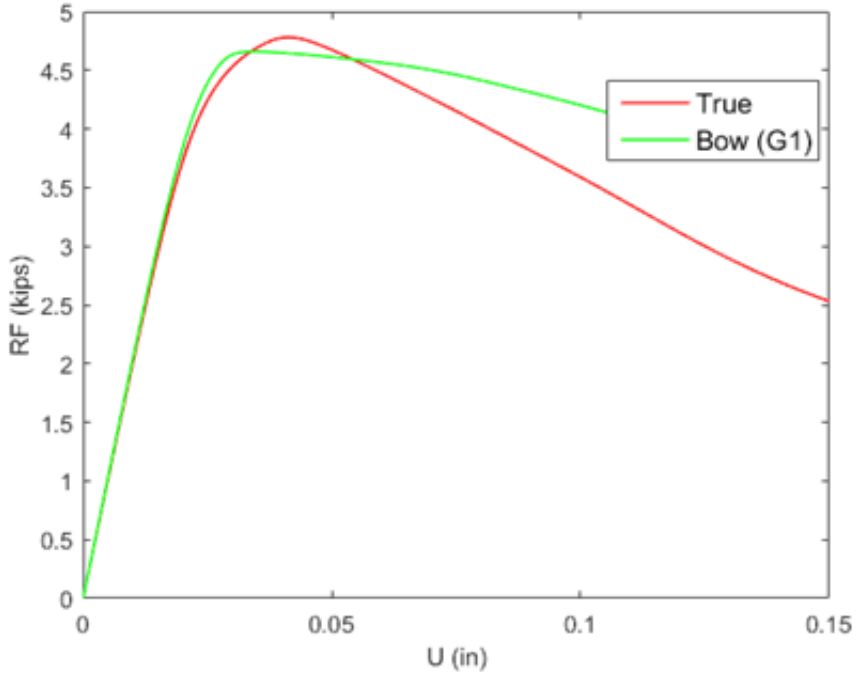

Figure 9. 58 Load-displacement curves of true geometry and model in 1D spectral representation of C sections (600S137-54)

9.3 Conclusions

This chapter demonstrates shell finite-element modeling using true measurements and imperfection simulations in both traditional and 1D spectral representations. Dense point clouds from a measured specimen require specific steps to be converted into accessible points to build up a finite element model. Procedures for this modeling are provided. Imperfections characterized from previous chapters, i.e. Chapter 7 and Chapter 8, are utilized to produce single mode imperfections. These imperfections are directly added to nodes of a perfect model as displacements so that finite-element models with simulated single mode imperfections can be realized together with mesh types and other properties. Results from true-geometry models and models with simulated imperfections are shown and compared where dominant single-mode imperfections can be found. Future work should consider models with combinations of different modes of imperfections so that stiffness and post-buckling behaviors can better approach the true-geometry models.

Chapter 10 Conclusions and Future Work

10.1 Conclusions

Geometric imperfections of cold-formed steel have been researched for decades, and the results have advanced the understanding of the interactions between geometric imperfections and structural performance. Current research related to such imperfections has the following two goals:

- Improvement of measurement technologies and acquisition of abundant and accurate measurements of imperfections.
- Thoroughly understanding the interactions between different classes of geometric imperfections and the structural behaviors of various types of thin-walled members.

In pursuit of these two goals, the author initiated several research projects in the Thin-Walled Structures Laboratory at Johns Hopkins University. The first goal can be achieved by improving the available measurement techniques. Traditional measurements of imperfections use calipers, rulers, displacement sensors, and other such devices. The contact-measurement technique restrains the collection of geometric information about a structural member because only three to five cross sections are chosen to be measured for certain dimensions and quantities of imperfections. The sparsity of the required measurement data hinders the understanding of geometric imperfections, especially cross-section imperfections, and their impacts on structural members. Therefore, an innovative measurement technique was used in which a laser scanner was installed on a rotary stage and driven to move along a linear motion stage. The laser scanner can rotate circumferentially on the rotary stage and project 800 laser points per profile to probe a targeted specimen at any desired angle.

A complex geometry generally requires more than one angle so that all features can be detected and recorded through adjustment of the scanning angles and the longitudinal movement of the laser

scanner. This technique, from its conceptualization to its detailed implementations, is described carefully and thoroughly in Chapter 3. It should be emphasized that the full-field measurement platform that was constructed requires less expenditures than most 3D non-contact measurement platforms since the design and construction can be done by a research group.

The data that were collected from the non-contact 3D measurement platform seem to open a new research direction in the study of geometric imperfections in cold-formed steel and perhaps even in the cold-formed steel industry. Large point clouds of measurements require intensive post-processing before they can be used in structural studies. For example, a cold-formed steel member that is six feet long requires from five to nine scan directions. The longitudinal resolution can be as small as 0.12 in, and around 600 cross sections x 800 points are recorded in one scan. Effective processing and analysis of data are very important since computation cost can be unreasonably high without proper management. Therefore, more than 50 pages were included in Chapter 4 to discuss image-processing algorithms, unique approaches, and application examples to provide the details associated with image-processing procedures. Two major image-processing stages, i.e., surface registration and feature recognition, were explained carefully. Two methods of feature recognition were explained in the chapter with Z, C, and BUC sections as examples. A thorough literature review of image processing, including the methods that inspired the development of the algorithm used in the author's research, is provided in Chapter 2.

The processing of measurements data after image processing broadens research areas. Such research includes geometric imperfections and the study of dimensions for potential quality control and true geometry validation for both traditional and 1D spectral imperfection simulation. Chapter 6 provides statistical summaries of dimensions along with histograms for three shapes and five types of structural members, i.e. Z, C (362S162-68), C (600S137-54), BUC (362S162-68), and

BUC (600S137-54) sections. Chapter 6 reports the results of the study of 19 700Z225-60 Z sections; 14 362S162-68 and 14 600S137-54 C sections; and four 362S162-68 and four 600S137-54 BUC sections. Probabilistic distributions of dimensions across all types of sections generally were non-Gaussian, especially the radii of the corners, angles, and lengths of the lips. It was observed that corners that close to the web can maintain better quality control than those close to the lips. Correlation matrixes among dimensions were estimated for each type of nominally-identical sections. These correlation matrixes can serve as a guide for the dimensional analyses of structural members and as a reference for fabrication factors in building specifications.

Geometric imperfections of a cold-formed steel member, typically studs and purlins, were characterized as cross-section and global imperfections using the conventional imperfection characterization method. In general, cross-section imperfections contain Type 1 (d_1) and Type 2 (d_2); Global imperfections can be categorized as bow (G1), camber (G2), and twist (G3). Sorted imperfections from characterization can be concluded statistically and provide a database for simulating imperfections in finite-element modeling of structural members. A simulated model with single-mode imperfections is assigned a specific, sinusoidal component where the amplitude of the sinusoidal wave is deterministic, but the shape of the cross-sectional deformation varies along the model. A modified method for characterizing imperfections is described following the conventional approach, and it is referred to as modal imperfection decomposition (MID). Global imperfections maintain their own shapes, but cross-section imperfections differ. The cross-section imperfections are classified into local and distortional imperfections, which are correlated with the two cross-section buckling modes. The magnitudes found from MID are smaller than those from conventional imperfections, and they are more accurate since noise from the measurements can be filtered out automatically in the MID approach. This study was presented in Chapter 7, where the concepts, findings, and comparisons with examples are stated.

Zeinoddini (2011) proposed a method called 1D spectral method in which imperfections along a specimen are Fourier-transformed into the frequency domain. Different from the general frequency definition, the frequency is calibrated into the reciprocal of a half-sine wavelength. Magnitudes, square root of power spectra, are considered as actual imperfections at its corresponding frequencies. This interesting representation of imperfections allows an insightful study of the imperfection components and a different way of simulating imperfections in modeling. Five modes of imperfections are transformed into power spectrum densities, where local and distortional bucklings at corresponding frequencies have much smaller magnitudes than expected. Each type of section has its own characteristic spectrum density curves, observations from which can be expressed mathematically. All of these equations were compared to Design PSD, which was proposed by Zeinoddini (2011). Different types and shapes of cold-formed steel members may have dissimilar mathematical expressions, and it is worthwhile to develop equations for each type of cold-formed steel member.

Shell finite element models of five single-mode imperfections were simulated with both traditional imperfection representation and 1D Spectral representation, and the results were compared with as-measured models. Dominant modes of imperfection can be identified where the ultimate load of a simulated model resembles that of the mean ultimate load of all as-measured models.

10.2 Future Work

Obviously, extensive research is needed in the area to complete and advance the design paradigm of geometric uncertainties. Four aspects should be considered in future work, i.e., measurement techniques, image processing, imperfection database, and experimental validation of imperfection modeling.

As described in the Chapter 3, the imperfection measurement platform has many limitations. The diameter of the rotary ring and the scanner's measurement distance restrict measurements of specimens up to 10 inches. Most tracks, panels, and decks cannot be measured using the imperfection measurement platform. In addition, the longitudinal resolution is around 0.12 inch controlled by a DC motor and its embedded encoder. The resolution is workable for long structural members, such as studs and purlins. However, a poor scan result may be achieved with few cross sections if an angle plates or other small-dimension samples are measured. First, improvements of the measurement platform should be focused on these two aspects before optimizing the other functions of the machine.

The second aspect is related to image processing using data collected from the laser imperfection measurement platform. As explained before, large point clouds may result in costly computation, while noise and outliers require careful treatment in order to extract geometric information precisely and correctly. These requirements complicate post-processing in three major procedures, and there are many sub-steps in the surface registration and feature recognition steps, especially the latter. The iterative closest point algorithm in surface registration should be optimized to reduce its computational cost and its search for corresponding to improve its accuracy. The current iterative closest point algorithm and noise filters focus only on cross-section errors, while longitudinal errors are contributed by dynamic motions. The 3D iterative closest point algorithm, as well as specific

filters, should be implemented so that longitudinal errors can be minimized in the future. Sub-steps in feature recognition, especially in integration of different measurements, are highly dependent on the measured geometry. If the section contains four corners on its cross section, three or four measurement pieces may be processed and integrated with its best-resolution area. However, the best-resolution area requires extensive trial-and-error efforts, and the result must be judged manually. This step is expected to be optimized with the deep-learning technique considering large point clouds that can be provided to train the learning algorithm. In addition, it would be desirable to integrate all of the image-processing procedures into one graphic user interface (GUI) that has all of the image-related algorithms and noise filtering embedded into it. The design of this image system could be based on the CUFSM GUI developed by researchers in the Thin-Walled Structures Laboratory.

The third aspect is related to the imperfection database, which should be attractive mostly to researchers in the cold-formed steel area. Abundant imperfection fields and statistical summary tables should be prepared regarding its dimensions and shapes. The author's research has shown that sections with specific dimensions may share similar imperfection types, which, indeed, are worth imperfection measurements for each type of structural members. The imperfection database should provide alternative approaches to researchers, i.e., traditional imperfection representation and 1D spectral imperfection representation. Regarding traditional imperfection representation, researchers can obtain statistical summaries of the desired type of specimens and their corresponding imperfection half-wavelengths. Also, researchers may consider using the base spectrum or even mathematical findings to simulate imperfections for specific types of structural members. Consideration should be given to providing samples of raw surface imperfections without any characterizations to users, which could benefit imperfection modeling validation.

The fourth part, considered as one of the most important research areas, should validate imperfection simulation with as-measured finite element models as well as experimental results. Relying on the 3D laser technique, the true geometries of various shapes of cold-formed steel structural members can be determined. Through modal imperfection decomposition and dimension quantities, the geometric imperfections can be attained from the true geometry. The Correlation matrix has been found among dimension quantities; geometric imperfections are transformed into the frequency domain, and power spectrum curves of imperfection magnitudes can be obtained. Monte Carlo simulations can be used to generate random dimensions with the guidance of the correlation matrix and the imperfections based on the base-power spectrum from 1D spectral representation. Failure modes from simulated imperfections can be compared with the true geometry, where load capacity and failure deformation shapes can be reviewed carefully. An imperfection design protocol can be proposed based on stochastic simulation of dimensions and geometric imperfections. The proposed design protocol will be validated through future experiments and used in shell finite element models to characterize the strength of cold-formed steel members and assemblages. This step can eliminate many of the assumptions that must be made in modeling and finally provide a much more accurate way to simulate imperfections in analysis.

Other than these four aspects, laser measurement techniques may be able to collaborate with building information modeling, especially in the construction field and in trace deformation along structural testing. Variations of dimensions inspired from this research are worth insightful exploration, and the fabrication factor in design specifications should be re-estimated based on the correlation matrixes for today's structural members.

Chapter 11 References

AISI (2012). North American Specification for the Design of Cold-Formed Steel Structural Members. C, American Iron and Steel Institute.

Almhdie, A., C. Leger, M. Deriche and R. Ledee (2007). "3D registration using a new implementation of the ICP algorithm based on a comprehensive looup matrix: application to medical imaging." Pattern Recognition Letters **28**: 1523-1533.

ASTM (2015). C955-Standard specification for load-bearing (transverse and axial) steel studs, runners (tracks), and bracing or bridging for screw application of gypsum panel products and metal plaster bases. West Conshohocken, PA, ASTM International.

Arbocz, J. and J. G. Williams (1977). "Imperfection survery on a 10-ft diameter shell structure." AIAA Journal **15 (7)**: 949-956.

Ayrton, W. E. and J. Perry (1886). "On struts." The Engineer **61**: 464-465, 513-415.

Bendels, G. H., P. Degener, R. Wahl, M. Kortgen and R. Klein (2004). Image-based registration of 3D-range data using feature surface elements. 5th International Symposium on virtual reality, archeology and culture heritage, Brussels and Oudenaard, Belgium.

Berry, P. A., R. Q. Bridge and J. M. Rotter (1996). "Imperfection measurement of cylinders using automated scanning with a laser displacement meter." Strain: 1-8.

Besl, P. J. and N. D. Mckay (1991). "A method for registration of 3-D shapes." Sensor Fusion 1611: 586-606.

Calladine, C. R. (1995). "Understanding imperfection-sensitivity in the buckling of thin-walled shells." Thin-Walled Structures **23**: 2150235.

Chen, Y. and G. Medioni (1991). Object modeling by registration of multiple range images. International Conference on Robotics and Automation, Sacramento, CA, IEEE.

Chetverikov, D., D. Svirko, D. Stepanov and P. Kresk (2002). The trimmed iterative closest point algorithm. 16th International Conference on Pattern Recognition, Quebec, Canada.

Dat, D. T. and T. P. Pekoz (1980). Report: The strength of cold-formed steel columns. Department of Structural Engineering Report. Ithaca, NY, Cornell University. **80**.

Dinis, P. B. and D. Camotim (2010). "Local/distortional mode interaction in cold-formed steel lipped channel beams." Thin-Walled Structures **48**(10-11): 771-785.

Dinis, P. B., D. Camotim and N. Silvestre (2007). "FEM-based analysis of the local plate/distortional mode interaction in cold-formed steel lipped channel columns." Computers and Structures **85**(19-20): 1461-1474.

Fischer, A. W. and B. W. Schafer (2016). Impact of fabrication tolerances on cold-formed steel section properties, stability, and strength. SSRC, Orlando, FL.

FrameCad (2015). "Product & Service." Manufacturing System. from https://framecad.com/en/products-services/construction/manufacturing-system.

Fratamico, D. C. (2017). Direct strength design and analysis of built-up cold-formed steel columns. Doctorate, Johns Hopkins University.

Fratamico, D. C., S. Torabian, K. J. R. Rasmussen and B. W. Schafer (2016). Experimental studies on the composite action in wood-sheathed and screw-fastened built-up cold-formed steel columns. SSRC, Orlando, FL.

Hancock, G. J. (2016). "Cold-formed steel structures: Research review 2013-2014." Advances in Structural Engineering: 1-16.

Harris, C. and M. Stephens (1988). A combined corner and edge detector. Alvey Vision Conference. **15**.

Johnson, A. and M. Herbert (1997). Surface registration by matching oriented points. International Conference on Recent Advances in 3-D Digital Imaging and Modeling.

Karman, T. v., E. G. Sechler and H. S. Tsien (1940). "The influence of curvature on the buckling characteristics of structures." J. Aeronaut. Sci.: 276-289.

Koiter, W. T. (1945). The stability of elastic equilibrium (English translated by E. Riks). Delft, Amsterdam.

Leng, J., B. W. Schafer and S. G. Buonopane (2012). Seismic computational analysis of CFS-NEES building.

Li, Z., M. T. Hanna, S. Adany and B. W. Schafer (2011). "Impact of basis, orthogonalization, and normalization on the constrained Finite Strip Method for stability solutions of open thin-walled members." Thin-Walled Structures **49**(9): 1108-1122.

Liu, P., K. D. Peterman, C. Yu and B. W. Schafer (2012). Characterization of cold-formed steel shear wall behavior under cyclic loading for the CFS-NEES building.

MBMA (2012). Metal building systems manual. Fabrication tolerances, Metal Building Manufacturers Association.

Mulligan, G. P. (1983). The influence of local buckling on the structural behavior of singly symmetric cold-formed steel columns. Ph.D., Cornell University.

Peterman, K. D. (2014). "Behavior of full-scale cold-formed steel buildings under seismic excitations." Johns Hopkins University, Baltimore.

Pulli, K. (1999). Multiview registration for large data sets. 3D Digital Imaging and Modeling, OT, Canada.

Rusinkiewicz, S. and M. Levoy (2001). "Efficient variants of the ICP algorithm." 3-D Digital Imaging and Modeling: 145-152.

Schafer, B. W. and T. Pekoz (1998). "Computational modeling of cold-formed steel: characterizing geometric imperfections and residual stresses." Journal of Constructional Steel Research **47**: 193-210.

Schafer, B. W. (2002). "Local, distortional, and Euler buckling of thin-walled columns." Journal of structural engineering **128**(3): 289-299.

Schafer, B. W. (2011). "Cold-formed steel structures around the world - A review of recent advances in applications, analysis and design." Steel Construction **4**(3): 141-149.

SCI (2015). "Cold-formed steel roof truss." 2016, from http://www.sanfordcontracting.com/systems/Cold-Form-Steel-Roof-Trusses.asp.

SFIA (2015). Case study. Sheridan colleage residence.

SFIA (2015). Case study. Cold-formed cashflow story.

SFIA. (2016). "Advantages of cold-formed steel framing." 2016.

Sebek, R. W. L. (1981). Imperfection surveys and data reduction of ARIANE interstages I/II AND II/III, thesis.

Simon, D. A. (1996). Fast and accurate shape-based registration. Ph.D., Carnegie Mellon University.

Singer, J., J. Arbocz and W. Tanchum (2002). Buckling experiments - experimental methods in buckling of thin-walled structures. New York, John Wiley & Sons, Inc.

SMDI (2010). Cold-formed steel in building construction.

Steder, B., R. B. Rusu, K. Konolige and W. Burgard (2011). Point feature extraction on 3D range scans taking into account object boundaries. Robotics and Automation, 2011 IEEE International Conference. Shanghai**:** 2601-2608.

Torabian, S., B. Zheng and B. W. Schafer (2015). "Experimental response of cold-formed steel lipped channel beam-columns." Thin-Walled Structures **89**: 152-168.

Torabian, S., D. C. Fratamico and B. W. Schafer (2016). "Experimental response of cold-formed steel zee-section beam-columns." Thin-Walled Structures **98**: 496-517.

Turk, G. and M. Levoy (1994). Zippered polygon meshes from range images. Special Interest Group on GRAPHics and Interactive Techniques, Orlando, FL.

Vieira JR., L. C. M., Y. Shifferaw and B. W. Schafer (2011). "Experiments on sheathed cold-formed steel studs in compression." Journal of Constructional Steel Research **67**(10): 1554-1566.

Young, B., Rasmussen, K.J.R. (2003). "Measurement techniques in the testing of thin-walled structural members." Experimental Mechanics **43**(1): 32-38.

Yu, W. W. (2000). Cold-formed steel design. United States of America, John Wiley & Sons.

Zeinoddini, V. (2011). Geometric imperfections in cold-formed steel members. Ph. D., Johns Hopkins University.

Zeinoddini, V. and B. W. Schafer (2011). "Global imperfections and dimensional variations in cold-formed steel members." International Journal of Structural Stability and Dynamics **11**(5): 829-854.

Zeinoddini, V. M. and B. W. Schafer (2012). "Simulation of geometric imperfections in cold-formed steel members using spectral representation approach." Thin-Walled Structures **60**: 105-117.

Zhao, X. and B. W. Schafer (2014). Laser scanning to develop three-dimensional fields for the precise geometry of cold-formed steel members. Recent Research and Developments in Cold-Formed Steel Design and Construction, St. Louis, MO.

Zhao, X., M. Tootkaboni and B. W. Schafer (2016). "Laser-based cross-section measurement of cold-formed steel members: model reconstruction and application." Thin-Walled Structures.

Appendix

Ap.1 Chapter 3

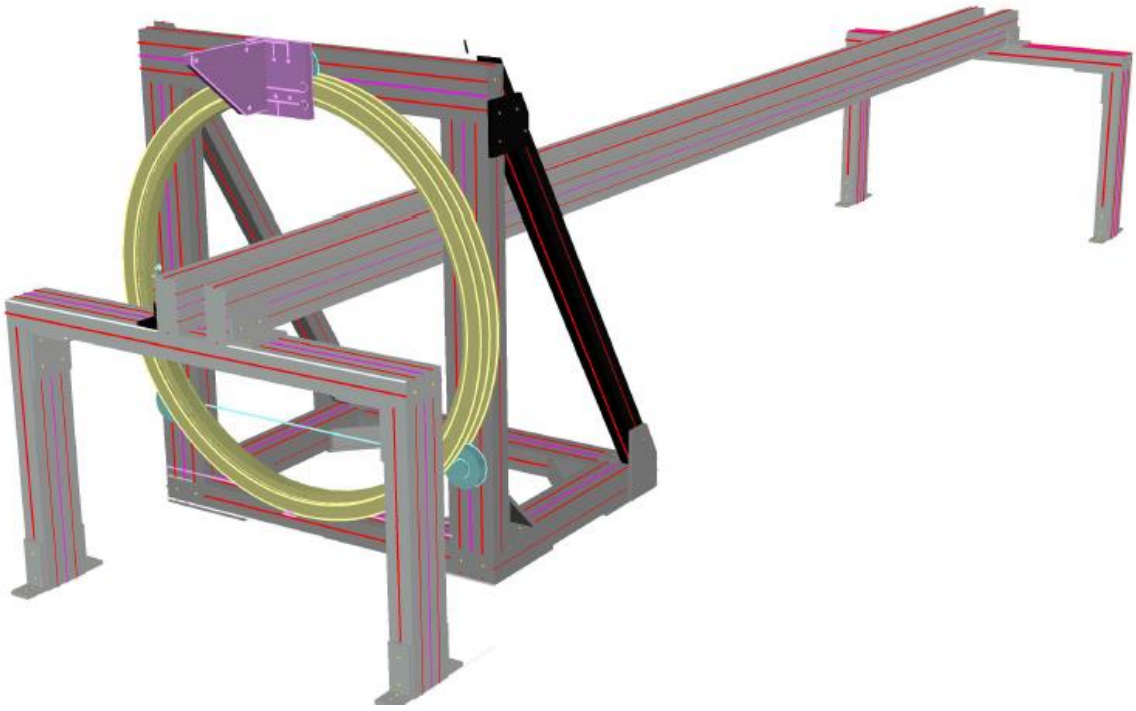

A. 1 Conceptual design of full-field non-contact measurement platform

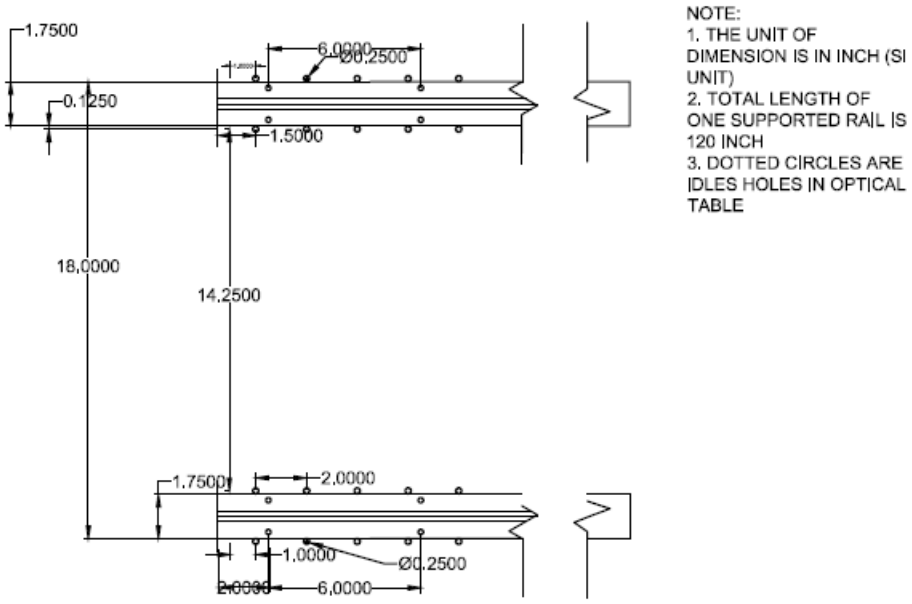

A. 2 Linear guide rail arrangement of linear motion system

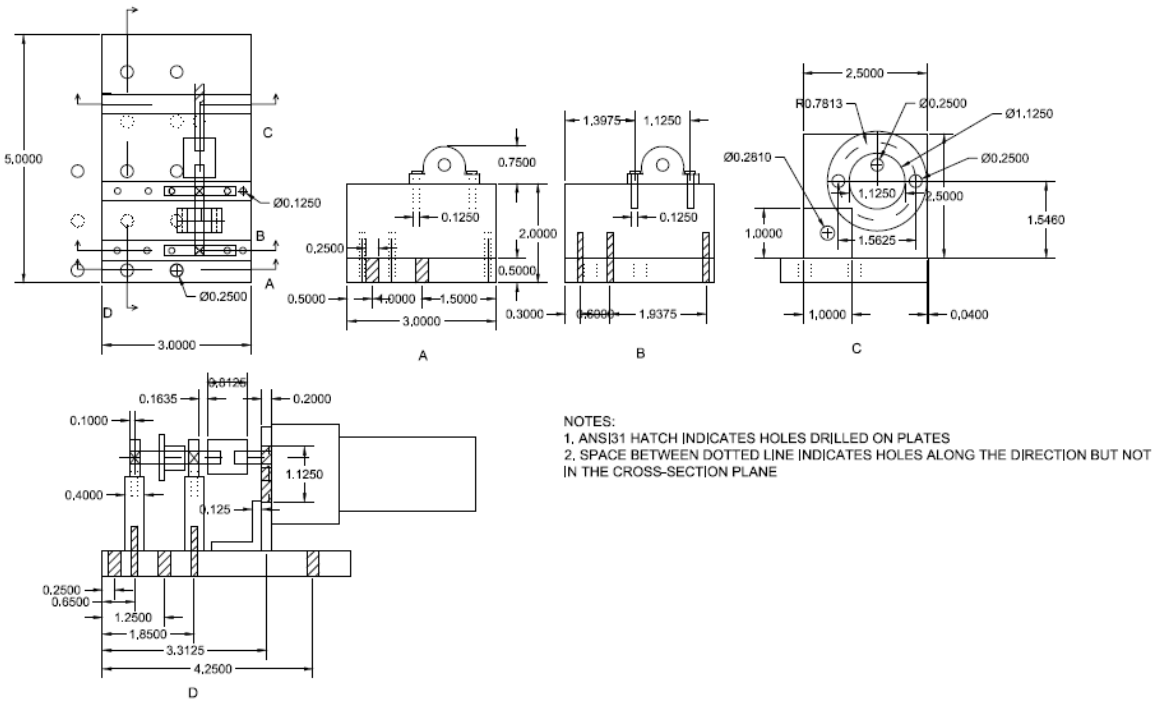

A. 3 Drive end design of linear motion system

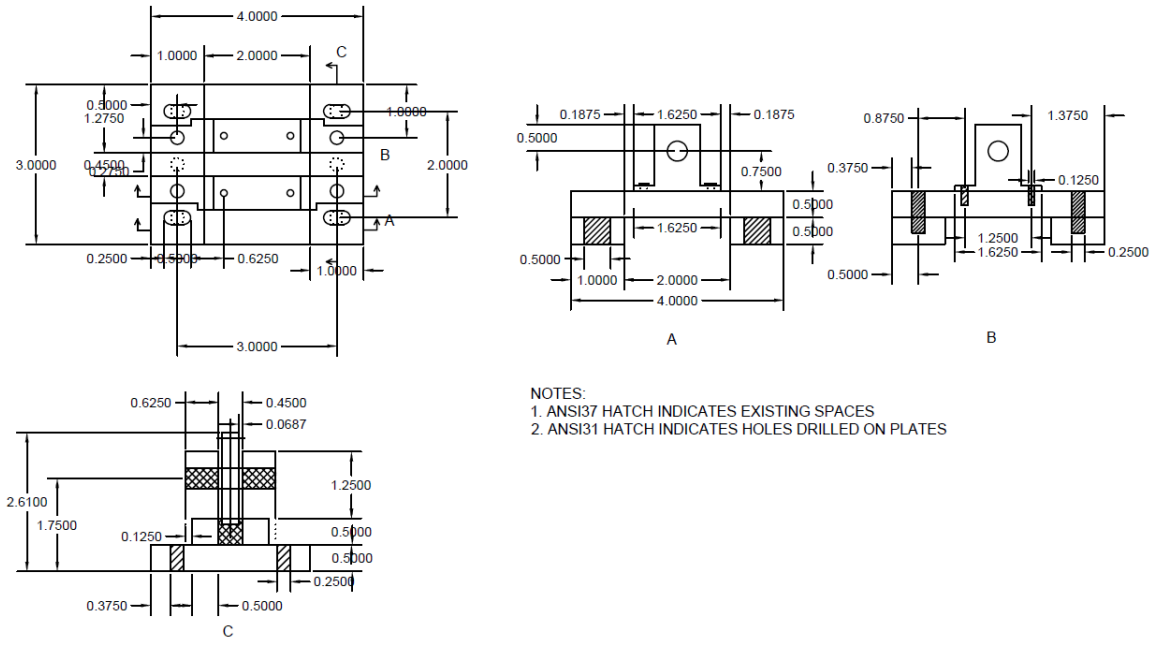

A. 4 Driven end design of linear motion system

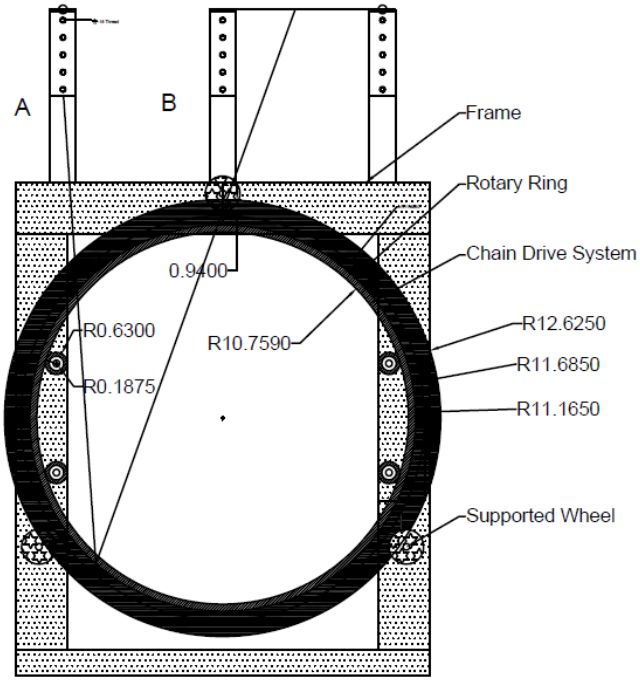

NOTES:
1. A ELEMENTS CAN MOVE HORIZONTALLY. FOR ZEE SECTION, WHERE ONE SIDE IS FURTHER TO LIP SHOULD BE CLOSE TO THE CENTER.
2. B ELEMENT WILL NOT BE IN THE SAME LONGITUDINAL LEVEL AS A ELEMENTS TO AVOID THE TANGLE OF LASER CORE.
3. ALL ELEMENTS ARE ABLE TO BE ADJUSTED VERTICALLY

A. 5 Conceptual design of rotary stage

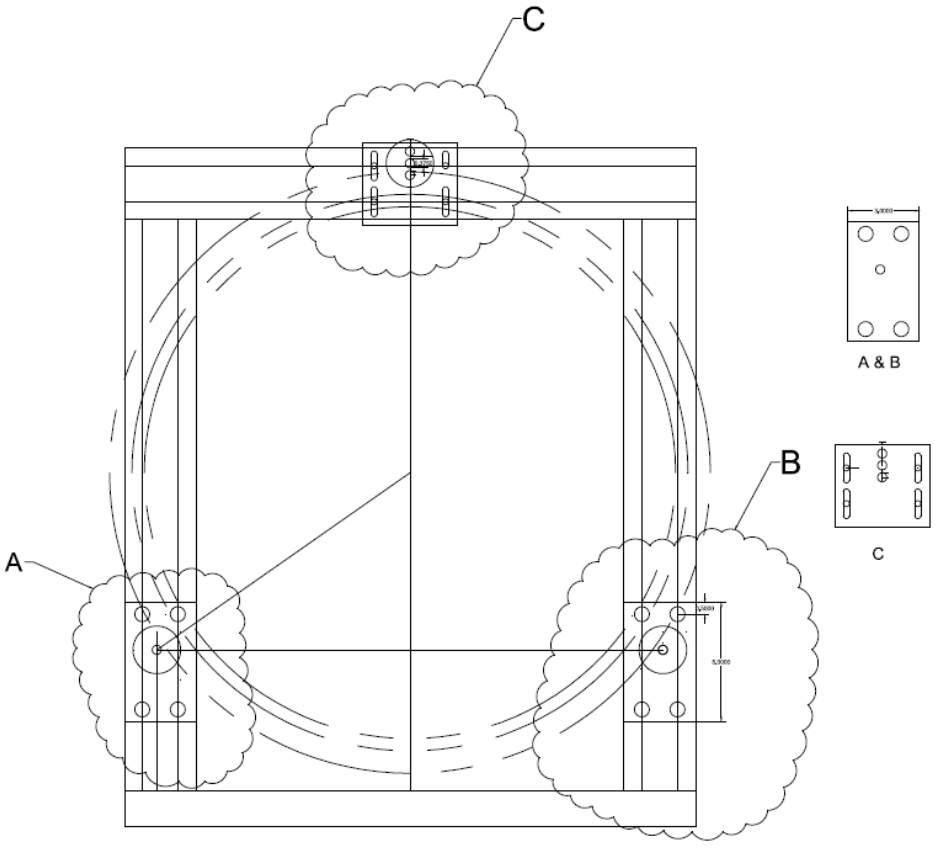

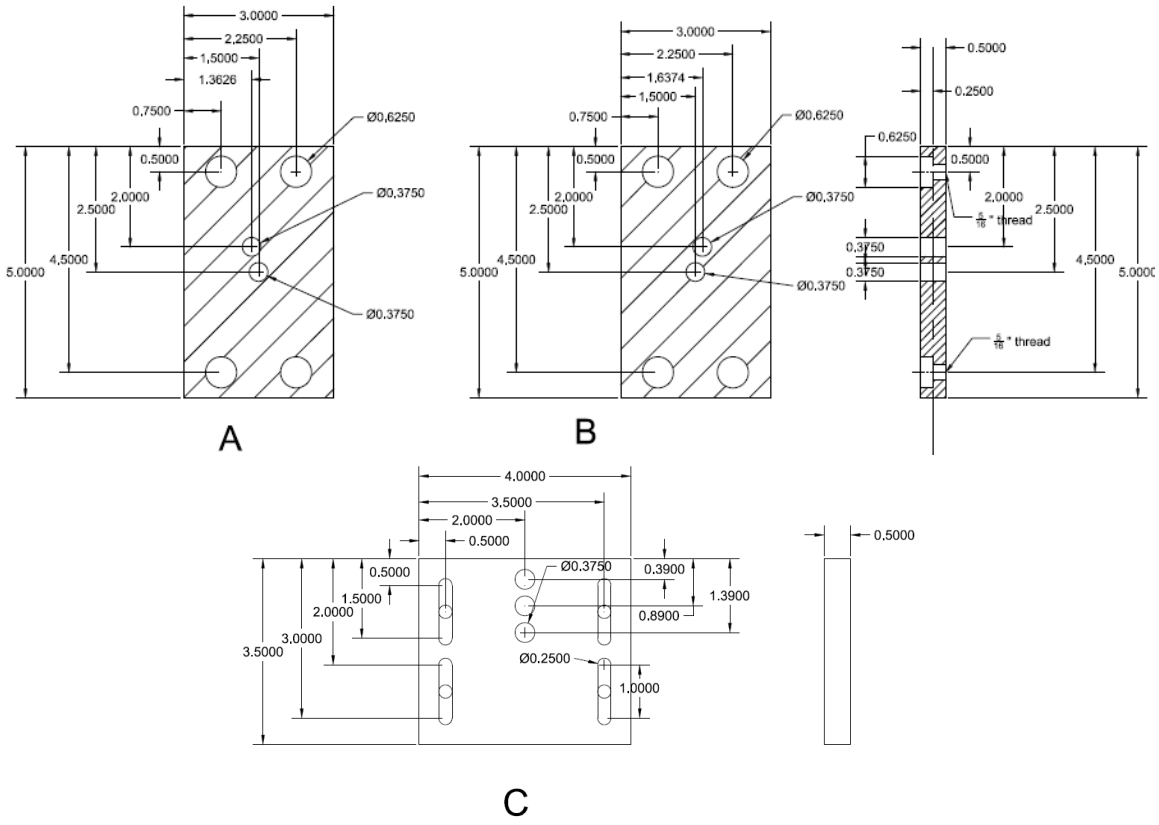

A. 6 Connection design between rotary ring and triangular frame

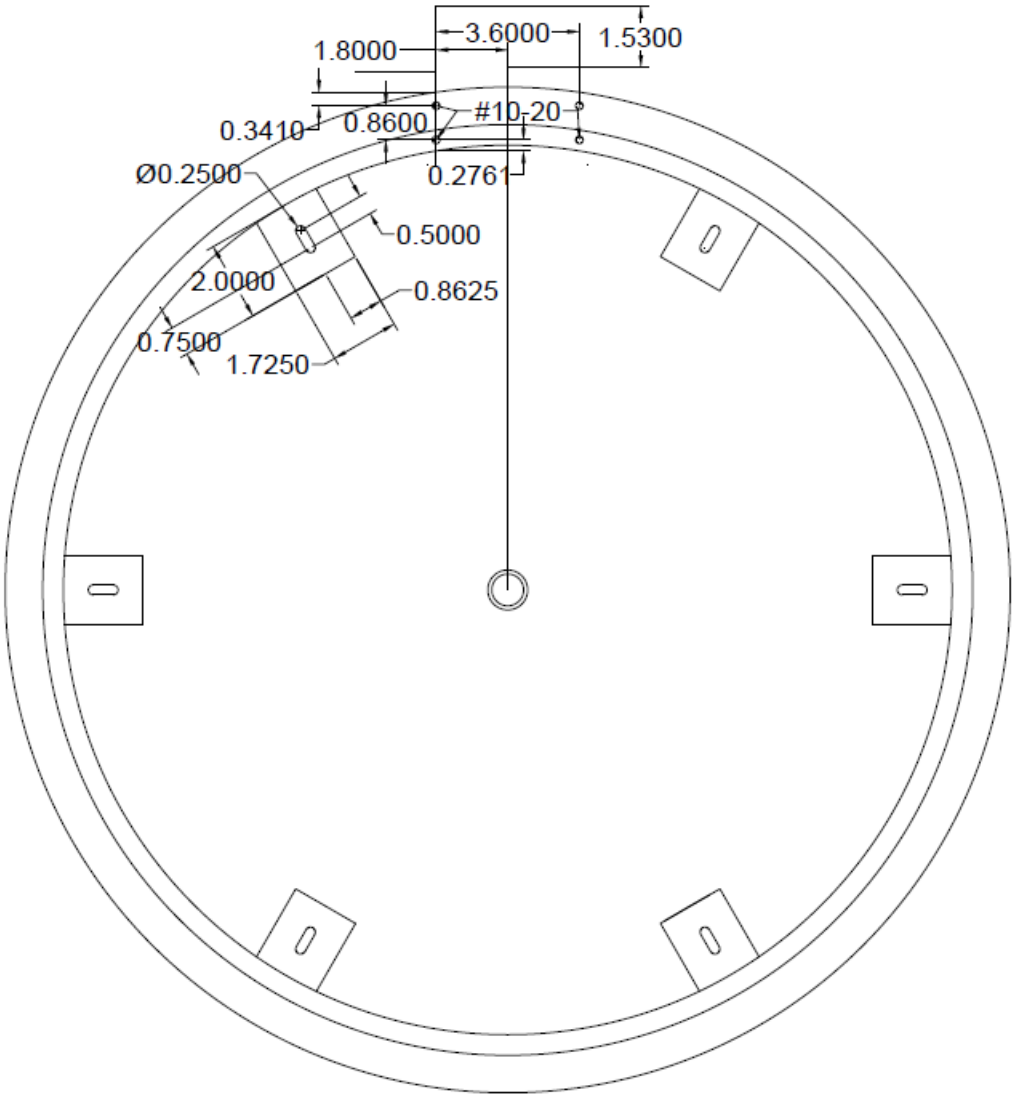

A. 7 Rotary ring design of rotary stage

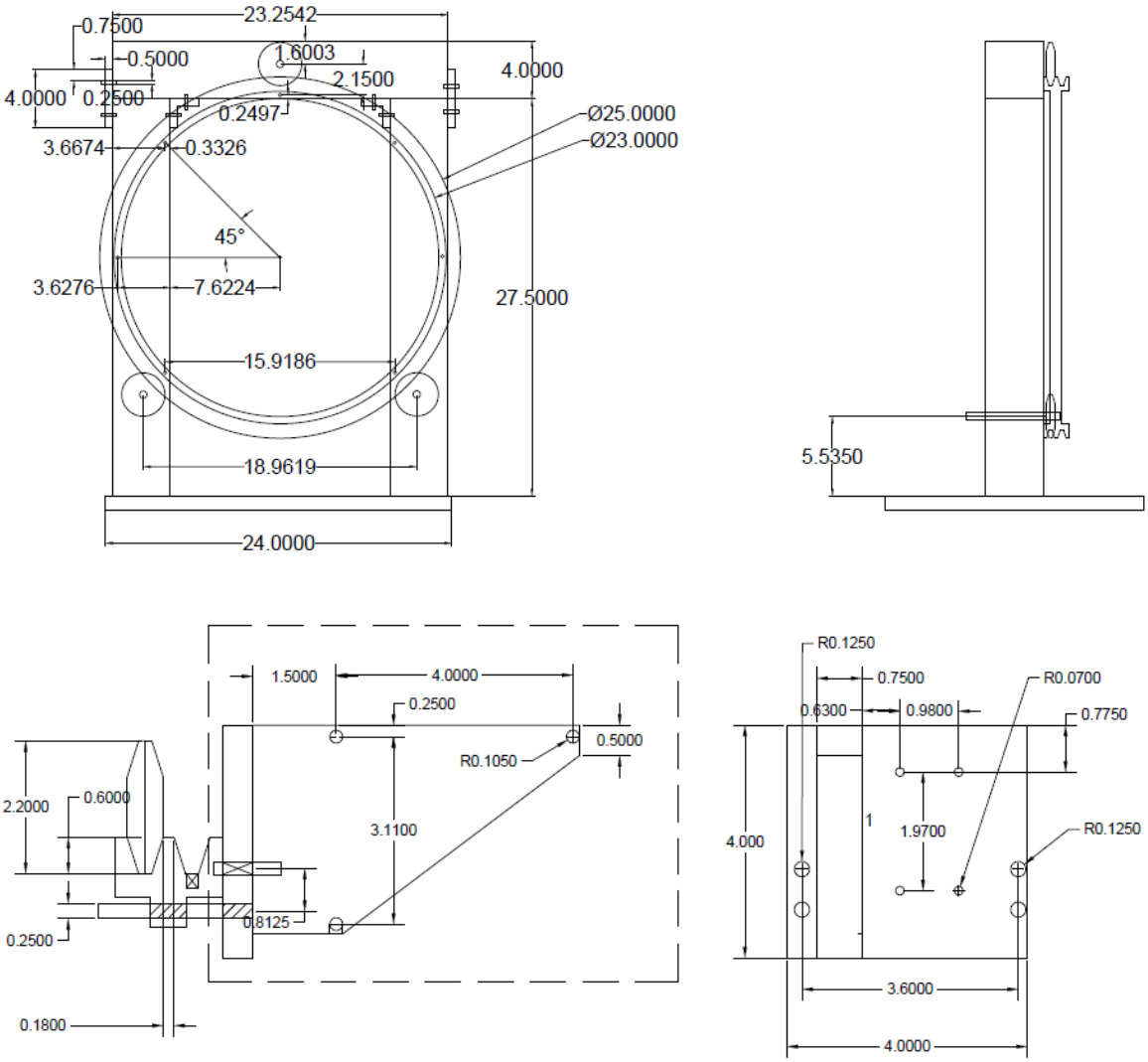

A. 8 Support frame design of rotary stage

Ap.2 Chapter 4

S0 File Conversion

CSV2Excel.m (Main function)

```
function []=CSV2Excel() % this function creates GUI shown in Figure 4.1 converting .csv file to .xlsx file
subfig=figure;
name=['File Conversion'];
set(subfig,'Name',name,'NumberTitle','off');
set(subfig,'MenuBar','none');
set(subfig,'position',[100 100 500 200])% define interface's dimension
```

```
%%%%BUTTON%%%%
SelectFile=uicontrol(subfig,...
   'Style','push','units','normalized',...
   'Position',[0.05 0.6 0.3 0.35],...
   'String','Select',...
   'Callback','CbFun(1);');

ConvertFile=uicontrol(subfig,...
   'Style','push','units','normalized',...
   'Position',[0.05 0.1 0.3 0.35],...
   'String','Convert',...
   'Callback','CbFun(2);');
```

S1 Data Trimmer

```
function []=impost1() %This function

global axestemp n_tex xmin_tex xmax_tex ymin_tex ymax_tex zmin_tex zmax_tex
global scanner_tex processor_tex
global file_tex

%basic figure window for the post-processor
subfig=figure;
name=['IMPERFECTION SCANNER POST-PROCESSOR STEP 1'];
set(subfig,'Name',name,'NumberTitle','off');
set(subfig,'MenuBar','none');
set(subfig,'position',[50 50 800 500])%

%define the axis where the plotting will happen
axestemp=axes('Units','normalized','Position',[0.06 0.1 0.53 0.8],'visible','off');
%
%DEFAULT INITIAL VALUES
n = 10;
%DEFAULT INITIAL PLOT
axes(axestemp)
xmin = 0;
xmax = 0;
ymin = 0;
ymax = 0;
zmin = -1000;
zmax = 150;
A = ones(n,n)*NaN;
mesh(A)
axis tight
set( gcf, 'toolbar', 'none' )
set( gcf, 'toolbar', 'figure' )

scannername = 'enter scanner name';
processorname = 'enter processor name';
```

```
%Create buttons on GUI
updateplot=uicontrol(subfig,...
   'Style','push','units','normalized',...
   'Position',[0.66 0.8 0.3 0.14],...
   'String','Update Plot',...
   'Callback',[...
      'impost1_cbfunc(1);']);
loadfile=uicontrol(subfig,...
'Style','push','units','normalized',...
'Position',[0.05 0.92 0.1 0.05],...
'String','Load File',...
'Callback',[...
   'impost1_cbdata(1);']);
savefile=uicontrol(subfig,...
'Style','push','units','normalized',...
'Position',[0.66 0.1 0.3 0.14],...
'String','Save File',...
'Callback',[...
   'impost1_cbdata(2);']);
%
%EDITABLE TEXT BOX WITH A TITLE
n_title=uicontrol(subfig,...
   'Style','text','units','normalized',...
  'Position',[0.66 0.7 0.05 0.08],...
   'String','Data Size');
xmin_title = uicontrol(subfig,...
   'style','text','units','normalized',...
   'Position',[0.66 0.61 0.06 0.08],...
   'String','x min');
xmax_title = uicontrol(subfig,...
   'style','text','units','normalized',...
   'Position',[0.82 0.61 0.06 0.08],...
   'String','x max');
ymin_title = uicontrol(subfig,...
   'style','text','units','normalized',...
   'Position',[0.66 0.52 0.06 0.08],...
   'String','y min');
ymax_title = uicontrol(subfig,...
   'style','text','units','normalized',...
   'Position',[0.82 0.52 0.06 0.08],...
   'String','y max');
zmin_title = uicontrol(subfig,...
   'style','text','units','normalized',...
   'Position',[0.66 0.43 0.06 0.08],...
   'String','z min');
zmax_title = uicontrol(subfig,...
   'style','text','units','normalized',...
   'Position',[0.82 0.43 0.06 0.08],...
   'String','z max');
scanner_title = uicontrol(subfig,...
```

```
    'style','text','units','normalized',...
    'position',[0.66 0.34 0.1 0.08],...
    'String','Scanner name');
processor_title = uicontrol(subfig,...
    'style','text','units','normalized',...
    'position',[0.66 0.25 0.1 0.08],...
    'String','Processor name');

n_tex=uicontrol(subfig,...
    'Style','edit','units','normalized',...
   'Position',[0.72 0.7 0.2 0.08]);
file_tex = uicontrol(subfig,...
    'style','edit','units','normalized',...
    'Position',[0.16 0.92 0.3 0.05]);
xmin_tex = uicontrol(subfig,...
    'Style','edit','units','normalized',...
   'Position',[0.73 0.61 0.08 0.08],...
    'String',num2str(xmin)); %Coord. Boundaries Input for min x
xmax_tex = uicontrol(subfig,...
    'Style','edit','units','normalized',...
   'Position',[0.89 0.61 0.08 0.08],...
    'String',num2str(xmax)); %Coord. Boundaries Input for max x
ymin_tex = uicontrol(subfig,...
    'Style','edit','units','normalized',...
   'Position',[0.73 0.52 0.08 0.08],...
    'String',num2str(ymin)); %Coord. Boundaries Input for min y
ymax_tex = uicontrol(subfig,...
    'Style','edit','units','normalized',...
   'Position',[0.89 0.52 0.08 0.08],...
    'String',num2str(ymax)); %Coord. Boundaries Input for max y
zmin_tex = uicontrol(subfig,...
    'Style','edit','units','normalized',...
   'Position',[0.73 0.43 0.08 0.08],...
    'String',num2str(zmin)); %Coord. Boundaries Input for min z
zmax_tex = uicontrol(subfig,...
    'Style','edit','units','normalized',...
   'Position',[0.89 0.43 0.08 0.08],...
    'String',num2str(zmax)); %Coord. Boundaries Input for max z
scanner_tex = uicontrol(subfig,...
    'Style','edit','units','normalized',...
   'Position',[0.77 0.34 0.2 0.08],...
   'String',scannername);%Enter the responsible person for scanning work
processor_tex = uicontrol(subfig,...
    'Style','edit','units','normalized',...
   'Position',[0.77 0.25 0.2 0.08],...
    'string',processorname); %Enter the responsible person for processing work
```

S2 Surface Registration

```
function [] = SurfaceRegistration()
```

```
global axestemp axestemp2
global iter val2 val val3 val4 val5 tv4 m fac
global listalldata listplotdata crosssectionm RefMenu TagMenu
global rot_tex x_tex z_tex
global xlbtex xubtex zlbtex zubtex datex dxtex dztex
% second GUI
subfig = figure;
name = ['3D Model Reconstruction'];
set(subfig,'Name',name,'NumberTitle','off');
set(subfig,'MenuBar','None');
set(subfig,'Position',[50 50 1000 600]);

%define the axis where the plotting will happen
axestemp = axes('Units','Normalized','Position',[0.08 0.45 0.35 0.45],'visible','off');
axestemp2 = axes('Units','Normalized','Position',[0.08 0.08 0.35 0.28],'visible','off');

%DEFAULT INITIAL VALUES
n = 10;
%DEFAULT INITIAL PLOT
axes(axestemp) %Generate 3D View
xmin = 0;
xmax = 0;
ymin = 0;
ymax = 0;
zmin = -1000;
zmax = 150;
A = ones(n,n)*NaN;
x = [1:1:n]'*ones(1,n);
y = [1:1:n]'*ones(1,n);
mesh(x,y,A)
xlabel('x(mm)')
ylabel('y(mm)')
zlabel('z(mm)')
axis tight
set( gcf, 'toolbar', 'none' )
set( gcf, 'toolbar', 'figure' )

axes(axestemp2) %Generate Cross Section View
a = ones(n,1)*NaN;
b = rand(n,1)*NaN;
plot(a,b);
xlabel('x(mm)')
ylabel('z(mm)')
axis tight
set( gcf, 'toolbar', 'none' )
set( gcf, 'toolbar', 'figure' )

% Define Parameters
m = 0; % mth cross section
iter = 0; % loading data counts
```

```
val2 = 0;val = 0;val3 = 0; val4 = 0; val5 = 0;
fac = 3.2152;
tv4 = 0;
% Design GUI
%%%loading data part%%%
loadfile=uicontrol(subfig,...
'Style','push','units','normalized',...
'Position',[0.05 0.93 0.18 0.04],...
'String','Load File',...
'Callback','LD_cb(1);'); % retrieve datafile & save raw data
clearfile2=uicontrol(subfig,...
'Style','push','units','normalized',...
'Position',[0.24 0.93 0.18 0.04],...
'String','Clear File',...
'Callback', 'LD_cb(2)'); %clear all data and restart

%%%plotting data part%%%
%overall plots
listalldata = uicontrol(subfig,...
   'style','listbox','units','normalized',...
   'position',[0.47,0.75,0.15,0.18],...
   'string',{'Wait for Data'},...
   'Callback','PT_cb(1)'); %list of data for processing
listalltitle = uicontrol(subfig,...
   'style','text','units','normalized',...
   'Position',[0.49 0.94 0.1 0.03],...
   'String','All Files'); %name to listbox 1
selectbutton = uicontrol(subfig,...
   'style','push','units','normalized',...
   'position',[0.49 0.71 0.1 0.04],...
   'String','Select Data',...
   'Callback','PT_cb(2)'); % select the data to plot
listplotdata = uicontrol(subfig,...
   'style','listbox','units','normalized',...
   'position',[0.47,0.5,0.15,0.15],...
   'string',{'Wait for Data'},...
   'Callback','PT_cb(3)'); %list of data being processed
listplottitle = uicontrol(subfig,...
   'style','text','units','normalized',...
   'Position',[0.49 0.66 0.1 0.03],...
   'String','Plotted Files'); %name to listbox 2
deletbutton = uicontrol(subfig,...
   'style','push','units','normalized',...
   'position',[0.49 0.46 0.1 0.04],...
   'String','Delete Data',...
   'Callback','PT_cb(4)'); % delete the data in plots
%%lower plots
crosssectiontitle = uicontrol(subfig,...
   'style','text','units','normalized',...
   'position',[0.49 0.40 0.1 0.03],...
```

```
    'String','Cross Section');
crosssectionm = uicontrol(subfig,...
    'style','edit','units','normalized',...
    'position',[0.49 0.35 0.1 0.04],...
    'String',m); % cross section that is plotted in the cross-section view
decm = uicontrol(subfig,...
    'style','push','units','normalized',...
    'position',[0.44 0.35 0.045 0.04],...
    'String','-',...
    'Callback','PT_cb(5)'); % decrease m
incm = uicontrol(subfig,...
    'style','push','units','normalized',...
    'position',[0.6 0.35 0.045 0.04],...
    'string','+',...
    'Callback','PT_cb(6)'); % increase m
plotbutton = uicontrol(subfig,...
    'style','push','units','normalized',...
    'position',[0.46 0.22 0.17 0.1],...
    'string','Plot Cross Section',...
    'Callback','PT_cb(7)');

%Optimization for Surface Registration Transformation Matrix
RefMenu = uicontrol(subfig,...
    'style','popupmenu','units','normalized',...
    'position',[0.65 0.88 0.15 0.04],...
    'string',{'0'},...
    'Callback','ICP_cb(1)'); % reference surface
RefTitle = uicontrol(subfig,...
    'style','text','units','normalized',...
    'position',[0.65 0.93 0.15 0.04],...
    'string','Reference Surface');
TagMenu = uicontrol(subfig,...
    'style','popupmenu','units','normalized',...
    'position',[0.81 0.88 0.15 0.04],...
    'string',{'0'},...
    'Callback','ICP_cb(2)'); % target surface
TagTitle = uicontrol(subfig,...
    'style','text','units','normalized',...
    'position',[0.81 0.93 0.15 0.04],...
    'string','Target Surface');
%%%Optimized Region%%%
RRTitle = uicontrol(subfig,...
    'style','text','units','normalized',...
    'position',[0.65 0.76 0.21 0.1],...
    'string','Optimized Region'); %optimized Region Text
xlbTitle = uicontrol(subfig,...
    'style','text','units','normalized',...
    'position',[0.65 0.71 0.1 0.04],...
    'string','x min');
xlbtex = uicontrol(subfig,...
```

```
    'style','edit','units','normalized',...
    'position',[0.65 0.65 0.1 0.05],...
    'string','-90'); % x lower boundary for Window Function
xubTitle = uicontrol(subfig,...
    'style','text','units','normalized',...
    'position',[0.76 0.71 0.1 0.04],...
    'string','x max');
xubtex = uicontrol(subfig,...
    'style','edit','units','normalized',...
    'position',[0.76 0.65 0.1 0.05],...
    'string','120'); %x upper boundary for Window Function
zlbTitle = uicontrol(subfig,...
    'style','text','units','normalized',...
    'position',[0.65 0.6 0.1 0.04],...
    'string','z min');
zlbtex = uicontrol(subfig,...
    'style','edit','units','normalized',...
    'position',[0.65 0.54 0.1 0.05],...
    'string','-90'); % z lower boundary for Window Function
zubTitle = uicontrol(subfig,...
    'style','text','units','normalized',...
    'position',[0.76 0.6 0.1 0.04],...
    'string','z max');
zubtex = uicontrol(subfig,...
    'style','edit','units','normalized',...
    'position',[0.76 0.54 0.1 0.05],...
    'string','150'); %z upper boundary for Window Function
calbutton = uicontrol(subfig,...
    'style','push','units','normalized',...
    'position',[0.65 0.46 0.2 0.07],...
    'string','Optimize!',...
    'Callback','ICP_cb(3)');
resultTitle = uicontrol(subfig,...
    'style','text','units','normalized',...
    'position',[0.88 0.81 0.11 0.05],...
    'string','Optimized Results');
daTitle = uicontrol(subfig,...
    'style','text','units','normalized',...
    'position',[0.88 0.76 0.1 0.04],...
    'string','rotation');
datex = uicontrol(subfig,...
    'style','text','units','normalized',...
    'position',[0.88 0.71 0.1 0.04]);
dxTitle = uicontrol(subfig,...
    'style','text','units','normalized',...
    'position',[0.88 0.66 0.1 0.04],...
    'string','x translation');
dxtex = uicontrol(subfig,...
    'style','text','units','normalized',...
    'position',[0.88 0.61 0.1 0.04]);
```

```
dzTitle = uicontrol(subfig,...
    'style','text','units','normalized',...
    'position',[0.88 0.56 0.1 0.04],...
    'string','z translation');
dztex = uicontrol(subfig,...
    'style','text','units','normalized',...
    'position',[0.88 0.51 0.1 0.04]);

%%% Manual Surface Registration%%%
reg_title = uicontrol(subfig,...
    'style','text','units','normalized',...
    'Position',[0.66 0.4 0.2 0.03],...
    'String','Registration');
rot_title=uicontrol(subfig,...
    'Style','text','units','normalized',...
   'Position',[0.66 0.35 0.1 0.04],...
    'String','rotation');
x_title=uicontrol(subfig,...
    'Style','text','units','normalized',...
   'Position',[0.66 0.29 0.1 0.04],...
    'String','x translat.');

z_title=uicontrol(subfig,...
    'Style','text','units','normalized',...
   'Position',[0.66 0.23 0.1 0.04],...
    'String','z translat.');

rot_tex = uicontrol(subfig,...
    'style','edit','units','normalized',...
    'position',[0.81 0.34 0.1 0.05],...
    'string','0');
x_tex = uicontrol(subfig,...
    'style','edit','units','normalized',...
    'position',[0.81 0.28 0.1 0.05],...
    'string','0');
z_tex = uicontrol(subfig,...
    'style','edit','units','normalized',...
    'position',[0.81 0.22 0.1 0.05],...
    'string','0');

dec1 = uicontrol(subfig,...
    'style','push','units','normalized',...
    'position',[0.77 0.34 0.03 0.05],...
    'string','-',...
    'callback','MN_cb(1)');
inc1 = uicontrol(subfig,...
    'style','push','units','normalized',...
    'position',[0.92 0.34 0.03 0.05],...
    'string','+',...
    'callback','MN_cb(2)');
```

```
dec2 = uicontrol(subfig,...
   'style','push','units','normalized',...
   'position',[0.77 0.28 0.03 0.05],...
   'string','-',...
   'callback','MN_cb(3)');
inc2 = uicontrol(subfig,...
   'style','push','units','normalized',...
   'position',[0.92 0.28 0.03 0.05],...
   'string','+',...
   'callback','MN_cb(4)');
dec3 = uicontrol(subfig,...
   'style','push','units','normalized',...
   'position',[0.77 0.22 0.03 0.05],...
   'string','-',...
   'callback','MN_cb(5)');
inc3 = uicontrol(subfig,...
   'style','push','units','normalized',...
   'position',[0.92 0.22 0.03 0.05],...
   'string','+',...
   'callback','MN_cb(6)');
rgstbutton = uicontrol(subfig,...
   'style','push','units','normalized',...
   'position',[0.66 0.14 0.2 0.07],...
   'string','Register!',...
   'callback','MN_cb(7)');

%Save Data
savefile=uicontrol(subfig,...
'Style','push','units','normalized',...
'Position',[0.66 0.03 0.15 0.1],...
'String','Save File',...
'Callback',[...
   'save_cbs(1)']);
sig_save = uicontrol(subfig,...
   'style','checkbox','units','normalized',...
   'Position',[0.82 0.03 0.08 0.1],...
   'string','Single',...
   'callback','save_cbs(2)');
mul_save = uicontrol(subfig,...
   'style','checkbox','units','normalized',...
   'Position',[0.91 0.03 0.08 0.1],...
   'string','Multiple',...
   'callback','save_cbs(3)');
```

S3 Feature Recognition

```
clear all;close all;clc
%% Load Data %%
%%%%Input 1 (Load Data)%%%%
```

```
spn = 'B8_2';% Input, specimen #
a1 = '120';% Input, angle #
Type = 'Cee'; % Input, type of CFS
%%%Loading Data%%%%
a2 = a1;
specname = strcat(Type,'_',spn,'_',a1);
if ~isempty(strfind(a1,'N'));
   ind1 = strfind(a1,'N');
   a2(ind1) = '_';
end
sub = strcat('c',a2);
savename = strcat('FR','_',specname);
tmp = load(specname); %%%Assume data is cell
tx = tmp.(sub);
ty = tx; tz = tx;

%% Define Variables %%
lg = size(tx,2);
gl = length(tx{1}(:,1)); % This is an assumption to the size of points in

%%%%%%%%Depends on different angles (Input)%%%%
% st = 1;%Data extracted from c.s.
st = round(gl*0.3);%100
% nd = round(gl*0.8);
nd = round(gl);
cnd = 1; %Details can refer to FeatRecg_BUC.m
n =  15;%Starting points assumption
ctl = 0.5; p = 0.8;
incn = 1;
vv = 0; % vv=0, boundary filter used
nn = 0; % 0 for angle POSITIVE; nn = 1 for angle NEGATIVE.
pt = 0;% recommend for only one cross section is tested, all data will be ploted
cs = 0; % selected cross section; 0 for all cross sections; can be an index array to cross sections
pt2 = 1;%If it is 1, criter1&criter2 will generate plot
mu = 0; %Determine if only one cs wanted to update or all improper cs. to be updated
mc = 0;%%%If mc=0, model update will be started;
ms = 0;%%%If some cross sections required to be adjusted with change of n,ms = 1
   %%%%if ms==1, define which cross section wanted to be adjusted&redfine
   %%%%n
   cs2 =46:48;n2 = 25;ctl2 = 0.5;vv2=0;

%%%%Initial Feature Recognition %%%%
[datan,crn,xc_f,yc_f] = FeatRecg_BUC(tx,ty,tz,st,nd,cnd,n,ctl,p,nn,vv,cs,pt,incn);
%%%%%%%%%%%%%%%%%%%%%%%%%%%%%%%%%%%%%%%%%%%%%%%%%%%%%%%%%%%%%%%%%%%%%%%%%%%%%%%
%%%%
%%%%Manual Model Update%%%%%
if ms == 1
   if cs2(1)==0
      'Define adjusted cross section #!'
   end
```

```
  [datav,crv,xc_f,yc_f] = FeatRecg_BUC(tx,ty,tz,st,nd,cnd,n2,ctl2,p,nn,vv2,cs2,0,incn);
  for ppp = 1:length(cs2)
     datan{cs2(ppp)} = [];
     datan{cs2(ppp)} = datav{cs2(ppp)};
  end
  crn(cs2,:) = crv(cs2,:);
end
%%%%Only works when entire cross sections have been processed%%%%
if cs == 0
 %%%%Define filtering & model updating Validation
   %%%%%%%Criterion 1%%%%%
   [bgdx,bgdz,eddx,eddz,ine,inb] = criter1(datan,crn,pt2);

   %%%%%%%Criterion 2%%%%
   [inr,r] = criter2(crn,pt2);
   %%%%%%%
```

```
    save(savename,'datan','crn');
end
```

Ap.3 Chapter 6

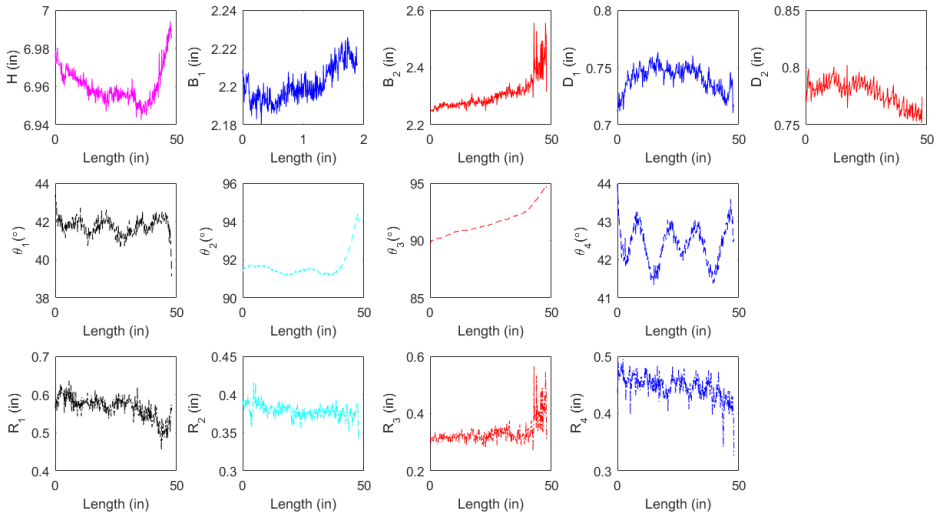

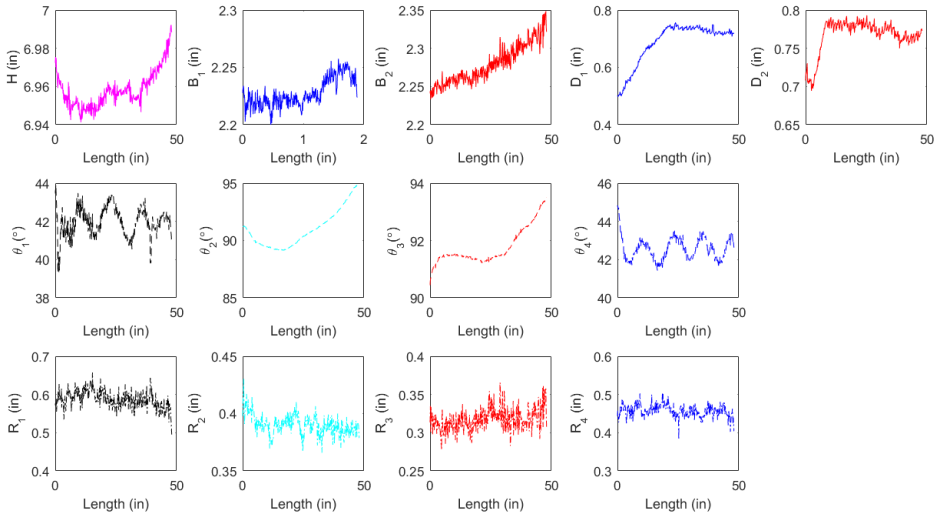

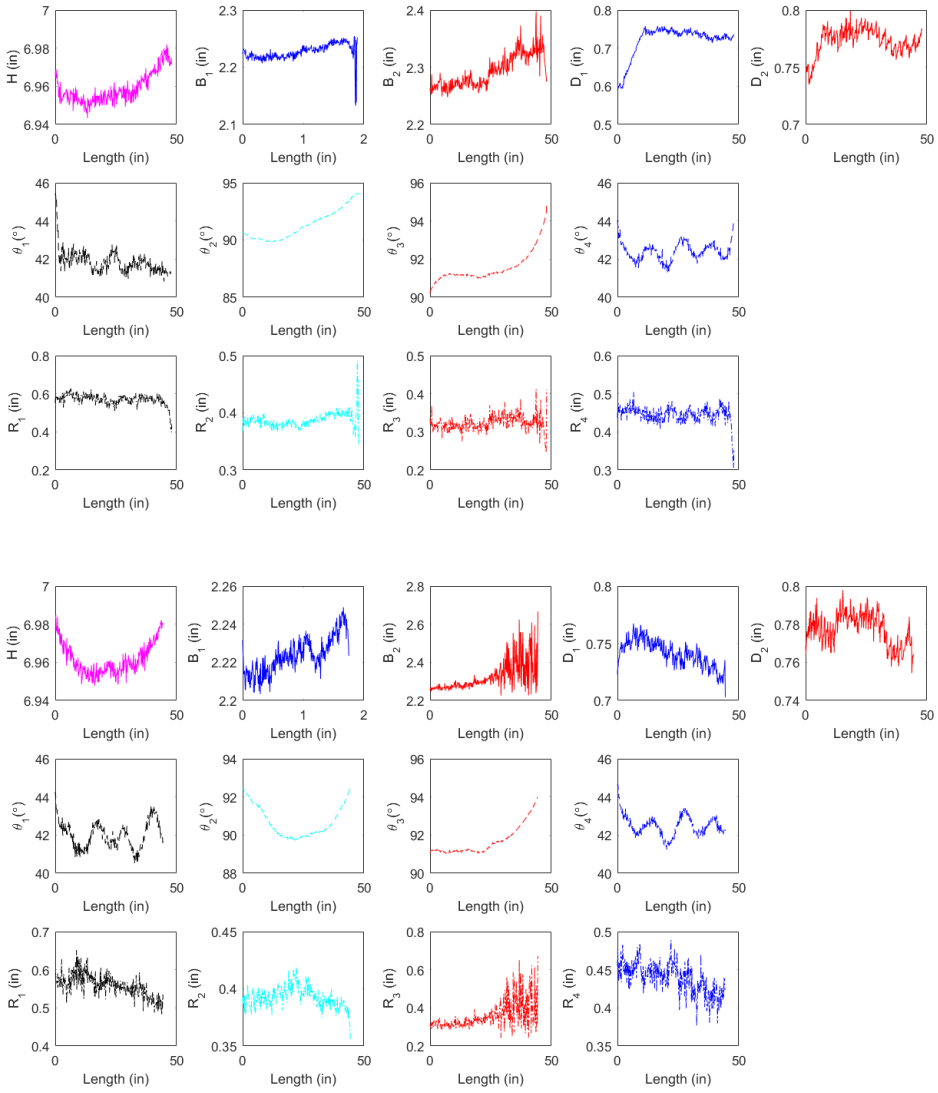
H (in)
B1 (in)
B2 (in)
D1 (in)
D2 (in)
θ1 (°)
θ2 (°)
θ3 (°)
θ4 (°)
R1 (in)
R2 (in)
R3 (in)
R4 (in)
Length (in)

H (in)
B1 (in)
B2 (in)
D1 (in)
D2 (in)
θ1 (°)
θ2 (°)
θ3 (°)
θ4 (°)
R1 (in)
R2 (in)
R3 (in)
R4 (in)
Length (in)

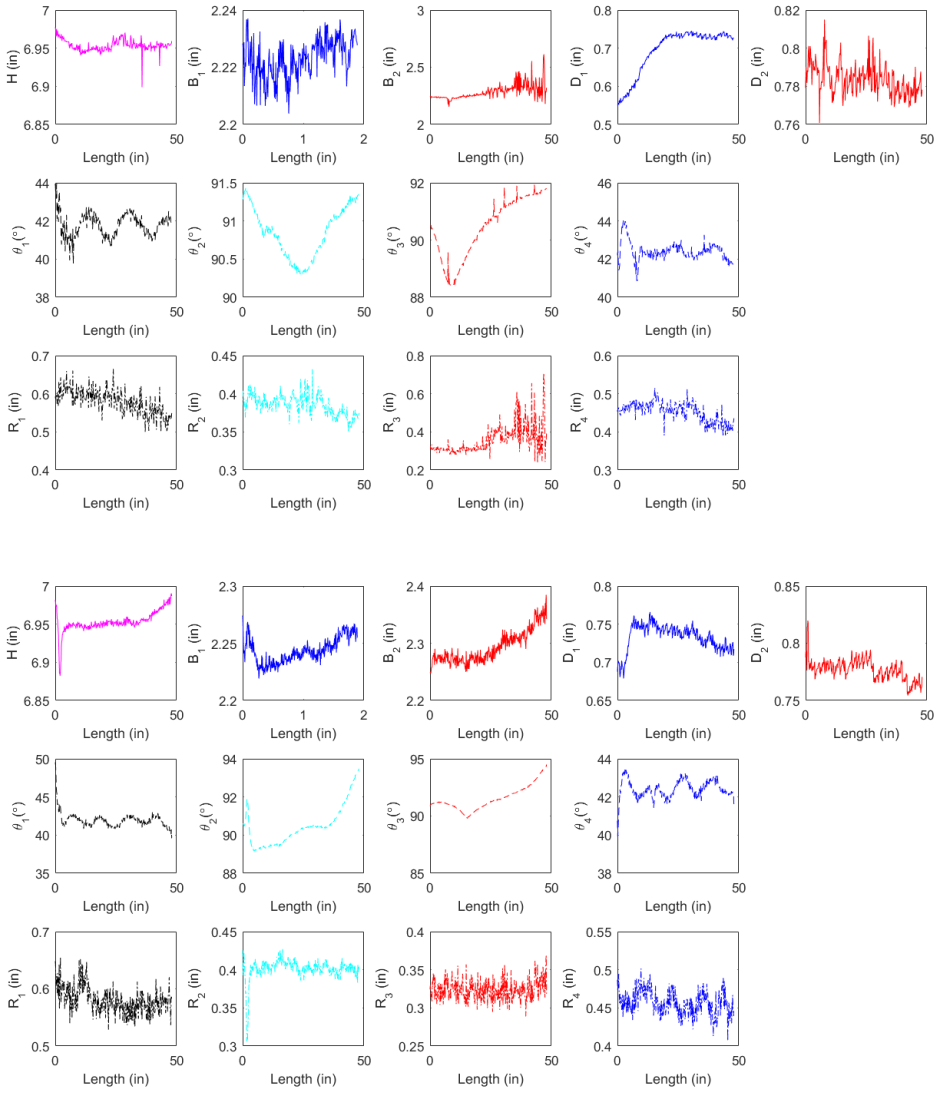
H (in)
B1 (in)
B2 (in)
D1 (in)
D2 (in)
θ1 (°)
θ2 (°)
θ3 (°)
θ4 (°)
R1 (in)
R2 (in)
R3 (in)
R4 (in)
Length (in)

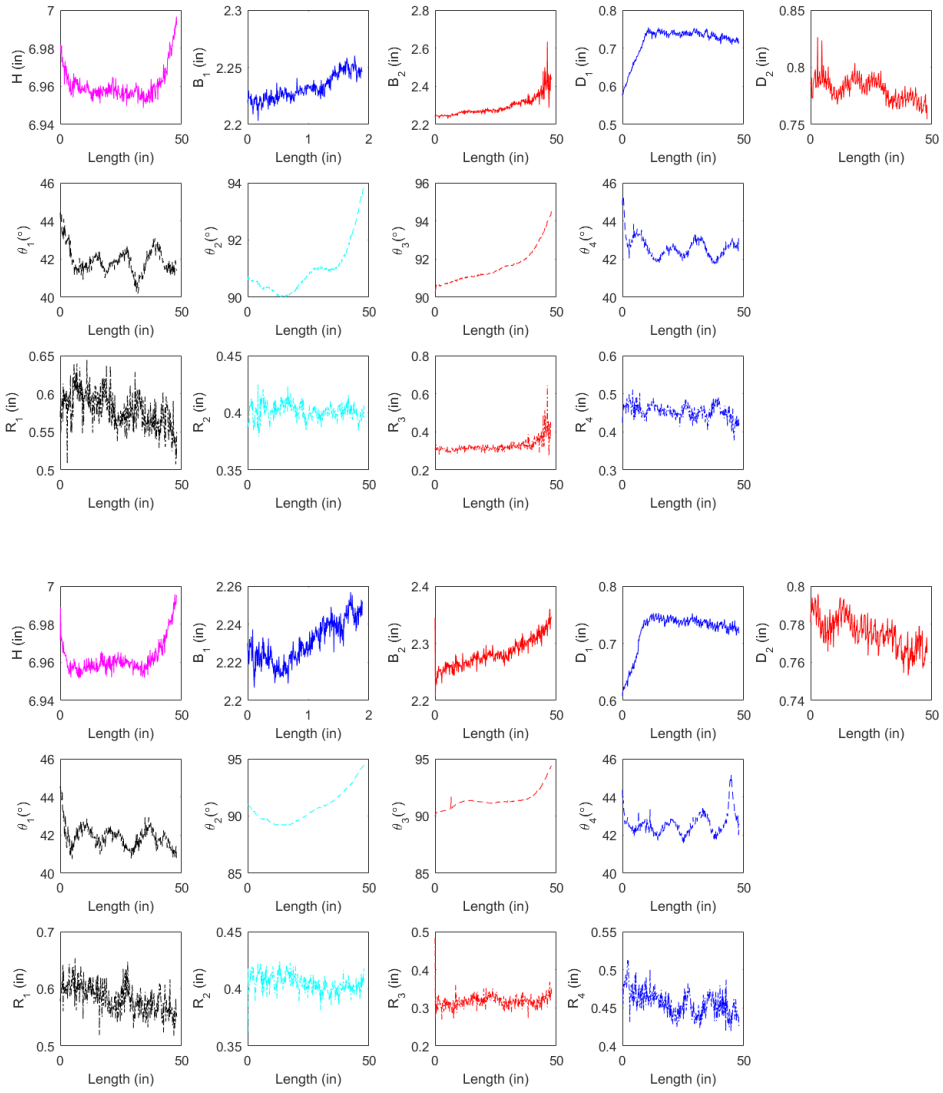
H (in)
B1 (in)
B2 (in)
D1 (in)
D2 (in)
θ1 (°)
θ2 (°)
θ3 (°)
θ4 (°)
R1 (in)
R2 (in)
R3 (in)
R4 (in)
Length (in)

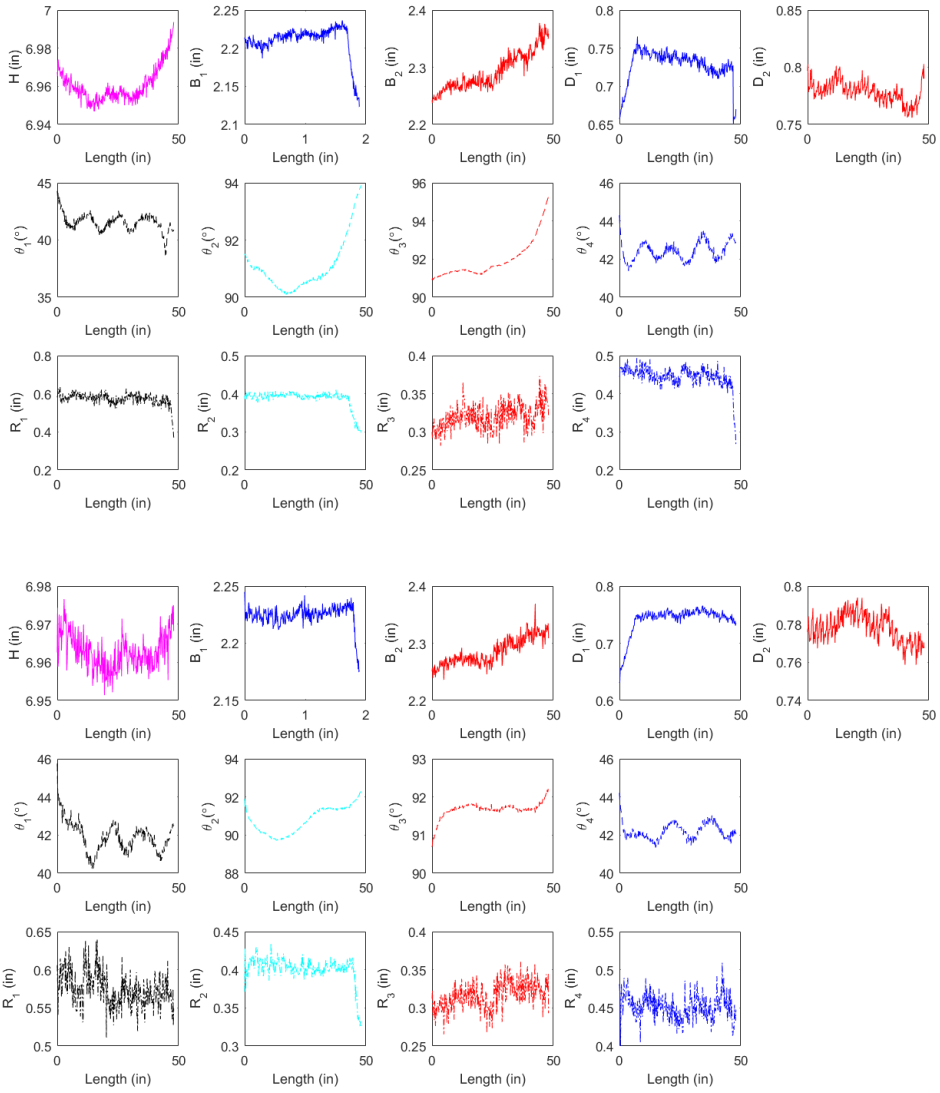
H (in)
B1 (in)
B2 (in)
D1 (in)
D2 (in)
θ1 (°)
θ2 (°)
θ3 (°)
θ4 (°)
R1 (in)
R2 (in)
R3 (in)
R4 (in)
Length (in)

H (in)
B1 (in)
B2 (in)
D1 (in)
D2 (in)
θ1 (°)
θ2 (°)
θ3 (°)
θ4 (°)
R1 (in)
R2 (in)
R3 (in)
R4 (in)
Length (in)

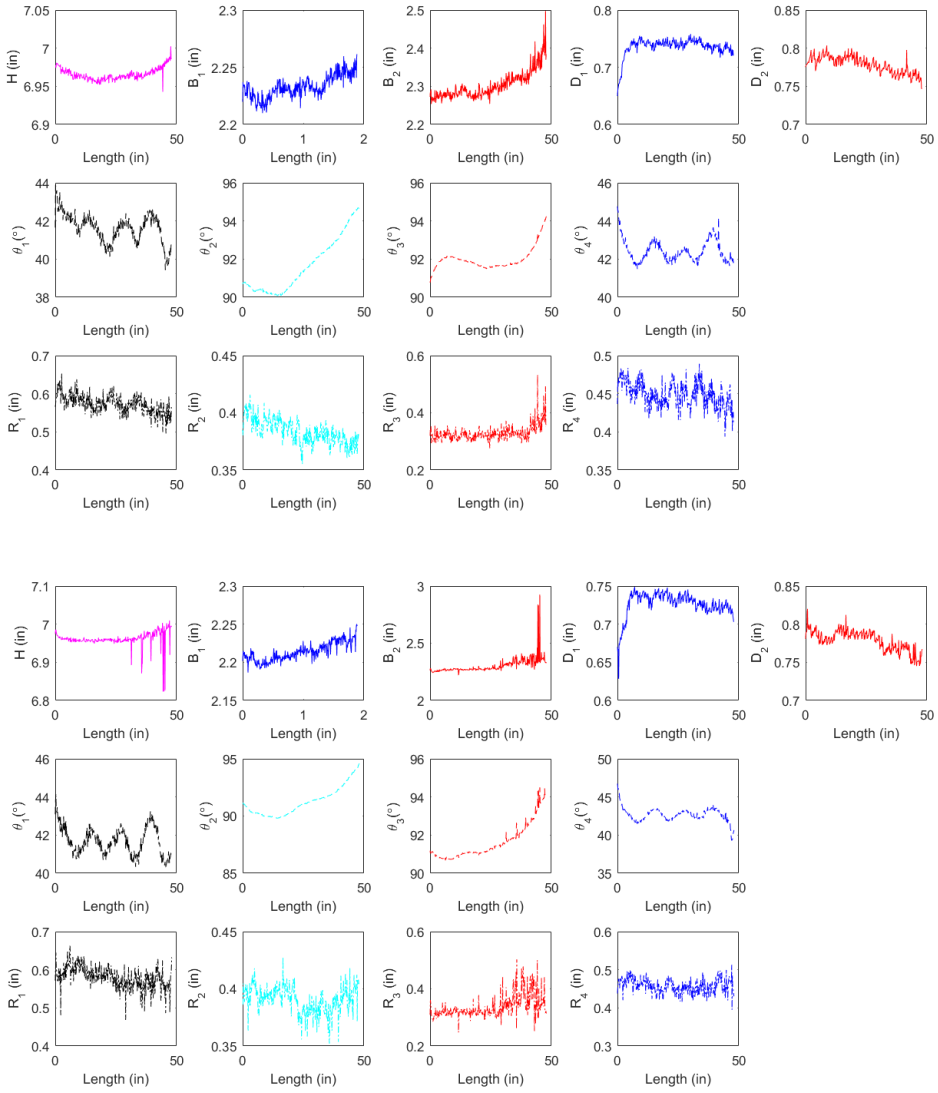
H (in)
B1 (in)
B2 (in)
D1 (in)
D2 (in)
θ1 (°)
θ2 (°)
θ3 (°)
θ4 (°)
R1 (in)
R2 (in)
R3 (in)
R4 (in)
Length (in)

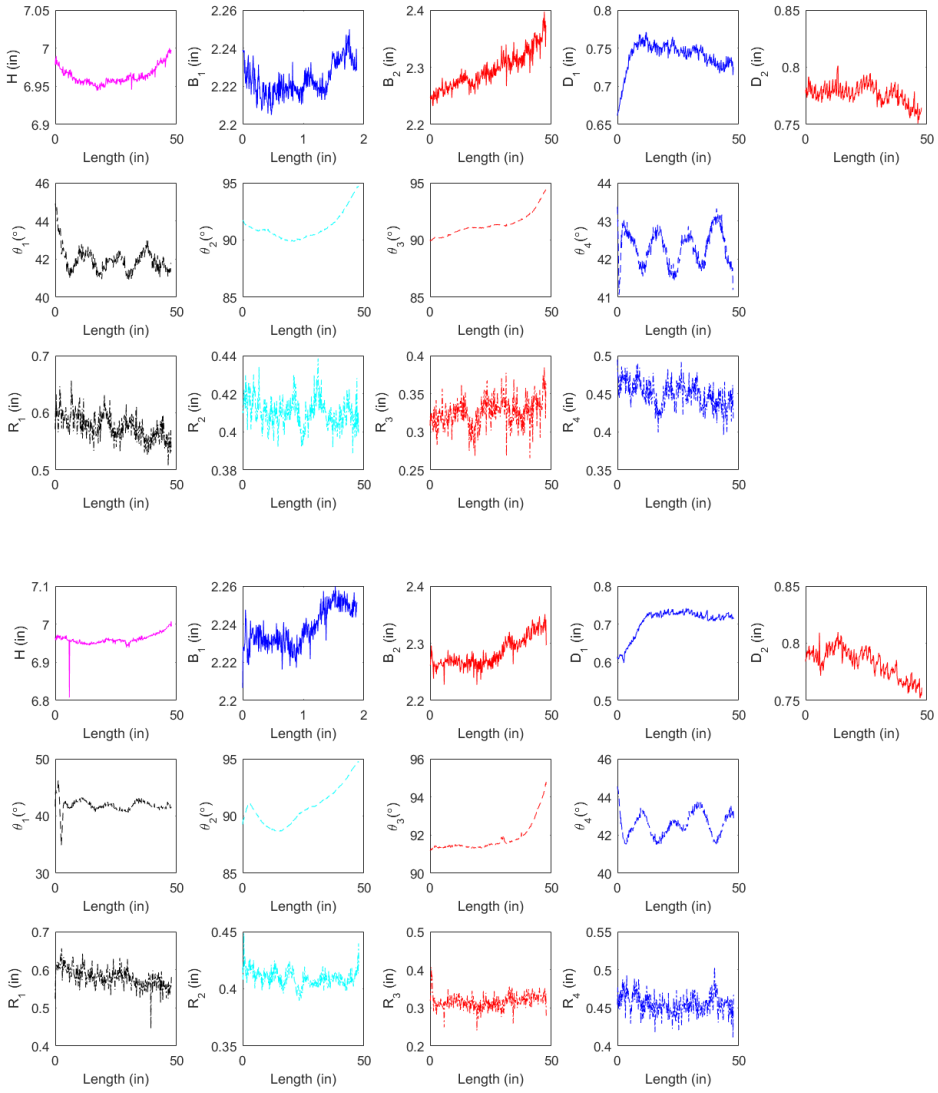
H (in)
B1 (in)
B2 (in)
D1 (in)
D2 (in)
θ1 (°)
θ2 (°)
θ3 (°)
θ4 (°)
R1 (in)
R2 (in)
R3 (in)
R4 (in)
Length (in)

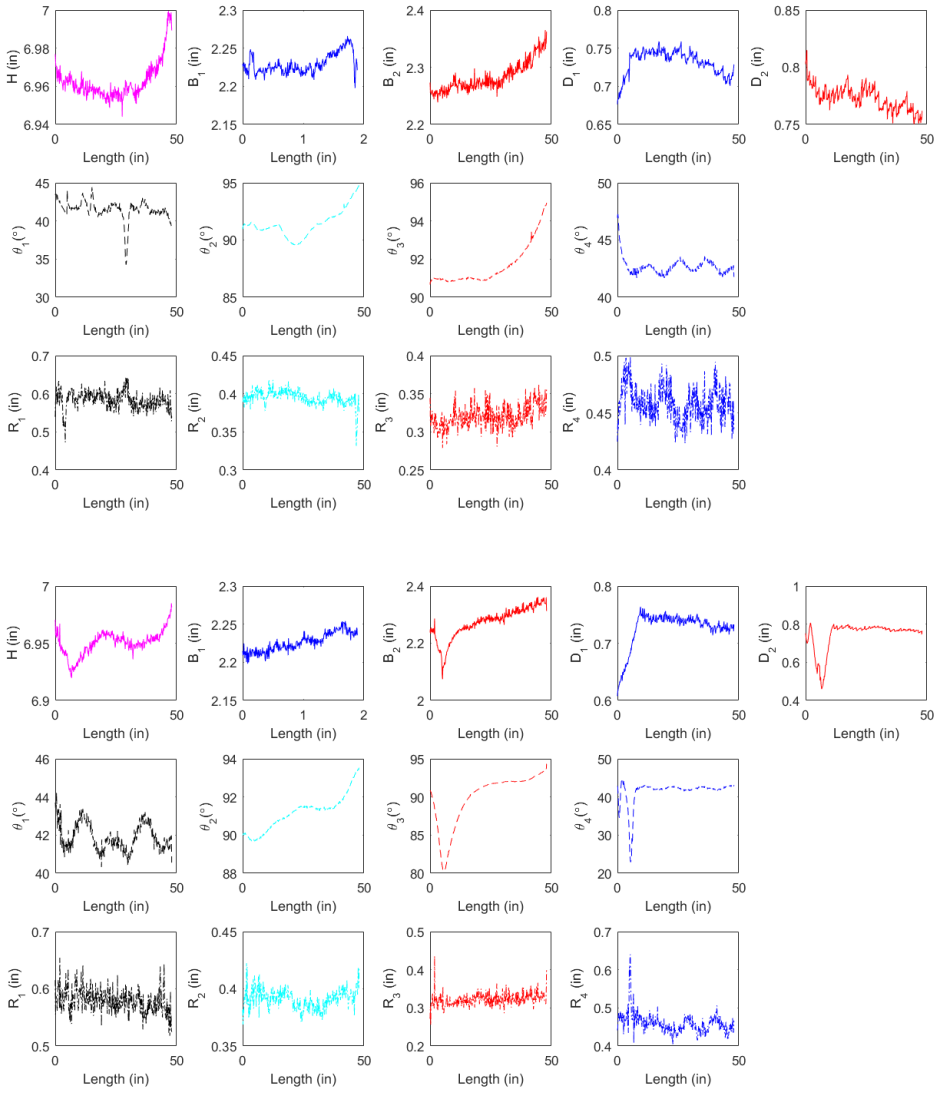
H (in)
B1 (in)
B2 (in)
D1 (in)
D2 (in)
θ1 (°)
θ2 (°)
θ3 (°)
θ4 (°)
R1 (in)
R2 (in)
R3 (in)
R4 (in)
Length (in)

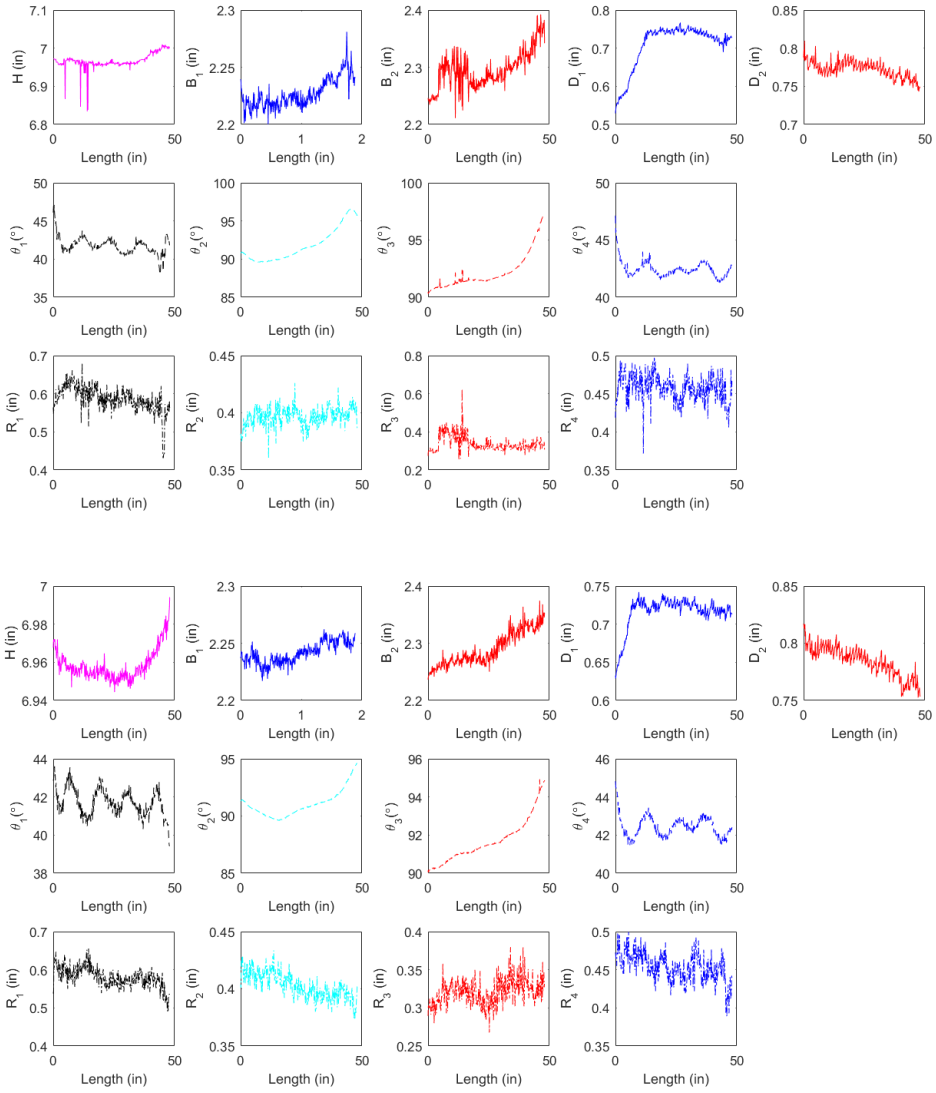
H (in)
B1 (in)
B2 (in)
D1 (in)
D2 (in)
θ1 (°)
θ2 (°)
θ3 (°)
θ4 (°)
R1 (in)
R2 (in)
R3 (in)
R4 (in)
Length (in)

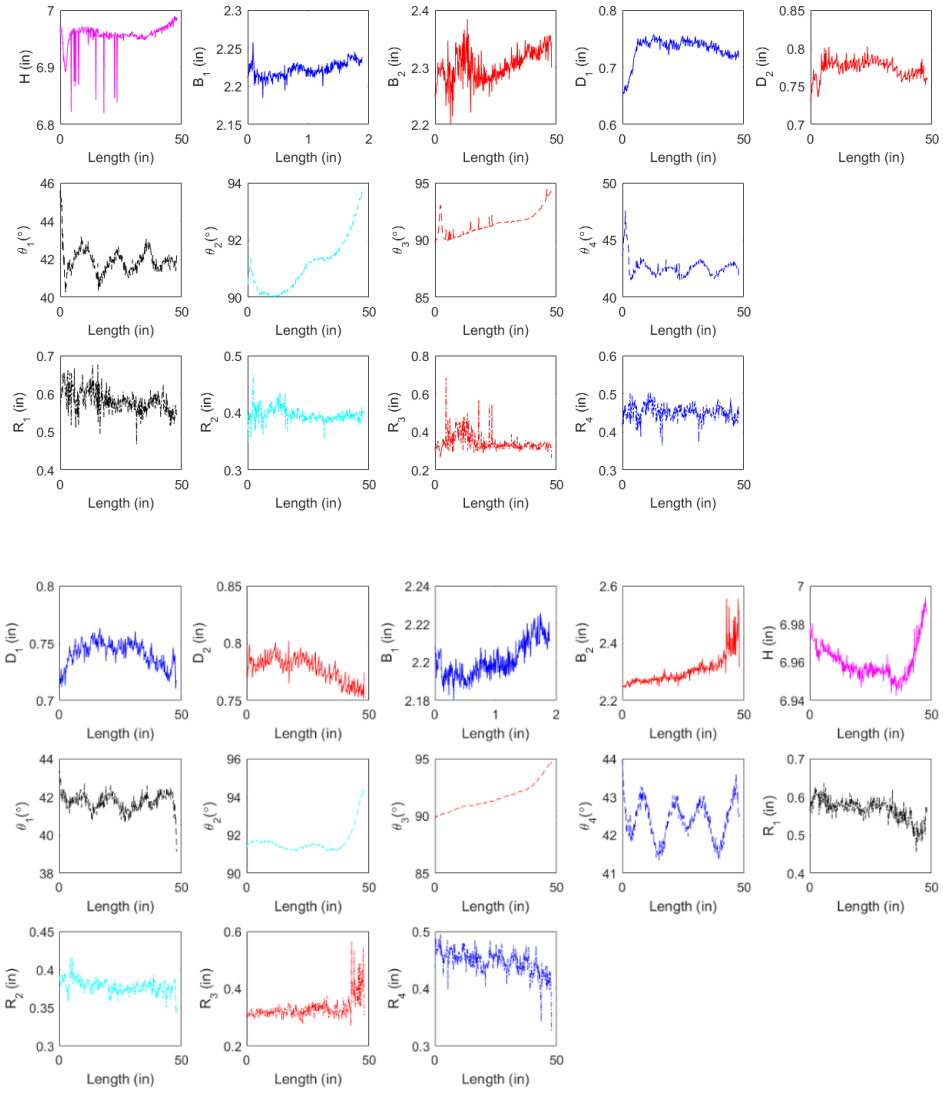
H (in)
B1 (in)
B2 (in)
D1 (in)
D2 (in)
θ1 (°)
θ2 (°)
θ3 (°)
θ4 (°)
R1 (in)
R2 (in)
R3 (in)
R4 (in)
Length (in)

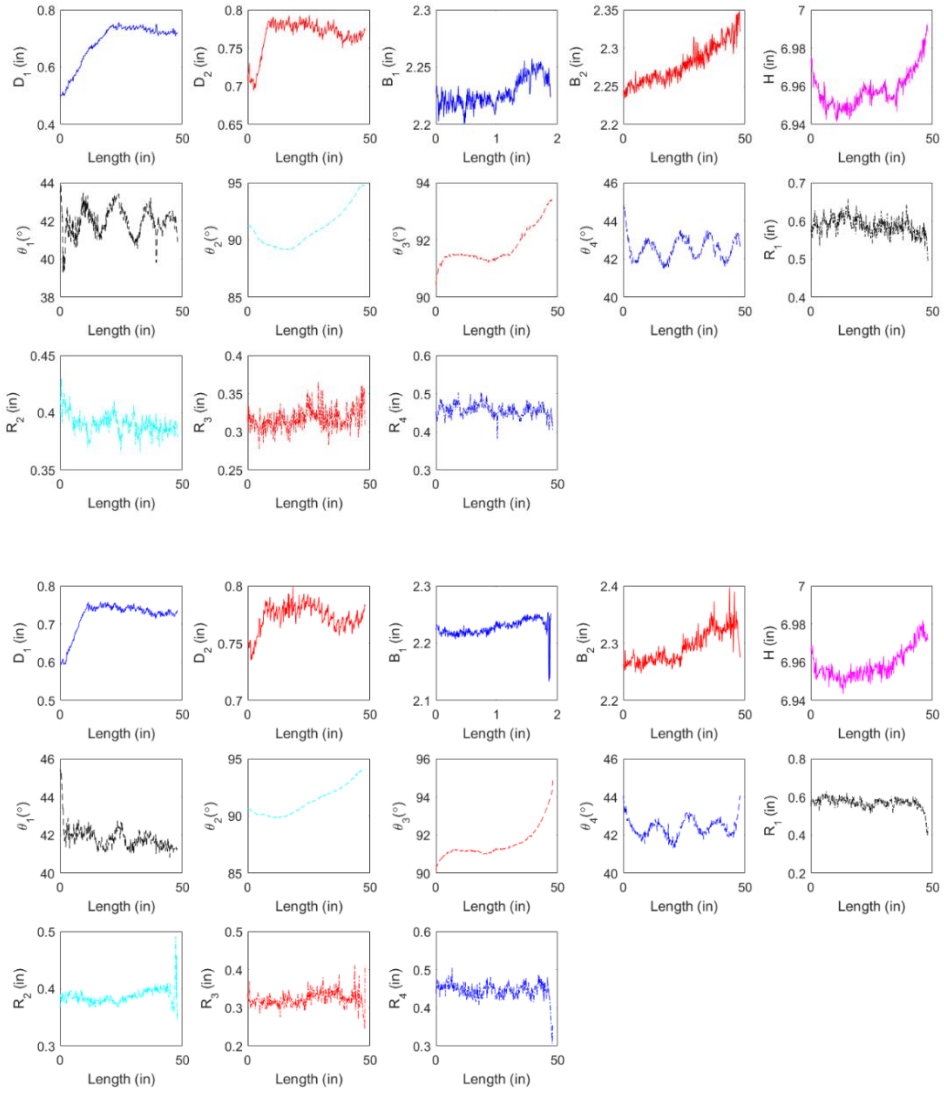
D1 (in)
D2 (in)
B1 (in)
B2 (in)
H (in)
θ1 (°)
θ2 (°)
θ3 (°)
θ4 (°)
R1 (in)
R2 (in)
R3 (in)
R4 (in)
Length (in)

D1 (in)
D2 (in)
B1 (in)
B2 (in)
H (in)
θ1 (°)
θ2 (°)
θ3 (°)
θ4 (°)
R1 (in)
R2 (in)
R3 (in)
R4 (in)
Length (in)

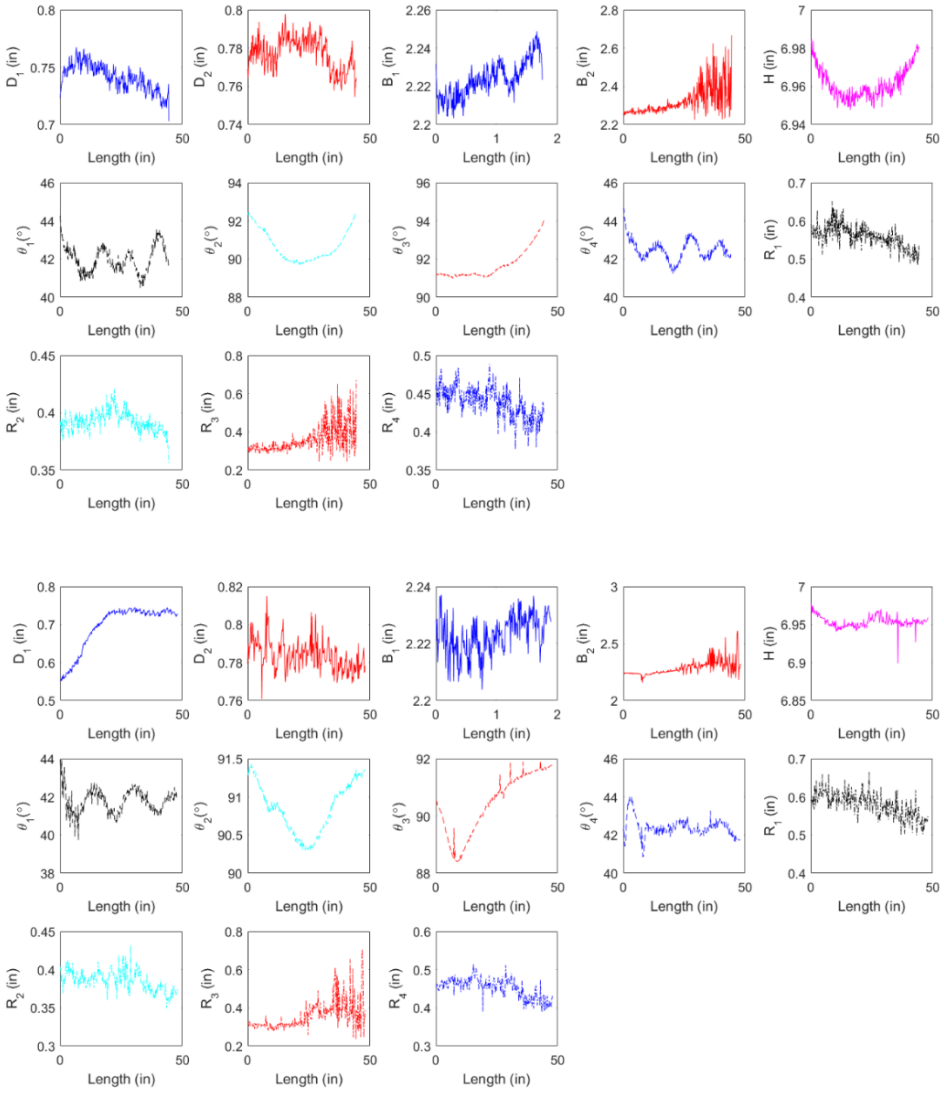
D1 (in)
D2 (in)
B1 (in)
B2 (in)
H (in)
θ1 (°)
θ2 (°)
θ3 (°)
θ4 (°)
R1 (in)
R2 (in)
R3 (in)
R4 (in)
Length (in)

D1 (in)
D2 (in)
B1 (in)
B2 (in)
H (in)
θ1 (°)
θ2 (°)
θ3 (°)
θ4 (°)
R1 (in)
R2 (in)
R3 (in)
R4 (in)
Length (in)

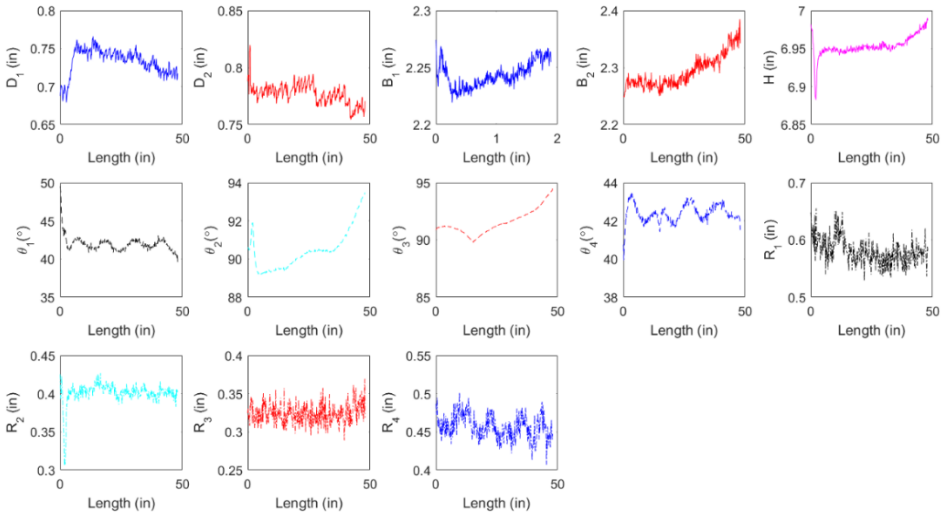
D1 (in)
D2 (in)
B1 (in)
B2 (in)
H (in)
θ1 (°)
θ2 (°)
θ3 (°)
θ4 (°)
R1 (in)
R2 (in)
R3 (in)
R4 (in)
Length (in)

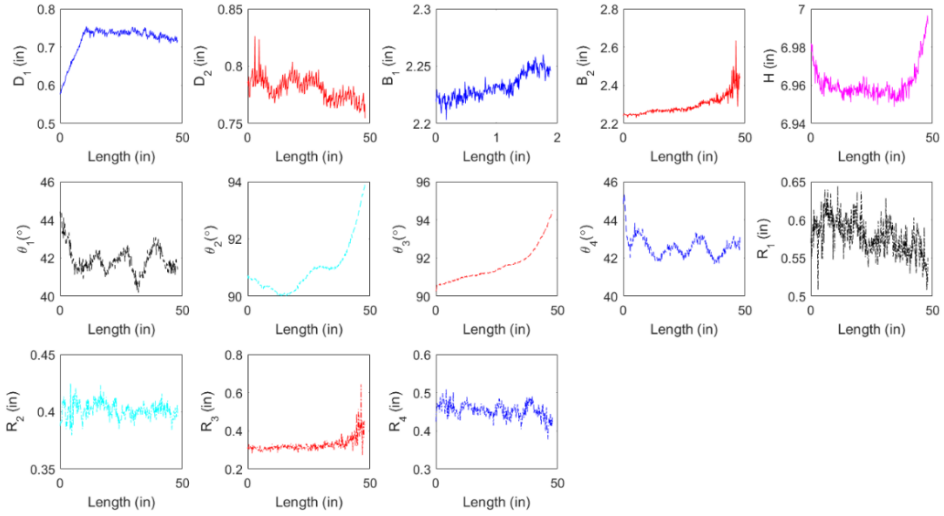
D1 (in)
D2 (in)
B1 (in)
B2 (in)
H (in)
θ1 (°)
θ2 (°)
θ3 (°)
θ4 (°)
R1 (in)
R2 (in)
R3 (in)
R4 (in)
Length (in)

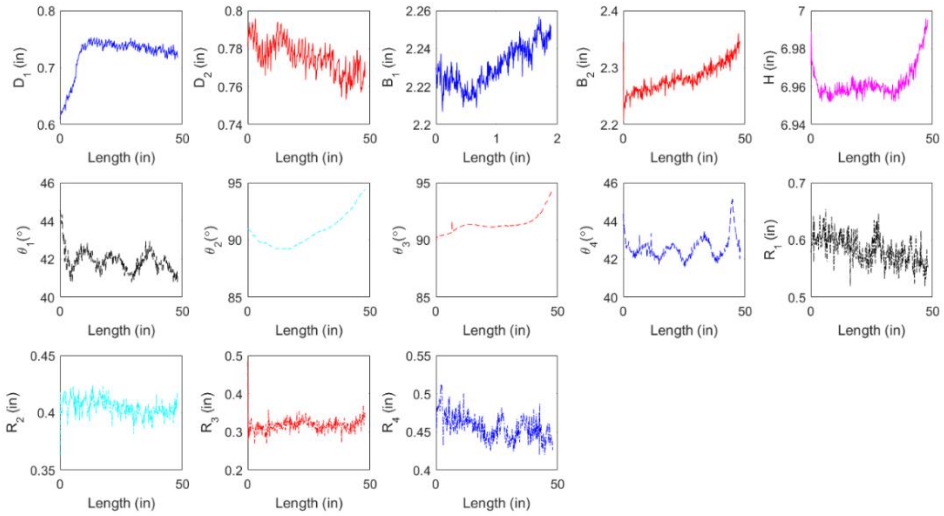
D1 (in)
D2 (in)
B1 (in)
B2 (in)
H (in)
θ1 (°)
θ2 (°)
θ3 (°)
θ4 (°)
R1 (in)
R2 (in)
R3 (in)
R4 (in)
Length (in)

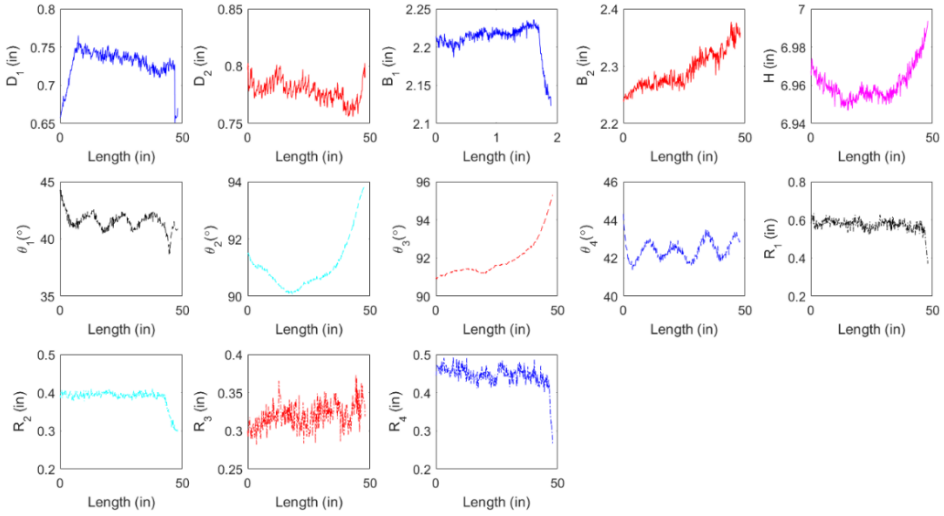
D1 (in)
D2 (in)
B1 (in)
B2 (in)
H (in)
θ1 (°)
θ2 (°)
θ3 (°)
θ4 (°)
R1 (in)
R2 (in)
R3 (in)
R4 (in)
Length (in)

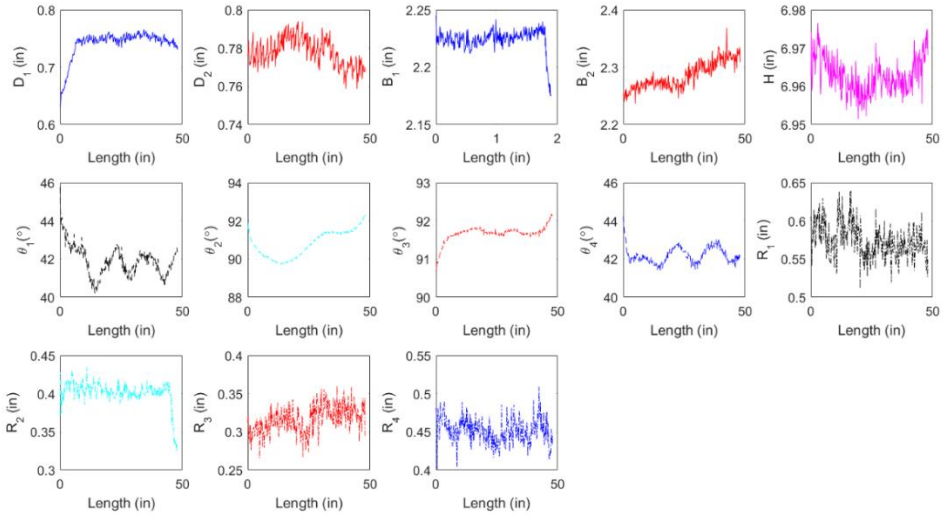
D1 (in)
D2 (in)
B1 (in)
B2 (in)
H (in)
θ1 (°)
θ2 (°)
θ3 (°)
θ4 (°)
R1 (in)
R2 (in)
R3 (in)
R4 (in)
Length (in)

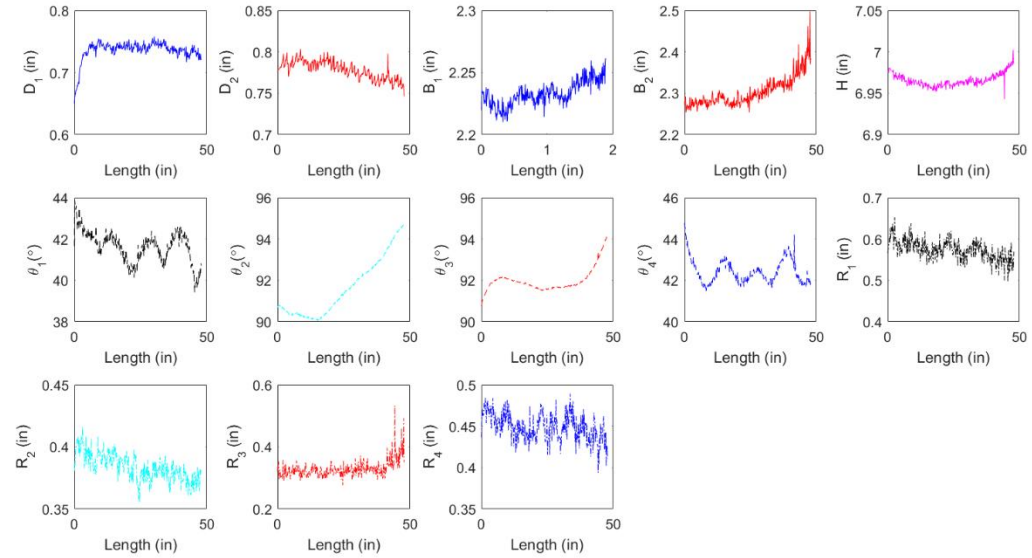
D1 (in)
D2 (in)
B1 (in)
B2 (in)
H (in)
θ1 (°)
θ2 (°)
θ3 (°)
θ4 (°)
R1 (in)
R2 (in)
R3 (in)
R4 (in)
Length (in)

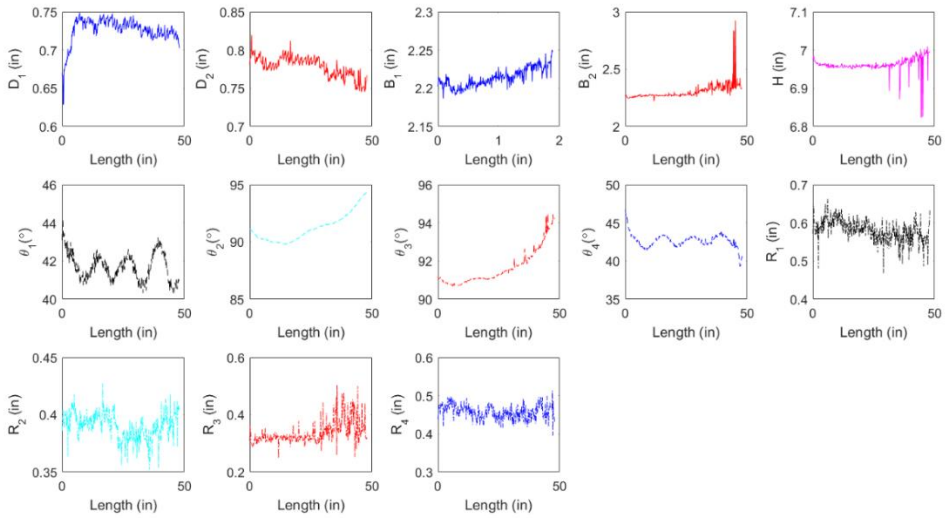
D1 (in)
D2 (in)
B1 (in)
B2 (in)
H (in)
θ1 (°)
θ2 (°)
θ3 (°)
θ4 (°)
R1 (in)
R2 (in)
R3 (in)
R4 (in)
Length (in)

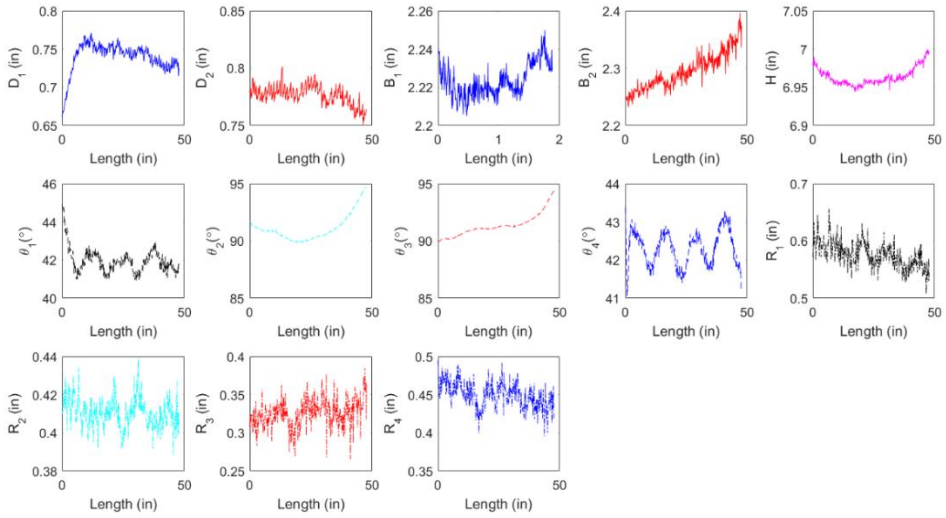
D1 (in)
D2 (in)
B1 (in)
B2 (in)
H (in)
θ1 (°)
θ2 (°)
θ3 (°)
θ4 (°)
R1 (in)
R2 (in)
R3 (in)
R4 (in)
Length (in)

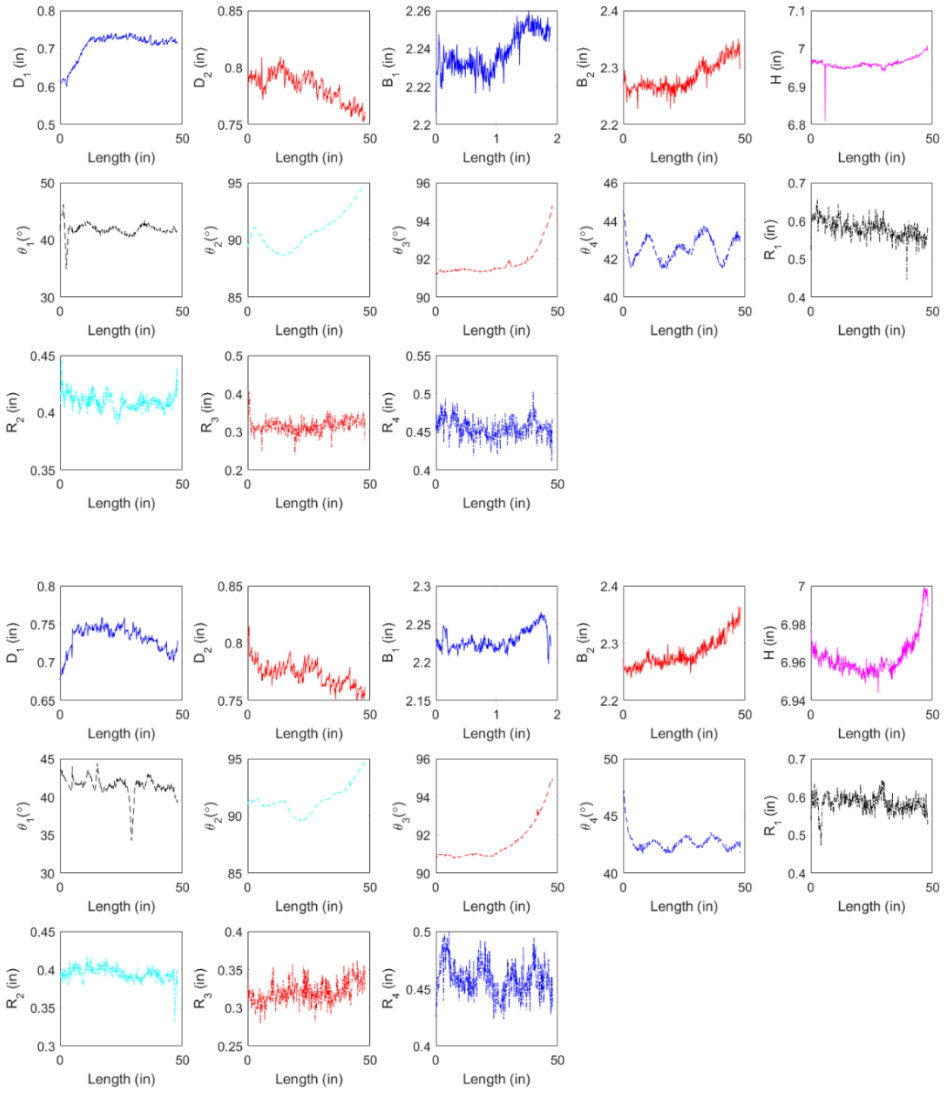
D1 (in)
D2 (in)
B1 (in)
B2 (in)
H (in)
θ1 (°)
θ2 (°)
θ3 (°)
θ4 (°)
R1 (in)
R2 (in)
R3 (in)
R4 (in)
Length (in)

D1 (in)
D2 (in)
B1 (in)
B2 (in)
H (in)
θ1 (°)
θ2 (°)
θ3 (°)
θ4 (°)
R1 (in)
R2 (in)
R3 (in)
R4 (in)
Length (in)

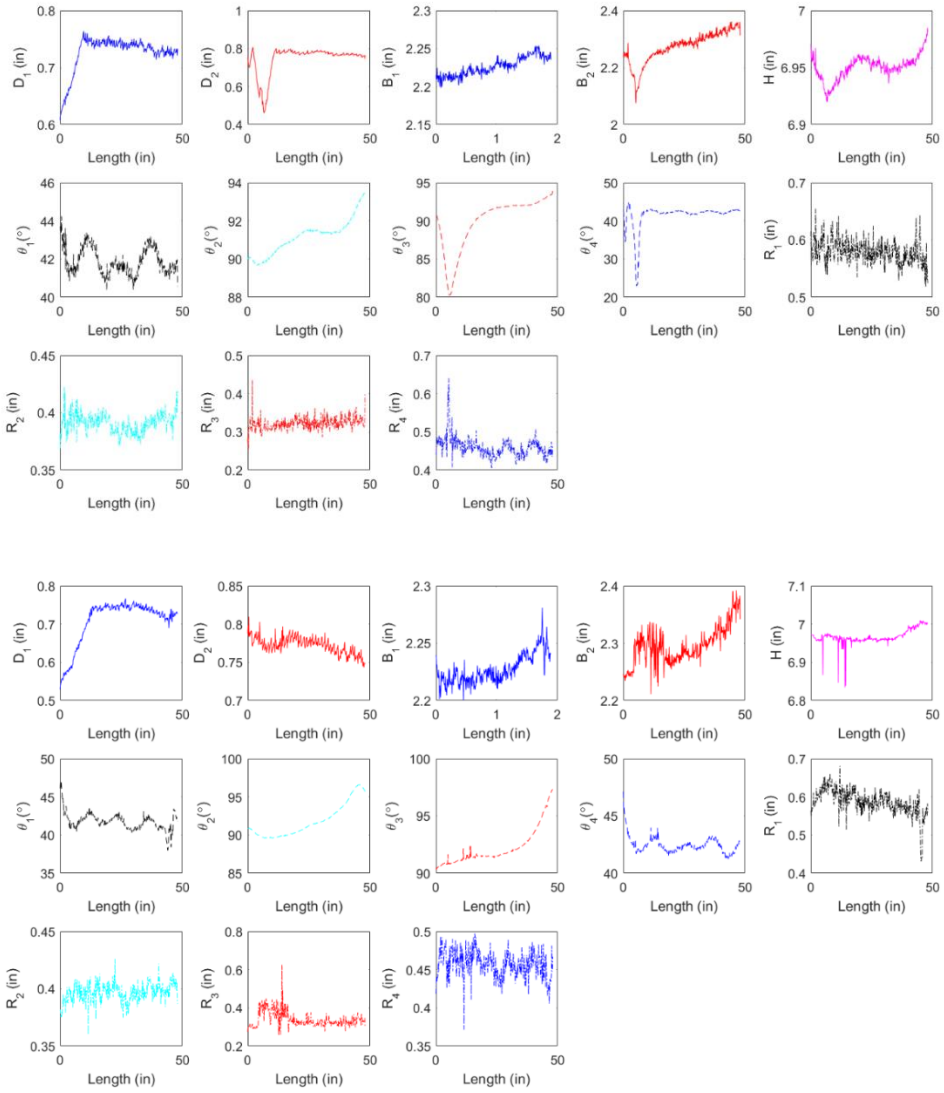
D1 (in)
D2 (in)
B1 (in)
B2 (in)
H (in)
θ1 (°)
θ2 (°)
θ3 (°)
θ4 (°)
R1 (in)
R2 (in)
R3 (in)
R4 (in)
Length (in)

D1 (in)
D2 (in)
B1 (in)
B2 (in)
H (in)
θ1 (°)
θ2 (°)
θ3 (°)
θ4 (°)
R1 (in)
R2 (in)
R3 (in)
R4 (in)
Length (in)

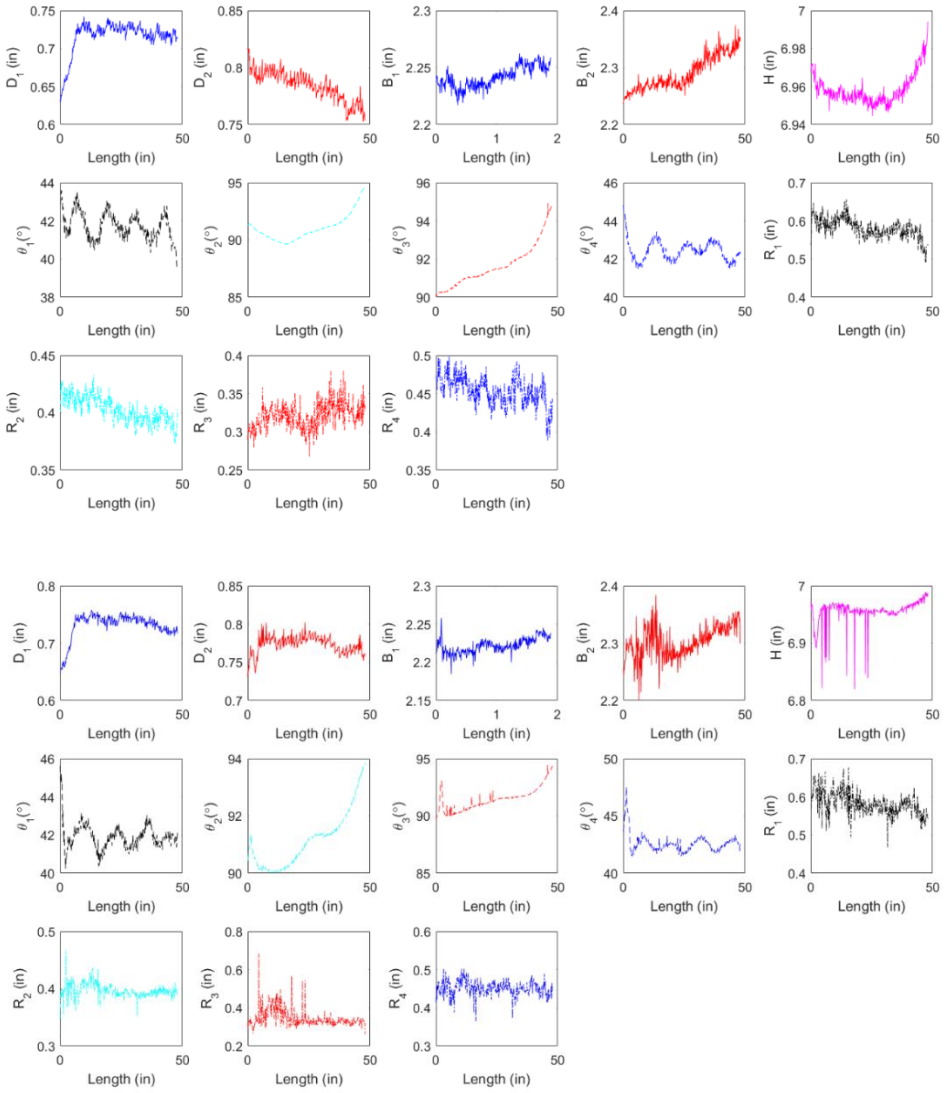

A. 9 Variations of dimensions along 700Z225-60 Z sections (Specimen 1 – Specimen 19)

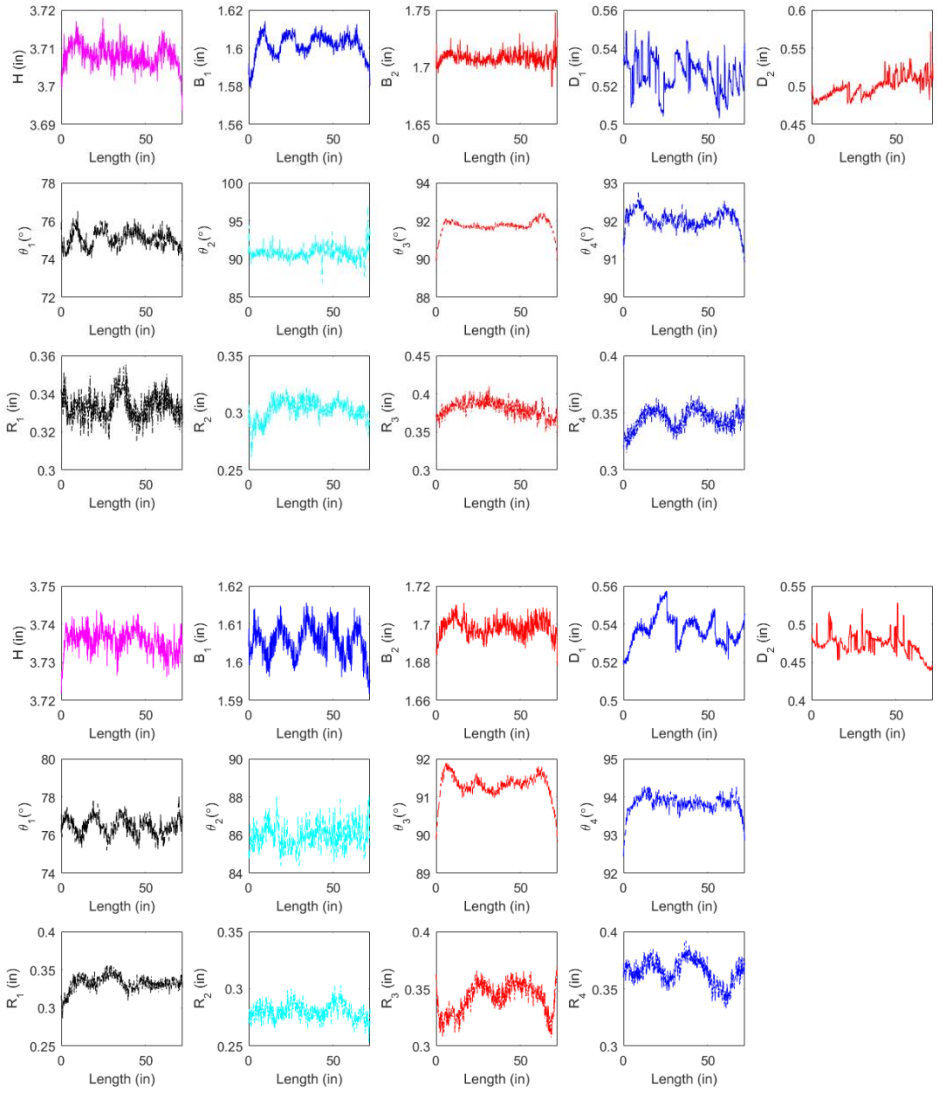
H (in)
B1 (in)
B2 (in)
D1 (in)
D2 (in)
θ1 (°)
θ2 (°)
θ3 (°)
θ4 (°)
R1 (in)
R2 (in)
R3 (in)
R4 (in)
Length (in)

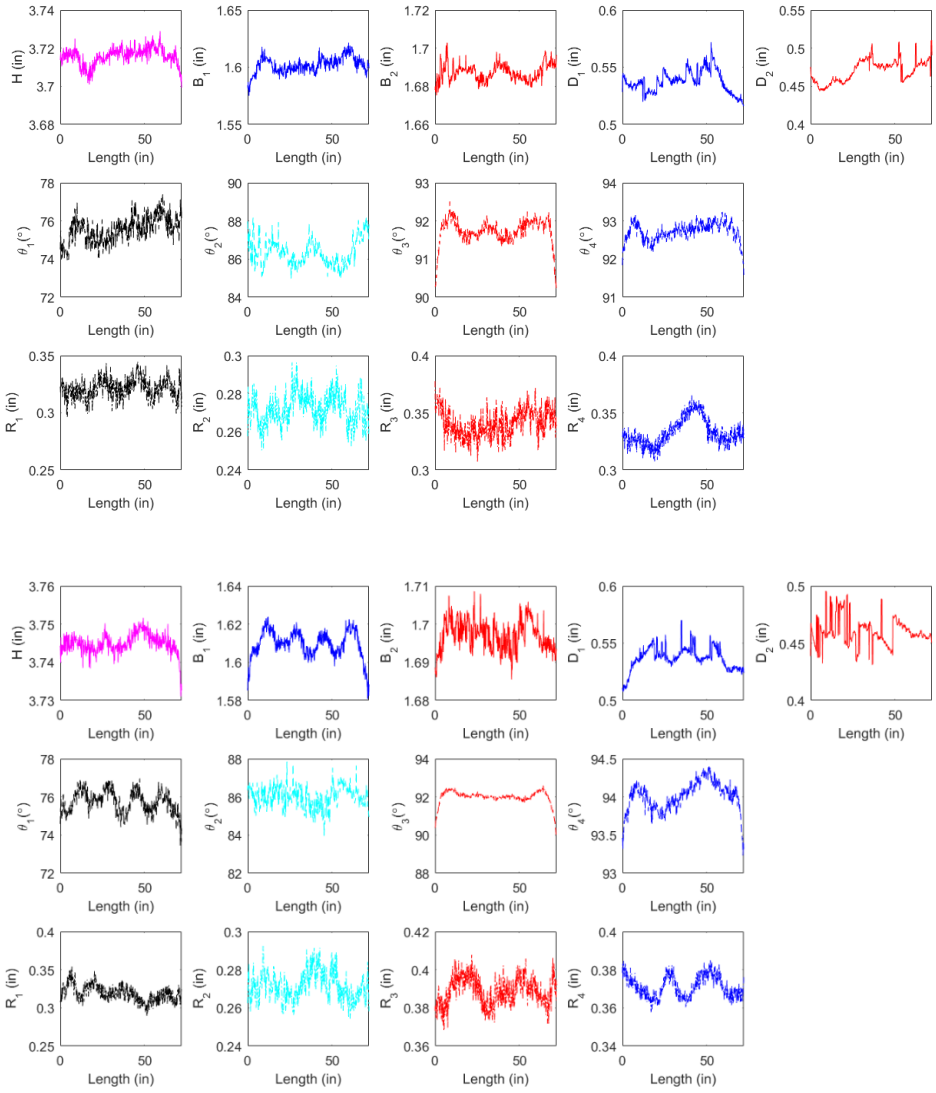
H (in)
3.74
3.72
3.7
3.68
B1 (in)
1.65
1.6
1.55
B2 (in)
1.72
1.7
1.68
1.66
D1 (in)
0.6
0.55
0.5
D2 (in)
0.55
0.5
0.45
0.4
θ1 (°)
78
76
74
72
θ2 (°)
90
88
86
84
θ3 (°)
93
92
91
90
θ4 (°)
94
93
92
91
R1 (in)
0.35
0.3
0.25
R2 (in)
0.3
0.28
0.26
0.24
R3 (in)
0.4
0.35
0.3
R4 (in)
0.4
0.35
0.3
0
50
Length (in)
H (in)
3.76
3.75
3.74
3.73
B1 (in)
1.64
1.62
1.6
1.58
B2 (in)
1.71
1.7
1.69
1.68
D1 (in)
0.6
0.55
0.5
D2 (in)
0.5
0.45
0.4
θ1 (°)
78
76
74
72
θ2 (°)
88
86
84
82
θ3 (°)
94
92
90
88
θ4 (°)
94.5
94
93.5
93
R1 (in)
0.4
0.35
0.3
0.25
R2 (in)
0.3
0.28
0.26
0.24
R3 (in)
0.42
0.4
0.38
0.36
R4 (in)
0.4
0.38
0.36
0.34
0
50
Length (in)

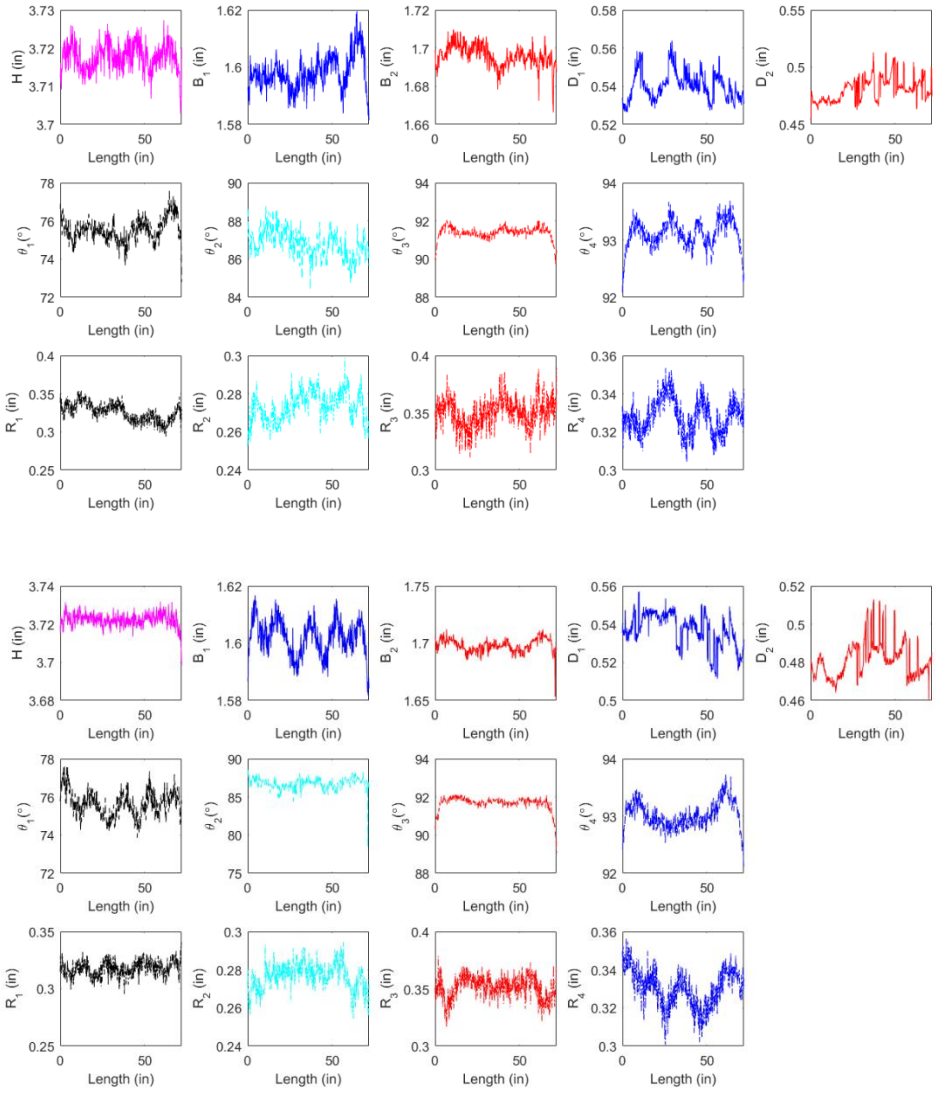
H (in)
B1 (in)
B2 (in)
D1 (in)
D2 (in)
θ1 (°)
θ2 (°)
θ3 (°)
θ4 (°)
R1 (in)
R2 (in)
R3 (in)
R4 (in)
Length (in)

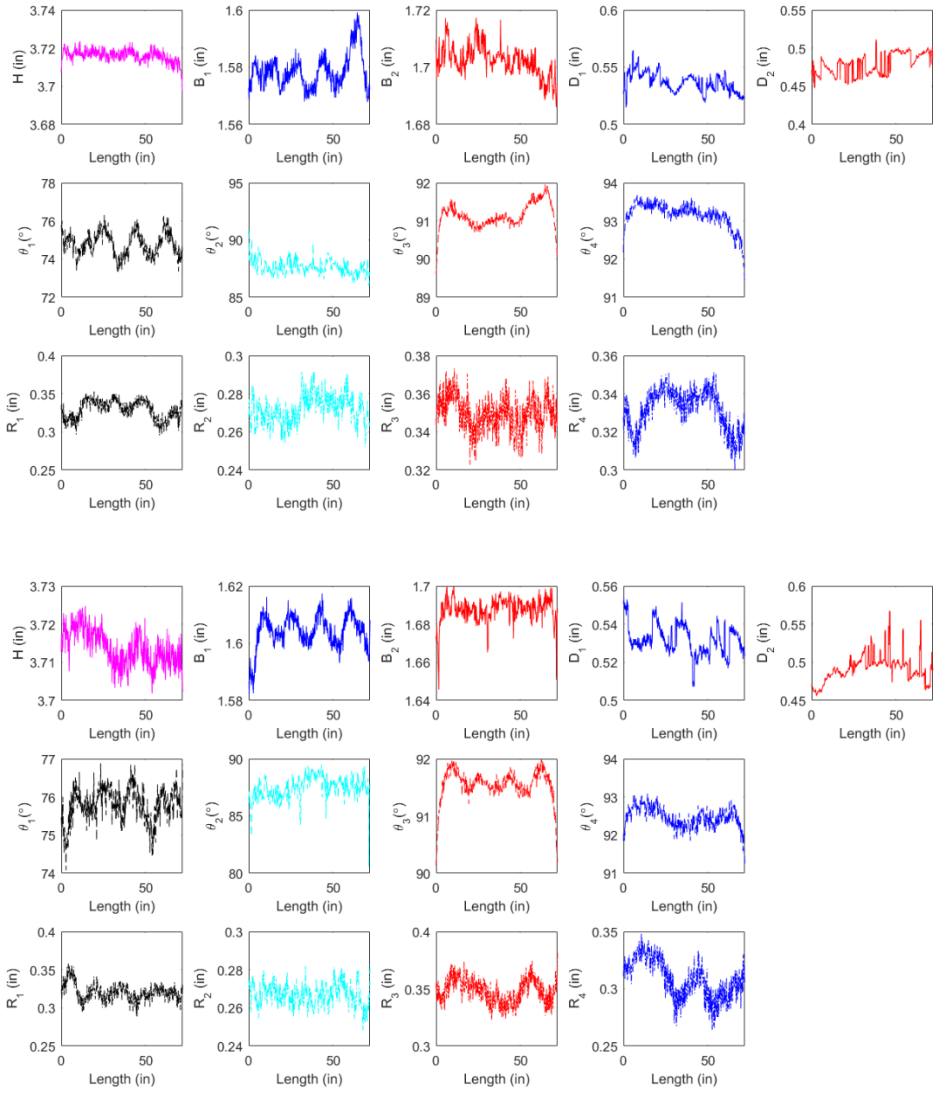
H (in)
B1 (in)
B2 (in)
D1 (in)
D2 (in)
θ1 (°)
θ2 (°)
θ3 (°)
θ4 (°)
R1 (in)
R2 (in)
R3 (in)
R4 (in)
Length (in)

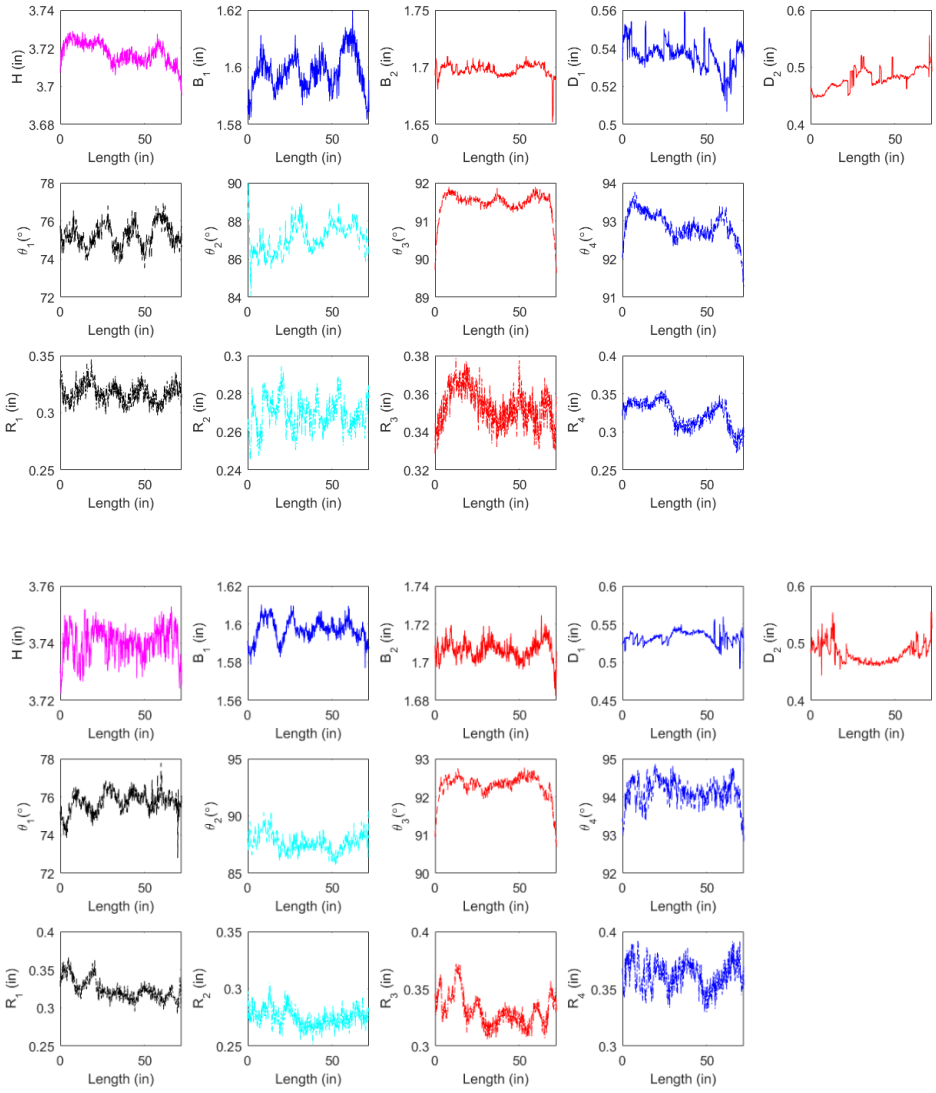
H (in)
B1 (in)
B2 (in)
D1 (in)
D2 (in)
θ1 (°)
θ2 (°)
θ3 (°)
θ4 (°)
R1 (in)
R2 (in)
R3 (in)
R4 (in)
Length (in)

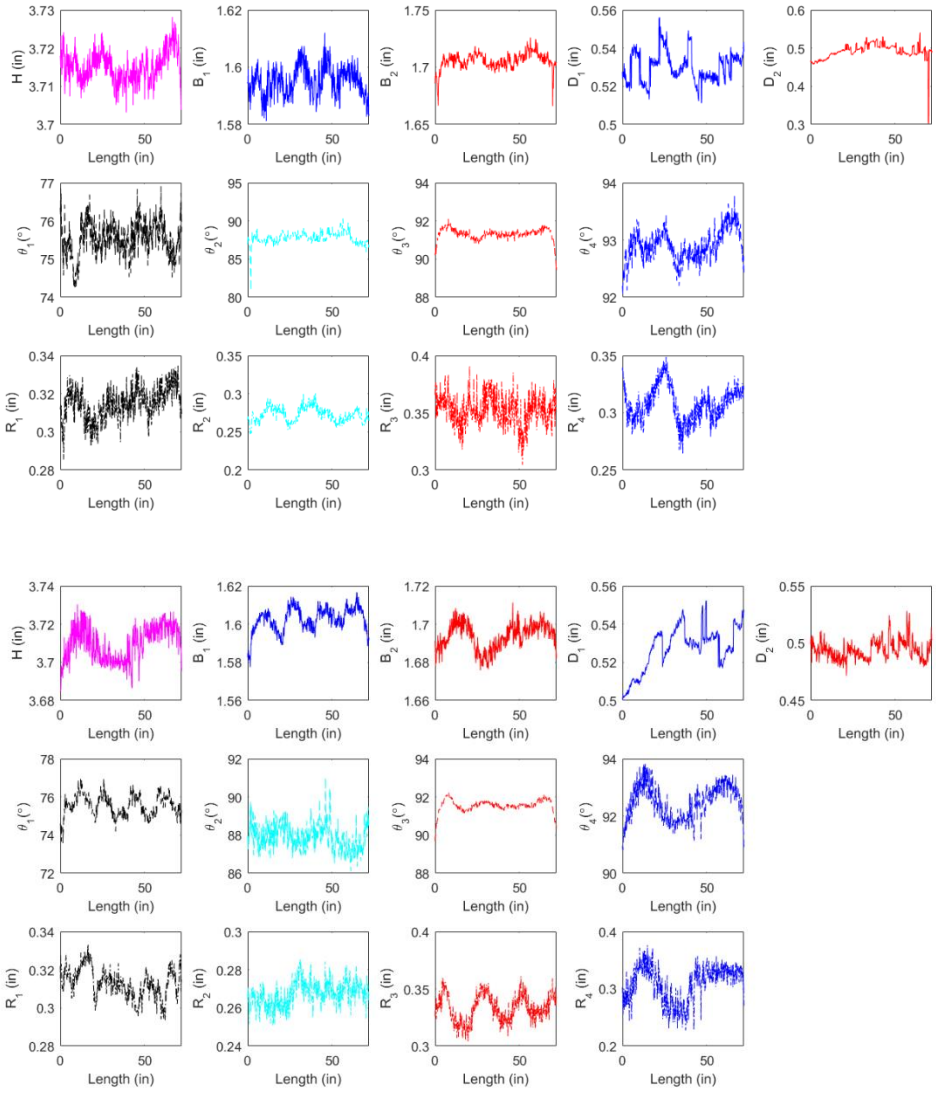
H (in)
B1 (in)
B2 (in)
D1 (in)
D2 (in)
θ1 (°)
θ2 (°)
θ3 (°)
θ4 (°)
R1 (in)
R2 (in)
R3 (in)
R4 (in)
Length (in)

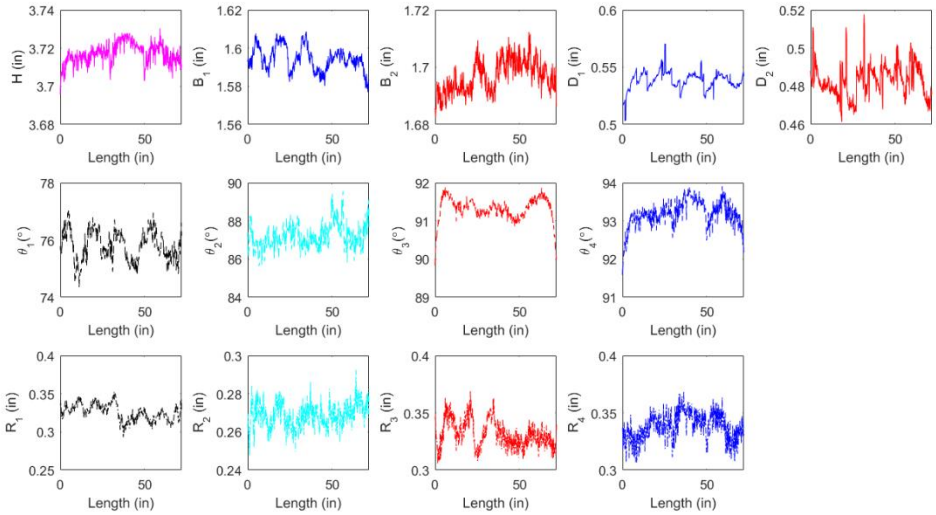

A. 10 Variations of dimensions along the length of C sections [362S162-68] (Specimen 1 – Specimen 14)

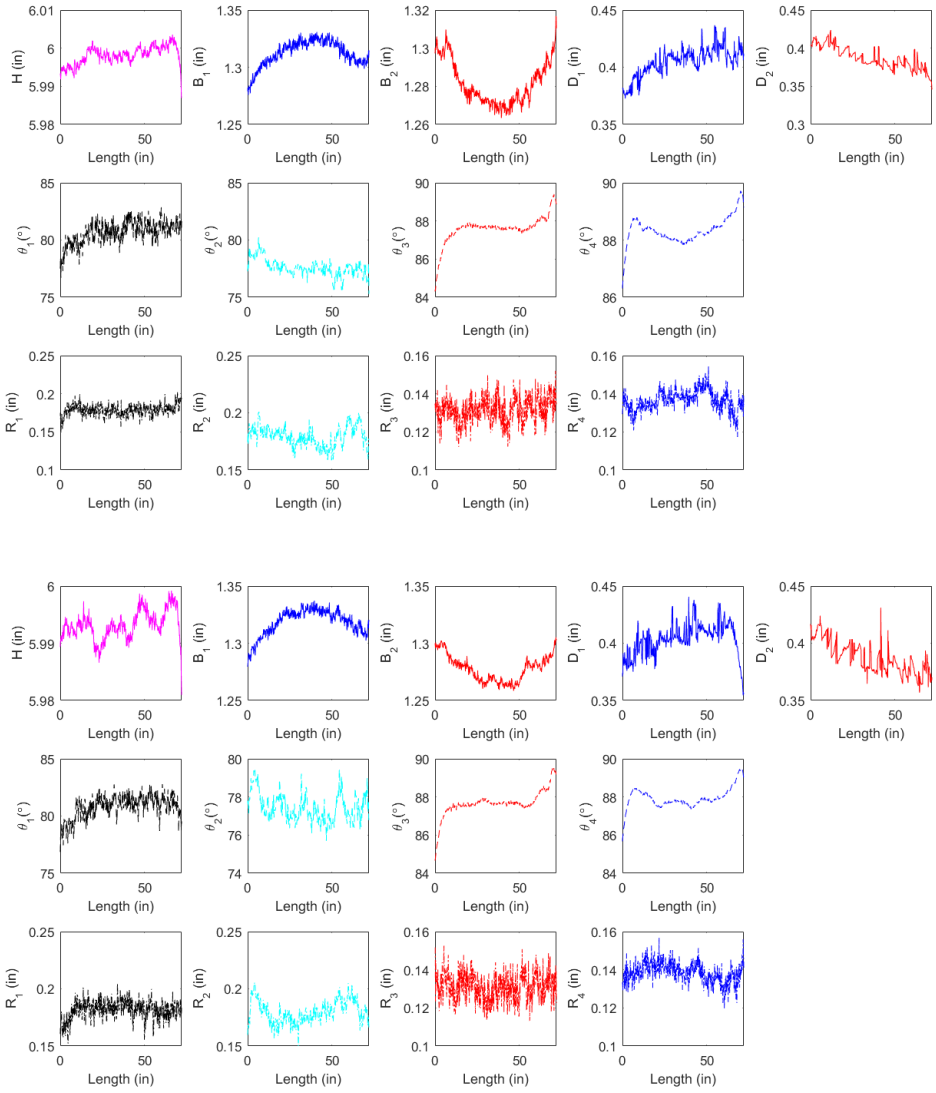
H (in)
B1 (in)
B2 (in)
D1 (in)
D2 (in)
θ1 (°)
θ2 (°)
θ3 (°)
θ4 (°)
R1 (in)
R2 (in)
R3 (in)
R4 (in)
Length (in)

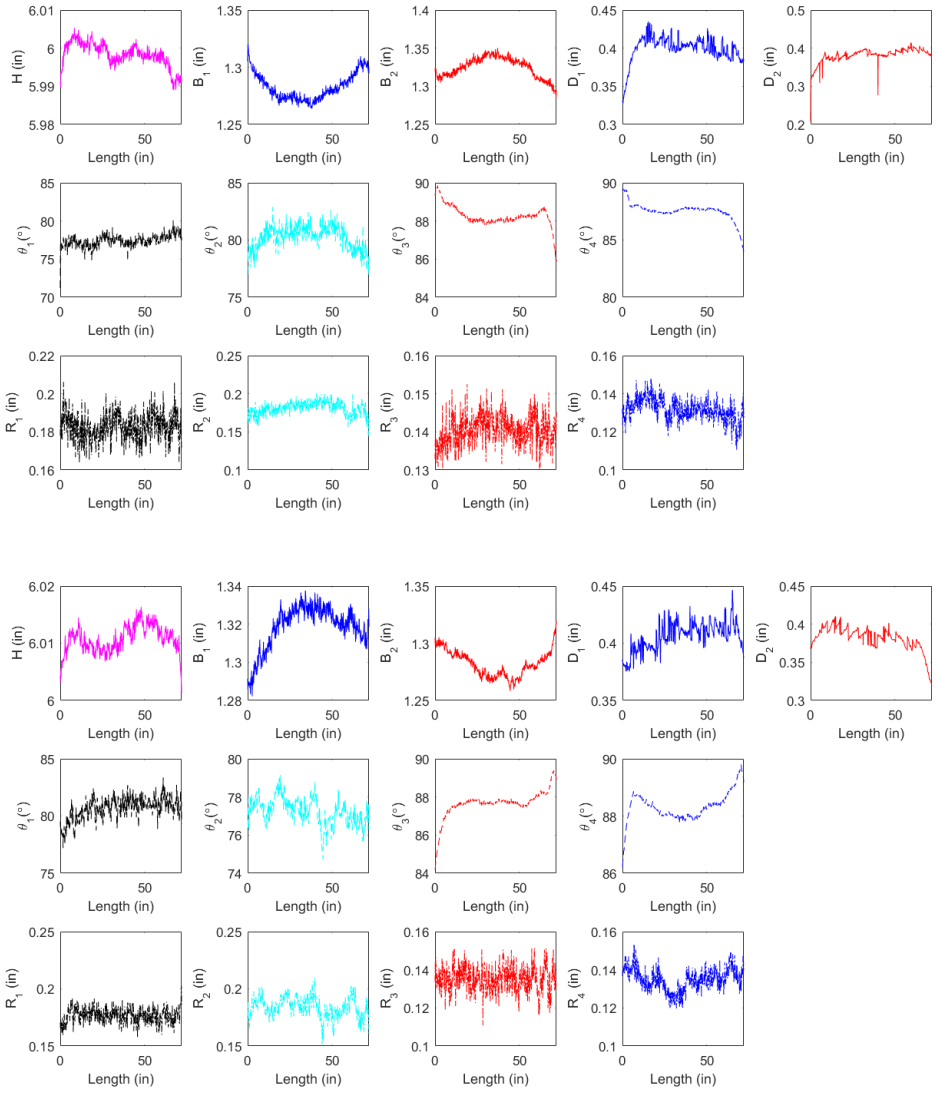
H (in)
B1 (in)
B2 (in)
D1 (in)
D2 (in)
θ1 (°)
θ2 (°)
θ3 (°)
θ4 (°)
R1 (in)
R2 (in)
R3 (in)
R4 (in)
Length (in)

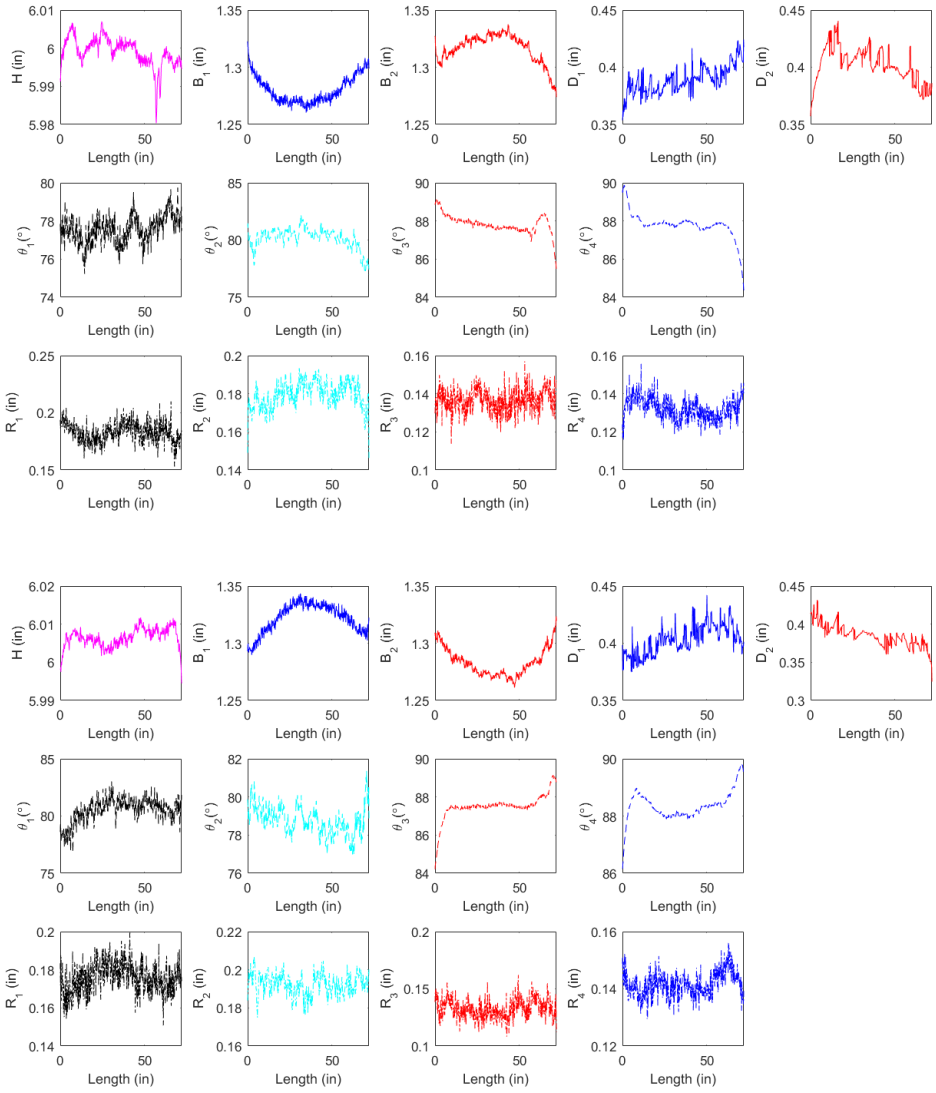
H (in)
B1 (in)
B2 (in)
D1 (in)
D2 (in)
θ1 (°)
θ2 (°)
θ3 (°)
θ4 (°)
R1 (in)
R2 (in)
R3 (in)
R4 (in)
Length (in)

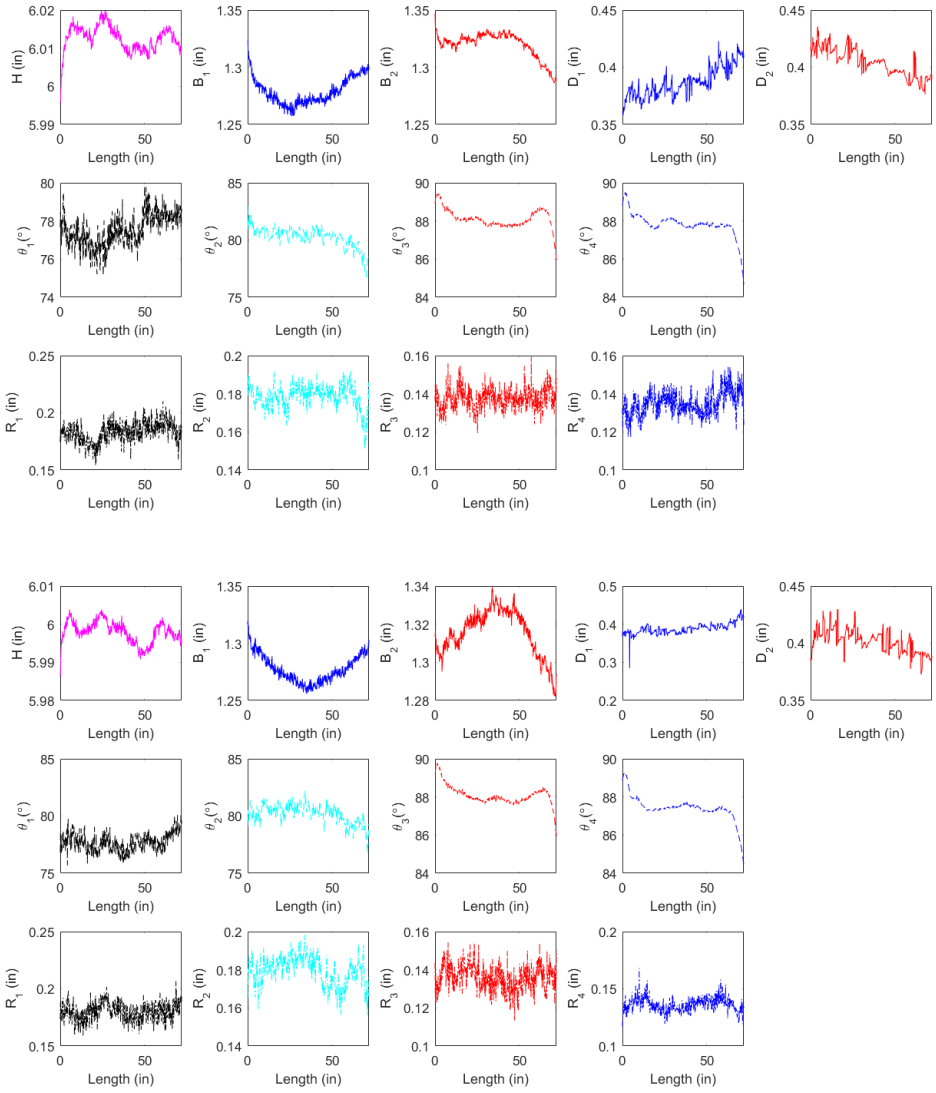
H (in)
B1 (in)
B2 (in)
D1 (in)
D2 (in)
θ1 (°)
θ2 (°)
θ3 (°)
θ4 (°)
R1 (in)
R2 (in)
R3 (in)
R4 (in)
Length (in)

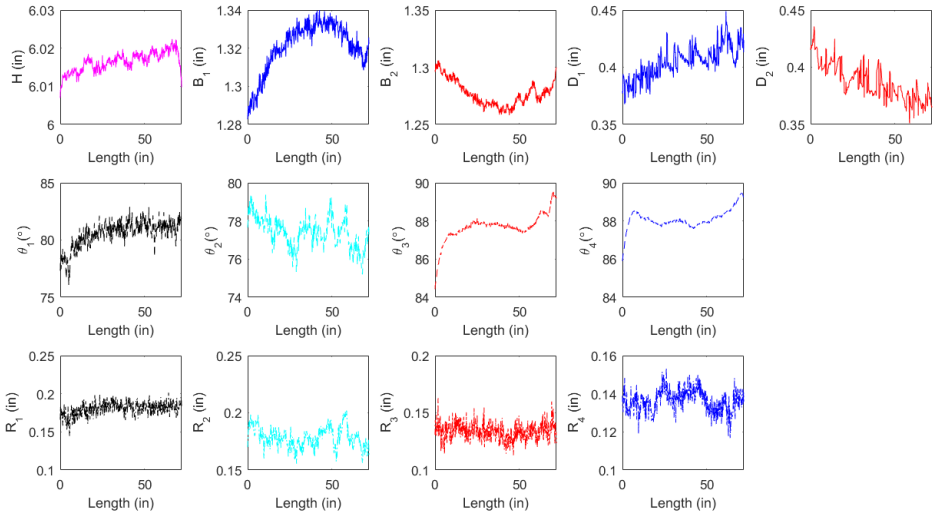
H (in)
B1 (in)
B2 (in)
D1 (in)
D2 (in)
θ1 (°)
θ2 (°)
θ3 (°)
θ4 (°)
R1 (in)
R2 (in)
R3 (in)
R4 (in)
Length (in)

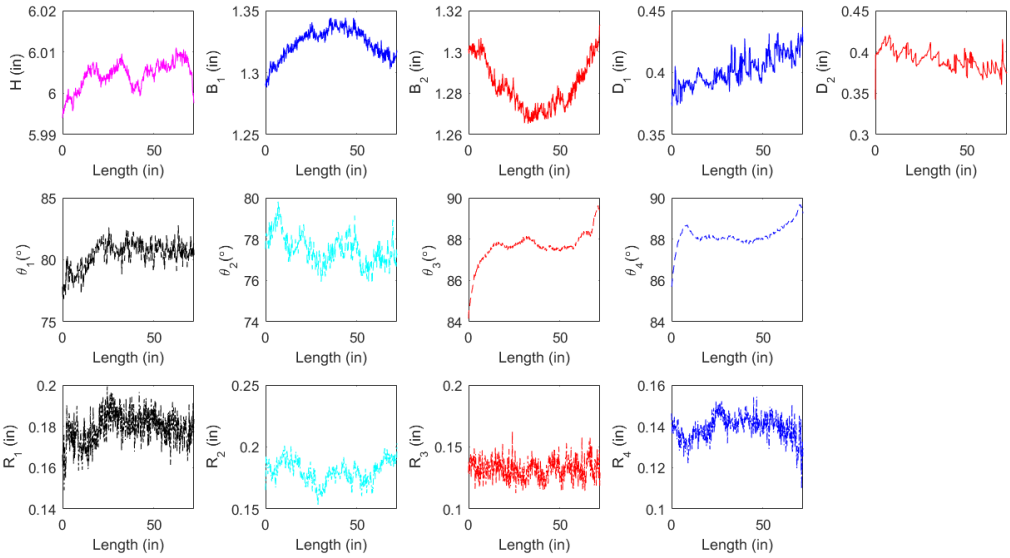
H (in)
B1 (in)
B2 (in)
D1 (in)
D2 (in)
θ1 (°)
θ2 (°)
θ3 (°)
θ4 (°)
R1 (in)
R2 (in)
R3 (in)
R4 (in)
Length (in)

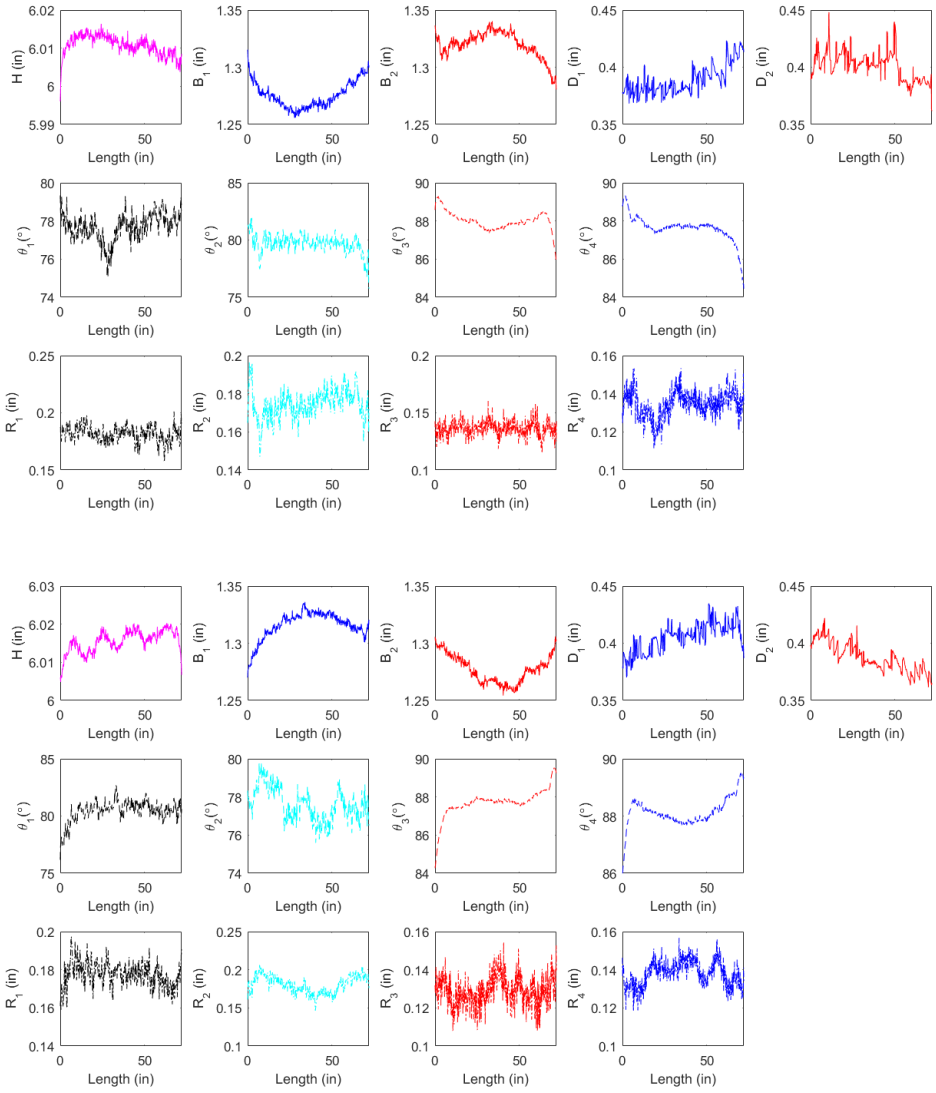
H (in)
B1 (in)
B2 (in)
D1 (in)
D2 (in)
θ1 (°)
θ2 (°)
θ3 (°)
θ4 (°)
R1 (in)
R2 (in)
R3 (in)
R4 (in)
Length (in)

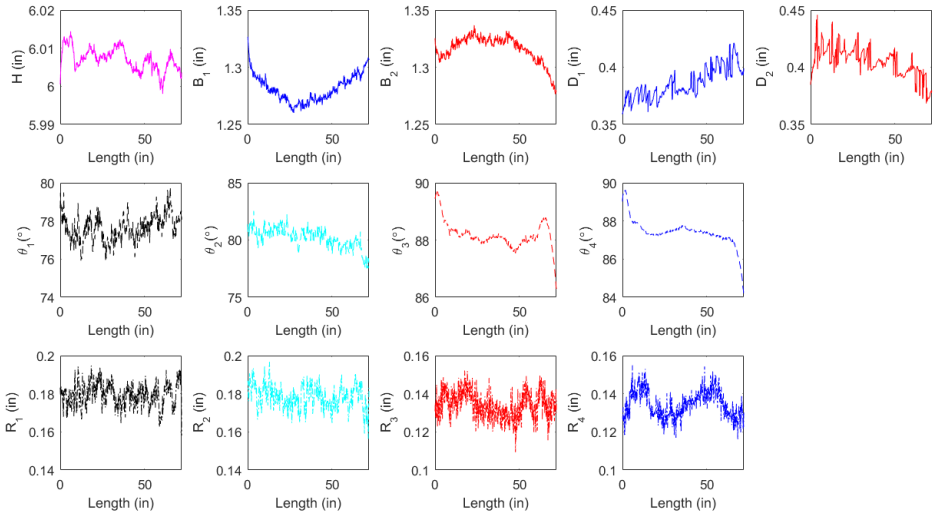

A. 11 Variations of dimensions along C sections [600S137-54] (Specimen 1 – Specimen 14)

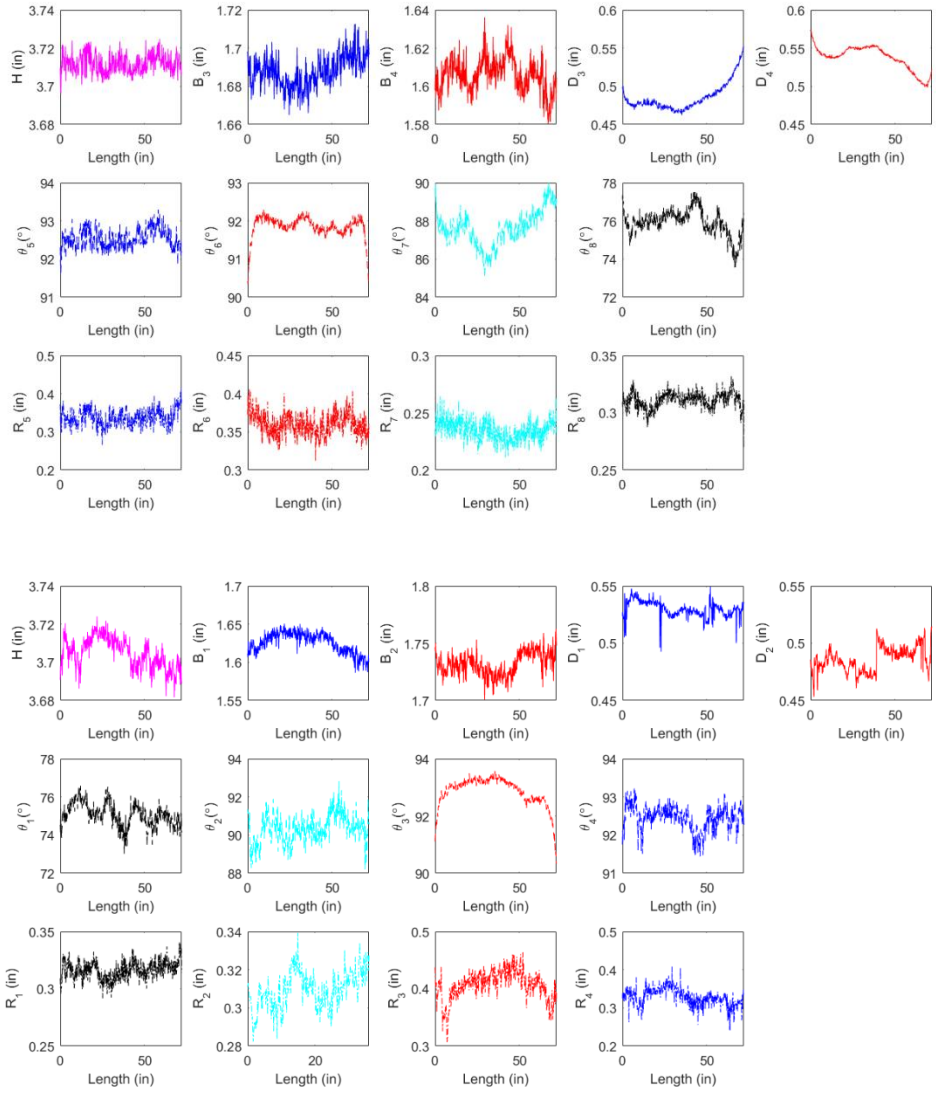
H (in)
B3 (in)
B4 (in)
D3 (in)
D4 (in)
θ5 (°)
θ6 (°)
θ7 (°)
θ8 (°)
R5 (in)
R6 (in)
R7 (in)
R8 (in)
B1 (in)
B2 (in)
D1 (in)
D2 (in)
θ1 (°)
θ2 (°)
θ3 (°)
θ4 (°)
R1 (in)
R2 (in)
R3 (in)
R4 (in)
Length (in)

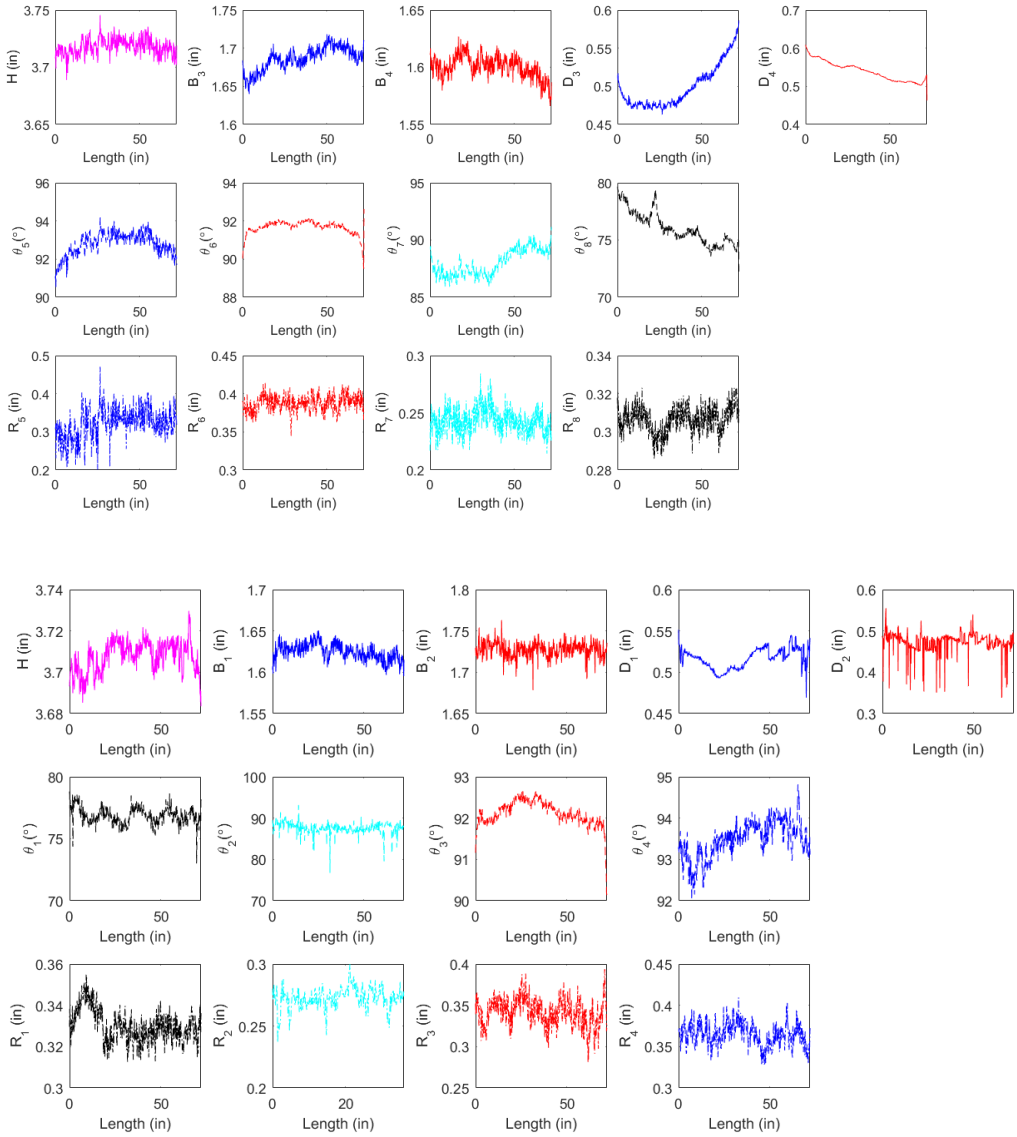
H (in)
B3 (in)
B4 (in)
D3 (in)
D4 (in)
θ5 (°)
θ6 (°)
θ7 (°)
θ8 (°)
R5 (in)
R6 (in)
R7 (in)
R8 (in)
H (in)
B1 (in)
B2 (in)
D1 (in)
D2 (in)
θ1 (°)
θ2 (°)
θ3 (°)
θ4 (°)
R1 (in)
R2 (in)
R3 (in)
R4 (in)
Length (in)

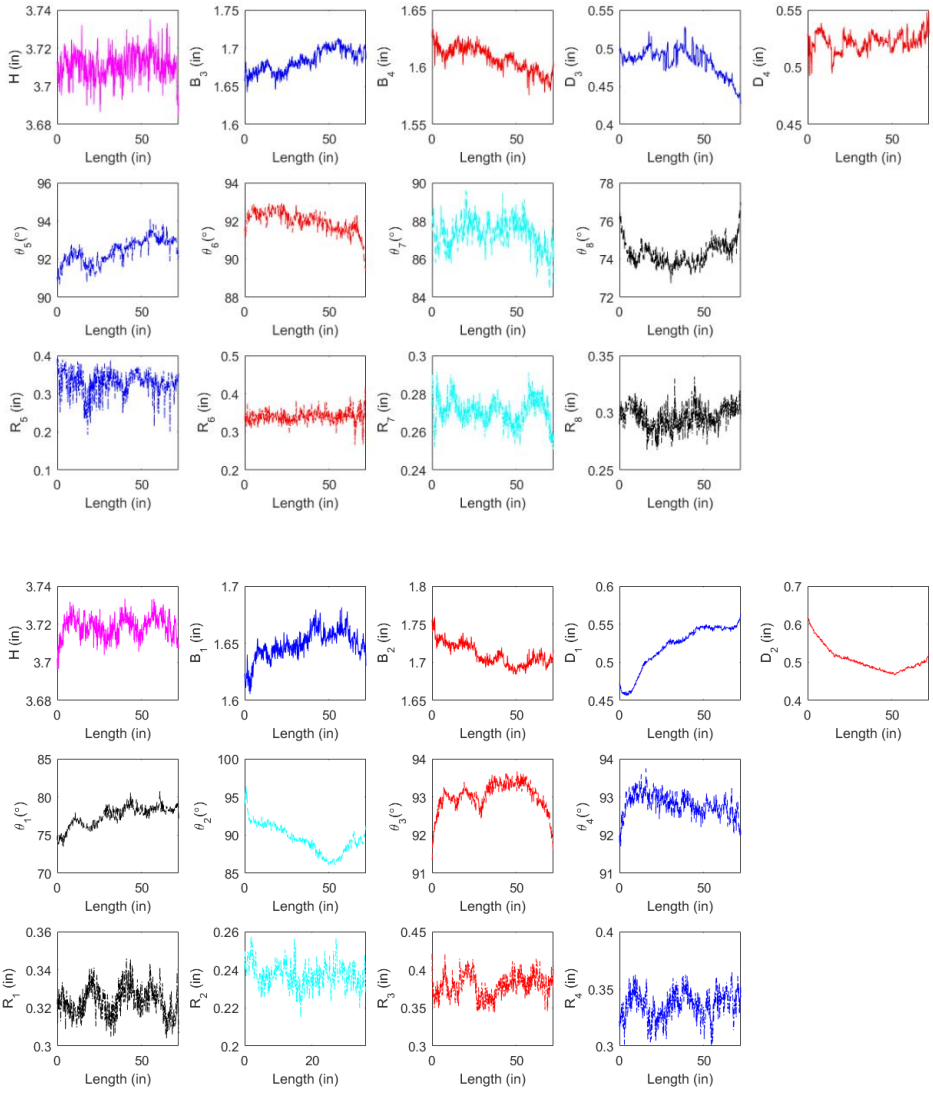
H (in)
B3 (in)
B4 (in)
D3 (in)
D4 (in)
θ5 (°)
θ6 (°)
θ7 (°)
θ8 (°)
R5 (in)
R6 (in)
R7 (in)
R8 (in)
B1 (in)
B2 (in)
D1 (in)
D2 (in)
θ1 (°)
θ2 (°)
θ3 (°)
θ4 (°)
R1 (in)
R2 (in)
R3 (in)
R4 (in)
Length (in)

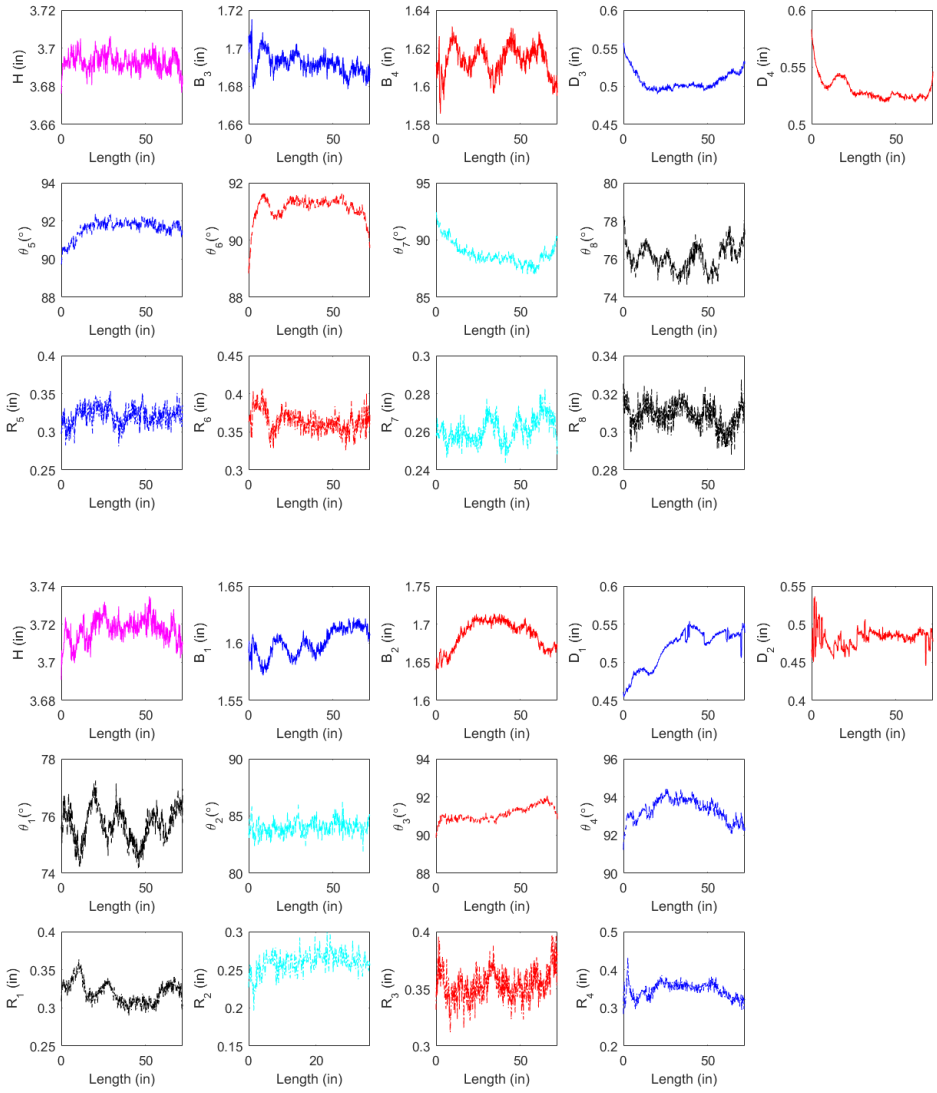

A. 12 Variations of dimensions along the BUC sections [362S162-68] (Specimens 1-14)

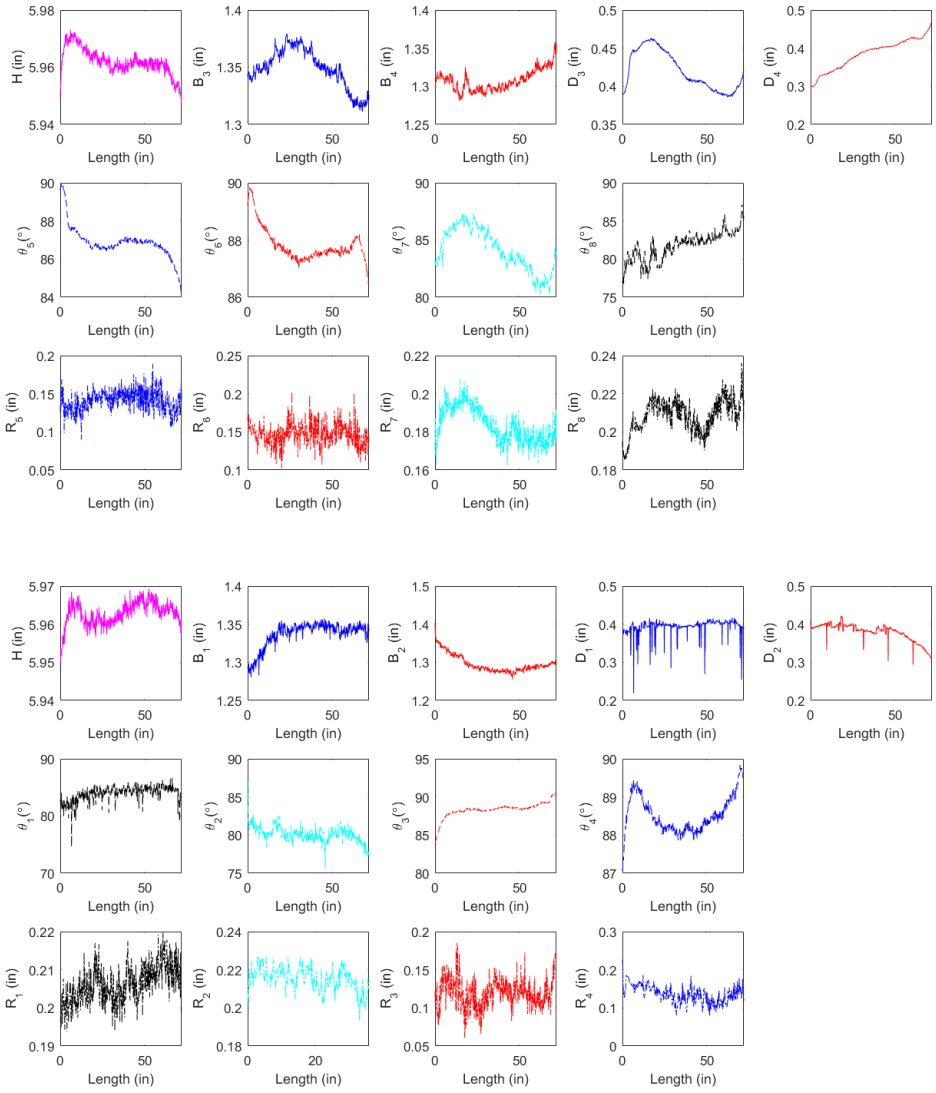
H (in)
B3 (in)
B4 (in)
D3 (in)
D4 (in)
θ5 (°)
θ6 (°)
θ7 (°)
θ8 (°)
R5 (in)
R6 (in)
R7 (in)
R8 (in)
H (in)
B1 (in)
B2 (in)
D1 (in)
D2 (in)
θ1 (°)
θ2 (°)
θ3 (°)
θ4 (°)
R1 (in)
R2 (in)
R3 (in)
R4 (in)
Length (in)

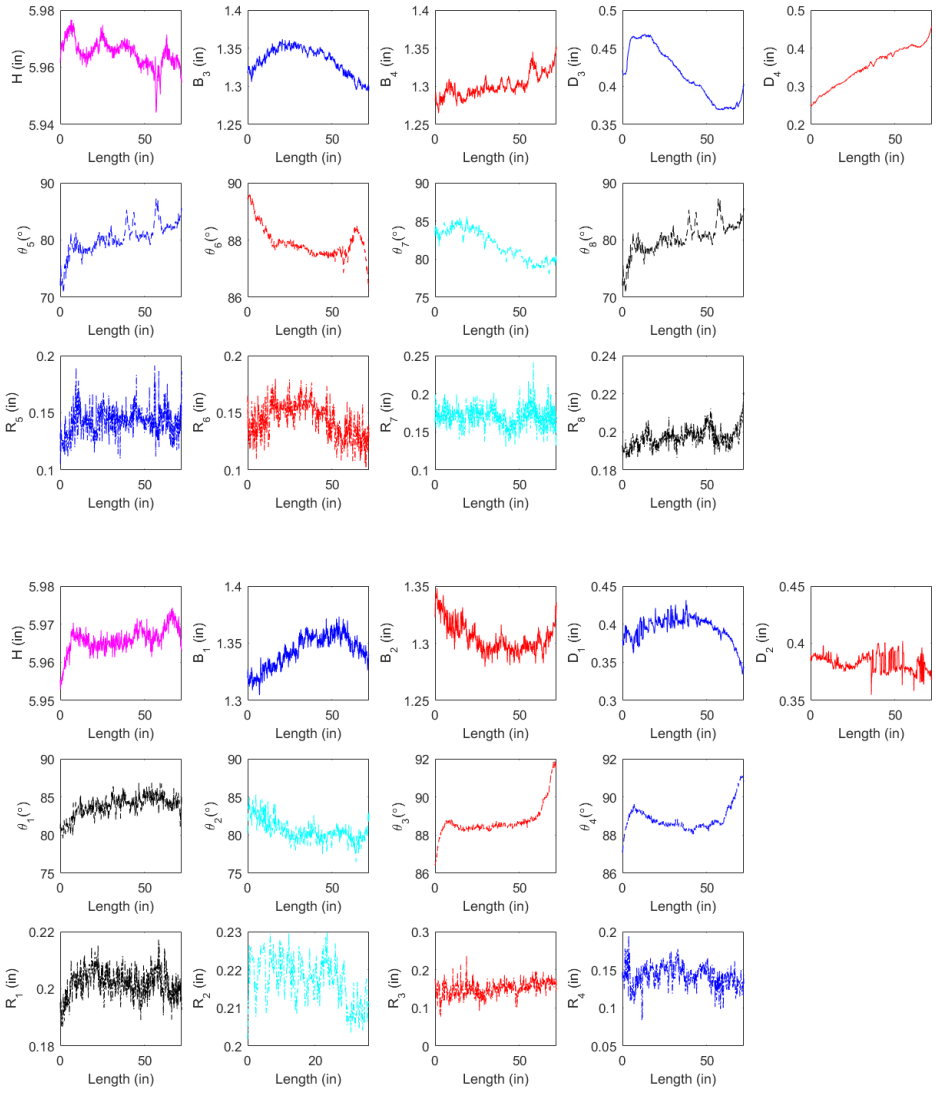
H (in)
B3 (in)
B4 (in)
D3 (in)
D4 (in)
θ5 (°)
θ6 (°)
θ7 (°)
θ8 (°)
R5 (in)
R6 (in)
R7 (in)
R8 (in)
H (in)
B1 (in)
B2 (in)
D1 (in)
D2 (in)
θ1 (°)
θ2 (°)
θ3 (°)
θ4 (°)
R1 (in)
R2 (in)
R3 (in)
R4 (in)
Length (in)

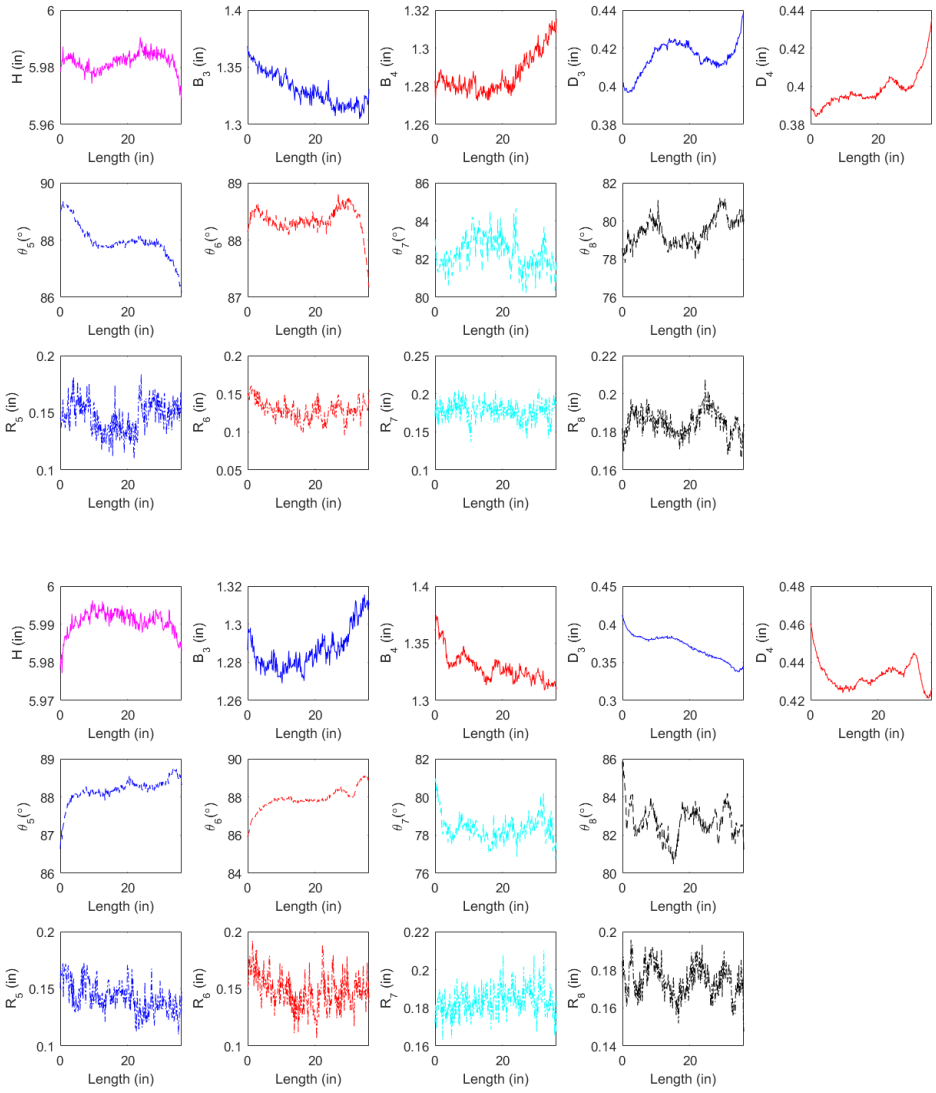
H (in)
B3 (in)
B4 (in)
D3 (in)
D4 (in)
θ5 (°)
θ6 (°)
θ7 (°)
θ8 (°)
R5 (in)
R6 (in)
R7 (in)
R8 (in)
Length (in)

H (in)
B3 (in)
B4 (in)
D3 (in)
D4 (in)
θ5 (°)
θ6 (°)
θ7 (°)
θ8 (°)
R5 (in)
R6 (in)
R7 (in)
R8 (in)
Length (in)

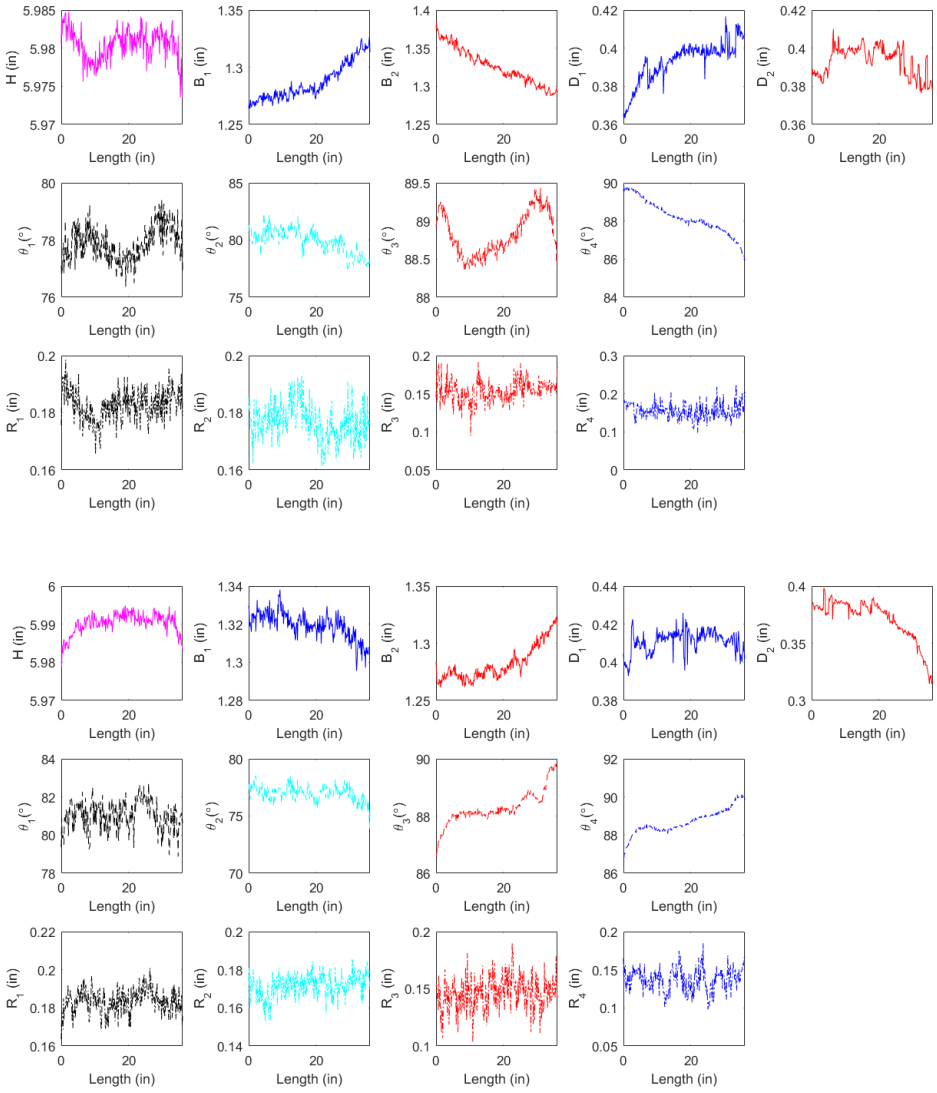

A. 13 Variations of dimensions along C sections [600S137-54] (Specimens 1-14)

Ap.4 Chapter 7

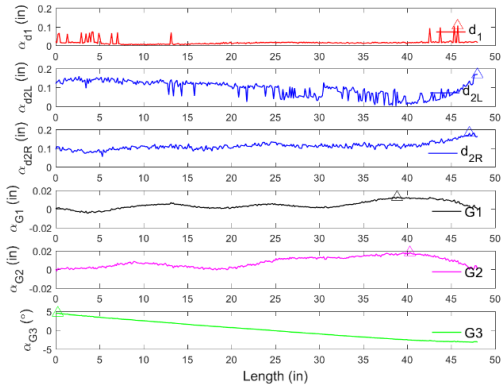

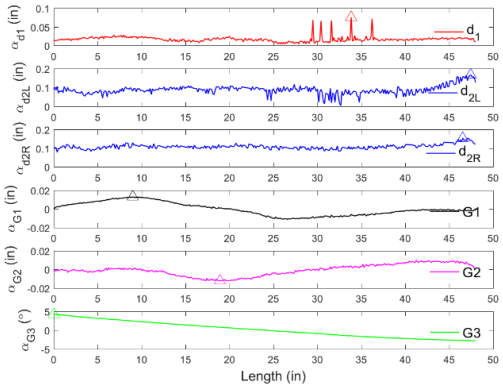

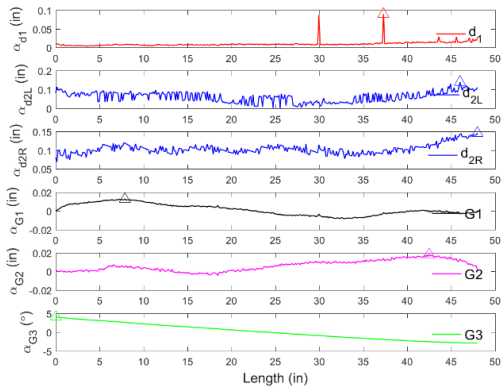

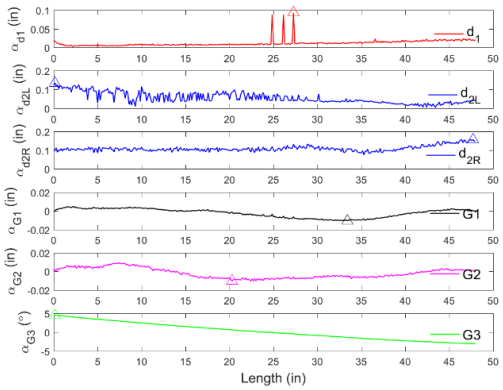

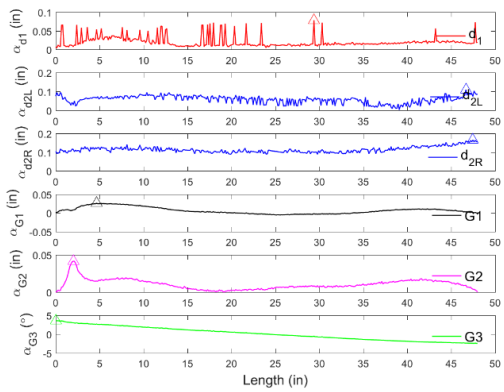

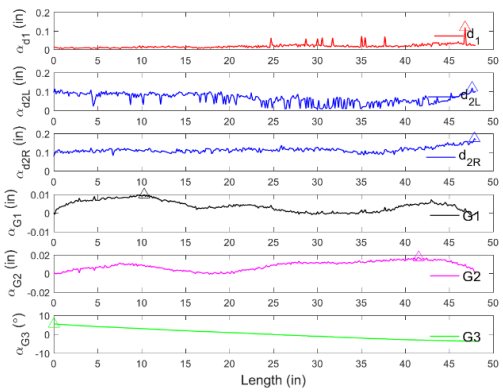

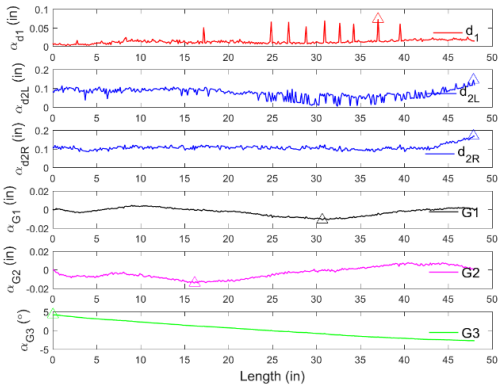
d1
d2L
d2R
G1
G2
G3
Length (in)

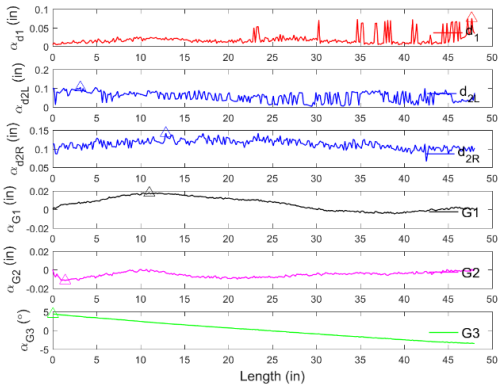
d1
d2L
d2R
G1
G2
G3
Length (in)

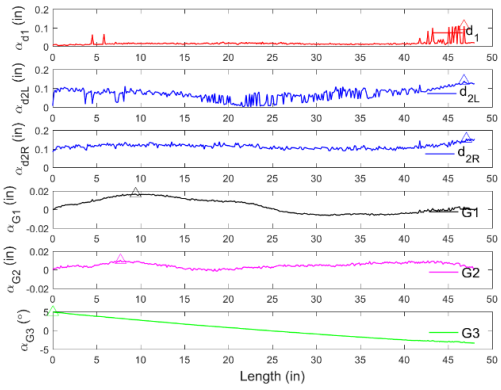
d1
d2L
d2R
G1
G2
G3
Length (in)

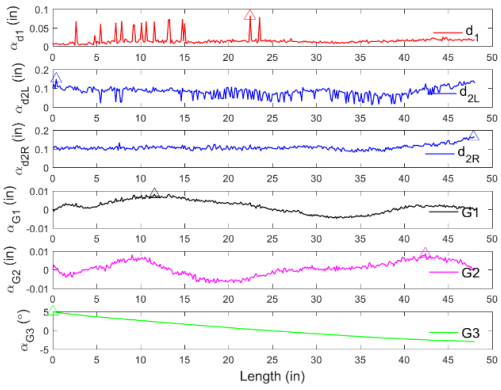
d1
d2L
d2R
G1
G2
G3
Length (in)

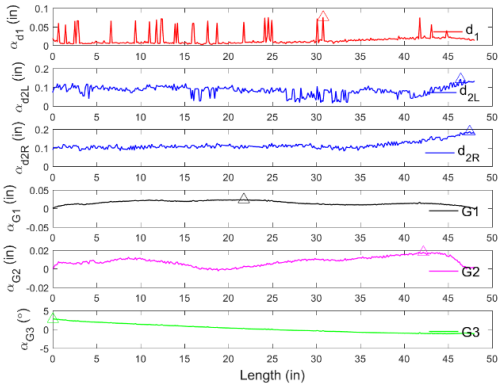
d1
d2L
d2R
G1
G2
G3
Length (in)

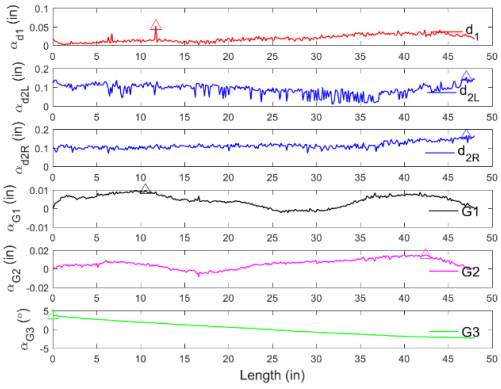
d1
d2L
d2R
G1
G2
G3
Length (in)

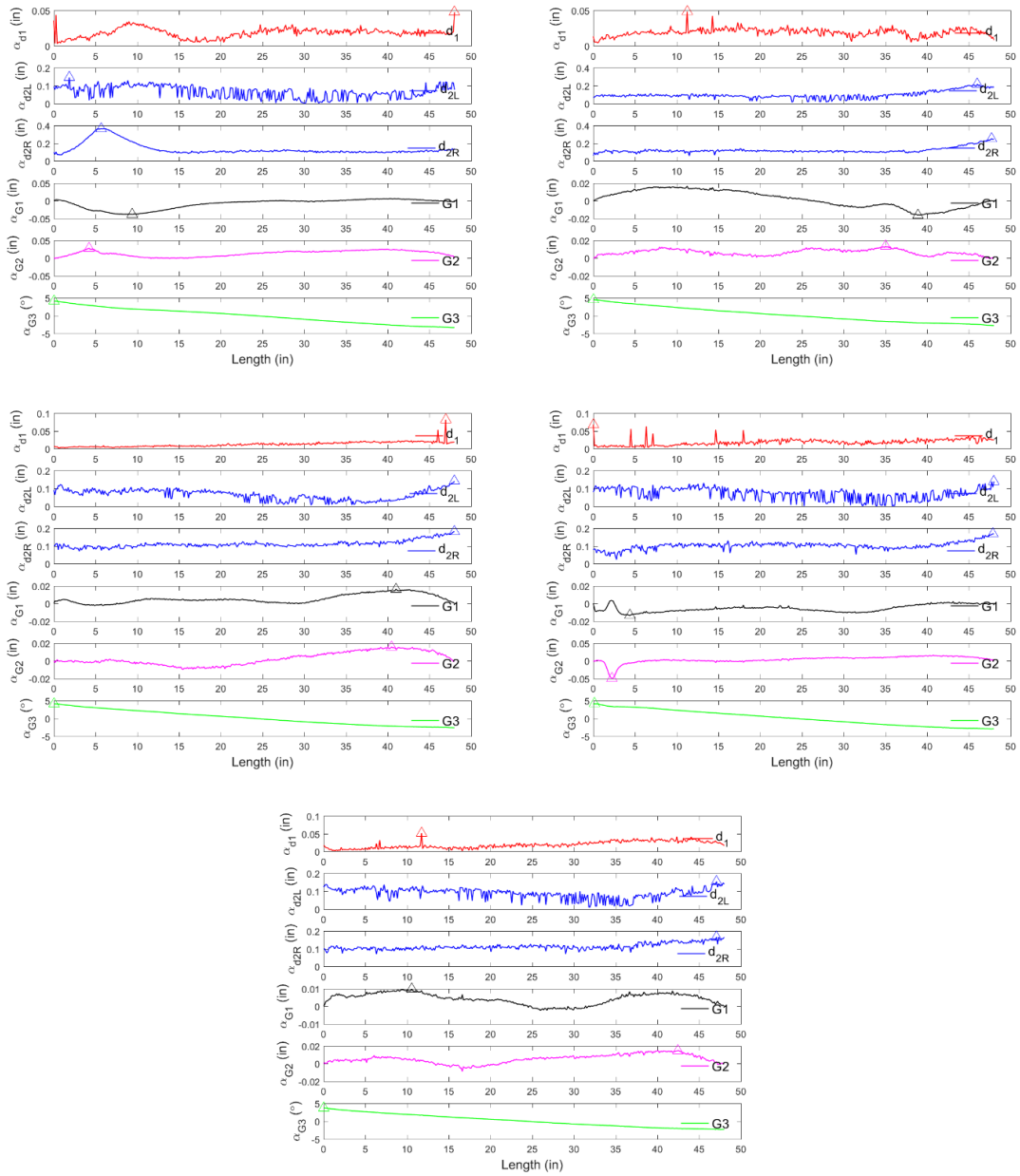

A. 14 Conventional imperfections along length of Z sections (Specimens 1-19)

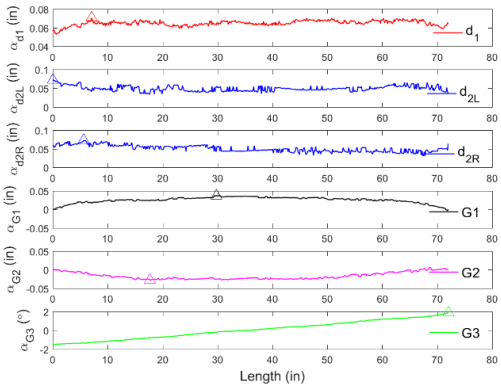
d1
d2L
d2R
G1
G2
G3
Length (in)

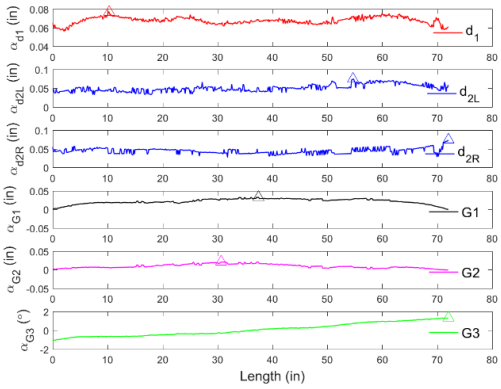
d1
d2L
d2R
G1
G2
G3
Length (in)

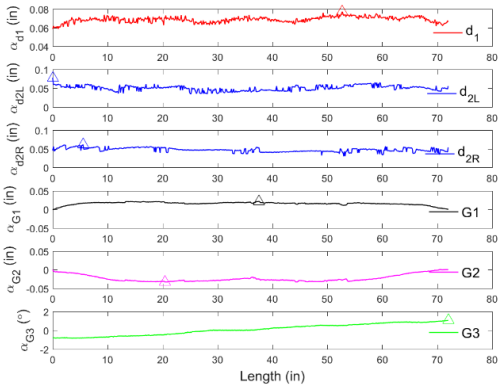
d1
d2L
d2R
G1
G2
G3
Length (in)

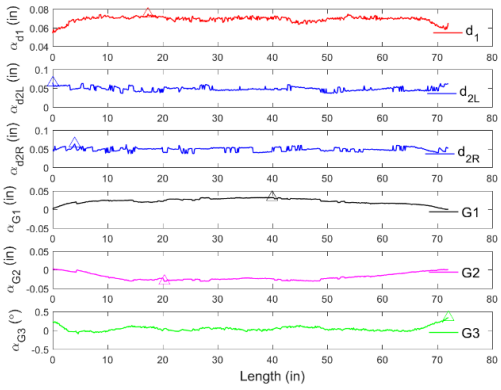
d1
d2L
d2R
G1
G2
G3
Length (in)

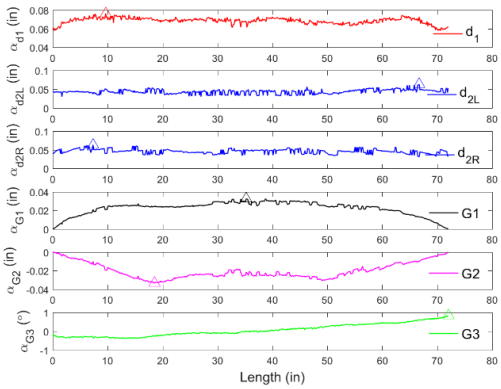
d1
d2L
d2R
G1
G2
G3
Length (in)

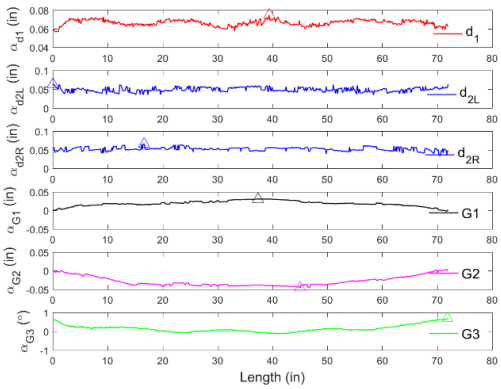
d1
d2L
d2R
G1
G2
G3
Length (in)

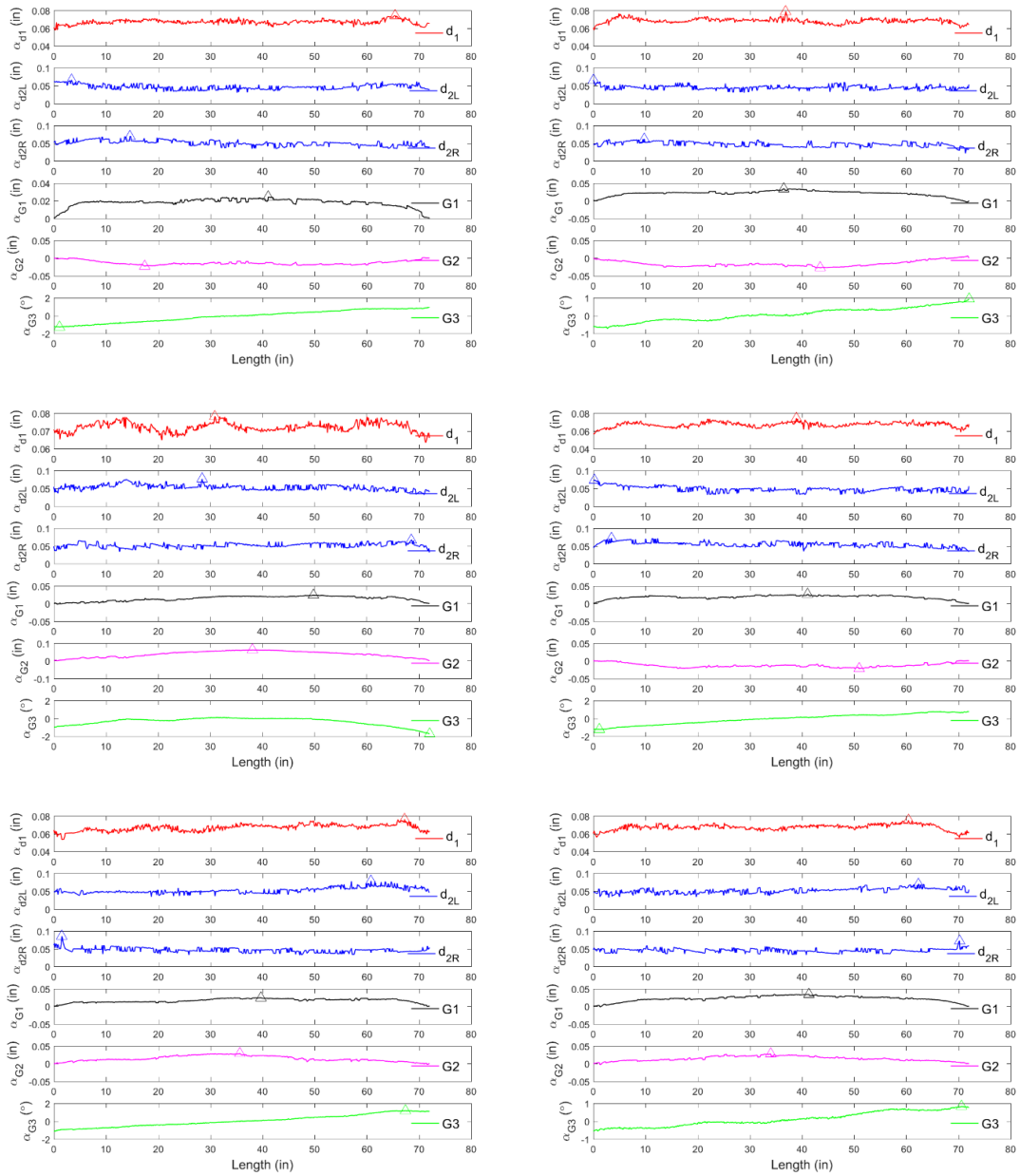

A. 15 Conventional imperfections along length of 362S162-68 of C sections. (Specimens 1-14)

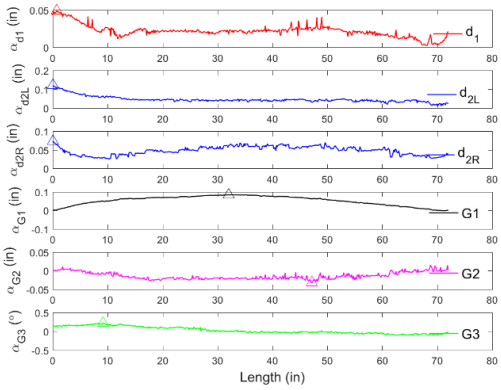
α_{d1} (in)
d_1
α_{d2L} (in)
d_{2L}
α_{d2R} (in)
d_{2R}
α_{G1} (in)
G1
α_{G2} (in)
G2
α_{G3} (°)
G3
Length (in)

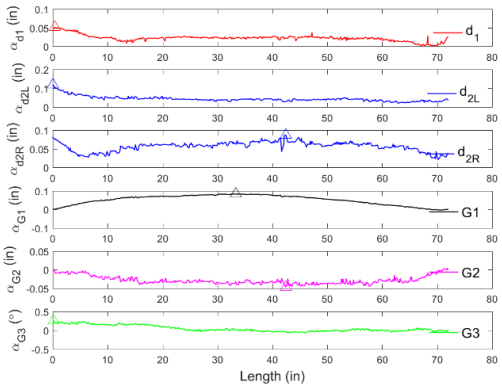
α_{d1} (in)
d_1
α_{d2L} (in)
d_{2L}
α_{d2R} (in)
d_{2R}
α_{G1} (in)
G1
α_{G2} (in)
G2
α_{G3} (°)
G3
Length (in)

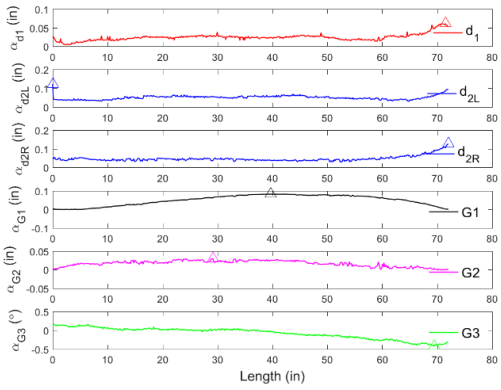
α_{d1} (in)
d_1
α_{d2L} (in)
d_{2L}
α_{d2R} (in)
d_{2R}
α_{G1} (in)
G1
α_{G2} (in)
G2
α_{G3} (°)
G3
Length (in)

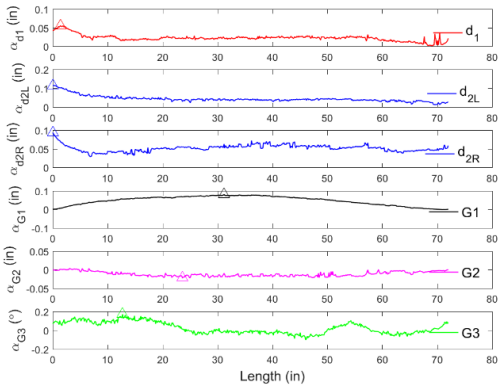
α_{d1} (in)
d_1
α_{d2L} (in)
d_{2L}
α_{d2R} (in)
d_{2R}
α_{G1} (in)
G1
α_{G2} (in)
G2
α_{G3} (°)
G3
Length (in)

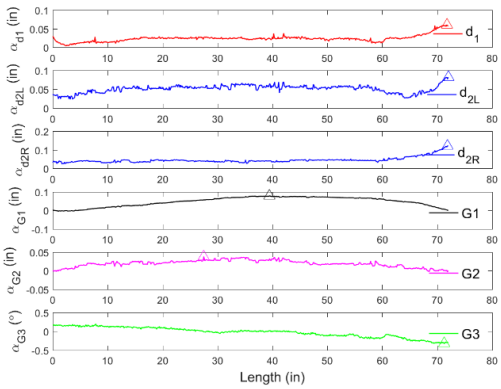
α_{d1} (in)
d_1
α_{d2L} (in)
d_{2L}
α_{d2R} (in)
d_{2R}
α_{G1} (in)
G1
α_{G2} (in)
G2
α_{G3} (°)
G3
Length (in)

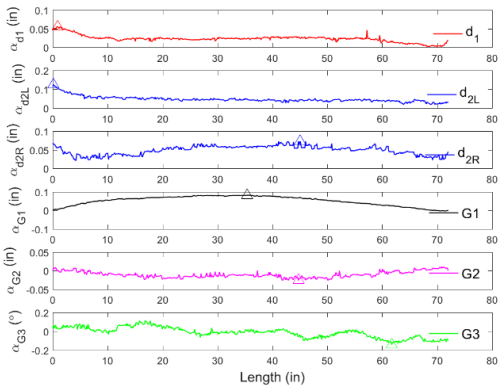
α_{d1} (in)
d_1
α_{d2L} (in)
d_{2L}
α_{d2R} (in)
d_{2R}
α_{G1} (in)
G1
α_{G2} (in)
G2
α_{G3} (°)
G3
Length (in)

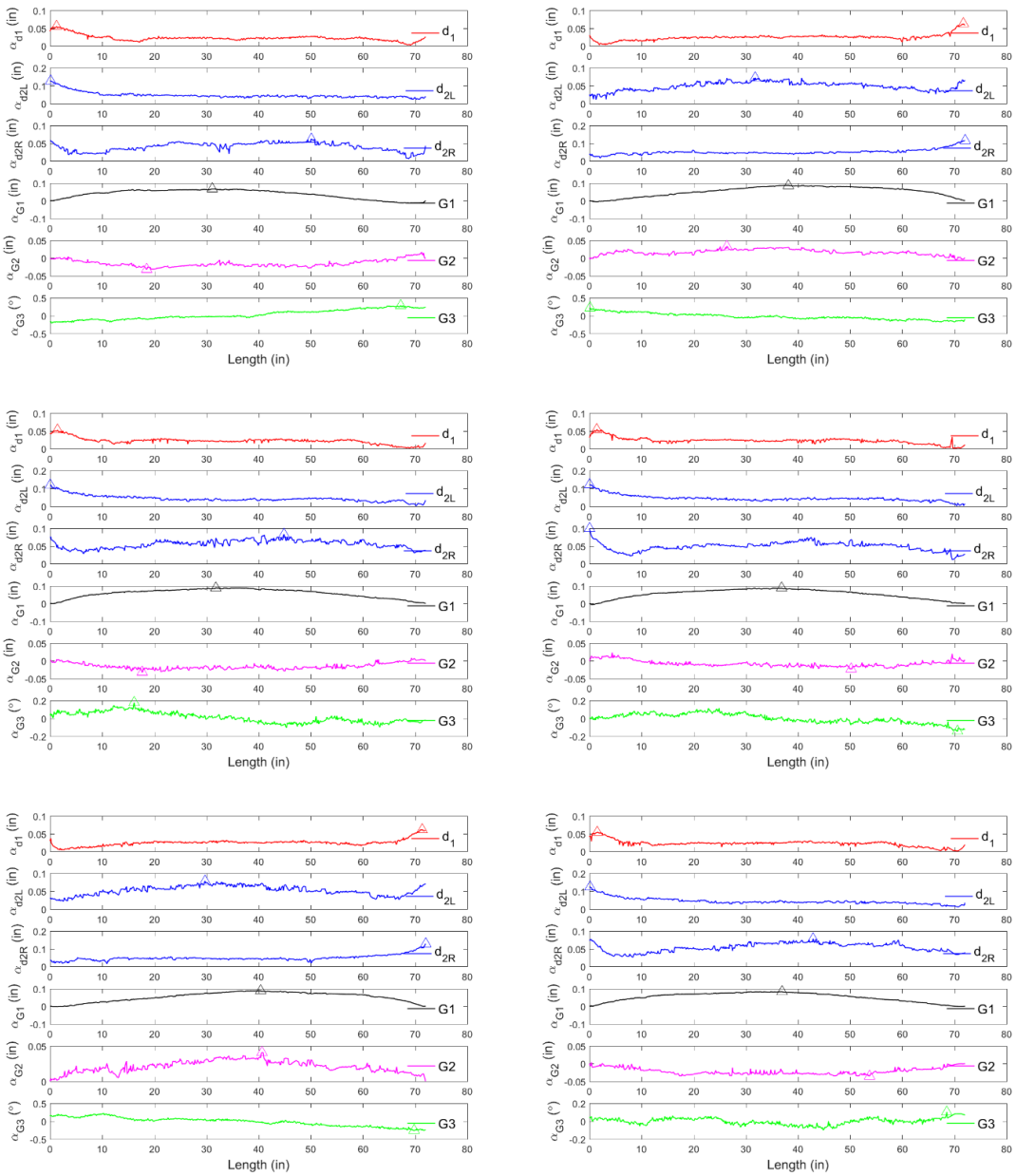

A. 16 Conventional imperfections along length of 600S137-54 of C sections (Specimens 1-14)

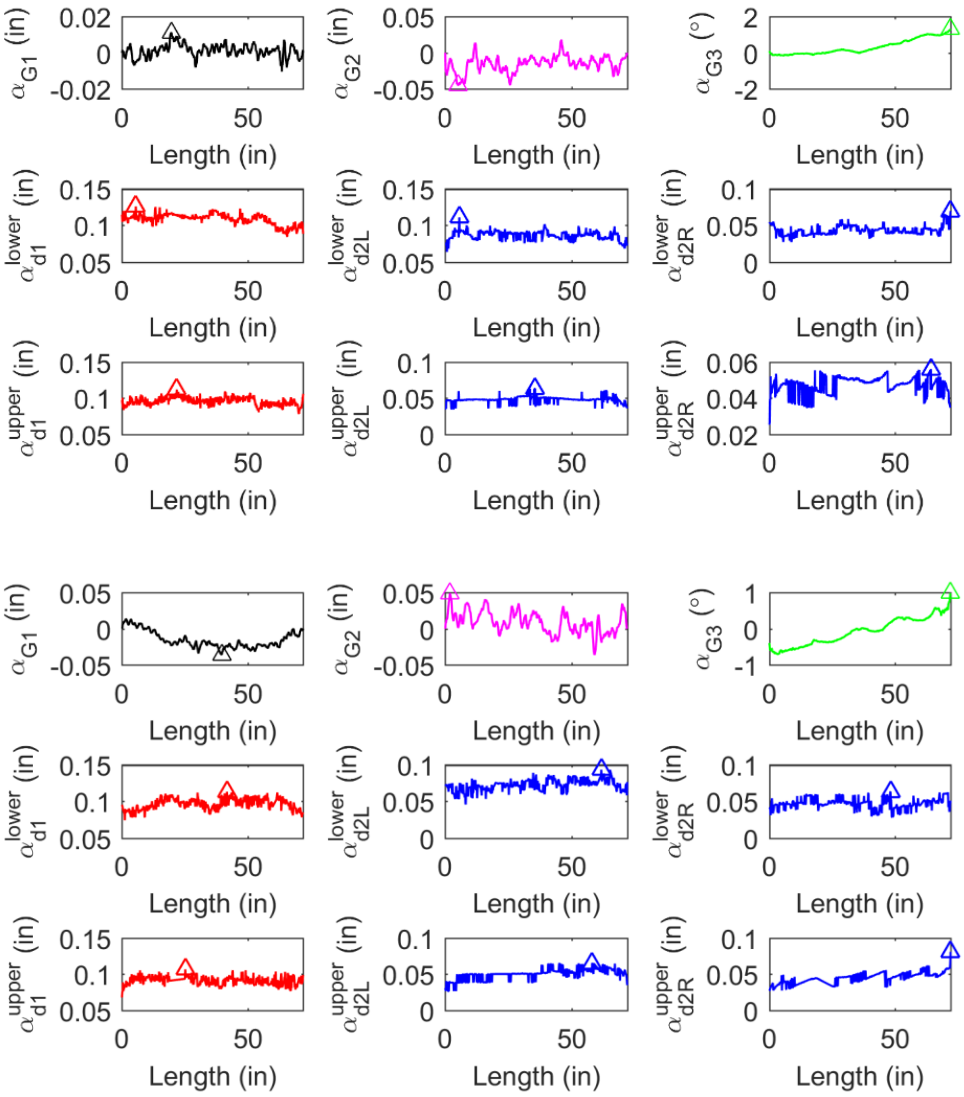

A. 17 Conventional imperfections along length of 362S162-68 of BUC

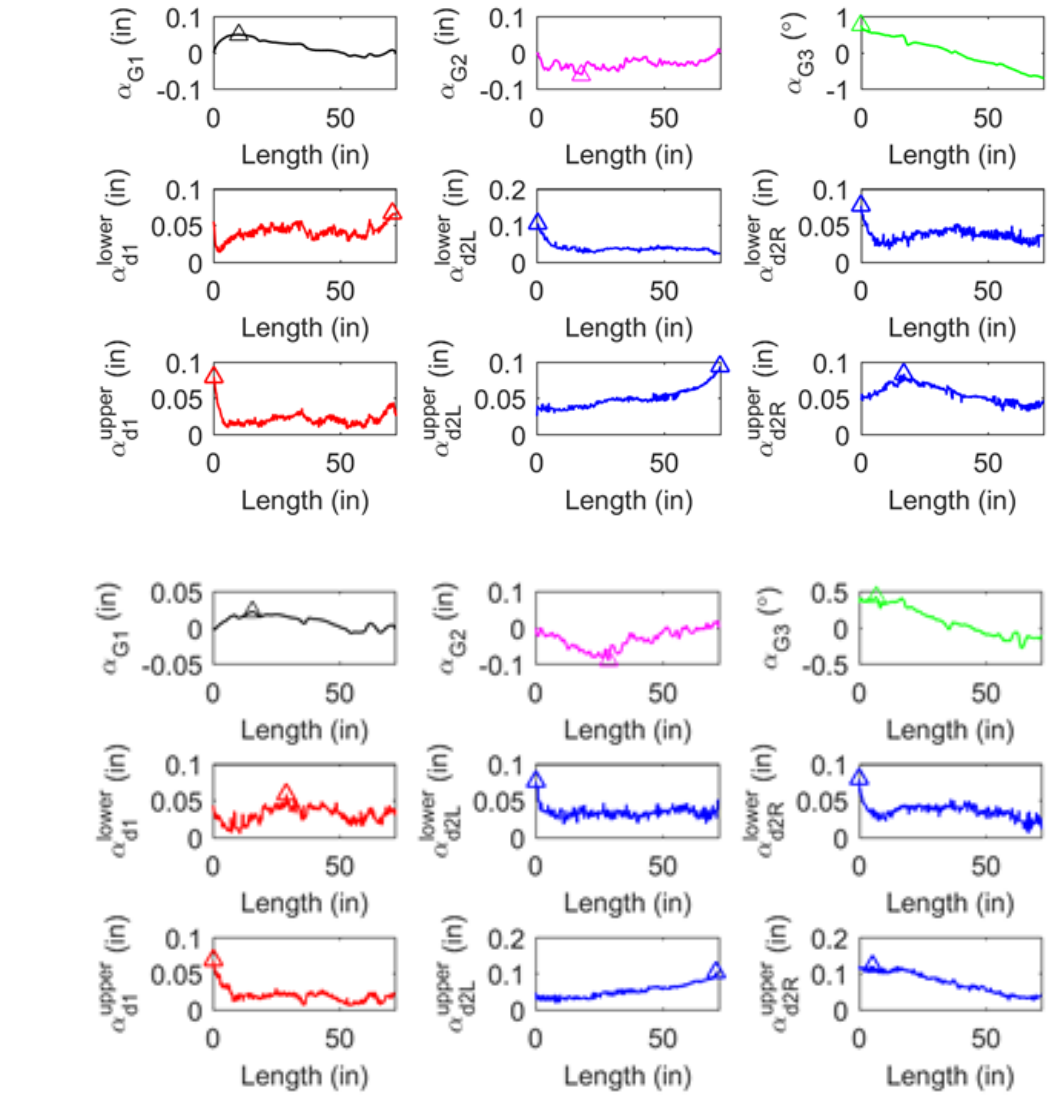
α_{G1} (in)
α_{G2} (in)
α_{G3} (°)
α^{lower}_{d1} (in)
α^{lower}_{d2L} (in)
α^{lower}_{d2R} (in)
α^{upper}_{d1} (in)
α^{upper}_{d2L} (in)
α^{upper}_{d2R} (in)
Length (in)

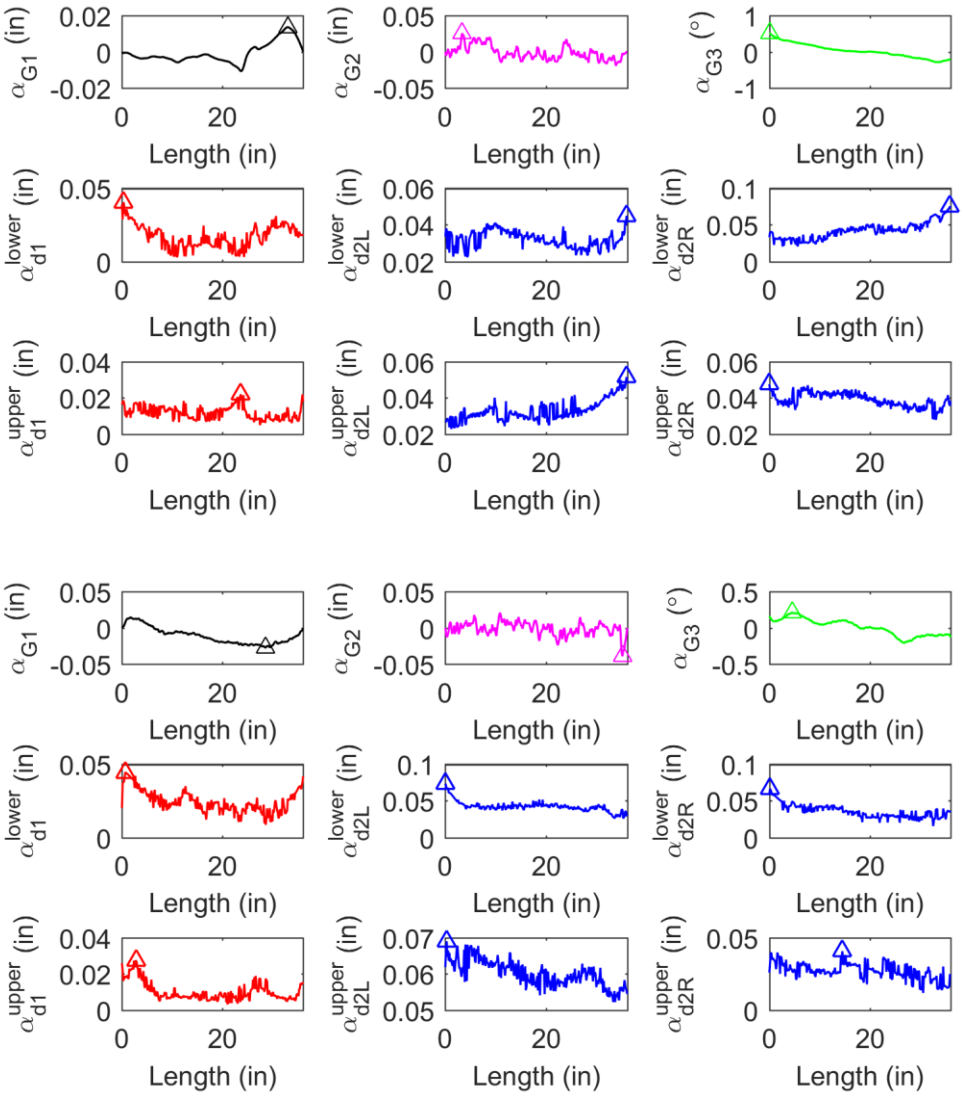

A. 18 Conventional imperfections along length of 600S137-54 of BUC

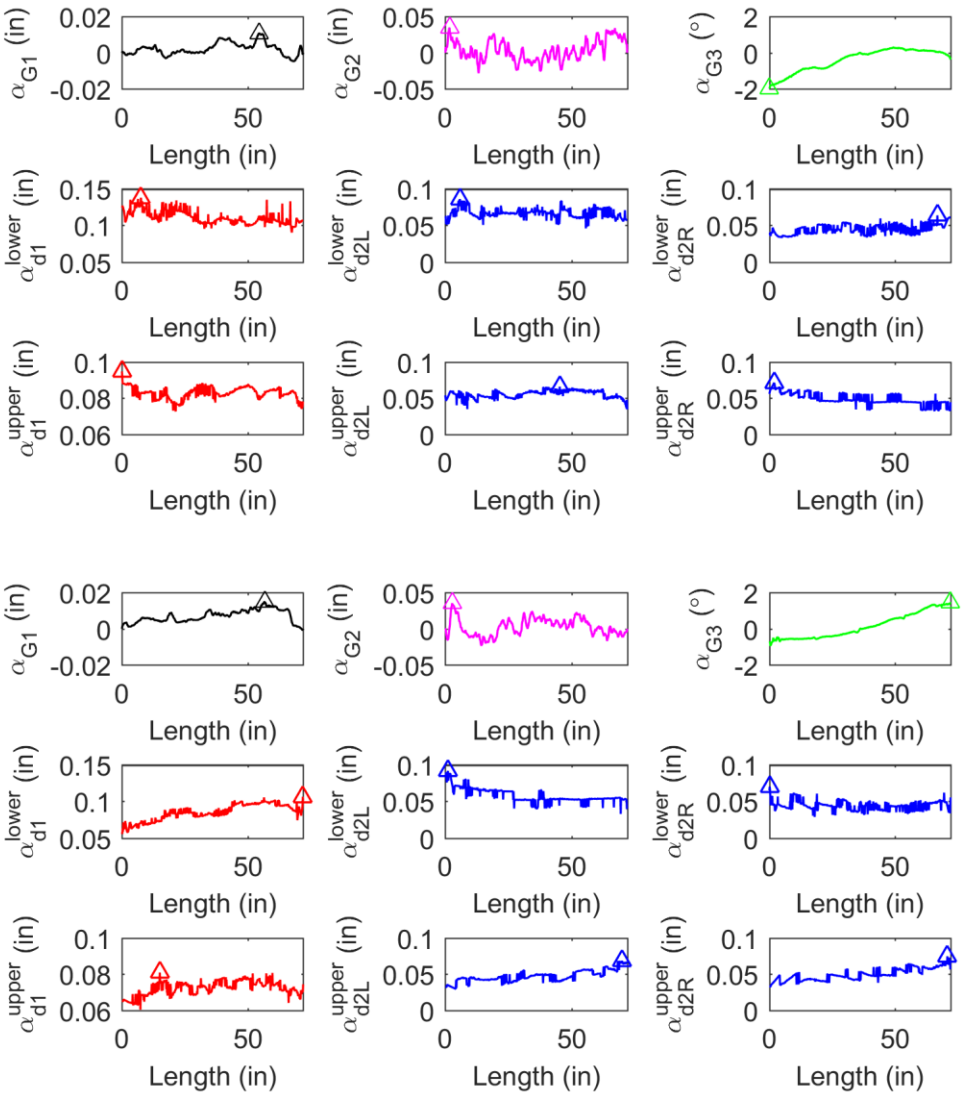

A. 19 Conventional imperfections along length of 600S138-54 of BUC

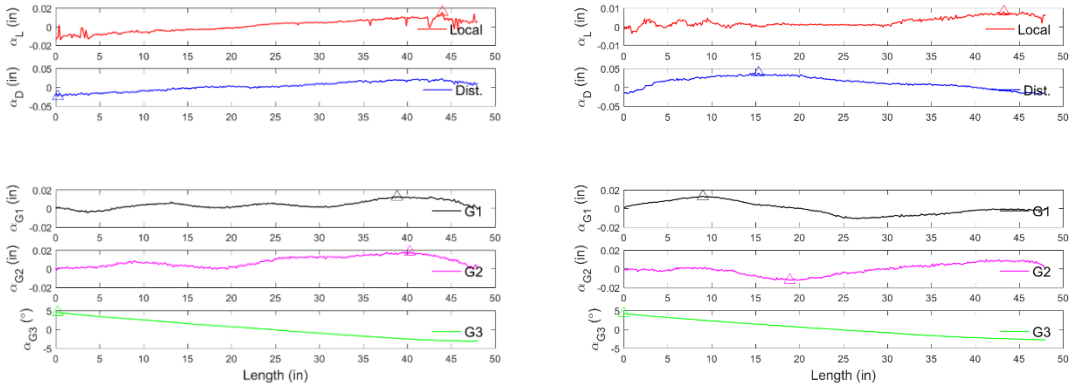

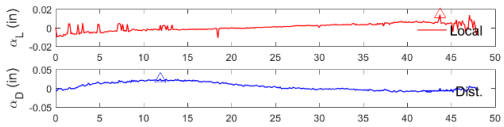
α_L (in)
Local
α_D (in)
Dist.

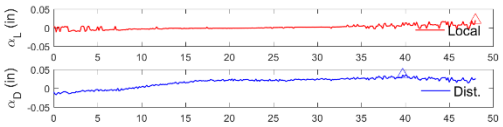
α_L (in)
Local
α_D (in)
Dist.

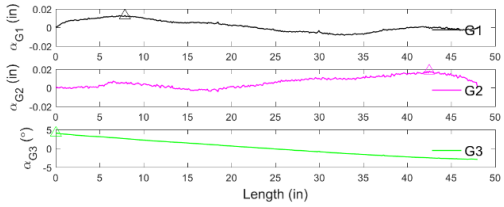
α_{G1} (in)
G1
α_{G2} (in)
G2
α_{G3} (°)
G3
Length (in)

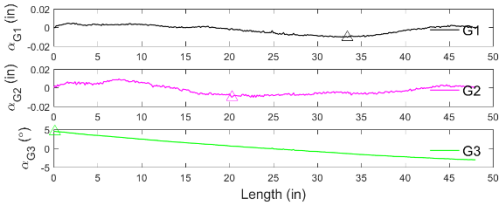
α_{G1} (in)
G1
α_{G2} (in)
G2
α_{G3} (°)
G3
Length (in)

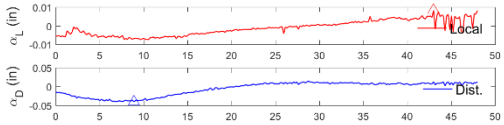
α_L (in)
Local
α_D (in)
Dist.

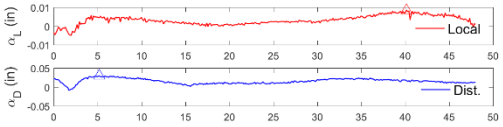
α_L (in)
Local
α_D (in)
Dist.

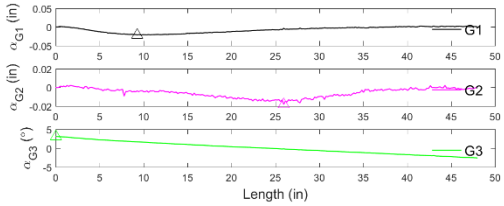
α_{G1} (in)
G1
α_{G2} (in)
G2
α_{G3} (°)
G3
Length (in)

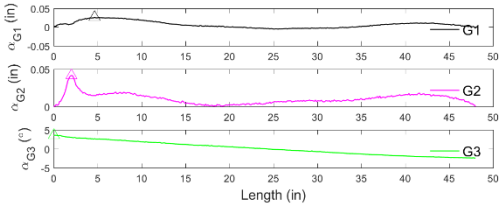
α_{G1} (in)
G1
α_{G2} (in)
G2
α_{G3} (°)
G3
Length (in)

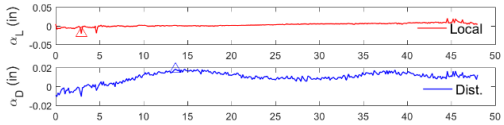
α_L (in)
Local
α_D (in)
Dist.

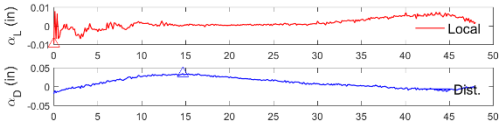
α_L (in)
Local
α_D (in)
Dist.

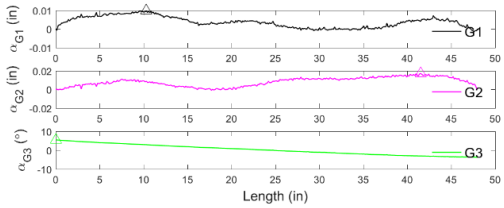
α_{G1} (in)
G1
α_{G2} (in)
G2
α_{G3} (°)
G3
Length (in)

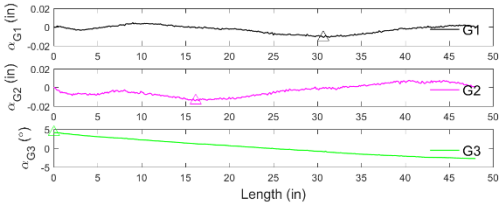
α_{G1} (in)
G1
α_{G2} (in)
G2
α_{G3} (°)
G3
Length (in)

α_L (in)
Local
α_D (in)
Dist.

α_L (in)
Local
α_D (in)
Dist.

α_{G1} (in)
G1
α_{G2} (in)
G2
α_{G3} (°)
G3
Length (in)

α_{G1} (in)
G1
α_{G2} (in)
G2
α_{G3} (°)
G3
Length (in)

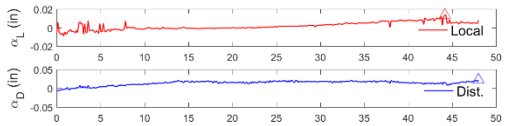
α_L (in)
Local
α_D (in)
Dist.

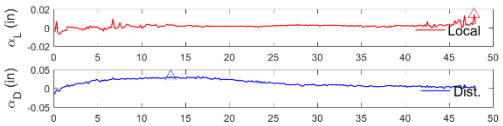
α_L (in)
Local
α_D (in)
Dist.

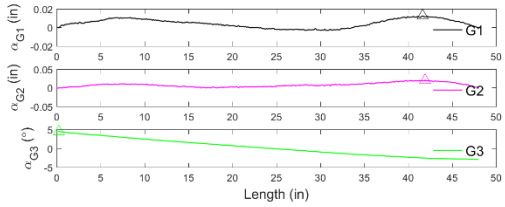
α_{G1} (in)
G1
α_{G2} (in)
G2
α_{G3} (°)
G3
Length (in)

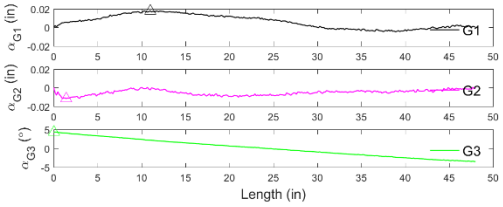
α_{G1} (in)
G1
α_{G2} (in)
G2
α_{G3} (°)
G3
Length (in)

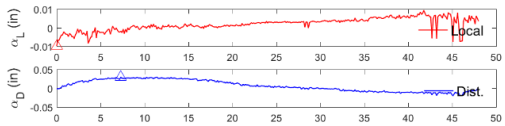
α_L (in)
Local
α_D (in)
Dist.

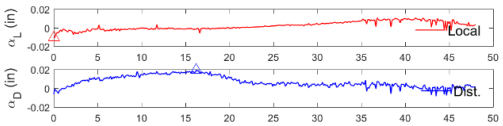
α_L (in)
Local
α_D (in)
Dist.

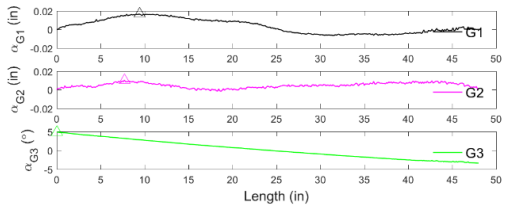
α_{G1} (in)
G1
α_{G2} (in)
G2
α_{G3} (°)
G3
Length (in)

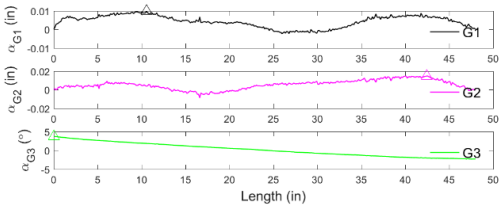
α_{G1} (in)
G1
α_{G2} (in)
G2
α_{G3} (°)
G3
Length (in)

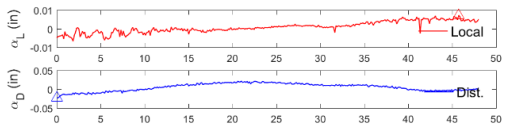
α_L (in)
Local
α_D (in)
Dist.

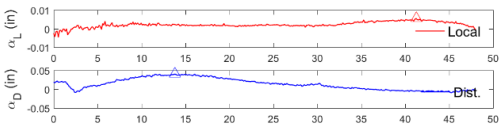
α_L (in)
Local
α_D (in)
Dist.

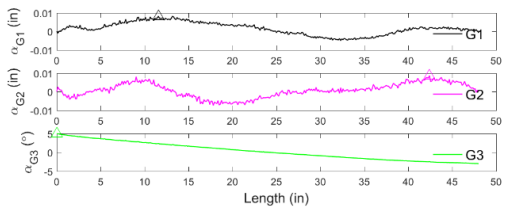
α_{G1} (in)
G1
α_{G2} (in)
G2
α_{G3} (°)
G3
Length (in)

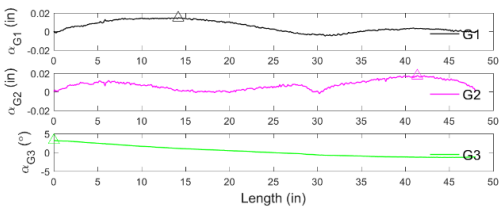
α_{G1} (in)
G1
α_{G2} (in)
G2
α_{G3} (°)
G3
Length (in)

α_L (in)
Local
α_D (in)
Dist.

α_L (in)
Local
α_D (in)
Dist.

α_{G1} (in)
G1
α_{G2} (in)
G2
α_{G3} (°)
G3
Length (in)

α_{G1} (in)
G1
α_{G2} (in)
G2
α_{G3} (°)
G3
Length (in)

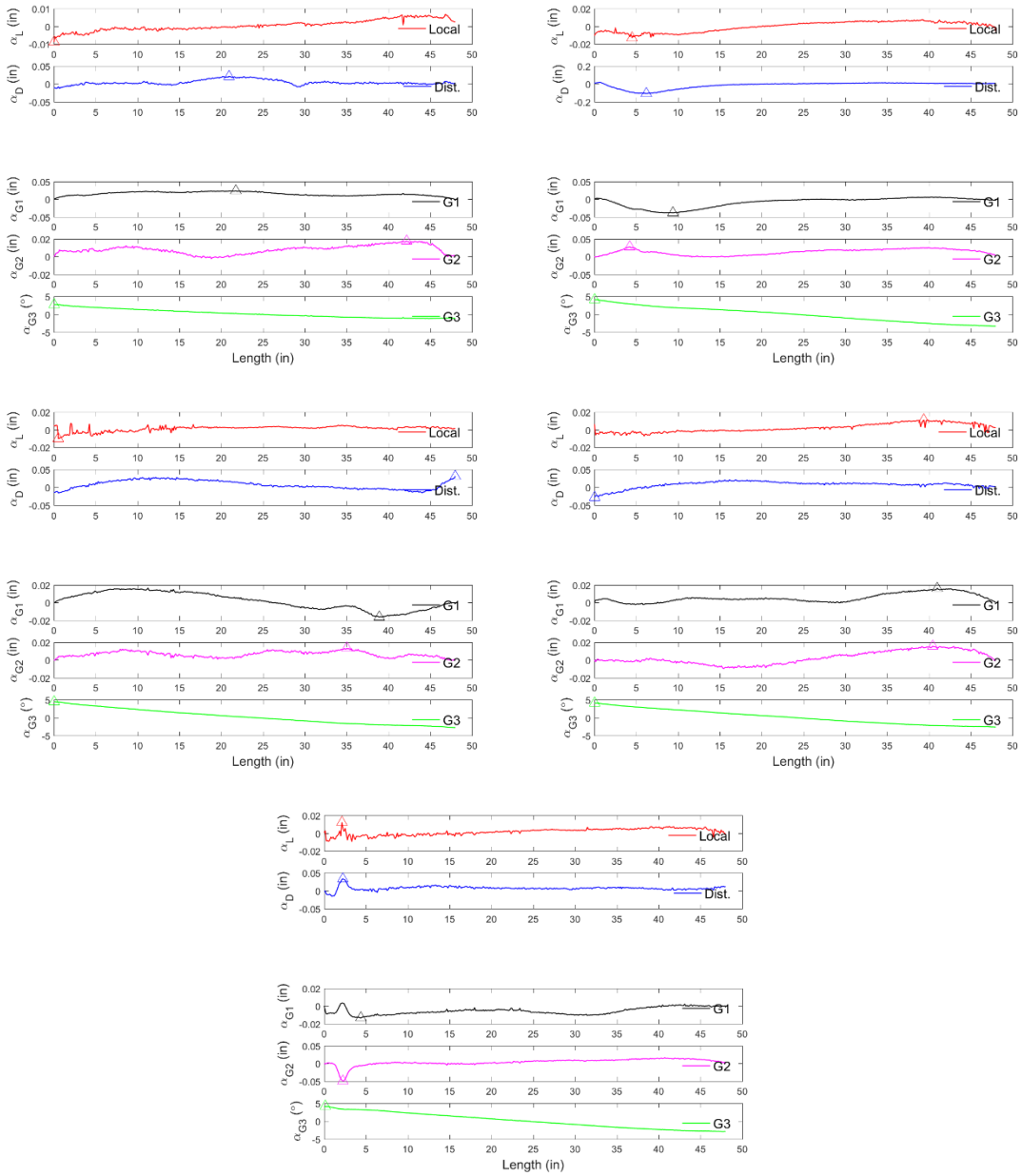

A. 20 Modal imperfections along length of Z sections (Specimens 1-19)

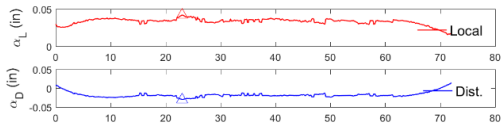
Local
Dist.

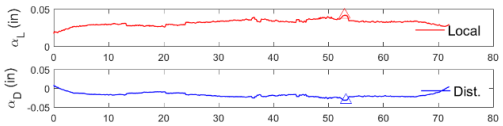
Local
Dist.

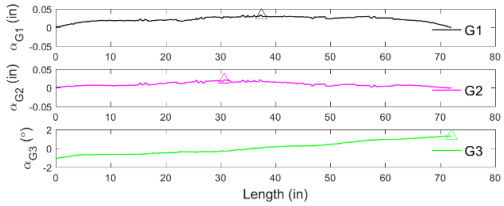
G1
G2
G3
Length (in)

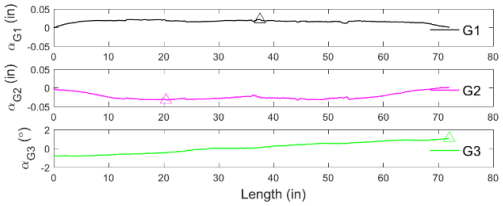
G1
G2
G3
Length (in)

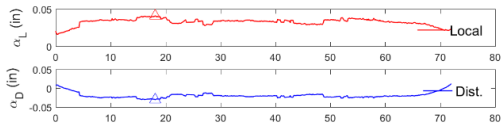
Local
Dist.

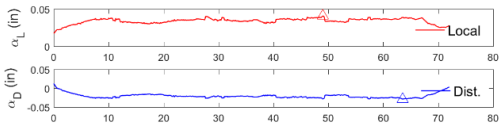
Local
Dist.

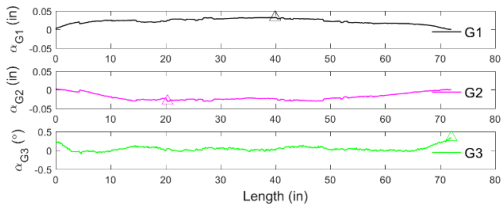
G1
G2
G3
Length (in)

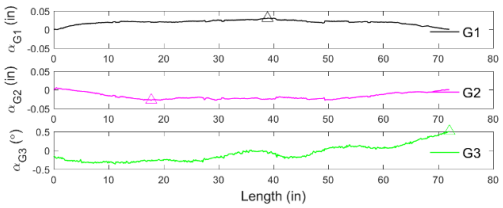
G1
G2
G3
Length (in)

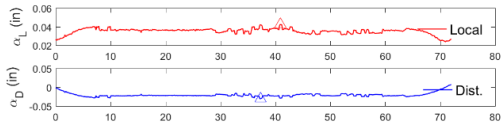
Local
Dist.

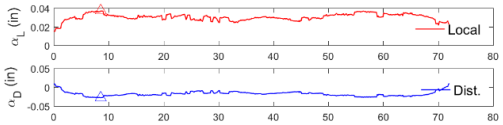
Local
Dist.

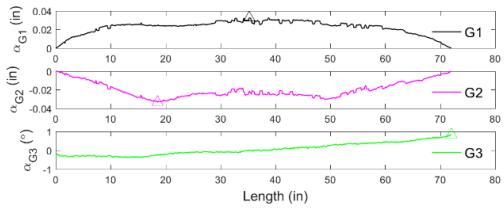
G1
G2
G3
Length (in)

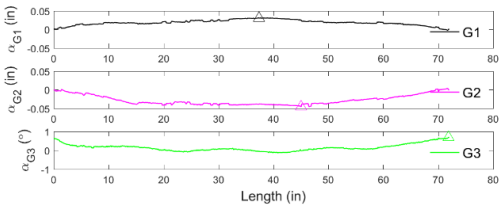
G1
G2
G3
Length (in)

Local
Dist.

Local
Dist.

G1
G2
G3
Length (in)

G1
G2
G3
Length (in)

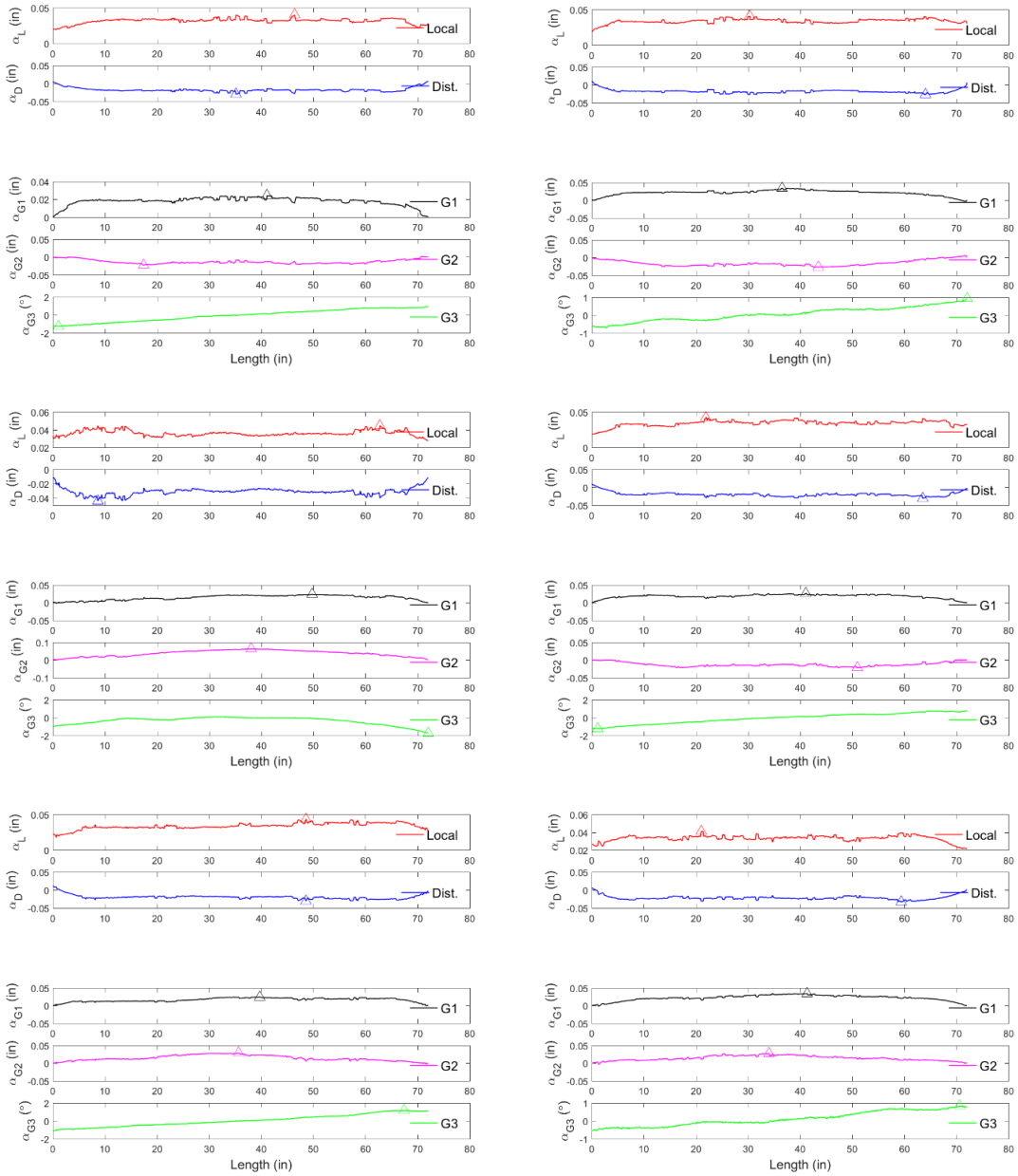

A. 21 Modal imperfections along length of C sections (362S162-68) (Specimens 1-14)

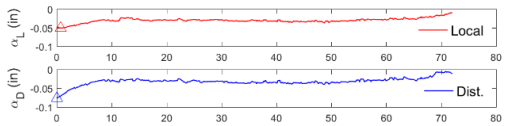
Local
Dist.

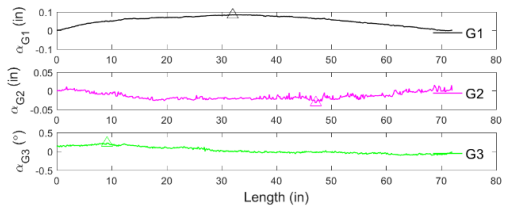
G1
G2
G3
Length (in)

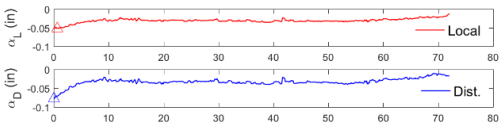
Local
Dist.

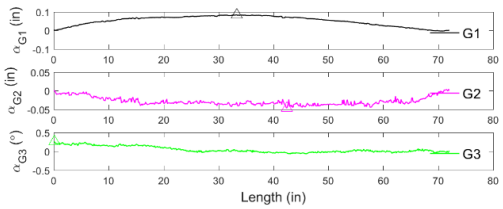
G1
G2
G3
Length (in)

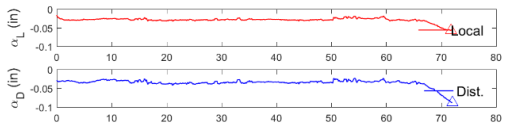
Local
Dist.

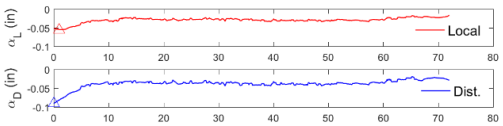
Local
Dist.

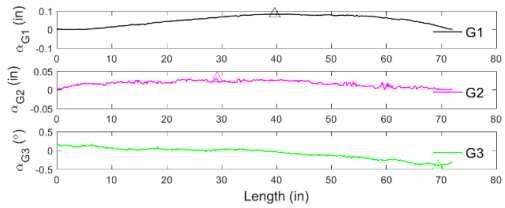
G1
G2
G3
Length (in)

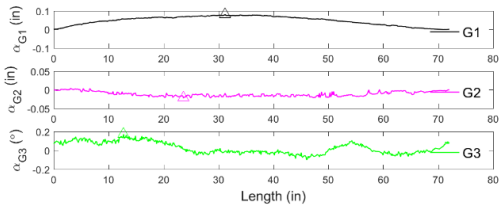
G1
G2
G3
Length (in)

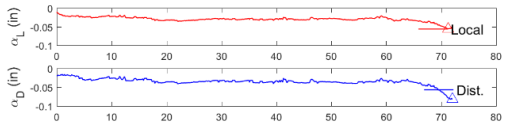
Local
Dist.

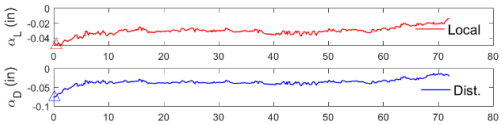
Local
Dist.

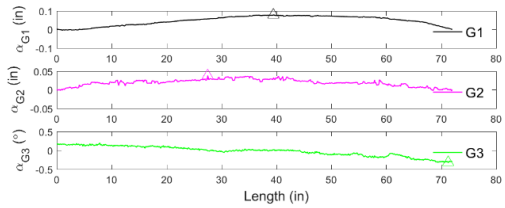
G1
G2
G3
Length (in)

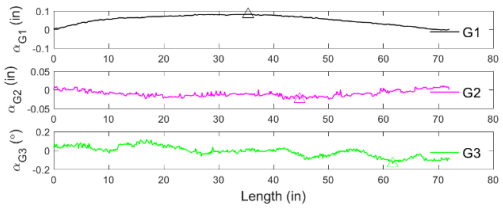
G1
G2
G3
Length (in)

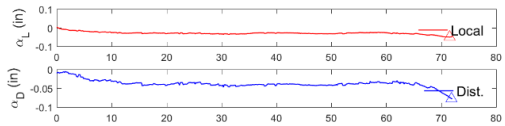
Local
Dist.

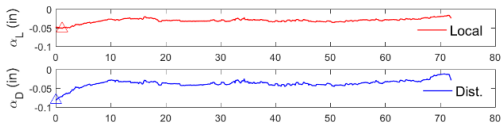
Local
Dist.

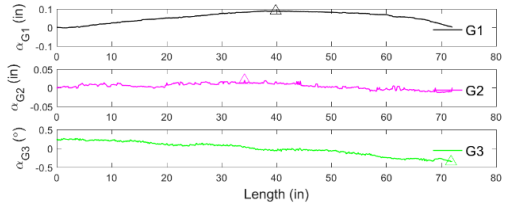
G1
G2
G3
Length (in)

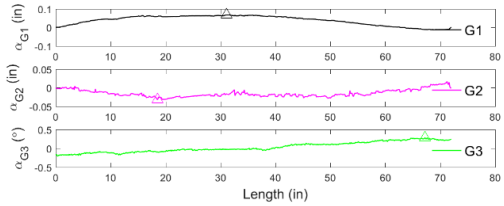
G1
G2
G3
Length (in)

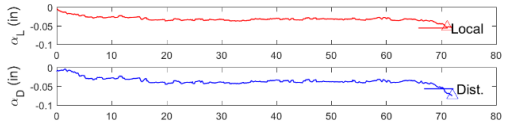
Local
Dist.

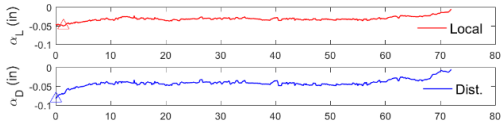
Local
Dist.

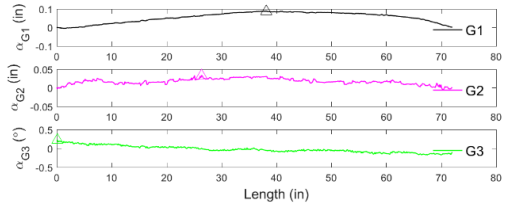
G1
G2
G3
Length (in)

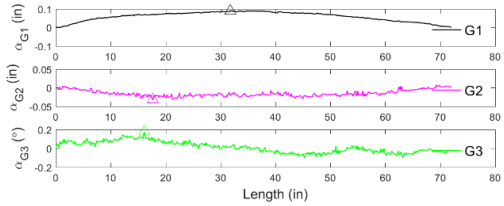
G1
G2
G3
Length (in)

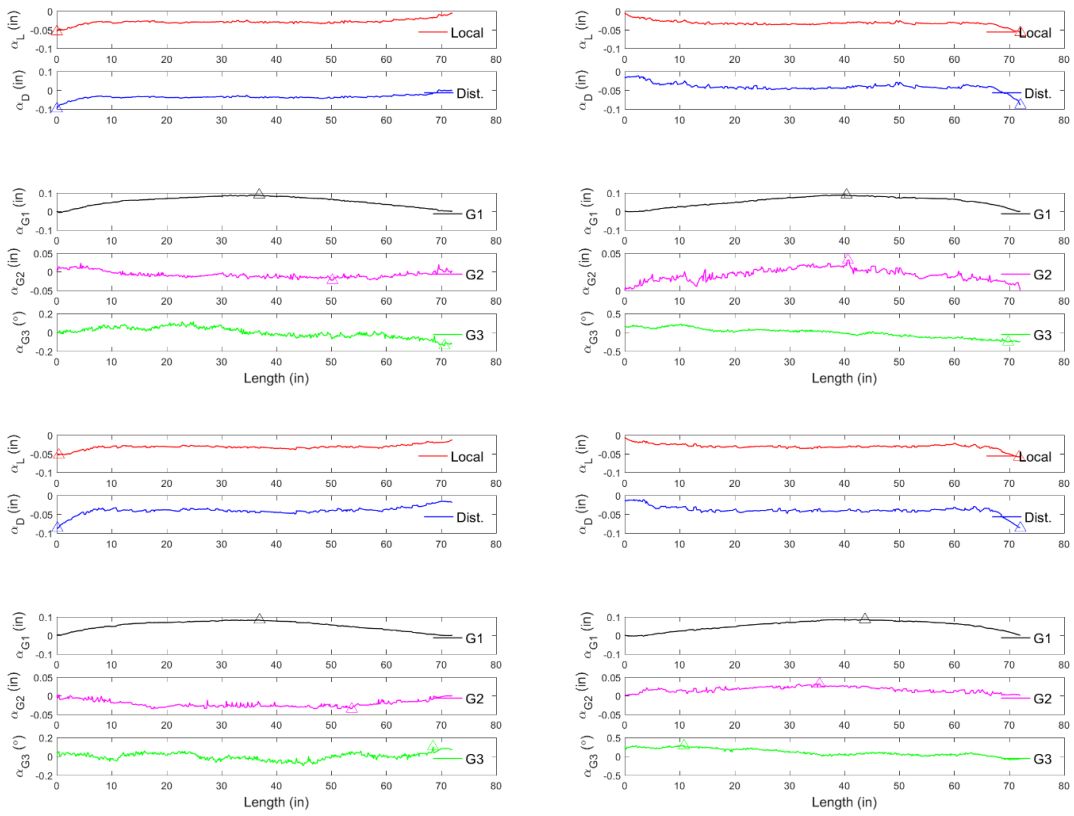

A. 22 Modal imperfections along length of C sections (600S137-54) (Specimens 1-14)

Ap.5 Chapter 8

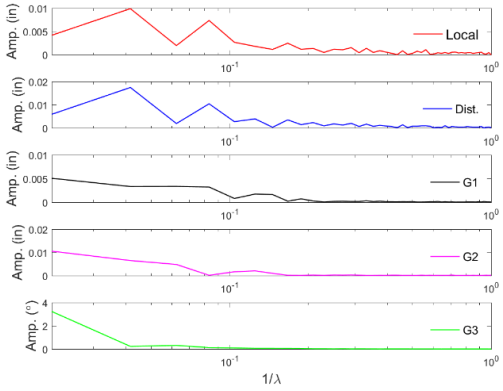

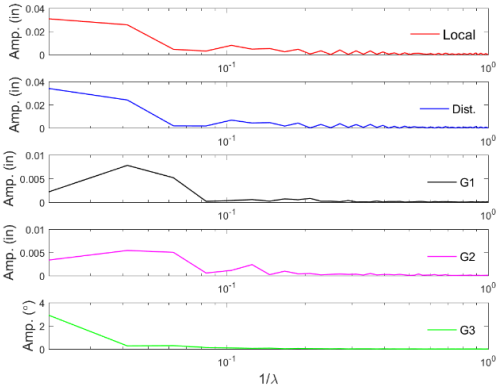

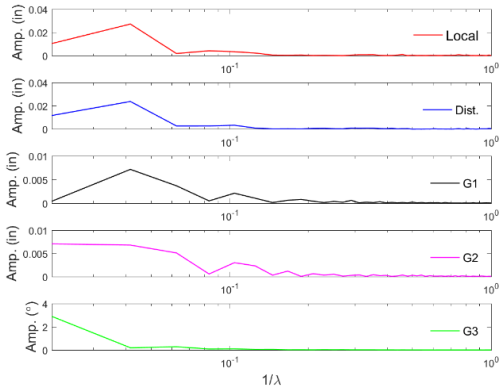

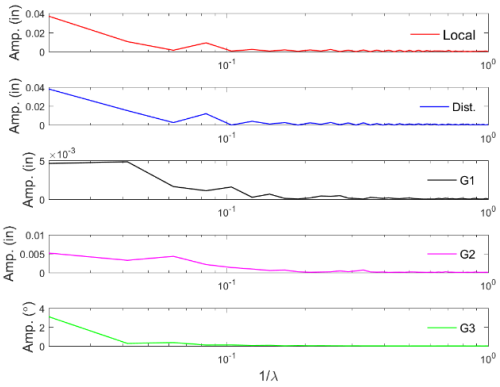

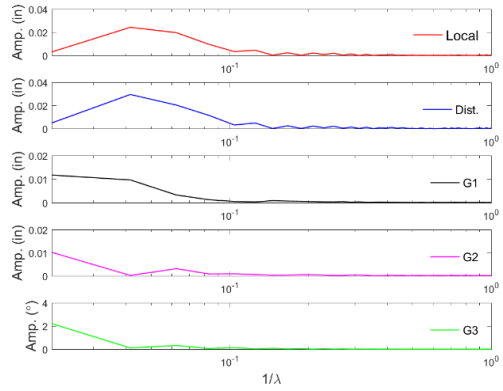

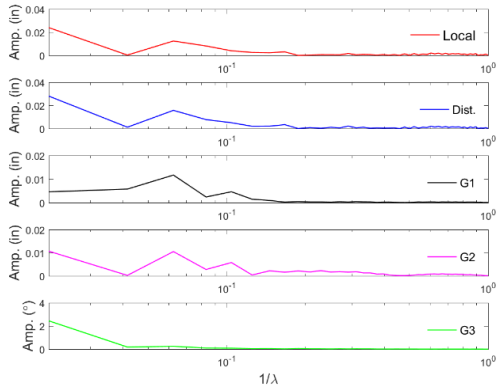

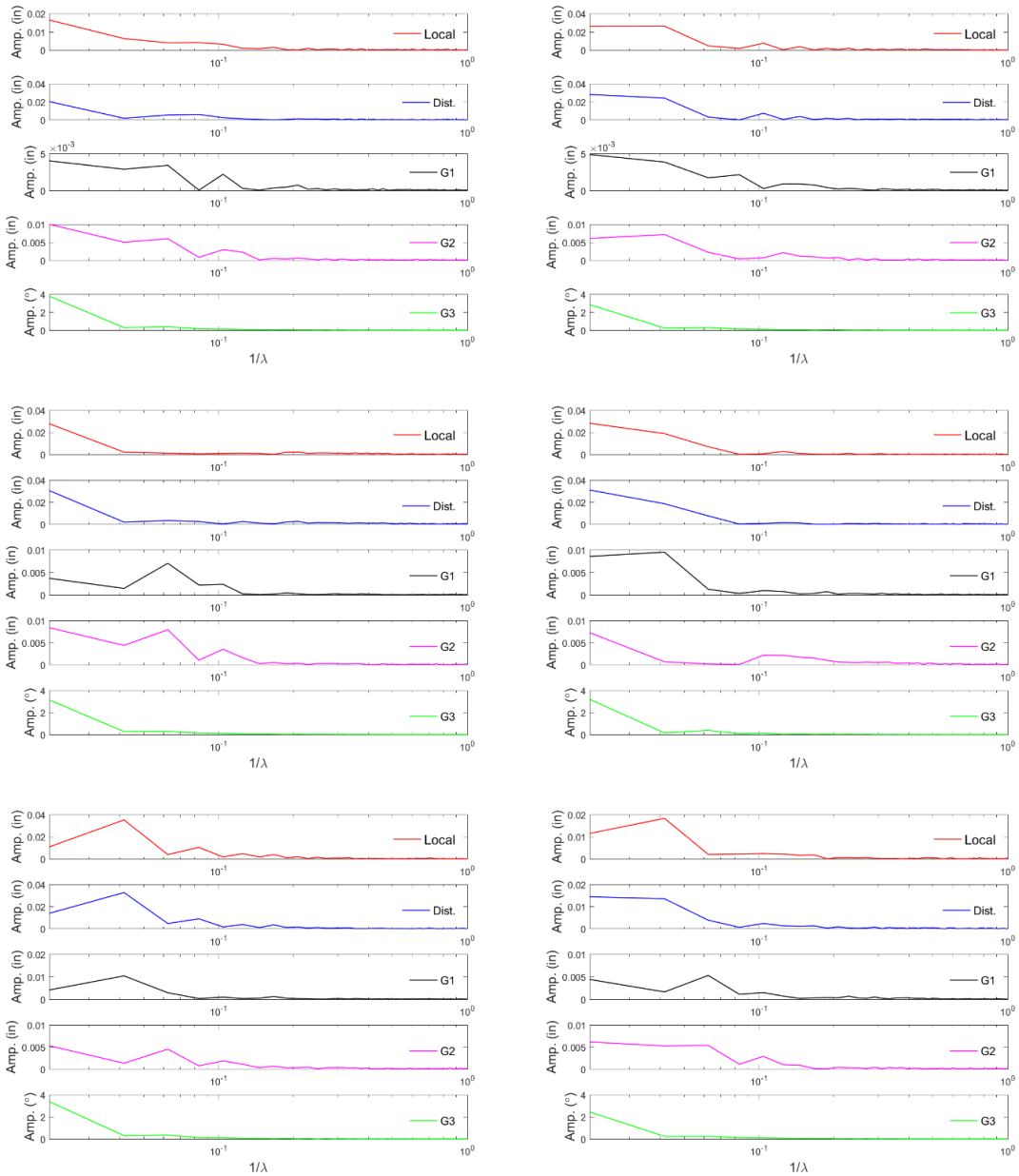
Local
Dist.
G1
G2
G3
Amp. (in)
Amp. (°)
1/λ

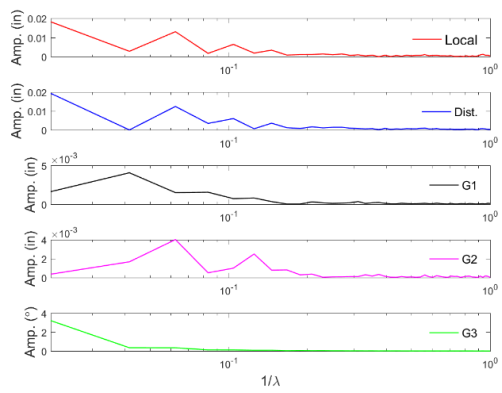
Local
Dist.
G1
G2
G3
Amp. (in)
Amp. (°)
1/λ

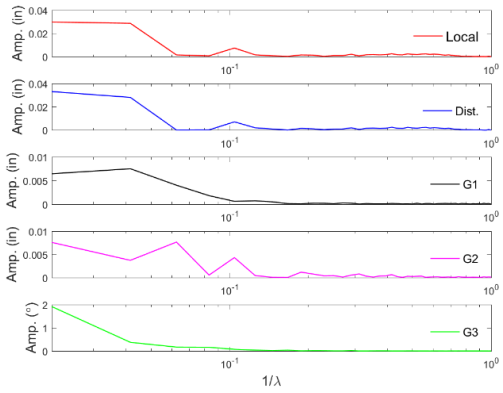
Local
Dist.
G1
G2
G3
Amp. (in)
Amp. (°)
1/λ

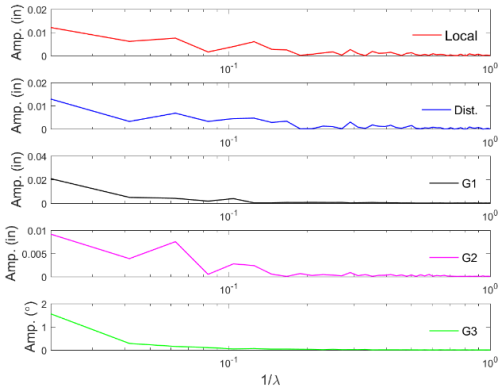
Local
Dist.
G1
G2
G3
Amp. (in)
Amp. (°)
1/λ

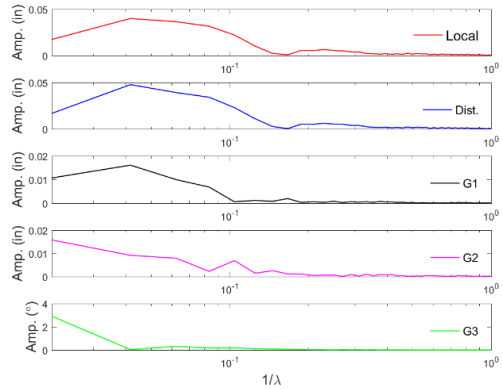
Local
Dist.
G1
G2
G3
Amp. (in)
Amp. (°)
1/λ

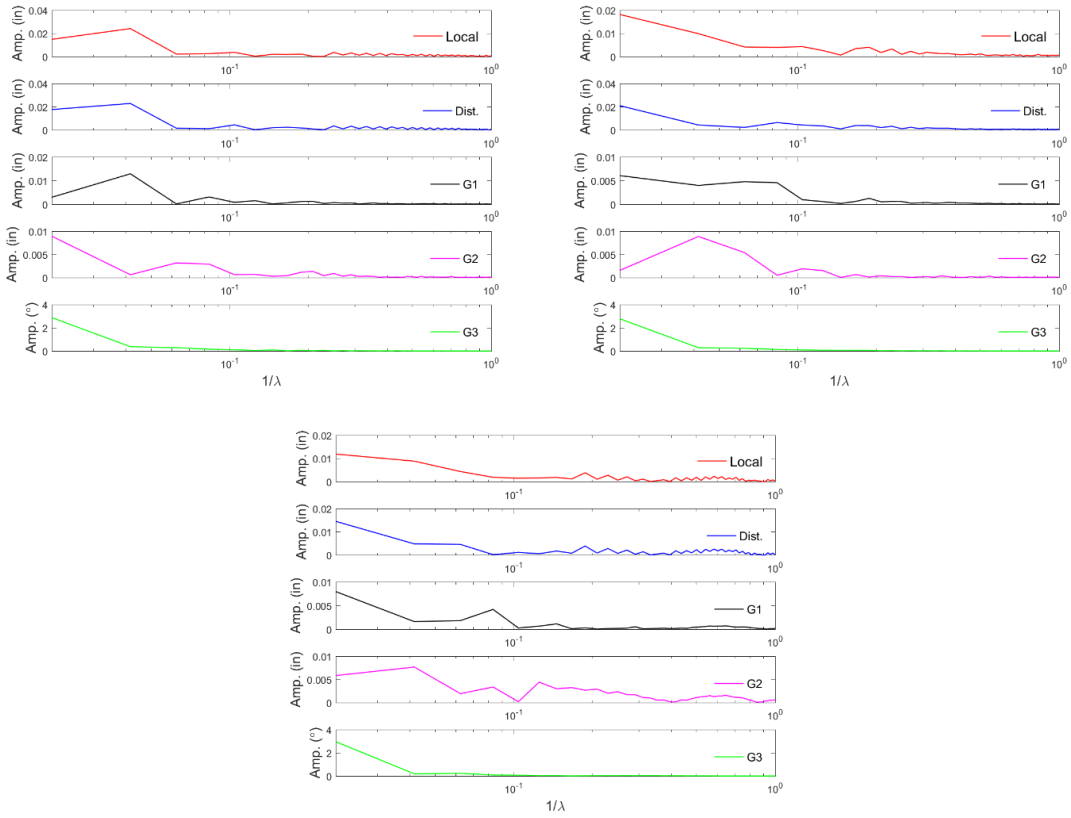

A. 23 1D spectral realization of Z section (700Z225-60) (Specimens 1-19)

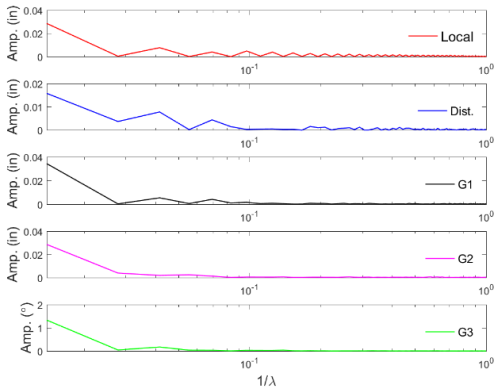
Local
Dist.
G1
G2
G3
Amp. (in)
Amp. (°)
1/λ

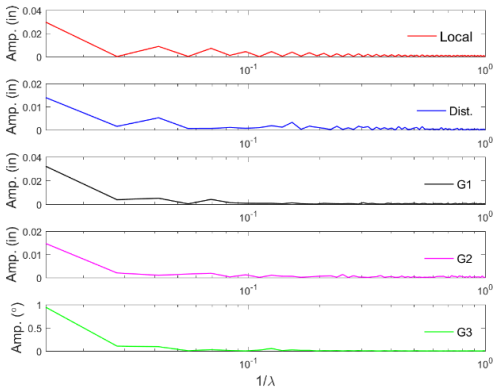
Local
Dist.
G1
G2
G3
Amp. (in)
Amp. (°)
1/λ

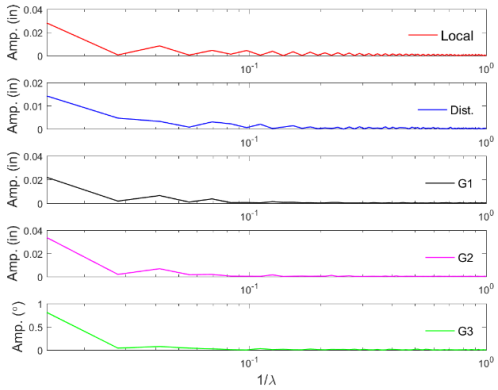
Local
Dist.
G1
G2
G3
Amp. (in)
Amp. (°)
1/λ

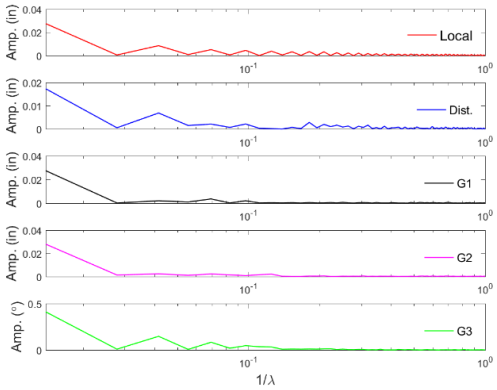
Local
Dist.
G1
G2
G3
Amp. (in)
Amp. (°)
1/λ

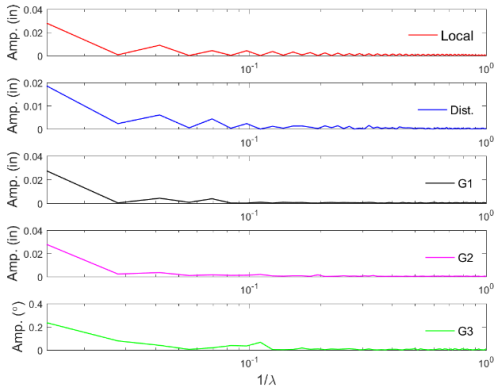
Local
Dist.
G1
G2
G3
Amp. (in)
Amp. (°)
1/λ

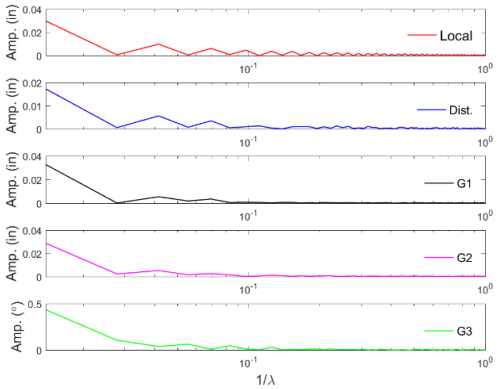
Local
Dist.
G1
G2
G3
Amp. (in)
Amp. (°)
1/λ

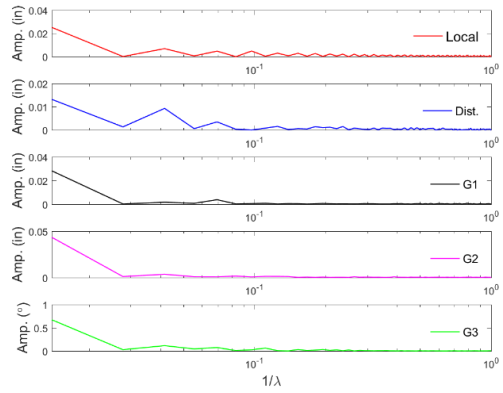
Local
Dist.
G1
G2
G3
Amp. (in)
Amp. (°)
1/λ

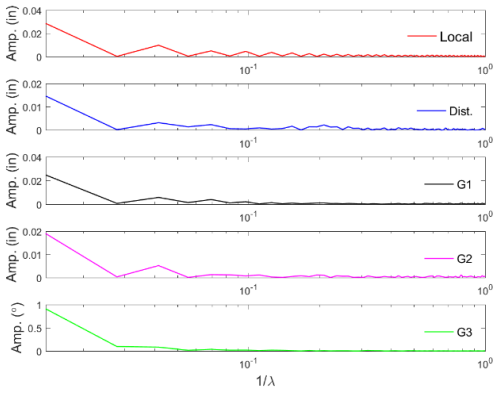
Local
Dist.
G1
G2
G3
Amp. (in)
Amp. (°)
1/λ

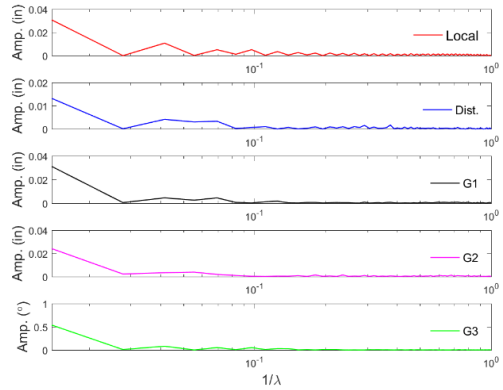
Local
Dist.
G1
G2
G3
Amp. (in)
Amp. (°)
1/λ

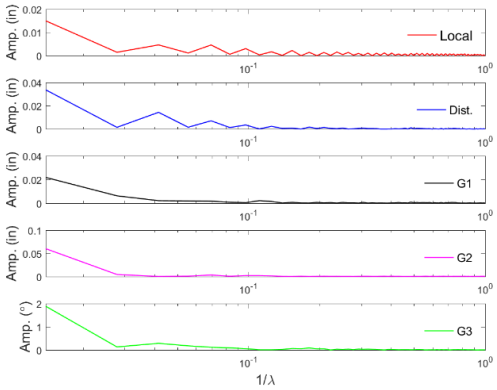
Local
Dist.
G1
G2
G3
Amp. (in)
Amp. (°)
1/λ

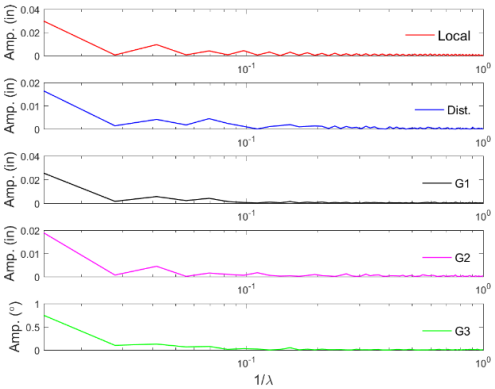
Local
Dist.
G1
G2
G3
Amp. (in)
Amp. (°)
1/λ

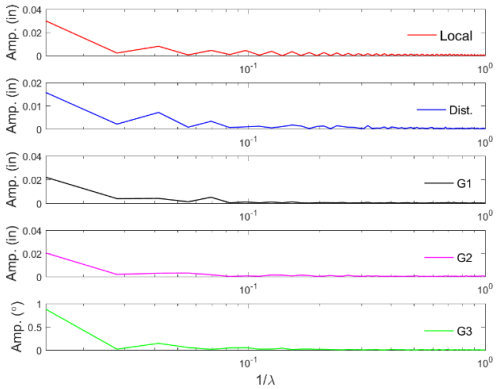
Local
Dist.
G1
G2
G3
Amp. (in)
Amp. (°)
1/λ

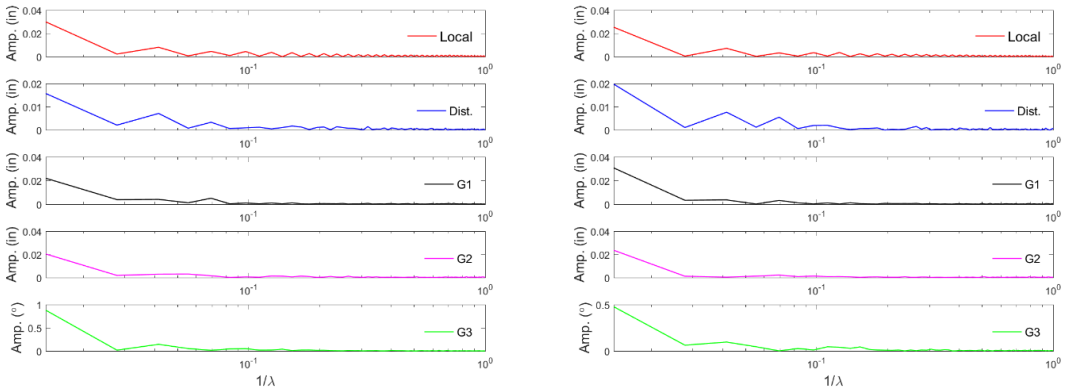

A. 24 1D spectral realization of C sections (362S162-68) (Specimens 1-14)

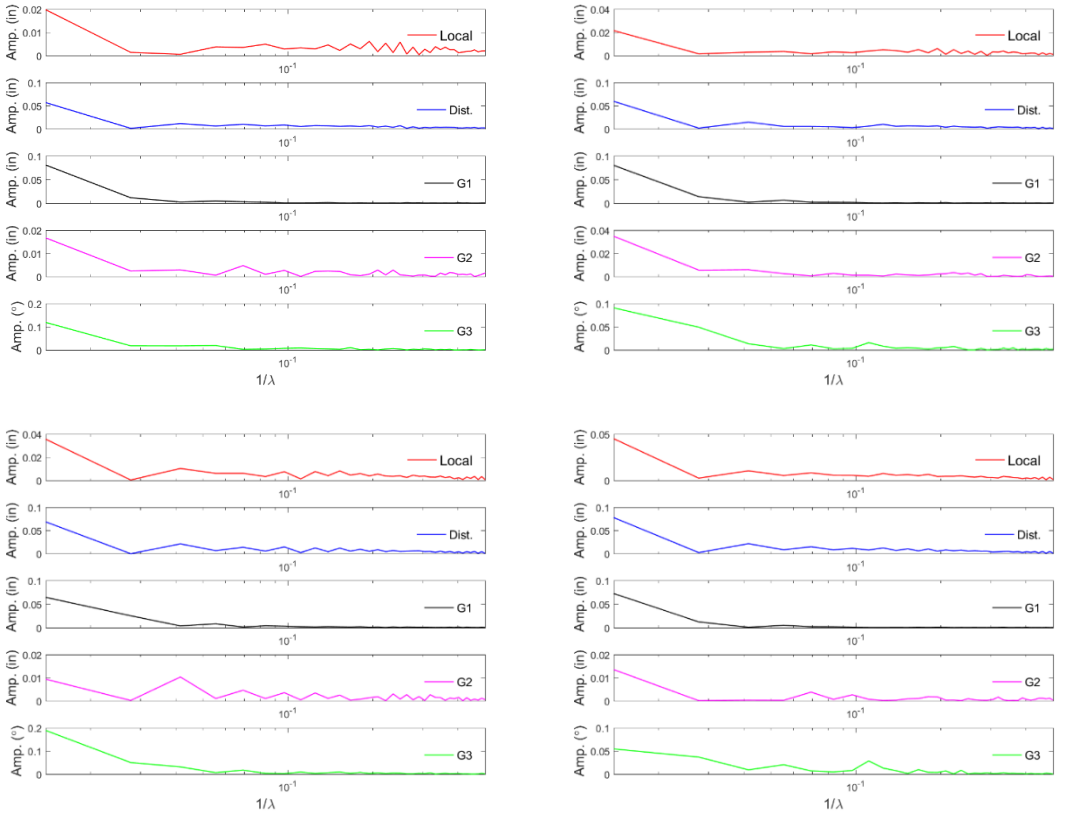

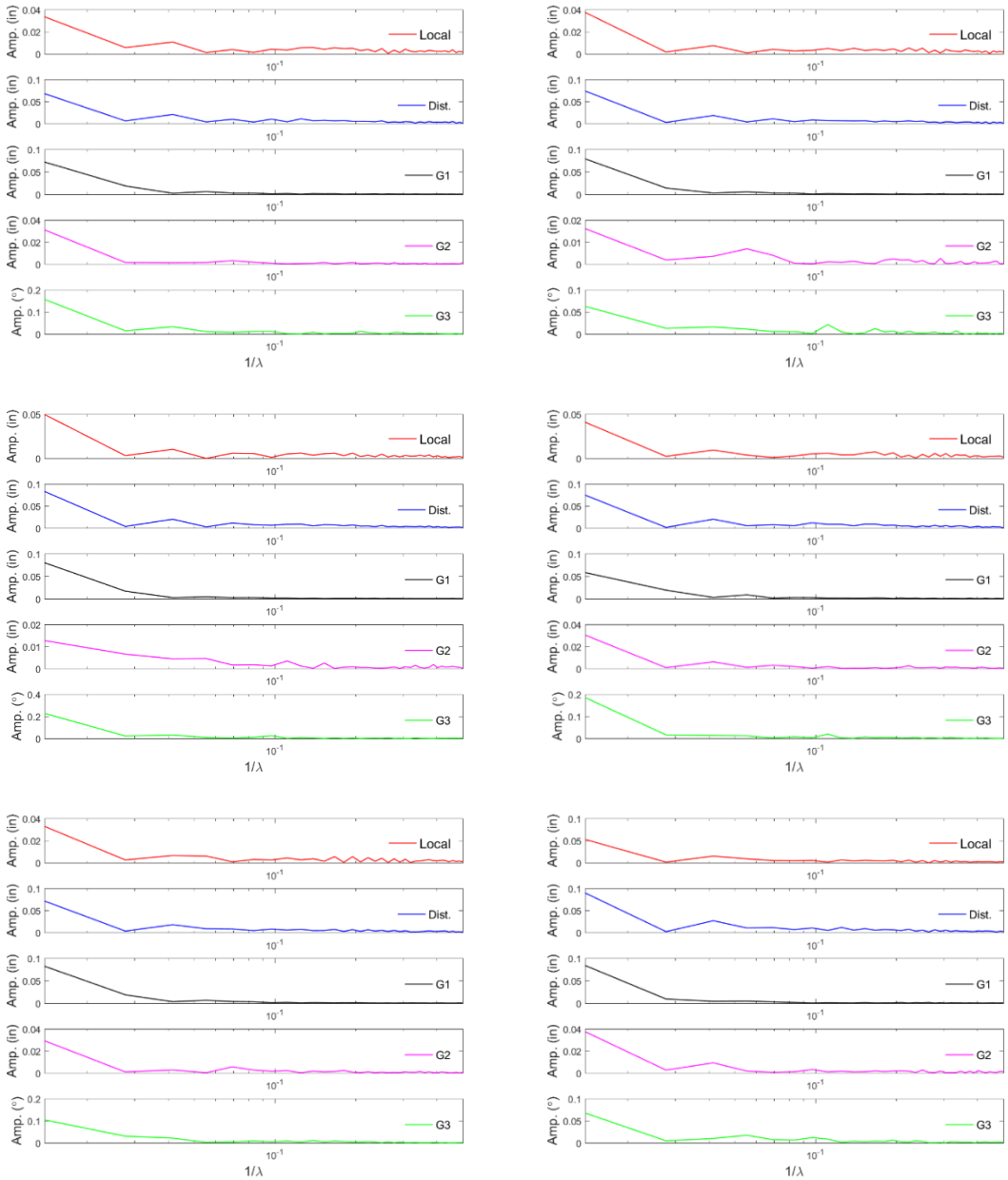
Local
Dist.
G1
G2
G3
Amp. (in)
Amp. (°)
1/λ

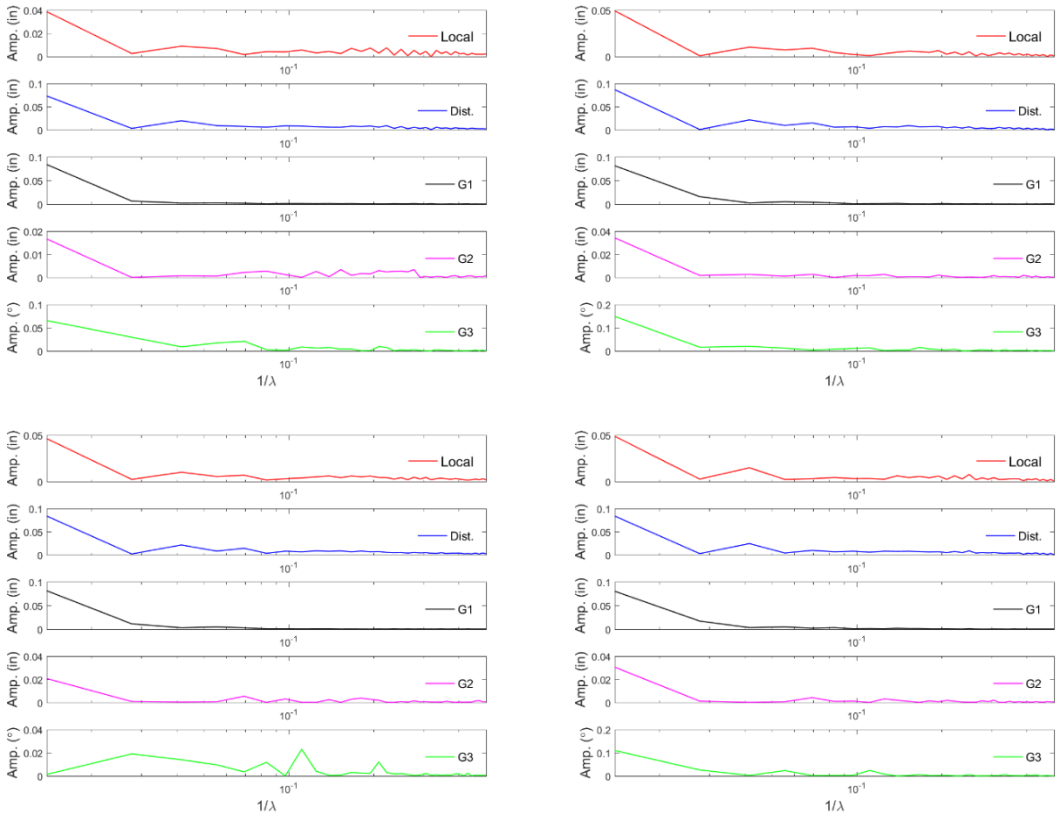

A. 25 1D spectral realization of C sections (600S137-54) (Specimens 1-14)

Curriculum Vita:

Xi Zhao was born in Yunnan, China on November 6, 1988 to Pengfei Zhao and Yan Shen. She achieved very good score in the national college entrance exam and was admitted by a 2+2 collaborative programs held by Sun Yat-sen University and the University of Hong Kong. She spent two years' study in Sun Yat-sen University and then went to study in the University of Hong Kong. This experience broadened her horizon and encouraged her to pursue higher education abroad.

As soon as she graduated in summer 2010 with a bachelor of science in civil engineering, she went to Johns Hopkins University, Baltimore, Maryland to continue her study. She was admitted into the master program at the beginning and then was switched to the doctorate program. She joined the Thin-Walled Structures Group under the guidance of Professor Benjamin Schafer at September 2012. She was interested in an innovative measurement technique of geometric imperfections in cold-formed steel structures and its application, which later became her doctorate research project. She also worked hard as a teaching assistant for several courses in Johns Hopkins University including Dynamics (Fall 2011), Mechanics of materials and statics (Fall 2014, 2015), and Prestressed concrete (Spring 2016). She finished her study and graduated with her Ph.D. degree in August, 2016.